RECENT ADVANCES in MATHEMATICAL METHODS, MATHEMATICAL MODELS and SIMULATION in SCIENCE and ENGINEERING

Proceedings of the 2014 International Conference on Mathematical Methods, Mathematical Models and Simulation in Science and Engineering (MMSSE 2014)

Interlaken, Switzerland
February 22-24, 2014

RECENT ADVANCES in MATHEMATICAL METHODS, MATHEMATICAL MODELS and SIMULATION in SCIENCE and ENGINEERING

Proceedings of the 2014 International Conference on Mathematical Methods, Mathematical Models and Simulation in Science and Engineering (MMSSE 2014)

Interlaken, Switzerland
February 22-24, 2014

All papers of the present volume were peer reviewed by no less than two independent reviewers. Acceptance was granted when both reviewers' recommendations were positive.

Mathematics and Computers in Science and Engineering Series – 23

ISSN: 2227-4588
ISBN: 978-1-61804-219-4

RECENT ADVANCES in MATHEMATICAL METHODS, MATHEMATICAL MODELS and SIMULATION in SCIENCE and ENGINEERING

Proceedings of the 2014 International Conference on Mathematical Methods, Mathematical Models and Simulation in Science and Engineering (MMSSE 2014)

Interlaken, Switzerland
February 22-24, 2014

Organizing Committee

General Chairs (EDITORS)

- Professor Maria Isabel García-Planas,
  Universitat Politècnica de Catalunya,
  Spain
- Professor George Vachtsevanos,
  Georgia Institute of Technology,
  Atlanta, Georgia,
  USA
- Professor Gen Qi Xu
  Department of Mathematics
  Tianjin University
  Tianjin, China

Senior Program Chair

- Professor Philippe Dondon
  ENSEIRB
  Rue A Schweitzer 33400 Talence
  France

Program Chairs

- Professor Filippo Neri
  Dipartimento di Informatica e Sistemistica
  University of Naples "Federico II"
  Naples, Italy
- Prof. Constantin Udriste,
  University Politehnica of Bucharest,
  Bucharest,
  Romania
- Professor Sandra Sendra
  Instituto de Inv. para la Gestión Integrada de Zonas Costeras (IGIC)
  Universidad Politécnica de Valencia
  Spain

Tutorials Chair

- Professor Pradip Majumdar
  Department of Mechanical Engineering
  Northern Illinois University
  Dekalb, Illinois, USA

Special Session Chair

- Professor Claudio Talarico,
  Gonzaga University, Spokane,
  USA

Workshops Chair

- Professor Ryszard S. Choras
  Institute of Telecommunications
  University of Technology & Life Sciences
  Bydgoszcz, Poland

Local Organizing Chair

- Professor Jan Awrejcewicz,
  Technical University of Lodz,
  Lodz, Poland

Publication Chair

- Professor Vincenzo Niola
  Departement of Mechanical Engineering for Energetics
  University of Naples "Federico II"
  Naples, Italy

Steering Committee

- Professor Aida Bulucea, University of Craiova, Romania
- Professor Zoran Bojkovic, Univ. of Belgrade, Serbia
- Professor Claudio Talarico, Gonzaga University, Spokane, USA
- Professor Imre Rudas, Obuda University, Budapest, Hungary

Program Committee

Prof. Lotfi Zadeh (IEEE Fellow,University of Berkeley, USA)
Prof. Leon Chua (IEEE Fellow,University of Berkeley, USA)
Prof. Michio Sugeno (RIKEN Brain Science Institute (RIKEN BSI), Japan)
Prof. Dimitri Bertsekas (IEEE Fellow, MIT, USA)
Prof. Demetri Terzopoulos (IEEE Fellow, ACM Fellow, UCLA, USA)
Prof. Georgios B. Giannakis (IEEE Fellow, University of Minnesota, USA)
Prof. George Vachtsevanos (Georgia Institute of Technology, USA)
Prof. Abraham Bers (IEEE Fellow, MIT, USA)
Prof. Brian Barsky (IEEE Fellow, University of Berkeley, USA)
Prof. Aggelos Katsaggelos (IEEE Fellow, Northwestern University, USA)
Prof. Josef Sifakis (Turing Award 2007, CNRS/Verimag, France)
Prof. Hisashi Kobayashi (Princeton University, USA)
Prof. Kinshuk (Fellow IEEE, Massey Univ. New Zeland),
Prof. Leonid Kazovsky (Stanford University, USA)
Prof. Narsingh Deo (IEEE Fellow, ACM Fellow, University of Central Florida, USA)
Prof. Kamisetty Rao (Fellow IEEE, Univ. of Texas at Arlington,USA)
Prof. Anastassios Venetsanopoulos (Fellow IEEE, University of Toronto, Canada)
Prof. Steven Collicott (Purdue University, West Lafayette, IN, USA)
Prof. Nikolaos Paragios (Ecole Centrale Paris, France)
Prof. Nikolaos G. Bourbakis (IEEE Fellow, Wright State University, USA)
Prof. Stamatios Kartalopoulos (IEEE Fellow, University of Oklahoma, USA)
Prof. Irwin Sandberg (IEEE Fellow, University of Texas at Austin, USA),
Prof. Michael Sebek (IEEE Fellow, Czech Technical University in Prague, Czech Republic)
Prof. Hashem Akbari (University of California, Berkeley, USA)
Prof. Yuriy S. Shmaliy, (IEEE Fellow, The University of Guanajuato, Mexico)
Prof. Lei Xu (IEEE Fellow, Chinese University of Hong Kong, Hong Kong)
Prof. Paul E. Dimotakis (California Institute of Technology Pasadena, USA)
Prof. M. Pelikan (UMSL, USA)
Prof. Patrick Wang (MIT, USA)

Prof. Wasfy B Mikhael (IEEE Fellow, University of Central Florida Orlando,USA)
Prof. Sunil Das (IEEE Fellow, University of Ottawa, Canada)
Prof. Panos Pardalos (University of Florida, USA)
Prof. Nikolaos D. Katopodes (University of Michigan, USA)
Prof. Bimal K. Bose (Life Fellow of IEEE, University of Tennessee, Knoxville, USA)
Prof. Janusz Kacprzyk (IEEE Fellow, Polish Academy of Sciences, Poland)
Prof. Sidney Burrus (IEEE Fellow, Rice University, USA)
Prof. Biswa N. Datta (IEEE Fellow, Northern Illinois University, USA)
Prof. Mihai Putinar (University of California at Santa Barbara, USA)
Prof. Wlodzislaw Duch (Nicolaus Copernicus University, Poland)
Prof. Tadeusz Kaczorek (IEEE Fellow, Warsaw University of Tehcnology, Poland)
Prof. Michael N. Katehakis (Rutgers, The State University of New Jersey, USA)
Prof. Pan Agathoklis (Univ. of Victoria, Canada)
Prof. P. Demokritou (Harvard University, USA)
Prof. P. Razelos (Columbia University, USA)
Dr. Subhas C. Misra (Harvard University, USA)
Prof. Martin van den Toorn (Delft University of Technology, The Netherlands)
Prof. Malcolm J. Crocker (Distinguished University Prof., Auburn University,USA)
Prof. S. Dafermos (Brown University, USA)
Prof. Urszula Ledzewicz, Southern Illinois University , USA.
Prof. Dimitri Kazakos, Dean, (Texas Southern University, USA)
Prof. Ronald Yager (Iona College, USA)
Prof. Athanassios Manikas (Imperial College, London, UK)
Prof. Keith L. Clark (Imperial College, London, UK)
Prof. Argyris Varonides (Univ. of Scranton, USA)
Prof. S. Furfari (Direction Generale Energie et Transports, Brussels, EU)
Prof. Constantin Udriste, University Politehnica of Bucharest , ROMANIA
Prof. Patrice Brault (Univ. Paris-sud, France)
Prof. Jim Cunningham (Imperial College London, UK)
Prof. Philippe Ben-Abdallah (Ecole Polytechnique de l'Universite de Nantes, France)
Prof. Photios Anninos (Medical School of Thrace, Greece)
Prof. Ichiro Hagiwara, (Tokyo Institute of Technology, Japan)
Prof. Andris Buikis (Latvian Academy of Science. Latvia)
Prof. Akshai Aggarwal (University of Windsor, Canada)
Prof. George Vachtsevanos (Georgia Institute of Technology, USA)
Prof. Ulrich Albrecht (Auburn University, USA)
Prof. Imre J. Rudas (Obuda University, Hungary)
Prof. Alexey L Sadovski (IEEE Fellow, Texas A&M University, USA)
Prof. Amedeo Andreotti (University of Naples, Italy)
Prof. Ryszard S. Choras (University of Technology and Life Sciences Bydgoszcz, Poland)
Prof. Remi Leandre (Universite de Bourgogne, Dijon, France)
Prof. Moustapha Diaby (University of Connecticut, USA)
Prof. Brian McCartin (New York University, USA)
Prof. Elias C. Aifantis (Aristotle Univ. of Thessaloniki, Greece)
Prof. Anastasios Lyrintzis (Purdue University, USA)
Prof. Charles Long (Prof. Emeritus University of Wisconsin, USA)
Prof. Marvin Goldstein (NASA Glenn Research Center, USA)
Prof. Costin Cepisca (University POLITEHNICA of Bucharest, Romania)
Prof. Kleanthis Psarris (University of Texas at San Antonio, USA)
Prof. Ron Goldman (Rice University, USA)
Prof. Ioannis A. Kakadiaris (University of Houston, USA)
Prof. Richard Tapia (Rice University, USA)
Prof. F.-K. Benra (University of Duisburg-Essen, Germany)
Prof. Milivoje M. Kostic (Northern Illinois University, USA)

Prof. Helmut Jaberg (University of Technology Graz, Austria)
Prof. Ardeshir Anjomani (The University of Texas at Arlington, USA)
Prof. Heinz Ulbrich (Technical University Munich, Germany)
Prof. Reinhard Leithner (Technical University Braunschweig, Germany)
Prof. Elbrous M. Jafarov (Istanbul Technical University, Turkey)
Prof. M. Ehsani (Texas A&M University, USA)
Prof. Sesh Commuri (University of Oklahoma, USA)
Prof. Nicolas Galanis (Universite de Sherbrooke, Canada)
Prof. S. H. Sohrab (Northwestern University, USA)
Prof. Rui J. P. de Figueiredo (University of California, USA)
Prof. Hiroshi Sakaki (Meisei University, Tokyo, Japan)
Prof. K. D. Klaes, (Head of the EPS Support Science Team in the MET Division at EUMETSAT, France)
Prof. Emira Maljevic (Technical University of Belgrade, Serbia)
Prof. Kazuhiko Tsuda (University of Tsukuba, Tokyo, Japan)
Prof. Milan Stork (University of West Bohemia , Czech Republic)
Prof. Lajos Barna (Budapest University of Technology and Economics, Hungary)
Prof. Nobuoki Mano (Meisei University, Tokyo, Japan)
Prof. Nobuo Nakajima (The University of Electro-Communications, Tokyo, Japan)
Prof. Victor-Emil Neagoe (Polytechnic University of Bucharest, Romania)
Prof. P. Vanderstraeten (Brussels Institute for Environmental Management, Belgium)
Prof. Annaliese Bischoff (University of Massachusetts, Amherst, USA)
Prof. Virgil Tiponut (Politehnica University of Timisoara, Romania)
Prof. Andrei Kolyshkin (Riga Technical University, Latvia)
Prof. Fumiaki Imado (Shinshu University, Japan)
Prof. Sotirios G. Ziavras (New Jersey Institute of Technology, USA)
Prof. Constantin Volosencu (Politehnica University of Timisoara, Romania)
Prof. Marc A. Rosen (University of Ontario Institute of Technology, Canada)
Prof. Alexander Zemliak (Puebla Autonomous University, Mexico)
Prof. Thomas M. Gatton (National University, San Diego, USA)
Prof. Leonardo Pagnotta (University of Calabria, Italy)
Prof. Yan Wu (Georgia Southern University, USA)
Prof. Daniel N. Riahi (University of Texas-Pan American, USA)
Prof. Alexander Grebennikov (Autonomous University of Puebla, Mexico)
Prof. Bennie F. L. Ward (Baylor University, TX, USA)
Prof. Guennadi A. Kouzaev (Norwegian University of Science and Technology, Norway)
Prof. Eugene Kindler (University of Ostrava, Czech Republic)
Prof. Geoff Skinner (The University of Newcastle, Australia)
Prof. Hamido Fujita (Iwate Prefectural University(IPU), Japan)
Prof. Francesco Muzi (University of L'Aquila, Italy)
Prof. Les M. Sztandera (Philadelphia University, USA)
Prof. Claudio Rossi (University of Siena, Italy)
Prof. Sergey B. Leonov (Joint Institute for High Temperature Russian Academy of Science, Russia)
Prof. Arpad A. Fay (University of Miskolc, Hungary)
Prof. Lili He (San Jose State University, USA)
Prof. M. Nasseh Tabrizi (East Carolina University, USA)
Prof. Alaa Eldin Fahmy (University Of Calgary, Canada)
Prof. Paul Dan Cristea (University "Politehnica" of Bucharest, Romania)
Prof. Gh. Pascovici (University of Koeln, Germany)
Prof. Pier Paolo Delsanto (Politecnico of Torino, Italy)
Prof. Radu Munteanu (Rector of the Technical University of Cluj-Napoca, Romania)
Prof. Ioan Dumitrache (Politehnica University of Bucharest, Romania)
Prof. Corneliu Lazar (Technical University Gh.Asachi Iasi, Romania)
Prof. Miquel Salgot (University of Barcelona, Spain)
Prof. Amaury A. Caballero (Florida International University, USA)

Prof. Maria I. Garcia-Planas (Universitat Politecnica de Catalunya, Spain)
Prof. Petar Popivanov (Bulgarian Academy of Sciences, Bulgaria)
Prof. Alexander Gegov (University of Portsmouth, UK)
Prof. Lin Feng (Nanyang Technological University, Singapore)
Prof. Colin Fyfe (University of the West of Scotland, UK)
Prof. Zhaohui Luo (Univ of London, UK)
Prof. Mikhail Itskov (RWTH Aachen University, Germany)
Prof. George G. Tsypkin (Russian Academy of Sciences, Russia)
Prof. Wolfgang Wenzel (Institute for Nanotechnology, Germany)
Prof. Weilian Su (Naval Postgraduate School, USA)
Prof. Phillip G. Bradford (The University of Alabama, USA)
Prof. Ray Hefferlin (Southern Adventist University, TN, USA)
Prof. Gabriella Bognar (University of Miskolc, Hungary)
Prof. Hamid Abachi (Monash University, Australia)
Prof. Karlheinz Spindler (Fachhochschule Wiesbaden, Germany)
Prof. Josef Boercsoek (Universitat Kassel, Germany)
Prof. Eyad H. Abed (University of Maryland, Maryland, USA)
Prof. Robert K. L. Gay (Nanyang Technological University, Singapore)
Prof. Andrzej Ordys (Kingston University, UK)
Prof. Harris Catrakis (Univ of California Irvine, USA)
Prof. T Bott (The University of Birmingham, UK)
Prof. Petr Filip (Institute of Hydrodynamics, Prague, Czech Republic)
Prof. T.-W. Lee (Arizona State University, AZ, USA)
Prof. Le Yi Wang (Wayne State University, Detroit, USA)
Prof. John K. Galiotos (Houston Community College, USA)
Prof. Oleksander Markovskyy (National Technical University of Ukraine, Ukraine)
Prof. Suresh P. Sethi (University of Texas at Dallas, USA)
Prof. Hartmut Hillmer(University of Kassel, Germany)
Prof. Bram Van Putten (Wageningen University, The Netherlands)
Prof. Alexander Iomin (Technion - Israel Institute of Technology, Israel)
Prof. Roberto San Jose (Technical University of Madrid, Spain)
Prof. Minvydas Ragulskis (Kaunas University of Technology, Lithuania)
Prof. Arun Kulkarni (The University of Texas at Tyler, USA)
Prof. Joydeep Mitra (New Mexico State University, USA)
Prof. Vincenzo Niola (University of Naples Federico II, Italy)
Prof. S. Y. Chen, (Zhejiang University of Technology, China and University of Hamburg, Germany)
Prof. Duc Nguyen (Old Dominion University, Norfolk, USA)
Prof. Tuan Pham (James Cook University, Townsville, Australia)
Prof. Jiri Klima (Technical Faculty of CZU in Prague, Czech Republic)
Prof. Rossella Cancelliere (University of Torino, Italy)
Prof. L.Kohout (Florida State University, Tallahassee, Florida, USA)
Prof. Dr-Eng. Christian Bouquegneau (Faculty Polytechnique de Mons, Belgium)
Prof. Wladyslaw Mielczarski (Technical University of Lodz, Poland)
Prof. James F. Frenzel (University of Idaho, USA)
Prof. Vilem Srovnal,(Technical University of Ostrava, Czech Republic)
Prof. J. M. Giron-Sierra (Universidad Complutense de Madrid, Spain)
Prof. Walter Dosch (University of Luebeck, Germany)
Prof. Rudolf Freund (Vienna University of Technology, Austria)
Prof. Erich Schmidt (Vienna University of Technology, Austria)
Prof. Alessandro Genco (University of Palermo, Italy)
Prof. Martin Lopez Morales (Technical University of Monterey, Mexico)
Prof. Ralph W. Oberste-Vorth (Marshall University, USA)
Prof. Vladimir Damgov (Bulgarian Academy of Sciences, Bulgaria)
Prof. P.Borne (Ecole Central de Lille, France)

Additional Reviewers

Matthias Buyle	Artesis Hogeschool Antwerpen, Belgium
Lesley Farmer	California State University Long Beach, CA, USA
Deolinda Rasteiro	Coimbra Institute of Engineering, Portugal
Sorinel Oprisan	College of Charleston, CA, USA
Santoso Wibowo	CQ University, Australia
Yamagishi Hiromitsu	Ehime University, Japan
Kei Eguchi	Fukuoka Institute of Technology, Japan
Shinji Osada	Gifu University School of Medicine, Japan
Tetsuya Yoshida	Hokkaido University, Japan
Xiang Bai	Huazhong University of Science and Technology, China
Philippe Dondon	Institut polytechnique de Bordeaux, France
José Carlos Metrôlho	Instituto Politecnico de Castelo Branco, Portugal
João Bastos	Instituto Superior de Engenharia do Porto, Portugal
Takuya Yamano	Kanagawa University, Japan
Hessam Ghasemnejad	Kingston University London, UK
Konstantin Volkov	Kingston University London, UK
Eleazar Jimenez Serrano	Kyushu University, Japan
Jon Burley	Michigan State University, MI, USA
Manoj K. Jha	Morgan State University in Baltimore, USA
Frederic Kuznik	National Institute of Applied Sciences, Lyon, France
Stavros Ponis	National Technical University of Athens, Greece
Ole Christian Boe	Norwegian Military Academy, Norway
Imre Rudas	Obuda University, Budapest, Hungary
Masaji Tanaka	Okayama University of Science, Japan
Francesco Rotondo	Polytechnic of Bari University, Italy
George Barreto	Pontificia Universidad Javeriana, Colombia
Dmitrijs Serdjuks	Riga Technical University, Latvia
Andrey Dmitriev	Russian Academy of Sciences, Russia
Tetsuya Shimamura	Saitama University, Japan
Francesco Zirilli	Sapienza Universita di Roma, Italy
Minhui Yan	Shanghai Maritime University, China
Valeri Mladenov	Technical University of Sofia, Bulgaria
Jose Flores	The University of South Dakota, SD, USA
James Vance	The University of Virginia's College at Wise, VA, USA
Genqi Xu	Tianjin University, China
Zhong-Jie Han	Tianjin University, China
Kazuhiko Natori	Toho University, Japan
Moran Wang	Tsinghua University, China
M. Javed Khan	Tuskegee University, AL, USA
Bazil Taha Ahmed	Universidad Autonoma de Madrid, Spain
Alejandro Fuentes-Penna	Universidad Autónoma del Estado de Hidalgo, Mexico
Miguel Carriegos	Universidad de Leon, Spain
Angel F. Tenorio	Universidad Pablo de Olavide, Spain
Abelha Antonio	Universidade do Minho, Portugal

Table of Contents

ISBN: 978-1-61804-219-4

ISBN: 978-1-61804-219-4

ISBN: 978-1-61804-219-4

Plenary Lecture 1

Discrete Lyapunov Controllers for an Actuator in Camless Engines

Professor Paolo Mercorelli
Leuphana University of Lueneburg
Germany
E-mail: mercorelli@uni.leuphana.de

Abstract: This paper deals with a hybrid actuator composed by a piezo and a hydraulic part controlled using two cascade Lyapunov controllers for camless engine motor applications. The idea is to use the advantages of both, the high precision of the piezo and the force of the hydraulic part. In fact, piezoelectric actuators (PEAs) are commonly used for precision positionings, despite PEAs present nonlinearities, such as hysteresis, satura- tions, and creep. In the control problem such nonlinearities must be taken into account. In this paper the Preisach dynamic model with the above mentioned nonlinearities is considered together with cascade controllers which are Lyapunov based. The sampled control laws are derived using the well known Backward Euler method. An analysis of the Backward and Forward Euler method is also presented. In particular, the hysteresis effect is considered and a model with a switching function is used also for the controller design. Simulations with real data are shown.

Brief Biography of the Speaker: Paolo Mercorelli received the (Laurea) M.S. degree in Electronic Engineering from the University of Florence, Florence, Italy, in 1992, and the Ph.D. degree in Systems Engineering from the University of Bologna, Bologna, Italy, in 1998. In 1997, he was a Visiting Researcher for one year in the Department of Mechanical and Environmental Engineering, University of California, Santa Barbara, USA. From 1998 to 2001, he was a Postdoctoral Researcher with Asea Brown Boveri, Heidelberg, Germany. From 2002 to 2005, he was a Senior Researcher with the Institute of Automation and Informatics, Wernigerode, Germany, where he was the Leader of the Control Group. From 2005 to 2011, he was an Associate Professor of Process Informatics with Ostfalia University of Applied Sciences, Wolfsburg, Germany. In 2010 he received the call from the German University in Cairo (Egypt) for a Full Professorship (Chair) in Mechatronics which he declined. In 2011 he was a Visiting Professor at Villanova University, Philadelphia, USA. Since 2012 he has been a Full Professor (Chair) of Control and Drive Systems at the Institute of Product and Process Innovation, Leuphana University of Lueneburg, Lueneburg, Germany.
Research interests: His current research interests include mechatronics, automatic control, signal processing, wavelets; sensorless control; Kalman filter, camless control, knock control, lambda control, robotics.

The full paper of this lecture can be found on page 19 of the Proceedings of the 2014 International Conference on Circuits, Systems and Control, as well as in the CD-ROM proceedings.

Plenary Lecture 2

EMG-Analysis for Intelligent Robotic based Rehabilitation

Professor Thomas Schrader
University of Applied Sciences Brandenburg
Germany
E-mail: thomas.schrader@computer.org

Abstract: The establishment of wireless sensor network (WSN) technology in physiotherapy and rehabilitation is a clue for improvement of the thera- peutic process, quality assessment and development of supporting tech- nologies such as robotics. Especially for complex therapeutic interventions such as sensorimotor training, a continuous monitoring during the ther- apy as well as for all sessions would be quite useful. For the usage of robotic support in rehabilitation various input informa- tion about the status of patient and his/her activity status of various muscles have to be detected and evaluated. The critical point for robotic intervention is the response time. Under physiotherapeutic and rehabilita- tion conditions, the robotic device should be able to react differently and in various patterns. A complex analysis procedure of input signals such as EMG is essential to ensure an effective response of the robot. However sensor nodes in a wireless (body) area network have limited resources for calculating and storage processes. A stepwise procedure with distributed analysis tasks is proposed. Electromyogram (EMG) measurements of eight muscles were collected and evaluated in an experimental setting of a sensorimotor training using different types of balance boards. Fast and easy methods for detection of activity and rest states based on time domain analysis using low pass IIR filter und dynamic threshold adaption. These procedures can be done on the sensor nodes themselves or special calculation nodes in the network. More advanced methods in frequency domain or analysis of dynamical system behavior request much more system power in calculation as well as storage. These tasks could be done on the level of mobile devices such as mobile phones or tablet computer. A broad range of resources can be provided by cloud/internet. Such level based organization of analysis and system control can be com- pared with biological systems such as human nervous system.

ISBN: 978-1-61804-219-4

Plenary Lecture 3

Atmospheric Boundary Layer Effects on Aerodynamics of NREL Phase VI Windturbine in Parked Condition

Professor Mohammad Moshfeghi
Sogang University, South Korea
E-mail: mmoshfeghi@sogang.ac.kr

Abstract: In a natural condition, the wind is affected by the groundcover and the type of terrains which impose vertical velocity profile to the wind. This wind profile, which is also called atmospheric boundary layer (ABL), dramatically influences the aerodynamic behaviors and loadings of horizontalaxis wind turbines. However, for the sake of simplicity, many numerical simulations only deal with the uniform wind speed. To consider the effects of the ABL, numerical simulations of the two-bladed NREL Phase VI wind turbines aerodynamicat the parked condition are conducted under both uniform and ABL. The Deaves-Harris (DH)model is applied to the ABL. The wind turbine blades are kept at the six o'clock position and are considered at two different pitch angles. The aerodynamic forces and moments of the uniform the DH model are compared.The results show that the pitch angle at which the HAWT is parked plays an important role on the blade loading. Also it is observed that for the fully separated conditions, the Down-blade and the blade in the uniform wind are under approximately similar aerodynamic loadings, while the Up-blade encounters more aerodynamic loads, which is even noticeable value for this small wind turbine. This in turn means that for an appropriate and exact design, effects of ABL should be considered with more care.

Brief Biography of the Speaker: Dr. Mohammad Moshfeghi works in Multi-phenomena CFD Engineerng Research Center (ERC) Sogang University, Seoul, South Korea. He is also Lecturer in Qazvin Azad University. He has a registered patent: "Split-Blade For Horizontal Axis Wind Turbines" (Inventors: Mohammad Moshfeghi, Nahmkeon Hur).

ISBN: 978-1-61804-219-4

Plenary Lecture 4

Laminar and Turbulent Simulations of Several TVD Schemes in Two-Dimensions

Professor Edisson S. G. Maciel
Federal University of Great Dourados, Brazil
E-mail: edisavio@edissonsavio.eng.br

Abstract: This work, first part of this study, describes five numerical tools to perform perfect gas simulations of the laminar and turbulent viscous flow in two-dimensions. The Van Leer, Harten, Frink, Parikh and Pirzadeh, Liou and Steffen Jr. and Radespiel and Kroll schemes, in their first- and second-order versions, are implemented to accomplish the numerical simulations. The Navier-Stokes equations, on a finite volume context and employing structured spatial discretization, are applied to solve the supersonic flow along a ramp in two-dimensions. Three turbulence models are applied to close the system, namely: Cebeci and Smith, Baldwin and Lomax and Sparlat and Allmaras. On the one hand, the second-order version of the Van Leer, Frink, Parikh and Pirzadeh, Liou and Sreffen Jr., and Radespiel and Kroll schemes is obtained from a "MUSCL" extrapolation procedure, whereas on the other hand, the second order version of the Harten scheme is obtained from the modified flux function approach. The convergence process is accelerated to the steady state condition through a spatially variable time step procedure, which has proved effective gains in terms of computational acceleration (see Maciel). The results have shown that, with the exception of the Harten scheme, all other schemes have yielded the best result in terms of the prediction of the shock angle at the ramp. Moreover, the wall pressure distribution is also better predicted by the Van Leer scheme. This work treats the laminar first- and second-order and the Cebeci and Smith second- order results obtained by the five schemes.

Brief Biography of the Speaker: Professor Edisson Sávio de Góes Maciel was born in Recife, Pernambuco, Brazil in 1969, February, 25. He studied in Pernambuco until obtains his Master degree in Thermal Engineering, in 1996, August. With the desire of study aerospace and aeronautical problems using numerical methods as tools, he obtains his Doctor degree in Aeronautical Engineering, in 2002, December, in ITA and his Post-Doctor degree in Aerospace Engineering, in 2009, July, also in ITA. He is currently Professor at UFGD (Federal University of Great Dourados) – Mato Grosso do Sul – Brasil. He is author in 47 papers in international journals, 2 books, 67 papers in international conference proceedings. His research interestes includes a) Applications of the Euler equations to solve inviscid perfect gas 2D and 3D flows (Structured and unstructured discretizations) b) Applications of the Navier-Stokes equations to solve viscous perfect gas 2D and 3D flows (Structured and unstructured discretizations) c) Applications of the Euler and Navier-Stokes to solve magneto gas dynamics flows 2D and 3D; (Structured and unstructured discretizations) d) Applications of algebraic, one-equation, and two-equations turbulence models to predict turbulent effects in viscous 2D flows (Structured and unstructured discretizations), e) Study of artificial dissipation models to centered schemes

ISBN: 978-1-61804-219-4

in 2D and 3D spaces (Structured and unstructures discretizations) f)Applications of the Euler and Navier-Stokes equations to solve reentry flows in the Earth atmosphere and entry flows in Mars atmosphere in 2D and 3D (Structured and unstructured discretizations).

The full paper of this lecture can be found on page 79 of the Proceedings of the 2014 International Conference on Mechanics, Fluid Mechanics, Heat and Mass Transfer, as well as in the CD-ROM proceedings.

ISBN: 978-1-61804-219-4

Plenary Lecture 5

The Flocking Based and GPU Accelerated Internet Traffic Classification

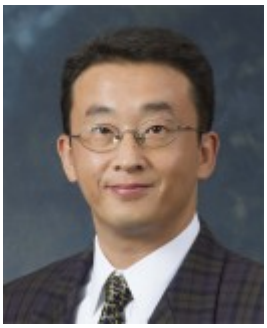

Professor Zhiguang Xu
Valdosta State University
USA
E-mail: zxu@valdosta.edu

Abstract: Mainstream attentions have been brought to the issue of Internet traffic classification due to its political, economic, and legal impacts on appropriate use, pricing, and management of the Internet. Nowadays, both the research and operational communities prefer to classify network traffic through approaches that are based on the statistics of traffic flow features due to their high accuracy and improved robustness. However, these approaches are faced with two main challenges: identify key flow features that capture fundamental characteristics of different types of traffic in an unsupervised way; and complete the task of traffic classification with acceptable time and space costs. In this paper, we address these challenges using a biologically inspired computational model that imitates the flocking behavior of social animals (e.g. birds) and implement it in the form of parallel programs on the Graphics Processing Unit (GPU) based platform of CUDA from NVIDIA™. The experimental results demonstrate that our flocking model accelerated by GPU can not only effectively select and prioritize key flow features to classify both well-known and unseen network traffic into different categories, but also get the job done significantly faster than its traditional CPU-based counterparts due to the high magnitude of parallelism that it exhibits.

Brief Biography of the Speaker: Prof. Zhiguang Xu received his Ph.D. in Computer Science from University of Central Florida, FL, USA in 2001. He is currently Professor of Computer Science in the Department of Math and Computer Science at Valdosta State University, GA, USA. His research and teaching interests include Computer Networking, Artificial Intelligence, Parallel and Distributed Computing, and Computer Science Education. Professor Xu is author or co-author of more than 25 published papers in refereed journals or conference proceedings. He has been awarded many grants from both academic and industrial entities. He is actively serving as committee member, reviewer, or lecturer of many national and international conferences and organizations.

The full paper of this lecture can be found on page 88 of the present volume, as well as in the CD-ROM proceedings.

ISBN: 978-1-61804-219-4

Plenary Lecture 6

The State of Civil Political Culture among Youth: Goals and Results of Education

Professor Irina Dolinina
Perm National Research University, Russia
E-mail: irina_edu@mail.ru

Abstract: Political culture is viewed as a phenomenon of social reality. Attitudes toward it (its meaning or significance) are historically conditioned. This research studies enduring presuppositions about (dispositions toward) society and the state, and how these are reflected in conscious stereotypes and cognitive structures among young people within the sociocultural mechanisms that form and modify the basic characteristics of political culture.

Brief Biography of the Speaker: Prof. Irina Dolinina was born in 1960, in Perm, Russia. She is Team Leader in the Research Project «Formation of the political culture of the students», and Professor of Philosophy and Law of the Faculty of Humanities, Perm National Research Technical University since 2012. She has received a lot of honors and awards (2012 - Diploma of the All-Russian Roswitha fund national education and the Education Committee of the State Duma of the Federal Assembly of the Russian Federation. 2013 - Diploma of the All-Russian Roswitha fund national education and the Education Committee of the State Duma of the Federal Assembly of the Russian Federation. Diploma-Russian contest "Best Science Book in the humanitarian sphere - 2013). Prof. Dolinina has various progessional organizations and activities.
(Expert on the legislative activities of the Council of Federation of Russia. Board member of the Interregional Association "For civic education." Director of the Research Centre of the political culture).

The full paper of this lecture can be found on page 57 of the Proceedings of the 2014 International Conference on Educational Technologies and Education, as well as in the CD-ROM proceedings.

ISBN: 978-1-61804-219-4

Modification of synthetic fuzzy logic to solve multicriteria problems realized by neural networks

J. Tussupov, L. La, A. Mukhanova

***Abstract*—**This article contains researches devoted to the development of new models and methods of solution for multicriteria problems of decision-making in conditions of uncertainty, the development of new safe schemes of access to data, questions of genetic algorithms work speed.

***Keywords*—** fuzzy logic, decision making, method of an indistinct synthetic assessment, neural networks and systems, multicriteria tasks.

I. INTRODUCTION

The method of synthetic fuzzy assessment is a method of the solution of multicriteria problems of decision-making in conditions of uncertainty. It is used for solving various problems when a complete assessment to some object with diverse properties is required [1], [2].

When using the method of synthetic fuzzy assessment, the most important task is to define a quantitative assessment of the importance of various criteria - weights. Weights are mostly defined by experts, variously set weights lead to different results of estimation. The project involves the modification of the method of synthetic fuzzy assessment realized by neural network where the method weights are defined at setting weight vectors of network.

Let's find out a definition for the method of synthetic fuzzy assessment [1]. Previously we will review necessary concepts and definitions.

The definition 1 [3] The fuzzy subset F of the set M will be called indicator $\mu_F: M \to [0,1]$.

The value $\mu_F(x)$ is interpreted as a degree of membership of the element x to a set F.

Here $M = \{S_1, \dots, S_t\}$ is a final set of assessed objects. The objects of $S = (s_1, \dots, s_n) \in R^n$ are vectors of dimension of n. We say that S is defined by n properties or attributes. The s_i value expresses the quantitative value of i, the property of the object of S. Let's describe the method. Concerning each property the object belongs to one of m classes. The object memebership to the one of the classes is determined by each property as follows.

Let the object of $S = (s_1, \dots, s_n)$ be set by n properties. By each property of i we can determine fuzzy sets $\mu_{v_j}(x_i)$, $j = 1, \dots, m$ (we will designate them as μ_{ij}) corresponding to m classes, as follows.

Let $s_i \in [y_{i1}, y_{i,m+1}] \subseteq R$, (could be $y_{i1} > y_{i,m+1}$). $[y_{i1}, y_{i,m+1}]$ breaks m intervals $[y_{i1}, y_{i2}), [y_{i2}, y_{i3}), \dots, [y_{im}, y_{i,m+1}]$. Then, if y_{ij} increase monotonously, the membership function $\mu_{v_j}(x_i) = \mu_{ij}(x_i)$ is defined as follows:

For each property of U_i let's determine fuzzy sets of $\mu_{v_j}(x_i), j = 1, \dots, m$, which we will designate as μ_{ij} as follows. Let $U_i = [y_{i_0}, y_{i_m}] \subset R$ – the universal sets for $\mu_{ij}(x_i)$, $[y_{i_0}, y_{i_m}]$ be broken into m intervals $[y_{i_0}, y_{i_1}), [y_{i_1}, y_{i_2}), \dots, [y_{i_{m-1}}, y_{i_m}]$. (Intervals correspond to linguistic v_i values and are defined by experts, i.e. if $S = (x_1, \dots, x_n)$, $x_i \in [y_{i_j}, y_{i_{j+1}})$ for the object, then S based on i corresponds to v_i value) Then

$$\mu_{ij}(x_i) = \begin{cases} \dfrac{|x_i - y_{i_j}|}{|y_{i_{j-1}} - y_{i_j}|}, & \text{if } \ y_{i_{j-1}} \le x_i < y_{i_j} \\ 0, & \text{in the contrary case.} \end{cases}$$

The values of $\mu_{ij}(x_i)$ turn diverse values of properties of x_i, $i = 1, \dots, n$ of the object of S into homogenious, belonging to the segment of $[0,1]$.

Given $S = (x_1, \dots, x_n)$. The first level of the model of the synthetic fuzzy assessment is described by the equation

$$w \cdot R = b,$$

where $w = (w_1, \dots, w_n)$, $0 \le w_i \le 1$ is a weight vector, $R = (r_{ij})_{n \times m}$, $r_{ij} = \mu_{i,j}(x_i)$, $b = (b_1, \dots, b_m)$, $b_j = \sum_{i=1}^{n} w_i r_{ij}$, $j = 1, \dots, m$. The weight vector is defined by experts of the subject domain of the solved problem.

Now let's describe the second level of the model of synthetic fuzzy assessment. It is supposed that at the first level we estimated the object of S on one factor, let be given c factors $\Phi_1, \dots, \Phi_c$ on which the assessment of S is made and $w^i \cdot R^i = b^i$, $i = 1, \dots, c$ are the equations describing the first level of the model of the synthetic fuzzy assessment on the factor of Φ_i, $w^i = (w_1^i, \dots, w_{n_i}^i)$ is a weight vector of i factor,

J.A. Tussupov is from L.N. Gumilyev Eurasian National University, Astana, Kazakhstan (corresponding author to provide phone: +7 701 789 27 10; e-mail: tussupov@mail.ru).

L.L. La is from L.N. Gumilyev Eurasian National University, Astana, Kazakhstan (e-mail: lira_la@hotmail.com)

A.A. Mukhanova is from L.N.Gumilyov Eurasian Natinal University, Astana, Kazakhstan (corresponding author to provide phone: +7 775 530 59 77; e-mail: ayagoz198302@mail.ru)

R^i is a matrix made of values of membership functions for fuzzy sets μ_{kj} for i factor, $b^i = (b_1^i, b_2^i, \dots, b_m^i)$ is a resultant vector of the first level of model for i factor, $R^i = (r_{kj}^i)_{n_i \times m}$.

Given $B = (b_{ij})_{c \times m}$,

$$b_{ij} = b_j^i = \sum_{k=1}^{n} w_k^i r_{kj}^i,$$

$i = 1, \dots, c,\ j = 1, \dots, m$. Thus, the second level of the model of synthetic fuzzy assessment is defined by $p = W \cdot B$ equation, where $W = (W_1, \dots, W_c)$ is a weight vector of the second level of the model of synthetic fuzzy assessment, $p = (p_1, \dots, p_m)$, $p_j = \sum_{i=1}^{c} W_i b_{ij}$ is a resultant vector of the second level. Similarly the 3rd, the 4th, etc. model levels are defined.

Given $I = (i_1, \dots, i_m)$ is a resultant vector of the last level of the model of synthetic fuzzy assessment, $i_k = \max\{i_s | s = 1, \dots, m\}$. Then we believe that the object of S is estimated by the linguistic v_k value.

II. The Modification of a Method of Synthetic Fuzzy Assessment

The given work involves one model of the modified method of synthetic fuzzy assessment realized by a neural network, where weights of method are defined by network weights. Let's describe the model and review some definitions.

Definition 1. [5] The artificial neural systems or neural networks are systems physically organized as system of cells which can do requests, store and use the empirical knowledge gained as a result of operation.

Let $M = \{S_1, \dots, S_t\}$ be a finite set of evaluated objects, $S = (x_1, \dots, x_n) \in R^n$, $L =< \{a_1, \dots, a_m\}, <>$ will be a finite lattice, where $a_i < a_j$если $i < j$.

Definition 2. [4] Indication of $\mu_A: M \to L$ is called fuzzy S subset of A sets of M.

It is believed that μ_A expresses a degree of membership of an element S to a fuzzy set of A or, in our case, we suppose that S with a degree of $\mu_A(S)$ possesses the estimated property. The task of $S \in M$ object assessment will consist in definition of $\mu_A(S)$.

We suppose that $a_i$accept values of the natural language, expressing some quality, for example, good, bad, etc.

Definition of $\mu_A(S)$ happens at some stages called model levels. Depending on quantity of levels we will distinguish one, two, etc. level models.

Let's try to describe the first level of model.

Let $S = (x_1, \dots, x_n) \in R^n, I_k = \left[y_k^{'}, y^{''}{}_k\right] \subset R, k = 1, \dots, n$ be segments of a set of the real numbers of R. The x_k variable accepts the values in I_k. Function $\mu_{I_k}: I_k \to L$ is defined by experts of subject domain of the solved task.

Further, we suppose that functions μ_{I_k} are either increasing or decreasing, i.e. $\mu_{I_k}(x_i) \le \mu_{I_k}(x_j)$, where as $x_i \le x_j$ (or $\mu_{I_k}(x_i) \ge \mu_{I_k}(x_j)$, $at\ x_i \le x_j$) which corresponds to the majority of real tasks of objects assessment.

The first level of model is described by the equation of

$$w \cdot T = b,$$

Where $w = (w_1, \dots, w_n)$, $0 \le w_k \le 1$, - weight vector, $T = (t_{kj})_{n \times m}$, $b = (b_1, \dots, b_m)$ – output vector, $b_j = \sum_{k=1}^{n} w_k t_{kj}$, $j = 1, \dots, m$.

$$t_{kj} = \begin{cases} \dfrac{|x_k - y^{''}{}_k|}{|y_k^{'} - y^{''}{}_k|} & if\ \mu_{I_k}(x_k) = a_j \\ 0, & on\ the\ contrary. \end{cases}$$

The object assessment at the degree of $k, k \ge 2$ occurs according to the following diagram.

1. Defined from factors on which the object $\Phi_{1,\dots,}\Phi_c$ is evaluated.

2. To each factor Φ_i corresponds to $n_i$of properties for an object assessment.

3. At each level, starting from the second, factors of the previous level appear as properties of the current level.

Now we will describe the second level of model. Given c of the factors of $\Phi_{1,\dots,}\Phi_c$ on which the assessment of S object is made, if $w^i \cdot T^i = b^i, i = 1, \dots, c$ equations describing the first level of model on a factor Φ_i, $w^i = (\omega_1^i, \dots, \omega_{n_i}^i)$ is a weight vector of i factor, $b^i = (b_1^i, b_2^i, \dots, b_m^i)$ - an output vector of the first level of model for factor, $T^i = \left(t_{kj}^i\right)_{n_1 \times m}$.

Here $B = \left(b_{ij}\right)_{c \times m}$,

$$b_{ij} = b_j^i = \sum_{k=1}^{n_i} w_k^i\, t_{kj}^i,$$

$i = 1, \dots, c,\ j = 1, \dots, m$. Form a matrix $B' = (b'_{ij})_{c \times m}$ as follows. If $b_{it} = \max\{b_{ij} | j = 1, \dots, m|\}, so\ b'_{it} = b_{it}$, и $b'_{ir} = 0$ for all $r \ne t,\ i = 1, \dots, c$. Then the second level of model of synthetic fuzzy assessment is defined by the equation $p = W \cdot B'$, где $W = (W_1, \dots, W_c)$ weight vector of the second level of model, W_i – weight of i factor, $p = (p_1, \dots p_m),\ p_j = \sum_{i=1}^{c} W_i b'_{ij}$ – output vector of the second level. The 3rd, the 4th, etc. are defined the same way by model levels.

Let $I = (i_1, \dots i_m)$ be an output vector of the last level of model of synthetic fuzzy assessment, $i_k = \max\{i_s | s = 1, \dots, m|\}$.Then we suppose that the object of S with a degree of $a_k \in L$ possesses estimated property.

III. Definition of Weight Vectors

Definition of weights is an important task when using the method of synthetic fuzzy assessment. Weights are usually defined by experts, variously defined weights lead to different results of assessment. The project also offers to realize the given method of assessment by neural network where the weights of the method are defined by the network weights.

Let's give the network definition on the example of two factorial, two-level models where the objects are estimated on three properties of x_1, x_2, x_3 on the first factor, on the second, on two properties of h_1, h_2. The lattice of $L =< \{a_1, a_2\}, \le >$ contains two elements. The network looks as follows (see figure 1).

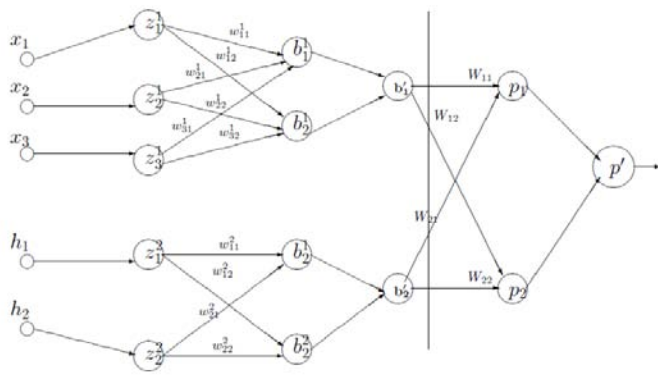

Fig. 1 network on the example of two factorial, two-level models

To calculation the weights of the method of synthetic fuzzy assessment we'll break the network into two parts corresponding to the first and second levels of model. In figure 1 this splitting is represented by the vertical line. Each of the parts is used for formation of two new networks. The first network realizes single-level model of synthetic fuzzy assessment, corresponds to the first level of initial model and is applied to calculate weights of the first level. It also consists of two subnets, each of which estimates an object on one of the factors. Let's describe it.

0 layer. The signals corresponding to the values of properties of an estimated object are given to the entrance layer (x_1, x_2, x_3)- for the first factor and (h_1, h_2) - for the second. Weights from the zero layer to the first are absent.

1 layer. t_{ij}^s calculation, $1 \le i \le 3$, $1 \le j \le 2$, $1 \le s \le 2$. It contains 5 neurons corresponding to the entrance signals of x_1, x_2, x_3 for the first factor, h_1, h_2 for the second. The values for the first factor, $\mu_{I_k}(x_k)$, $z_k^1 = |x_k - y''_k|/|y'_k - y''_k|$, $k = 1,2,3$ are calculated on this layer. The vector (t_{k1}^1, t_{k2}^1) is formed for each neuron as follows. If $\mu_{I_k}(x_k) = a_j$, то $t_{kj}^1 = z_k^1$, $t_{ks}^1 = 0$ для $s \ne j$. The signals of t_{kl}^1, $l = 1,2$, $k = 1,2,3$ go to l neuron of the second layer. The similar calculations are made for the second factor.

2 layer. Contains 2 neurons for each factor. Neurons correspond to values a_1, a_2 of the lattice of L.

These are calculated in the second layer $b^i = (b_1^i, b_2^i)$, $i = 1,2$, где $b_j^i = \sum_{k=1}^{n_i} w_{kj}^i t_{kj}^i$, $n_i = 3,2$, $j = 1,2$, w_{kj}^i - the weight of lines going from k neuron of the first layer to j neuron of the second layer of the i factor. The weights from the second layer to the third are absent.

3 layer. The third layer is outgoing for the first level and corresponds to the calculation of a matrix of B'. The layer contains one neuron for each factor. The vector of (b'^i_1, b'^i_2) is formed for the factor of Φ_i $i = 1,2$, as follows: such t is calculated that $b_t^i = \max\{b_j^i | j = 1,2\}$ so, $b'^i_t = b_t^i$ и $b'^i_r = 0$ для $r \ne t$, $i = 1,2$, further the vector of (b''^i_1, b''^i_2) is formed, where t coordinate is equal to "1", and the others to "0". The vectors of (b''^i_1, b''^i_2) $i = 1,2$ move to the output or the network. We believe that on i factor the object with a degree of a_t possesses the estimated property.

The second network consists of the third layer of the first network and the second part of the general network. It will be used for finding weights of the second level. Let's try to describe it.

1 layer. Consists of two neurons, one for each factor. The vector of (b'^i_1, b'^i_2), $i = 1,2$, calculated on the third layer of the first network, moves to the enter of the neuron. The signals of b'^i_j, $i = 1,2$ move to j neuron of the second layer.

2 layer. Corresponds to calculation of the output vector of the second level $p = (p_1, p_2)$. The 2nd layer consists of two neurons on which $p_j = \sum_{i=1}^{2} W_{ij} b'^i_j$ are calculated, where W_{ij} are weights corresponding to network lines going from i neuron of the 1st layer to j neuron of the 2nd layer. Weights from the second layer to the third are absent.

3 layer. Finds out the maximum coordinate of the vector of $p = (p_1, p_2)$. The 3rd layer contains one neuron. Given $p_k = \max\{p_j | j = 1,2\}$, the vector of $p' = (p'_1, p'_2)$ is formed, where k coordinate is equal to 1, and the others to 0. The vector of $p' = (p'_1, p'_2)$ moves to the network exit. We believe that the object with a degree of a_k possesses the estimated property.

IV. Network training

The modified option of generalized δ-rule is used for training of the both networks [5]. Let's consider training of the first network. The training set consists of pairs $\{< (x_1, \dots, x_n), \overline{b_i} >\}$, where $S = (x_1, \dots, x_n)$ is an estimated object and $\overline{b_i}$ vector of length of m, i coordinate is equal to 1, the values of other coordinates are equal to 0. It is believed that for the pair of $< (x_1, \dots, x_n), \overline{b_i} >$ the object of $S = (x_1, \dots, x_n)$ with a degree of a_i possesses the estimated property.

Let's attach to all scales of a network some significance close to "0". Given $\overline{b_j}$ - real value of an output for the input of $S = (x_1, \dots, x_n)$ from the pair of $\{< (x_1, \dots, x_n), \overline{b_i} >\}$, $\overline{b_j}$ is a vector of length of m, j coordinate of which is equal to "1", and the others "0". $\overline{t_S} = \overline{b_i} - \overline{b_j} = (t_1, \dots, t_m)$. Let's designate $\sigma_i = t_i$. Notice that σ_i will be equal to "0" if $i =$ j and is equal to "1" if $i \ne j$. Then the weights of a network change as follows. $w_{ki}^s(n) = w_{ki}^s(n-1) + \delta_i$ for each of $s = 1, \dots, c$ factors, where $\delta_i = \eta \sigma_i f_k$, n - a step of training, $n = 1, \dots, |\{< (x_1, \dots, x_n), \overline{b_i} >\}|$, f_k - value of output signal from k neuron of the layer 1, η is a coefficient of *training speeds* which allows to operate the average size of weights change, δ_i is a correction connected with an output from k neuron of the layer 1, $w_{ki}^s(n)$ a value of weight after the correction, $w_{ki}^s(n-1)$ the value of weight before the correction.

Note the following.

1. After each step of training, network weights can increase only.

2. At each step of training if there is a pair on the input $\{< (\mathrm{x}_1, \ldots, \mathrm{x}_n), \overline{b_k} >\}$, it only changes the weights corresponding to the lines directed to k neuron and on which nonzero signals from neurons of the first layer flow.
3. Upon the completion of the process of training let's put $\mathrm{w}_{ik} = w_{is} = \max\{w_{ij} \mid j = 1, \ldots \mathrm{m}\}$ for $1 \le k, s \le m$, $1 \le i \le n$. Let's believe that w_{ik}, $1 \le i \le n$ is a weight of i property of a method of synthetic fuzzy assessment.

Let $\{< (x_1, \ldots, x_n), \overline{b_i} >\}$ be a training set. From 1 and 2 we have that in the received trained network for each of the factors we'll have $(x_1, \ldots, x_n)$ for input and $\overline{b_i}$ for output.

Training of the second network is performed similarly.

After the completion of the training process both networks are united so that the output layer of the first network, which consists of neurons on which (b'^i_1, b'^i_2), $i = 1,2$ is calculated will coincide with the first layer of the second network and form the 3rd layer of the general network. Thus the input layer will be zero.

The received network realizes offered two-level model of the method of synthetic fuzzy assessment.

V. Application of Models and Methods of the Solution of Multicriteria Tasks in the Practical Purposes. One Appendix for the Method of Synthetic Fuzzy Assessment. Assessment of Air Quality

In this section one appendix of the method of synthetic fuzzy assessment is offered: assessment of air quality. We will give the description of the method on the example of two-level model.

At the first level three factors whose vectors of assessment form a matrix of an assessment of the second level are considered. The first and third factors contain 15 properties each, the second factor only one property. As a result of an assessment the object will belong to one of five classes corresponding to the following degrees of purity of air Very pure, pure, Average, Dirty, Very dirty

The data have been taken according to the State Standards of the Republic of Kazakhstan No. 14-5-2244/I from 31.03.2011 about "Sanitary and epidemiologic requirements to atmospheric air", and interstate standard of pure rooms and related controlled environments, part 1. Classification of air purity" State Standard 14644-1-2002, the appendices of hygienic standards 2.1.6.2177-07 "The Maximum Permissible Concentration (MPC) of microorganisms - producers, bacterial preparations and their components in atmospheric air in the settlements". Let's describe the factors.

I. Content of harmful chemicals (mg / м^3). This factor is characterized by the following 15 properties: content of epichlorohydrin, toluol, phenol, aniline, formaldehyde, butyl alcohol, methyl anhydride, isopropyl alcohol, acetone, CO carbon oxide, dioxide of sulfur, hydrogen sulfide, oxide of nitrogen, nitrogen dioxide.

II. Concentration of particles (particles / куб.м)

III. Concentration of microorganisms producers, bacterial preparations and their components (mg/m^3). This factor is characterized by the following 15 properties: maintenance of Acetobacter methylicum, Actinomyces roseolus, Alcaligines denitrificans, Aspergillus awamori, Bacillus amyloliquefaci ens, Bacillus licheniformis, Bacillus licheniformis, Bacillus polymyxa, Bacillus subtilis, Brevibacterium flavum, Candida tropicalis, Clostridium acetobutilicum, Penici llium canescens, Trichoderma viride, Yarrowia lipolytica.

At the first level we form matrixes $R = (r_{ij})_{n \times m}$ according to formulas given in section 1. For example, for the first factor it will be the matrix of $(r_{ij})_{15 \times 5}$ calculated according to table 1. We will show only some part of the table.

Table 1. Criteria of an assessment of air purity of the room according to the content of harmful chemicals

Criteria	Attributes	Linguistic assessment				
		VP	P	A	D	VD
Concrnytation of harmful chemicals (мг\m^3)	Epichloroh ydrin	[0-0,05)	[0,05-0,1)	[0,1-0,2)	[0,2-0,3)	[0.3-0,5]
	Toluene	[0-0,2)	[0,2-0,4)	[0,4-0,6)	[0,6-0,8)	[0,8-1,0]
	Phenol	[0-0,001)	[0,001-0,002)	[0,002-0,003)	[0,003-0,004)	[0,004-0,005]
	Aniline	[0-0,01)	[0,01-0,02)	[0,02-0,03)	[0,03-0,06)	[0,06-0,1]
	Formaldehyde	[0-0,001)	[0,001-0,002)	[0,002-0,003)	[0,003-0,004)	[0,004-0,005]
	Alcohol butyl	[0-0,02)	[0,02-0,05)	[0,05-0,1)	[0,1-0,2)	[0,2-0,5]
	Metil anhydride	[0-0,01)	[0,01-0,03)	[0,03-0,05)	[0,05-0,1)	[0,1-0,2]
	Alcohol isopropyl	[0-0,2)	[0,2-0,4)	[0,4-0,6)	[0,6-0,8)	[0,8-1,0]

The vector of an assessment is calculated by a formula $b^i = w^i R^i$, $i = 1,2,3$. At the second level the matrix of R consists of three lines corresponding to vectors of an assessment for three factors. The vector of an assessment of the second level - $b = wR$, here w^i, w are weight vectors.

The following procedure of decision-making on object membership to a vector of an assessment of b is offered to a class. Given $b = (b_1, \ldots, b_m)$ is a vector of the second level of the model, the size of j expresses the degree of memebership of the object to the j class. Through $\tilde{\mathrm{p}}$ we'll designate an integer closest to $\sum_{j=1}^{m} jp_j$. Then object will be estimated by linguistic $v_{\tilde{\mathrm{p}}}$ value, or in other words that it belongs to $\tilde{\mathrm{p}}$ class.

VI. Research and Development of New Safe Schemes of Access to Data. The Scheme of Division of a Secret with a Key of Multiple Use and Protection Against Participants – Malefactors

In this subsection the scheme of division of a secret with a key of multiple use and protection against participants – malefactors has been offered.

In [6] A. Shamir offered the scheme of secret division, the essence of which is that parts of the "secret", we will call it a

key, are distributed between participants of group of people so that only certain subgroups of these people can restore it. We will provide the description (t, w) of Shamir's threshold scheme [6]. Previously, let's review the formulation of the interpolation theorem of Lagrange.

Theorem. For $n+1$ pairs of numbers $(x_0, y_0), (x_1, y_1), \ldots, (x_n, y_n)$, where all x_i are various, the only polynomial $L(x)$ of n degrees, where $L(x_i) = y_i$. Here the polynom is $L(x) = \sum_{j=0}^{n} y_j l_j(x)$, where the basic polynoms are determined by a formula:

$$l_j(x) = \prod_{i=0, j\neq i}^{n} \frac{(x - x_i)}{(x_j - x_i)} = \frac{(x - x_0)}{(x_j - x_0)} \cdots \frac{(x - x_{j-1})}{(x_j - x_{j-1})} \frac{(x - x_{j+1})}{(x_j - x_{j+1})} \cdots \frac{(x - x_n)}{(x_j - x_n)}.$$

Let's enter the following definition.

The definition 1. Let t, w be positive integers, $t \leq w$. $t, w)$ - Shamir's threshold scheme, which is a method of distribution of a key of D between ω participants, so that t participants can calculate a key, but any group of $t-1$ of participants can't make it.

Let $P = \{P_i | 1 \leq i \leq w\}$ be a great number of participants of group wishing to divide a key. The disinterested person, the dealer to whom the group addressed, chooses simple $p \geq w + 1$. Further he acts as follows. Let Z_p be a field of deductions on the module p.

1. The dealer gives to each participant of group some number i, $1 \leq i \leq w$. This information is open.

2. Chooses $a_1, \ldots, a_{t-1} \in Z_p$ incidentally, independently.

3. Makes a polynom of $q(x) = D + a_1 x + \ldots + a_{t-1} x^{t-1}$, where $D \in Z_p$, D is a confidential key.

4. Given $D_i = q(i)$, $1 \leq i \leq w$, $D_i \in Z_p$. The dealer gives D_i to the i participant of group. We will call D_i - a share of i participant, D_i is a confidential number known only to the i participant.

For key restoration, the group of more than t participants present their shares $q(i_k)$, $1 \leq k \leq l$, $l \geq t$, and using, for example, Lagrange's interpolation theorem, builds the only polynom of degree of $t-1$ crossing t points $(i_k, q(i_k))$, which free member is equal to D. The following properties are thus carried out.

1. The knowledge of t shares is enough to calculate a key of D.

2. The knowledge of any $t-1$ shares doesn't give any information on a key of D.

But Shamir's threshold scheme possesses a number of the vulnerable parties

1. Expendability of a key. After the first use the key needs to be replaced as it becomes known to t participants, for (t, w)- the threshold scheme.

2. Lack of protection against being malefactor participants of the scheme.

In [7] one approach to definition of the scheme of division of a secret with a key of multiple use was considered. Let's solve the second problem. Let's assume that the group of t participants of the scheme decided to restore a key, at this k participants - malefactors want to mislead other $t-k$ participants, having shown false shares to learn true shares of honest participants. Shamir's scheme doesn't allow to be protected from such malefactors. For the solution of this problem, in [6] A. Shamir offered to choose keys of D much less, than some set number S. But the following example shows that any k of participating malefactors, can mislead other $t-k$ participants of group, having given out false shares of D_i', thus at the generated polynom of $q'(x)$ the free member of D' will be less S.

Example [8]. Let's assume that the group of t participants of the scheme decided to restore a key. Participating malefactors with numbers of $i_1, \ldots, i_k$ build such polynom $\Delta(x)$ that $\Delta(0) = -1$, $\Delta(j_s) = 0$, $s = 1, \ldots, t-k$, j_s - numbers of honest participants of the scheme show false shares of $D'_{i_l} = q(i_l) + \Delta(i_l)$, $1 \leq l \leq k$ key restoration.

Honest participants of the scheme of j_s, $s = 1, \ldots, t-k$ show the shares of D_{j_s} and $q'(x)$ polynom of $t-1$ degree crossing t points (i_l, D'_{i_l}), (j_s, D_{j_s}), $1 \leq l \leq k$, $1 \leq s \leq t-k$. For $q'(x)$ we have $q'(i) = q(i) + \Delta(i)$, $1 \leq i \leq t$.

From uniqueness of $q'(x)$ follows that $q'(x) = q(x) + \Delta(x)$, $\forall x \in Z_p$. Therefore, the calculated key equal to the free member of $q'(x)$ is equal to $D' = D - 1 < S$.

In this section one scheme of division of the secret has been offered, which is (t, w) modification of Shamir's, M. Tomp's, H. Wall's threshold scheme with a key of multiple use, thus probability of deception of honest participants of the scheme by participants - malefactors will be less than set ε.

Let's give the scheme description. Let be given ω participants of the scheme. Some number i corresponds to each participant of the scheme. This information is open. Let $P(\omega)$ be a set of all subsets of a set $\{1,2,\ldots,\omega\}$. We'll correspond each subset of $a \in P(\omega)$ to binary sequence of $\tilde{\alpha} = < \alpha_1, \ldots, \alpha_\omega >$, where $\alpha_i = 1$, if $i \in a$ и $\alpha_i = 0$, if $i \notin a$.

1. For each sequence of $\tilde{\alpha}$, $\sum_{i=1}^{\omega} \alpha_i = t$ the dealer generates in a random way, shifts $\pi_{\tilde{\alpha}}$ sets $\{1, \ldots, \omega\}$.

2. For the set sequence α dealer builds $q_{\tilde{\alpha}}(x)$ polynom of $t-1$ degree with the free member of $D < S$, $S < p$.

3. To each i participant of the scheme the share is given

$$\left\{(i, \tilde{\alpha}, \pi_{\tilde{\alpha}}(i), q_{\tilde{\alpha}}(x_i)) | x_i = \pi_{\tilde{\alpha}}(i), \sum_{i=1}^{\omega} \alpha_i = t\right\}.$$

The key of the scheme represents a set of pairs $\{(\tilde{\alpha}, D_{\tilde{\alpha}}) | \sum_{i=1}^{\omega} \alpha_i t\}$. The knowledge of each of the pairs belonging to the key opens access to the secret.

Note. a) For $\tilde{\alpha}' \neq \tilde{\alpha}''$ can appear that $D_{\tilde{\alpha}'} = D_{\tilde{\alpha}''}$. But these equalities won't have any impact on safety of the key.

b) The sequence of $\tilde{\alpha}$ for a is build only for the convenience of implementation of the scheme.

The process of restoration of the key by participants of the scheme will happen as follows. Let great number of participants of $b = \{j_1, \ldots, j_t\}$ decides to receive pair from the key for the subset of b.

ISBN: 978-1-61804-219-4

1. The sequence of $\tilde{\alpha}$ is build corresponding to a subset of b.

2. Participants give out confidential shares $\pi_{\tilde{\alpha}}(j_s), q_{\tilde{\alpha}}(x_{j_s}))$, $1 \le s \le t$, $x_{j_s} = \pi_{\tilde{\alpha}}(j_s)$ and (α, D_α) pair is generated from the key.

After the use the (α, D_α) pair becomes invalid and it has to be removed from the key. The rest of the key will function further.

VII. Properties of the Scheme of Secret Division

1. The key of the scheme is reusable. After use by the group of participants, the key remains suitable for further use as the knowledge about one parts of the key doesn't give any information on other parts.

2. The probability of deception of 1 participant of the group even by $t-1$ participants - malefactors is less $\varepsilon = (S-1)(t-1)/(p-t)$.

Indeed, for some set of participants $a \in P(\omega)$, $a = \{j_1, \ldots, j_t\}$ (a corresponds to binary sequence of $\tilde{\alpha}$), who decided to recover a key, k participants - malefactors $\{i_1, \ldots, i_k\}$ want to mislead remaining $t-k$ participants $\{j_1, \ldots, j_{t-k}\}$. Participants - malefactors show false shares $(\pi_{\tilde{\alpha}}(i_l), D'_{i_l})$, $1 \le l \le k$, honest participants their own shares $(\pi_{\tilde{\alpha}}(j_s), D_{j_s})$ $1 \le s \le t-k$, further $q'(x)$ polynomial with a degree of $t-1$, which crosses these points is generated. Honest participants will be misled, only if the constant term of this polynomial appears to be not less than S.

Given $D'' < S$. Let's study $q''(x)$ polynomial with a degree of $t-1$, crossing points of $(0, D'')$, $(\pi_{\tilde{\alpha}}(i_l), D'_{i_l})$, $1 \le l \le k$. Then the probability that $q''(x_{j_s}) = D_{j_s}$ where $x_{j_s} = \pi_{\tilde{\alpha}}(j_s)$, $1 \le s \le t-k$ will be less than $(t-1)/(p-k-1)$. It follows from this that $q''(x)$, polynomial can be defined only for $p-k-1$ in values of x. $q''(x)$ can be crossed with $q(x)$ no more than in $t-1$ points. As various D'' define different polynomials, the probability that the generated key of D' will appear less than S will be less than $\varepsilon = (S-1)(t-1)/(p-k-1)$.

VIII. The Development of Modifications of Genetic Algorithms. Researches on Questions of Operating Speed

Let's review some data from [9] and [10].

The genetic algorithm — is an algorithm which allows to find the satisfactory solution to analytically insoluble problems through sequential selection and a combination of required parameters with use of the mechanisms reminding biological evolution. The first the publication which can be related to genetic algorithms, belongs to N. A. Barichelli. Let's say the simplified definition of the genetic algorithm.

Operation of the genetic algorithm look like:

1. We initiate the initial population — we select way of population for chromosomes in a random;

2. We calculate the value of adaptibility function for each chromosome;

3. We select chromosomes which will participate in transposition (chromosomes with higher values of adaptibility function participate);

4. We create new generation by means of the operator of transposition, i.e. carry out paired recombination of the initial chromosomes;

5. We initiate accidental mutations.

The process is to be repeated until then the chromosome with the maximum value won't be found.

We will give some definitions from the same sources:

Definition 1 Chromosome — a vector (or a line) from some numbers. Each line item (bit) of a chromosome is called a gene.

Definition 2 Individual (a genetic code, an individual) — a set of chromosomes (a task solution candidate).

Definition 3 Crossingover (crossover) — operation where two chromosomes exchange their parts.

Definition 4 Mutation — random change of one or several line items in a chromosome.

Definition 5 Population — set of individuals.

Definition 6 Suitability (fitness) — criterion or function, an extremum, which should be found.

Definition 7 Locus - a gene line item in a chromosome (discharge in binary representation of number).

Definition 8 Allele set of genes going in a row.

Let's solve the optimization problem $F(x) \to max$. Let L be the chromosome consisting of genes whose alleles of each genes are values of $\{0,1\}$.

The sizes of population of chromosomes can be in limits of $[1, 2^L]$. Let N be the size of population of chromosomes.

The set of chromosomes shall contain all values necessary to recombinate them and obtain any of binary sequences of length of L. From [10] follows: probability of that all the L loci will contain complete set of alleles everyone: $P_1 = (1-(1/2)^{(N-1)})^L$ and the minimum size of population necessary for operability of the genetic algorithm: $N = 1 + log(1/(1-P_1^{(1/L)}))$, where P_1 is required probability of that the accidental set of chromosomes will contain all necessary elements for each locus; L — chromosome length. Probabilities of a mutation of a chromosome: $P_2 = L * (1-(1-10*(1/2)^{(N-1)})^{(1/N)})$.

The given size of population is necessary, but not sufficient for effective operation of the genetic algorithm.

This is happening because of premature convergence — an algorithm stop before the achievement of a global maximum. The reason of it is put in the algorithm nature: the higher the adaptibility of a chromosome, the higher is probability of its take participation in transposition. Thus, the chromosomes which function of adaptibility significantly exceeds the minimum value of population, forces out other chromosomes from population. But if adaptibility of such chromosomes, is much less than the global maximum of adaptibility function, and the size of population isn't sufficient for variety maintenance, there is a premature convergence to values far from a global maximum [10].

This problem can be solved by the support of the big size of population to provide the variety of data for operation of the genetic algorithm.

We will consider one modification of the classical genetic algorithm to reduce the size of population and an algorithm operating time.

1. Initialization of the initial population. Let's refuse an accidental choice of the initial population of chromosomes. We create the initial generation so that it wasn't concentrated round some area, i.e. had a wide spacing of values and possessed rather high adaptibility. It is possible to offer the following procedure of a choice of the initial population.

For determinancy, let's think that chromosomes represent binary notation of an integral number. Let a be the smallest of numbers, i.e. $a = 0$, and b the greatest, $b = 2^L + 2^{L-1} + \ldots + 2^0$. The initial population represents sequence from N numbers of $a_1, \ldots, a_N$ defined as follows.

We'll part an interval of $[a, b]$ into kN approximately equal parts. We will calculate function value of adaptibility in points of partition and we will sort them in ascending order. Given $F(x_1) \le F(x_2) \le \ldots \le F(x_{kN})$. (Note that x_i, $i = 1, \ldots, kN$ aren't arranged in ascending order of indexes). Thus $a_1 = x_{(k-1)N+1}, a_2 = x_{(k-1)N+2}, \ldots, a_2 = x_{kN}$. The choice of k depends on the initial task.

2. Calculation of the function value of adaptibility. We calculate the value of adaptibility function for each chromosome from population.

3. Choice of chromosomes for a crossingover. We select chromosomes which will participate in transposition by one of the well-known methods. The size of population necessary for operability participating in a crossingover is calculated by a formula:

$$N = 1 + log_2(1/(1 - P_1^{(1/L)})).$$

4. Formation of new generation. In case of paired recombination of the initial chromosomes, chromosomes from area of a global maximum while transposition with chromosomes from other areas can give unadapted descendants. As a result they will be lost for further reproduction. To avoid it, we will add the new generation of N most fitted parent individuals and N individuals received as a result of a crossingover from chromosomes, selected on a step 3.

IX. Conclusion

The project has given the following results.

1. The modification of the method of synthetic fuzzy assessment realized by neural network has been offered. Yet the method weight coincides with the network weight.

2. The two-level, multiple-factor model modified for air quality assessment has been developed.

3. The scheme of division of a secret with a key of multiple use and protection against participants - malefactors has been developed.

4. The modification of classical genetic algorithm which reduces the size of population and algorithm's operating time has been offered.

References

[1] B.Q. Hu, S.M. Lo, M. Liu, C.M. Zhao. On the Use of Fuzzy Synthetic Evaluation and Optimal Classification for Fire Risk Ranking of Buildings // Neural Computing and Application. – 2009. – No 2.

[2] Ni-Bin Chang, H. W. Chen and S. K. Ning Identification of river water quality using the Fuzzy Synthetic Evaluation approach // Journal of Enviromental Management. – V.63, I.3. – P. 293-305.

[3] Заде Л.А. Размытые множества и их применение в распознавании образов и кластер анализе. – Москва: Мир, 1980 – С.208-247.

[4] Аверкин, А.Н., Батыршин, И.З., Блишун, А.Ф., Силов, В.Б., Тарасов, В.Б. Нечеткие множества в моделях управления и искусственного интеллекта. – Москва: Наука, 1986. – 312 с.

[5] Уоссермен Ф. Нейрокомпьютерная техника: Теория и практика. – СПб.: Питер, 1992.

[6] Adi Shamir. How to Share a Secret // Communications of the ACM. – 1979. – V.22, No 11. – P. 612-613.

[7] Е.Р. Байсалов, Ж.М. Тунликбаева. Многоразовая схема разделения секрета // Труды межд. конф. «Actual problems of computer sciences». – Алматы: КазНУ, 2003. – С.143-145.

[8] M. Tompa, H. Woll How to Share a Secret with Cheaters // Proceedings on Advances in cryptology. – 1987. – P. 261-265.

[9] Mitchell M. An Introduction to Genetic Algorithms. – Cambridge, MA: The MIT Press, 1996.

[10] John R. Koza Genetic Programming On the Programming of Computers by Means of Natural Selection. – Cambridge, MA: The MIT Press, 1998.

Tussupov Jamalbek is Doctor of physic and mathematical science, full professor, chair of information systems department, L.N.Gumilyov Eurasian Natinal University, Astana, Kazakhstan

La Lira is associated professor, L.N.Gumilyov Eurasian Natinal University, Astana, Kazakhstan

Mukhanova Ayagoz is third year doctoral student, master of Information systems, L.N.Gumilyov Eurasian Natinal University, Astana, Kazakhstan

Gaussian type differential equation

Conny Adams, Tshidiso Masebe, Jacob Manale

***Abstract*—Lie point symmetries and a new approach utilizing Euler's type formulas for the solution of second order ordinary linear differential equations are applied to determine symmetries for a differential equation derived from a Gaussian function whose antiderivate cannot be expressed in closed form. The effectiveness of the approach is tested by constructing invariant solutions of the symmetries if any.**

***Index Terms*—Gaussian function, invariant solution, partial differential equation, point symmetries.**

I. Introduction

THE Gaussian function

$$\int_0^\infty e^{-ax^2}dx \tag{1}$$

is classified as an integral whose antiderivative cannot be expressed in closed form (i.e. cannot be expressed analytically in terms of a finite number of certain well known functions) [4].

The current undertaking seeks to determine the solution of its derived differential equation using Lie Symmetry method. Lie Symmetry method is a mathematical theory that synthesizes symmetry of differential equation [2].

In order to apply Lie Symmetry method to the Gaussian type function, we need to first present it as a differential equation by substituting

$$a = t,$$

and letting

$$u = \int_0^\infty e^{-tx^2}dx \tag{2}$$

resulting in

$$u_x = -2txe^{-tx^2}. \tag{3}$$

If we differentiate equation (3) with respect to t then the resulting partial differential equation becomes

$$u_{tx} = \frac{1}{t}u_x - x^2u_x. \tag{4}$$

Equation (4) is a partial differential equation with independent variables t and x, and differential variable u.

C.M. Adams is with the Department of Mathematics, University of South Africa, Pretoria, 0001, RSA e-mail: connieadams@webmail.co.za

T.P. Masebe is with the Department of Mathematics,Science and Technology Education, Tshwane University of Technology, Pretoria, 0001, RSA e-mail: masebetp@tut.ac.za.

J.M. Manale is with the Department of Mathematical Sciences, University of South Africa, Pretoria, 0001 RSA (phone: +27-11-670-9172; fax: +27-11-670-9171; e-mail: Manaljm@unisa.ac.za

Manuscript received December 13, 2013;

II. Solution of determining equation

The infinitesimal generator for point symmetry admitted by equation (4) is of the form

$$X = \xi^1(t,x)\frac{\partial}{\partial t} + \xi^2(t,x)\frac{\partial}{\partial x} + \eta(t,x)\frac{\partial}{\partial u} \tag{5}$$

Its first and second prolongations are given by

$$X^{(2)} = X + \eta_x^{(1)}\frac{\partial}{\partial u_x} + \eta_{tx}^{(2)}\frac{\partial}{\partial u_{tx}} \tag{6}$$

where X is defined by equation (5). The invariance condition for (4) is given by

$$\begin{aligned} &X^{(2)}(u_{tx} - \frac{1}{t}u_x + x^2u_x)|_{u_{tx}=\frac{1}{t}u_x - x^2u_x} = \\ &(\eta_{tx}^{(2)} - \frac{1}{t}\eta_x^{(1)} + \frac{1}{t^2}\xi^1u_x + 2x\xi^{(2)}u_x + x^2\eta_x^{(1)})|_{u_{tx}=\frac{1}{t}u_x - x^2u_x} = 0 \end{aligned} \tag{7}$$

We define the following from ([1],[2])

$$\begin{aligned} \eta &= fu + g \\ \eta_t^{(1)} &= g_t + f_tu + [f - \xi_t^1]u_t - \xi_t^2u_x \\ \eta_x^{(1)} &= g_x + f_xu + [f - \xi_x^2]u_x - \xi_x^1u_t \\ \eta_{tx}^{(2)} &= g_{tx} + f_{tx}u + [f_t - \xi_{tx}^2]u_x + [f_x - \xi_{tx}^1]u_t \\ &\quad + u_{tx}[f - \xi_t^1 - \xi_x^2] - \xi_t^2u_{xx} - \xi_x^1u_{tt} \end{aligned} \tag{8}$$

The substitutions of $\eta_x^{(1)}$ and $\eta_{tx}^{(2)}$ in the invariance condition (7) yield the determining equation

$$\begin{aligned} &g_{tx} + f_{tx}u + [f_t - \xi_{tx}^2]u_x + [f_x - \xi_{tx}^1]u_t + (\frac{1}{t}u_x - x^2u_x)[f - \xi_t^1 - \xi_x^2] \\ &- \xi_t^2u_{xx} - \frac{1}{t}g_x - \frac{1}{t}f_xu - \frac{1}{t}u_x[f - \xi_x^2] + \frac{1}{t}u_t\xi_x^1 + \frac{1}{t^2}\xi^1u_x - \xi_x^1u_{tt} \\ &+ 2x\xi^2u_x + x^2g_x + x^2f_xu + x^2u_x[f - \xi_x^2] - x^2\xi_x^1u_t = 0 \end{aligned} \tag{9}$$

We set the coefficients of $u_{xx}, u_{tt}, u_x, u_t, u$ and those free of these variables to zero. We thus have the following defining equations

$$u_{xx} \quad : \quad \xi_t^2 = 0, \tag{10}$$

$$u_{tt} \quad : \quad \xi_x^1 = 0, \tag{11}$$

$$u_t \quad : \quad f_x = 0, \tag{12}$$

$$u_x \quad : \quad f_t - \frac{1}{t}\xi_t^1 + \frac{1}{t^2}\xi^1 + 2x\xi^2 + x^2\xi_t^1 = 0, \tag{13}$$

$$u \quad : \quad f_{tx} = 0, \tag{14}$$

$$u^0 \quad : \quad g_{tx} = \frac{1}{t}g_x - x^2g_x. \tag{15}$$

We differentiate defining equation (13) with respect to t and apply equation (10) to obtain the equation

$$f_{tt} - (\frac{1}{t}\xi_t^1)_t + (\frac{1}{t}\xi^1)_t + x^2\xi_{tt}^1 = 0 \tag{16}$$

ISBN: 978-1-61804-219-4

The derivative of equation (16) with respect to x and the application of equations (11) and (12) result in that

$$2x\xi^1_{tt} = 0$$

whence

$$\xi^1_{tt} = 0 \tag{17}$$

Thus we have that

$$\xi^1 = at + b \tag{18}$$

which can be expressed using Euler formula with infinitesimal ω as

$$\xi^1 = \frac{a\ \sin(\frac{\omega t}{i}) + b\phi\ \cos(\frac{\omega t}{i})}{-i\omega} \quad \text{where} \quad \phi = \sin(\frac{\omega}{i}) \quad \text{and} \quad a = a(x), b = b(x). \tag{19}$$

We differentiate equation (19) with respect to t and obtain expressions for ξ^1_t, and ξ^1_{tt}

$$\xi^1_t = a\ \cos(\frac{\omega t}{i}) - b\phi\ \sin(\frac{\omega t}{i}), \tag{20}$$

$$\xi^1_{tt} = \frac{-\omega}{i}\ a\ \sin(\frac{\omega t}{i}) - \frac{\omega}{i}\ b\ \phi\ \cos(\frac{\omega t}{i}), \tag{21}$$

Similarly we differentiate defining equation (13) with respect to x and obtain

$$(x\xi^2)_x = -x\xi^1_t \tag{22}$$

We integrate equation (22) with respect to x and simplify to obtain the expression for ξ^2, given as

$$\xi^2 = -\frac{1}{2}x\xi^1_t + A \tag{23}$$

which translate to

$$\xi^2 = -\frac{1}{2}ax\ \cos(\frac{\omega t}{i}) + \frac{1}{2}bx\phi\ \sin(\frac{\omega t}{i}) + A. \tag{24}$$

The equation (16) imply that

$$f_{tt} = (\frac{1}{t}\xi^1_t)_t - (\frac{1}{t}\xi^1)_t - x^2\xi^1_{tt}$$

which translate to

$$\begin{aligned} f_{tt} = &-\frac{\omega a}{it}\ \sin(\frac{\omega t}{i}) - \frac{\omega b}{it}\phi\ \cos(\frac{\omega t}{i}) - \frac{a}{t^2}\cos(\frac{\omega t}{i}) \\ &+ \frac{b\phi}{t^2}\sin(\frac{\omega t}{i}) - \frac{a}{t}\ \cos(\frac{\omega t}{i}) + \frac{b\phi}{t}\ \sin(\frac{\omega t}{i}) \\ &- \frac{a}{it^2\omega}\ \sin(\frac{\omega t}{i}) - \frac{b\phi}{it^2\omega}\ \cos(\frac{\omega t}{i}) + \frac{ax^2\omega}{i}\ \sin(\frac{\omega t}{i}) \\ &+ \frac{b\phi x^2\omega}{i}\ \cos(\frac{\omega t}{i}) \end{aligned} \tag{25}$$

The integration of equation (25) results in the expression for f_t and f given as

$$\begin{aligned} f_t = &\frac{a}{t}\ \cos(\frac{\omega t}{i}) - \frac{b}{t}\phi\ \sin(\frac{\omega t}{i}) - \frac{ai}{\omega t^2}\sin(\frac{\omega t}{i}) \\ &- \frac{bi\phi}{\omega t^2}\cos(\frac{\omega t}{i}) - \frac{ia}{\omega t}\ \sin(\frac{\omega t}{i}) - \frac{ib\phi}{t\omega}\ \cos(\frac{\omega t}{i}) \\ &+ \frac{a}{\omega^2 t^2}\ \cos(\frac{\omega t}{i}) - \frac{b\phi}{\omega^2 t^2}\ \sin(\frac{\omega t}{i}) - ax^2\ \cos(\frac{\omega t}{i}) \\ &+ b\phi x^2\ \sin(\frac{\omega t}{i}) \end{aligned} \tag{26}$$

and

$$\begin{aligned} f = &\frac{ai}{t\omega}\ \sin(\frac{\omega t}{i}) + \frac{ib}{t\omega}\phi\ \cos(\frac{\omega t}{i}) - \frac{a}{\omega^2 t^2}\cos(\frac{\omega t}{i}) \\ &+ \frac{b\phi}{\omega^2 t^2}\sin(\frac{\omega t}{i}) - \frac{a}{\omega^2 t}\ \sin(\frac{\omega t}{i}) - \frac{ib\phi}{t\omega}\ \sin(\frac{\omega t}{i}) \\ &+ \frac{ia}{\omega^3 t^2}\ \sin(\frac{\omega t}{i}) + \frac{ib\phi}{\omega^3 t^2}\ \cos(\frac{\omega t}{i}) - \frac{iax^2}{\omega}\ \sin(\frac{\omega t}{i}) \\ &- \frac{bi\phi x^2}{\omega}\ \cos(\frac{\omega t}{i}) + B \end{aligned} \tag{27}$$

respectively. From the defining equation (11) we have that

$$\xi^1_x = \frac{\dot{a}\ \sin(\frac{\omega t}{i}) + \dot{b}\phi\ \cos(\frac{\omega t}{i})}{-i\omega} = 0 \tag{28}$$

This result in that

$$\begin{aligned} &\dot{a} = 0 \ \text{ and } \ \dot{b} = 0 \\ &\text{Hence } \ a = C_1 \ \text{ and } \ b = C_2 \end{aligned} \tag{29}$$

The defining equation (12) $f_x = 0$ imply that the last terms of f i.e.

$$-\frac{iax^2}{\omega}\ \sin(\frac{\omega t}{i}) - \frac{bi\phi x^2}{\omega}\ \cos(\frac{\omega t}{i}) = 0 \tag{30}$$

A. Infinitesimals

The linearly independent solutions of the defining equations (10) to (15) result in the infinitesimals

$$\xi^1 = -C_1\frac{\sin(\frac{\omega t}{i})}{i\omega} - C_2\phi\frac{\cos(\frac{\omega t}{i})}{i\omega} \tag{31}$$

$$\xi^2 = -\frac{1}{2}xC_1\cos(\frac{\omega t}{i}) + \frac{1}{2}x\phi C_2\sin(\frac{\omega t}{i}) + A \tag{32}$$

$$\begin{aligned} f = &\frac{C_1 i}{t\omega}\ \sin(\frac{\omega t}{i}) + \frac{iC_2}{t\omega}\phi\ \cos(\frac{\omega t}{i}) - \frac{C_1}{\omega^2 t^2}\cos(\frac{\omega t}{i}) \\ &+ \frac{C_2\phi}{\omega^2 t^2}\sin(\frac{\omega t}{i}) - \frac{C_1}{\omega^2 t}\ \sin(\frac{\omega t}{i}) - \frac{iC_2\phi}{t\omega}\ \sin(\frac{\omega t}{i}) \\ &+ \frac{iC_1}{\omega^3 t^2}\ \sin(\frac{\omega t}{i}) + \frac{iC_2\phi}{\omega^3 t^2}\ \cos(\frac{\omega t}{i}) + B \end{aligned} \tag{33}$$

B. Symmetries

The Symmetries according to infinitesimals (31) to (33) are:

$$\begin{aligned} X_1 = &\frac{\sin(\frac{\omega t}{i})}{i\omega}\frac{\partial}{\partial t} - \frac{1}{2}x\cos(\frac{\omega t}{i})\frac{\partial}{\partial x} \\ &\{ + \frac{i}{t\omega}\ \sin(\frac{\omega t}{i}) - \frac{1}{\omega^2 t^2}\cos(\frac{\omega t}{i}) \\ &- \frac{1}{\omega^2 t}\ \sin(\frac{\omega t}{i}) + \frac{i}{\omega^3 t^2}\ \sin(\frac{\omega t}{i})\}u\frac{\partial}{\partial u} \end{aligned} \tag{34}$$

$$\begin{aligned} X_2 = &-\phi\frac{\cos(\frac{\omega t}{i})}{i\omega}\frac{\partial}{\partial t} + \frac{1}{2}x\phi\sin(\frac{\omega t}{i})\frac{\partial}{\partial x} \\ &\{ + \frac{i}{t\omega}\phi\ \cos(\frac{\omega t}{i}) + \frac{\phi}{\omega^2 t^2}\sin(\frac{\omega t}{i}) \\ &- \frac{i\phi}{t\omega}\ \sin(\frac{\omega t}{i}) + \frac{i\phi}{\omega^3 t^2}\ \cos(\frac{\omega t}{i})\}u\frac{\partial}{\partial u} \end{aligned} \tag{35}$$

$$X_3 = \frac{\partial}{\partial x} \tag{36}$$

$$X_4 = u\frac{\partial}{\partial u} \tag{37}$$

ISBN: 978-1-61804-219-4

The function $g(t,x)$ could not be determined and thus lead to an infinite symmetry generator

$$X_\infty = g(t,x)u\frac{\partial}{\partial u} \tag{38}$$

III. Invariant Solutions

A. Invariant solution through the symmetry X_2

We consider the symmetry given by equation (32). The invariants are determined from solving the equation

$$\begin{aligned} X_2 I = &-\phi\frac{\cos(\frac{\omega t}{i})}{i\omega}\frac{\partial I}{\partial t} + \frac{1}{2}x\phi\sin(\frac{\omega t}{i})\frac{\partial I}{\partial x} \\ &\{ + \frac{i}{t\omega}\phi\ \cos(\frac{\omega t}{i}) + \frac{\phi}{\omega^2 t^2}\sin(\frac{\omega t}{i}) \\ &- \frac{i\phi}{t\omega}\ \sin(\frac{\omega t}{i}) + \frac{i\phi}{\omega^3 t^2}\ \cos(\frac{\omega t}{i})\}u\frac{\partial I}{\partial u} = 0 \end{aligned} \tag{39}$$

The characteristic equation of (39) is given by

$$\begin{aligned} &-\frac{dt}{\phi\frac{\cos(\frac{\omega t}{i})}{i\omega}} = \frac{dx}{\frac{1}{2}x\phi\sin(\frac{\omega t}{i})} = \\ &\frac{du}{u\{\frac{i}{t\omega}\phi\ \cos(\frac{\omega t}{i}) + \frac{\phi}{\omega^2 t^2}\sin(\frac{\omega t}{i}) - \frac{i\phi}{t\omega}\ \sin(\frac{\omega t}{i}) + \frac{i\phi}{\omega^3 t^2}\ \cos(\frac{\omega t}{i})\}} \end{aligned} \tag{40}$$

From equation (40) we have that

$$-\frac{dt}{\phi\frac{\cos(\frac{\omega t}{i})}{i\omega}} = \frac{dx}{\frac{1}{2}x\phi\sin(\frac{\omega t}{i})} \tag{41}$$

simplifies to

$$\frac{2}{x}dx = -\omega i\tan(\frac{\omega t}{i})dt \tag{42}$$

The solution to equation (42) is given by

$$C + 2\ln x = -\ln\cos|(\frac{\omega t}{i})| \tag{43}$$

which result in that the first invariant is given by

$$C_1 = x^2\cos(\frac{\omega t}{i}) \tag{44}$$

Also from equation (40) we have that

$$\begin{aligned} &-i\omega\frac{dt}{\phi\cos(\frac{\omega t}{i})}\{\frac{i}{t\omega}\phi\ \cos(\frac{\omega t}{i}) + \frac{\phi}{\omega^2 t^2}\sin(\frac{\omega t}{i}) \\ &-\frac{i\phi}{t\omega}\ \sin(\frac{\omega t}{i}) + \frac{i\phi}{\omega^3 t^2}\ \cos(\frac{\omega t}{i})\} \\ &= \frac{du}{u} \end{aligned} \tag{45}$$

We simplify left hand side of equation (45) by multiplying through by $\frac{-i\omega}{\cos(\frac{\omega t}{i})}$, and for smaller value of ω we have the approximation

$$dt\{\frac{1}{t} - \frac{1}{t^2} - 0 + \frac{1}{t^2}\} = \frac{du}{u}$$

Hence the equation becomes

$$\frac{dt}{t} = \frac{du}{u} \tag{46}$$

The solution to equation (46) is

$$\frac{u}{t} = C_2 \tag{47}$$

Since C_1 is independent of u, every invariant solution is of the form

$$\frac{u}{t} = F(x^2\cos(\frac{\omega t}{i})) \tag{48}$$

or equivalently

$$u = tF(x^2\cos(\frac{\omega t}{i})) \tag{49}$$

Differentiating equation (49) we obtain

$$u_x = 2xtF'\cos(\frac{\omega t}{i}) \tag{50}$$

$$u_{xt} = 2xF'\cos(\frac{\omega t}{i}) - 2xt\frac{\omega}{i}F'\sin(\frac{\omega t}{i}) - x^3t\frac{\omega}{i}F''\sin(\frac{2\omega t}{i}) \tag{51}$$

We substitute for equations (50) and (51) in equation (4) and obtain

$$\begin{aligned} &2xF'\cos(\frac{\omega t}{i}) - 2xt\frac{\omega}{i}F'\sin(\frac{\omega t}{i}) - x^3t\frac{\omega}{i}F''\sin(\frac{2\omega t}{i}) \\ &-2xF'\cos(\frac{\omega t}{i}) + 2x^3tF'\cos(\frac{\omega t}{i}) = 0 \end{aligned} \tag{52}$$

If we let $\omega \to 0$ equation (52) simplifies to

$$2x^3tF' = 0$$

or

$$F' = 0 \tag{53}$$

Hence

$$F = A \tag{54}$$

The solution is given by

$$u = At \tag{55}$$

where A is a constant.

B. Invariant solution through the symmetry X_1

We consider the symmetry given by equation (31). The invariants are determined from solving the equation

$$\begin{aligned} X_1 I = &-\frac{\sin(\frac{\omega t}{i})}{i\omega}\frac{\partial I}{\partial t} - \frac{1}{2}x\cos(\frac{\omega t}{i})\frac{\partial I}{\partial x} \\ &\{ + \frac{i}{t\omega}\ \sin(\frac{\omega t}{i}) - \frac{1}{\omega^2 t^2}\cos(\frac{\omega t}{i}) \\ &-\frac{1}{\omega^2 t}\ \sin(\frac{\omega t}{i}) + \frac{i}{\omega^3 t^2}\ \sin(\frac{\omega t}{i})\}u\frac{\partial I}{\partial u} = 0 \end{aligned} \tag{56}$$

The characteristic equation of (56) is given by

$$\begin{aligned} &-\frac{dt}{\frac{\sin(\frac{\omega t}{i})}{i\omega}} = \frac{dx}{-\frac{1}{2}x\cos(\frac{\omega t}{i})} \\ &= \frac{du}{u\{\frac{i}{t\omega}\ \sin(\frac{\omega t}{i}) - \frac{1}{\omega^2 t^2}\cos(\frac{\omega t}{i}) - \frac{1}{\omega^2 t}\ \sin(\frac{\omega t}{i}) + \frac{i}{\omega^3 t^2}\ \sin(\frac{\omega t}{i})\}} \end{aligned} \tag{57}$$

From equation (57) we have that

$$-\frac{dt}{\frac{\sin(\frac{\omega t}{i})}{i\omega}} = \frac{dx}{-\frac{1}{2}x\cos(\frac{\omega t}{i})} \tag{58}$$

simplifies to

$$\frac{2}{x}dx = \omega i\cot(\frac{\omega t}{i})dt \tag{59}$$

ISBN: 978-1-61804-219-4

The solution to equation (59) is given by

$$A + 2\ln x = -\ln\sin|(\frac{\omega t}{i})| \tag{60}$$

which result in that the first invariant is given by

$$A_1 = x^2\sin(\frac{\omega t}{i}) \tag{61}$$

Also from equation (57) we have that

$$\begin{aligned} &-i\omega\frac{dt}{\sin(\frac{\omega t}{i})}\{\frac{i}{t\omega}\ \sin(\frac{\omega t}{i}) - \frac{1}{\omega^2 t^2}\cos(\frac{\omega t}{i}) \\ &-\frac{1}{\omega^2 t}\ \sin(\frac{\omega t}{i}) + \frac{i}{\omega^3 t^2}\ \sin(\frac{\omega t}{i})\} \\ &= \frac{du}{u} \end{aligned} \tag{62}$$

We simplify left hand side of equation (62) by multiplying through by $\frac{-i\omega}{\sin(\frac{\omega t}{i})}$, and for smaller value of ω we have the approximation

$$dt\{\frac{1}{t} - \frac{1}{t^2} - 0 + \frac{1}{t^2}\} = \frac{du}{u}$$

Hence the equation becomes

$$\frac{dt}{t} = \frac{du}{u} \tag{63}$$

The solution to equation (63) is

$$\frac{u}{t} = A_2 \tag{64}$$

Since A_1 is independent of u, every invariant solution is of the form

$$\frac{u}{t} = F(x^2\sin(\frac{\omega t}{i})) \tag{65}$$

or equivalently

$$u = tF(x^2\sin(\frac{\omega t}{i})) \tag{66}$$

Differentiating equation (66) we obtain

$$u_x = 2xtF'\sin(\frac{\omega t}{i}) \tag{67}$$

$$\begin{aligned} u_{xt} &= 2xF'\sin(\frac{\omega t}{i}) + 2xt\frac{\omega}{i}F'\cos(\frac{\omega t}{i}) \\ &+ x^3 t\frac{\omega}{i}F''\sin(\frac{2\omega t}{i}) \end{aligned} \tag{68}$$

We substitute for equations (67) and (68) in equation (4) and obtain

$$\begin{aligned} &2xF'\sin(\frac{\omega t}{i}) + 2xt\frac{\omega}{i}F'\cos(\frac{\omega t}{i}) + x^3 t\frac{\omega}{i}F''\sin(\frac{2\omega t}{i}) \\ &-2xF'\sin(\frac{\omega t}{i}) + 2x^3 tF'\sin(\frac{\omega t}{i}) = 0 \end{aligned} \tag{69}$$

If we let $\omega \to 0$ in equation (69) we get no solution.

C. Invariant solution through the symmetry X_3

The invariant solution through symmetry $X_3 = \frac{\partial}{\partial x}$ yields that

$$u = H(t) \tag{70}$$

where $H(t)$ denotes some function of t, consistent with equation (71)

D. Conclusion

The approach produced symmetries which provided a linear invariant solutions. This is consistent with the result in [4] that

$$\int_0^\infty e^{-tx^2}dx = \frac{1}{2}\sqrt{\frac{\pi}{t}}, \quad t > 0 \tag{71}$$

REFERENCES

[1] Blumen,G.W. Anco,S.C. 2002. Symmetries and Integration methods for Differential Equations. New York. Springer-Verlag.

[2] Hydon, P.E 2000. Symmetry methods for Differential Equations. New York. Cambridge University Press .

[3] Ibragimov, N.H.1999. Elementary Lie Group Analysis and Ordinary Differential Equations. London. J. Wiley & Sons Ltd.

[4] Wikipedia Foundation.2013. List of integrals[Online].en.wikipedia.org Available from http://www.wikipedia.org/wiki/list of integrals [Accessed:07/12/2013]

A Note on Geometric Mean of Positive Matrices

Wen-Haw Chen

***Abstract*—The geometric mean of two positive definite matrices was first given by Pusz and Woronowicz in 1975. It has many properties of the geometric mean of two positive numbers. In 2004, Ando, Li and Mathias listed ten properties that a geometric mean of m matrices should satisfy and give a definition of geometric mean of m matrices by a iteration which satisfies these ten properties. For the geometric mean of two positive matrices, there is an interesting relationship between matrix geometric mean and the information metric. That is, consider the set of all positive definite matrices as a Riemannian manifold with the information metric, then the geometric mean matrices is the middle point of a geodesic. In this paper, we present two different proofs, the variation and the exponential map for the relationship.**

***Index Terms*—Geometric means, Positive definite matrices, Geodesics.**

I. Introduction

It has been an interestiong topic of studying geometric means on positive definite matrices in many disciplines of science such as operator theory, physics, engineering and statistics etc. The geometric mean of two positive definite matrices was first given by Pusz and Woronowicz [17] which is defined by

$$A\#B = A^{\frac{1}{2}}(A^{-\frac{1}{2}}BA^{-\frac{1}{2}})^{\frac{1}{2}}A^{\frac{1}{2}},$$

and the detailed study was in Kubo and Ando's paper [12]. It has some similar properties as the geometric mean of positive numbers. For example, it satisfies the arithmetic-geometric-harmonic-mean unequality.

On the other hand, the geomotric mean of positive definite matrices may be defined geometrically. Information geometry began as the geometric study of statistical estimation. This involved viewing the set of probability distributions which constitute a statistical model as a Riemannian manifold with the Fisher metric. In 1945, C. R. Rao [18] had already pointed out in his paper that the Fisher information matrix determines a Riemannian metric on a statistical manifold. In addition, there is an interesting relationship between matrix geometric mean and the information metric.

Consider the set of all positive matrices as a manifold. Then the tangent space of a point A can be identified as the space of Hermitian matrices. Define the Riemannian metric at A by the differential

$$ds = ||A^{-\frac{1}{2}}dAA^{-\frac{1}{2}}||_2 = [Tr((A^{-1}dA)^2)]^{\frac{1}{2}},$$

then the geodesic connecting A, B is

$$\gamma(t) = A^{\frac{1}{2}}(A^{-\frac{1}{2}}BA^{-\frac{1}{2}})^t A^{\frac{1}{2}}$$

W. -H. Chen is with the Department of Applied Mathematics, Tunghai University, Taichung 40704, Taiwan, R. O. C. e-mail: whchen@thu.edu.tw

where $0 \leq t \leq 1$ and the geometric mean of A, B is the middle point of the geodesic which connecting A and B. We will verify that some properties is still hold such as monotonicity and harmonic-geometric-arithmetic inequality. Moreover, a definition of geometric mean for three or more positive definite matrices by a iteration will be introduced. We find that such the geometric mean will inherits some properties of the geometric mean of two positive definite matrices.

II. Fisher information matric of a statistical model

We first introduce the Fisher information matric of a statistical model.

Definition 1. *Consider an n-dimensional statistical model $S = \{p_\theta \,|\, \theta \in \Theta\}$ where $p_\theta = p(x;\theta)$ are probability distribution functions and Θ is a subset of $\mathbb{R}^n$. Then the Fisher information matrix of S at θ is the $n \times n$ matrix $G(\theta) = \big[g_{ij}(\theta)\big]$ where $g_{ij}(\theta)$ is defined by*

$$\begin{aligned} g_{ij}(\theta) &= E_\theta\big[\frac{\partial}{\partial\theta^i}\log p(x;\xi)\frac{\partial}{\partial\theta^j}\log p(x;\xi)\big] \\ &= \int_{\mathcal{X}}\big[\frac{\partial}{\partial\theta^i}\log p(x;\xi)\frac{\partial}{\partial\xi^j}\log p(x;\theta)\big]p(x;\theta)\,dx. \end{aligned}$$

We assume that Θ is an open subset of $\mathbb{R}^n$ and for each $x \in \mathcal{X}$, the function $\xi \mapsto p(x;\xi)$ $(\Xi \to \mathbb{R})$ is C^∞ so that we can define $\frac{\partial}{\partial\xi^i}p(x;\xi)$ and $\frac{\partial}{\partial\xi^i}\frac{\partial}{\partial\xi^j}p(x;\xi)$.

In addition, we assume that the order of integration and differentiation may be freely rearranged. For example, we shall often use formulas such as

$$\int_{\mathcal{X}}\frac{\partial}{\partial\xi^i}p(x;\xi)\,dx = \frac{\partial}{\partial\xi^i}\int_{\mathcal{X}}p(x;\xi)\,dx = \frac{\partial}{\partial\xi^i}1 = 0.$$

We also assume that $p(x;\xi) > 0$ for all $\xi \in \Xi$ and all $x \in \mathcal{X}$.

By the assumptions, it is easy to see that G is positive semidefinite. We assume that G is positive definite.

Now we can define the Riemannian metric $g_\theta = <,>_\theta$ on the tangent space $T_\theta(S)$ at θ by

$$< (\partial_i)_\theta, (\partial_j)_\theta >_\theta = g_{ij}(\theta) = E_\theta[\partial_i l_\theta \partial_j l_\theta], \quad (\partial_i)_\theta, (\partial_j)_\theta \in T_\theta(S).$$

We call this the Fisher metric or the information metric.

An important example is the multivariate normal distributions with 0 expectation. The distributions are given by

$$p_A(x) = \frac{1}{\sqrt{(2\pi)^n det(A)}}\exp\{-\frac{1}{2}x^T A^{-1}x\},$$

where A is positive definite real matrix and $x \in \mathbb{R}^n$. The tangent space at a point p_A can be identified as the set of all symmetric real matrices and the information metric was given

ISBN: 978-1-61804-219-4

by Skovgaard. The formula is

$$g_A(H_1,H_2) = \frac{1}{2}Tr(A^{-1}H_1A^{-1}H_2)$$
$$= \frac{1}{2}Tr(A^{-\frac{1}{2}}H_1A^{-\frac{1}{2}}A^{-\frac{1}{2}}H_2A^{-\frac{1}{2}}),$$

where H_1, H_2 are symmetric real matrices. It coincides with the Hilbert-Schmidt inner product scaled by $\frac{1}{2}$. In next section, we will find that the geometric mean of two matrices is the middle point of geodesic when we consider the set of real positive definite matrices as a Riemannian manifold with the information metric.

III. Geometric mean of two positive definite matrices

We know that the arithmetic mean can be extend to matrices which is defined by

$$\frac{A_1+\cdots+A_n}{n},$$

for n matrices $A_1,\cdots,A_n$ where $n \geq 2$. When we want to extend the geometric mean to matrices, we obtain that the product AB of two matrices A and B should be well defined. So we can restrict to the square matrices and the positive number is replaced by positive definite matrix.

Note that the product of two positive definite matrices is not always positive definite. For example, let $A = \begin{bmatrix}1 & 2\\ 2 & 5\end{bmatrix}$ and $B = \begin{bmatrix}1 & -1\\ -1 & 2\end{bmatrix}$. Then $AB = \begin{bmatrix}-1 & 3\\ -3 & 8\end{bmatrix}$ is not positive definite since AB is not symmetric. Hence we can not defined the geometric mean to be $(AB)^{\frac{1}{2}}$, since the geometric mean of two positive definite matrices should be positive definite. But we obtain that XBX^* is always positive definite for any positive definite matrix B and for any matrix X.

In fact, the geometric mean of two positive definite matrices A and B is defined by

$$A\#B = A^{\frac{1}{2}}(A^{-\frac{1}{2}}BA^{-\frac{1}{2}})^{\frac{1}{2}}A^{\frac{1}{2}}.$$

The set of all Hermitian matrices is denote by H_n, and the set of all positive definite matrices is denote by P_n.

Next we show that the geometric mean of two positive definite matrices A, B is the middle point of the geodesic which connect A and B when P_n is viewed as a Riemannian manifold.

Consider P_n as a manifold. The tangent space of a point A can be identified as H_n. Define the Riemannian metric at A by the differential

$$ds = ||A^{-\frac{1}{2}}dAA^{-\frac{1}{2}}||_2 = [Tr((A^{-1}dA)^2)]^{\frac{1}{2}}.$$

If $\gamma : [a,b] \to P_n$ is a differentiable curve in P_n, then we define its length as

$$L(\gamma) = \int_a^b ||\gamma^{-\frac{1}{2}}(t)\gamma'(t)\gamma^{-\frac{1}{2}}(t)||_2\, dt.$$

For each invertible X, $\Gamma_X(A) = X^*AX$ is a bijection of P_n onto P_n. If γ is a differentiable curve in P_n, then the composition $\Gamma_X \circ \gamma$ is another differentiable curve in P_n.

Lemma 1. *For each invertible X and for each differentiable curve γ*

$$L(\Gamma_X \circ \gamma) = L(\gamma).$$

Theorem 1. *The geodesic connecting A, B is*

$$\gamma(t) = A^{\frac{1}{2}}(A^{-\frac{1}{2}}BA^{-\frac{1}{2}})^tA^{\frac{1}{2}}$$

where $0 \leq t \leq 1$ and the geometric mean of A, B is the middle point of the geodesic which connecting A and B.

A. Proof by variation

By the lemma, we may assume that $A = I$, $\gamma(t) = B^t$. Let $l(t)$ be a curve such that $l(0) = l(1) = 0$. Then the variations of energy function is given by

$$\frac{d}{d\epsilon}[\int_0^1(\sqrt{g_{\gamma(t)+\epsilon l(t)}(\gamma'(t)+\epsilon l'(t),\gamma'(t)+\epsilon l'(t))})^2\, dt]|_{\epsilon=0}$$
$$= Tr(\int_0^1 -(B^t)^{-1}(\log B)^2 l(t)dt + (B^t)^{-1}(\log B)l(t)|_0^1 + \int_0^1 (B^t)^{-1}(\log B)^2 l(t)\, dt).$$

Since $l(0) = l(1) = 0$, the first term vanishes here and the derivative at ϵ is 0. On the other hand

$$g_{\gamma(t)}(\gamma'(t),\gamma'(t)) = Tr((B^t)^{-1}(B^t\log B)(B^t)^{-1}(B^t\log B))$$
$$= Tr((\log B)^2)$$

does not depend on t, we conclude that $\gamma(t) = B^t$ is the geodesic curve between I and B.

B. Proof by exponential map

Let X and Y be Banach space and U be an open subset of X. A map $f : U \to Y$ is said to be differential at $u \in U$ if there exist a bounded linear operator T from X to Y such that

$$\lim_{v\to 0}\frac{||f(u+v)-f(u)-T(v)||_Y}{||v||_X} = 0,$$

We call T the derivative of f at u and denote T by $Df(u)$. Note that $Df(u)(w) = \frac{d}{dt}|_{t=0}f(u+tw)$.

Now let I be an open interval and $H_n(I)$ be the collection of all Hermitian matrices whose eigenvalues are in I. Then a function f in $C^1(I)$ induces a map from $H_n(I)$ into H_n, where $C^1(I)$ is the space of continuously differentiable real-valued function on I. If $f \in C^1(I)$ and $A \in H_n(I)$, then we define $f^{[1]}(A)$ as the matrix whose i,j entry is

$$f^{[1]}(\lambda_i,\lambda_j) = \begin{cases}\frac{f(\lambda_i)-f(\lambda_j)}{\lambda_i-\lambda_j} & \lambda_i \neq \lambda_j\\ f'(\lambda_i) & \lambda_i = \lambda_j\end{cases},$$

where $\lambda_1,\ldots,\lambda_n$ are the eigenvalues of A. This is called the Loewner matrix of f at A.

The function f on $H_n(I)$ is differentiable. Its derivative at A, denoted as $Df(A)$, is a linear map on H_n. We have

$$Df(A)(H) = \frac{d}{dt}|_{t=0}f(A+tH).$$

An interesting expression for this derivative in terms of Loewner matrices is given in the following theorem.

Theorem 2. *[5] Let $f \in C^1(I)$ and $A \in H_n(I)$. Then*

$$\begin{aligned} Df(A)(H) &= f^{[1]}(A) \bullet H \\ &= U[f^{[1]}(\Lambda) \bullet (U^*HU)]U^*, \end{aligned}$$

where Λ is diagonal and $A = U\Lambda U^*$ and $\bullet$ denotes the Schur product.

We write De^H for the derivative of the exponential map at a point H of H_n. This is a linear map on H_n and the action is given by

$$De^H(K) = \frac{d}{dt}|_{t=0}(e^{H+tK}) = \lim_{t\to 0} \frac{e^{H+tK} - e^H}{t}.$$

Theorem 3. *[6] For all H and K in H_n we have*

$$||e^{-\frac{H}{2}} De^H(K) e^{-\frac{H}{2}}||_2 \geq ||K||_2.$$

Proof: Fir we claim that $||X^*KX||_2 = ||K||_2$ if $X^*X = I$. Note that

$$\begin{aligned} ||X^*KX||_2 &= (Tr[(X^*KX)(X^*KX)^*])^{\frac{1}{2}} \\ &= (Tr[KK^*])^{\frac{1}{2}} \\ &= ||K||_2. \end{aligned}$$

Now since H is Hermitian, $H = U\Lambda U^*$ where Λ is a diagonal matrix and $UU^* = I$. By Theorem 2 we have

$$\begin{aligned} De^H(K) &= U[[x_{ij}] \bullet U^*KU]U^* \\ &= U[[x_{ij}] \bullet B]U^* \end{aligned}$$

where $x_{ij} = \begin{cases} \frac{e^{\lambda_i} - e^{\lambda_j}}{\lambda_i - \lambda_j} & \lambda_i \neq \lambda_j \\ e^{\lambda_i} & \lambda_i = \lambda_j \end{cases}$ and $B = U^*KU$.

Note that $e^{-\frac{H}{2}} = U \begin{bmatrix} e^{-\frac{\lambda_1}{2}} & 0 & 0 \\ 0 & \ddots & 0 \\ 0 & 0 & e^{-\frac{\lambda_n}{2}} \end{bmatrix} U^*$. Hence we have

$$\begin{aligned} &||e^{-\frac{H}{2}} De^H(K) e^{-\frac{H}{2}}||_2 \\ &= ||U \begin{bmatrix} e^{-\frac{\lambda_1}{2}} & 0 & 0 \\ 0 & \ddots & 0 \\ 0 & 0 & e^{-\frac{\lambda_n}{2}} \end{bmatrix} U^*U[[x_{ij}]\bullet \\ &B]U^*U \begin{bmatrix} e^{-\frac{\lambda_1}{2}} & 0 & 0 \\ 0 & \ddots & 0 \\ 0 & 0 & e^{-\frac{\lambda_n}{2}} \end{bmatrix} U^*||_2 \\ &= || \begin{bmatrix} e^{-\frac{\lambda_1}{2}} & 0 & 0 \\ 0 & \ddots & 0 \\ 0 & 0 & e^{-\frac{\lambda_n}{2}} \end{bmatrix} [[x_{ij}] \bullet B] \begin{bmatrix} e^{-\frac{\lambda_1}{2}} & 0 & 0 \\ 0 & \ddots & 0 \\ 0 & 0 & e^{-\frac{\lambda_n}{2}} \end{bmatrix} ||_2 \\ &= |||[a_{ij}b_{ij}]|||_2 \end{aligned}$$

where $[b_{ij}] = B$,

$$\begin{aligned} a_{ij} &= e^{-\frac{\lambda_i}{2}} \frac{e^{\lambda_i} - e^{\lambda_j}}{\lambda_i - \lambda_j} e^{-\frac{\lambda_j}{2}} \\ &= \frac{\sinh(\frac{\lambda_i - \lambda_j}{2})}{\frac{\lambda_i - \lambda_j}{2}} \end{aligned}$$

if $\lambda_i \neq \lambda_j$
and $a_{ij} = 1$ if $\lambda_i = \lambda_j$.

Since $\frac{\sinh(x)}{x} \geq 1$ for all $x \neq 0$, $a_{ij} \geq 1$ for all i, j.

Hence

$$\begin{aligned} ||e^{-\frac{H}{2}} De^H(K) e^{-\frac{H}{2}}||_2 &= |||[a_{ij}b_{ij}]|||_2 \\ &= (\sum_{ij} a_{ij}^2 b_{ij}\overline{b_{ij}})^{\frac{1}{2}} \\ &\geq (\sum_{ij} b_{ij}\overline{b_{ij}})^{\frac{1}{2}} \\ &= ||B||_2 \\ &= ||U^*KU||_2 \\ &= ||K||_2. \end{aligned}$$

■

Theorem 4. *[6] Let $H(t)$, $a \leq t \leq b$ be any curve in H_n and let $\gamma(t) = e^{H(t)}$. Then we have*

$$L(\gamma) \geq \int_a^b ||H'(t)||_2 \, dt.$$

Proof: By the chain rule, we have

$$\gamma'(t) = e^{H(t)}H'(t) = \frac{d}{dh}|_{h=0}[e^{H(t)+hH'(t)}] = De^{H(t)}(H'(t)).$$

Theorem 3 implies that

$$\begin{aligned} ||\gamma^{-\frac{1}{2}}(t)\gamma'(t)\gamma^{-\frac{1}{2}}(t)||_2 &= ||e^{-\frac{H(t)}{2}} De^{H(t)}(H'(t)) e^{-\frac{H(t)}{2}}||_2 \\ &\geq ||H'(t)||_2. \end{aligned}$$

Integrating over t we complete the proof. ■

Now we define a metric δ_2 on P_n. For any $A, B \in P_n$, we define $\delta_2(A, B)$ by

$$\delta_2(A, B) = \inf\{L(\gamma) : \gamma \text{ is a curve from } A \text{ to } B\}.$$

According to Lemma 1, each Γ_X is an isometry for the length L. Hence it is also an isometry for the metric δ_2, that is,

$$\delta_2(A, B) = \delta_2(\Gamma_X(A), \Gamma_X(B)),$$

for all A, B in P_n and invertible X.

If $\gamma(t)$ is any curve joining A and B in P_n, then $H(t) = \log\gamma(t)$ is a curve joining $\log A$ and $\log B$ in H_n. Since $\int_a^b ||H'(t)||_2 \, dt$ is the length of $H(t)$ in H_n and H_n is a convex subspace of Euclidean space M_n, $\int_a^b ||H'(t)||_2 \, dt$ is bounded below by the length of the straight line segment $(1-t)\log A + t \log B$ which joining $\log A$ and $\log B$ where $0 \leq t \leq 1$. Hence by Theorem 4,

$$L(\gamma) \geq ||\log A - \log B||_2$$

and we have the following theorem.

Theorem 5. *[6] For each pair of points A, B in P_n we have*

$$\delta_2(A, B) \geq ||\log A - \log B||_2.$$

In other words for any two matrices H and K in H_n

$$\delta_2(e^H, e^K) \geq ||H - K||_2.$$

Thus the exponential map

$$\exp : (H_n, ||\cdot||_2) \to (P_n, \delta_2)$$

increases distances.

We write $[H, K]$ for the line segment joining H and K and $[A, B]$ for the geodesic from A to B where H, K in H_n and A, B in P_n.

Theorem 6. *[6] Let A and B be commuting matrices in P_n. Then the exponential function maps the line segment $[\log A, \log B]$ in H_n to the geodesic $[A, B]$ in P_n. In this case*

$$\delta_2(A, B) = ||\log A - \log B||_2.$$

Proof: We claim that

$$\gamma(t) = \exp((1-t)\log A + t \log B),$$

where $0 \le t \le 1$ is the unique curve of shortest length joining A and B in the space (P_n, δ_2). Since A and B commute, $\gamma(t) = A^{1-t}B^t$ and $\gamma'(t) = (\log B - \log A)\gamma(t)$. Thus

$$\begin{aligned} L(\gamma) &= \int_0^1 ||\gamma^{-\frac{1}{2}}\gamma'(t)\gamma^{-\frac{1}{2}}||_2 \, dt \\ &= \int_0^1 ||\log A - \log B||_2 \, dt \\ &= ||\log A - \log B||_2. \end{aligned}$$

Theorem 5 says that no curve can be shorter than this.

Now suppose $\tilde{\gamma}$ is another curve that joins A and B and has the same length as that of γ. Then $\tilde{H(t)} = \log \tilde{\gamma}(t)$ is a curve that joins $\log A$ and $\log B$ in H_n, and by Theorem 4, this curve has length $||\log A - \log B||_2$. But in a Euclidean space the straight line segment is the unique shortest curve between two points. So $\tilde{H(t)}$ is a reparametrization of the line segment $[\log A, \log B]$. ∎

When A and B commute, the natural parametrisation of the geodesic $[A, B]$ is given by

$$\gamma(t) = A^{1-t}B^t, \; 0 \le t \le 1,$$

in the sense that $\delta_2(A, \gamma(t)) = t\delta_2(A, B)$ for each t. The general case is obtained from this and the isometries Γ_X.

Theorem 7. *[6] Let A and B be any two elements of P_n. Then there exists a unique geodesic $[A, B]$ joining A and B. This geodesic has a parametrization*

$$\gamma(t) = A^{\frac{1}{2}}(A^{-\frac{1}{2}}BA^{-\frac{1}{2}})^t A^{\frac{1}{2}}, \; 0 \le t \le 1,$$

which is natural in the sense that

$$\delta_2(A, \gamma(t)) = t\delta_2(A, B)$$

for each t. Furthermore, we have

$$\delta_2(A, B) = ||\log(A^{-\frac{1}{2}}BA^{-\frac{1}{2}})||_2.$$

Proof: The matrices I and $A^{-\frac{1}{2}}BA^{-\frac{1}{2}}$ commute. By Theorem 6, the geodesic $[I, A^{-\frac{1}{2}}BA^{-\frac{1}{2}}]$ is naturally parametrized as

$$\gamma_0(t) = (A^{-\frac{1}{2}}BA^{-\frac{1}{2}})^t.$$

Applying the isometry $\Gamma_{A^{\frac{1}{2}}}$ we obtain the curve

$$\gamma(t) = \Gamma_{A^{\frac{1}{2}}}(\gamma_0(t)) = A^{\frac{1}{2}}(A^{-\frac{1}{2}}BA^{-\frac{1}{2}})^t A^{\frac{1}{2}}$$

joining the points $\Gamma_{A^{\frac{1}{2}}}(I) = A$ and $\Gamma_{A^{\frac{1}{2}}}(A^{-\frac{1}{2}}BA^{-\frac{1}{2}}) = B$. Since $\Gamma_{A^{\frac{1}{2}}}$ is an isometry, this curve is the geodesic $[A, B]$. The equality $\delta_2(A, \gamma(t)) = t\delta_2(A, B)$ follows from the similar property for $\gamma_0(t)$ noted earlier. We see that by Lemma 1

$$\begin{aligned} \delta_2(A, B) &= \delta_2(I, A^{-\frac{1}{2}}BA^{-\frac{1}{2}}) \\ &= ||\log I - \log(A^{-\frac{1}{2}}BA^{-\frac{1}{2}})||_2 \\ &= ||\log(A^{-\frac{1}{2}}BA^{-\frac{1}{2}})||_2. \end{aligned}$$

∎

IV. Geometric mean of three or more matrices

Ando, Li and Mathias [2] listed ten properties that a geometric mean of m matrices should satisfy, which we call the ALM properties. For simplicity, we report this list in the case $m = 3$.

1) Consistency with scalars. If A, B, C commute then $G(A, B, C) = (ABC)^{\frac{1}{3}}$.
2) Joint homogeneity. $G(\alpha A, \beta B, \gamma C) = (\alpha\beta\gamma)^{\frac{1}{3}}G(A, B, C)$, for α, β, $\gamma > 0$.
3) Permutation invariance. For any permutation $\pi(A, B, C)$ of (A, B, C), it holds that $G(A, B, C) = G(\pi(A, B, C))$.
4) Monotonicity. If $A \ge A_0$, $B \ge B_0$, and $C \ge C_0$, then $G(A, B, C) \ge G(A_0, B_0, C_0)$.
5) Continuity from above. If $\{A_n\}$, $\{B_n\}$, $\{C_n\}$ are monotonic decreasing sequences converging to A, B, C, respectively, then $\{G(A_n, B_n, C_n)\}$ converges to $G(A, B, C)$.
6) Congruence invariance. For any invertible S, it holds that
$$G(S^*AS, S^*BS, S^*CS) = S^*G(A, B, C)S.$$
7) Joint concavity. For $0 < \lambda < 1$,
$$\begin{aligned} &G(\lambda A_1 + (1-\lambda)A_2, \lambda B_1 + (1-\lambda)B_2, \lambda C_1 + (1-\lambda)C_2) \\ &\qquad \ge \lambda G(A_1, B_1, C_1) + (1-\lambda)G(A_2, B_2, C_2). \end{aligned}$$
8) Self-duality. $G(A^{-1}, B^{-1}, C^{-1}) = (G(A, B, C))^{-1}$.
9) Determinant identity.
$$\det G(A, B, C) = (\det A \det B \det C)^{\frac{1}{3}}.$$
10) Harmonic-geometric-arithmetic mean inequality.
$$(\frac{A^{-1} + B^{-1} + C^{-1}}{3})^{-1} \le G(A, B, C) \le \frac{A + B + C}{3}.$$

They also give a definition of geometric mean of m matrices by a iteration. Denote $G_2(A_1, A_2) = A_1 \# A_2$ and suppose the mean G_{m-1} of $m-1$ matrices is already defined. Given $A_1, \ldots, A_m$, define m sequences by

$$A_i^{j+1} = G_{m-1}(A_1^j, A_2^j, \ldots, A_{i-1}^j, A_{i+1}^j, \ldots, A_m^j)$$

for $j = 1, 2, \ldots$ and $A_i^1 = A_i$. They proved that the sequences $\{A_i^j\}_{j=1}^{\infty}$ converge to a common matrix which satisfy the ALM properties. We denote by G_m^{ALM}.

ISBN: 978-1-61804-219-4

V. Conclusion

So far, we state the proof of our main theorem. That is, the geometric mean is the middle point of the geodesic. This allows us to find the real meaning geometrically.

Consider the ALM geometric mean G_m^{ALM}, when $m = 3$, another geometric mean is defined in the same way by Bini, Meini and Poloni [9] which denote by G_3^{BMP}, but the iteration is replaced by

$$A_1^{j+1} = G_2(A_2^j, A_3^j)\#_{\frac{1}{3}} A_1^j,$$
$$A_2^{j+1} = G_2(A_1^j, A_3^j)\#_{\frac{1}{3}} A_2^j,$$
$$A_3^{j+1} = G_2(A_1^j, A_2^j)\#_{\frac{1}{3}} A_3^j,$$

where $A\#_t B$ is defined by $A^{\frac{1}{2}}(A^{-\frac{1}{2}}BA^{-\frac{1}{2}})^t A^{\frac{1}{2}}$. it has been proved that the three matrix sequences have common limit which is different from the G_3^{ALM}, and satisfies the ALM properties.

The idea which the geometric mean can be view as the middle point of a geodesic is a very important result. In fact, for two positive numbers, we know that the arithmetic mean is the middle point of the geodesic connect these two scalar. In addition, for m positive numbers, the arithmetic mean minimizes the sum of the squared distances to the given points x_k

$$\bar{x} = \frac{1}{m}\sum_{k=1}^{m} x_k = \text{argmin}_{x>0} \sum_{k=1}^{m} \text{d}_e^2(x, x_k),$$

where $\text{d}_e(x, y) = |x - y|$ is the Euclidean distance in $\mathbb{R}$, and the geometric mean also minimizes the sum of the squared hyperbolic distances to the given points x_k

$$\tilde{x} = \sqrt[m]{x_1 x_2 \cdots x_m} = \text{argmin}_{x>0} \sum_{k=1}^{m} \text{d}_h^2(x, x_k),$$

where $\text{d}_h(x, y) = |\log x - \log y|$ is the hyperbolic distance between x and y on positive number. So Moakher [14] and Bhatia and Holroo [7] given a definition of geometric mean of m positive definite matrices $A_1, \ldots, A_m$ which is defined by

$$G(A_1, \ldots, A_m) = \text{argmin}_{X \in P_n} \sum_{j=1}^{m} \delta_2^2(X, A_j)$$

. We call $G(A_1, \ldots, A_m)$ the barycenter or the center of mass. It can be show that there is a unique X_0 such that $\sum_{j=1}^{m} \delta_2^2(X, A_j)$ is minimised. When $m = 2$, we have $G(A, B) = A\#B$.

In fact, the barycenter also satisfies the ALM properties and is not always the same as G_m^{ALM}. So there are many different geometric mean which satisfy the ALM properties.

The barycenter mean has been used in diverse applications such as elasticity, signal processing, medical imaging and computer vision. The explicit formula for the barycenter mean is still unknown.

Acknowledgment

The authors would like to thank the Taiwan National Science Council for partially financial support for this work.

References

[1] T. Ando, *Concavity of certain maps on positive definite matrices and applications to Hadamard products*, Linear Algebra and its Applications, Vol. 26, (1979), 203-241.

[2] T. Ando, C.-K. Li, and R. Mathias, *Geometric means*, Linear algebra and its applications, Vol. 385, (2004), 305-334.

[3] S. Amari, and H. Nagaoka, *Methods of information geometry*, American Mathematical Society, 2000.

[4] W. N. Anderson, and G. E. Trapp, *Operator means and electrical networks*, Proc. 1980 IEEE International Symposium on Circuits and Systems, (1980), 523-527.

[5] R. Bhatia, *Matrix analysis*, Springer, 1997.

[6] R. Bhatia, *Positive definite matrices*, Princeton University Press, 2009.

[7] R. Bhatia, and J. Holbrook, *Riemannian geometry and matrix geometric means*, Linear algebra and its applications, Vol. 413, No. 2, (2006), 594-618.

[8] R. Bhatia, and R. L. Karandikar, *Monotonicity of the matrix geometric mean*, Mathematische Annalen, Vol. 353, No. 4, (2012), 1453-1467.

[9] D. Bini, B. Meini, and F. Poloni, *An effective matrix geometric mean satisfying the Ando-Li-Mathias properties*, Mathematics of Computation, Vol. 79, No. 269, (2010), 437-452.

[10] M. P. Do Carmo, *Riemannian geometry*, Birkhäuser Boston, 1992.

[11] Y. Eidelman, V. D. Milman, and A Tsolomitis, *Functional analysis: an introduction*, American Mathematical Society, 2004.

[12] F. Kubo, and T. Ando, *Means of positive linear operators*, Mathematische Annalen, Vol. 246, No. 3, (1980), 205-224.

[13] J. D. Lawson, and Y. Lim, *The geometric mean, matrices, metrics, and more*, The American Mathematical Monthly, Vol. 108, No. 9, (2001), 797-812.

[14] M. Moakher, *A differential geometric approach to the geometric mean of symmetric positive-definite matrices*, SIAM Journal on Matrix Analysis and Applications, Vol. 26, No. 3, (2005), 735-747.

[15] D. Petz, *Matrix Analysiis with some Applications*,

[16] D. Petz, *Means of positive matrices: Geometry and a conjecture*, Annales Mathematicae et Informaticae, Vol. 32, (2005), 129-139.

[17] W. Pusz, and S. L. Woronowicz, *Functional calculus for sesquilinear forms and the purification map*, Vol. 8, No. 2, (1975), 159-170.

[18] C. R. Rao, *Information and accuracy attainable in the estimation of statistical parameters*, Bulletin of the Calcutta Mathematical Society, Vol. 37, No. 3, (1945), 81-91.

[19] M. Schechter, *Principles of functional analysis*, American Mathematical Society, 2002.

[20] L. T. Skovgaard, *A Riemannian geometry of the multivariate normal model*, Scandinavian Journal of Statistics, Vol. 11, (1984), 211-223.

Two Methods of Obtaining a Minimal Upper Estimate for the Error Probability of the Restoring Formal Neuron

A. I. Prangishvili, O. M. Namicheishvili, M. A. Gogiashvili

***Abstract*—**It is shown that a minimal upper estimate for the error probability of the formal neuron, when the latter is used as a restoring (decision) element, can be obtained by the Laplace transform of the convolution of functions as well as by means of the generating function of the factorial moment of the sum of independent random variables. It is proved that in both cases the obtained minimal upper estimates are absolutely identical.

***Keywords*—**generating function, probability of signal restoration error, restoring neuron, upper estimate.

I. Introduction

LET us consider the formal neuron, to the inputs of which different versions $X_1, X_2, \ldots, X_n, X_{n+1}$ of one and the same random binary signal X arrive via the binary channels $B_1, B_2, \ldots, B_n, B_{n+1}$ with different error probabilities $q_i \left(i = \overline{1, n+1}\right)$, and the neuron must restore the correct input signal X or, in other words, make a decision Y using the versions $X_1, X_2, \ldots, X_n, X_{n+1}$. When the binary signal X arrives at the inputs of the restoring element via the channels of equal reliability, the decision-making, in which some value prevails among the signal versions, i.e. the decision-making by the majority principle, was for the first time described by J. von Neumann [1], and later V. I. Varshavski [2] generalized this principle to redundant analog systems.

In the case of input channels with different reliabilities, adaptation of the formal neuron is needed in order to restore the correct signal. Adaptation is interpreted as the control process of weights $a_i \left(i = \overline{1, n+1}\right)$ of the neuron inputs, which makes these weights match the current probabilities $q_i \left(i = \overline{1, n+1}\right)$ of the input channels. The purpose of this control is to make inputs of high reliability to exert more influence on decision-making (i.e. on the restoration of the correct signal) as compared with inputs of low reliability. Restoration is carried out by vote-weighting by the relation

$$Y = \operatorname{sgn}\left(\sum_{i=1}^{n+1} a_i X_i\right) = \operatorname{sgn} Z\,, \tag{1}$$

where

$$Z = \sum_{i=1}^{n+1} a_i X_i\ . \tag{2}$$

Both the input signal X and its versions $X_i (i = \overline{1, n})$ are considered as binary random variables coded by the logical values $(+1)$ and (-1). It is formally assumed that the threshold Θ of the restoring neuron is introduced into consideration by means of the identity $\Theta \equiv a_{n+1}$, where $(-\infty < a_{n+1} < \infty)$ and the signal $X_{n+1} \equiv -1$. The main point of this formalism is that the signal $X_{n+1} \equiv -1$ is dumped from some imaginary binary input B_{n+1} for any value of the input signal X, whereas the value q_{n+1} is the a priori probability of occurrence of the signal $X = +1$ or, which is the same, the error probability of the channel B_{n+1}. Quite a vast literature [3—7] is dedicated to threshold logic which takes into consideration the varying reliability of channels, but in this paper we express our viewpoint in the spirit of the ideas of W. Pierce [8].

Let us further assume that

$$\operatorname{sgn} Z = \begin{cases} -1 & \text{if } Z < 0 \\ +1 & \text{if } Z \geq 0 \end{cases}. \tag{3}$$

When $Z = 0$, the solution Y at the output of the restoring formal neuron has the form +1 according to (3). The probability that the restored value Y of the signal X is not correct is expressed by the formula

$$Q = \operatorname{Prob}\{Y \neq X\} = \operatorname{Prob}\{\eta < 0\}\,. \tag{4}$$

Here $\eta = XZ$ is a discrete random variable with probability distribution density $f(v)$. This variable is the sum

This work is performed according to plan of joint research of the Georgian Technical University and Georgian University of the Patriarchate of Georgia.

A. I. Prangishvili is with the Faculty of Informatics and Control Systems in Georgian Technical University, 0171 Tbilisi, Georgia (e-mail: a_prangi@gtu.ge).

O. M. Namicheishvili is with the Faculty of Informatics and Control Systems in Georgian Technical University 0171 Tbilisi, Georgia (e-mail: o.namicheishvili@gtu.ge).

M. A. Gogiashvili is with the School (Faculty) of Informatics, Mathematics and Natural Sciences in St. Andrew the First-Called Georgian University of the Patriarchate of Georgia, 0162 Tbilisi, Georgia (e-mail: maia.gogiashvili@yahoo.com).

of independent discrete variables $\eta_i = a_i XX_i$, and the function $f_i(v_i)$ describes the probability distribution density of individual summands η_i. For the realizations of random variables η and η_i we introduce the symbols v and v_i, respectively.

It is easy to observe that the variable η_i takes the values $+a_i$ and $-a_i$ with probabilities $1-q_i$ and q_i, respectively. Therefore, if we use the Dirac delta function $\delta(t)$, then the probability density $f_i(v_i)$ can be represented as follows

$$\left.\begin{array}{l} f_i(v_i) = (1-q_i)\delta(v_i - a_i) + q_i\delta(v_i + a_i) \\ v_i = +a_i, -a_i \\ i = \overline{1, n+1} \end{array}\right\}. \qquad (5)$$

Such formalism is completely justified and frequently used due to the following two properties of the delta-function

$$\left.\begin{array}{l} \delta(t) \ge 0, \forall t \in \mathbb{R} \\ \int_{-\infty}^{+\infty} \delta(t)dt = 1 \end{array}\right\}.$$

However $f_i(v_i)$ can also be represented as

$$\left.\begin{array}{l} f_i(v_i) = q_i^{(a_i - v_i)/2a_i} \cdot (1-q_i)^{(a_i + v_i)/2a_i} \\ v_i = +a_i, -a_i \\ i = \overline{1, n+1} \end{array}\right\}. \qquad (6)$$

The random variable η is the sum of independent discrete random variables η_i. Its distribution density $f(v)$ can be defined in the form of convolution of probability distribution densities of summands $f_i(v_i)$:

$$f(v) = \overset{n+1}{\underset{i=1}{*}} f_i(v_i), \qquad (7)$$

where $*$ (superposition of the addition and multiplication signs) is the convolution symbol.

It is obvious that in view of formula (7) the error probability at the decision element output can be written in two equivalent forms

$$\begin{array}{l} Q = \mathrm{Prob}(v < 0) = \int_{-\infty}^{0} f(v)dv = \int_{-\infty}^{0} \overset{n+1}{\underset{i=1}{*}} f_i(v_i)dv = \\ = \int_{-\infty}^{0} \overset{n+1}{\underset{i=1}{*}} \left[(1-q_i)\delta(v_i - a_i) + q_i\delta(v_i + a_i)\right]dv \end{array} \qquad (8)$$

and

$$\begin{array}{l} Q = \sum_{v<0} f(v) = \sum_{v<0} \overset{n+1}{\underset{i=1}{*}} f_i(v_i) = \\ = \sum_{v<0} \overset{n+1}{\underset{i=1}{*}} \left[q_i^{(a_i - v_i)/2a_i} \cdot (1-q_i)^{(a_i + v_i)/2a_i}\right], \end{array} \qquad (9)$$

where the probability distribution density $f_i(v_i)$ is defined by (5) in the first case and by (6) in the second case. Integration or summation in both cases is carried out continuously or discretely over all negative values of the variable v. Formulas (8) and (9) give an exact value of the error probability of restoration of a binary signal by the formal neuron.

Note that for practical calculations, formula (9) can be written in a more convenient form. Indeed, the complete number of discrete values of the variable v is 2^{n+1} since

$$v = \widetilde{a}_1 + \widetilde{a}_2 + \cdots + \widetilde{a}_n + \widetilde{a}_{n+1},$$

where $\widetilde{a}_i$ is equal either to $+(a_i)$ or to $-(a_i)$, whereas the proper sign of the weight a_i is meant to be within the round brackets.

By formula (9), to each discrete value of the sum v there corresponds the term Q_j ($j = \overline{1, 2^{n+1}}$) which is the product of $(n+1)$ co-factors of the form q_k or $(1-q_k)$.

In particular

$$\left.\begin{array}{l} Q_j \equiv f(v) = \overset{n+1}{\underset{i=1}{*}} f_i(v_i) \equiv \widetilde{q}_1 \cdot \widetilde{q}_2 \cdot \cdots \widetilde{q}_n \cdot \widetilde{q}_{n+1} \\ j = \overline{1, 2^{n+1}} \end{array}\right\},$$

where

$$\widetilde{q}_k = \begin{cases} q_k & \text{if} \quad v_k = -(a_k) \\ 1-q_k & \text{if} \quad v_k = +(a_k) \end{cases}$$

for any $k\left(k = \overline{1, n+1}\right)$.

Thus formula (9) can also be written in the form

$$Q = \sum_{v<0} Q_j = \sum_{v<0} \widetilde{q}_1 \cdot \widetilde{q}_2 \cdot \cdots \cdot \widetilde{q}_n \cdot \widetilde{q}_{n+1}, \qquad (10)$$

which is more adequate for cognitive perception and practical realization.

II. FINDING A MINIMAL UPPER ESTIMATE BY THE FIRST METHOD

From the expression

$$Q = \mathrm{Prob}(\eta < 0) = \int_{-\infty}^{0} f(v)dv$$

it follows that for a real positive number s ($s > 0$)

$$Q \le \int_{-\infty}^{0} e^{-sv} f(v)dv \le \int_{-\infty}^{\infty} e^{-sv} f(v)dv.$$

But the left-hand part of this inequality is the Laplace transform of the function $f(v)$

$$\mathfrak{L}[f(v)] = \int_{-\infty}^{\infty} e^{-sv} f(v)dv,$$

where $\mathfrak{L}$ is the Laplace transform operator.

Therefore

$$Q \le \mathfrak{L}[f(v)]. \qquad (11)$$

The random value η with realizations v is the sum of independent random variables η_i having realizations v_i. In that case, as is known, the Laplace transform for the convolution $f(v)$ of functions $f_i(v_i)$ is equal to the product of Laplace transforms of convoluted functions:

$$\mathfrak{L}[f(v)] = \prod_{i=1}^{n+1} \mathfrak{L}[f_i(v_i)].$$

The latter implies that

$$Q \le \prod_{i=1}^{n+1} \mathfrak{L}[f_i(v_i)]. \qquad (12)$$

By expression (5) for functions $f_i(v_i)$ and the Laplace transform definition, we obtain

$$\mathfrak{L}[f_i(v_i)] = \int_{-\infty}^{\infty} e^{-sv_i} f_i(v_i) dv_i = \\ = \int_{-\infty}^{\infty} e^{-sv_i} \left[(1-q_i)\delta(v_i - a_i) + q_i \delta(v_i + a_i)\right] dv_i .$$

Using this expression in formula (12) we have

$$Q \le \prod_{i=1}^{n+1} \int_{-\infty}^{\infty} e^{-sv_i} \left[(1-q_i)\delta(v_i - a_i) + q_i \delta(v_i + a_i)\right] dv_i . \qquad (13)$$

Here we should make use of one more property of the Dirac delta function

$$\int_{-\infty}^{\infty} g(t)\delta(t - t_0) dt = g(t_0).$$

With this property taken into account, from formula (13) we obtain

$$Q \le \prod_{i=1}^{n+1} \left[(1-q_i)e^{-a_i s} + q_i e^{+a_i s}\right]. \qquad (14)$$

Here s, as mentioned above, is an arbitrary real positive number. Before we continue simplifying the right-hand part of inequality (14), we have to define a value of s for which expression (14) gives *a minimal upper estimate*.

Passing to the natural logarithm of inequality (14) we come to the expression

$$\ln Q \le \sum_{i=1}^{n+1} \ln\left[(1-q_i)e^{-a_i s} + q_i e^{+a_i s}\right].$$

Let us define here partial derivatives with respect to arguments a_i by using the elementary fact that

$$y' = \frac{dy}{dx} = f'(x) \cdot e^{f(x)}$$

if $y = e^{f(x)}$, and also the fact that $\frac{d}{dx} \ln f(x) = f'(x) \cdot \frac{1}{f(x)}$.

Hence we obtain

$$\frac{\partial \ln Q}{\partial a_i} \le \sum_{i=1}^{n+1} \frac{1}{[(1-q_i)e^{-a_i s} + q_i e^{+a_i s}]} \cdot [s q_i e^{+a_i s} - s(1-q_i)e^{-a_i s}].$$

For the right-hand part of this inequality to be equal to zero, it suffices that the following condition be fulfilled

$$s q_i e^{+a_i s} - s(1-q_i)e^{-a_i s} = 0,$$

whence it follows that

$$e^{+2a_i s} = \frac{1-q_i}{q_i},$$

or, which is the same,

$$a_i s = \frac{1}{2} \ln \frac{1-q_i}{q_i}.$$

If the weights a_i of the neuron inputs are put into correspondence with error probabilities q_i of these inputs by the relations

$$a_i = \ln \frac{1-q_i}{q_i}, \qquad (15)$$

then the sought value of s will be

$$s = \frac{1}{2}. \qquad (16)$$

Using equality (16) in formula (14), we obtain a minimal upper estimate for the error probability Q of the restoring neuron. Indeed, for the right-hand part of expression (14) the following chain of identical transforms is valid:

$$q_i e^{\frac{a_i}{2}} + (1-q_i)e^{-\frac{a_i}{2}} = 2\sqrt{q_i(1-q_i)} \cdot \frac{q_i e^{\frac{a_i}{2}} + (1-q_i)e^{-\frac{a_i}{2}}}{2\sqrt{q_i(1-q_i)}} = \\ = 2\sqrt{q_i(1-q_i)} \cdot \frac{\sqrt{\frac{q_i}{1-q_i}} \cdot e^{\frac{a_i}{2}} + \sqrt{\frac{1-q_i}{q_i}} \cdot e^{-\frac{a_i}{2}}}{2}.$$

Let us take into account here that

$$\left.\begin{aligned} \sqrt{\frac{q_i}{1-q_i}} &= \exp\left[\ln\left(\sqrt{\frac{q_i}{1-q_i}}\right)\right] = \exp\left[-\frac{1}{2}\ln\frac{1-q_i}{q_i}\right] \\ \sqrt{\frac{1-q_i}{q_i}} &= \exp\left[\ln\left(\sqrt{\frac{1-q_i}{q_i}}\right)\right] = \exp\left[+\frac{1}{2}\ln\frac{1-q_i}{q_i}\right] \end{aligned}\right\}.$$

Besides, we denote

$$\frac{1}{2}\left(a_i - \ln\frac{1-q_i}{q_i}\right) = \lambda_i.$$

Then we have

$$q_i e^{\frac{a_i}{2}} + (1-q_i)e^{-\frac{a_i}{2}} = 2\sqrt{q_i(1-q_i)} \cdot \frac{e^{\lambda_i} + e^{-\lambda_i}}{2}.$$

The second co-factor in the right-hand part of this expression is the hypebolic cosine of the argument λ_i:

$$\frac{e^{\lambda_i} + e^{-\lambda_i}}{2} = \operatorname{ch} \lambda_i.$$

Therefore

$$q_i e^{\frac{a_i}{2}} + (1-q_i)e^{-\frac{a_i}{2}} = 2\sqrt{q_i(1-q_i)} \cdot \operatorname{ch} \lambda_i = \\ = 2\sqrt{q_i(1-q_i)} \cdot \operatorname{ch}\left(\frac{a_i - \ln\frac{1-q_i}{q_i}}{2}\right).$$

Finally, for estimate (14) we can write

$$Q \le \prod_{i=1}^{n+1} \left\{2\sqrt{q_i(1-q_i)} \cdot \operatorname{ch}\left(\frac{a_i - \ln\frac{1-q_i}{q_i}}{2}\right)\right\}.$$

For the error probability Q, the right-hand part of the above inequality is the upper estimate Q^+:

$$Q^+ = \prod_{i=1}^{n+1}\left[2\sqrt{q_i(1-q_i)}\cdot \mathrm{ch}\left(\frac{a_i - \ln\frac{1-q_i}{q_i}}{2}\right)\right].$$

The minimum $Q^+_{\min}$ of this upper estimate Q^+ is equal to

$$Q^+_{\min} = \prod_{i=1}^{n+1}\left[2\sqrt{q_i(1-q_i)}\right] = 2^{n+1}\cdot\prod_{i=1}^{n+1}\left[\sqrt{q_i(1-q_i)}\right]. \quad (17)$$

It is attained when for the zero argument the hyperbolic cosine attains the minimum equal to 1.

This estimate confirms in a certain sense the advantage of the choice of weights of the restoring neuron in compliance with the error probabilities of input signals according to the following relations

$$\left.\begin{array}{l} a_i = \ln\dfrac{1-q_i}{q_i} \\ i = \overline{1,n+1} \end{array}\right\}.$$

III. OBTAINING A MINIMAL UPPER ESTIMATE BY THE SECOND METHOD

Simulteously, for the probability Q it is useful to obtain a minimal upper estimate in the closed analytic form by one more new approach.

As is known [9], the generating function $\gamma_v(S)$ of the factorial moment of the sum η of independent random variables η_i is equal to the product of generating functions $\gamma_{v_i}(S)$ of the factorial moments of individual summands, i.e.

$$\gamma_v(S) = \prod_{i=1}^{n+1}\gamma_{v_i}(S), \quad (18)$$

where

$$\gamma_v(S) = \mathrm{M}\left[S^{\eta}\right] = \sum_v S^v\cdot f(v), \quad (19)$$

$$\left.\begin{array}{l} \gamma_{v_i}(S) = \mathrm{M}\left[S^{\eta_i}\right] = \sum\limits_{v_i} S^{v_i}\cdot f_i(v_i) \\ i = \overline{1,n+1} \end{array}\right\}. \quad (20)$$

Here M is the mathematical expectation symbol and S is an arbitrary complex number for which series (19) and (20) exist on some segment of the real axis containing the point $S=1$.

Since in relation (20), summation is carried out on the set of two possible values $+a_i$ and $-a_i$ of the variable v_i, using (6) we have

$$\left.\begin{array}{l} \gamma_{v_i}(S) = (1-q_i)S^{a_i} + q_iS^{-a_i} \\ i = \overline{1,n+1} \end{array}\right\}. \quad (21)$$

The substitution of (21) into relation (18) gives

$$\gamma_v(S) = \prod_{i=1}^{n+1}\left[(1-q_i)S^{a_i} + q_iS^{-a_i}\right].$$

When $v<0$, the value S^v satisfies the condition

$$S^v = \frac{1}{S^{(v(}} > 1,$$

if of course

$$0 < S < 1. \quad (22)$$

Let us assume that inequality (22) is fulfilled. Then the following relation is valid:

$$Q = \sum_{v<0} f(v) < \sum_{v<0} S^v\cdot f(v).$$

Since every summand $S^v\cdot f(v)$ is non-negative, we have the inequality

$$\sum_{v<0} S^v f(v) \le \sum_v S^v\cdot f(v).$$

Therefore

$$Q < \gamma_v(S). \quad (23)$$

The right-hand part of this expression can be taken as the upper estimate Q^+ of the error probability Q of the restoring neuron

$$Q^+ = \prod_{i=1}^{n+1}\left[(1-q_i)S^{a_i} + q_iS^{-a_i}\right].$$

The latter relation is easily rewritten in the equivalent form

$$Q^+ = \prod_{i=1}^{n+1}Q_i^+ = \prod_{i=1}^{n+1}\left[(1-q_i)w_i + \frac{q_i}{w_i}\right], \quad (24)$$

where

$$Q_i^+ = (1-q_i)w_i + \frac{q_i}{w_i}$$

and, along with this,

$$w_i = S^{a_i}, 0 < w_i < \infty, (i = \overline{1,n+1}). \quad (25)$$

Now we can find the minimum $Q^+_{\min}$ of expression (24) and the value w_{0i} of w_i will attach a minimum to the upper estimate of the error probability Q^+ of the restoring neuron. For this, we use the conditions

$$\left.\begin{array}{l} \dfrac{\partial Q^+}{\partial w_i} = 0 \\ i = \overline{1,n+1} \end{array}\right\}.$$

Hence

$$w_{0i} = \sqrt{\frac{q_i}{1-q_i}}, \ (i = \overline{1,n+1}). \quad (26)$$

If (26) is substituted into expression (24), then by the second method for a minimal upper estimate of the error probability of the restoring neuron we obtain the relation

$$Q^+_{\min} = 2^{n+1}\cdot\prod_{i=1}^{n+1}\left[\sqrt{q_i(1-q_i)}\right], \quad (27)$$

which coincides with result (17) obtained by the first method.

The weights $a_i (i = \overline{1,n+1})$ which match the error probabilities $q_i \left(i = \overline{1,n+1}\right)$ are defined from relations (26) with notation (25) taken into account:

$$\left.\begin{array}{l} a_i = \dfrac{1}{2\ln S}\cdot \ln\dfrac{q_i}{1-q_i} \\ i=\overline{1,n+1} \end{array}\right\}.$$

Since the value S satisfies condition (22), we have $\ln S < 0$ and therefore

$$\left.\begin{array}{l} a_i = K\cdot \ln\dfrac{1-q_i}{q_i} \\ i=\overline{1,n+1} \end{array}\right\}, \qquad (28)$$

where

$$\left.\begin{array}{l} K = \dfrac{1}{2\left|\ln S\right|} \\ 0<K<\infty \end{array}\right\}. \qquad (29)$$

Thus, the weights $a_i (i=\overline{1,n+1})$, which are consistent with the error probabilities $q_i \left(i=\overline{1,n+1}\right)$ and attach a minimum to the upper estimate of the error probability of the restoring neuron, are defined to within the a general positive factor K.

IV. Conclusion

A minimal upper estimate of the error probability of the restoring formal neuron is defined by formula (17) or, which is the same, by formula (27). In both cases the result can be written in the form

$$Q^{+}_{\min} = \exp\left(-\sum_{i=1}^{n+1} A(q_i)\right), \qquad (30)$$

where

$$A(q_i) = \left|\ln\left[2\sqrt{q_i(1-q_i)}\right]\right|. \qquad (31)$$

In view of relations (31) confirming the non-negativity of the values $A(q_i)$, formula (30) implies that an increase of the number n of inputs of the formal decision neuron bings about a monotone decrease of the minimal upper estimate of the error probability of restoration of the binary signal $Q^{+}_{\min}$ by the exponential law if, certainly, the error probabilities $q_i \left(i=\overline{1,n+1}\right)$ at these inputs are not equal to $\frac{1}{2}$ when the minimal upper estimate of the error probability $Q^{+}_{\min}$ is equal to 1.

This result is demonstrates an essenatial inner connection with Shannon's theorem [10]. According to this theorem, the number of messages of length n (duration τ) composed of individual symbols – both in the absence and in the presence of fixed and probabilistic constraints (in the latter case it is assumed that the source is ergodic) – grows by the asymptotically exponential law as n (or τ) increases. In particular we understand this connection as follows: as the number n of inputs of the restoring formal neuron increases, the initial information to be used in making the decision Y increases by the exponential law if there are a number of possible versions of the input signal, while the minimal upper estimate $Q^{+}_{\min}$ of the probability Q that the made decision is erroneous decreases by the same exponential law.

References

[1] J. Neumann, "Probabilistic logics and synthesis of reliable organisms from unreliable components", in *Automata Studies: Annals of Mathematics Studies*, no. 34 (in Russian, translated from English), Moscow: Publishing House for foreign literature IIL, 1956, pp. 68-139.

[2] I. Varshavsky "Functional Possibilities and Synthesis of Threshold Elements" (in Russian), *Dokl. AN SSSR*, vol. 139, no. 5, pp. 1071-1074, 1961.

[3] M. Dertouzos *Threshold logic* (in Russian, translated from English). Moscow: Mir, 1966.

[4] C. R. Lageweg, S. D. Cotofana, S. Vassiliadis, "A full adder implementation using set based linear threshold gates", in *Proc. 9th IEEE International Conference on Electronics, Circuits and Systems*, New York, 2002, pp. 665–669.

[5] V. Beiu, J. M. Quintana, M. J. Avedillo, "VLSI Implementation of threshold Logic: A Comprehensive Survey", *IEEE Trans. Neural Networks*, vol.. 14, pp. 1217–1243, May 2003.

[6] R. Zhang, P. Gupta, L. Zhong, N. K. Jha, "Threshold Network Synthesis and Optimization and Its Application to Nanotechnologies", *IEEE Transaction On Computer-Aided Design Of Integrated Circuits And Systems*, vol. 24, pp. 107–118, January 2005.

[7] T. Gowda, S. Vrudhula, N. Kulkarni, K. Berezowski, "Identification of Threshold Functions and Synthesis of Threshold Networks", *IEEE Transactions on Computer-Aided Design Of Integrated Circuits And Systems*, vol. 30, pp. 665-677, May 2011.

[8] W. Pierce, *Failure-tolerant computer design* (in Russian, translated from English), Moscow: Mir, 1968.

[9] G. A. Korn, T. M. Korn, *Mathematical handbook for scientists and engineers* (in Russian, translated from English), Moscow: Nauka, 1977, p. 832

[10] S. Goldman, *Information theory* (in Russian, translated from English), Moscow: Publishing House for foreign literature IIL, 1957.

About Development of the Aggregate Mathematical Models for Complex Non-Linear Systems with Deviated Arguments

Jamshid Gharakhanlou, Oleksandr V. Konoval, Ivan V. Kazachkov

Abstract: - The considered problem has concern to one of the problems on system analysis for nuclear power plants (NPP) in touch with the modelling and simulation of the complex non-linear objects with deviating arguments (e.g. potentially hazardous objects in nuclear power safety including severe accidents at the nuclear power plants). Development and implementation of the aggregate mathematical models for analysis and computer simulations of the passive protection systems against severe accidents and mathematical modelling and simulation of the potentially hazardous objects (PHO) with account of different time shifts accounting the real features of the PHO are analyzed. The methods and results obtained may be of interest for planning and decision making in the field of environmental and other research and practical applications.

Keywords: - Aggregate mathematical model, potentially hazardous object, non-linear dynamical system, deviated arguments, computer simulation, control parameters

1. VITALITY OF THE PROBLEM

Problem of a development of the aggregate mathematical models for analysis and simulation of the different complex systems (inviroment, industry, nuclear power safety, etc.) is of paramount interest for the modern computer modelling and simulation tasks.

Importance of such models and computer simulations with their use is due to prediction of any available negative environmental influence of the PHO, searching both positive as well as negative unknown properties of the complex systems. For example, simulation of the potentially hazardous objects is considered in touch with a need of a tactical and strategic planning and decision making support in a lot of the environmental and other tasks for analysis the peculiarities of the real systems with account of different time delays and time forecasting terms as peculiarities of the real systems.

Development of the aggregate mathematical models for complex systems with deviating arguments provided the possibilities to systematic investigation of the crucial situations in their evolution and peculiarities in controlling parameters: singularities of solutions, bifurcations of the regimes, catastrophes, etc. Certainly the results obtained have concern to the other dynamical systems of similar type [1-3].

In general, the aggregate dynamical models for complex non-linear systems are considered in touch with potentially hazardous objects (for instance, assessment of the nuclear power safety and other type hazards).

A number of physical processes, e.g. from severe accidents at the NPPs [4-11], peculiarities of the penetration dynamics of a liquid corium jet into the other liquid medium of coolant, vapour flow, etc. are dependent on some deviating arguments, for example delays in time by action of some parameters.

Differential equations of the model have been analyzed and computer simulation has been presented. Base for such investigation is statistical data on the objects functioning, as well as some information about deviating arguments (time delays by any parameters and time forecasts). Both are of importance to get closer to the real systems with their specific features.

Also a number of the other physical processes, e.g. peculiarities of the penetration dynamics of a liquid corium jet into the other liquid (coolant, vapour flow, etc.) are dependent on some deviating arguments, for example, time delays by some parameters [5, 6, 8-11].

2. TO THE STATEMENT OF THE PROBLEM

The non-linear complex systems of diverse nature could be considered as statistical dynamical systems that consist of a number of different parameters, which are interconnected. The PHO is too complicated dynamical system for deterministic modelling, it is reasonable constructing the aggregate model based on the statistical data.

Differential equations for different kind of such cases are analyzed and available time deviating arguments are found and disputed [1-9]. The aggregate models for potentially hazardous objects with time shifts are considered in touch with estimation of the nuclear power safety, forecasts and revealing the critical features to be studied and managed.

The other types of hazardous, critical or specific situations and computer simulation has been presented for the case of jet penetration dynamics into the pool of volatile coolant, with time shifts (delays and forecasts for diverse parameters) and without them.

The possibility for model application to tactical and strategic planning of the objects' development is discussed. Analysis of the shifted arguments and their influence on the model behaviors are presented.

2.1. DEVELOPMENT OF THE AGGREGATE MODELS

According to [1, 2], the aggregate dynamical model of the PHO may be represented as follows:

$$\frac{dx_i}{dt} = (N_i - x_i) \cdot (a_{i0} + \sum_{j=1}^{n} a_{ij} \cdot (N_j - x_j)), \qquad (1)$$

where are: $x_i(t)$ - the PHO characteristic parameters, N_i - the limit values of *i*-th parameters, a_{ij} - the coefficients,

which may be the function of time in a general case, *n*- the number of parameters of the PHO, *i=1,2..n.* Here the parameters x_i are [1]: x_1 - number of the workers, x_2 - number of managers, x_3 - total amount of product, x_4 - expenditures for the repairing, x_5 - for elimination of negative influence on the environment, x_6 - the safety culture level.

2.1.1. PARAMETERS OF THE MODELS

According to the problem stated (tactical or strategic planning, calculation of the dynamic evolution of the parameters, etc.) the limit values N_i may vary.

The non-linear ordinary differential equation array (1) with the corresponding initial data allowed conducting the simulation of PHO determining the peculiarities of evolution in time until the achievement of the planning values or any kind of other regimes, for example saturation, critical points in the system, catastrophes, etc.

The variables may change in the range from 0 to N_i (N_6=1 is chosen just for simplicity). The first step in a development of the model consists in calculation of the constants in (1) using the statistical data collected. For a lot of diverse PHO this is crucial problem due to absence or uncertainty of the statistical data about its functioning.

A serious problem is the identification of the model, which requires computing the coefficients a_{ij} satisfying the model developed to the real object.

2.1.2. DIMENSIONLESS FORM OF THE MODEL

All variables are divided on their characteristic scales: $y_i = x_i / N_i, b_{ij} = a_{ij} N_j, b_{i0} = a_{i0}, y_6 = x_6$ and equation array (1) is transformed to the form:

$$\begin{aligned}
\frac{dy_1}{dt} &= [b_{10} + b_{11}(1-y_1) + b_{12}(1-y_2) + b_{13}(1-y_3)](1-y_1),\\
\frac{dy_2}{dt} &= [b_{20} + b_{21}(1-y_1) + b_{22}(1-y_2) + b_{23}(1-y_3)](1-y_2),\\
\frac{dy_3}{dt} &= [b_{30} + b_{31}(1-y_1) + b_{32}(1-y_2) + b_{33}(1-y_3) +\\
&\quad + b_{34}(1-y_4) + b_{35}(1-y_5) + b_{36}y_6)](1-y_3)\\
\frac{dy_4}{dt} &= [b_{40} + b_{43}(1-y_3) + b_{44}(1-y_4) +\\
&\quad b_{45}(1-y_5) + b_{46}y_6)](1-y_4)\\
\frac{dy_5}{dt} &= [b_{50} + b_{53}(1-y_3) + b_{54}(1-y_4) +\\
&\quad + b_{55}(1-y_5) + b_{56}y_6)](1-y_5)\\
\frac{dy_6}{dt} &= [b_{60} + b_{61}(1-y_1) + b_{62}(1-y_2) + b_{63}(1-y_3)](1-y_6),
\end{aligned} \qquad (2)$$

where the restriction $N_4 + N_5 \le N_3$ is applied because total amount of expenses (repairing, restoring and elimination of negative consequences to the environment) is less than total product. For the dimensionless time t some characteristic interval T is chosen.

2.2. BASIC FEATURES OF THE MODEL

Coefficients a_{ij} and b_{ij} in the equations (1), (2) are estimated as follows. In a first equation (1) $a_{11} \le 0$, $a_{16} \le 0$, $a_{1j} \ge 0$, *j=2-5*. The more people are working at the object, the more the first term in the first equation (1) decreases further growing rate of the workers. Then $a_{16} \le 0$ due to increase of the safety culture leads a shortcut of the employees with increase of the productivity and safety at the PHO.

Then $a_{1j} \ge 0$, (*j=2-5)* due to the fact that a number of managers, quantity of a product, expenses on the repairing, etc. can only lead to increase of the workers needed. Similarly $a_{21} \ge 0$, $a_{23} \ge 0$, and the rest of the coefficients in the second equation of the system (1) must be negative because only growing of the workers' number and product may result in managers' growing. All other factors result in decrease of the managers' amount. In a third equation only coefficient $a_{33} \le 0$ may be negative because the product growing causes further productivity falling. The other factors act to its growing.

The forth equation gives $a_{44} \le 0$, $a_{46} \le 0$: increase of all expenses tend to their decrease afterwards. And the increase of safety culture makes tendency to decrease of all expenses. In the fifth equation only the last 3 coefficients supposed negative: $a_{5j} \le 0$, *j=4-6*, where $a_{54} \le 0$ because expenses' growing for repairing tend less going to ecology, etc., $a_{55} \le 0$ because if paid for this, then decreases later on.

Further, $a_{56} \le 0$ because grow of the safety culture decreases money for preventing the environmental pollution. The last equation must contain the last three coefficients negative: $a_{6j} \le 0$ (*j=4-6*): the payments for the repairing, etc. influence directly a safety culture: the higher it is, the less are expenditures. And increase of the safety culture depends on its own level.

2.2.1. ESTIMATION OF THE SAFETY LEVEL

According to [1] the indicator of the safety culture is:

$$V = q\frac{1+\alpha_1 y_1 + \beta_1 y_2}{1+\alpha_2 y_1 + \beta_2 y_2} \cdot \frac{y_3 y_4 y_6}{y_5}, \qquad (3)$$

where q characterizes the current level of technology in a society, α_i, β_i - coefficients. The equation (3) shows $V \to 0$ by $y_3, y_4, y_6 \to 0$, and $V \to \infty$ by $y_5 \to 0$. By $y_1, y_2 \to 0$ the indicator of general safety level is determined not only by the personnel amount but also by level of individual and social interests.

2.2.3. THE SHIFTED ARGUMENTS OF THE MODEL

The delays in a system are available for example due to information transfer and processing, etc. Some referring values like achievement of the desired future levels are also available. The time delays τ, in turn, are too some functions of time in general case, which complicate the problem dramatically. For the constant time delays, the model (2) is presented in the form:

$$\begin{aligned}
&\frac{dz_1}{dt} = [b_{10} + b_{11}z_1(t-\tau_{11}) + b_{12}z_2(t-\tau_{12}) + b_{13}z_3(t-\tau_{13})]z_1(t-\tau_{10}),\\
&\frac{dz_2}{dt} = [b_{20} + b_{21}z_1(t-\tau_{21}) + b_{22}z_2(t-\tau_{22}) + b_{23}z_3(t-\tau_{23})]z_2(t-\tau_{20}),\\
&\frac{dz_3}{dt} = [b_{30} + b_{31}z_1(t-\tau_{31}) + b_{32}z_2(t-\tau_{32}) + b_{33}z_3(t-\tau_{33}) +\\
&+b_{34}z_4(t-\tau_{34}) + b_{35}z_5(t-\tau_{35}) + b_{36}z_6(t-\tau_{36})]z_3(t-\tau_{30}),\\
&\frac{dz_4}{dt} = [b_{40} + b_{43}z_3(t-\tau_{43}) + b_{44}z_4(t-\tau_{44}) + \qquad (4)\\
&b_{45}z_5(t-\tau_{45}) + b_{46}z_6(t-\tau_{46})]z_4(t-\tau_{40}),\\
&\frac{dz_5}{dt} = [b_{50} + b_{53}z_3(t-\tau_{53}) + b_{54}z_4(t-\tau_{54}) + b_{55}z_5(t-\tau_{55}) + b_{56}z_6(t-\tau_{56})]z_5(t-\tau_{50}),\\
&\frac{dz_6}{dt} = [b_{60} + b_{61}z_1(t-\tau_{61}) + b_{62}z_2(t-\tau_{62}) +\\
&b_{63}z_3(t-\tau_{63}))]z_6(t-\tau_{60}),
\end{aligned}$$

where τ_{ij} =const, z_i=1-y_i. The mathematical model (4) for the PHO with deviated arguments τ_{ij} describes evolution in time depending on its history. In a similar way the positive time shifts can be introduced to the system (4) with respect to the processes of some planning levels for the future parameters.

2.3. Examples of Calculations by the PHO Aggregate Dynamical Model

Some numerical computer simulations have been performed based on the mathematical model obtained. A few examples given in Figs 1, 2 below show available specific features in the systems, which may be of interest, so that influence of the parameters and their interconnections are important for more in deep investigations. The papameters in Fig. 1 were computed for t>0 while the ones in Fig. 2 were computed for both t>0 and t<0 (prehistory).

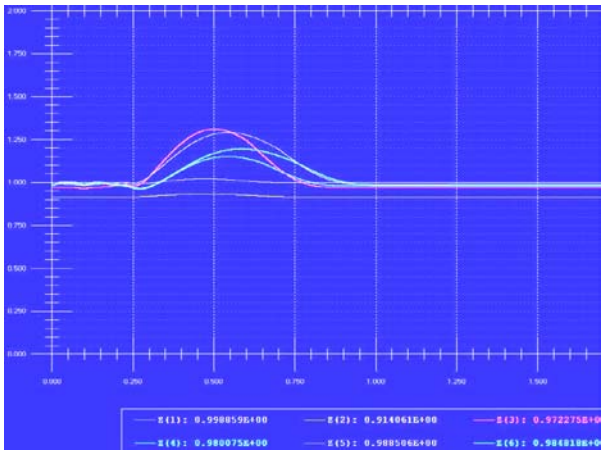

Fig 1. Functions z_i against time t

Functions z_i for t>0 are the results of numerical simulations by the model obtained. And for *prehistory* of the object (t<0) the papameters were computed by the interpolation methods.

The results in Fig. 1 correspond to the case when PHO has some critical regimes, which are gradually approaching the the stable state.

The results presented in Fig. 2 show another case when PHO being very stable (even without any remarkable development) could have very much oscillating prehistory, which might be even dramatic or in some cases catastrophic.

The mathematical model thus developed and the corresponding software done for its realization have shown possibilities for investigation of the features of the different PHO, revealing their critical regimes, specific cases of the parameters' influence on the development of PHO, optimization of the parameters by the criterium stated, etc.

This aggregate dynamical model is of general purpose. The most complex is important problem of the model identification in each specific case of the PHO, which requires detail experimental statistical data about the PHO fuctioning. More concrete problems with modeling and simulation are considered here further on as two scenarios of the severe accidents at the nuclear power plants (NPP), which may be of interest for the development and implementation of the passive protection systems against severe accidents.

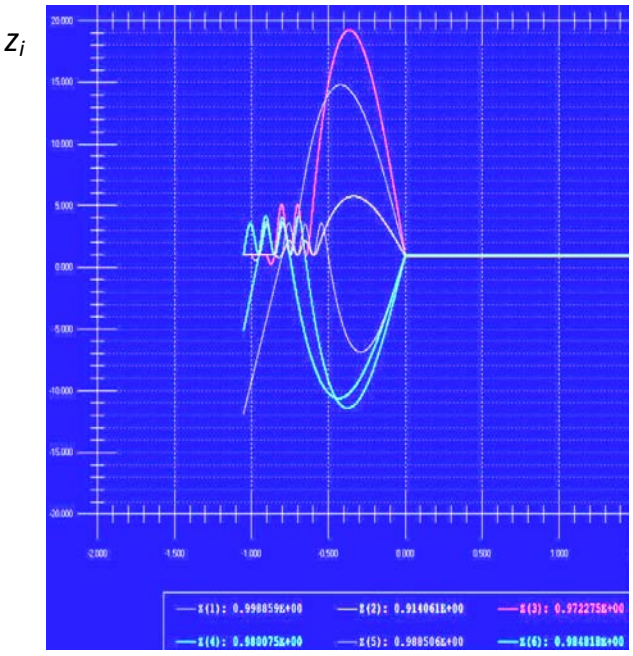

Fig 2. Functions z_i against time t with account of prehistory

2.4. Non-linear Model for the Corium Jet Penetrating Pool of Coolant

One-dimensional non-linear mathematical model for the jet of melted corium penetrating the pool of volatile coolant under the reactor vessel [12], with account of the time delays by parameters may be presented as follows

$$\rho_1 \frac{d(hv_1)}{dt} = (\rho_1 - \rho_2) g h(t-\tau_1) - \beta_c \rho_2 v_1^2 (t-\tau_2), \quad (5)$$

where τ_1, τ_2 are time delays. Here h is a penetration length, $v_1 = dh/dt$ - velocity of penetration, ρ_1, ρ_2 - densities of the jet and pool, respectively, g- acceleration due to gravity, β_c - coefficient.

The melt-water interaction phenomena are important for the conditions governing behaviors of corium coolability inside containment during severe accidents at the NPP, as well as their modeling are analysis. The problem may be of interest for many other industrial and technological situations where interaction of high-temperature melts and solid materials with liquids and vapours mainly predetermine the character of the thermal hydraulic processes and the features of the severe accidents at NPP.

The dimensionless form of the equation (5) may be written as

$$\frac{d(hv_1)}{dt^2} + \beta_c \rho_{2/1} \left(\frac{dh(t-\tau_2)}{dt} \right)^2 + \frac{\rho_{2/1} - 1}{Fr} h(t-\tau_1) = 0. \quad (6)$$

Here Fr is a Foude number and $\rho_{2/1} = \rho_2 / \rho_1$.

The initial condition is stated as

$$t = \tau_2,\ h = 0,\ dh/dt = 1, \quad (7)$$

but for numerical solution of the Cauchy problem (6), (7) it is actually needed to state all the values of the fuctions on the whole interval by τ_2, which is the peculiarity of the problem with time delays.

2.5. Modeling of the Corium Melt Pool Cooling from the Submerged Bottom Nozzles

Based on the method for heterogeneous turbulent jet by Prof. Nakorchevskyi [13] the mathematical models and computer soft have been developed for modeling and simulation of the mixing and cooling in a pool of melted corium by volatile coolant supplied from the bottom as shown in Fig. 3 taken from [14]:

By the results of the volatile coolant jet mixing in a turbulent layer velocity distribution for the coolant and melt were computed and then all the parameters by the corium melt cooling were obtained. The integral flow rate was computed as

$$Q = \frac{\sum_{i=1}^{N} q(x_i)(x_i - x_{i-1})}{H}, \quad (8)$$

where $q(x_i)$ is the ejection coefficient in the jet mixing layer, x_i – the point by coordinate x directed by a jet movement, H- the height of the corium layer, N- the number of the calculation point in numerical simulation.

The time for coolant flow in a corium melt layer was computed according to relation $\Delta t = H/u$, where u – average velocity of the coolant in a mixing layer:

$$u = \frac{\sum_{i=1}^{N} u_{mi}(x_i - x_{i-1})}{H}. \quad (9)$$

where u_{mi} are the computed velocity values on the jet axis at the corresponding point x_i. Energy balance takes into account heat from the melt going on vaporization of a coolant at the nozzle inlet:

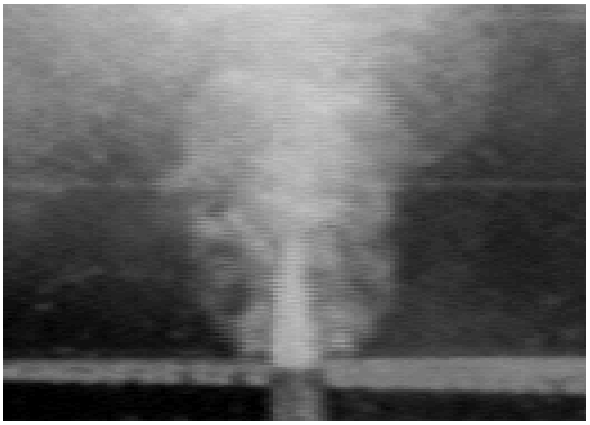

Fig. 3. Experimental picture of the pool cooled down from the nozzles at the bottom of the layer.

$$c_2 M_2 (T_{20} - T_2) = q_c \Delta t h_{lv}, \quad (10)$$

where q_c is the coolant flow rate, h_{lv} is the specific phase change heat (vaporization heat), c_2 – heat capacity, M_2 – mass of the melt to be cooled down, T_{20} , T_2 – the initial and current temperatures, correspondingly.

Heat balance (10) leads to

$$T_2 = T_{20} - \frac{q_c \Delta t h_{lv}}{c_2 M_2}. \quad (11)$$

The equations (10), (11) allow considering the heat balance of the melt and coolant in a form $c_2\rho_2 QV(T_2 - T) = c_1\rho_1(1-Q)V(T - T_1)$, where V, T are the average volume and temperature in a mixing layer. Thus, it yields:

$$T = \frac{c_2\rho_2 Q T_2 + c_1\rho_1(1-Q)T_1}{c_2\rho_2 Q + c_1\rho_1(1-Q)}. \quad (12)$$

The results of calculations by (12) are presented in Fig. 4, which evidently shows good correlation of these theoretical results and experimental results by [14].

3. Conclusion

The aggregate dynamical model of a general purpose and the two scenarios of the passive NPP protection systems against severe accidents were considered for analysis of the melt corium interaction with coolant and the factors influencing the containment failure, with account of the complicating real factors and parameters' time delays. In the first scenario, corium melt jet is going from the destroyed reactor vessel to the under reactor pool of coolant, and the time delays have concern to an account of the influence of volatile coolant on the melt jet penetrating into a pool. In the

second scenario, cooling of the melted corium pool is supposed by supply of the coolant through the nozzles on the basement (for example, similar to the construction of the EPR – European Pressurized Reactor). The time delays are available there on the coolant jets' inlets into the corium pool at the moment of a destroy of the concrete sacrificial layer and burning the nozzles' covers (supply of coolant), as well as by phase interchanges of the corium drops involved into the cooling layer, etc.

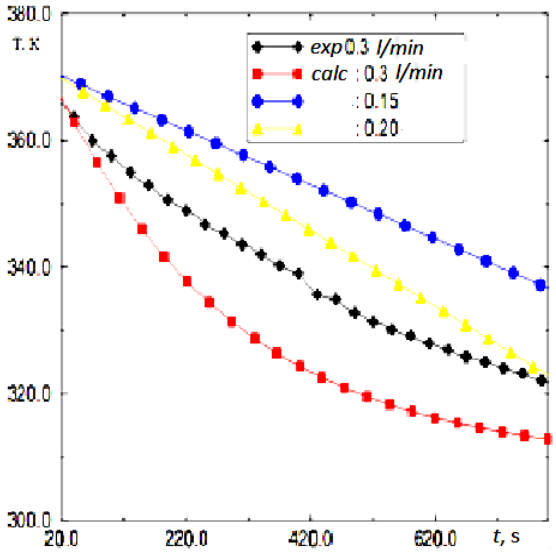

Fig. 4. Comparison of calculations by model against the experimental data for the pool cooled down from the nozzles at the bottom of the layer.

REFERENCES:

[1] I.V. Kazachkov, Ye.V. Chesnokov and O.M. Kazachkova. Modelling of Potentially Hazardous Objects with Time Shifts// WSEAS Trans. on Business & Economics.- 2004.- Issue 3.- №1.- P. 37-43.

[2] Jamshid Gharakhanlou, I.V. Kazachkov. Development and Investigation of Aggregate Models for Nuclear Objects with Time Shifts// J. Nuclear and Radiation Safety.- 2 (54).- 2012.- P. 36-41.

[3] Jamshid Gharakhanlou, I.V. Kazachkov. Mathematical modeling of potentially hazardous nuclear power objects with shifted arguments// J. Nuclear and Radiation Safety.- 3 (55) .- 2012.- P. 21-26. (In Russian).

[4] V.V.Begun, S.V. Begun, I.V. Kazachkov, et al. *Safety culture on nuclear power plants of Ukraine.*- Kyiv.- NTUU "KPI".- Granma.- 2012.- 544 pp. (In Ukrainian).

[5] M.L. Corradini, B.J. Kim, M.D. Oh, Vapor explosions in light water reactors: A review of theory and modeling, Progress in Nuclear Energy, Vol.22, No.1, 1988, pp. 1-117.

[6] M. Saito, et al. Experimental study on penetration behaviors of water jet into Freon-11 and Liquid Nitrogen, ANS Proceedings, Natl. Heat Transfer Conference, Houston, Texas, USA, July 24-27, 1988.

[7] M. Epstein, H.K. Fauske. Steam film instability and the mixing of core-melt jets and water/ ANS proceedings. National heat transfer conference. Aug. 4-7. Denver, Colorado, 1985.

[8] I.V.Kazachkov, O.V. Konoval. Modeling of spreading of the melted corium inside the pool of emergency heat removal during severe accidents at NPP// Nuclear physics and energy.- 2012.- V. 13.- № 1.- P. 46-55 (In Ukrainian).

[9] I.V. Kazachkov and Ali Hasan Moghaddam. *Modeling the thermal hydraulic processes by severe accidents at the NPPs*.- Monograph.- Kyiv, NTUU "KPI".- Zhytomyr.- Polissya.- 2008.- 170pp. (In Russian).

[10] H.O. Haraldsson, I.V. Kazachkov, T.N. Dinh and B.R. Sehgal. Analysis of thin jet breakup depth in immiscible fluids/ Abstracts of the 3rd International Conference on Advances in Fluid Mechanics, 24-26 May Montreal, Canada, 2000.

[11] H.S. Park, I.V. Kazachkov, B.R. Sehgal, Y. Maruyama and J. Sugimoto. Analysis of Plunging Jet Penetration into Liquid Pool in Isothermal Conditions/ ICMF 2001: 4th Int. Conference on Multiphase Flow, New Orleans, Louisiana, U.S.A., May 27 - June 1, 2001.

[12] I.V. Kazachkov. The mathematical models for penetration of a liquid jets into a pool// WSEAS Trans. on fluid mechanics.- 2011.- Issue 2.- Vol. 6, April.- P. 71-91.

[13] A.I. Nakorchevkyi, B.I. Basok. Hydrodynamics and heat-mass transfer in heterogeneous systems and pulsating flows/ Ed. A.A. Dolinskyi.- Kyiv: Naukova Dumka.- 2001.- 346 pp. (In Russian).

[14] *Kazachkov I.V., Paladino D., Sehgal B.R.* Ex-vessel coolability of a molten pool by coolant injection from submerged nozzles // 9-th Int. Conf. Nucl. Energy Devel (April 8 - 12, 2001. Nice, France). - P. 43 - 49.

Mathematical modelling the dynamics of colliding droplets with application to transport phenomena

Kamila B. Bulekbaeva, Maira T. Turalina, and Arnold M. Brener

***Abstract*—**The paper deals with the mathematical model for describing the dynamics of droplet-droplet collisions and merging in gas-droplet systems which are based on the energy analysis. The problems of describing the droplets defragmentation during collisions as well as the problems of liquid patterns stability are not considered. The effect of liquid mixing inside the droplets has been described with the help of the Hadamard- Rybczynski equation, and the renewal of the interface was estimated according to the Danckwerts model. The obtained results can be applied to engineering calculating the chemical apparatuses and devices characterized by active hydrodynamic regimes.

***Keywords*—** Droplets merging, Colliding droplets, Energy analysis, Heat and mass transfer.

I. Introduction

In many chemical apparatuses and other devices characterized by the liquid-gas interaction under active hydrodynamic regimes, the bulk of a liquid phase is usually dispersed [1, 2, 3, 4]. Although the fine dispersion has a large specific interfacial area, the internal mixing intensity inside small droplets can be small [2 - 6]. Therefore the droplets collisions, mergers and secondary crushing play a major role for contributing update specific interface and for intensifying the transport phenomena [7 -14].

The theoretical description of these processes involves great mathematical difficulties, and the corresponding problems are far from satisfactory resolution [7 -12]. Detailed experimental investigation of droplet collision processes is also linked with difficult challenges [10, 12, 15, 16, 17, 18].

This paper deals with an energy analysis of the dynamics of the droplets collision and coalescence in gas-droplet dispersions. The problems of describing the droplets defragmentation during collisions as well as the problems of liquid patterns stability are not considered in this paper.

II. Theoretical Details

Let us consider the collision and subsequent merger of two droplets of the radiuses r_1 and r_2, respectively (Fig.1). The impulse balance reads

$$\vec{p}_1 + \vec{p}_2 = \vec{p}\,. \tag{1}$$

For convenience, we project ratio (2.60) in the direction of motion of the one of droplets and introduce the local coordinate system (u,v) (Fig. 1)

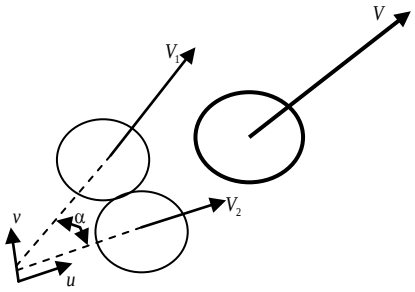

Fig. 1 Diagram of droplets collision

Thus we obtain

$$(m_1 + m_2)V_v = m_1 V_1 \sin\alpha\,, \tag{2}$$

$$(m_1 + m_2)V_u = m_1 V_1 \cos\alpha + m_2 V_2\,, \tag{3}$$

where m_1, m_2 are the masses of the colliding droplets.

From formulas (2), (3), we obtain the expression for the magnitude of a velocity of the droplet, formed by the merger of colliding droplets

$$V = \frac{\sqrt{m_1^2 V_1^2 + m_2^2 V_2^2 + 2m_1 m_2 V_1 V_2 \cos\alpha}}{m_1 + m_2}\,. \tag{4}$$

Using the formula for the droplet mass $m = \rho\frac{4}{3}\pi r^3$, we get the following expression for the velocity of the droplet formed after merger

K.B. Bulekbaeva is with the Taraz Innovative-Humanitarian University, Taraz, Kazakhstan (e-mail: nurhat2000@ mail.ru).

M.T. Turalina is with the Taraz Dulati State University, Taraz, Kazakhstan.

A.M. Brener is with the State University of South Kazakhstan, Shymkent, Kazakhstan (e-mail: amb_52@mail.ru; brener@fromru.com).

ISBN: 978-1-61804-219-4

$$V = \frac{\sqrt{\chi^2 V_1^2 + V_2^2 + 2\chi V_1 V_2 \cos\alpha}}{1+\chi}, \quad (5)$$

where V_1 and V_2 are the values of the velocities of the colliding droplets; α is the angle between the droplets velocities before the collision; $\chi = r_1/r_2$.

For two droplets of the equal diameters we have

$$V = \frac{\sqrt{V_1^2 + V_2^2 + 2V_1 V_2 \cos\alpha}}{2}. \quad (6)$$

The change in the total kinetic energy after the collision and the merge of droplets reads

$$\Delta E_K = \frac{(m_1+m_2)V^2 - m_1 V_1^2 - m_2 V_2^2}{2}. \quad (7)$$

Hence, using (5), we obtain

$$\Delta E_K = \frac{m_1 V_1^2}{2}\frac{2\chi(\cos\alpha - s) - s}{s(1+\chi)^2} + \frac{m_2 V_2^2}{2}\frac{2\chi(s\cos\alpha - 1) - \chi^2}{(1+\chi)^2}, \quad (8)$$

where $s = \frac{V_1}{V_2}$.

For droplets of the equal diameters formula (8) can be rewritten as a function of the kinetic energy of one of the droplets

$$\Delta E_K = \frac{E_1}{4}\frac{4s\cos\alpha - 3(1+s^2)}{s^2}, \quad (9)$$

where $E_1 = \frac{mV_1^2}{2}$.

If the velocities of droplets are equal before the collision, we obtain

$$\Delta E_K = \frac{mV_1^2}{8}(4\cos\alpha - 6), \quad (10)$$

It is obvious that $(-\Delta E_K)$ is a complete energy of the dissipation at the merge of droplets. Magnitude of the total energy dissipation can take the maximum for certain ratios of velocities. This extremum is found from the condition

$$\frac{d(\Delta E_K)}{ds} = 0. \quad (11)$$

Hence we obtain

$$s_{extr} = \frac{3}{2\cos\alpha}. \quad (12)$$

Fig. (2) depicts some results of calculating the change in the total kinetic energy of a system of two droplets during their collision and merge.

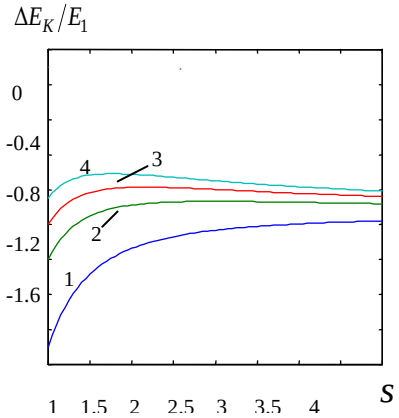

1- $\alpha = \frac{\pi}{2}$; 2- $\alpha = \frac{\pi}{3}$; 3- $\alpha = \frac{\pi}{4}$; 4- $\alpha = \frac{\pi}{6}$

Fig.2 Change of the kinetic energy of the system of two droplets

The change in a free surface energy after the merge of the liquid droplets with the identical physical properties is determined as follows

$$\Delta E_S = 4\pi\sigma\left(\sqrt[3]{(r_1^3 + r_2^3)^2} - r_1^2 - r_2^2\right), \quad (13)$$

where σ is the surface tension.

For two droplets of equal diameters we have:

$$\Delta E_S = 4\pi\sigma r^2\left(\sqrt[3]{4} - 2\right) \approx -1{,}68\pi\sigma r^2. \quad (14)$$

It is easy to see that

$$\Delta E_K + \Delta E_S < 0. \quad (15)$$

Thus, the process of merging droplets seems to be energetically favorable under the any initial velocities of droplets, as it is accompanied by a decrease in a total surface energy of the droplets. At the same time the energy that is freed during the collision and merging of droplets induces the formation of vortices inside the droplet and thereby it contributes to the intensive liquid mixing inside the droplet and updating the interface (Fig. 3).

ISBN: 978-1-61804-219-4

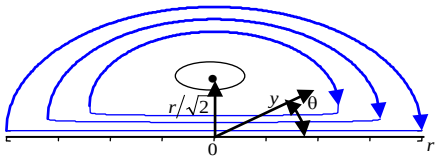

Fig. 3 Diagram of the vortex inside the droplet

Let us give an estimation for this effect, with the help of the known Hadamard - Rybczynski solution for the axis-symmetric vortex components [12, 19] :

$$W_r = -\frac{V_S}{2(1+\beta)}\left(1-\frac{y^2}{r^2}\right)\cos\theta, \tag{16}$$

$$W_\theta = \frac{V_S}{2(1+\beta)}\left(1-\frac{2y^2}{r^2}\right)\sin\theta, \tag{17}$$

where V_S - the surface velocity of the droplet; y, θ - radial and angular coordinates; $r = \sqrt[3]{r_1^3 + r_2^3}$ - the radius of the formed droplet; $\beta = \mu/\mu_g$ - the ratio between dynamic viscosities of the liquid and gas.

The evaluation of the dissipation energy during the vortex motion of the fluid inside the droplet can be obtained from the following relationship

$$E_{dis} = \mu\int_0^r \left|\frac{d\overline{W}_\theta}{dr}\right| dSdr. \tag{18}$$

Hence we get

$$E_{dis} = 4\pi\mu\int_0^r \left|\frac{d\overline{W}_\theta}{dr}\right| r^2 dr = \mu\frac{V_S r^2}{(1+\beta)}, \tag{19}$$

where for the average tangential velocity of the vortex, we have

$$\overline{W}_\theta = \frac{2}{\pi}\int_0^{\frac{\pi}{2}} W_\theta d\theta = \frac{V_S}{\pi(1+\beta)}\left(1-\frac{2y^2}{r^2}\right). \tag{20}$$

From the energy balance

$$\Delta E_{dis} + \Delta E_S + \Delta E_K = 0 \tag{21}$$

we get

$$V_S = -\frac{(1+\beta)(\Delta E_S + \Delta E_K)}{\mu r^2} \tag{22}$$

As an estimation of the characteristic time for updating the interfacial surface due to fluid mixing in a droplet we take the conditional time of the passage of the fluid particles along the radius of the vortex inside the droplet [4]:

$$\tau = \frac{r}{\overline{W}_r\sqrt{2}}. \tag{23}$$

The estimation for the average radial velocity component of the vortex reads

$$\overline{W}_r = -\frac{2}{\pi r}\iint_{\theta,y}\frac{V_S}{2(1+\beta)}\left(1-\frac{y^2}{r^2}\right)\cos\theta dyd\theta = \frac{V_S}{3\pi(1+\beta)}. \tag{24}$$

Thus we get

$$\tau = -\frac{3\pi\mu r^3/\sqrt{2}}{\Delta E_K + \Delta E_S}. \tag{25}$$

Taking into account (9) and (14), the expression for calculating the update time of the surface takes the form

$$\tau = \frac{18\mu\bar{r}/\sqrt{2}}{\rho\bar{r}V_1^2\left[3\left(1+s^2\right)-4s\cos\alpha\right]+24\sigma\left(2-\sqrt[3]{4}\right)}. \tag{26}$$

where $\bar{r}$ is the average radius of the colliding drops.

III. APPLICATION AND CONCLUSION

The described above hydrodynamic model can be used for calculating the convective mass-transfer coefficient inside the droplet with the help of Danckwerts approach [14, 19, 20].

Thus we obtain

$$k_i = \sqrt{\frac{D}{\tau}} = \sqrt{D\sqrt{2}\frac{\left|\Delta E_K + \Delta E_S\right|}{3\pi\mu r^3}}, \tag{27}$$

where D is a diffusion coefficient inside the droplet.

According to the same model, we obtain the formula for calculating the effective coefficient of convective heat transfer inside the droplet. Indeed, according to the analogy between heat and mass transfer [14, 20], we can write an expression for the effective heat transfer to the drop:

$$\frac{\alpha_{ef}}{C_p\rho} = \sqrt{\frac{\lambda}{C_p\rho\tau}}. \tag{28}$$

Hence we obtain

$$\alpha_{ef} = \sqrt{\frac{\lambda C_p\rho}{\tau}}. \tag{29}$$

Next, we have the expression for the Nusselt number as

$$Nu = \frac{\alpha_{ef}\,\bar{r}}{\lambda} = \bar{r}\sqrt{\frac{C_p\rho}{\lambda\tau}}\,. \tag{30}$$

Here the time of the surface update is calculated with the help of formulas (25) or (26).

As a result we have

$$Nu = \frac{\alpha_{ef}\,\bar{r}}{\lambda} = \sqrt{\frac{C_p\rho\sqrt{2}\left\{\rho\bar{r}V_1^2\left[3\left(1+s^2\right)-4s\cos\alpha\right]+24\sigma\left(2-\sqrt[3]{4}\right)\right\}}{18\lambda\mu\bar{r}}} \tag{31}$$

The average value of the Nusselt number, which can be recommended as quality assessment for engineering calculations is determined by averaging expression (2.91) for different values of the collision angles and ratios between droplets velocities

$$N\bar{u} = \frac{1}{2\pi}\int_0^{\pi/2}\int_1^5 Nudsd\alpha\,. \tag{32}$$

After the numerical integration we obtain

$$N\bar{u} = \bar{r}\sqrt{\frac{C_p\rho}{\lambda\bar{\tau}}}\,, \tag{33}$$

Where

$$\bar{\tau} = \frac{2{,}14\mu\bar{r}}{0{,}47\rho\bar{r}V^2+1{,}68\sigma}\,. \tag{34}$$

Substituting (34) into (33) we obtain the dimensionless equation for calculating the effective Nusselt number in the collision and coalescence of the droplets

$$N\bar{u} = \sqrt{\frac{0{,}47\,\mathrm{Re}+1{,}68We}{2{,}14St}}\,, \tag{35}$$

where $\mathrm{Re} = \frac{\rho\bar{r}V}{\mu}$ - Reynolds number; $We = \frac{\sigma}{\mu V}$ -modified Weber number; $St = \frac{\lambda}{C_p\rho V\bar{r}}$ - Stanton number.

Fig. 4 shows some results of calculations according to criterial ratio (35). The graphs show that the Nusselt number increases monotonically with increasing Reynolds number of the droplets.

At the same time, the rate of heat transfer during the collision and merging of droplets increases with increasing droplets velocities even at the fixed Reynolds number. This can be explained by the stronger dependence of the Nusselt number on the Stanton number than its dependence on the Weber number.

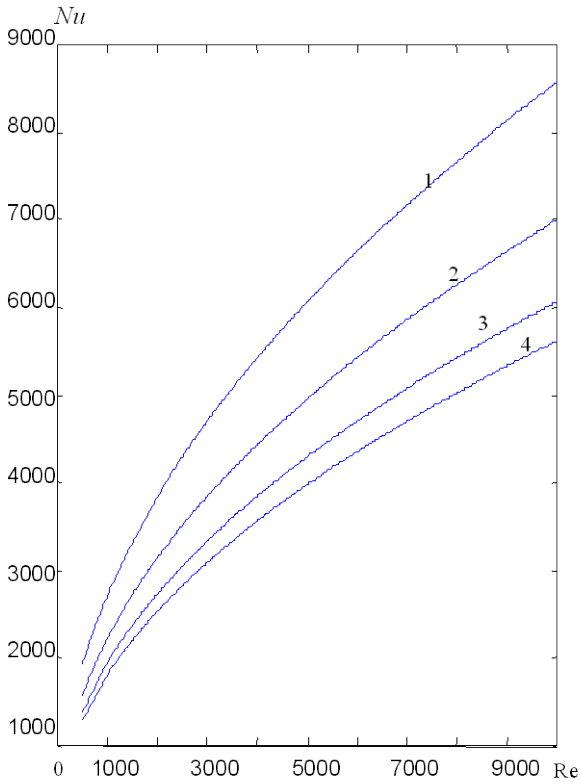

1- $We = 3{,}75$; $St = 3\cdot10^{-5}$; 2- $We = 5$; $St = 4{,}5\cdot10^{-5}$; 3- $We = 8$; $St = 6{,}5\cdot10^{-5}$; 4- $We = 10$; $St = 7{,}5\cdot10^{-5}$.

Fig. 4 The effective Nusselt number

Thus, the energy analysis makes it possible to obtain estimates of the characteristics of mixing and updating the interface under the collisions and merge of the droplets in the apparatus with active hydrodynamic regimes. These results play a great role both while calculating the mass-transfer coefficients and heat transfer coefficients according to the Danckwerts model of interface updating.

REFERENCES

[1] A. Orell, J.W. Westwater, "Spontaneous interfacial cellular convection accompanying mass transfer", *AIChE Jour.*, vol. 8, № 3, 1962, pp. 350-363.

[2] Haber S., Hetsroni G., Solan A., "On the low Reynolds number motion of two droplets", *Int. J. Multiphase Flow*, vol.1, 1973, pp. 57-71.

[3] J.C. Berg, A. Acrivos, "The effect of surface-active agents on convection cells induced by surface tension", *Chem. Eng. Sci.*, vol. 20, № 8, 1965, pp. 737-746.

[4] Manga M., Stone H.A., "Collective hydrodynamics of deformable drops and bubbles in dilute low Reynolds number suspensions", *J. Fluid Mech.*, vol. 300, 1995, pp. 231-263.

[5] Levan M.D., "Motion of a Droplet with Newtonian Interface", *Jour. of Colloid and Interface Sci.*, vol. 83, No. 1, 1981, pp. 11-17.

[6] K.A. Smith, "On convective instability induced by surface-tension gradients", *Jour. Fluid Mech.*, vol. 28, № 2, 1966, pp. 401-407.

[7] S.P. Lin, "Stabilizing effects of surface-active agents on a film flow", *AIChE Jour.*, vol.16, № 3, 1970, pp. 375-382.

[8] K.H. Wang, V. Ludwiksson, E.N. Lightfoot, "Hydrodynamic stability of Marangoni films. A preliminary analysis of the effects of interphase mass transfer", *AIChE Jour*., vol. 17, №6, 1971, pp. 1402-1412.
[9] Macklin W.C., Metaxas G.J., "Splashing of drops on liquid layers", *Jour. of Applied Physics*, vol. 47, No. 9, 1976, pp. 3963-3970.
[10] Manzello S.L., Yang J.C., "An experimental study of a water droplet impinging on a liquid surface", *Experiments in Fluids*, 32, 2002, pp. 580-689.
[11] Ching B., Golay M.W., Johnson T.J., "Droplet impacts upon liquid surface", *Science*, vol.226, No. 4674, 1984, pp. 535-537.
[12] Othniel Hermes, *Hadamard-Rybczynski Equation*. Bellum Publ., 2012
[13] Macklin W.C., Hobbs P.V., "Subsurface phenomena and the splashing of drops on shallow liquids" *Science*, vol. 166, No 3901, 1969, pp. 107-108.
[14] Danckwerts P.V. *Gas-liquid reactions*, McGraw-Hill Book Co., New-York, 1970.
[15] Archipov V.A., Ratanov G.S., Trofimov V.F., "Experimental investigation of the interaction of colliding droplets", *Jour. of Appl. Mech. and Tech. Phys.*, vol. 326, is. 1, 2008, pp. 196-200.
[16] Winnikow S., Chao B.T., "Droplet motion in purified systems", *Phys. of Fluids*, vol. 9, 1966, pp. 50-61.
[17] Brenn G, Frohn A., "Collision and coalescence of droplets of various liquids", *Jour. Aerosol Sci*., vol. 20, No. 8, 1989, pp. 1027-1030.
[18] Brenn G, Frohn A., "Collision and merging of two equal droplets of prophanol", *Experiments in Fluids*, vol. 7, 1989, pp. 441-446.
[19] Mertaniemi H., Forchheimer R., Ikkala O., Ras R.H.A., "Rebounding Droplet-Droplet Collisions on Superhydropholic Surfaces: from the Phenomenon to Droplet Logic", *Advanced Materials*, vol. 24, is. 42, 2012, pp. 5738-5743.
[20] Khan W., "An extension of Danckwerts theoretical surface renewal model to mass transfer at contaminated turbulent interfaces", *Math. and Comp. Modelling*, vol. 14, 1990, pp. 750-754.

P-extensions of lattices and its Applications to Formal Concept Analyses

A. Basheyeva, A. Nurakunov, J.Tussupov, and A.Satekbayeva

***Abstract*—** The main purpose of the paper is to present one approach of extension of a given lattice to lattice with some properties of Boolean lattices and its applications to concept lattices. Also we provide some examples and applications.

***Keywords*—** Formal Concept Analysis, a formal context, concept lattices, extension of lattice.

I. Introduction

In practice often the Formal concept lattices are very big and it is difficult to study and say about properties of such lattices. To reduce or correct the big formal concept lattices to lattices with well studied properties is usual problem of the Theory of Formal Concept Analysis [4].

From the point view of the Lattice Theory and Formal Concept Analysis it is natural to correct given lattice to lattice with a well studied properties without losing relations (order) between elements.

Doing this we will extend a given lattice to other lattice guiding by the following two principles of completions:

- extended lattice should have the "well-known" properties;
- extended lattice should preserve partial order of given lattice.

Under "well-known" property we mean a property that is natural defined in Lattice theory, as well as, a property that can be expressed by the first order formulas. For example, the "well-known" property is "to be complete lattice" or "to be distributive lattice".

Also for finite lattices we will use the next principle:

- The difference between given a lattice and the extended lattice should be "difficult to distinguish".

This work has been supported by grants of the Ministry of Education and Science of Republic Kazakhstan: "Contribution on two leading problems of the Universal algebra and Lattice theory" (Grant # 0112PK02245) and "The formal methods of the specification and their application in the development of programs"

J.Tussupov is from L.N. Gumilyev Eurasian National University, Astana, Kazakhstan (corresponding author to provide phone: +7 701 789 27 10; e-mail: tussupov@mail.ru).

A. Basheyeva is from L.N. Gumilyev Eurasian National University, Astana, Kazakhstan (e-mail: basheeva@mail.ru).

A. Nurakunov is from Institute of Theoretical and Applied Mathematics, Bishkek, Kyrgyzstan (e-mail: a.nurakunov@gmail.com).

A.Satekbayeva is from L.N. Gumilyev Eurasian National University, Astana, Kazakhstan (e-mail: satekbayeva@gmail.com).

For given finite lattice and finite extended lattice which satisfies to condition 1) and 2) our measure of "difficult to distinguish" is a rational number that is equal to the number of added elements divided by the number of all elements of extendeded lattice.

Terminology corresponds to G. Birkhoff [1] on Lattice Theory, S. Burris - H. P. Sankappanavar [2] on Universal Algebra, H. M. MacNeille [6] on Partially ordered sets and B. Gunter - Willy [4] for formal concept analysis.

II. Preliminaries and definitions

The authors assume that the readers are familiar with the basic concepts of lattice theory, universal algebra and formal concept analysis.

Definition 1. Let P be a set of some properties of lattices and L be a lattice. A latice L^* is called P- *extensions* of L if L is embedding to L^* as poset and L^* satisfies to all properties from P.

We note that not for any finite lattice L and a set of properties P there are P- extensions of L.

We will extend given lattice to lattice with some properties of Boolean lattices. The reason of such consideration is the following theorem that provides existence of P- extension:

Theorem 1. *Let P be a set of some properties of finite Boolean lattices. For any finite lattice L there is a lattice L^* such that P are valid on L^* and L is embedded into L^* as partially order set.*

From the above theorem and fact that every nontrivial universal Horn class contains the class of all distributive lattices, in particular, the class of all boolean lattices we get:

Corollary 2. *Let P be a consistent set of the universal Horn sentences. Then for any finite lattice L there are P- extensions of L.*

We recall some main classes of lattices in which we will find extensions.

- A lattice L is called *distributive* if it satisfies to distributive law:

$$\forall xyz[x \wedge (y \vee z) = (x \wedge y) \vee (x \wedge z)];$$

- A lattice L is called *modular* if it satisfies to modular law:

$$\forall xyz[x \leq y \Rightarrow x \vee (y \wedge z) = y \wedge (x \vee z)];$$

- A lattice L is called *meet (join) semi-distributive* if it satisfies to meet (join) semi-distributive law:

$$\forall xyz[x \wedge y = x \wedge z \Rightarrow x \wedge y = x \wedge (y \vee z)]$$

ISBN: 978-1-61804-219-4

$$(\forall xyz[x \vee y = x \vee z \Rightarrow x \vee y = x \vee (y \wedge z)])$$

An element a of the lattice L is called an *atom* if $0 < b \leq a$ implies $b = a$ for all $b \in L$. A lattice L is called *atomic (coatomic)* if every element of L is a sum of some atoms (an intersection of some coatoms) of L.

Let L be an arbitrary lattice and $\mathcal{B}(L)$ a set of all subsets of the set L. Obviously, $\mathcal{B}(L)$ is a boolean lattice for any lattice L. A lattices L that are isomorphic to the lattice $\mathcal{B}(X)$ for some set X is called a lattice of the set of subsets.

Further we will often use the following lattices: N_5 is a lattice with basic set $\{0, a, b, c, 1\}$ and partial order $0 < a < 1$, $0 < b < c < 1$, and M_3 is a lattice with basic set $\{0, a, b, c, 1\}$, and partial oder $0 < a < 1$, $0 < b < 1$, $0 < c < 1$ (see Figure 1). The lattice N_5 is called pentagon and M_3 is diamond.

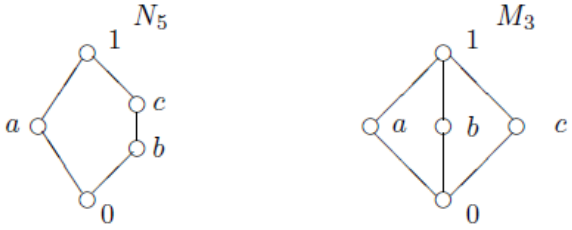

Fig. 1. Lattices N_5 and M_3

III. Minimal P- extensions of the finite lattices

Further we will consider finite lattices only. For a finite set A we sign $|A|$ the number of elements of the set A . Let L be a finite lattice, P a set of the properties of the lattices and $\mathcal{P}$ a set of all P- extensions of L. A number

$$d_p(L) = \begin{cases} 1, & \text{if } \mathcal{P}(L) = \emptyset \\ \min\{\dfrac{|\bar{L}| - |L|}{|\bar{L}|} : \bar{L} \in \mathcal{P}(L)\}, & \text{if } \mathcal{P}(L) \neq \emptyset \end{cases}$$

is called a *P-defect* of the lattice L.

So, we have $0 \leq d_p(L) \leq 1$ for any finite lattice L. Furthermore, $d_p(L) = 0$ if and only if L satisfies to all properties from P and $d_p(L) = 1$ if and only if L does not have P- extensions.

Definition 2. A *P- extension* L^* of finite lattice L is called *a* minimal *P- extension* if $d_p(L) = (|L^*| - |L|)|L^*|$.

We note that a lattice can have more than one nonisomorphic minimal extension.

In some cases, the problem of finding the minimal P-extensions of certain lattices is quite simple. In particular, we study the lattices pentagon N_5 and diamond M_3 on distributive, modular and semidistributive extensions.

Let D, M and $SD_\wedge$ be distributive, modular and meet semidistributive properties, respectively. And let N_5^c and M_3^b are lattices on the Figure 2. Note that both lattices are isomorphic, but fixed elements a, b, c have different partial orders.

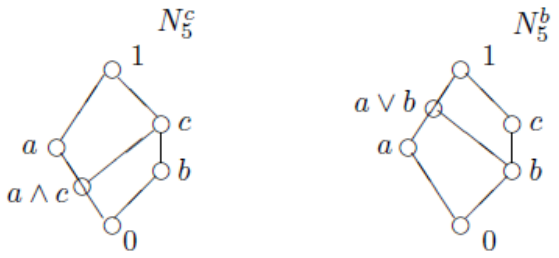

Fig. 2. Minimal D- extension and M- extension of N_5

Lemma 1. *The lattices N_5^c and N_5^b are all minimal D-extensions and M-extension of the lattice N_5.*

Lemma 2. *Let $\mathcal{B}(3)$, $SD_\wedge(3)$ and $SD_\wedge(3)^+$ are lattices on the Figure 3.*

1. *The lattices $\mathcal{B}(3)$ up to isomorphism is unique minimal D- extensions of the lattice M_3 and $d_D(M_3) = 3/8$;*
2. *The lattices $\mathcal{S}D_\wedge(3)$ and $\mathcal{S}D_\wedge(3)^+$ up to isomorphism are all the minimal $\mathcal{S}D_\wedge$- extensions of the lattice M_3 and $d_{SD_\wedge}(M_3) = 2/7$.*

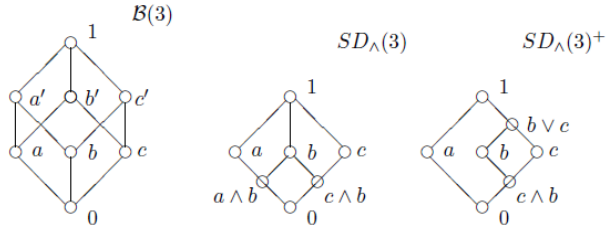

Fig. 3. Lattices $\mathcal{B}(3)$, $SD_\wedge(3)$ and $SD_\wedge(3)^+$

IV. Concept lattice of suppressors of the plant viruses and extensions

In this section we will construct a minimal $\mathcal{S}D_\wedge$- extensions of one concept lattice, that is naturally arised in study of the suppressors of plant viruses.

In the review paper [7] the current knowledge on activities and biochemical mechanisms of selected virus-encoded suppressors of RNAi (VSRs) with regard to their biological role of suppressing RNAi in plants was described. By the database of this paper we get the context $\mathcal{S} =< Sup, Sil; I >$, where the set of objects Sup is the set of suppressors that is produced by plant viruses to suppress the immune system of the cells of plants; Sil is a set of attributes that are a variety of immune mechanisms of plant cells, the binary relation I consists of the pairs $(s, r) \in Sup \times Sil$ such that a pair (s, r) belongs to I if and only if suppressor $s \in Sup$ and suppress immune mechanism $r \in Sil$. The context $\mathcal{S}$ is represented as Context Table $\mathcal{S}$ on Figure 4.

Sup\Sil	Interaction with RISC	siRNA binding	Interference with siRNA methylation	Interference with siRNA synthesis
P0	x			

2b	x	x		x
122K		x		
P19		x	x	
P21		x		x
AC4		x		
HC-Pro		x	x	x
126K			x	
16K				x
V2				x
CP/p38				x
P6				x

Sup (abbreviation of Suppressors) is a set consists suppressors P0, 2b, 122K, P19, P21, AC4, HC-Pro, 126K, 16K, V2, CP/p38, P6; and Sil (abbreviation RNA Silencing) is a set consists immune mechanisms Interaction with RISC, siRNA binding, Interference with siRNA methylation, Interference with siRNA synthesis.

Fig. 4. Context Table $\mathcal{S}$

From the context $\mathcal{S}$ we construct concept lattice $FCL(\mathcal{S})$ pictured on Figure 5.

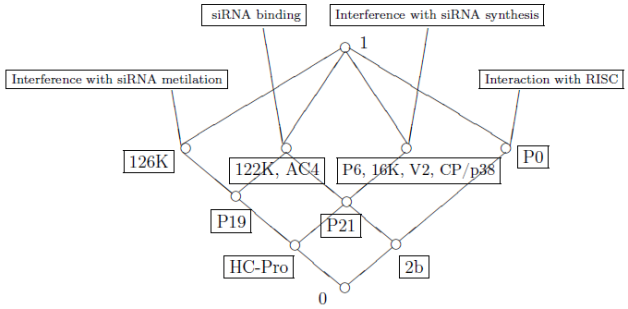

Fig 5. Concept lattice $FCL(\mathcal{S})$

Put $a = [P0]$, $b = [P6,16K,V2,CP/p38]$ and $c = [122K, AC4]$. It is easy to see that $a \wedge b = a \wedge c$ and $a \wedge b \neq a \wedge (b \vee c)$. This means that the lattice is not meet semidistributive. We consider minimal meet semidistributive extensions ($SD_{\wedge}$- extension of $FCL(\mathcal{S})$. Using the methods of extensions we produce the lattice $FCL(\mathcal{S})^*$ pictured on Figure 6. We are omitting details presentation and reasoning.

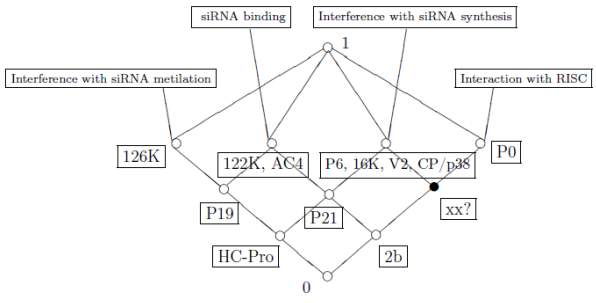

Fig 6. Concept lattice $FCL^*(\mathcal{S})$

The authors, being no experts in virology, have courage to assume the following:

- there is a suppressor [xx?] which participates in the process of suppression of immune Interference with siRNA synthesis and Interaction with RISC mechanisms, but doesn't participate in process of suppression of immune siRNA binding and Interference with siRNA methylation mechanisms;
- $[16K]$ or $[V2]$ or $[CP/p38]$ or $[P6]$ supressor participates in the process of suppression of the Interaction with RISC immune mechanism.

The authors would like to note that in the publication [5] have been shown that the suppressor of $P1$, which is not included in the *Sup*, participates in a locking of process of Interaction with RISC. Probably this known suppressor is an Interference with siRNA synthesis suppressor.

V. Conclusion

In the paper was introduce a definition of P-extension of lattice, where P is a set of some properties of lattices. The existence of such extensions for every finite lattice and any properties of Boolean lattices was shown. In particular, there were found all distributive and meet semi-distributive extensions of pentagon and diamond lattices. Using these results and database of suppressors we construct meet semi-distributive, co-atomistic lattice of suppressors of plant viruses.

Acknowledgment

The authors are grateful to Prof. R. T. Omarov for providing information and consultation on the virology of plants.

This work has been supported by grants of the Ministry of Education and Science of Republic Kazakhstan: "Contribution on two leading problems of the Universal algebra and Lattice theory" (Grant # 0112PK02245) and "The formal methods of the specification and their application in the development of programs".

References

[1] G. Birkhoff, *"Lattice theory"*, Third Edition, AMS Colloquium Publications 25, American Mathematical Society, Providence, RI, 1967.

[2] Stanley Burris, H. P. Sankappanavar (1981), *"A Course in Universal Algebra"*, Springer-Verlag, 1981, pp. 331.

[3] Richard Dedekind, *"Essays on the Theory of Number"*, Open Court Publishing Company, Chicago, 1901.

[4] G. Ganter, R. Wille, *"Formal Concept Analysis"*, Mathematical Foundations. Springer, 1999.- 314 p.

[5] Gillet, F.-X. et al. (2013), *"The RYMV-Encoded Viral Suppressor of RNA Silencing P1 Is a Zinc-Binding Protein with Redox-Dependent Flexibility"*, J. Mol. Biol. 425(2013), 2423-2435.

[6] H. M. MacNeil, *"Partially Ordered Sets"*, Trans. Amer. Math. Soc. 42(1937), 90-96.

[7] Rustem T. Omarov and Herman B. Scholtof (2012), *"Biological Chemistry of Virus-Encoded Suppressors of RNA Silencing: An Overview"*, Methods in Molecular Biology, Springer Science+Business Media, LLC, 2012.

Aynur Basheyeva is master of Mathematics, Eurasian National University, Astana, Kazakhstan

Anvar Nurakunov is associated professor, Institute of Theoretical and Applied Mathematics, Bishkek, Kyrgyzstan
Aizhan Satekbayeva is PhD student on “Information Systems”, master of Mathematics, Eurasian National University, Astana, Kazakhstan
J.Tussupov is doctor of physical and mathematical sciences, professor, head of Information Systems Department, Eurasian National University, Astana, Kazakhstan

General theory of micropolar ferromagnetic elastic thin shells

Samvel H. Sargsyan

***Abstract*—** Three-dimensional equations and boundary conditions for micropolar ferromagnetic body are considered: these are equations of micropolar theory of elasticity for shell with consideration of mass forces and moments of electromagnetic nature, equations of quasistationar electrodynamics of ferromagnetic body for shell domain, equations of quasistationar electrodynamics for infinity space, surrounding the shell, boundary conditions with consideration of Maxwell's magnetic tensor of stresses for mechanical part of the problem, boundary conditions of transmission of electrodynamic part of the problem on external surface of the shell and conditions in infinity. Rather general hypotheses are formulated, which are adequate to qualitative properties of asymptotic solution of the above mentioned three-dimensional boundary-value problem in domain of thin shell, and applied two-dimensional theory of magnetoelasticity of micropolar ferromagnetic thin shells is constructed: these are equations and boundary conditions of mechanics of micropolar thin shells with consideration of averaged forces and moments of electromagnetic nature and system of integrodifferential equations of electromagnetic field. The constructed applied theory is basic for studying different concrete problems of determination of stress-strain state of elastic micropolar ferromagnetic thin shells.

***Keywords*—**applied theory, elastic, ferromagnetic, micropolar, thin shell.

I. Introduction

In mechanics of solids during the studying of problems for materials, which have electromagnetic properties, both mass forces and mass couple of forces are present. In papers [2]-[7] the fact that massively distributed moments appear in ferromagnetics is pointed out. Because of the presence of massively distributed moments tensor of mechanical stresses will be asymmetric [8]-[11]. This means that it is natural to study the problem of determination of stress-strain state in ferromagnetic body on the basis of micropolar (asymmetric, momental) theory of elasticity.

Since magnetoelastic effects are very important in thin bodies, therefore the construction of mathematical models of micropolar ferromagnetic elastic thin shells and plates is actual.

Review of works on construction of mathematical models of micropolar elastic thin shells and plates without consideration of magnetoelastic interaction is done in papers [12],[13]. The main problem of the general theory of micropolar elastic thin shells and plates is in approximate, but adequate reduction of three-dimensional boundary-value problem of the micropolar theory of elasticity to two-dimensional problem. From this point of view the use of qualitative aspects of the result of the asymptotic method of integration of boundary-value problem of three-dimensional micropolar theory of elasticity in thin domain of the shell or plate is effective for formulation of adequate hypotheses and for construction of applied theories of micropolar elastic thin shells and plates. In papers [14]-[18] general applied theories of micropolar elastic thin shells and plates are constructed on the basis of asymptotically confirmed hypotheses method [19]-[21]. On the basis of the same approach general applied theories of micropolar thermoelasticity [22], [23] and magnetoelasticity [24], [25] of thin shells and plates are constructed (for non ferromagnetic materials).

In the present paper the mentioned approach is developed and general applied theory with free fields of displacements and rotations of micropolar ferromagnetic elastic thin shells is constructed. Applied theories of micropolar ferromagnetic elastic thin plates and bars will be obtained as private cases of the theory, constructed for shells.

It should be noted that in frame of classical theory of elasticity problems of strength, vibration and stability of ferromagnetic elastic solids, thin shells, plates and bars are studied in papers [26]-[32]. In monograph [32] all main provisions of theory of ferromagnetic elastic thin shells and plates are introduced on the basis of classical approach.

II. Problem Statement

An isotropic shell of constant thickness $2h$ is considered as three-dimensional micropolar dielectric ferromagnetic (magnetically soft) elastic body. It is assumed that the undeformed shell is located in initially given stationary magnetic field, for which we have equations of magnetostatics: in the inner region of the body-shell

$$rot\vec{H}_* = 0, \quad div\vec{B}_* = 0, \qquad \vec{B}_* = \mu_0\left(\vec{H}_* + \vec{M}_*\right), \quad \vec{M}_* = \chi\vec{H}_*, \tag{1}$$

in the outer region of the body-shell, which is the whole three-dimensional space except of the region of the shell (electrodynamic properties of this region are identified with the properties of the vacuum):

$$rot\vec{H}_*^{(e)} = 0, \quad div\vec{B}_*^{(e)} = 0, \quad \vec{B}_*^{(e)} = \mu_0\vec{H}_*^{(e)}, \quad \vec{M}_*^{(e)} = 0. \tag{2}$$

Here $\vec{H}_*, \vec{H}_*^{(e)}; \vec{B}_*, \vec{B}_*^{(e)}; \vec{M}_*, \vec{M}_*^{(e)}$ are vectors of intensity, induction and magnetization of the given magnetic field in the body-shell and in surrounding infinite space; μ_0 is the

ISBN: 978-1-61804-219-4

magnetic constant $\left(\mu_0 = 4\pi \cdot 10^{-7}\,\frac{H}{M^2}\right)$; χ is the magnetic susceptibility of the body-shell material.

Continuity conditions for normal components of the induction vector and tangential components of the intensity vector of the magnetic field must be satisfied on the boundary surfaces of the body-shell. Corresponding conditions in infinity [2] for systems of equations of magnetostatics (2) also should be taken into account.

It is assumed that external surface forces act on the body. For studying the stress strain state of three-dimensional shell we'll start from basic equations and boundary conditions of spatial static (dynamic) problem of linearized micropolar theory of ferromagnetoelasticity with free fields of displacements and rotations (for dielectric material). These are equations and boundary conditions of mechanics of deformable solid and magnetostatics of perturbed magnetic field (both in the inner region of the body-shell and in outer region), conjugation conditions and conditions in infinity.

1. Equations and boundary conditions of mechanics of deformable micropolar elastic body with consideration of volume forces and moments of magnetic nature [10]:

Equilibrium equations:

$$\begin{aligned} &\nabla_m \sigma^{mk} + \rho_0 F^k = 0, \\ &\nabla_m \mu^{mk} + e^{nmk}\sigma_{nm} + \rho_0 C^k = 0. \end{aligned} \tag{3}$$

Physical relations of elasticity:

$$\begin{cases} \sigma_{mn} = (\mu+\alpha)\gamma_{mn} + (\mu-\alpha)\gamma_{nm} + \lambda\gamma_{kk}\delta_{nm} \\ \mu_{mn} = (\gamma+\varepsilon)\kappa_{mn} + (\gamma-\varepsilon)\kappa_{nm} + \beta\kappa_{kk}\delta_{nm} \end{cases} \tag{4}$$

Geometric relations:

$$\gamma_{mn} = \nabla_m V_n - e_{kmn}\omega^k, \qquad \chi_{mn} = \nabla_m \omega_n. \tag{5}$$

Here indexes m,n,k accept values 1,2,3; $\hat{\sigma},\hat{\mu}$ are tensors of force and moment stresses; $\hat{\gamma},\hat{\chi}$ are tensors of deformations and bending-torsions; $\vec{V},\vec{\omega}$ are vectors of displacements and free rotation; e^{mnk} are Levi-Civita's tensor components; δ_{nm} are Kronecker symbols; $\lambda,\mu,\alpha,\beta,\gamma,\varepsilon$ are elastic constants of the shell micropolar material [33]; ρ_0 is the density of the shell material; $\rho_0\vec{F}$, $\rho_0\vec{C}$ are intensities of massively distributed forces and moments of magnetic nature [10], [30]-[32]:

$$\rho_0 F^k = \mu_0 M_*^n \nabla_n H_*^k + \mu_0 M_*^n \nabla_n h^k + \mu_0 m^n \nabla_n H_*^k, \tag{6}$$

$$\rho_0 C^k = \varepsilon^{nmk}\mu_0\left(M_{*n}H_{*m} + M_{*n}h_m + m_n H_{*m}\right). \tag{7}$$

It should be noted that $\vec{h},\vec{b},\vec{m}$ are vectors of intensity, induction and magnetization of perturbed magnetic field of body-shell.

Further we'll use curvilinear orthogonal coordinates $\alpha_k\,(k=1,2,3)$ accepted in the theory of shells [34], but the above accepted notations for displacement and free rotation vectors' physical components, force and moment stresses tensors' components remain the same.

Mechanical boundary conditions on surfaces $\alpha_3 = \pm h$ of the shell are the followings $i = 1,2$ [30]-[32]:

$$\sigma_{3i} = \pm q_i^{\pm} + \left[\sigma_{3i}^M\right], \qquad \sigma_{33} = \pm q_3^{\pm} + \left[\sigma_{33}^M\right], \tag{8}$$

$$\mu_{3i} = \pm m_i^{\pm}, \qquad \mu_{33} = \pm m_3^{\pm}, \qquad i = 1,2, \tag{9}$$

where symbol $[A]$ indicates jump of quantity A on surfaces $\alpha_3 = \pm h$ of the shell; $\sigma_{3i}^M, \sigma_{33}^M, \sigma_{3i}^{M,e}, \sigma_{33}^{M,e}$ are components of magnetic tensor of Maxwell stresses on the mentioned surfaces respectively from the side of the body and vacuum:

$$\begin{aligned} \sigma_{mn}^M &= \mu_1 H_{*m} H_{*n} - \frac{1}{2}\mu_0 H_{*k}\delta_{mn} + \\ &+ \mu_1\left(H_{*m}h_n + h_m H_{*n}\right) - \mu_0 H_{*n}h_k\delta_{mn}, \end{aligned} \tag{10}$$

$$\begin{aligned} \sigma_{mn}^{M,e} &= \mu_0\left(H_{*m}^{(e)}H_{*n}^{(e)} - \frac{1}{2}\mu_0 H_{*k}^{(e)}H_{*k}^{(e)}\delta_{mn} + \right. \\ &\left. + \left(H_{*m}^{(e)}h_n^{(e)} + h_m^{(e)}H_{*n}^{(e)}\right) - \mu_0 H_{*n}^{(e)}h_k^{(e)}\delta_{mn}\right) \end{aligned} \tag{11}$$

Depending on how the external load is applied or the shell's points are adjusted, mechanical boundary conditions on the shell edge Σ can be written down in force and moment stresses ((8), (9)), displacements and rotations or in mixed form.

In case of the dynamic problem forces and moments of inertia $\rho_0\frac{\partial^2 \nu_k}{\partial t^2}, I_0\frac{\partial^2\omega_k}{\partial t^2}$ should be added in the mentioned equations, where I_0 is a constant, which characterizes inertial properties of the particle during its rotation. In this case initial conditions should be also given for components of vectors $\vec{\nu},\ \vec{\omega},\ \frac{\partial\vec{\nu}}{\partial t},\ \frac{\partial\vec{\omega}}{\partial t}$.

2. Equations of magnetostatics for perturbed magnetic field in body- shell [30]-[32]:

$$rot\vec{h} = 0, \quad div\vec{b} = 0, \quad \vec{b} = \mu_0\left(\vec{h} + \vec{m}\right), \quad \vec{m} = \chi\vec{h}\,. \tag{12}$$

3. Equations of magnetostatics for perturbed magnetic field in outer area from the body-shell (in vacuum) [30]-[32]:

$$rot\vec{h}^{(e)} = 0, \quad div\vec{b}^{(e)} = 0, \quad \vec{b}^{(e)} = \mu_0\vec{h}^{(e)}, \quad \vec{m}^{(e)} = 0. \tag{13}$$

Here $\vec{h}^{(e)},\vec{b}^{(e)},\vec{m}^{(e)}$ are vectors of intensity, induction and magnetization of perturbed magnetic field of outer area of three-dimensional body-shell (of vacuum).

Boundary conditions of conjugation of magnetostatic part of the problem are the followings [21], [27]:

$$e_{nmk}\left\{n_m^0\left[h_k\right] - n_p^0 V_{p,m}\left[H_{*k}\right]\right\} = 0, \tag{14}$$

$$n_m^0\left[b_m\right] - n_p^0 V_{p,m}\left[B_{*m}\right] = 0, \tag{15}$$

where n_m^0 are components of the shell boundary surface's ($\alpha_3 = \pm h$ or Σ) normal unit vector before the deformation.

Conditions of decay in infinity should be added to equations (13) of magnetostatic problem:

$\vec{h}^{(e)} \to 0$ when $r \to \infty$.

III. Main Hypotheses of Theory of Magnetostatics of Micropolar Ferromagnetic Elastic Thin Shells

It is assumed that the shell thickness is small compared with typical radii of curvature of the shell middle surface. We'll proceed from the following basic concept: in the static case magnetoelastic appearance in a thin three-dimensional

body, forming a shell, is composed of internal state, covering all the shell and surrounding three-dimensional space, and boundary layers, localizing near the surface of the shell edge Σ. Construction of general applied two-dimensional model of magnetoelasticity of micropolar ferromagnetic thin shells is closely connected with construction of the internal problem, covering all the shell and surrounding three-dimensional infinity space.

Considering that the hypotheses method, along with extremely visibility, very quickly and relatively simply leads to final results for engineering practice, theory of micropolar ferroelasticity of thin shells will be constructed on the basis of this method. From the mechanical part of the stated problem the hypotheses, which have asymptotic justification, are identical to those, which were accepted in papers [16]-[18] for construction of theory of micropolar elastic thin shells. From the magnetostatic part of the problem some hypotheses will be also accepted for perturbed magnetic field in body-shell and surrounding space.

Thus, following rather general assumptions (hypotheses) are formulated for the construction of theory of micropolar ferromagnetic elastic thin shells:

1. During the deformation initially straight and normal to the middle surface fibers rotate freely in space as a whole rigid body at an angle, without changing their length and without remaining perpendicular to the deformed middle surface.

The accepted hypothesis is mathematically written as follows:

$$V_i = u_i(\alpha_1,\alpha_2)+\alpha_3\psi_i(\alpha_1,\alpha_2),\quad V_3 = w(\alpha_1,\alpha_2),$$
$$\omega_i = \Omega_i(\alpha_1,\alpha_2),\quad \omega_3 = \Omega_3(\alpha_1,\alpha_2)+\alpha_3\iota(\alpha_1,\alpha_2).\quad (i=1,2)\ (16)$$

Thus, normal to the middle surface displacement and tangential free rotations are constant functions along the shell thickness, and the tangential displacements and normal free rotation are changed by a linear law.

It should be noted that from the point of view of displacements the hypothesis (16), in essence, is Timoshenko's kinematic hypothesis in the classical theory of elastic shells [35]-[38]. Hypothesis (16) in whole, as in papers [14]-[18], is called Timoshenko's generalized kinematic hypothesis in the micropolar theory of shells.

2. In the generalized Hook's law (4) force stress σ_{33} can be neglected in relation to the force stresses σ_{ii} in formulas for deformations γ_{ii}. Analogically, moment stresses μ_{3i} can be neglected in relation to moment stresses μ_{i3} $(i=1,2)$ in formulas for bending-torsions χ_{i3}.

3. Using the assumption of thin-walled shell, we assume

$$1+\frac{\alpha_3}{R_i}\approx 1 \qquad (i=1,2).$$

4. During the determination of deformations, bending-torsions, force and moment stresses, first for the force stresses σ_{3i} and moment stress μ_{33} we'll take:

$$\sigma_{3i} = \overset{0}{\sigma}_{3i}(\alpha_1,\alpha_2),\ i=1,2 \qquad \mu_{33} = \overset{0}{\mu}_{3i}(\alpha_1,\alpha_2). \qquad (17)$$

After determination of mentioned quantities, values of σ_{3i} and μ_{33} will be finally defined by the addition to the corresponding values (17) summed up, obtained by integration of the corresponding equilibrium equations from (3) (equations, which have derivatives by from quantities σ_{3i} $(i=1,2)$, μ_{33}), for which condition will be required, that quantities, averaged along the shell thickness, are equal to zero.

It is assumed that components of the vector $\vec{h}$ of perturbed magnetic field in thin shell are changed by linear low along the shell thickness:

$$h_k = \overset{0}{h}_k(\alpha_1,\alpha_2)+\alpha_k\overset{1}{h}_k(\alpha_1,\alpha_2)\quad (k=1,2,3). \qquad (18)$$

6. During the determination of perturbed magnetic field of surrounding the shell infinite space, the shell can be replaced with its middle surface [38], [39]. In this case surface toque with components $\left(\left[h_1^{(e)}\right],\left[h_2^{(e)}\right],0\right)$ flows along that surface and magnetic charge $\left[h_3^{(e)}\right]$ is distributed. For the jointing of internal and external problems this hypothesis is asymptotically justified in paper [39].

IV. Determination of Tensors' Components of Deformations, Bending-Torsions, Force and Moment Stresses

On the basis of Timoshenko's generalized kynematic hypothesis (16) following formulas for tensors' components of deformations and bending-torsions will be obtained from geometric relations (5):

$$\gamma_{ii} = \Gamma_{ii}(\alpha_1,\alpha_2)+\alpha_3K_{ii}(\alpha_1,\alpha_2),$$
$$\gamma_{ij} = \Gamma_{ij}(\alpha_1,\alpha_2)+\alpha_3K_{ij}(\alpha_1,\alpha_2), \qquad (19)$$
$$\gamma_{i3} = \Gamma_{i3}(\alpha_1,\alpha_2),\quad \gamma_{3i} = \Gamma_{3i}(\alpha_1,\alpha_2),\quad \gamma_{33}=0,$$
$$\chi_{ii} = \kappa_{ii}(\alpha_1,\alpha_2),\quad \chi_{ij} = \kappa_{ij}(\alpha_1,\alpha_2),$$
$$\chi_{i3} = \kappa_{i3}(\alpha_1,\alpha_2)+\alpha_3l_{i3}(\alpha_1,\alpha_2), \qquad (20)$$
$$\chi_{33} = \kappa_{33}(\alpha_1,\alpha_2),\quad \chi_{3i}=0,$$

where

$$\Gamma_{ii} = \frac{1}{A_i}\frac{\partial u_i}{\partial\alpha_i}+\frac{1}{A_iA_j}\frac{\partial A_i}{\partial\alpha_j}u_j+\frac{w}{R_i},$$

$$\Gamma_{ij} = \frac{1}{A_i}\frac{\partial u_j}{\partial\alpha_i}-\frac{1}{A_iA_j}\frac{\partial A_i}{\partial\alpha_j}u_i-(-1)^j\Omega_3,$$

$$K_{ii} = \frac{1}{A_i}\frac{\partial\psi_i}{\partial\alpha_i}+\frac{1}{A_iA_j}\frac{\partial A_i}{\partial\alpha_j}\psi_j,$$

$$K_{ij} = \frac{1}{A_i}\frac{\partial\psi_j}{\partial\alpha_i}-\frac{1}{A_iA_j}\frac{\partial A_i}{\partial\alpha_j}\psi_i-(-1)^j\iota, \qquad (21)$$

$$\Gamma_{i3} = -\vartheta_i+(-1)^j\Omega_j,\quad \Gamma_{3i} = \psi_i-(-1)^j\Omega_j,$$

$$\vartheta_i = -\frac{1}{A_i}\frac{\partial w}{\partial\alpha_i}+\frac{u_i}{R_i},\ \kappa_{ii} = \frac{1}{A_i}\frac{\partial\Omega_i}{\partial\alpha_i}+\frac{1}{A_iA_j}\frac{\partial A_i}{\partial\alpha_j}\Omega_j+\frac{\Omega_3}{R_i}$$

$$\kappa_{ij} = \frac{1}{A_i}\frac{\partial\Omega_j}{\partial\alpha_i}-\frac{1}{A_iA_j}\frac{\partial A_i}{\partial\alpha_j}\Omega_i, \qquad (22)$$

$$\kappa_{i3} = \frac{1}{A_i}\frac{\partial\Omega_3}{\partial\alpha_i}-\frac{\Omega_i}{R_i},\qquad l_{i3} = \frac{1}{A_i}\frac{\partial\iota}{\partial\alpha_i}.$$

Here and below $i,j=1,2;\ i\neq j$.

Following formulas for stress and moment stresses will be obtained using expressions (19), (20) for deformation components, static hypotheses 2, 4, generalized Hook's low (4), equilibrium equations (3) and boundary conditions (8), (9):

$$\sigma_{ii} = \frac{E}{1-\nu^2}\left(\Gamma_{ii} + \nu\Gamma_{jj}\right) + \alpha_3 \frac{E}{1-\nu^2}\left(K_{ii} + \nu K_{jj}\right),$$
$$\sigma_{ij} = \left((\mu+\alpha)\Gamma_{ij} + (\mu-\alpha)\Gamma_{ji}\right) +$$
$$+ \alpha_3\left((\mu+\alpha)K_{ij} + (\mu-\alpha)K_{ji}\right),$$
$$\sigma_{i3} = (\mu+\alpha)\Gamma_{i3} + (\mu-\alpha)\Gamma_{3i},$$
$$\sigma_{33} = \overset{0}{\sigma}_{33}(\alpha_1,\alpha_2) + \alpha_3 \overset{1}{\sigma}_{33}(\alpha_1,\alpha_2),$$
$$\overset{0}{\sigma}_{33}(\alpha_1,\alpha_2) = \frac{q_3^+ - q_3^-}{2} + \frac{1}{2}\left[\left(\sigma_{33}^{M,e} - \sigma_{33}^M\right)^+ - \left(\sigma_{33}^{M,e} - \sigma_{33}^M\right)^-\right],$$
$$\overset{1}{\sigma}_{33}(\alpha_1,\alpha_2) = -\frac{1}{A_1A_2}\left[\frac{\partial(A_2\sigma_{13})}{\partial\alpha_1} + \frac{\partial(A_1\sigma_{23})}{\partial\alpha_2}\right] +$$
$$+ \frac{\overset{0}{\sigma}_{11}}{R_1} + \frac{\overset{0}{\sigma}_{22}}{R_2} - f_3^M =$$
$$= \frac{1}{2h}\left\{\left(q_3^+ + q_3^-\right) + \left[\left(\sigma_{33}^{M,e} - \sigma_{33}^M\right)^+ + \left(\sigma_{33}^{M,e} - \sigma_{33}^M\right)^-\right]\right\},$$
$$\overset{0}{\sigma}_{3i} = (\mu+\alpha)\Gamma_{3i} + (\mu-\alpha)\Gamma_{i3}, \qquad (23)$$
$$\sigma_{3i} = \overset{0}{\sigma}_{3i}(\alpha_1,\alpha_2) +$$
$$+ \alpha_3\left\{-\frac{1}{A_iA_j}\left[\frac{\partial\left(A_j \overset{0}{\sigma}_{ii}\right)}{\partial\alpha_i} + \frac{\partial\left(A_i \overset{0}{\sigma}_{ji}\right)}{\partial\alpha_j}\right] +\right.$$
$$\left. + \frac{1}{A_iA_j}\frac{\partial A_j}{\partial\alpha_i}\overset{0}{\sigma}_{jj} - \frac{1}{A_iA_j}\frac{\partial A_i}{\partial\alpha_j}\overset{0}{\sigma}_{ij} - \frac{\sigma_{i3}}{R_i} + f_i^M\right\} +$$
$$+ \left(\frac{\alpha_3^2}{2} - \frac{h^2}{6}\right)\left\{-\frac{1}{A_iA_j}\left[\frac{\partial\left(A_j \overset{1}{\sigma}_{ii}\right)}{\partial\alpha_i} + \frac{\partial\left(A_i \overset{1}{\sigma}_{ji}\right)}{\partial\alpha_j}\right] +\right.$$
$$\left. + \frac{1}{A_iA_j}\frac{\partial A_j}{\partial\alpha_i}\overset{1}{\sigma}_{jj} - \frac{1}{A_iA_j}\frac{\partial A_i}{\partial\alpha_j}\overset{1}{\sigma}_{ij} + c_i^M\right\}.$$
$$\mu_{ii} = (\beta+2\gamma)k_{ii} + \beta\left(k_{jj} + \iota\right),$$
$$\overset{0}{\mu}_{33} = (\beta+2\gamma)\iota + \beta(k_{11} + k_{22}),$$
$$\mu_{ij} = (\gamma+\varepsilon)\kappa_{ij} + (\gamma-\varepsilon)\kappa_{ji},$$
$$\mu_{3i} = \overset{0}{\mu}_{3i}(\alpha_1+\alpha_2) + \alpha_3 \overset{1}{\mu}_{3i}(\alpha_1,\alpha_2),$$
$$\overset{0}{\mu}_{3i} = \frac{m_i^+ - m_i^-}{2},$$
$$\overset{1}{\mu}_{3i} = \frac{1}{A_i}\frac{\partial\mu_{ii}}{\partial\alpha_i} + \frac{1}{A_iA_j}\frac{\partial A_j}{\partial\alpha_i}\left(\mu_{ii} - \mu_{jj}\right) +$$
$$+ \frac{1}{A_j}\frac{\partial\mu_{ji}}{\partial\alpha_j} + \frac{1}{A_iA_j}\frac{\partial A_i}{\partial\alpha_j}\left(\mu_{ji} + \mu_{ij}\right) +$$
$$+ \frac{\overset{0}{\mu}_{i3}}{R_i} + \left(\sigma_{j3} - \overset{0}{\sigma}_{3j}\right) + m_i^M = \frac{m_i^+ + m_i^-}{2h}, \qquad (24)$$
$$\mu_{i3} = \frac{4\gamma\varepsilon}{\gamma+\varepsilon}\kappa_{i3} + \alpha_3\frac{4\gamma\varepsilon}{\gamma+\varepsilon}l_{i3},$$
$$\mu_{33} = \overset{0}{\mu}_{33}(\alpha_1,\alpha_2) +$$
$$+ \alpha_3\left\{-\frac{1}{A_1A_2}\left(\frac{\partial\left(A_2 \overset{0}{\mu}_{13}\right)}{\partial\alpha_1} + \frac{\partial\left(A_1 \overset{0}{\mu}_{23}\right)}{\partial\alpha_2}\right) +\right.$$
$$\left. + \left(\frac{\mu_{11}}{R_1} + \frac{\mu_{22}}{R_2}\right) - \left(\overset{0}{\sigma}_{12} - \overset{0}{\sigma}_{21}\right) - m_3^M\right\} + \left(\frac{\alpha_3^2}{2} - \frac{h^2}{6}\right)\cdot$$
$$\cdot\left\{-\frac{1}{A_1A_2}\left(\frac{\partial\left(A_2 \overset{1}{\mu}_{13}\right)}{\partial\alpha_1} + \frac{\partial\left(A_1 \overset{1}{\mu}_{23}\right)}{\partial\alpha_2}\right) - \left(\overset{1}{\sigma}_{12} - \overset{1}{\sigma}_{21}\right) - \Lambda_3^M\right\}.$$

Here $\overset{0}{\sigma}_{ii}, \overset{0}{\sigma}_{ij}, \overset{0}{\mu}_{i3}, \overset{1}{\sigma}_{ii}, \overset{1}{\sigma}_{ij}, \overset{1}{\mu}_{i3}$ are accordingly constant and linear by α_3 parts of force stresses σ_{ii}, σ_{ij} and moment stresses μ_{i3}. We also have following expressions for $f_k^M \ (k=1,2,3)$, $c_i^M \ (i=1,2)$, $m_k^M \ (k=1,2,3)$, Λ_3^M:

$$f_1^M = \mu_0\left\langle\left\{\overset{0}{M}_{*1}\left(\frac{1}{A_1}\frac{\partial \overset{0}{H}_{*1}}{\partial\alpha_1} + \frac{1}{A_1A_2}\frac{\partial A_1}{\partial\alpha_2}\overset{0}{H}_{*2}\right) +\right.\right.$$
$$+ \overset{0}{M}_{*2}\left(\frac{1}{A_2}\frac{\partial \overset{0}{H}_{*1}}{\partial\alpha_2} - \frac{1}{A_1A_2}\frac{\partial A_2}{\partial\alpha_1}\overset{0}{H}_{*2}\right) +$$
$$\left.\left. + \frac{\overset{0}{H}_{*1}\overset{0}{M}_{*3} + \overset{0}{H}_{*3}\overset{0}{M}_{*1}}{R_1} + \overset{0}{M}_{*3}\overset{1}{H}_{*1}\right\} +\right.$$
$$+ \left\{\overset{0}{m}_1\left(\frac{1}{A_1}\frac{\partial \overset{0}{H}_{*1}}{\partial\alpha_1} + \frac{1}{A_1A_2}\frac{\partial A_1}{\partial\alpha_2}\overset{0}{H}_{*2}\right) +\right.$$
$$\left.\left. + \overset{0}{m}_2\left(\frac{1}{A_2}\frac{\partial \overset{0}{H}_{*1}}{\partial\alpha_2} - \frac{1}{A_1A_2}\frac{\partial A_2}{\partial\alpha_1}\overset{0}{H}_{*2}\right) +\right.\right.$$

$$+\frac{\overset{0}{H}_{*1}\overset{0}{m}_3+\overset{0}{H}_{*3}\overset{0}{m}_1}{R_1}+\overset{0}{m}_3\overset{1}{H}_{*1}\Bigg\}+$$

$$+\left\{\overset{0}{M}_{*1}\left(\frac{1}{A_1}\frac{\partial\overset{0}{h}_1}{\partial\alpha_1}+\frac{1}{A_1A_2}\frac{\partial A_1}{\partial\alpha_2}\overset{0}{h}_2\right)+\right.$$

$$+\overset{0}{M}_{*2}\left(\frac{1}{A_2}\frac{\partial\overset{0}{h}_1}{\partial\alpha_2}-\frac{1}{A_1A_2}\frac{\partial A_2}{\partial\alpha_1}\overset{0}{h}_2\right)+$$

$$\left.+\frac{\overset{0}{h}_1\overset{0}{M}_{*3}+\overset{0}{h}_3\overset{0}{M}_{*1}}{R_1}+\overset{0}{M}_{*3}\overset{1}{h}_1\right\}\Bigg\rangle,$$

$$f_2^M=\mu_0\Bigg\langle\left\{\overset{0}{M}_{*1}\left(\frac{1}{A_1}\frac{\partial\overset{0}{H}_{*2}}{\partial\alpha_1}-\frac{1}{A_1A_2}\frac{\partial A_1}{\partial\alpha_2}\overset{0}{H}_{*1}\right)+\right.$$

$$+\overset{0}{M}_{*2}\left(\frac{1}{A_2}\frac{\partial\overset{0}{H}_{*2}}{\partial\alpha_2}+\frac{1}{A_1A_2}\frac{\partial A_2}{\partial\alpha_1}\overset{0}{H}_{*1}\right)+$$

$$+\overset{0}{M}_{*3}\overset{1}{H}_{*2}+\frac{\overset{0}{H}_{*2}\overset{0}{M}_{*3}+\overset{0}{H}_{*3}\overset{0}{M}_{*2}}{R_2}\Bigg\}+$$

$$+\left\{\overset{0}{m}_1\left(\frac{1}{A_1}\frac{\partial\overset{0}{H}_{*2}}{\partial\alpha_1}-\frac{1}{A_1A_2}\frac{\partial A_1}{\partial\alpha_2}\overset{0}{H}_{*1}\right)+\right.$$

$$+\overset{0}{m}_2\left(\frac{1}{A_2}\frac{\partial\overset{0}{H}_{*2}}{\partial\alpha_2}+\frac{1}{A_1A_2}\frac{\partial A_2}{\partial\alpha_1}\overset{0}{H}_{*1}\right)+$$

$$+\overset{0}{m}_3\overset{1}{H}_{*2}+\frac{\overset{0}{H}_{*2}\overset{0}{m}_3+\overset{0}{H}_{*3}\overset{0}{m}_2}{R_2}\Bigg\}+\left\{\overset{0}{M}_{*1}\left(\frac{1}{A_1}\frac{\partial\overset{0}{h}_2}{\partial\alpha_1}-\frac{1}{A_1A_2}\frac{\partial A_1}{\partial\alpha_2}\overset{0}{h}_1\right)+\right.$$

$$+\overset{0}{M}_{*2}\left(\frac{1}{A_2}\frac{\partial\overset{0}{h}_2}{\partial\alpha_2}+\frac{1}{A_1A_2}\frac{\partial A_2}{\partial\alpha_1}\overset{0}{h}_1\right)+$$

$$\left.+\overset{0}{M}_{*3}\overset{1}{h}_2+\frac{\overset{0}{h}_2\overset{0}{M}_{*3}+\overset{0}{h}_3\overset{0}{M}_{*2}}{R_2}\right\}\Bigg\rangle,$$

$$f_3^M=\mu_0\Bigg\{\overset{0}{M}_{*1}\frac{1}{A_1}\frac{\partial\overset{0}{H}_{*3}}{\partial\alpha_1}+\overset{0}{M}_{*2}\frac{1}{A_2}\frac{\partial\overset{0}{H}_{*3}}{\partial\alpha_2}+$$

$$+\overset{0}{M}_{*1}\frac{1}{A_1}\frac{\partial\overset{0}{h}_3}{\partial\alpha_1}+\overset{0}{M}_{*2}\frac{1}{A_2}\frac{\partial\overset{0}{h}_3}{\partial\alpha_2}+\overset{0}{m}_1\frac{1}{A_1}\frac{\partial\overset{0}{H}_{*3}}{\partial\alpha_1}+$$

$$+\overset{0}{m}_2\frac{1}{A_2}\frac{\partial\overset{0}{H}_{*3}}{\partial\alpha_2}-\frac{\overset{0}{M}_{*1}\overset{0}{H}_{*1}+\overset{0}{m}_1\overset{0}{H}_{*1}+\overset{0}{M}_{*1}\overset{0}{h}_1}{R_1}-$$

$$-\frac{\overset{0}{M}_{*2}\overset{0}{H}_{*2}+\overset{0}{m}_2\overset{0}{H}_{*2}+\overset{0}{M}_{*2}\overset{0}{h}_2}{R_2}\Bigg\}.$$

$$c_1^M=\mu_0\Bigg\langle\left\{\overset{1}{M}_{*1}\left(\frac{1}{A_1}\frac{\partial\overset{0}{H}_{*1}}{\partial\alpha_1}+\frac{1}{A_1A_2}\frac{\partial A_1}{\partial\alpha_2}\overset{0}{H}_{*2}\right)+\right.$$

$$+\overset{1}{M}_{*2}\left(\frac{1}{A_2}\frac{\partial\overset{0}{H}_{*1}}{\partial\alpha_2}-\frac{1}{A_1A_2}\frac{\partial A_2}{\partial\alpha_1}\overset{0}{H}_{*2}\right)+$$

$$+\overset{0}{M}_{*1}\left(\frac{1}{A_1}\frac{\partial\overset{1}{H}_{*1}}{\partial\alpha_1}+\frac{1}{A_1A_2}\frac{\partial A_1}{\partial\alpha_2}\overset{1}{H}_{*2}\right)+$$

$$+\overset{0}{M}_{*2}\left(\frac{1}{A_2}\frac{\partial\overset{1}{H}_{*1}}{\partial\alpha_2}-\frac{1}{A_1A_2}\frac{\partial A_2}{\partial\alpha_1}\overset{1}{H}_{*2}\right)+\overset{1}{M}_{*3}\overset{1}{H}_{*1}+$$

$$+\frac{\overset{1}{H}_{*1}\overset{0}{M}_{*3}+\overset{0}{H}_{*1}\overset{1}{M}_{*3}+\overset{1}{H}_{*3}\overset{0}{M}_{*1}+\overset{0}{H}_{*3}\overset{1}{M}_{*1}}{R_1}\Bigg\}+$$

$$+\left\{\overset{1}{m}_1\left(\frac{1}{A_1}\frac{\partial\overset{0}{H}_{*1}}{\partial\alpha_1}+\frac{1}{A_1A_2}\frac{\partial A_1}{\partial\alpha_2}\overset{0}{H}_{*2}\right)+\right.$$

$$+\overset{0}{m}_2\left(\frac{1}{A_2}\frac{\partial\overset{0}{H}_{*1}}{\partial\alpha_2}-\frac{1}{A_1A_2}\frac{\partial A_2}{\partial\alpha_1}\overset{0}{H}_{*2}\right)+$$

$$+\overset{0}{m}_1\left(\frac{1}{A_1}\frac{\partial\overset{1}{H}_{*1}}{\partial\alpha_1}+\frac{1}{A_1A_2}\frac{\partial A_1}{\partial\alpha_2}\overset{1}{H}_{*2}\right)+$$

$$+\overset{0}{m}_2\left(\frac{1}{A_2}\frac{\partial\overset{1}{H}_{*1}}{\partial\alpha_2}-\frac{1}{A_1A_2}\frac{\partial A_2}{\partial\alpha_1}\overset{1}{H}_{*2}\right)+\overset{1}{m}_3\overset{1}{H}_{*1}+$$

$$+\frac{\overset{1}{H}_{*1}\overset{0}{m}_3+\overset{0}{H}_{*1}\overset{1}{m}_3+\overset{1}{H}_3\overset{0}{m}_1+\overset{0}{H}_{*3}\overset{1}{m}_1}{R_1}\Bigg\}+$$

$$+\left\{\overset{1}{M}_{*1}\left(\frac{1}{A_1}\frac{\partial\overset{0}{h}_1}{\partial\alpha_1}+\frac{1}{A_1A_2}\frac{\partial A_1}{\partial\alpha_2}\overset{0}{h}_2\right)+\right.$$

$$+\overset{1}{M}_{*2}\left(\frac{1}{A_2}\frac{\partial\overset{0}{h}_1}{\partial\alpha_2}-\frac{1}{A_1A_2}\frac{\partial A_2}{\partial\alpha_1}\overset{0}{h}_2\right)+$$

(25)

$$+\overset{0}{M}_{*1}\left(\frac{1}{A_1}\frac{\partial \overset{1}{h}_1}{\partial\alpha_1}+\frac{1}{A_1A_2}\frac{\partial A_1}{\partial\alpha_2}\overset{1}{h}_2\right)+$$
$$+\overset{0}{M}_{*2}\left(\frac{1}{A_2}\frac{\partial \overset{1}{h}_1}{\partial\alpha_1}+\frac{1}{A_1A_2}\frac{\partial A_1}{\partial\alpha_2}\overset{1}{h}_2\right)+$$
$$+\overset{0}{M}_{*2}\left(\frac{1}{A_2}\frac{\partial \overset{1}{h}_1}{\partial\alpha_2}-\frac{1}{A_1A_2}\frac{\partial A_2}{\partial\alpha_1}\overset{1}{h}_2\right)+\overset{1}{M}_{*3}\overset{1}{h}_1+$$
$$+\frac{\overset{1}{h}_1\overset{0}{M}_{*3}+\overset{0}{h}_1\overset{1}{M}_{*3}+\overset{1}{h}_3\overset{0}{M}_{*1}+\overset{0}{h}_3\overset{1}{M}_{*1}}{R_1}\Bigg\}\Bigg\rangle,$$

$$c_2^M=\mu_0\Bigg\langle\Bigg\{\overset{1}{M}_{*1}\left(\frac{1}{A_1}\frac{\partial \overset{1}{H}_{*2}}{\partial\alpha_1}-\frac{1}{A_1A_2}\frac{\partial A_1}{\partial\alpha_2}\overset{1}{H}_{*1}\right)+$$
$$+\overset{0}{M}_{*2}\left(\frac{1}{A_2}\frac{\partial \overset{1}{H}_{*2}}{\partial\alpha_2}+\frac{1}{A_1A_2}\frac{\partial A_2}{\partial\alpha_1}\overset{1}{H}_{*1}\right)+$$
$$+\overset{1}{M}_{*1}\left(\frac{1}{A_1}\frac{\partial \overset{0}{H}_{*2}}{\partial\alpha_1}-\frac{1}{A_1A_2}\frac{\partial A_1}{\partial\alpha_2}\overset{0}{H}_{*1}\right)+$$
$$+\overset{1}{M}_{*2}\left(\frac{1}{A_2}\frac{\partial \overset{0}{H}_{*2}}{\partial\alpha_2}+\frac{1}{A_1A_2}\frac{\partial A_2}{\partial\alpha_1}\overset{0}{H}_{*1}\right)+\overset{1}{M}_{*3}\overset{1}{H}_{*2}+$$
$$+\frac{\overset{0}{H}_{*2}\overset{1}{M}_{*3}+\overset{1}{H}_{*2}\overset{0}{M}_{*3}+\overset{0}{H}_{*3}\overset{1}{M}_{*2}+\overset{1}{H}_{*3}\overset{0}{M}_{*2}}{R_2}\Bigg\}+$$
$$+\Bigg\{\overset{0}{m}_1\left(\frac{1}{A_1}\frac{\partial \overset{1}{H}_{*2}}{\partial\alpha_1}-\frac{1}{A_1A_2}\frac{\partial A_1}{\partial\alpha_2}\overset{1}{H}_{*1}\right)+$$
$$+\overset{0}{m}_2\left(\frac{1}{A_2}\frac{\partial \overset{1}{H}_{*2}}{\partial\alpha_2}+\frac{1}{A_1A_2}\frac{\partial A_2}{\partial\alpha_1}\overset{1}{H}_{*1}\right)+$$
$$+\overset{1}{m}_1\left(\frac{1}{A_1}\frac{\partial \overset{0}{H}_{*2}}{\partial\alpha_1}-\frac{1}{A_1A_2}\frac{\partial A_1}{\partial\alpha_2}\overset{0}{H}_{*1}\right)+$$
$$+\overset{1}{m}_2\left(\frac{1}{A_2}\frac{\partial \overset{0}{H}_{*2}}{\partial\alpha_2}+\frac{1}{A_1A_2}\frac{\partial A_2}{\partial\alpha_1}\overset{0}{H}_{*1}\right)+\overset{1}{m}_3\overset{1}{H}_{*2}+$$
$$+\frac{\overset{0}{H}_{*2}\overset{1}{m}_3+\overset{0}{H}_{*2}\overset{0}{m}_3+\overset{0}{H}_{*3}\overset{1}{m}_2+\overset{1}{H}_{*3}\overset{0}{m}_2}{R_2}\Bigg\}+ \tag{26}$$
$$+\Bigg\{\overset{0}{M}_{*1}\left(\frac{1}{A_1}\frac{\partial \overset{1}{h}_2}{\partial\alpha_1}-\frac{1}{A_1A_2}\frac{\partial A_1}{\partial\alpha_2}\overset{1}{h}_1\right)+$$
$$+\overset{0}{M}_{*2}\left(\frac{1}{A_2}\frac{\partial \overset{1}{h}_2}{\partial\alpha_2}+\frac{1}{A_1A_2}\frac{\partial A_2}{\partial\alpha_1}\overset{1}{h}_1\right)+$$
$$+\overset{1}{M}_{*1}\left(\frac{1}{A_1}\frac{\partial \overset{0}{h}_2}{\partial\alpha_1}-\frac{1}{A_1A_2}\frac{\partial A_1}{\partial\alpha_2}\overset{0}{h}_1\right)+$$
$$+\overset{1}{M}_{*2}\left(\frac{1}{A_2}\frac{\partial \overset{0}{h}_2}{\partial\alpha_2}+\frac{1}{A_1A_2}\frac{\partial A_2}{\partial\alpha_1}\overset{0}{h}_1\right)+$$
$$+\overset{1}{M}_{*3}\overset{1}{h}_2+\frac{\overset{0}{h}_2\overset{1}{M}_{*3}+\overset{1}{h}_2\overset{0}{M}_{*3}+\overset{0}{h}_3\overset{1}{M}_{*2}+\overset{1}{h}_3\overset{0}{M}_{*2}}{R_2}\Bigg\}\Bigg\rangle.$$

$$m_1^M=\mu_0\Bigg(\overset{0}{M}_{*2}\overset{0}{H}_{*3}-\overset{0}{M}_{*3}\overset{0}{H}_{*2}+\overset{0}{m}_2\overset{0}{H}_{*3}-$$
$$-\overset{0}{m}_3\overset{0}{H}_{*2}+\overset{0}{M}_{*2}\overset{0}{h}_3-\overset{0}{M}_{*3}\overset{0}{h}_2\Bigg),$$
$$m_2^M=\mu_0\Bigg(\overset{0}{M}_{*3}\overset{0}{H}_{*1}-\overset{0}{M}_{*1}\overset{0}{H}_{*3}+\overset{0}{m}_3\overset{0}{H}_{*1}-,$$
$$-\overset{0}{m}_1\overset{0}{H}_{*3}+\overset{0}{M}_{*3}\overset{0}{h}_1-\overset{0}{M}_{*1}\overset{0}{h}_3\Bigg), \tag{27}$$
$$m_3^M=\mu_0\Bigg(\overset{0}{M}_{*1}\overset{0}{H}_{*2}-\overset{0}{M}_{*2}\overset{0}{H}_{*1}+\overset{0}{m}_1\overset{0}{H}_{*2}-$$
$$-\overset{0}{m}_2\overset{0}{H}_{*1}+\overset{0}{M}_{*1}\overset{0}{h}_2-\overset{0}{M}_{*2}\overset{0}{h}_1\Bigg),$$
$$\Lambda_3^M=\mu_0\Bigg(\overset{1}{M}_{*1}\overset{0}{H}_{*2}-\overset{1}{M}_{*2}\overset{0}{H}_{*1}+\overset{0}{M}_{*1}\overset{1}{H}_{*2}-\overset{0}{M}_{*2}\overset{1}{H}_{*1}+ \tag{28}$$
$$+\overset{1}{m}_1\overset{0}{H}_{*2}-\overset{1}{m}_2\overset{0}{H}_{*1}+\overset{0}{M}_{*1}\overset{1}{h}_2-\overset{0}{M}_{*2}\overset{1}{h}_1\Bigg).$$

$\sigma_{3i}^{M,e}(\alpha_3=\pm h)-\sigma_{3i}^{M,e}(\alpha_3=\pm h)$,

$\sigma_{33}^{M,e}(\alpha_3=\pm h)-\sigma_{33}^{M,e}(\alpha_3=\pm h)$ are expressed as follows:

$$\sigma_{31}^{M,e}(\alpha_3=\pm h)-\sigma_{31}^{M,e}(\alpha_3=\pm h)=$$
$$=\frac{\mu_0\chi}{\mu_r}\vartheta_1\left[H_{*3}^{(e)}(\alpha_3=\pm h)\right]^2+\mu_0\chi\vartheta_1\left[H_{*1}^{(e)}(\alpha_3=\pm h)\right]^2+$$
$$+\mu_0\chi\vartheta_2H_{*1}^{(e)}(\alpha_3=\pm h)\cdot H_{*3}^{(e)}(\alpha_3=\pm h)=$$
$$=\left\{\frac{\mu_0\chi}{\mu_r}\left[H_{*3}^{(e)}(\alpha_3=\pm h)\right]^2+\mu_0\chi_1\left[H_{*1}^{(e)}(\alpha_3=\pm h)\right]^2\right\}\vartheta_1+$$
$$+\mu_0\chi H_{*1}^{(e)}(\alpha_3=\pm h)\cdot H_{*2}^{(e)}(\alpha_3=\pm h)\cdot\vartheta_2,$$
$$\sigma_{32}^{M,e}(\alpha_3=\pm h)-\sigma_{32}^{M,e}(\alpha_3=\pm h)=$$
$$=\frac{\mu_0\chi}{\mu_r}\vartheta_2\left[H_{*3}^{(e)}(\alpha_3=\pm h)\right]^2+\mu_0\chi\vartheta_2\left[H_{*1}^{(e)}(\alpha_3=\pm h)\right]^2+ \tag{29}$$

$$+\mu_0\chi\vartheta_1 H_{*1}^{(e)}(\alpha_3=\pm h)\cdot H_{*2}^{(e)}(\alpha_3=\pm h)=$$
$$=\mu_0\chi H_{*1}^{(e)}(\alpha_3=\pm h)\cdot H_{*2}^{(e)}(\alpha_3=\pm h)\vartheta_1+$$
$$+\left\{\frac{\mu_0\chi}{\mu_r}\left[H_{*3}^{(e)}(\alpha_3=\pm h)\right]^2+\mu_0\chi_1\left[H_{*2}^{(e)}(\alpha_3=\pm h)\right]^2\right\}\vartheta_2,$$
$$\sigma_{33}^{M,e}-\sigma_{33}^{M}=\frac{\mu_0\chi^2}{\mu_r}H_{*3}^{(e)}\cdot H_{*1}^{(e)}\cdot\vartheta_1+$$
$$+\frac{\mu_0\chi^2}{\mu_r}H_{*3}^{(e)}\cdot H_{*2}^{(e)}\cdot\vartheta_2+\frac{\mu_0\chi^2}{2\mu_r^2}\left(H_{*3}^{(e)}\right)+\frac{\mu_0\chi^2}{\mu_r}H_{*3}^{(e)}\cdot h_3.$$

V. Main Equations of Magnetoelasticity of Micropolar Ferromagnetic Thin Shells (Mechanical Part of the Problem)

In order to reduce three-dimensional system (3)-(7) of the micropolar theory of magnetoelasticity to two-dimensional (for mechanical part of the general magnetoelastic problem), which is already done for displacements, rotations, deformations, bending-torsions, force and moment stresses, instead of the components of the tensors of force and moment stresses statically equivalent to them integral characteristics are introduced [15]-[18]-forces $T_{ii}, S_{ij}, N_{i3}, N_{31}$, moments $M_{ii}, H_{ij}, L_{ii}, L_{ij}, L_{i3}, L_{33}$ and hypermoments Λ_{i3}:

$$T_{ii}=\int_{-h}^{h}\sigma_{ii}d\alpha_3,\quad S_{ij}=\int_{-h}^{h}\sigma_{ij}d\alpha_3,\quad N_{i3}=\int_{-h}^{h}\sigma_{i3}d\alpha_3,$$
$$N_{3i}=\int_{-h}^{h}\sigma_{3i}d\alpha_3,\quad M_{ii}=\int_{-h}^{h}\alpha_3\sigma_{ii}d\alpha_3,\quad H_{ij}=\int_{-h}^{h}\alpha_3\sigma_{ij}d\alpha_3,$$
$$L_{ii}=\int_{-h}^{h}\mu_{ii}d\alpha_3,\quad L_{33}=\int_{-h}^{h}\mu_{33}d\alpha_3,\quad L_{ij}=\int_{-h}^{h}\mu_{ij}d\alpha_3,\quad (30)$$
$$L_{i3}=\int_{-h}^{h}\mu_{i3}d\alpha_3,\quad \Lambda_{i3}=\int_{-h}^{h}\alpha_3\mu_{i3}d\alpha_3.$$

Using expressions (23), (24) for force and moment stresses and formulas (30), we'll obtain:

Elasticity relations:

$$T_{ii}=\frac{2Eh}{1-\nu^2}\left[\Gamma_{ii}+\nu\Gamma_{jj}\right],\qquad S_{ij}=2h\left[(\mu+\alpha)\Gamma_{ij}+(\mu-\alpha)\Gamma_{ji}\right],$$
$$M_{ii}=\frac{2Eh^3}{3(1-\nu^2)}\left[K_{ii}+\nu K_{jj}\right],$$
$$H_{ij}=\frac{2h^3}{3}\left[(\mu+\alpha)K_{ij}+(\mu-\alpha)K_{ji}\right],\quad (31)$$
$$N_{i3}=2h(\mu+\alpha)\Gamma_{i3}+2h(\mu-\alpha)\Gamma_{3i},$$
$$N_{3i}=2h(\mu+\alpha)\Gamma_{3i}+2h(\mu-\alpha)\Gamma_{i3}.$$
$$L_{ii}=2h\left[(\beta+2\gamma)k_{ii}+\beta(k_{jj}+\iota)\right],$$
$$L_{ij}=2h\left[(\gamma+\varepsilon)\kappa_{ij}+(\gamma-\varepsilon)\kappa_{ji}\right],$$
$$L_{33}=2h\left[(\beta+2\gamma)\iota+\beta(\kappa_{11}+\kappa_{22})\right],$$
$$L_{i3}=2h\frac{4\gamma\varepsilon}{\gamma+\varepsilon}\kappa_{i3},\quad \Lambda_{i3}=\frac{2h^3}{3}\frac{4\gamma\varepsilon}{\gamma+\varepsilon}l_{i3}.\quad (32)$$

Now using formulas from (23), (24) for $\sigma_{3i},\sigma_{33},\mu_{3i},\mu_{33}$ and satisfying boundary conditions (8), (9) on surfaces $\alpha_3=\pm h$, we'll obtain following equilibrium equations of magnetoelasticity for ferromagnetic shells.

Equilibrium equations:

$$\frac{1}{A_1}\frac{\partial T_{11}}{\partial\alpha_1}+\frac{1}{A_1A_2}\frac{\partial A_2}{\partial\alpha_1}(T_{11}-T_{22})+\frac{1}{A_2}\frac{\partial S_{21}}{\partial\alpha_2}+$$
$$+\frac{1}{A_1A_2}\frac{\partial A_1}{\partial\alpha_2}(S_{21}+S_{12})+\frac{N_{13}}{R_1}+2hf_1^M=-\left(q_1^+ + q_1^-\right)-P_1^M,$$
$$\frac{1}{A_1}\frac{\partial S_{12}}{\partial\alpha_1}+\frac{1}{A_2}\frac{\partial T_{22}}{\partial\alpha_2}+\frac{1}{A_1A_2}\frac{\partial A_1}{\partial\alpha_2}(T_{22}-T_{11})+$$
$$+\frac{1}{A_1A_2}\frac{\partial A_2}{\partial\alpha_1}(S_{12}+S_{21})+\frac{N_{23}}{R_2}+2hf_2^M=-\left(q_2^+ + q_2^-\right)-P_2^M,$$
$$\frac{T_{11}}{R_1}+\frac{T_{22}}{R_2}-\frac{1}{A_1A_2}\left[\frac{\partial(A_2N_{13})}{\partial\alpha_1}+\frac{\partial(A_1N_{23})}{\partial\alpha_2}\right]-2hf_3^M=$$
$$=\left(q_3^+ + q_3^-\right)+P_3^M,$$
$$N_{31}-\left[\frac{1}{A_1}\frac{\partial M_{11}}{\partial\alpha_1}+\frac{1}{A_1A_2}\frac{\partial A_2}{\partial\alpha_1}(M_{11}-M_{22})+\frac{1}{A_2}\frac{\partial H_{21}}{\partial\alpha_2}+\right.$$
$$\left.+\frac{1}{A_1A_2}\frac{\partial A_1}{\partial\alpha_2}(H_{21}+H_{12})+\frac{2h^3}{3}c_1^M\right]=h\left(q_1^+ - q_1^-\right)+hq_1^M,\quad (33)$$
$$N_{32}-\left[\frac{1}{A_2}\frac{\partial M_{22}}{\partial\alpha_2}+\frac{1}{A_1A_2}\frac{\partial A_1}{\partial\alpha_2}(M_{22}-M_{11})+\right.$$
$$\left.+\frac{1}{A_1}\frac{\partial H_{12}}{\partial\alpha_1}+\frac{1}{A_1A_2}\frac{\partial A_2}{\partial\alpha_1}(H_{12}+H_{21})+\frac{2h^3}{3}c_2^M\right]=$$
$$=h\left(q_2^+ - q_2^-\right)+hq_2^M.$$
$$\frac{1}{A_1}\frac{\partial L_{11}}{\partial\alpha_1}+\frac{1}{A_1A_2}\frac{\partial A_2}{\partial\alpha_1}(L_{11}-L_{22})+\frac{1}{A_2}\frac{\partial L_{21}}{\partial\alpha_2}+$$
$$+\frac{1}{A_1A_2}\frac{\partial A_1}{\partial\alpha_2}(L_{21}+L_{12})+\frac{L_{13}}{R_1}+(N_{23}-N_{32})+2hm_1^M=-\left(m_1^+ + m_1^-\right),$$
$$\frac{1}{A_1}\frac{\partial L_{12}}{\partial\alpha_1}+\frac{1}{A_2}\frac{\partial L_{22}}{\partial\alpha_2}+\frac{1}{A_1A_2}\frac{\partial A_1}{\partial\alpha_2}(L_{22}-L_{11})+\quad (34)$$
$$\frac{1}{A_1A_2}\frac{\partial A_2}{\partial\alpha_1}(L_{12}+L_{21})+\frac{L_{23}}{R_2}+(N_{31}-N_{13})+2hm_2^M=-\left(m_2^+ + m_2^-\right),$$
$$\frac{L_{11}}{R_1}+\frac{L_{22}}{R_2}-\frac{1}{A_1A_2}\left[\frac{\partial(A_2L_{13})}{\partial\alpha_1}+\frac{\partial(A_1L_{23})}{\partial\alpha_2}\right]-$$
$$-(S_{12}-S_{21})-2hm_3^M=\left(m_3^+ + m_3^-\right),$$
$$L_{33}-\frac{1}{A_1A_2}\left[\frac{\partial(A_2\Lambda_{13})}{\partial\alpha_1}+\frac{\partial(A_1\Lambda_{23})}{\partial\alpha_2}\right]-(H_{12}-H_{21})-$$
$$-\frac{2h^3}{3}\Lambda_3^M=h\left(m_3^+ - m_3^-\right).$$

Here P_1^M, P_2^M, P_3^M are determined with the help of components of Maxwell tensor of stresses on boundary surfaces $\alpha_3=\pm h$:

$$P_1^M = -\left[\left(\sigma_{31}^{M,e} - \sigma_{31}^M\right)^+ + \left(\sigma_{31}^{M,e} - \sigma_{31}^M\right)^-\right],$$
$$P_2^M = -\left[\left(\sigma_{32}^{M,e} - \sigma_{32}^M\right)^+ + \left(\sigma_{32}^{M,e} - \sigma_{32}^M\right)^-\right], \quad (35)$$
$$P_3^M = -\left[\left(\sigma_{32}^{M,e} - \sigma_{32}^M\right)^+ + \left(\sigma_{32}^{M,e} - \sigma_{32}^M\right)^-\right].$$

Thus, main equations of magnetoelasticity of micropolar thin shells are constructed for mechanical part of the problem (equilibrium equations (33), (34), elasticity relations (31), (32),and geometric relations (21), (22)).

VI. Main Integra-Differential Equations of Magnetoelasticity of Micropolar Ferromagnetic Thin Shells (the Whole Magnetostatic Part of the Problem)

First we'll study the magnetostatic part of the problem for perturbed magnetic field in the area of body-shell (equations (12)). We'll use hypothesis 5. In order to obtain expressions for $\overset{1}{h}_1(\alpha_1,\alpha_2)$, $\overset{1}{h}_2(\alpha_1,\alpha_2)$, first for h_3 we accept $h_3 = \overset{0}{h}_3(\alpha_1,\alpha_2)$. Then, using the first two componential equations of vector equation $rot\vec{h} = 0$ and the system (12), we'll obtain:

$$\overset{1}{h}_i(\alpha_1,\alpha_2) = \frac{1}{A_i}\frac{\partial \overset{0}{h}_3(\alpha_1,\alpha_2)}{\partial\alpha_1}. \quad (36)$$

Then substituting expressions for h_1 and h_2 from (18) into scalar equation $div\vec{b} = 0\left(div\vec{h} = 0\right)$, integrating it by α_3 and holding only linear terms, we obtain:

$$\overset{1}{h}_3(\alpha_1,\alpha_2) = -\frac{1}{A_1A_2}\left[\frac{\partial\left(\overset{0}{h}_1 A_2\right)}{\partial\alpha_1} + \frac{\partial\left(\overset{0}{h}_2 A_1\right)}{\partial\alpha_2}\right]. \quad (37)$$

Thus, we have formulas (18) with consideration of (36), (37) for components of intensity of perturbed magnetic field in the area of body-shell.

Now we'll study the magnetostatic part of the problem for perturbed magnetic field in the surrounding space of body-shell (equations (13)). Using hypothesis 6, the geometry of integration domain is greatly simplified for the problem of magnetostatic of perturbed magnetic field in the outer area of body-shell (system of equations (13)). Now the mentioned area can be considered as three-dimensional space with a cut along the shells middle surface, along which surface toque flows and on which surface magnetic charge is distributed.

Knowing Green's tensors for external problem (13) of magnetostatic for the infinite space R^3, surrounding the shell, interconnected magnetostatic problem (12), (13) can be reduced to integradifferential equations in the domain of the shell middle surface Ω (here two different problems should be discussed: the first problem, when only the surface toque $\left(\left[h_1^e\right],\left[h_2^e\right],0\right)$ is given along the cut and the second problem, when only magnetic distributed charge of intensity $\left[h_3^e\right]$ is given along the cut). Problems of Green's functions tensor are formulated for the external problem of magnetostatic (system of equations (13)) of perturbed magnetic field, when the integration domain is the whole three-dimensional space and focused factors are given for point $\left(\alpha_1^0,\alpha_2^0\right)\in\Omega$ (toque or magnetic charge):

The first problem:

$$rot\vec{h}^{(e)} = \vec{I}, \quad div\vec{h}^{(e)} = 0,$$
$$\vec{I} = \left\{\delta\left(\alpha_1^0,\alpha_2^0\right),\delta\left(\alpha_1^0,\alpha_2^0\right),0\right\}. \quad (38)$$

The second problem:

$$rot\vec{h}^{(e)} = 0, \quad div\vec{h}^{(e)} = \delta\left(\alpha_1^0,\alpha_2^0\right). \quad (39)$$

Here $\delta\left(\alpha_1^0,\alpha_2^0\right)$ is Dirac delta function; $\left(\alpha_1^0,\alpha_2^0\right)\in\Omega$, $(\alpha_1,\alpha_2,\alpha_3)\in R^3$.

It should be noted that Green's functions tensor for the whole three-dimensional infinite space for problems (38), (39) is easy to construct with the help of corresponding integral transformations [40].

When Green's functions tensor is given for the first problem, following expression will be obtained for normal component of the perturbed magnetic field, when surface toque with components $\left(h_1^{(e)}(\alpha_3=+h)-h_1^{(e)}(\alpha_3=-h)\right)$, $\left(h_2^{(e)}(\alpha_3=+h)-h_2^{(e)}(\alpha_3=-h)\right)$ flows along the shell middle surface Ω:

$$h_3^{(e)}(\alpha_1,\alpha_2,\alpha_3) = \iint_\Omega K_{13}\left(\alpha_1-\alpha_1^0,\alpha_2-\alpha_2^0\right)\cdot$$
$$\cdot\left[h_1^{(e)}(\alpha_3=+h)-h_1^{(e)}(\alpha_3=-h)\right]d\Omega + \quad (40)$$
$$+\iint_\Omega K_{23}\left(\alpha_1-\alpha_1^0,\alpha_2-\alpha_2^0\right)\left[h_2^{(e)}(\alpha_3=+h)-h_2^{(e)}(\alpha_3=-h)\right]d\Omega.$$

Here $(\alpha_1,\alpha_2,\alpha_3)\in R^3$, $\left(\alpha_1^0,\alpha_2^0\right)\in\Omega$, $K_{13}\left(\alpha_1-\alpha_1^0,\alpha_2-\alpha_2^0\right)$ and $K_{23}\left(\alpha_1-\alpha_1^0,\alpha_2-\alpha_2^0\right)$ are Green's functions tensor components for the first problem.

Boundary conditions of conjugation (14), (15) will be used for determination of $h_k^{(e)}(\alpha_3=+h)-h_k^{(e)}(\alpha_3=-h)$, $k=1,2,3$. Taking into consideration expressions for displacements V_k $(k=1,2,3)$ from formulas (16), we obtain:

$$h_i - h_i^{(e)} = \vartheta_i\left(H_{*3}-H_{*3}^{(e)}\right) \text{ when } \alpha_3=\pm h, \quad i=1,2,$$
$$\mu_r h_3 - h_3^{(e)} = -\vartheta_1\left(B_{*1}-B_{*1}^{(e)}\right)-\vartheta_2\left(B_{*2}-B_{*2}^{(e)}\right) \text{ when } \alpha_3=\pm h, \quad (41)$$

where ϑ_i has the form from formula (22). Taking into consideration formulas (18), (36), (37) on the basis of (41) we'll obtain:

$$h_1^{(e)}(\alpha_3=+h)-h_1^{(e)}(\alpha_3=-h) =$$
$$= 2h\frac{1}{A_1}\frac{\partial \overset{0}{h}_3(\alpha_1,\alpha_2)}{\partial\alpha_1} + \frac{\chi}{\mu_1}\vartheta_1\left[B_{*3}^{(e)}(\alpha_3=+h)-B_{*3}^{(e)}(\alpha_3=-h)\right],$$
$$h_2^{(e)}(\alpha_3=+h)-h_2^{(e)}(\alpha_3=-h) =$$
$$= 2h\frac{1}{A_2}\frac{\partial \overset{0}{h}_3(\alpha_1,\alpha_2)}{\partial\alpha_2} + \quad (42)$$
$$+\frac{\chi}{\mu_1}\vartheta_2\left[B_{*3}^{(e)}(\alpha_3=+h)-B_{*3}^{(e)}(\alpha_3=-h)\right],$$

$$h_3^{(e)}(\alpha_3=+h)-h_3^{(e)}(\alpha_3=-h)=$$
$$=-2h\left\{\frac{1}{A_1A_2}\frac{\partial\left(\overset{0}{h}_1 A_2\right)}{\partial\alpha_1}+\frac{1}{A_1A_2}\frac{\partial\left(\overset{0}{h}_2 A_1\right)}{\partial\alpha_2}\right\}+$$
$$+\frac{\chi}{\mu_0}\left[B_{*1}^{(e)}(\alpha_3=+h)-B_{*1}^{(e)}(\alpha_3=-h)\right]\vartheta_1+ \quad (43)$$
$$+\frac{\chi}{\mu_0}\left[B_{*2}^{(e)}(\alpha_3=+h)-B_{*2}^{(e)}(\alpha_3=-h)\right]\vartheta_2.$$

Expression for $h_3^{(e)}$ at $\alpha_3=0,\ (\alpha_1,\alpha_2)\in\Omega$ will be as follows:

$$h_3^{(e)}(\alpha_1,\alpha_2,\alpha_3)\Big|_{\alpha_3=0}=\frac{h_3^{(e)}(z=+h)+h_3^{(e)}(z=-h)}{2}. \quad (44)$$

With consideration of formulas (42), second formula from (41) and on the basis of (40) following integradifferential equations will be obtained in the domain of the shell middle surface Ω:

$$\mu_r\overset{0}{h}_3(\alpha_1,\alpha_2)+\frac{\chi}{\mu_0}\vartheta_1\frac{B_{*1}^{(e)}(\alpha_3=+h)+B_{*1}^{(e)}(\alpha_3=-h)}{2}+$$
$$+\frac{\chi}{\mu_0}\frac{B_{*2}^{(e)}(\alpha_3=+h)+B_{*2}^{(e)}(\alpha_3=-h)}{2}=$$
$$=\iint_\Omega K_{13}\left(\alpha_1-\alpha_1^0,\alpha_2-\alpha_2^0\right)\cdot \quad (45)$$
$$\cdot\left[2h\frac{1}{A_1}\frac{\partial\overset{0}{h}_3\left(\alpha_1^0,\alpha_2^0\right)}{\partial\alpha_1}+\frac{\chi}{\mu_1}\vartheta_1\left(B_{*3}^{(e)}(\alpha_3=+h)-B_{*3}^{(e)}(\alpha_3=-h)\right)\right]d\Omega+$$
$$+\iint_\Omega K_{23}\left(\alpha_1-\alpha_1^0,\alpha_2-\alpha_2^0\right)\cdot$$
$$\cdot\left[2h\frac{1}{A_2}\frac{\partial\overset{0}{h}_3\left(\alpha_1^0,\alpha_2^0\right)}{\partial\alpha_2}+\frac{\chi}{\mu_1}\vartheta_2\left(B_{*3}^{(e)}(\alpha_3=+h)-B_{*3}^{(e)}(\alpha_3=-h)\right)\right]d\Omega.$$

Analogically, if Green's functions tensor is given for the second problem ((39)), we'll obtain for $h_1^{(e)}(\alpha_1,\alpha_2,\alpha_3)$ and $h_2^{(e)}(\alpha_1,\alpha_2,\alpha_3)$:

$$h_1^{(e)}(\alpha_1,\alpha_2,\alpha_3)=\iint_\Omega P_1\left(\alpha_1-\alpha_1^0,\alpha_2-\alpha_2^0\right)\left[h_3^{(e)}\right]d\Omega, \quad (46)$$

$$h_2^{(e)}(\alpha_1,\alpha_2,\alpha_3)=\iint_\Omega P_2\left(\alpha_1-\alpha_1^0,\alpha_2-\alpha_2^0\right)\left[h_3^{(e)}\right]d\Omega, \quad (47)$$

where $P_1\left(\alpha_1-\alpha_1^0,\alpha_2-\alpha_2^0\right)$, $P_2\left(\alpha_1-\alpha_1^0,\alpha_2-\alpha_2^0\right)$ are corresponding functions from Green's tensor for the second problem and $(\alpha_1,\alpha_2,\alpha_3)\in R^3$, $\left(\alpha_1^0,\alpha_2^0\right)\in\Omega$.

Applying formulas [41]

$$h_1^{(e)}(\alpha_1,\alpha_2,\alpha_3)\Big|_{\alpha_3=0}=\frac{h_1^{(e)}(\alpha_3=+h)+h_1^{(e)}(\alpha_3=-h)}{2},$$
$$h_2^{(e)}(\alpha_1,\alpha_2,\alpha_3)\Big|_{\alpha_3=0}=\frac{h_2^{(e)}(\alpha_3=+h)+h_2^{(e)}(\alpha_3=-h)}{2}, \quad (48)$$

with consideration of (43) and the first formula from (5.6), following system of integradifferential equations will be obtained in the domain of the shell middle surface Ω:

$$\overset{0}{h}_1(\alpha_1,\alpha_2)+\frac{\chi}{\mu_1}\vartheta_1\frac{B_{*3}^{(e)}(\alpha_3=+h)+B_{*3}^{(e)}(\alpha_3=-h)}{2}=$$
$$=\iint_\Omega P_1\left(\alpha_1-\alpha_1^0,\alpha_2-\alpha_2^0\right)\Bigg\{-2\mu_r h\Bigg[\frac{1}{A_1A_2}\frac{\partial\left(\overset{0}{h}_1 A_2\right)}{\partial\alpha_1}+ \quad (49)$$
$$+\frac{1}{A_1A_2}\frac{\partial\left(\overset{0}{h}_2 A_1\right)}{\partial\alpha_2}\Bigg]+\frac{\chi}{\mu_0}\left(B_{*1}^{(e)}(\alpha_3=+h)-B_{*3}^{(e)}(\alpha_3=-h)\right)\vartheta_1+$$
$$+\frac{\chi}{\mu_0}\left(B_{*2}^{(e)}(\alpha_3=+h)-B_{*2}^{(e)}(\alpha_3=-h)\right)\vartheta_2\Bigg\}d\Omega,$$
$$\overset{0}{h}_2(\alpha_1,\alpha_2)+\frac{\chi}{\mu_1}\vartheta_2\frac{B_{*3}^{(e)}(\alpha_3=+h)+B_{*3}^{(e)}(\alpha_3=-h)}{2}=$$
$$=\iint_\Omega P_2\left(\alpha_1-\alpha_1^0,\alpha_2-\alpha_2^0\right)\Bigg\{-2\mu_r h\Bigg[\frac{1}{A_1A_2}\frac{\partial\left(\overset{0}{h}_1 A_2\right)}{\partial\alpha_1}+ \quad (50)$$
$$+\frac{1}{A_1A_2}\frac{\partial\left(\overset{0}{h}_2 A_1\right)}{\partial\alpha_2}\Bigg]+\frac{\chi}{\mu_0}\left(B_{*1}^{(e)}(\alpha_3=+h)-B_{*3}^{(e)}(\alpha_3=-h)\right)\vartheta_1+.$$
$$+\frac{\chi}{\mu_0}\left(B_{*2}^{(e)}(\alpha_3=+h)-B_{*2}^{(e)}(\alpha_3=-h)\right)\vartheta_2\Bigg\}d\Omega..$$

As we'll see internal and external problems of magnetostatics for perturbed magnetic field are reduced to the systems of integrodifferential euqations (45), (49), (50) in the shell middle surface.

VII. Mathematical Model of Micropolar Ferromagnetic Elastic Thin Shells

Thus, main equations of the general theory with free fields of displacements and rotations of magnetoelasticity of micropolar ferromagnetic thin shells are constructed. These are equilibrium equations (33), (34), elasticity relations (31), (32), geometric relations (21), (22), integrodifferential equations (45), (49), (50). Boundary conditions on the contour Γ of the shell middle surface Ω should be added to the mentioned equations.

Acceptance of hypothesis 6 means that for the problem of outer domain of the body-shell magnetostatic processes can be neglected in thin layer, enclosed between the surfaces $\alpha_3=\pm h$. This means that for the problem of outer domain of the body-shell radiation is important only from surfaces $\alpha_3=\pm h$ and it can be neglected from surface Σ. This means that averaged along the shell thickness values of components of perturbed magnetic field in the points of the boundary contour Γ of the shell middle surface Ω are equal to zero, in

addition, force magnetic interaction (magnetic tensor of Maxwell's stresses) on the shell edge surface Σ can be neglected.

Based on the above, zero boundary conditions on contour Γ of the shell middle surface should be added for components of magnetic field, perturbed in the shell:

$$\overset{0}{h}_k(\alpha_1,\alpha_2)\Big|_{\Gamma}=0,\quad k=1,2,3. \tag{6.1}$$

For the mechanical part of the problem boundary conditions on Γ remain the same as they used to without magnetomechanical interactions [15]-[17]. If the contour Γ coincides with the coordinate line $\alpha_1 = const$, these boundary conditions will expressed as follows:

$$\begin{aligned}
&T_{11}=T_{11}^{*}\ \text{or}\ u_1=u_1^{*},\quad S_{12}=S_{12}^{*}\ \text{or}\ u_2=u_2^{*},\\
&N_{13}=N_{13}^{*}\ \text{or}\ w=w^{*},\quad M_{11}=M_{11}^{*}\ \text{or}\ K_{11}=K_{11}^{*},\\
&H_{12}=H_{12}^{*}\ \text{or}\ K_{12}=K_{12}^{*},\quad L_{11}=L_{11}^{*}\ \text{or}\ \kappa_{11}=\kappa_{11}^{*},\\
&L_{12}=L_{12}^{*}\ \text{or}\ \kappa_{12}=\kappa_{12}^{*},\quad L_{13}=L_{13}^{*}\ \text{or}\ \kappa_{13}=\kappa_{13}^{*},\\
&\Lambda_{13}=\Lambda_{13}^{*}\ \text{or}\ l_{13}=l_{13}^{*}.
\end{aligned} \tag{51}$$

It should be noted that transverse shears and related deformations are completely taken into account in the constructed mathematical model of magnetoelasticity of micropolar ferromagnetic thin shells.

If on the basis of Dalamber's principle forces, moments and hypermoments of inertia $2\rho h\frac{\partial^2 u_i}{\partial t^2}$, $2\rho h\frac{\partial^2 w}{\partial t^2}$, $\frac{2h^3}{3}\rho\frac{\partial^2 \psi_i}{\partial t^2}$, $2Ih\frac{\partial^2 \Omega_i}{\partial t^2}$, $2Ih\frac{\partial^2 \Omega_3}{\partial t^2}$, $\frac{2h^3}{3}I\frac{\partial^2 \iota}{\partial t^2}$ are added in equilibrium equations (33), (34) and initial conditions for quantities $u_i, w, \frac{\partial u_i}{\partial t}, \frac{\partial w}{\partial t}$, $\psi_i, \frac{\partial \psi_i}{\partial t}$, Ω_i, Ω_3, $\frac{\partial \Omega_i}{\partial t}, \frac{\partial \Omega_3}{\partial t}, \iota, \frac{\partial \iota}{\partial t}$ are given at $t=0$, then dynamic model of magnetoelsaticity of micropolar ferromagnetic thin shells will be obtained.

Main equations and boundary conditions (initial conditions) of the general theory of magnetoelasticity of the static (dynamic) deformation of micropolar ferromagnetic elastic thin plates and bars can be obtained as private cases of the constructed model of shells.

If we accept $\alpha = 0$ in the model with free fields of displacements and rotations (33), (34), (31), (32), (21), (22), (45), (49), (50), (51), (52), (53) of magnetoelasticity of micropolar ferromagnetic thin shells, system of main equations and boundary conditions of magnetoelasticity of static (dynamic) deformation of ferromagnetic thin shells on the basis of the classical theory of elasticity will be obtained, where transverse shear deformations will be completely taken into account.

The constructed model ((33), (34), (31), (32), (21), (22), (45), (49), (50)) of magnetoelasticity of micropolar ferromagnetic thin shells with free fields of displacements and rotations is a general model. With the help of this model private models with constrained rotation can be obtained, assuming $\alpha \to \infty$.

Concrete applied problems about determination of stress-strain state, natural and forced vibrations, static and dynamic stability will be studied on the basis of the constructed general theory of magnetoelasticity of ferromagnetic micropolar elastic thin shells, plates and bars.

It is also important to note that the construction of general theory and studying of concrete problems of magnetoelasticity of ferromagnetic micropolar elastic thin shells, plates and bars open possibility of developing experimental methods for determination of elastic constants of the ferromagnetic micropolar body.

REFERENCES

[1] P. Jerman, *Mechanics of comtinua*. Moscow: Mir, 1965. (in Russian).

[2] I.E. Tamm, *Basic theory of electricity*. Moscow: Nauka, 1976. (in Russian).

[3] W.G. Brown, "Theory of Magnetoelastic Effect in Ferromagnetism" , in *Jounal of Applied Physics.* vol.36, 1965.

[4] K.B. Vlasov, "Dynamic constants of magnetopolarized environments". *Izv. NA USSR. Physical series*. vol. 10, N12, 1958 (in Russian).

[5] K.B. Vlasov, "Equations of state, determining magnetoelastic properties of ferromagnetic monocrystals" *in Journal of experimental and theoretical physics*, vol. 38, N 3, 1960 (in Russian).

[6] A.I. Akhiezer, V.B. Baryakhtar and S.V. Peletminskij, *Spin waves*. Moscow: Nauka. 1967 (in Russian).

[7] V.A. Jelnorovich, *Models of material solids, having internal electromagnetic and mechanical moments*. Moscow: P/h of Moscow Univercity, 1980 (in Russian).

[8] H.F. Tiersten, "Coupled Magnetomechanical Equations for Magnetically Saturated Insulators", in *Jour. of Math. Phys.*, vol. 5, N9, 1964, pp. 1298-1318.

[9] G.A. Maugin, *Continuum Mechanics of Electromagnetic solids*. North-Holand, ets. 1988.

[10] A. C. Eringen, *Microcontinuum Field Theories. I. Foundations and Solids.* Springer, 1998.

[11] G.E. Baxdasaryan and D.D. Asanyan, "Main equations and relations of asymmetric theory of magnetoelasticity of ferromagnetic body", *Problems of mechanics of thin deformable bodies*. Yerevan, 2002, pp. 37-47. (in Russian).

[12] J. Altenbach, H. Altenbach and V. Eremeyev, "On generalized Cosserat-Type Theories of Plates and Shells: a Short Review and Bibliography" in *Arch. Appl. Mech.* Special Issue. 2009. Doi 10. - 1007/s 00419-009-0365-3.

[13] H. Altenbach and V. Eremeyev, "On the linear theory of micropolar plates" in *Z. Angew. Math. Mech. (ZAMM)*, vol. 89, N 4, 2009, pp. 242-256.

[14] S.H. Sargsyan, "Effective Manifestations of Characteristics of Strength and Rigidity of Micropolar Elastic Thin Bars" in *Jour. of Materials Science and Engineering*, vol.2, N1, 2012, pp.98-108.

[15] S.H. Sargsyan, "Mathematical Model of Micropolar Elastic Thin Plates and Their Strength and Stiffness Characteristics" in *Journal of Applied Mechanics and Technical Physics*, vol. 53, N2, 2012, pp. 148-155. (in Russian).

[16] S.H. Sargsyan, "General theory of micropolar elastic thin shells" in *Physical mesomechanics*, vol. 14, N1, 2011, pp. 55-66. (in Russian).

[17] S.H. Sargsyan, "Mathematical Models of Micropolar Elastic Thin Shells" in *Advanced Structured Materials. Shell-like Structures. Non-classical Theories and Applications*. Springer. vol. 15, 2011, pp. 91-100.

[18] S.H. Sargsyan, "The General Dynamic Theory of Micropolar Elastic Thin Shells" in *Doklady NA of Russia*, vol. 436, N2, 2011, pp. 195-198. (in Russian).

[19] S.H. Sargsyan, "Boundary value problems of thin plates in nonsymmteric theory of elasticity" in *Applied mathematics and mechanics*,vol. 72, N 1, 2008, pp. 129-147. (in Russian).

[20] S.H. Sargsyan, "Theory of micropolar elastic thin shells" in *Applied mathematics and mechanics*, vol.76, N 2. 2012, pp. 325-343. (in Russian).

[21] S.H. Sargsyan, "Construction of mathematical model of micropolar elastic thin bars with the help of the asymptotic method" in *Izvestiya of higher educational institutions. North Caucasian region. Natural Sciences.* N5, 2012, pp. 31-37. (in Russian).
[22] S. H. Sargsyan, "Thermoelastisity of Thin Shells on the Basis of Asymmetrical Theory of Elasticity" in *Jour. of Thermal Stresses*, vol.32, N 8, 2009, pp. 791-818.
[23] S. H. Sargsyan, "Thermoelasticity of Micropolar Thin Shells" in *Proceedings of International Conference "Topical Problems of Continuum Mechanics" dedicated to centenary of academician Nagush Arutyunyan.* October 08-12, 2012. Tsakhkadzor, Armenia. Erevan. Vol.2. 2012, pp. 184-188. (in Russian).
[24] S.H. Sargsyan and L.S. Sargsyan, "Magnetoelasticity of Thin Shells and Plates Based on the Asymmetrical Theory of Elasticity" in *Advances in Mechanics and Mathematics. Mechanics of Generalized Continua. One Hundred Years After the Cosserats*, Springer, vol. 21, 2010, pp. 325-337.
[25] S.H. Sargsyan and L.S. Sargsyan, "Mathematical Models of Magnetoelasticity of Micropolar Conductive (No Ferromagnetic) Thin Shells" in *Mechanics*, vol. 65, N 2, 2012, pp. 34-45. (in Russian).
[26] G.E. Baxdasaryan and M.V. Belubekyan, "Stability of ferromagnetic plates in a gas flow in the presence of a magnetic field" in *Izvestiya NA USR Armenia. Mechanics*, vol.25, N3, 1972, pp.18-28. (in Russian).
[27] F.C. Moon, *Magneto-solid Mechanics*. New York, ets. Wiley. 1984.
[28] Y. Shindo, "The Linear Magnetoelastic problem for a soft Ferromagnetic Elastic Solid with a Finite crack" in *Applied Mechanics (ASME)*. vol. 44, 1997, pp. 47-50.
[29] Yu.N. Podilchuk and L.N. Tereshchenko, "Stress Concentration in a Soft Ferromagnetic with an Elliptic Inclusion in a Homogeneous Magnetic Field" in *Applied. Mechanics*, vol. 40, N1, 2004, pp. 83-93. (in Russian).
[30] V.V. Panasyuk, V.E. Andrejkiv and V.Z. *Parton, Fundamentals of fracture mechanics of materials.* Kiev: Naukova dumka, 1988. (in Russian).
[31] Y.H. Pao and C.S. Yen, "A Linear Theory for Soft Ferromagnetic Elastic Solids" in *Int. Jour. Eng. Sci*. vol. 11, N 4, 1973, pp. 415-436.
[32] G.E. Baxdasaryan, *Oscillation and stability of magnetoelastic systems*. Yerevan: Publ. House of Yerevan University, 1999. (in Russian).
[33] W. Nowacкi, *Theory of Asymmetric Elasticity*. Oxford: Pergamon Press, 1986.
[34] A.L. Goldenvejzer, *Theory of elastic thin shells*. Moscow. 1953. (in Russian).
[35] P.L. Pelech, *Theory of shells with shear stiffness*. Kiev: Naukova Dumka, 1973. (in Russian).
[36] Ya.M. Grigorenko and A.T. Vasilenko, *Theory of shells of variable stifffness.* Kiev: Naukova Dumka, 1981. (in Russian).
[37] E.I. Grigolyuk and G.M. Kulikov, *Multilayered reinforced shells. Calculation of pneumatic tires.* Moscow: Engineering, 1988. (in Russian).
[38] G.E. Baxdasaryan, "Equations of magnetoelastic vibrations of thin perfectly conducted shells" in *Applied mechanics*, vol. XIX, N12, 1983, pp. 87-91. (in Russian).
[39] S.H. Sargsyan *General two-dimensional theory of magnetoelasticity of thin shells.* Yerevan: Ph of NAS Armenia,1992. (in Russian).
[40] G.T. Markov and A.F. Chaplin, *Purturbed electromagnetic waves*. Moscow: "Radno i svyaz", 1983. (in Russian).
[41] A.N. Tikhonov and A.A. Samarskij, *Equations of Mathematical Physics*. Moscow: Nauka, 1972. (in Russian).

Samvel H. Sargsyan was born on December 5, 1944 in Leninakan, Armenia. He was a student in Leninakan branch of Yerevan Polytechnic Institute, faculty of Mechanics, major "Devices of Correct Mechanics" in 1962-1967, aspirant in Yerevan State University, faculty of Mathematics and Mechanics in 1970-1973. He is a candidate of physical and mathematical sciences since 1974, doctor of physical and mathematical sciences since 1987, professor since 1989, Corresponding Member of NAS Armenia since 2006.

He was Head chair of Theoretical Mechanics in Leninakan branch of Yerevan Politechnical Institute in1986-1994, Rector of Gyumri State Pedagogical Institute after M. Nalbandyan in 1994-1997, Head chair of Mathematical Analysis and Differential Equations in Gyumri State Pedagogical Institute since 1995 till now. List of previous publications:

1. S.H. Sargsyan, *General two-dimensional theory of magnetoelasticity of thin shells.* Yerevan: NAS Armenia, 1992 (in Russian)
2. S.H. Sargsyan, "General theory of micropolar elastic thin shells", *Physical mesomechanics*, vol. 15, N1-2, 2012, pp. 69-79.
3. S.H. Sargsyan, "Theory of micropolar elastic thin shells", *Applied mathematics and mechanics*, vol.76, 2012, pp. 235-249.

Scientific interests: Mechanics of thin walled systems (bars, plates and shells), Thermo-electro-magnetic mechanics of thin plates and shells, Mechanics of micropolar thin walled systems (bars, plates and shells), Discreet-continual models of mechanics.

Professor Sargsyan is Member of International Association of Applied Mathematics and Mechanics (GAMM), Member of Euromech, Member of National Committee of Theoretical and Applied Mechanics of Russia.

Numerical investigation of mhd free convection effectson non-newtonian fluid over a vertical porous plate

Rasul alizadeh, Alireza darvish

Abstract— The transient MHD Free Convection Effects on non-Newtonian Fluid over a Vertical Porous Plate has been investigated. The governing boundary layer equations and boundary conditions are cast into a dimensionless form by similarity transformation and the resulting system of equations is solved by a finite difference method. Using the obtained solutions, we have investigated different system parameters such as suction and injection velocities, power-Law index and also the magnetic field parameter. The results which are in good agreement with theoretical models have been compared and investigated. Results are found for power-law fluids.

Keywords— Unsteady, Free convection, MHD, Power-Law, Porous plate, Vertical plate.

I. INTRODUCTION

The problem of the free convection of a non-Newtonian fluid passing a porous plate under the influence of a magnetic field has attracted the interest of different groups because of its applications in geophysics, astrophysics, engineering, and also in the boundary layer control in the field of aerodynamics. Also non-Newtonian fluids have been considered a lot in modern technologies due to their growing use. Different works have been done in this context. Sattar et al. [1] obtained analytical and numerical solutions for free convection flow along a porous plate with variable suction and injection. Soundalgekar and Wavre [2] investigated unsteady free convection flow along vertical porous plate with different boundary conditions and viscous dissipation effect. Raptis and Kafousias [3] studied the influence of a magnetic field upon the steady free convection flow through a porous medium bounded by an infinite vertical plate with a constant suction velocity, and when the plate tempreture is also constant. The unsteady free convection flows over vertical plate studied by authors Gokhale. [4]. Cheng and Lau [5] and Cheng and Teckchandani [6] obtained numerical solutions for the convective flow in a porous medium bounded by two isothermal parallel plates in the presence of withdrawal of the fluid. Hassanien et al. [7] studied the flow and heat transfer in a power-law fluid over a non-isothermal stretching sheet. Also the various effects of MHD upon the behaviour of the non-newtonian fluid have been widely investigated in past few years[8,9,10,11].

As the most of the fluids in the modern applications are not strictly newtonian, the analysis considering the non-Newtonian behavior of these fluids in such flows are pay special attentions recently. In this context, viscoelastic boundary-layer flow along a vertical porous plate has been the subject of a large number of publications. It is worth mentioning here that many of the inelastic non-Newtonian fluids encountered in chemical engineering processes, are known to follow the empirical Ostwaald–de Waele model or the so-called ‘‘power-law model’’ in which the shear stress varies according to a power function of the strain rate. Hence, the purpose of this work is to study the effect of MHD on unsteady free-convection flow over a vertical porous plate.

II. MATHEMATIC MODELLING

A two-dimensional, unsteady free convective flow of a non-Newtonian fluid has been considered which passes through a finite vertical porous plate. It is also assumed that the surface absorbs the fluid with a constant velocity.

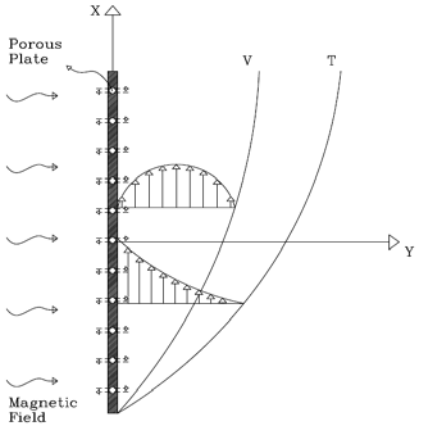

Fig. 1. Sketch of the physical model.

Rasul alizadeh :PHD student , Department of mechanic,science and research branch , azad university , Tehran , iran ; e-mail: r_alizadeh86@yahoo.com).

Alireza darvish : Guilan university , rasht, iran (e-mail: adb_baran@yahoo.com).

A system of rectangular coordinates xyz is taken such that $y = 0$ on the plate and the x -axis is along its leading edge. As shown in Fig. 1, a uniform magnetic field of strength B_0 is applied along the y -axis. The plate is maintained at a constant temperature T_w greater than the constant temperature T_∞ of the surrounding fluid.

The governing equations include mass conservation in a continuous medium (Eq. 1), The Navier-Stokes equation (Eq. 2) and also the energy equation (Eq. 3). Under the boundary layer and the Boussinesq approximations [12] and [13], the unsteady two-dimensional laminar boundary layer free convective flow is governed by the equations:

$$\frac{\partial u}{\partial x}+\frac{\partial v}{\partial y}=0 \tag{1}$$

$$\frac{\partial u}{\partial t}+u\frac{\partial u}{\partial x}+v\frac{\partial u}{\partial y}=\frac{1}{\rho}\frac{\partial}{\partial y}\left[\mu\frac{\partial u}{\partial y}\right]+g\beta\left(T-T_\infty\right)-\frac{\sigma B_0^2}{\rho}u \tag{2}$$

$$\frac{\partial T}{\partial t}+u\frac{\partial T}{\partial x}+v\frac{\partial T}{\partial y}=\alpha\frac{\partial^2 T}{\partial y^2} \tag{3}$$

where u and v are the velocity components along x and y directions respectively, ρ is the density, t is the time, μ is the fluid dynamic viscosity, α is the effective fluid thermal diffusivity, β is the coefficient of thermal expansion, g is the acceleration due to gravity, T is the temperature of the fluid, σ the electric conductivity and B_0 the applied magnetic field.

The Navier-Stokes equation includes different parameters. The non-Newtonian fluid model used in this study is the power-law model (Eq. 4) [14].

$$\tau = m\left|\frac{\partial u}{\partial y}\right|^{N-1}\frac{\partial u}{\partial y} \tag{4}$$

Where τ is the stress tensor, m is the consistency coefficient and N is the power-law index. When N= 1 the Eq. 4 represent a newtonian fluid with the dynamic coefficient of viscosity m.

If N < 1, the fluid is said to be ‘‘pseudoplastic’’ and if N > 1, the fluid is called ‘‘dilatant’’.

It should be noted that the second term of the Navier-Stokes equation express the summation of the gravitation and pressure gradients effect. Assuming that the pressure gradient inside and outside the boundary layer is the same, this term can be shown as Eq. 5.

$$-g-\frac{1}{\rho}\frac{\partial P}{\partial x}=\frac{1}{\rho}g\left(\rho_\infty-\rho\right) \tag{5}$$

The density may be represented by a linear function of temperature for small temperature differences and the change in density is related to the thermal expansivity, β, which can be approximated as Eq. 6.

$$\beta\cong-\frac{1}{\rho}\left(\frac{\rho_\infty-\rho}{T_\infty-T}\right)_P \tag{6}$$

Using this thermal expansivity the Eq. 5 can be expressed as Eq. 7.

$$\rho_\infty-\rho\cong\rho\beta(T-T_\infty) \tag{7}$$

The third term of Navier-Stokes equation explain the effect of magnetic field on the fluid motion which shows the interaction of the electromagnetic field and the fluid charges.

$$\vec{f}=\frac{1}{V}\left[\left(\sum_\ell q^\ell\right)\vec{E}+\left(\sum_\ell q^\ell\vec{v}^\ell\right)\times\vec{B}\right]=\sigma\vec{E}+\vec{j}\times\vec{B} \tag{8}$$

Using a generalized Ohm’s law for fluids in motion the electric current can be formulated as Eq. 9.

$$\vec{j}=\sigma(\vec{E}+\vec{v}\times\vec{B}) \tag{9}$$

As the fluid is usually assumed to be “almost electro-neutral”, the electric component of the force can be neglected. Under the assumptions that the magnetic Reynolds number of the flow is small enough, the induced magnetic field can also be neglected. By taking the magnetic induction $\vec{B}$ perpendicular to the plate, i.e. $\vec{B}\equiv(0,B_0,0)$, the pendermotive force has one non-vanishing component in x-direction given by:

$$\vec{f}=\sigma(\vec{v}\times\vec{B})\times\vec{B}=-\sigma B_0^2 u \tag{10}$$

Introducing the following dimensionless quantities:

$$x=\frac{X}{L},\quad y=\frac{Y}{L}Gr^{1/4},\quad u=\frac{UL}{\upsilon_o}Gr^{-1/2},\quad v=\frac{VL}{\upsilon_o}Gr^{-1/4},\quad \bar{\mu}=\frac{\mu}{\mu_o},$$

$$\bar{\mu}=\left|\frac{\partial U}{\partial Y}\right|^{N-1},\ \mu_o=m\left(\frac{\upsilon_o Gr^{\frac{3}{4}}}{L^2}\right)^{N-1},\ t=\frac{\upsilon_o t'}{L^2}Gr^{1/2},\quad \theta=\frac{T-T_\infty}{T_w-T_\infty}, \tag{11}$$

$$Gr=\frac{g\beta L^3(T_w-T_\infty)}{\upsilon_o^2},\quad MN=\frac{\sigma B_0^2 L^2}{\mu_o Gr^{1/2}},\ \mathrm{Pr}=\frac{\upsilon_o}{\alpha},\ \mu=m\left|\frac{\partial u}{\partial y}\right|^{N-1}$$

Where L is the length of the plate, Gr is the Grashof number, Pr is the Prandtl number, μ_o is the reference dynamic viscosity, υ_o is the reference kinematic viscosity. V_0 is the normal velocity at the plate having positive value for suction and negative for blowing. The governing equations in dimensionless form could be:

$$\frac{\partial U}{\partial X}+\frac{\partial V}{\partial Y}=0 \tag{12}$$

$$\frac{\partial U}{\partial t'}+U\frac{\partial U}{\partial X}+V\frac{\partial U}{\partial Y}=N\frac{\partial^2 U}{\partial Y^2}\left|\frac{\partial U}{\partial Y}\right|^{N-1}+\theta-(MN)U \tag{13}$$

$$\frac{\partial\theta}{\partial t'}+U\frac{\partial\theta}{\partial X}+V\frac{\partial\theta}{\partial Y}=\frac{1}{\mathrm{Pr}}\frac{\partial^2\theta}{\partial Y^2} \tag{14}$$

Under these assumptions, the appropriate boundary conditions for the velocity and temperature fields are:

$$\begin{aligned}
&t'\le 0\ ,\ U=0\ ,\ V=0\ ,\ \theta=0\\
&t'>0,\ U=0\ ,V=-V_0\ ,\ \theta=1\quad \text{at } Y=0\\
&\theta=0\ ,\ U=0\qquad\qquad \text{at } X=0\\
&Y\to\infty\qquad\qquad\qquad \text{at } \theta=0\ ,U\to 0
\end{aligned} \tag{15}$$

III. RESULTS AND DISCUSSIONS

Solving the obtained differential equation system, different system parameters are investigated. These include the suction and injection velocities, power-Law index, the magnetic field parameter and also the distribution of the velocities and

temperature versus various positions on the plate. It was observed that magnetic field does affect the transient velocity and temperature field of free convection flow of an electrically conducting fluid near a vertical porous plate surface temperature.

Figs. 2 and 3 describe the behavior of transient velocity and temperature for fluids with different value of power-law index N. It can be observed that the temperature decreases monotonously with increasing the n but the velocity has a different behavior for small and large N.

Figs. 4 and 5 describe the behavior of transient velocity and temperature with changes in the values of the length of plate X. It is observed that the velocity and temperature increases with increasing X.

Figs. 6 and 7 show the effect of suction parameter ‘‘V_0’’ on the transient velocity and temperature. It is observed that the transient velocity and temperature decrease with increasing .

Figs. 8 and 9 describe the behavior of transient velocity and temperature with changes in the values of the magnetic field parameter “MN”. It is observed that the velocity decreases with increases in ‘‘MN’’ parameters. However, the temperature increases with an increase in ‘‘MN’’ parameters.

Figs. 10 and 11 show the effect of Prandtl number ‘‘Pr’’ on the transient velocity and temperature. It is observed that the transient velocity and temperature decrease with increasing the Prandtl number ‘‘Pr’’.

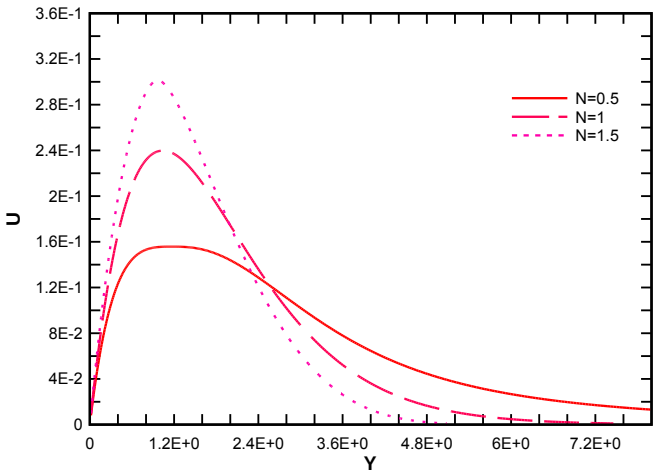

Fig.2. Transient velocity profiles for different values of parameter n
X=2 , Pr=10 , V0=0 ,MN=1

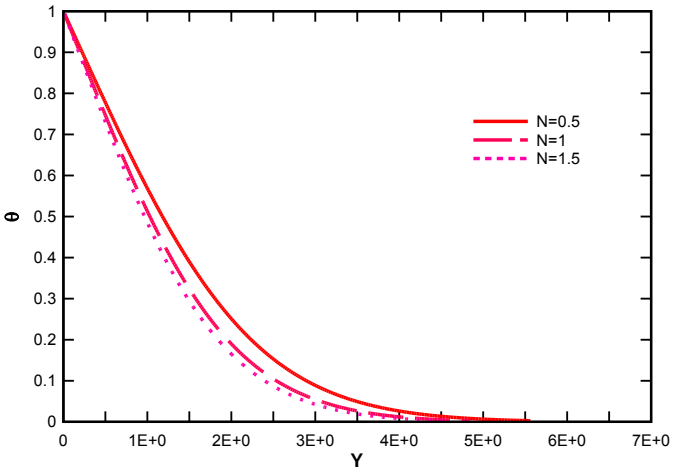

Fig.3. Transient temperature profiles for the different values of parameter n
X=2 , Pr=10 , V0=0 ,MN=1

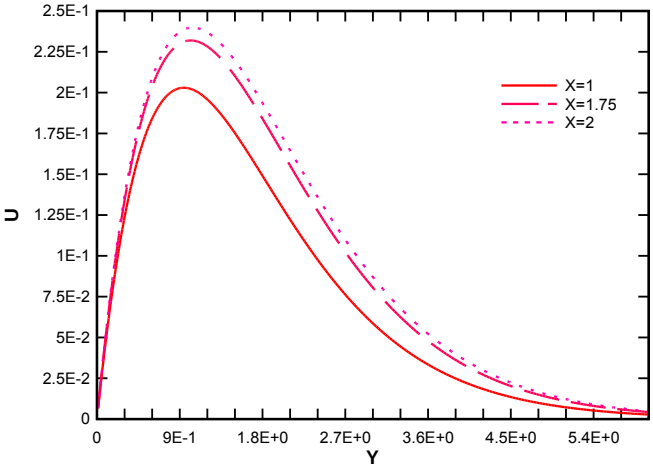

Fig.4. Comparison of velocity profiles at different values of X
MN=1, Pr=10, V0=0, N=1

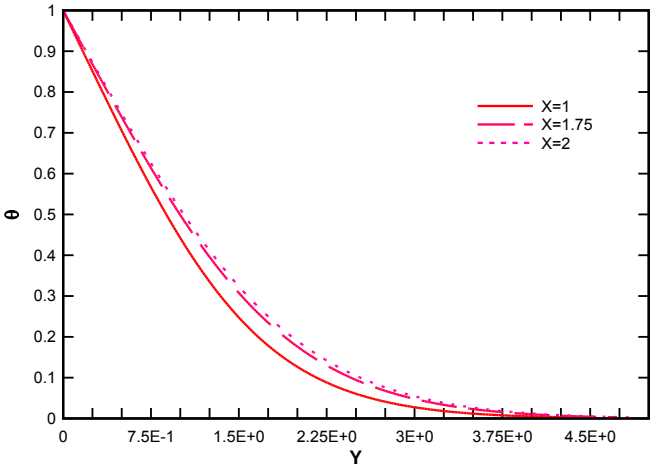

Fig.5. Comparison of temperature profiles for different values of X
MN=1 , Pr=10 , V0=0 ,N=1

ISBN: 978-1-61804-219-4

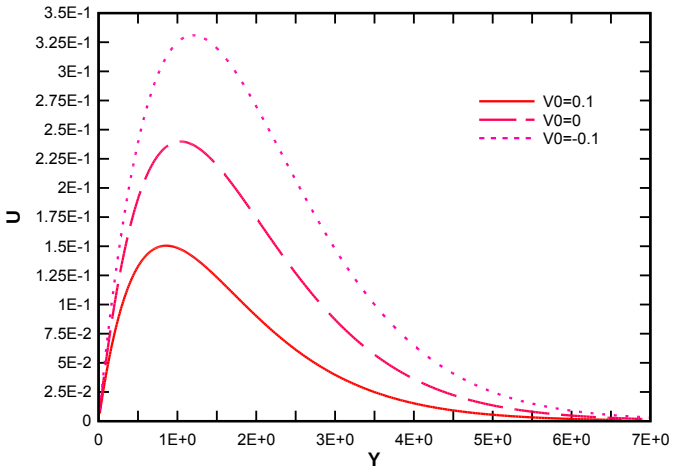

Fig.6. Transient velocity profiles for the different values of parameter V0, X=2 , Pr=10 , N=1 ,MN=1

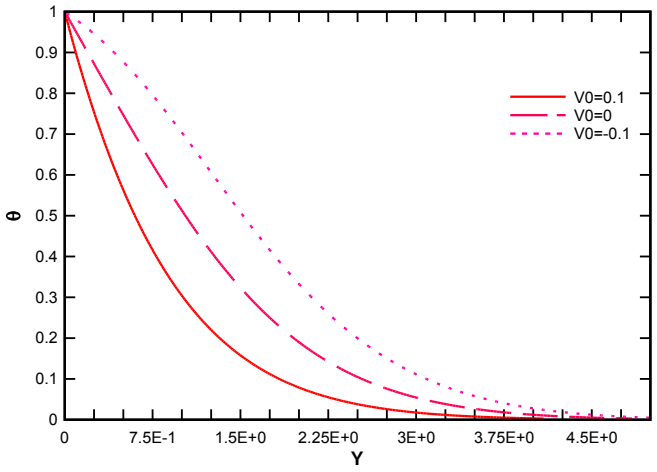

Fig. 7. Transient temperature profiles for the different values of parameter V0 , X=2 , Pr=10 , N=1 ,MN=1

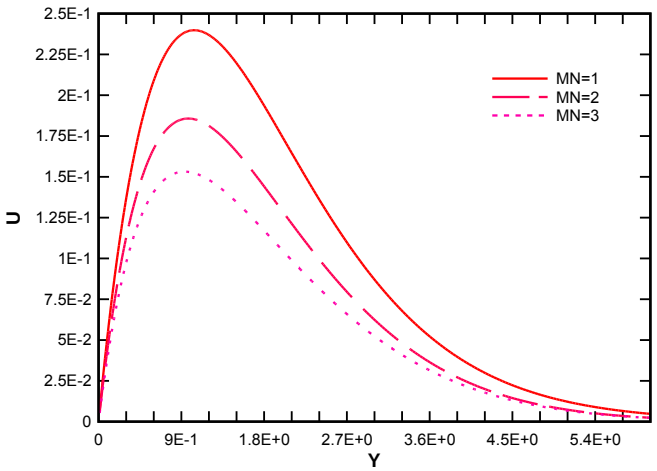

Fig. 8. Transient velocity profiles for the different values of parameter MN , X=2 , Pr=10 , V0=0 ,N=1

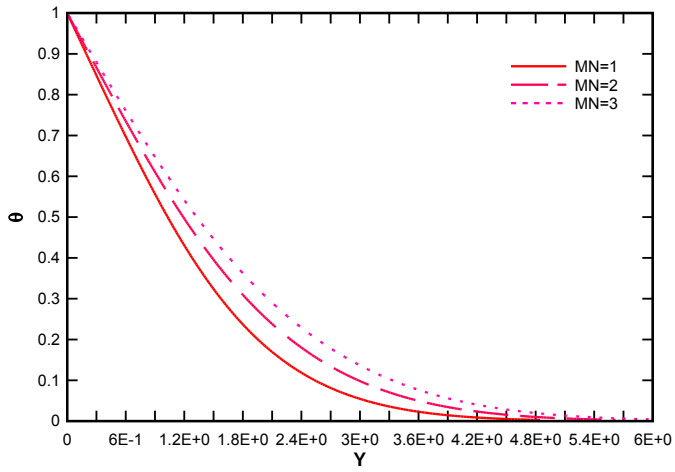

Fig. 9. Transient temperature profiles for the different values of parameter MN , X=2 , Pr=10 , V0=0 ,N=1

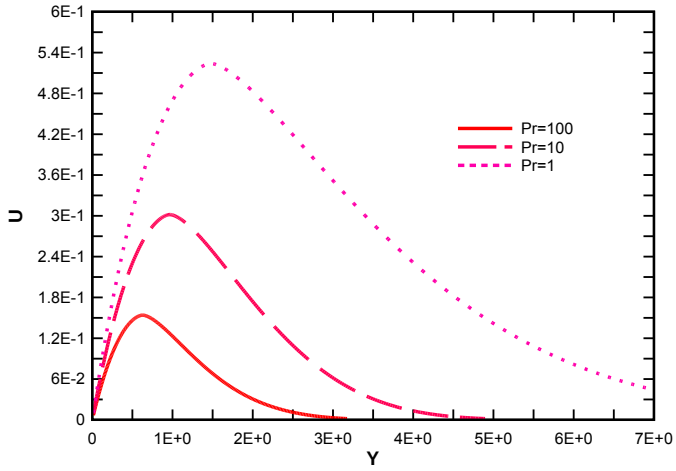

Fig.10. Transient velocity profiles for the different values of parameter Pr

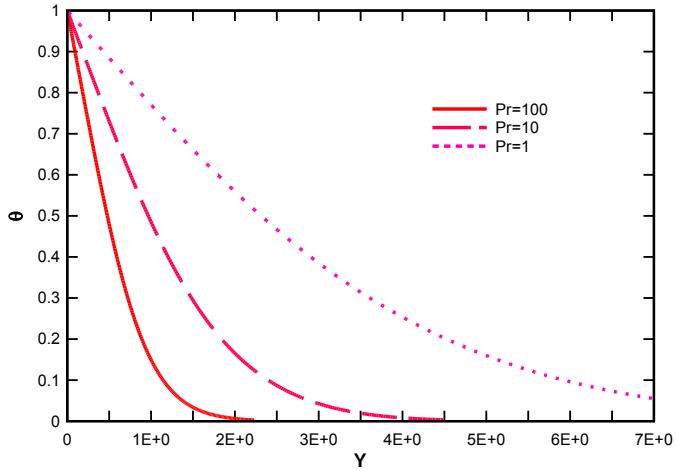

Fig.11. Transient temperature profiles for the different values of parameter Pr

IV. CONCLUSION

Considering all the effective parameters for the non-Newtonian fluid passing a vertical porous plate in a magnetic field, we have numerically solved the governing equations. These

ISBN: 978-1-61804-219-4

include continuity, momentum and energy equations which together make a system of differential equations that is solved using finite difference method. Incorporating this solution approach, different system parameters have been investigated.
Based on the obtained graphical results, the following conclusions were deduced:

- Velocity of fluid increases with a decrease of the magnetic parameter MN, the Prandtl number Pr and the suction velocity.
- The effect of increasing values of Prandtl number is to decrease temperature significantly.
- The temperature increases when MN parameters increase.

- The temperature increases when the flow behavior index N decrease.

REFERENCES

[1] Sattar MA, Rahman MM, and Alam MM. Free convection flow and heat transfer through a porous vertical plate immersed in a porous medium with variable suction. Journal of Energy, Heat and Mass Transfer, 21, pp.17-21 (2000).
[2] Soundalgekar VM and Wavre PD. Unsteady free convection flow past an infinite vertical plate with constant suction and mass transfer. International Journal of Heat and Mass Transfer, 20, (1977) pp.1363-1373.
[3] A.A. Raptis, N.kafousias, Heat transfer in flow through a porous medium bounded by infinite vertical plate under the action of magnetic field, Int. J. Energy Res. 10, (1986), pp. 97-100.
[4] M.Y. Gokhale, Magnetohydrodynamic transient-free convection past a semi-infinite vertical plate with constant heat flux, Can. J. Phys. 69, (1991), pp.1451–1453.
[5] Cheng, P.; Lau, K. H.: In: Proc. 2nd united Nation's Symp. Development use geotherm. Resources, 1591±±1598 (1977).
[6] Cheng, P.; Teckchandani, L.: In: Symposium Nat. phys. prop. Earth's crust, Vail, Colorado, 2±±6 August (1976).
[7] I.A. Hassanien, A.A. Abdullah, R.S. Gorla, Math. Comput. Model. 28 (1997) 105.
[8] Emad M. Abo-Eldahab, Ahmed M. Salem, MHD free-convection flow of a non-Newtonian power-law fluid at a stretching surface with a uniform free-stream, Journal of Applied Mathematics and Computation, (2005) 169
[9] M.A. Abd El-Naby, Elsayed M.E. Elbarbar, Nader Y. AbdElazem, Finite difference solution of radiation effects on MHD unsteady free-convection flow over vertical porous plate, Journal of Applied Mathematics and Computation, (2004) 151.
[10] Youn J. Kim, Unsteady MHD convection flow of polar fluids past a vertical moving porous plate in a porous medium, International Journal of Heat and Mass Transfer, (2001) 44.
[11] P.R. Sharma and G. Singh, Unsteady MHD free convection and heat transfer along a vertical porous plate with variable suction and internal heat generation, Int. J. of Appl. Math and Mech, (2008) 4.
[12] S. Kakac, Y. Yener, Convective Heat Transfer, CRC Press Inc, Boca Raton, FL, 1995.
[13] W.M. Rohsenow, J.P. Hartnett, Y.I. Cho (Eds.), Handbook of Heat Transfer, McGraw-Hill,
New York, 1998.
[14] R.B. Bird, W.E. Stewart, E.N. Lightfood, Transport Phenomena, John Wiley, New York, 1960.
[15] H. S. Takhar, P. Ganesan, K. Ekambavahar, and V. M. Soundalgekar, Transient free convection past a semi-infinite vertical plate with variable surface temperature, Internat. J. Numer. Methods Heat Fluid Flow 7 (1997), 280–296.

Numerical Simulation of a Nonlinear Problem of a Fast Diffusive Filtration with a Variable Density and Nonlocal Boundary Conditions

M. Aripov, Z. Rakhmonov

Abstract. In this paper we study the global solvability or no solvability of a nonlinear filtration problem in the case of fast diffusion. The conditions of existence and nonexistence of solutions for nonlinear filtering problem globally in time is finding. In the case of the global solvability of the asymptotic behavior of the solution obtained by means of asymptotic formula carried out numerical calculations. Results of numerical experiments showed that the results agreed with physics of a nonlinear filtration.

***Keywords*:** filtration, diffusion, nonlinear, asymptotic behavior, critical exponent, numerical analysis.

I. Introduction

In this paper, we consider the following polytrophic filtration equation:

$$\rho(x)\frac{\partial u}{\partial t}=\frac{\partial}{\partial x}\left(\left|\frac{\partial u^m}{\partial x}\right|^{p-2}\frac{\partial u^m}{\partial x}\right),\ (x,\ t)\in R_+\times(0,+\infty),\ (1)$$

subject to a nonlinear boundary flux and initial value conditions

$$-\left|\frac{\partial u^m}{\partial x}\right|^{p-2}\frac{\partial u^m}{\partial x}(0,\ t)=\ u^q(0,\ t),\quad t\in(0,+\infty),\quad (2)$$

$$u(x,0)\ =\ u_0(x),\ x\in R_+,\qquad (3)$$

where $\rho(x)=|x|^n$, $m>0,\ p>1,\ q>0$, $n\in R$ and $u_0(x)$ is a nontrivial, nonnegative, bounded and appropriately smooth function. In this paper we assume that p satisfies

$$p<1+1/m$$

The particular feature of equation (1) is its power- and gradient-dependent diffusivity. Equation (1) and its *N*-dimensional version arise in some physical models such as population dynamics, chemical reactions, heat transfer, etc. In particular, equation (1) may be used to describe the no stationary flow in a porous medium of fluids with a power dependence of the tangential stress on the velocity of displacement under polytrophic conditions. In this case, equation (1.1) is called the non-Newtonian polytrophic filtration equation, which has been intensively studied since the last century (see [3, 4] and references therein). The nonlinear boundary condition (2) can be used to describe the influx of energy input at the boundary $x=0$. For instance, in the heat transfer process (2) represents the heat flux, and hence the boundary conditions represent a nonlinear radiation law at the boundary. This kind of boundary condition appears also in combustion problems when the reaction happens only at the boundary of the container, for example because of the presence of a solid catalyzer, see [5] for a justification.

Equation (1) is called a parabolic equation with variable density [14].

In [6], Galaktionov and Levine studied the problem (1)-(3) for $p=2$, $n=0$ and for $m=1$, $n=0$. They proved that for the problem (1)-(3) the critical global exponent is $q_0=(m+1)/2$ and the critical Fujita exponent is $q_c=m+1$ (for $p=2$, $n=0$), while for the $m=1$, $n=0$ critical global exponent is $q_0=2(p-1)/p$ and the critical Fujita exponent is $q_c=2(p-1)$.

Wang and Yin [4], Li and Mu [7] studied problem (1)-(3) in the case of slow diffusion and fast diffusion, respectively, they showed that the critical global existence exponent and critical Fujita exponent are

This work was supported by the Grant "YOF-4-10" Republic of Uzbekistan, Nonlinear Diffusion reaction processes Russia-Uzbek joint project.

M.M. Aripov is with the National University of Uzbekistan, Tashkent, 100174 Uzbekistan (corresponding author to provide phone: +998946265232; e-mail: mirsaidaripov@mail.ru).

Z. R. Rakhmonov is with the National University of Uzbekistan, Tashkent, 100174 Uzbekistan (e-mail: zraxmonov@inbox.ru.).

$$q_0 = (m+1)(p-1)/p$$

and

$$q_c = (m+1)(p-1).$$

Recently, Jiang and Zheng [8] studied the following single equation:

$$\begin{cases} u_t = (|u_x|^{\beta}(u^m)_x)_x, & x>0,\ 0<t<T, \\ -|u_x|^{\beta}(u^m)_x(0,t) = u^p(0,t), & 0<t<T, \\ u(x,0) = u_0(x), & x>0 \end{cases}$$

where $m \ge 1,\ p>0,\ \beta>0.$ They obtained the critical global existence exponent $p_0 = (2\beta+m+1)/(\beta+2)$ and the critical Fujita exponent $p_c = 2\beta+m+1.$ These results are the extensions of those of Galaktionov and Levine [6].

Qi [9] studied the following Cauchy problem

$$\begin{aligned} &u_t = \Delta u^m + |x|^{\sigma} u^p, && x \in R^N, \quad t>0 \\ &u(x,0) = u_0(x), && x \in R^N, \end{aligned}$$

and established the critical Fujita exponent $p_c = m + (2+\sigma)/N$ for $m > (N-2)_+/N$.

In [18], some Fujita type results extended to

$$|x|^m u_t = \Delta u^k + |x|^n u^q, \quad x \in R^N, \quad t>0,$$

with $q > k \ge 1$ and $0 < m \le n < qm+q-1$ and the critical Fujita exponent was given as $q_c = k + (2+n)/(N+m)$.

The Cauchy problem of another nonlinear diffusive equation of the form

$$u_t = div(|\nabla u|^{p-2}\nabla u) + |x|^n u^q, \qquad (4)$$

where $p > (N+1)/(2N),\ q>1,$ was also considered by some authors. For the problem (4) with $p>2$ and $n=0$, Qi [10, 11] obtained that $q_c = p-1+p/N$ is the critical Fujita exponent of (4) and q_c belongs to the blow-up case. If $n \ne 0$ in (4), Qi and Wang [12] proved that the critical Fujita exponent $q_c = p-1+(p+n)/N$ for $(N+1)/(2N) < p < 2$.

Z. Li, Ch. Mu and W. Du [19] consider the Cauchy problem for p-Laplace equation with variable density.

Regular property of the Cauchy problem for the equations

$$s(x)\frac{\partial u}{\partial t} = div\left(u^{k-1}|Du|^{\lambda-1}Du\right), \quad (x,t) \in R^{N+1}$$

where $s(x) = |x|^{-l}$, $l \ge 0$, $Du \equiv \left(\frac{\partial u}{\partial x_1}, ..., \frac{\partial u}{\partial x_N}\right)$, was considered by authors of the work[].

Martynenko and Tedeev [13, 14], studied the Cauchy problem for the following two equations with variable coefficients:

$$\rho(x)u_t = div(u^{m-1}|\nabla u|^{\lambda-1}\nabla u) + u^p, \quad x \in R^N,\ t>0$$

and

$$\rho(x)u_t = div(u^{m-1}|\nabla u|^{\lambda-1}\nabla u) + \rho(x)u^p, \quad x \in R^N,\ t>0$$

where $\lambda>0,\ m+\lambda-2>0,\ p>m+\lambda-1,\ \rho(x) = |x|^{-n},$ or $\rho(x) = (1+|x|)^{-n}.$ It was shown that under some restrictions on the parameters, any nontrivial solution to the Cauchy problem blows up in a finite time. Moreover, the authors established a sharp universal estimate of the solution near the blow-up point.

Authors of the work [17] investigated properties of weak solutions of the Cauchy problem for the following equation with variable coefficients:

$$\rho(x)u_t = div(|x|^n u^{m-1}|\nabla u|^{\lambda-1}\nabla u) + u^p, \quad x \in R^N,\ t>0$$

where $\lambda>0,\ m+\lambda-2>0,\ p>m+\lambda-1,\ \rho(x) = |x|^{\delta-2}.$

Properties of the more general equation (1) with nonlocal nonlinear boundary condition were considered in [16] where were obtained the critical exponent of the Fujita type and second critical value.

The main purpose of this paper is to find conditions for the existence and non-existence results for global solutions of problem (1) - (3) on the basis of the self- analysis and the method of standard equations [2], to obtain the critical exponent of the global existence of solutions and the critical exponent of Fujita type. In the case of the existence of solutions for the whole time the leading term of the asymptotic behavior of solutions of the problem (1)-(3). Based on the asymptotic behavior of solutions offered suitable initial approximations for the iterative process for the case of fast

diffusion ($1<p<1+1/m$) depending on the values of the numerical parameters. At some points for the proof of theorems we used the method applied in [1, 2, 4, 7].

II. ESTIMATES FOR SOLUTIONS

Formulate the results on global solvability or no solvability of the problem (1) - (3).

We introduce the notation

$$q_0=\big(m(n+1)+1\big)(p-1)\big/(p+n),$$

$$q_c=m(p-1)+(p-1)/(n+1),$$

where $n>-1$.

Theorem 1. *If* $0\le q\le q_0$, *then each solution of the problem (1)-(3) exists globally.*

Proof. Theorem 1 is proved by the method of comparison of solutions. Equation (1) admits in the domain $Q_\infty=\{(t,x):\ 0<t<+\infty,\ x\in R\}$ self-similar solutions in the form of

$$u_+(t,x)=(T+t)^{-\gamma}\ f\left(\xi+h\right),\ \ \xi=|x|(T+t)^{-\sigma} \qquad (5)$$

where

$$\gamma=\frac{p-1}{q(p+n)-(p-1)\big(m(n+1)+1\big)},$$

$$\sigma=\frac{q-m(p-1)}{q(p+n)-(p-1)\big(m(n+1)+1\big)},$$

numeric $h>0$. Construct an sub-solution of problem (1)-(3). To $u_+(t,x)$ was an sub-solution of problem (1)-(3) $f\left(\xi+h\right)$ function must satisfy the following inequalities [6, 7]

$$\frac{d}{d\xi}\left(\left|\frac{df^m}{d\xi}\right|^{p-2}\frac{df^m}{d\xi}\right)+\sigma(\xi+h)^{n+1}\frac{df}{d\xi}+\gamma(\xi+h)^n\ f\le 0 \qquad (6)$$

$$-\left|\left(f^m\right)'\right|^{p-2}\left(f^m\right)'(0)\ge f^q(0) \qquad (7)$$

Consider the following function

$$\overline{f}\left(\xi+h\right)=\left(a+b\left|\xi+h\right|^{\frac{p+n}{p-1}}\right)^{-\frac{p-1}{1-m(p-1)}} \qquad (8)$$

where $b=\dfrac{1-m(p-1)}{m(p+n)}\sigma^{1/(p-1)}>0$, $a>0$,

$i_+=\max(0,i)$.

Therefore, as

$$\overline{f}'(\xi)=-\frac{\sigma^{1/(p-1)}}{m}(\xi+h)^{(n+1)/(p-1)}\ D^{-\frac{p-1}{1-m(p-1)}-1}$$

$$\left(\overline{f}^m\right)'(\xi)=-\sigma^{1/(p-1)}(\xi+h)^{(n+1)/(p-1)}\ D^{-\frac{m(p-1)}{1-m(p-1)}-1}$$

$$\left((\xi+h)^{n+1}\left|\left(\overline{f}^m\right)'\right|^{p-2}\left(\overline{f}^m\right)'\right)'(\xi)=-(n+1)\sigma(\xi+h)^n\ \overline{f}+$$

$$+\sigma(\xi+h)^{\frac{p(n+1)}{p-1}}\ D^{-\frac{p-1}{1-m(p-1)}-1},$$

where $D=a+b\left|\xi+h\right|^{(p+n)/(p-1)}$, it is easy to see that under the condition of Theorem 1 for (6), we have

$$-\left(\frac{\big(q-m(p-1)\big)(n+1)}{q(p+n)-(p-1)\big(m(n+1)+1\big)}-\right.$$

$$\left.-\frac{p-1}{q(p+n)-(p-1)\big(m(n+1)+1\big)}\right)(\xi+h)^n\ \overline{f}\le 0 \qquad (9)$$

Now check the condition (7). Substituting the function $\overline{f}\left(\xi+h\right)$ instead of $f\left(\xi\right)$ in (7), we obtain the following expression:

$$\sigma(\xi+h)D^{-\frac{p-1}{1-m(p-1)}}\Big|_{\xi=0}\ge D^{-\frac{q(p-1)}{1-m(p-1)}}\Big|_{\xi=0}, \qquad (10)$$

where $D=a+b\left|\xi+h\right|^{(p+n)/(p-1)}$. Let $a=Mh^{(p+n)/(p-1)}$, where constant $M>0$, then for (10) we have

$$\sigma h\left(Mh^{(p+n)/(p-1)}+bh^{(p+n)/(p-1)}\right)^{-\frac{p-1}{1-m(p-1)}}\ge$$

$$\left(Mh^{(p+n)/(p-1)}-bh^{(p+n)/(p-1)}\right)^{-\frac{q(p-1)}{1-m(p-1)}}$$

and this inequality holds for (10)

$$0<h\le\sigma^{-\frac{1-m(p-1)}{p(q-1)}}\ (M+b)^{-(p+n)/(p-1)} \qquad (11)$$

In conclusion, we note that the resulting self-similar solution $u_+(t,x)$ is sub-solution of the problem (1)-(3).

According to the principle of making comparisons that $u(t,x) \le u_+(t,x)$ in $(x,t) \in (0,+\infty)\times(0,+\infty)$. ■

Theorem 2. *If* $q > q_c$ *then the problem (1.6) admits global solutions with small initial data.*

Theorem 2 is proved similarly to the proof of Theorem 1.

Theorem 3. *If* $q > q_0$, *then the solution of the problem (1) - (3) with appropriately large initial data blows up in a finite time.*

Proof. Theorem 3 is proved similarly to the proof of Theorem 1. We seek a solution of (1) - (3) in the form

$$u_-(x,t) = (T-t)^{-\gamma}\,\vartheta(\xi),\ \xi = |x|(T-t)^{-\sigma}. \tag{12}$$

where $\vartheta(\xi)$ satisfies

$$\frac{d}{d\xi}\left(\left|\frac{d\vartheta^m}{d\xi}\right|^{p-2}\frac{d\vartheta^m}{d\xi}\right) - \sigma\xi^{n+1}\frac{d\vartheta}{d\xi} - \gamma\xi^n\vartheta \ge 0 \tag{13}$$

$$-\left|\left(\vartheta^m\right)'\right|^{p-2}\left(\vartheta^m\right)'(0) \le \vartheta^q(0) \tag{14}$$

Analyzing the problem (13), (14) taking into account the method of standard equations and comparison theorems of solutions can establish the conditions of Theorem 3. ■

Theorem 4. *If* $q_0 < q < q_c$, *then each nontrivial solution of the problem (1)-(3) blows up in a finite time.*

Proof. Let

$$u_1(x,t) = (\tau+t)^{-\frac{n+1}{m(p-1)(n+1)+p-1}} H(\varsigma),$$
$$\varsigma = |x|(\tau+t)^{-\frac{1}{m(p-1)(n+1)+p-1}},$$

where $\tau \ge 0$,

$$H(\varsigma) = \left(c_1 + b_1|\varsigma|^{\frac{p+n}{p-1}}\right)_+^{-\frac{p-1}{1-m(p-1)}},$$

$$b_1 = \frac{1-m(p-1)}{(p+n)m}\left(\frac{1}{m(p-1)(n+1)+p-1}\right)^{\frac{1}{p-1}}.$$

It is easy to verify that $H'(\varsigma) = 0$ and for $\varsigma \in \{\varsigma > 0 |\, H(\varsigma) \ge 0\}$ $H(\varsigma)$ satisfies

$$\frac{d}{d\varsigma}\left(\left|\frac{dH^m}{d\varsigma}\right|^{p-2}\frac{dH^m}{d\varsigma}\right) + \frac{1}{m(p-1)(n+1)+p-1}\varsigma^{n+1}\frac{dH}{d\varsigma} + \frac{n+1}{m(p-1)(n+1)+p-1}\varsigma^n H = 0$$

By using the well-known properties of weak solutions of the problem (1)-(3), we deduce that there exists $t_0 \ge 0$ such that $u(0,t_0) > 0$. Therefore, there exists sufficiently large $\tau > 0$ and small $c > 0$ such that for all $x > 0$

$$u(x,t_0) \ge u_1(x,t_0),\ x \in (0,+\infty)$$

A direct calculation shows that $u_1(x,t)$ is a sub-solution of the problem (1)-(3) in $(0,+\infty)\times(t_0,+\infty)$. By the comparison principle, we obtain that

$$u(x,t) \ge u_1(x,t),\ (x,t) \in (0,+\infty)\times(t_0,+\infty).$$

We declare that there exists $t_* > t_0$ and T large enough that

$$u_1(x,t_*) \ge u_-(x,0),\ x \in (0,+\infty), \tag{15}$$

where $u_-(x,t)$ is given by (12). A simple calculation shows that (15) is valid provided

$$(\tau+t_*)^{-\frac{n+p}{m(p-1)(n+1)+p-1}} \gg T^{-\frac{p-1}{q(p+n)-m(p-1)(n+1)-p+1}} \tag{16}$$

$$(\tau+t_*)^{-\frac{1}{(m(p-2)+k)(n+1)+p-1}} \ll T^{-\frac{q-m(p-1)}{q(p+n)-m(p-1)(n+1)-p+1}}. \tag{17}$$

Since $q < q_c$,

$$\frac{(p-1)/(n+1)}{q(p+n)-m(p-1)(n+1)-p+1} > \frac{q-m(p-2)-k}{q(p+n)-m(p-1)(n+1)-p+1}.$$

Therefore there exists $t_* > t_0$ and *T* large enough that (16) and (17) are both valid. Thus

$$u(x,t_*) \ge u_1(x,t_*) \ge u_-(x,0),\ x \in (0,+\infty),$$

which with the comparison principle implies that $u(x,t)$ blows up in a finite time. ■

ISBN: 978-1-61804-219-4

III. ASYMPTOTICS OF SOLUTIONS OF SIMILAR PROBLEMS

The next stage of the research is to study the asymptotic behavior of self-similar solutions of the problem (1) - (3) enable us to obtain numerical results.

We show that the function (8) obtained by the method of standard equations [2] is the asymptotic behavior of a similar problem (6), (7).

Theorem 5. When $\xi \to +\infty$ vanishing at infinity the solution of (6), (7) has the asymptotic

$$f(\xi) \sim C\bar{f}(\xi),$$

where

$$C = \left(\sigma\left((n+1)\left(m(p-1)-1\right)+p+n\right)\right)^{1/\left[1-m(p-1)\right]}.$$

Note that the main difficulty in the numerical study of the problem (1)-(3) arises because of the uniqueness of the solution is not. Therefore, the question arises of selecting a good initial approximation preserving properties of nonlinearity. Depending on the parameters of the equation, this difficulty is overcome by the right choice of initial approximations, which are taken as established above asymptotic formulas. On the basis of the above qualitative studies were produced by numerical calculations. The numerical results show rapid convergence of the iterative process due to the successful choice of the initial approximation. Below are some results of numerical experiments for different values of the numerical parameters.

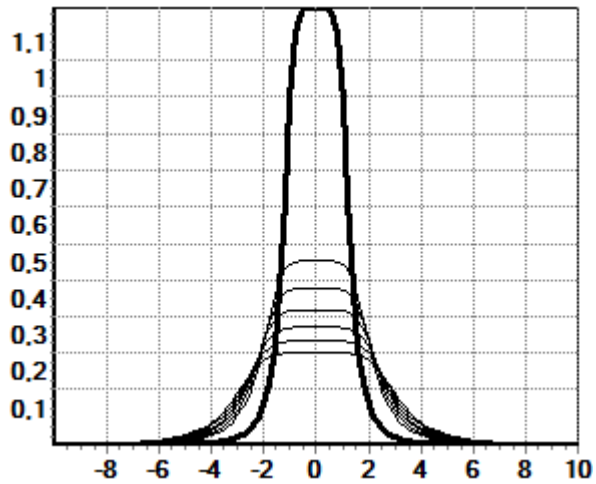

m=1.5, p=1.32, q=2.9, n=0.8, a=0.75

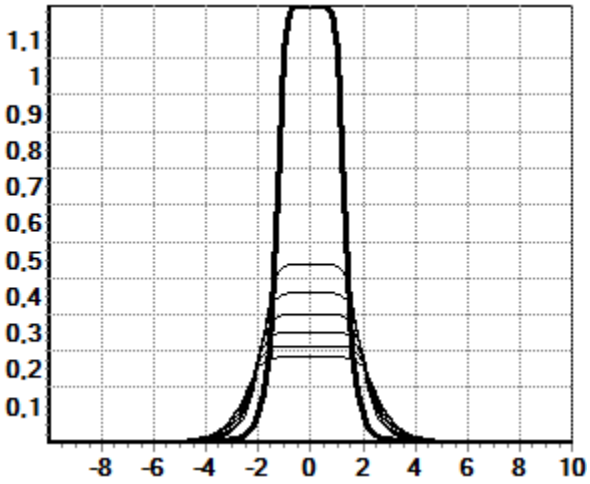

m=1.5, p=1.32, q=2.9, n=1.5, a=0.75

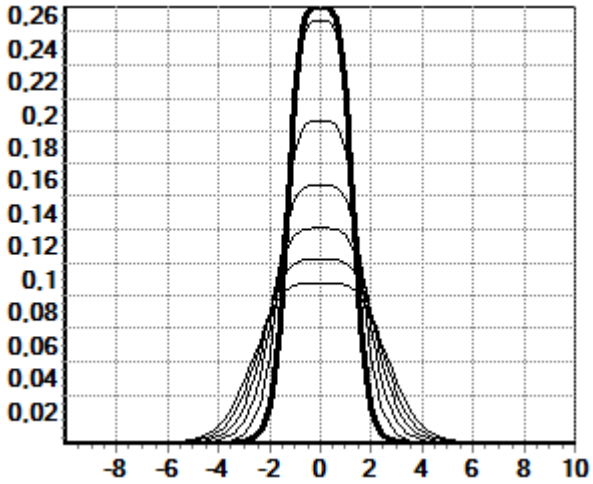

m=1.7, p=1.45, q=1.9, n=0.5, a=2

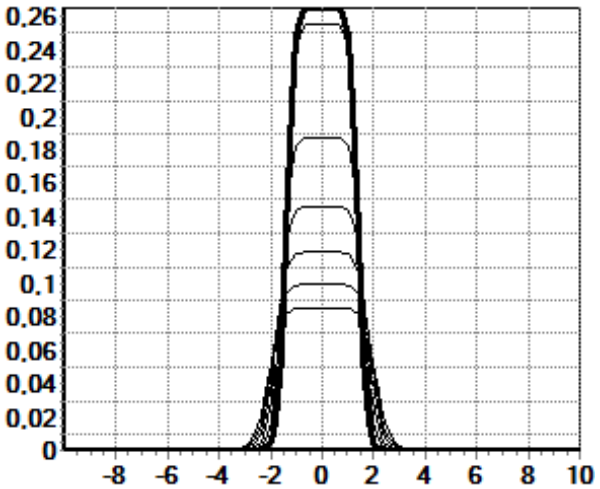

m=1.7, p=1.45, q=1.9, n=2, a=2

References

[1]. A.A.Samarskii, V.A.Galaktionov, S.P.Kurduomov, A.P.Mikhajlov, Blow-up in quasilinear parabolic equations, M., Nauka, 1987 (in Russian).

[2]. M.Aripov, Standard Equation's Methods for Solutions to Nonlinear problems (Monograph), Tashkent, FAN, 1988.

[3]. C. Jin, J. Yin, Critical exponents and non-extinction for a fast diffusive polytropic filtration equation with nonlinear boundary sources, Nonlinear Anal. 67 (2007) 2217–2223.

[4]. Z. Wang, J. Yin, C. Wang, Critical exponents of the non-newtonian polytropic filtration equation with nonlinear boundary condition, Appl. Math. Lett. 20 (2007) 142–147.

[5]. F.J. Mancebo, J.M. Vega, A model of porous catalyst accounting for incipiently no isothermal effects, J. Differential Equations 151 (1999) 79–110.

[6]. V.A. Galaktionov, H.A. Levine, On critical Fujita exponents for heat equations with nonlinear flux boundary condition on the boundary, Israel J. Math. 94 (1996) 125–146.

[7]. Zhongping Li, Chunlai Mu, Critical exponents for a fast diffusive polytropic filtration equation with nonlinear boundary flux, J. Math. Anal. Appl. 346 (2008) 55-64.

[8]. Z. X. Jiang and S. N. Zheng, Doubly degenerate parabolic equation with nonlinear inner sources or boundary flux, Doctor Thesis, Dalian University of Tcchnology, In China, 2009.

[9]. Y. W. Qi The critical exponents of parabolic equations and blow-up in RN, Proc. Roy. Soc. Edinburgh Sect. A **128** (1998), no. 1, 123–136.

[10]. Y. W. Qi, Critical exponents of degenerate parabolic equations, Sci. China Ser. A **38** (1995), no. 10, 1153–1162.

[11]. Y. W. Qi, The global existence and nonuniqueness of a nonlinear degenerate equation, Nonlinear Anal. 31 (1998), no. 1-2, 117–136.

[12]. Y. W. Qi and M. X. Wang, Critical exponents of quasilinear parabolic equations, J. Math. Anal. Appl**. 267** (2002), no. 1, 264–280.

[13]. A. V. Martynenko and A. F. Tedeev, The Cauchy problem for a quasilinear parabolic equation with a source and nonhomogeneous density, Comput. Math. Math. Phys. **47** (2007), no. 2, 238–248.

[14]. A. V. Martynenko and A. F. Tedeev, On the behavior of solutions to the Cauchy problem for a degenerate parabolic equation with inhomogeneous density and a source, Comput. Math. Math. Phys. **48** (2008), no. 7, 1145–1160.

[15]. Tedeyev AF Conditions for the existence and nonexistence of a compact support in time of solutions of the Cauchy problem for quasilinear degenerate parabolic equations. Siberian Math. Jour. 2004, v.45, № 1, 189-200.

[16]. Aripov MM Rakhmonov ZR Asymptotic behavior of self-similar solutions of a nonlinear problem polytropic filtration with a nonlinear boundary condition. Jour. Comp. Tech., 2013, v.18, 4,.50-55.

[17]. Mersaid Aripov, Shakhlo A. Sadullaeva. To properties of solutions to reaction-diffusion equation with double nonlinearity with distributed parameters. *J. Sib. Fed. Univ. Math. Phys.*, **6**:2 (2013), 157–167.

[18]. *Wanjuan Du and Zhongping Li*. Critical exponents for heat conduction equation with a nonlinear Boundary condition. Int. Jour. of Math. Anal. vol. 7, 11, 2013, 517-524.

[19]. *Li Z., Mu Ch. and Du W*. Critical Fujita exponent for a fast diffusive equation with variable coefficients. Bull. Korean Math. Soc. 50. 2013, №1, 105-116.

A Set Application of the Method of Moments using with a Expansion Function the Haar Wavelet

Aldo Artur Belardi and Antonio Honorato Picinini Neto

***Abstract* - This paper presents the mathematical basis, and some results, concerning the application of the Haar Wavelets as the expansion function in the Method of Moments. As an example, the surface charge density on a finite, thin plane plate, and the Eddy current problem, in which the main computational performance aspects are evaluated. Some computational optimization techniques are used, and their main aspects are stressed in the paper.**

Key Words: Moments, Wavelets, Haar

I. INTRODUCTION

Regarding the formulation, in order to illustrate the proposed methodology, the main theoretical aspects of the Method of Moments and of the Haar wavelets, are here presented. For simplification, the one and two dimension applications are taken into consideration.

a. Method of Moments

Although the Method of Moments is a known numerical one, and the complete description and details of this method have already been presented in many papers, in order to guide the reader through the overall method explanation, a brief summary is here shown. In a simplified way, it can be mentioned that the basis of the Method of Moments is the application of approximation functions, like the following one [1].

$$f(x) = \sum_n \alpha_n \boldsymbol{L} g_n \qquad (1)$$

In the aforementioned expression, α_n is the unknown coefficients, g_n is the expansion function, the pulse or the Haar wavelets, and "**L**" a mathematical operator. When the inner product, using a weighed function W_m, is carried out.

$$\sum_n \alpha_n < \boldsymbol{L} g_n, W_m > = < f, W_m > \quad \text{para} \quad m = 1, 2 \ldots\ldots N \qquad (2)$$

The previous expression can be represented in a matrix form by [A][α]=[B], where [α] is the unknown approximated solution coefficients column vector, and the matrixes [A] and [B] are given by:

$$\left[A\right] = \begin{vmatrix} < \boldsymbol{L} g_1, W_1 > & \ldots . < \boldsymbol{L} g_n, W_1 > \\ < \boldsymbol{L} g_1, W_2 > & \ldots < \boldsymbol{L} g_n, W_2 > \\ < \boldsymbol{L} g_1, W_n > & \ldots . < \boldsymbol{L} g_n, W_n > \end{vmatrix}; \left[B\right] = \begin{vmatrix} < f, W_1 > \\ < f, W_2 > \\ < f, W_n > \end{vmatrix} \qquad (3)$$

As a first application, the potential distribution on a finite and straight wire that can be calculated using the next equation is taken into consideration [2]:

$$V(x, y = 0, z = 0) = \frac{1}{4\pi\varepsilon} \int \frac{\rho(r')}{R(x, x')} dl' \qquad (4)$$

Thus making use of the method of moments, knowing the approximated solution function f(x), the expansion function g(x) and the weighting function W(x), the potential on a finite straight wire can be estimated by the inner product of these functions:

$$V(x) = \langle g, W, f \rangle \frac{1}{R} = \int_{-a}^{a} \frac{g(x) W(x) f(x)}{R(x)} dx \qquad (5)$$

Consequently, the surface density can be approximated by the N term expansion. If the wire is divided into uniform segments Δ=L/N, after applying the weight delta function of Dirac $W_m = \delta(x_m - x') = 1$, the inner product will become:

$$V(x) = \left\langle W_m, f, \boldsymbol{L} g \right\rangle = \delta \left(x - x_m\right) x \; x \frac{1}{4\pi\varepsilon} \sum_{n=1}^{N} \alpha_n \int_0^L \frac{g_n(x')}{\sqrt{(x_m - x')^2 + a^2}} dx' \qquad (6)$$

ISBN: 978-1-61804-219-4

Assuming the charges placed in the center of each subdivision in relation to the axis, substituting the values of x by the distance of the charge position to the point $P(x_m)$, we will have an integral that is only function of the x'. For a fixed potential V, the equation can be represented, using matrix notation, by $[V_m] = [Z_{mn}]\,[\alpha_n]$, in which Z_{mn} is defined by [3]:

$$Z_{mn} = \int_0^L \frac{g_n(x')}{\sqrt{(x_m - x')^2 + a^2}} dx' \qquad (7)$$

The same approach can be used, if a two-dimensional application is considered. If a square plane plate is considered as an example, we should remember that the potential in a finite and very thin plane plate can be evaluated by [4]:

$$V(x, y, z = 0) = \frac{1}{4\pi\varepsilon} \int_{-a}^{a} dx' \int_{-b}^{b} dy' \frac{\rho(x', y')}{[(x - x')^2 + (y - y')^2]^{1/2}} \qquad (8)$$

Thus, after applying the method of the moments, knowing the function of the approximated solution f(x,y), the expansion function g(x,y) and the weighed function W(x,y), the potential in a square plane plate, will be estimated by the inner product of these functions [5]:

$$V(x, y) = \langle g, W, f \rangle \frac{1}{R} = \int_{-a}^{a} \frac{g(x, y) W(x, y) f(x, y)}{R(x, y)} dx \qquad (9)$$

where,

$$R(x, y) = \sqrt{(x - x')^2 + (y - y')^2} \qquad (10)$$

Dividing the plate in equal segments and applying the weighed function as being the delta function of Dirac, we had that $W_m = \delta(x - x_m)\delta(y - y_m)$, being the inner product in the point given by:

$$V(x, y, z = 0) = \langle W_m, f, \boldsymbol{L}g \rangle = \delta(x - x_m)\,\delta(y - y_m) \times \frac{1}{4\pi\varepsilon} \int_{-a}^{a} dx' \int_{-b}^{b} dy' \frac{\sum_{n=1}^{N} \alpha_n g_n(x', y')}{[(x_m - x')^2 + (y_m - y')^2]^{1/2}} \qquad (11)$$

Assuming the charges placed in the center of each sub division in relation to each axes, substituting the values of x and y by the distance of the charge position to the point $P(x_m, y_m)$, we will have an integral that is only function of x' e y'. For a fixed potential V, the equation can be represented, using the matrix notation, by $[V_m]=[Z_{mn}][\alpha_n]$, in which Z_{mn} is defined by:

$$Z_{mn} = \int_{-a}^{a} dx' \int_{-b}^{b} \frac{g_n(x', y')}{4\pi\varepsilon \sqrt{(x_m - x')^2 + (y_m - y')^2}} dy' \qquad (12)$$

b. The Wavelets

The analysis through the wavelets has been a good alternative in replacement of the classical analyses that utilize the Fourier series, chiefly when treating acoustic signals, interpreting seismic signals and in the solution of numerical methods applied to electromagnetism and electrostatics [6][7][8]. In general the wavelets can be defined by:

$$\psi_{a,b}(x) = |a|^{-1/2} \psi\left(\frac{x - b}{a}\right) \quad a, b \in R, a \neq 0 \qquad (13)$$

Some kinds of wavelets are mentioned in the literature, making it possible for new family models to be built from them, which adapt more appropriately to each case. Fig. 1 represents the Morlet or Modulated Gaussian wavelet, which is expressed by:

$$\psi(x) = e^{i\omega_0 x} e^{-x^2/2} \qquad (14)$$

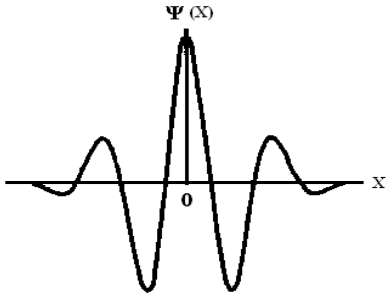

Fig. 1 - Morlet

The Fig. 2 represents the Mexican hat wavelet, which is expressed by:

$$\psi(x) = (1 - x^2)e^{-x^2/2} \qquad (15)$$

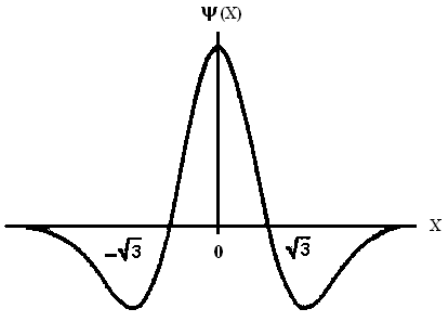

Fig. 2 - Mexican hat

The Fig. 3 represents the Shannon wavelet, which is expressed by:

$$\psi(x) = \frac{\sin(\frac{\pi x}{2})}{\frac{\pi x}{2}} \cos(\frac{3\pi x}{2}) \qquad (16)$$

$$\varphi(x) = \begin{cases} \dfrac{\sin(\pi x)}{\pi x}, & x \neq 0 \\ 1, & x = 0 \end{cases}$$

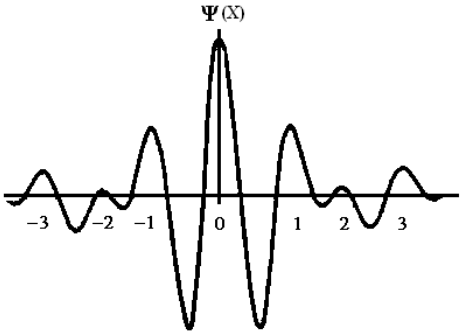

Fig. 3 - The Shannon wavelet

c. The Haar Wavelets

It was previously mentioned that many functions can be used as the expansion function: Among them, the pulse function, the truncate cosine function and the wavelets can be mentioned. Thus, after applying the method of the moments, and considering the Haar wavelets, a function f(x,y) can be approximated by:

$$f(x,y) = \sum_{k=-\infty}^{\infty} c_k \phi(x,y) + \sum_{j=-\infty}^{\infty} \sum_{k=-\infty}^{\infty} d_{j,k} f_P(x,y) \psi_{j,k}(x,y) \qquad (17)$$

In this equation "j", and "k" are the resolution and the translation levels, respectively.

Moreover, once the Haar wavelets, and the so-called mother function and scale function father are applied, the formulation, for two-dimensional applications, will result in a product combination, given by [9][10]:

$$\phi^{(H)}(x) = \begin{cases} 1 & 0 \leq x < 0.5, \text{ and} \\ 0 & \text{for other intervals} \end{cases} \qquad (18)$$

$$\psi_{j,k}^{(H)}(x) = \left[\phi(x)\ \psi(x)\psi(2x)\psi(2x-1)\ldots\psi\left(2^j x - k\right) \right]$$

$$\psi_{j,k}^{(H)}(y) = \left[\phi(y)\ \psi(y)\psi(2y)\psi(2y-1)\ldots\psi\left(2^j y - k\right) \right] \qquad (19)$$

$$\left\{ \psi_{j,k}^{(H)}(x),(y) \right\} = \phi(x)\phi(y), \phi(x)\psi(y), \ldots, \psi(2x-1)\psi(2y-1)$$

II. FORMULATION

a. Finite Straight

Thus, making use of the method of moments, and the wavelets the Haar the potential on a finite straight wire can be estimated by the inner product of these functions. As an illustration, the Fig. 4 represents the Haar function regarding one dimensions and two level of resolution [11].

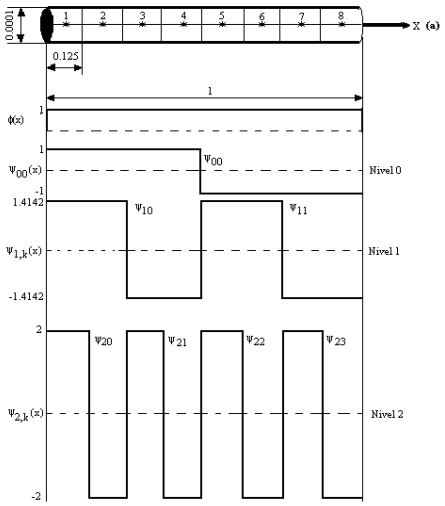

Fig. 4 - The Haar wavelet in a finite straight

The mathematical solution is:

$$V(r)=\frac{1}{4\pi\varepsilon}\left[\int_0^L \frac{c_0\phi(x)}{R(x,x')}dx+\int_0^L \frac{\sum_{n=1}^{N} c_{j,k}\psi_{j,k}^{(H)}(x')}{R(x,x')}dx\right] \quad (20)$$

$$V(r)4\pi\varepsilon = c_0\int_0^L \frac{\phi(x)}{\sqrt{(x-x')^2+a^2}}dx + \left[\sum_{j=-\infty}^{\infty}\sum_{k=-\infty}^{\infty} c_{j,k}\int_0^L \frac{\psi_{j,k}^{(H)}(x')}{\sqrt{(x-x')^2+a^2}}dx\right] \quad (21)$$

b. The thin plane plate

The same approach can be used, if a two-dimensional application is considered.
It was previously mentioned that many functions can be used as the expansion function. Among them, the pulse function, the truncate cosine function and the wavelets, the general aspects of the wavelets are shown.
As an illustration, the Fig. 5 represents the Haar function regarding two dimensions and one level of resolution, for a point $P(x_m, y_m)$.
On the other hand, if the potential in a finite and very thin plane plate is taken into account as an application, it can be evaluated by[12]:

$$V(x,y)4\pi\varepsilon = a_j b_j \int_{-a}^{a}\int_{-b}^{b} \frac{\phi(x,y)}{\sqrt{(x_m-x')^2+(y_m-y')^2}}dxdy + \sum_{j=-\infty}^{\infty}\sum_{k=-\infty}^{\infty} a_{j,k}b_{j,k}\int_{-a}^{a}\int_{-b}^{b} \frac{\psi_{j,k}^{(H)}(x,y)}{\sqrt{(x_m-x')^2+(y_m-y')^2}}dxdy \quad (22)$$

At each point we have:

$$\left\{c_k\psi_{j,k}^{(H)} d_{j,k}\psi_{j,k}^{(H)}\right\} = a_0b_0\phi(x)\phi(y)+a_0b_{00}\phi(x)\psi_{00}(y)+a_0b_{10}\phi(x)\psi_{10}(2y) + a_0b_{11}\phi(x)\psi_{11}(2y-1)+a_{00}b_0\psi_{00}(x)\phi(y)+\ldots+a_{11}b_{11}\psi_{11}(2x-1)\psi_{11}(2y-1) \quad (23)$$

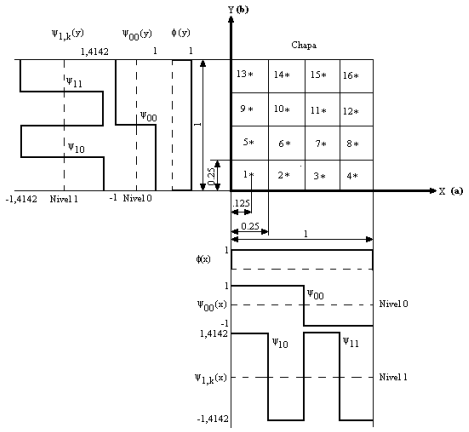

Fig.5 - Representation of the Haar function for two-dimensions and one level of resolution.

c. The Eddy Current problem

Let us consider the conducting wire to be composed of filaments, having their length is represented by c and current density by J(r'), according to Fig. 6.

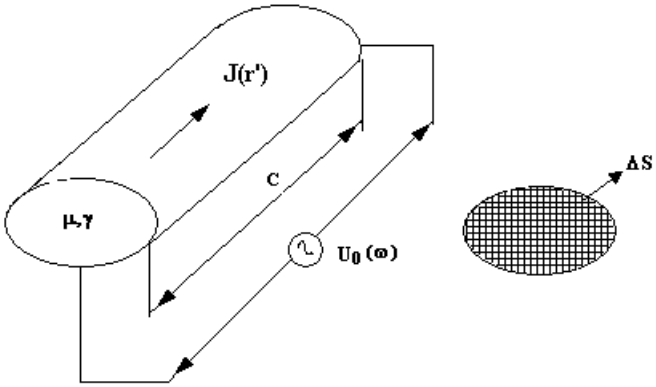

Fig. 6 - Current in the conductor

The two-dimensional fields can be obtained by using two or more current distributions J_1, J_2... on surface S, which is the interface between the conductor and the air.
By integrating it is possible to simplify the equations the most, so that there will not be complex integrals or approximations, as follows [13][14]:

$$A(r) = \frac{\mu}{2\pi}\int_s J(r')\ln\frac{1}{|r-r'|}ds' \quad (24)$$

In which r and r´ are respectively the origin and source points. The current density can be expressed by:

$$J(r) = J_e + J_s = -j\omega\gamma A(r) + \gamma U_0/c \quad (25)$$

In which $\mathbf{U_0}$ is the applied voltage, **c** and **s** are the length and the sectional area of the conductor. Considering Fredholm integral, a second order equation is obtained:

$$J(r) = \frac{j\omega\mu\gamma}{2\pi}\int_{\mathbf{s}} J(r')\ln|r-r'|ds' + J_s \quad (26)$$

In which the math operator in the previous equation is given by:

$$\boldsymbol{L} = 1 - \frac{j\omega\mu\gamma}{2\pi}\int_{\mathbf{s}} \ln|r-r'|ds' \quad (27)$$

By dividing the domain into N elements, the current density can be approximated by:

$$J(r) = \sum^{n} J_1\psi_1 \quad (28)$$

By choosing the pulse as the expansion and weighting functions, the coefficients of matrix A can be determined by the following expression [15][16]:

$$a_{mn} = \left\langle \boldsymbol{L}\psi_n, \mathbf{W}_m \right\rangle = \int_s P_m(x,y)ds - \frac{j\omega\mu\gamma}{2\pi}\int_s\int_s P_m(x,y) \\ *\ln\left[\left(x_m - x_n\right)^2 + \left(y_m - y_n\right)^2\right]^{1/2} P_n(x,y)dsds' \quad (29)$$

or

$$a_{mn} = \Delta S_m - \frac{j\omega\mu\gamma}{2\pi}\Delta S_m\Delta S_n * \\ *\ln\left[\left(x_m - x_n\right)^2 + \left(y_m - y_n\right)^2\right]^{1/2} \\ b_{mn} = \left\langle J_s, W_m \right\rangle = J_s\Delta S_m \quad (30)$$

Let us consider the sides of the elements resulting of the divisions performed in the superficial part of the conductor are square and defined as h.

By eliminating the other ΔS_m terms in the equations a_{mn} and b_m, considering the relative positions of the different charges that will form the elements of matrix A, and the relations d/h> 2 and d/h=1, the following will be obtained:

$$a_{mn} = 1 - \frac{j\omega\mu\gamma}{4\pi}h^2\ln\left[\left(x_m - x_n\right)^2 + \left(y_m - y_n\right)^2\right] \quad (31)$$

$$a_{mn} = 1 - 1,0065\frac{j\omega\mu\gamma}{4\pi}h^2 * \\ *\ln\left[\left(x_m - x_n\right)^2 + \left(y_m - y_n\right)^2\right] \quad (32)$$

if m=n

$$a_{mn} = 1 - \frac{j\omega\mu\gamma}{2\pi}h^2\ln(0,44705h) \quad (33)$$

By solving matrix $A\{J\}=\{J_s\}$ the current matrix will be obtained.

III. APPLICATION

a. Finite wire

Applying the aforementioned formulation, we got some results related to two applications: the first one related to a finite and straight wire, and another one regarding a thin plane plate. It is assumed in the two applications a constant potential distribution equal to1V, conform Fig. 7.

Table I presents the results regarding the charge surface density on a 1.0m straight wire, when it is divided in to 16 equal segments, as a function of the resolution (j) and the translation (k) levels. Those results can be considered as the ones suitable to validate this approach [17].

TABLE I
Charge surface density (pc/m) on straight finite as a function of the resolutions levels

	Expansion Function			
Point	Haar Wavelet (Level)			Pulse
	2	3	4	
1	8.835	9.376	9.957	9.957
2	8.835	9.376	8.764	8.764
3	8.835	8.274	8.411	8.411
4	8.835	8.274	8.219	8.219
5	7.970	8.059	8.102	8.102
…	…	…	…	…
12	7.970	8.059	8.102	8.102
13	8.835	8.274	8.219	8.219
14	8.835	8.274	8.411	8.411
15	8.835	9.376	8.764	8.764
16	8.835	9.376	9.957	9.957

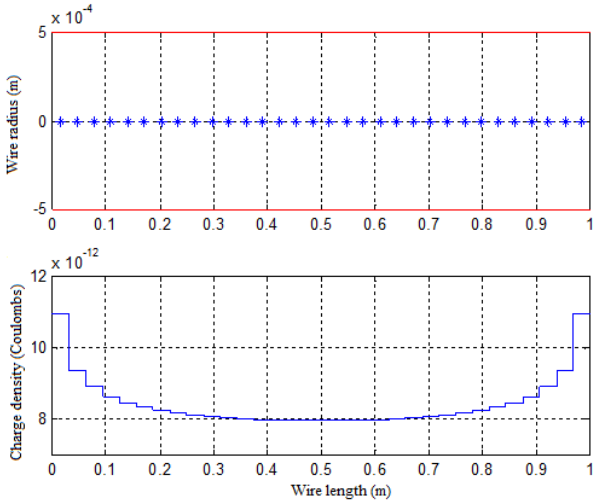

Fig. 7 - The surface charge (pC/m) on a 1.0m straight wire for 32 subdivisions

b. The thin plane plate

After applying the aforementioned formulation, some results were obtained. For example, the Fig. 8 represents the surface charge density in a square plate (1.0mx1.0m), submitted to a potential of 1.0 V. In this case, it was adopted 16 subdivision for each of the axes, and the level 5 of resolution was applied to the Wavelets. Concerning the characteristic of the method, it should be emphasized that the application of the Haar wavelets originates scattered matrixes. Thus, we will have nulls coefficients that can result in a computing time reduction.

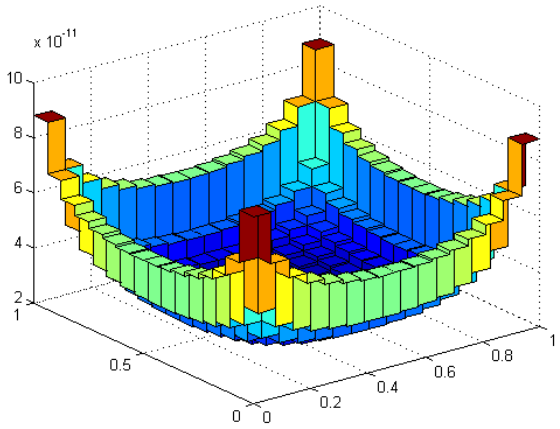

Fig. 8 - The surface charge (pC/m) on a 1.0 by 1.0m plate for 16 subdivisions

The Table II presents the comparative results, regarding the computing time values function of the adopted axe division number, with or without applying the null value detection routine [18].

TABLE II
Computing time(s) function of the axe subdivisions and of the null value detection use

Divisions	Computing time (s)		Difference
Plane Plate	Without	With	(%)
4x4	0.321	0.25	22.12
8x8	7.931	5.488	30.80
16x16	451.960	222.60	50.75
32x32	27,273.738	11,994.487	56.02

In applying for a finite flat plate, we measured the execution time of the program, varying the number of divisions in each of the axes, measuring both the amount held in floating point operations as the runtime. The Table III shows the values obtained for the total execution time and the amount of floating point operations performed, using as expansion function the Haar wavelet.

TABLE III
Calculation floating point operations and the execution time depending on the number of divisions of the plate

Divisions	Floating point operations	Runtime (s)
4X4	29.075	0,321
8X8	1.236.699	7,931
16X16	70.025.893	451,96

Taking advantage of the fact that the Haar matrix is sparse, we reduce the execution time of the program by entering a comparison that, when the null value is detected, the transaction between the arrays is performed. The Table IV presents the results comparing the values of the runtime and the number of floating point operations, with and without detection of null values.

TABLE IV
Amount of floating point operations and execution time (s), depending on the number of divisions of the plate with and without detection of nulls

	Nulls value				Diference
Div.	Without detection		With detection		(%)
	Flops operation	Runtime	Flops operation	Runtime	Runtime
4X4	29.075	0,321	25.491	0,250	22,12
8X8	1.236.699	7,931	843.483	5,488	30,80
16X16	70.025.893	451,96	39.748.261	222,60	50,75

ISBN: 978-1-61804-219-4

According to the results, reduced on average 40% run time of the program. The Fig. 9 (blue color) shows the values obtained for the runtime with and without detection of null values, depending on the number of divisions of finite flat plate.

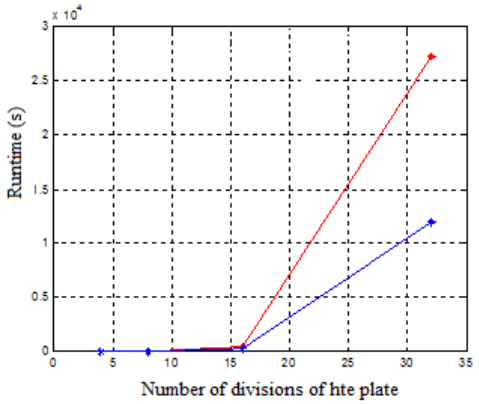

Fig.9 - The computing time (s) as a function of the subdivision axe number

When the plate was divided into 16 equal segments on each axis, a total of 256 coefficients were generated with 54% of them are zero. Taking advantage of the fact that the Haar matrix is sparse, applying the matrix algebra we can write that

$$[Z_{mn}]*[\rho]=[V] \quad (34)$$

where, Z_{mn} is a square matrix that is not necessarily a scattered one, since it depends on the expansion function that was chosen. Thus, taking advantages of the fact that the Haar matrix is a scattered matrix, applying the matrix algebra, it will result [19]:

$$[Z'_{mn}]*[\rho']=[V'] \quad (35)$$

else,

$$\left[Z'_{mn}\right]=[H]\left[Z_{mn}\right]\left|H^{T}\right| \quad (36)$$

$$[\rho']=\left[H^{T}\right]^{-1}*[\rho] \text{ and } [V']=[H]\ [V] \quad (37)$$

$$[H]\times[Z_{mn}]\times\left[H^{T}\right]\times\left[H^{T}\right]^{-1}\times[\rho]=[H]\times[V] \quad (38)$$

As estimation, when the null value detection routine is carried using the null value detection routine. The Fig. 10 represents the Haar matrix and Fig. 11 and 12 presents the Z'_{mn} matrix configuration for the threshold equal to 0.01%, and 0.05%, respectively. The dark part is the no null values.

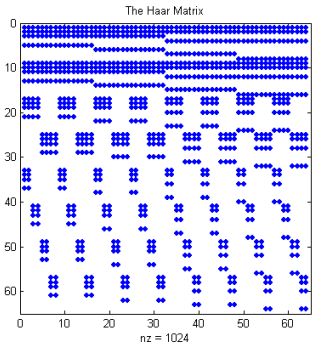

Fig.10 - The Haar matrix

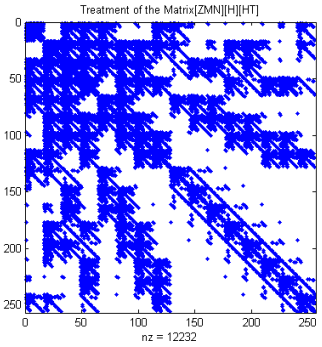

Fig.11 - Value of the threshold of 0.01% (23528 non-zero elements)

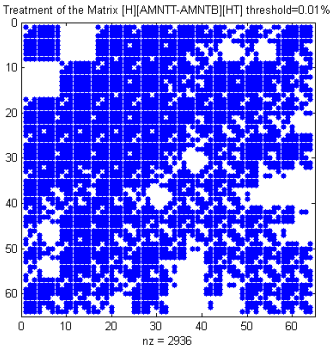

Fig. 12 - Value of a threshold of 0.05% (12232 non-zero elements)

The Table V, shows the computing time, when the threshold level and the axe subdivision number are taken into account.

TABLE V
Computing time(s) as a function of the axe subdivisions and of the adopted threshold level

Subdivision	Threshold levels (%)			
	0.00001	0.01	0.05	0.1
16x16	0.27	0.21	0.16	0.12
32x32	25.486	11.49	4.516	2.073

The Fig. 13 represents the error variation for the charge surface density, considering a square plane plate, and 16 axe subdivisions, as a function of the selected threshold.

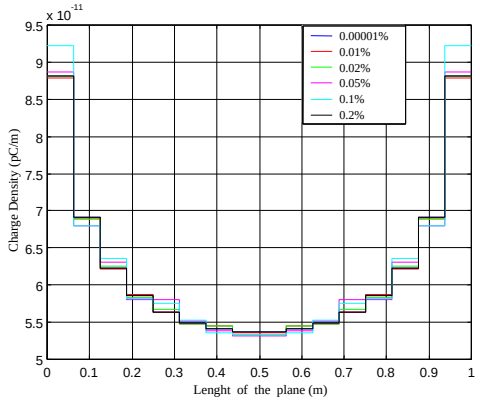

Fig. 13 - Variation of the charge surface density as a function of a selected threshold

Therefore, the variation of the threshold allowed a significant reduction in execution time without significantly changing the value of the surface charge density.
Moreover, it should be mentioned that the Cholesky decomposition method were also implemented [8]. The Fig.14 represents the matrix configuration after applying it, assuming a threshold level equal to 0.01%. In this case, approximate increase of 64% was obtained in the null value element of the matrix.

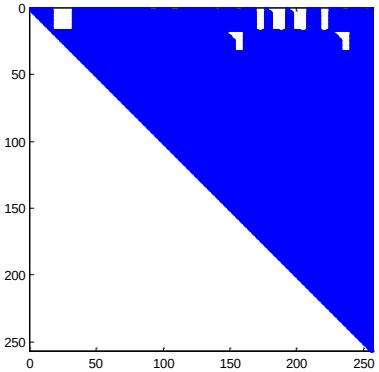

Fig. 14 - Matrix configuration after applying the Cholesky decomposition for the threshold equal to 0.01%

Regarding the computational performance, the average computing time decreased from 0.21 to 0.02 (s), for 16 axe subdivision, and a reduction time from 11.49 to 0.351(s).

c. Eddy current problem

In the application here presented, a copper conductor with the conductivity of 1.72 (μΩcm) and resistivity of 100% as shown on Table VI [20].
The Fig. 15 shows the reactions of the electromagnetic field and the involved energy considering the influence between the charges using the developed program.

TABLE VI
Material Characteristics

Material Type	Resistance (μΩcm)	Conductivity (%)
Aluminum (99.9)	2.65	64.84
Bronze	12	14
Copper	***1.72***	***100***
Nickel	37	4.5
Gold	2.36	76

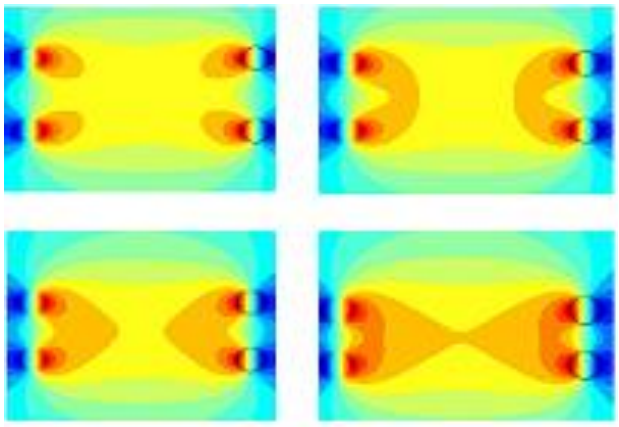

Fig. 15 - Electric field simulation

Therefore the final equation for each one of the elements that compose the current matrix can be expressed by:

$$A(x,y) = 1 - \frac{j\omega\mu\gamma}{4\pi} * h^2 * *a_j b_j \int_{-a}^{a}\int_{-b}^{b} \ln\left[\phi(x,y)\left(\sqrt{(x_m - x_n)^2 + (y_m - y'_n)^2}\right)\right]dxdy + + \sum_{j=-\infty}^{\infty}\sum_{k=-\infty}^{\infty} a_{j,k} b_{j,k} * * \int_{-a}^{a}\int_{-b}^{b} \ln\left[\psi_{j,k}^{(H)}(x,y)\left(\sqrt{(x_m - x_n)^2 + (y_m - y_n)^2}\right)\right]dxdy \quad (39)$$

ISBN: 978-1-61804-219-4

The solution of the previous equation can be obtained by using the expression $[a_{mn}]*[Coef]=[U_0]$ [21][22].
The Fig. 16 shows the superficial charge distribution on the conductor, taking into consideration the effects of losses.

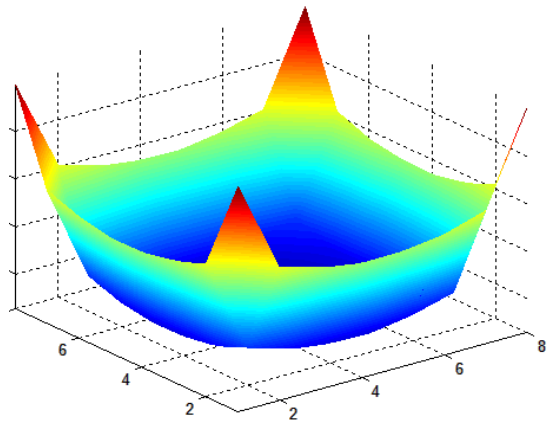

Fig.16 - Superficial charge distribution

The Fig. 17 was obtained through the use of the application toolbox and shows the results of the coefficients in relation to the several resolution levels. The numerical values are available in the application as well [23].

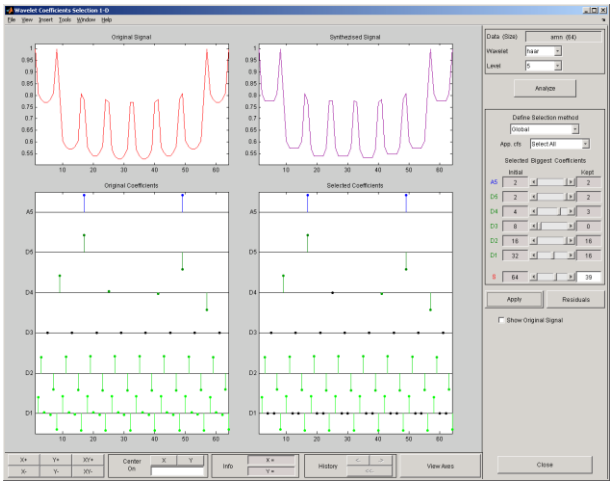

Fig. 17 - Wavelet Coefficients as a function of the resolution level

The Fig. 18 shows the statistical data for a 0.01% threshold with level 5 resolution.

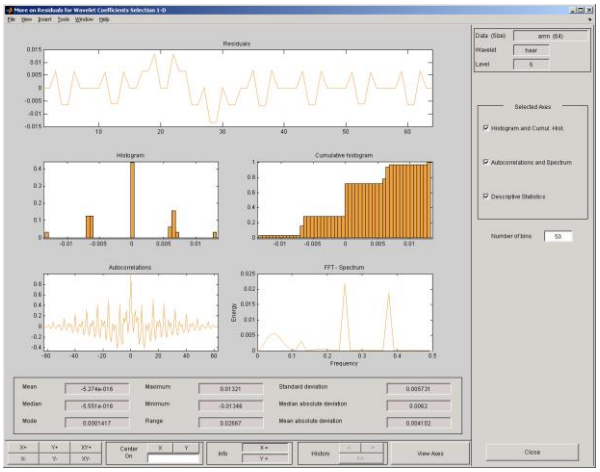

Fig. 18 - Statistical data of the usage of the Haar wavelet with a level 5 resolution

The Fig. 19 shows several the coefficients in different resolution levels from matrix a_{mn}

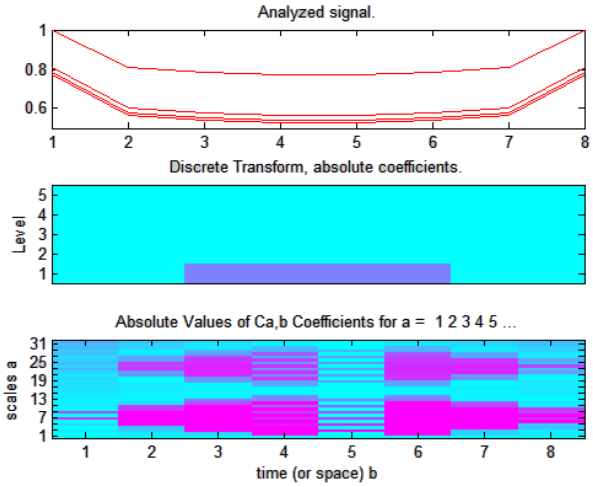

Fig. 19 - Superficial charge distribution with different resolution levels

IV. CONCLUSION

This article has simply a series of applications of wavelets, such as the surface density in a finite straight wire and a flat plate, and the determination of eddy currents using the pulse and as a expansion function of the Haar wavelet.
The proposed methodology permits the determination of the available numerical coefficients in the application as a function of the resolution level, this way avoiding the complex solution of the inner product, usually composed of double integrals that do not possess a very immediate solution.
By performing the product of the current matrix by the Haar wavelet $[a_{mn}][Coefficients][Haar]=[U_0][Haar]$ and in some cases reductions in execution time of up to 40% has been achieved.

ISBN: 978-1-61804-219-4

With this reduction in run time no significative variation in the a_{mn} elements that could compromise the final results has been found.

Although the proposed application is relatively simple, the presented methodology is likely to be applied to problems of greater complexity, such as a refinement can be achieved in energy in locking electric motors, cardiac signals, transmission lines, electromagnetic compatibility, financial market, corrosion or thermal treatment, neurological treatments and etc.

REFERENCES

[1] Harrington R. F. Field Computation by Moment Methods, New York, Macmillan Company, 1968.

[2]Clayton P. R. ; Syed N. A. Introduction to Electromagnetic Fields.1.ed. New York, McGraw-Hill, 1998.

[3]Constantine A. B. Advanced Engineering Eletromagnetics, 2.ed.New York, John Wiley & Sons, 1989.

[4]Harrington, R.F., Time-Harmonic Electromagnetic Fields, Graw-Hill, New York, 1961.

[5]Phillips, B.L. A technique for the numerical solution of certain integral equations of the second kind, 1962.

[6]Liang J.; Elangovan S.; Devotta J. B. X. A Wavelet Multiresolution Analysis Approach to Fault Detection and Classification in Transmission Lines. Elsevier Computer physics communications, p.327-332,1999.

[7]Mallat S. Wavelets for a Vision. IEEE Proceedings of the IEEE, v84, n.4, p.604-614, 1996.

[8]Cohen A. ; Kovacevic J. Wavelets: The mathematical background. IEEE Proceedings of the IEEE, v84, n.4, p.514-522, 1996.

[9]Morettin P. A., Ondas e Ondaletas 1°ed, São Paulo, Edusp, 1999, pp. 1-55.

[10]Morettin P. A., 7° Escola de Séries Temporais e Econometria. 1.ed, São Paulo, Edusp, 1997, pp. 20-34.

[11]D. E. Newland, Random Vibrations Spectral and Wavelet Analysis, Addison Wesley Longman 1993, pp. 315-333.

[12]Aboufadel E.; Schlicker S., Discovering Wavelets, John Wiley & Sons 1999, pp. 1-42.

[13] Kriezis E.E.; Stavaros M. P.,Tegopoulos J. A., "Eddy Currents: Theory and Applications", Proceedings of the IEEE, vol. 80, n° 10, 1992.

[14] Lopez L. A N. M., Transformadas de Wavelet e Lógica Fuzzy na Inspeção por Eddy-Current em Tubos de Geradores de Vapor de Centrais Nucleares, Tese de Doutorado,Universidade de São Paulo, USP, Brasil, 2003.

[15]Stoll, R. L., The analysis of eddy currents, Clarendon Press, 1974.

[16] Kaitec, "The 14th Kori Unit 4 Steam Generator Tube Eddy Current Examination – Final Report", Nov. 2004.

[17]Belardi A. A. ,Cardoso J. R., Sartori C. F., "Wavelets Application in Electrostatic and their Computing Aspects", Electric and Magnetic Fields, EMF 2003, Germany, 2003, pp. 43-46.

[18]Belardi A. A. ,Cardoso J. R., Sartori C. F., "Application of Haar's Wavelets in the method to solve electrostatic problems", Compel Vol. 23, N°3, 2004, pp. 606-612.

[19]Datta B. N., Numerical Linear Algebra and Applications, 1.ed. New York, Brooks/Cole Publishing Company 1995, pp. 222-225

[20]KPS, "The 5th Ulchin Unit 4 Steam Generator Tube Eddy Current Examination – Final Report", Mar. 2005.

[21]Bossavit, A. , A numerical approach to transient nonlinear eddy current problems in applied electromagnetic in materials, Elsevier, 1990.

[22] Salon S., Peng J.P.,Three dimensional eddy currents using a four component finite element formulation IEEE Transactions on Magnetics, 1994.

[23]Palm, W., Introduction to Matlab 7 and Simulink for Engineers, McGraw-Hill,2003, pp. 55-97.

The Flocking Based and GPU Accelerated Internet Traffic Classification

Zhiguang Xu

***Abstract*—**Mainstream attentions have been brought to the issue of Internet traffic classification due to its political, economic, and legal impacts on appropriate use, pricing, and management of the Internet. Nowadays, both the research and operational communities prefer to classify network traffic through approaches that are based on the statistics of traffic flow features due to their high accuracy and improved robustness. However, these approaches are faced with two main challenges: identify key flow features that capture fundamental characteristics of different types of traffic in an unsupervised way; and complete the task of traffic classification with acceptable time and space costs. In this paper, we address these challenges using a biologically inspired computational model that imitates the flocking behavior of social animals (e.g. birds) and implement it in the form of parallel programs on the Graphics Processing Unit (GPU) based platform of CUDA from NVIDIA™. The experimental results demonstrate that our flocking model accelerated by GPU can not only effectively select and prioritize key flow features to classify both well-known and unseen network traffic into different categories, but also get the job done significantly faster than its traditional CPU-based counterparts due to the high magnitude of parallelism that it exhibits.

***Keywords*—**CUDA, Flocking Algorithms, Internet Traffic Classification; Parallel Computing.

I. Introduction

A significant number of applications are rapidly emerging as the Internet becomes one of the essential parts of everyone's daily life. In particular, recently, Peer-to-Peer (P2P) and multimedia applications have substantially increased their presence in the Internet. However, these applications may induce serious technical, economic, legal, and security problems, for instance, the arms race between the file sharing community and intellectual property representatives RIAA (Recording Industry Association of America) and MPAA (Motion Picture Association of America); the battle between malicious hackers and security enforcement companies; and the network neutrality debate between ISPs and content/service providers in cloud [1]. In all these cases, network traffic classification plays a central role in not only using, operating, and regulating the current network resources; but also planning, designing, and financing the network architectures in the future.

In general, four types of approaches have been adopted to classify network traffic and applications. *Transport layer port-based approach* is the fastest but performs poorly when dealing with P2P applications that assign ports dynamically or use well-known ports. *Payload-based approach* is more accurate but needs to inspect packet payloads therefore causes tremendous privacy concerns. *Host behavior-based approach* aggregates social interaction information of observed hosts so is effective only when such hosts are located at topologically appropriate places. Finally, *Flow features-based approach* relies on the statistics of flow features for traffic classification. Such flow features include the distribution of packet sizes in the flow, duration of the flow, interval between packet arrivals in the flow, etc. Many classification algorithms such as Support Vector Machine (SVM), Decision Tree, and Neural Network [2] are then used to classify network traffic into pre-defined categories such as WWW, P2P, GAMES, DABABASE, etc.

Flow features-based network traffic classification has drawn great attentions from both the research and operational communities due to its high accuracy and improved robustness. However, it is faced with two main challenges: first, since supervised training is a common key step in most of the features-based classification algorithms listed above, it is needed to select key features and training samples and define traffic categories ahead of time. Apparently, the task of classifying today's highly dynamic network traffic is calling for unsupervised classification techniques without a priori knowledge of the network flows. Second, existing flow features-based network traffic classification algorithms are very space-hungry and time-consuming, especially when dealing with huge amount of traffic flows.

Therefore, in this paper, we propose a biologically inspired computational model that imitates the *flocking* behavior of social animals (e.g. birds). Each bird represents a single network flow and flies towards other birds of the same feather without supervision or training. Given reasonable time, similar birds would flock together through simple communications and effectively classify the network flows they represent into different categories. To accelerate the flocking-based classification process which is highly parallel, we implement the model in the form of parallel programs on the GPU-based platform of CUDA. Experimental results show that this flocking based and GPU accelerated approach is able to classify not only common types of network traffic and applications but also those unseen ones in a significantly faster way.

ISBN: 978-1-61804-219-4

The rest of the paper is organized as following. Section II briefly reviews related works in three areas: flow features-based traffic classification, flocking algorithms, and the parallel computing architecture with CUDA. Section III describes our flocking-based model in detail. Notice that both feature selection and traffic category definition are carried out while network flows are classified instead of ahead of time. Section IV discusses specific steps to parallelize our model in CUDA. We then present the experimental results in section V. Section VI concludes the paper.

II. RELATED WORK

In this section, three areas of related work are briefly reviewed.

A. Flow features-based Internet traffic classification

Substantial attention has been invested in utilizing flow features for traffic classification [1]. Zander first introduced the machine learning method [4]. Then Support Vector Machine, Decision Tree, and Neural Network were brought to the field [5, 6, 7]. Tan developed a Genetic Algorithm to select the subset of best features and optimized the weight of each feature selected using Particle Swarm Optimization (PSO) [2].

Flow features-based approach has practical advantages over other traffic classification approaches developed in early Internet. However, more work needs to be done on automatic and dynamic selection of key features and expedition of the classification process at low cost.

B. Flocking algorithms for data clustering

After decades of efforts, flocking based techniques have expanded its use from applications like animation, data visualization, and optimization tasks to massive data clustering. The basic flocking model was first proposed by Craig Reynolds in [9] where he referred to each individual as a "boid". In addition to the three basic flocking rules of separation, alignment, and cohesion as shown in Fig. 1, in order to cluster documents, a fourth rule, the feature similarity rule, was added into the basic action rules to influence the motion of the boids [3], where each of such boid represented a document. The resulting Multiple Species Flocking (MSF) model allowed groups of heterogeneous documents being organized into homogeneous subgroups.

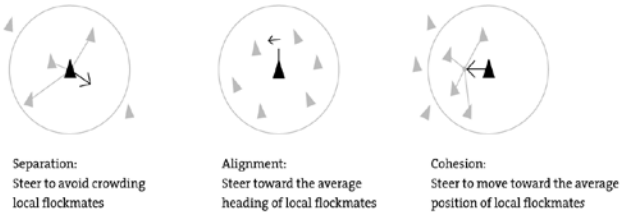

Fig. 1 Basic Flocking Rules

One limitation of flocking simulation, along with most naturally inspired algorithms such as bee colony construction and particle swarm optimization, is its exponential time complexity, i.e., as the size of data grows, it becomes increasingly difficult, sometimes impractical, to receive results within a reasonable amount of time. However, these algorithms are typically highly parallel, i.e., there is no central control; each boid behaves autonomously to achieve global goals in teams.

CUDA, a GPU-based platform from NVIDIA, as described below, expedites the execution of such parallel programs through massive number of parallel threads.

C. Parallel computing architecture with CUDA

Recently, Graphics Processing Unit (GPU) has received attention for its ability to solve highly parallel problems much faster than the traditional sequential Central Processing Unit (CPU). CUDA is one of such GPU-based computing architectures that aims to solve thousands (or millions) of similar and relatively simple tasks with huge throughput thanks to the highly multi-threaded processing units equipped on the CUDA-capable graphics cards [8].

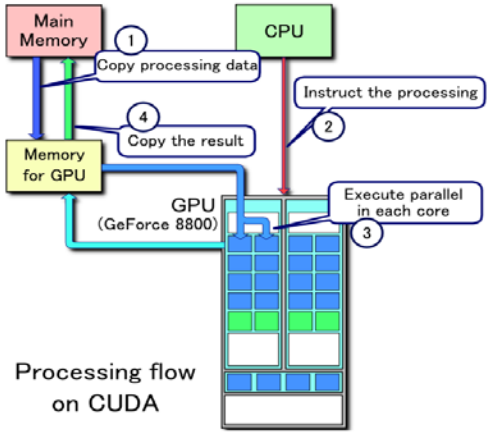

Fig. 2 Processing Flow in CUDA

Fig. 2 shows a high-level processing flow in CUDA. Notice that all data must be moved from the main memory to memory for GPU before being processed (Step 1 in Fig. 2) and back on the opposite direction afterwards (Step 4 in Fig. 2). In fact, the CUDA memory and cache hierarchy for GPU is far more complicated than a single yellow box as shown in Fig. 2. It consists of registers, shared memory, local memory, global memory, constant memory, and **texture** memory, etc. A proper use of the CUDA memory hierarchy is of special importance when implementing our flocking-based Internet traffic classification model. We need to cut the among of data that have to be moved back and forth between the main memory and the memory for GPU, keep and reuse data in GPU memory as much as we can, and push those frequently needed data up the CUDA **memory** hierarchy for faster reads and writes. Details will be discussed in Section IV.

ISBN: 978-1-61804-219-4

III. FLOCKING MODEL DESIGN

A. Preliminaries

In Internet, a single packet is combined with other relevant packets to form a session. Traffic flows can then be classified in the unit of session.

Definition 1 (TCP Session): If host A and host B communicate with each other through the TCP protocol, and their corresponding TCP ports are "portA" and "portB", a TCP session flow p includes all the data packets between the SYN and FIN packets transmitted between portA and portB.

Definition 2 (UDP Session): If host C and host D communicate with each other through the UDP protocol, and their corresponding UDP ports are "portC" and "portD", a UDP session flow p includes all the data packets transmitted between portC and portD within time period t.

Notice that being able to classify UDP flows is of significant importance to us due to their high popularity in today's Internet traffic.

Definition 3 (Feature Vector): Suppose $s(p)$ is an attribute of session p, then the feature vector of d attributes of session p is $f(p)=[s_1(p), s_2(p), \cdots, s_d(p)]^T$.

In this paper, we adopt 45 features to identify different TCP/UDP-based network applications and their sessions [2], i.e. $d=45$. Such features include duration of a session, number of packets host receives/sends in a session, bytes of payload a host receives/sends in a session, etc. Experiments show that among these 45 features, some play greater roles in characterizing the sessions than others; some features are completely redundant. Often, we want to select a subset of the full feature set which can, by itself, fully capture the knowledge of the traffic and classify it consequently. Such a subset is called a reduct.

Definition 4 (Reduct and Core): Given a full set of all attributes S, a reduct is a subset of attributes $R \subseteq S$ such that first, $[X]_R = [X]_S$, that is, the equivalent classes induced by R are the same as those induced by S; and second, R is minimal, that is, $[X]_{R-\{a\}} \neq [X]_S$ for any attribute $a \in R$. Reduct set is not unique. The intersection of all reduct sets is called the core of S, that is, $Core(S) = \bigcap R$.

B. Flow Feature Selection Based on Reduct Set

Ideally, we want to find the best (i.e. the smallest) reduction of the full attribute set, however, it's NP hard. So there are many researches in approximating it. In this paper, as a pre-processing step of the entire traffic classification procedure, we calculate the reduct set that consists of the most significant flow features by implementing a radix sort-based reduct approximation algorithm [10].

It is worth mentioning that this step is offline, one-time, unsupervised, and results in a RFV (Reduced Feature Vector) $r(p)=[s_1(p), s_2(p), \cdots, s_m(p)]^T$ for each session p where m is the size of the reduct set R. Supposedly, $m \leq d$.

C. Flocking Algorithm for Traffic Classification

Once the reduct set of the flow features are selected, we treat network sessions as boids and use the flocking algorithm described in the following to classify them.

Step 1: each session is summarized as a RFV, and then a similarity matrix is built based on the cosine distance between each session and all other sessions.

Definition 5 (Similarity Matrix): Given N sessions, each represented as a reduced feature vector, the $N \times N$ similarity matrix s is constructed by calculating the cosine distance of each pair of sessions, say a and b.

$$s(a,b) = \frac{\sum_{i=1}^{m} r_i(a) \times r_i(b)}{\sqrt{\sum_{i=1}^{m} (r_i(a))^2} \times \sqrt{\sum_{i=1}^{m} (r_i(b))^2}} \quad (1)$$

Step 2: once the similarity matrix is calculated, each boid is given a random velocity and placed at a random position in a 2-D plane. Thereafter, each boid moves at a constant speed but changes its direction each step of the way by following the enhanced flocking rules below, in all of which $\vec{v}$ is the velocity and $\vec{p}$ is the position of a boid before being normalized.

Case I: for similar boids, i.e., $s(a,b) \leq s_1$

If ($d(a,b) < d_2$)

$\vec{v} = -\sum_{b=1}^{m} \frac{\vec{p}_a - \vec{p}_b}{d^2(a,b)}$ // Separation Rule

If ($d(a,b) \leq d_1$ and $d(a,b) \geq d_2$)

$\vec{v} = \frac{1}{n} \sum_{b=1}^{n} \vec{v}_b$ // Strong Alignment Rule

$\vec{v} = \frac{1}{n} \sum_{b=1}^{n} \vec{p}_b$ // Strong Cohesion Rule

If ($d(a,b) > d_1$)

$\vec{v} = \sum_{b=1}^{k} \frac{\vec{v}_b}{d^2(a,b)}$ // Weak Alignment Rule

$\vec{v} = \sum_{b=1}^{k} \frac{\vec{p}_b}{d^2(a,b)}$ // Strong Cohesion Rule

Case II: for dissimilar boids, i.e., $s(a,b) > s_1$

If ($d(a,b) < d_2$)

$\vec{v} = -\sum_{b=1}^{l} \frac{\vec{p}_a - \vec{p}_b}{d^2(a,b)}$ // Separation Rule

Let's assume $d(a,b)$ be the distance between boid a and another boid b, and all such distances are contained in a $N \times N$ distance matrix. For those similar boids to a according to the similarity matrix and a pre-defined threshold value s_1: first, for the m "tightly" close neighbors of a where $d(a,b)$ is less than d_2, a pre-defined threshold, separation rule is taking effect; second, for the n "loosely" close neighbors of a where

$d(a,b)$ is greater than d_2 but less than d_1, another pre-defined threshold, strong alignment and cohesion rules are taking effect; and third, for the k non-neighbors of a where $d(a,b)$ is greater than d_1, weak alignment and cohesion rules are taking effect. For those dissimilar boids of a, only separation rule takes effect for the l "tightly" close neighbors of a.

After several iterations, the boids sharing similar features will automatically group together and become a flock. Other boids with dissimilar features will stay away from this flock. They will discover and form their own flocks.

IV. PARALLEL IMPLEMENTATION WITH CUDA

There are two fundamental challenges of implementing our flocking based traffic classification process in CUDA.

The first one is to identify opportunities for parallelization. Each of such opportunity needs to comply with the Single Program Multiple Data (SPMD) paradigm of CUDA where multiple instances of the same program, i.e. multiple threads of the same CUDA kernel, act on one set of data. Each instance uses a unique index to manipulate the piece of data that is assigned to it.

The second one is to make appropriate use of the CUDA memory hierarchy. Data migration between the main memory and the memory for GPU and frequent reads from the slow GPU global memory are usually the bottleneck of the CUDA parallel programs. Therefore, cutting the amount of such operations is the key to a successful program acceleration.

There are three areas in the flocking-based model described above that can be parallelized: calculating the similarity matrix, calculating the distance matrix, and updating each flock's velocity by following the flocking rules. Fig. 3 below shows a high level processing flow.

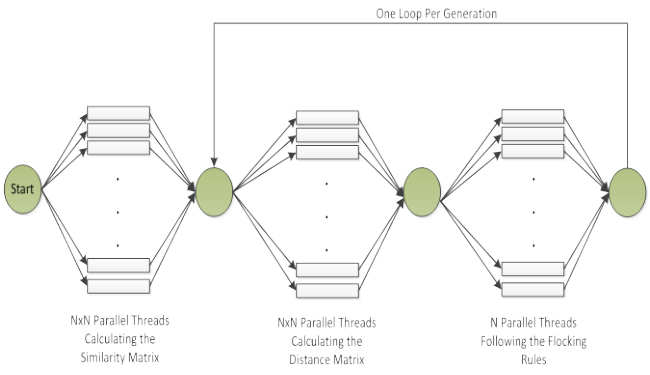

Fig. 3 High-level Processing Flow

In Fig. 3, N stands for the number of network sessions to be classified. The first kernel of $N \times N$ threads are created to calculate the Similarity Matrix (SM) based on the Reduced Feature Vectors (RFVs) of such sessions. The largest constraint here is the shortage of fast memory on GPU to hold the massive RFVs as the input of the algorithm. In order to prevent from being forced to make frequent reads from the GPU global memory, which is associated with delays at hundreds of clock cycles per read, we cache the data in the faster CUDA shared memory. See Fig. 4 below for details.

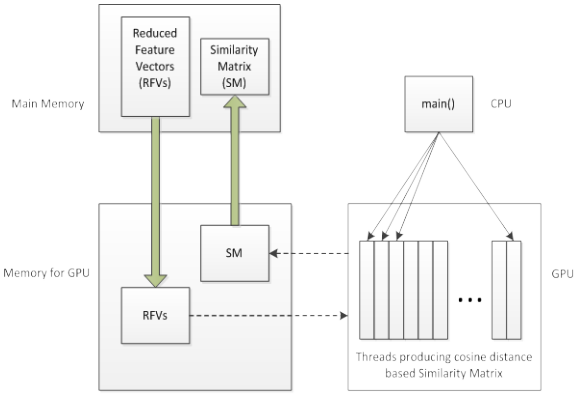

Fig. 4 Producing SM in CUDA

We then enter the main loop of the program that consists of two CUDA kernels per iteration.

One is to create $N \times N$ parallel threads to calculate the Distance Matrix (DM) for the N boids on the 2-D space. Each of such boid represents a network session. For the same reason as in the previous kernel, the Boid Vectors (BVs) as the input data for the algorithm will be placed in the CUDA shared memory for faster reads. Each BV contains both the velocity and the position of a boid. See Fig. 5 below for details.

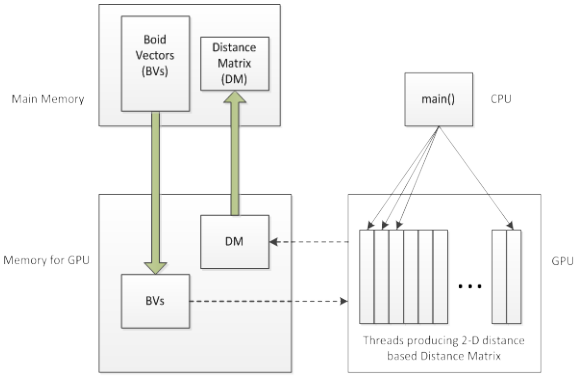

Fig. 5 Producing DM in CUDA

The other kernel of N threads is created to update the moving direction of each boid based on the influence from other boids simply by following the three enhanced flocking rules as described in Section III.C above. For each boid, similar ones will have impact on it through one or two of the alignment, coherent, and separation rules depending on the distance in between them whereas dissimilar boids will impact it through the separation rule if and only if they are "tightly" close neighbors. Since the Similarity Matrix, the Distance Matrix, and the previous Boid Vectors (p-BVs) will all be needed as inputs for the algorithm here to produce the new Boid Vector, a careful usage of the GPU memory is very

ISBN: 978-1-61804-219-4

important. Since SM is not changed once generated by the first kernel (see Fig. 4), it is placed in the CUDA global memory and stays there across generations of the boids. DM and p-BVs, on the other hand, have to be re-calculated for each generation, therefore, they will have to be read from the main memory at the beginning of each kernel execution. See Fig. 6 below for details.

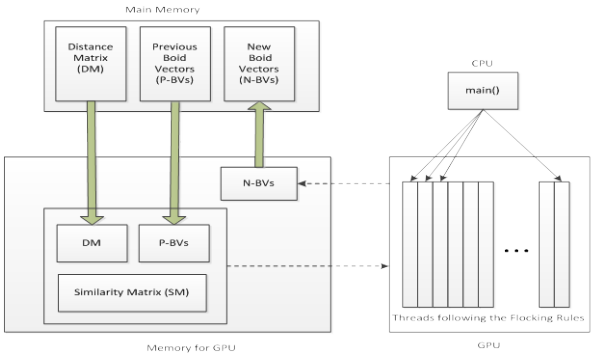

Fig. 6 Following the Flocking Rules in CUDA

V. EXPERIMENTAL RESULTS

A. Experimental Environment and Data

The flocking based network traffic classification model proposed in this paper was implemented in CUDA 5.5 and executed on a PC equipped with an Intel Core i7 CPU at the processor speed of 2.6 GHz, 8 GB RAM, a NVIDIA™ GeForce GTX 480 graphics card, and a NVIDIA™ Tesla C2070 graphics card. For performance comparison purposes, an equivalent sequential implementation was written in C.

The data set used in the experiments presented in this section was collected on the Valdosta State University campus network from January 7th, 2013 through January 13th, 2013 and from July 8th, 2013 through July 14th, 2013, respectively. Each of the traffic sessions in the data set fell into one of the 12 categories as listed in Table 1 below (same categories can be found in [2]). We were in full control of all of the data-generating applications during these two time windows, however, such categories were not made available to our flocking based classification programs. They were used for the performance validation purposes (in particular, the classification precision rate and recall rate) as presented in the next section.

Table 1 Network Traffic Categories

Category	Example Application
WWW	Web
P2P (File Sharing)	eDonkey, BitTorrent
P2P (Multimedia)	Sopcast, PPStream, PPTV
P2P (Instant Messaging)	Skype, MSN
Attack	Worm, Virus
Multimedia	Windows Media Player
Games	WOW
Email	IMAP, POP 3, SMTP
Interactive	ssh, rlogin
Database	Postgres, sqlnet
Bulk	ftp
Services	X11, DNS, LDAP

B. Experimental Results and Analysis

First of all, let's check the classification rates. In Fig. 7, the classification precision and recall rates are presented. They were obtained on the Tesla C2070 GPU when processing the traffic volume of 40,000 sessions. Apparently, our flocking-based model was able to effectively classify network traffic into different categories by selecting key flow features. Notice that our model didn't need a priori knowledge about these features and categories; it acquired them during the classification process unsupervisedly.

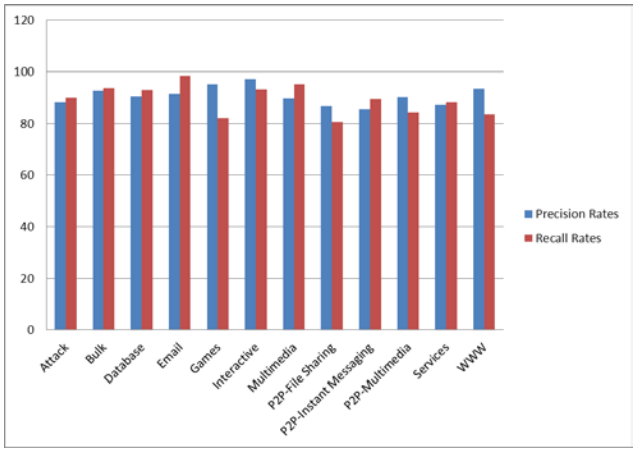

Fig. 7 Following the Flocking Rules in CUDA

Next, let's check the Average Classification Rate. We present the average classification rate of all 12 categories, which were obtained, again, on the Tesla C2070 GPU. Fig. 8 below shows that as the traffic volume grew, both the average precision rate and the average recall rate increased too. This is intuitive because in our flocking model, flocks will be formed more accurately when there are larger number of boids.

ISBN: 978-1-61804-219-4

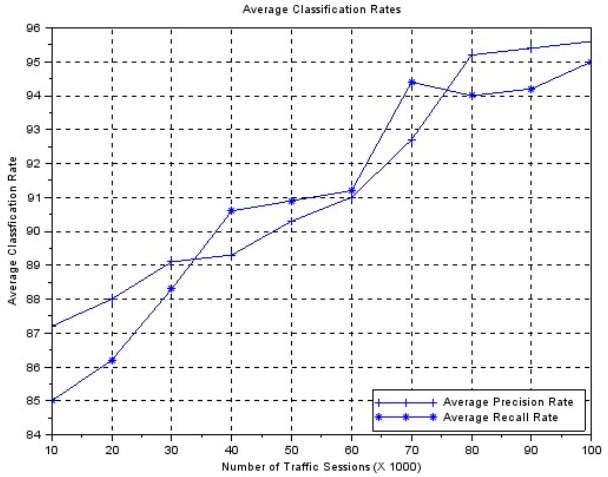

Fig. 8 Average Classification Rate

And third, let's check the Classification Runtime Speedup Ratio, GPU vs. CPU. Our experiments demonstrated that the traffic classification on GPU had substantially smaller runtime than its CPU counterpart (Fig. 9). The runtime acceleration was around 10 folds when the traffic volume was 10,000 sessions. We think such relatively low improvement was due to low utilization of GPU processing elements. Then the runtime acceleration rate grew and peeked on both of our graphics cards (around 60 folds and 50 folds respectively) when the traffic volume was 40,000 sessions. After that, the runtime acceleration degraded. We believe it was because of a significant increase in CUDA global memory reading and writing requirements as the traffic volume kept getter larger.

Notice that although the Tesla C2070 GPU was far more powerful than GeForce GTX 480, there was no significant difference between the runtime speedup delivered by these two graphics cards. The reason was, we think, the performance bottleneck of our programs lied mostly in the memory access rather than the computational delays.

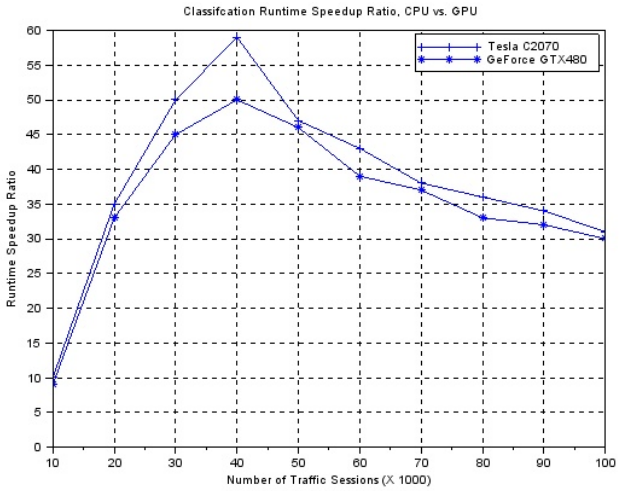

Fig. 9 Runtime Speedup Ratio, GPU vs. CPU

VI. CONCLUSION

Internet traffic classification is an actively researched area in recent years due to its high impact on using, operating, regulating , planning, and financing the Internet resources not only for today but also in the future.

In this paper, we present a GPU accelerated Internet traffic classification model inspired by the flocking behavior of social animals (like birds) in nature. The data that this model depends on is a reduct set of key flow features selected from the statistics of forty five flow features. Then the model automatically classifies the traffic flows/sessions into twelve categories without a priori knowledge of such categories. The experimental results show that the GPU-based parallel platforms outperform their CPU counterparts in execution time by a factor of 10X to 60X, while maintaining high classification precision and recall rates at around 90%.

REFERENCES

[1] H. Kim, K. Claffy, and M. Fomenkov, "Internet Traffic Classification Demystified: Myths, Caveats, and the Best Practices," *ACM CoNEXT 2008*, December 10-12 2008, Madrid, Spain.

[2] J. Tan, X. Chen, and M. Du, "An Internet Traffic Identification Approach Based on GA and PSO-SVM," *Journal of Computers*, Vol 7, No. 1, January 2012, pp. 17–29.

[3] J. Charles, R. Patton, T. Potok, and X. Cui, "Flocking-Based Document Clustering on the Graphics Processing Unit," in *Studies in Computational Intelligence*, 2008, vol. 129, pp. 129.

[4] S. Zander and T. Nguyen, "Antomated traffic classification and application identification using machine learning," *in Proceeding of the IEEE Conference on Local Computer Networks 30th Anniversary, 2005*, Sydney, NSW, pp. 250-257.

[5] A. Este, F. Gringoli, and L. Salgarelli, "Support Vector Machines for TCP Traffic classification," in *Computer Networks*, 2009, Vol 53, pp. 2476-2490.

[6] R. B, W. Zhong, and J. Liu, "Peer-to-Peer traffic identification by mining IP layer data streams using concept-adapting very fast decision tree," in *Proceeding of the 20th IEEE International Conference on Tools with Aritfitial Intelligence*, 2008, Dayton, OH, pp. 525-532.

[7] T. Auld, A. Moore, S. Gull, "Bayesian Neural Networks for Internet Traffic Classification," in *IEEE Transaction on Neural Networks*, Vol 18, No. 1, 2007, pp. 223–239.

[8] V. Lee, et al., "Debunking the 100X GPU vs. CPU Myth: An Evaluation of Throughput Computing on CPU and GPU," *ISCA 10, Proceedings of the 37th Annual International Symposium on Computer Architecture*, New York, NY, USA, 2010, pp. 451-460.

[9] C. Reynold, "Flocks, Herds, and Schools: A Distributed Behaviour Model," *ACM Computer Graphics*, 1987, Vol 21, pp. 25-34.

[10] M. Sun, J. Chen, Y. Zhang, and S. Shi: "A New Method of Feature Slection for Flow Classification," *2012 International Conference on Applied Physics and Industrial Engineering, Physics Procedia*, Vol 24, Part C, 2012, pp. 1729-1736.

The Selection and Training Framework for Managers in Business Innovation and Transformation Projects

An applied mathematics hyper- heuristics model

Antoine Trad, prof. dr.
Webster University
Geneva, Switzerland

and

Prof. Damir Kalpic, PhD
University of Zagreb
Faculty of Electrical Engineering and Computing
Zagreb, Croatia

Abstract—The riskiest factor in transforming a traditional Business Environment (BE) into an innovative and lean business oriented environment, is the role of the Business and (e-)Business Transformation Manager (BTM), in the implementation phase of a complex project transformation. The optimal profile of such a BTM, for the project implementation phase, has not been sufficiently investigated in a holistic and educational manner.

The main characteristic of a suitable BTM profile is the main goal of the authors' selection and training framework (STF) research project, started in the year 2010. In this research paper, the authors try to prove that the STF research methodology, design and prototype [36] can be applied in a "real world case"; that is in fact the research project's final phase. That would be considered as the research work's managerial benefits. This final phase is labeled the "STF research empirical model" and this paper presents its grounded theory based hyper-heuristics reasoning model [27].

This reasoning model offers the optimal BTM profile characteristics that have to cope with complex business transformation projects (BTP). These BTPs need a specific set of skills, especially for the final and the very difficult implementation phase [37]. These skills are fed in the form of factors into the reasoning model. That is in fact based on a mixed research method, which will deliver the most important BTM characteristics.

The literature review phase showed that a BTM favorite characteristic is to be an architect of adaptive business information systems (AofABIS) [58].

The BTP's technical implementation phase is the major cause of high failure rates. The BTMs need hands-on skills; these skills should encompass: 1) knowledge of dynamic business process architectures and business processes & services (BPs) technologies, 2) automated real-time unbundled business environments [17], 3) extreme & agile project management, 4) knowledge of just-in-time integration, 5) organizational behavior, 6) management science methodologies 7) enterprise architecture & integration and other concrete BTP implementation phase know-how artefacts. Therefore the researcher recommends a technocrats profile [6] as a "base profile" for such BTPs; that needs to be complemented with cross-functional skills [51].

More specifically, this research focuses on the influence of the BTMs' hands-on business architecture experience, background and education, in managing complex BTP implementations, where such transformations integrate avant-garde innovation, knowledge and technology components. "We know that those organizations that are consistently successful at managing innovation-related changes, outperform their peers in terms of growth and financial performance" [7].

Keywords-Hyper-heuristics, pseudo beam search, tree reasoning model, business transformation manager's profile, transformation project implementation, failure rates and empirical research phase.

I. INTRODUCTION

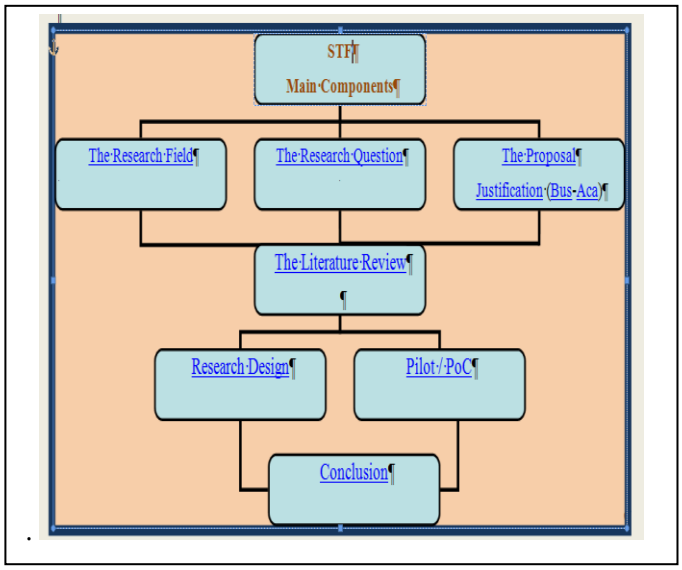

Fig. 1. The research design is the actual research phase and the authors are developing the hyper-heuristics reasoning model [52]

THE authors based there research on a mixed method, that is mainly based on a Hyper-heuristic decision tree [4], that is a real-world artefact that can be used by companies to select and train their BTM's. This research should propose the optimal BTM's profile characteristic that is
a variant of the an architect of adaptive business information systems [38].

The authors has based his research model on the main fact that only around 12% of business organizations successfully manage innovation-related business transformations initiatives. Therefore, there is a need for an automated hyper-heuristics reasoning model for the selection and training of future BTMs. BTMs who would have the needed characteristics for implementing a complex business process management (BPM) based systems [8].

One crucial implementation problem that is related to the profile of the BTM is the just-in-time (JIT) managerial practices and solutions related to the BTP. Such a problem can be only researched with a mixed-model that is very similar to the (re)-scheduling of activities model. Solving the given problem involves the determination of a actions and related solutions for multiple activities for the business information systems' (BIS) integration team. These mixed models are based on quantitative survey analysis, beam search and grounded hyper-heuristics; that is in fact a dual-objective decision-making [3].

This research article's main purpose is to offer a generic overview of the STF's mixed "ground hyper-heuristics based reasoning model", shortly the "STF_MHM". As this research aims, to qualify the BTMs': 1) profile capacities, 2) background and 3) skills; these characteristics are fed as factors in the STF_MHM; that in turn should deliver the most important BTM profile characteristic and recommendations. These "found" factors are also fundamental for the future coordination of the BTP of the BE; within the global transformed business enterprise. That enterprise that is eventually transformed into an "Enterprise 2.0" environment. BTMs who are also basically technocrats and advanced knowledge workers, support and design the transformation of the (e-) business environment in a pro-active hands-on manner [22][37][39].

"Hyper-heuristics are increasingly used in function and combinatorial optimization". In this research the hyper-heuristics approach is used, in order to find a combination of heuristics that solve a complex research question. The authors has decided to apply an adequate research model rather than to try to solve a simplistic problem using a fixed heuristic or descriptive statistics. Those are the standard methods in marketing research. In fact, the STF_MHM can be used as a template to solve future problems related to profile selections [4]. The actual research shows that the BTM is an architect of "adaptive" business information systems [38].

II. HOLISTIC MANAGEMENT OF COMPLEXITY

The authors based there research on a mixed method, that is mainly based on a hyper-heuristics approach. Organizations and BTMs need more than basic business information systems to exploit the avant-garde technologies in order to successfully achieve the BTP. Such BTMs and organizations need holistic just in time (JIT) decision methodologies like the BTM2, for (e-)business process architecture and BTPs [9]. This research shows that the BTM is a AofABIS; and s/he needs also to be: 1) a knowledgeable AofABIS, 2) flexible and 3) self-confident BTM [16].

III. BTM IS A AOFABIS

Understanding the BEs and the factors that affect their survival and competitiveness, is only the first step towards a successful BTP. The TBM must have in depth knowledge of: ELBE architecture and its development management, business people integration, agile project management and coordination of computer engineers. The BTM acts as solution designer and implementation architect [1][2].

The STF_MHM will offer the relationships between different factors and build an adequate algorithm to "rate & weight" these factors. Accordingly, this research project unifies resources from two distinct but related areas: business processes related information technologies and BTPs, it develops concepts for the BTM's selection and proposes a method to weight and inter-relate his or her various skills with factors.

This research project presents an original set of factors and fulfills the need for an efficient STF_MHM, in the form of a real world framework and recommendations, which affect the BTM's selection techniques. BTM selectors, professional analysts, project managers, auditors and advanced computer science students, will benefit from this research project.

Estimating of BTM skills requires a profound knowledge of the enterprise business architecture, business processes (BPs), services technologies and business project management issues. That rounds up the profile of a AofABIS. The BTM is in fact a AofABS, where s/he acts as a coordinator of enterprise architecture(s) teams and coordinates their various activities. The STF will also support him or her in managing problems in real-time. [38].

IV. THE RESEARCH QUESTION

As already mentioned in this article, the research topic's "research question" (RQ) was hammered [44]and the final research question is: ***"Which business transformation manager characteristic is most important for the implementation phase of a (e)business transformation project?"*** [44][50]. The targeted business domain is airline business.

V. THE LITERATURE REVIEW

To justify the essence of the researched subject, the authors relied on a significant number of sources, which

confirm the need or justification for the STF. This research's literature review proved the high failure rates in (e-)business transformations initiatives [51].

The literature review formed a large building block in the STF research design and methodology [26]. What mostly struck the authors was that after so many years and efforts, the failure rates are still extremely high and are even constantly increasing; probably due to the complexity of the implementation phase [21][20].

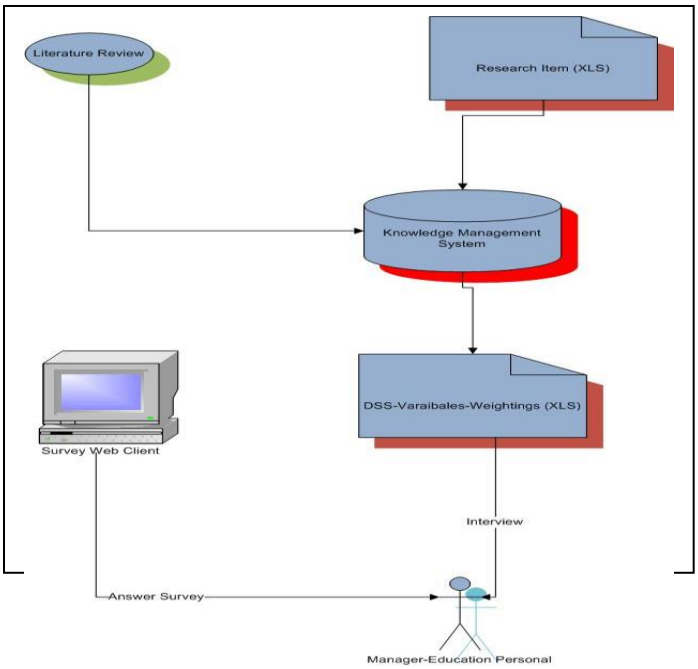

Fig. 2. The STF_MHM tools interaction [52].

The researcher proved the existence of a knowledge gap, as well as the necessity of the STF research project [52][57] [60].

What also astonished the authors, during the literature review process was the superficial approach of businesses and managers towards the innovation-related business transformation processes. This research question and topic appear to be undiscovered and under-estimated. The probable reason is the approach of too much scoping of the research question and simplifying the research method to the level of "marketing like" descriptive statistics.

VI. THE RESEARCH MODEL AND THE KNOWLEDGE GAP

As already described in previous research papers, which are related to this research project; the knowledge gap was acknowledged and confirmed. That is because the literature and methodologies treating BTMs' characteristics and AofABs in BTP's implementation phase are practically inexistent [1].

With the fact that the knowledge gap was defined, the authors will proceed with the STF_MHM development, which defines the empirical phase's "reasoning model" and its real world implementation.

VII. AUTHORS EMPIRICAL EXPERIENCES AND BACKGROUND

This STF research project is a distillation of the authors' experiences during at least the last 28 years as lecturers, senior software consultants, system designers, project managers and auditors in the domains of business engineering and respective information systems consultancy. In their carriers, the authors often encountered projects with serious problems and are aware of a very high rate of unsuccessfully terminated BTPs. That is the authors' main motivation to pursue the STF research to contribute to this endemic problem related to complex BTPs and to promote an effective BTM selection concept.

The authors designed and implemented an intelligent re-scheduling system (IRS) for the SwissAir airline. The IRS was based on the heuristics pseudo beam search decision tree [41].

VIII. THE RESEARCH DESIGN AND METHODOLOG-MIXED METHOD

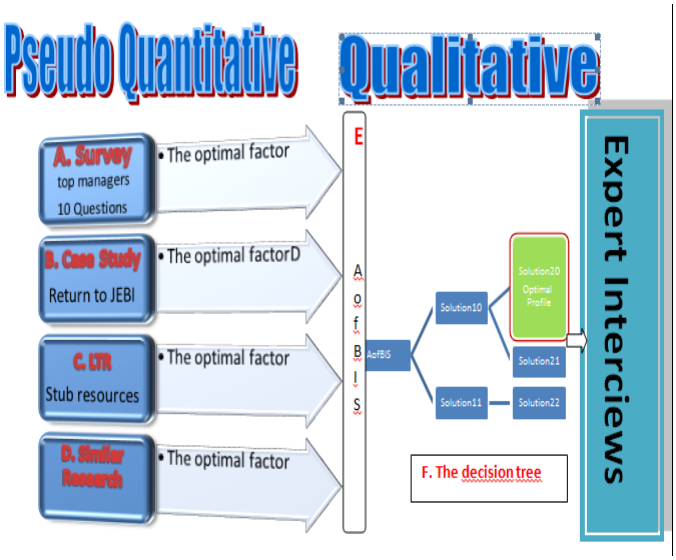

Fig. 3. The mixed method flow diagram [52] .

The STF's aim is to manage the most important risk factor for the selection of the future BTM, who is responsible of the BTPs' execution. The STF should help BTM selectors (like the human resources) avoid failures through the cross-functional assessment and the right selection of the optimal BTM. This assessment and selection will be insured by the evaluation and monitoring of the BTM's ability to integrate innovative business processes' (BP) technologies into the existing BE [28].

At this point in time, the STF_MHM research process hammered the research question (RQ), finalized the literature review (LTR) phase and survey design. The authors have decided to select Analytical Applicative Research (AAR) methodology, for the STF research project [11] because it was compatible with the STF_MHM (a heuristics model based on categories of factors). These factors where extracted from the

ISBN: 978-1-61804-219-4

LTR, survey outcomes, case studies and similar research projects.

AAR is a type of research that is mostly applied in education research, which fits right the STF, because it inspects the BTMs' skills and educational background [18]. In this research the authors want to prove that the BTM's profile is very much influenced by his or her business education and background. The AAR is certainly not the only qualitative research method that would fit the STF research; but, it defines exactly how the STF works, and also because it makes possible to insure the change through: a) actions) and b) research. These two steps can happen at the same time [12].

The STF's AAR is a spiral model which structures implement the action-research steps; because the spiral model matches perfectly the AAR's iterative approach. The AAR's reasoning algorithm fits the STF's empirical research model [10].

As this research project is based on AAR and on a positivist qualitative approach, the authors designed a factors tree-based reasoning model [15]. This model should help to define the BTMs' optimal profile, through the selection of factors that are deduced from selected empirical phase case studies from Farhoomand's collections [6]. These factors are then tuned and processed, through the STF's heuristics model. The prototype's processing outcomes are presented to various transformation specialists in the form of a questionnaire. The results of the questionnaires are correlated and the STF research project will at the end make a list of qualitative recommendations. Besides the recommendations, the STF_MHM delivers a concrete framework to be used in BTPs by various types of specialists; and that is considered the research managerial benefit.

The mixed method's resultant data sets will be stored in the STF's knowledge management system's database that has a query interface. This interface will help future researchers and managers to define data patterns to hammer a BTM profile.

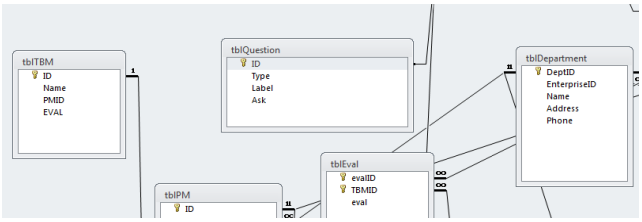

Fig. 4. The STF's entity relational model [35].

For this grounded complex phase, there were credible reasons for long planning and for investing efforts in combining various research technics [23], this mixed research method is the base for this holistic research project [26].

This research method that is conducted in the context of a cycle of doctorate in business administration was validated by the researcher's supervisor prof. M. Kalika, Business Science Institute (BSI).

This method consists of the following phases (as shown in Fig. 3.):

A. The case study reasoning and analysis

of a set of case studies from Farhoomands' collections and other case studies that were selected during the literature review.

B. SAP's BTM2 works

confirm the holistic approach and the profile of AofABIS. This method confirms the importance of the architectural view in BTPs.

C. LTR

The conclusions of the terminated literature review [50].

D. The quantitative data results

Come from similar and complementary works, like Kelada's [61] and Walsh's [22].

E. The quantitative phase

Will help to find the best questions, hence factors; that will be fed into the mixed-model initial node. That is done using the efficient frontier concept. This frontier is the filter that decreases the number of factors and problems [3]

F. The outputs from the pseudo-quantitative phase (A to G)

are qualitatively filtered and deliver the optimal factor. That factor is the root node for the decision tree.

G. The STF tree (qualitative/hyper-heuristics decision tree)

is a beam search heuristics model that uses the input from the previous phase (A to G) and proposes a possible solution, hence a profile.

H. The qualitative hyper-heuristics decision making process (DMP) model

will try to confirm the outcomes of the previous phases (A to G); and deliver managerial recommendations (or managerial benefits) on how to solve such problems.

I. The concept (A to H)

may be used as a template (a meta pattern) for similar problems [4].

IX. THE DATA COLLECTION

The STF's data-model and resulting data-collections are based on the following data artefacts:

A. The STF has an entity relational model (ERM), as shown in Fig. 4.

B. The STF survey interface will be filled by selected qualified persons. This survey will be delivered in an office word document form.

C. The survey questions will be filled by managers and then filtered to deliver the most important factor (that is equivalent to a question or problem). That process is automated by the use of office scripting functions (Visual basic for applications, VBA).

D. The resultant factor(s) from step "C, will be then analyzed in the STF tree; and a set of recommendations and solutions are presented as the recommendations. These recommendations are in fact the research project's resultant theory.

X. ARTIFACTS: HYPOTHESIS, VARIABLES, QUESTIONS, FACTORS AND WEIGHTINGS

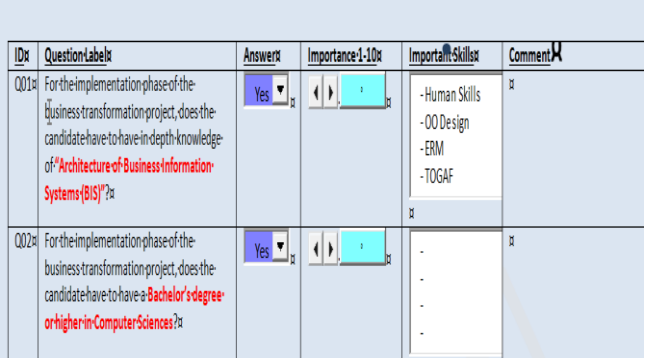

Fig. 5. The STF Survey Questions [35].

The survey questions are built from the research hypothesis. As already presented, this research is based on a mixed method that has the following artifact sets:

A. Hypothesis

The minimal set of hypothesis, which resulted from the literature review phase:

I. H1: The BTM is an adaptive business and enterprise architect.

II. H2: The BTM must know BPs related technologies and agile project management.

III. H3: The BTM must know and be capable of implementing the STF_MHM model, in order to monitor its evolution and insure the BTPs integrity.

IV. H4: The BTM must be of an engineering and business background, with substantial ICT experience (a technocrat profile [6]

V. H5: The BTM is a member of the middle management [32].

B. References

Has a defined set of factors and dependent variables, which result from point A). These factors are used in the decision making process (DMP) [34]

C. The survey questions

Are based on factors; resulted from the literature review phase and laboratory exercises [35].

D. These questions

are used to develop surveys which will be used in the quantitative part of the mixed method.

E. The surveys outputs

are fed into the mixed model that is based on the beam search, hyper-heuristics; and a dual-objective decision-making. It contains a tunable objective function (or reasoning engine). This objective function includes the weightings of various factors, problems, actions and solutions. The initial set of weightings result from the survey and they can be tuned [3].

XI. THE SURVEY

The STF survey templates were developed from a set of resulting factors and questions, which were derived from the research hypothesis. A group of experienced executive managers and TBMs (limited to 10) will fill the surveys. The research process previews to survey very experienced domain specialists and generate the collected data sets to be used in the final quantitative process. The surveys confirmed the research projects hypothesis. The considered types of specialists and managers, to be surveyed or interviewed are:

I. Business and information technology school professors and directors
II. Managers of information systems
III. Senior project managers
IV. Human resources specialists
V. Educational professionals
VI. Transformation managers
VII. Executive Managers
VIII. Senior Business Analyst and Auditors [52]

XII. CASE STUDY ANALYSIS

The case study analysis and other research resources are used to assist the filtering of the data that came out of the quantitative analysis; that concluded the survey data acquisition phase. The collection of case studies from A. Farhoomand and SAP's BTM2 perfectly correspond to the research filtering phase [6][2].

XIII. GROUNDED HYPER-HEURISTICS DECISION TREE

The aim of grounded hyper-heuristics approach is to implement a grounded process that generates solutions in an acceptable period of time (just in time). It is a "rule of thumb," and a guide to implement problem solving decisions making systems (DMP), like the STF. In business information

ISBN: 978-1-61804-219-4

technology, heuristics refers specifically to algorithms, like the STF's goal function.

The STF uses a grounded hyper-heuristics process that includes tuning and getting results by trial and error; with a factors based system. Data that comes out of the surveys' acquisition process are verified and filtered to build an efficient tree algorithm and to process solutions in the form of recommendations. Like all heuristics based systems, the STF reasoning engine will not be always perfect and adapted to all possible requirements, but it should be enhanced to make it capable of finding optimal results [33][34].

The grounded hyper-heuristics theory has become established as a qualitative methodology of choice for researchers in similar fields, using a holistic approach. It is apparent to many researchers that there are significant difficulties associated with defining what the grounded heuristics theory method actually is, and how it should be applied concretely in research projects or decision support systems. In addition, its popularity has tended to keep other qualitative approaches under-explored; it is an agile method that can be adapted to complex projects. Grounded hyper-heuristic method is a useful form of qualitative methodology for complex holistic research projects, because it develops a pluralistic approach to qualitative research and offers a possibility to develop a real world framework [27].

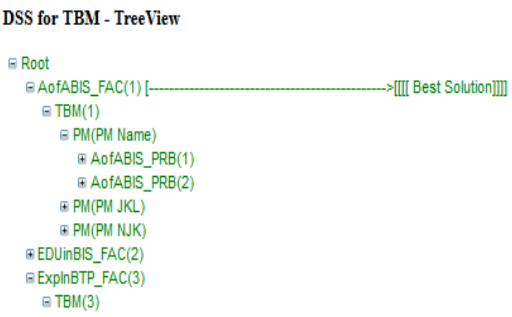

Fig. 6. *A view on the STF's tree solution node [35].*

The STF applies the positivist AAR that is designed on a model identical to the grounded hyper-heuristics model. This heuristics model is based on a pseudo beam search tree method and has the following elements [24][41]

A. *Factors set*

are the research dependent variables that are based on factors. The BTM's category, factors and dependent variables will be used as parameters for the configuration of the STF_MHM process. This processing will deliver the needed set of possible solutions in the form of the BTM's optimal profile.

B. *The filtering process*

Is executed after the survey data collection, and the filtered factor is the AofABIS, to be used for the qualitative part of the mixed process.

C. *Initial node*

Helps the establishment of the initial BTM's profile characteristics; that comes from the surveys and selected research resources, like case studies.

D. *Tree reasoning*

The STF's goal is to select the optimal BTM who can implement the BTP successfully, for that reason the BTM needs a set of skills that are represented in the form of the STF_MHM factors (which have the format: BTM_xxx, where xxx is adapted to the type of the needed skill. For example, xxx that stands for AofABIS, represents the BTM's factor for "business architecture skills", that, if selected, has to be considered in the selection process.

E. *Solution*

These factors will be fed in the STF's AAR heuristics motor in order to bring up the optimal BTM profile. This research's AAR model is based on a heuristics motor, that can be configured, weighted and tuned using BTM's factors.

XIV. THE STF_MHM AND THE DMP SOLUTIONS

STF's set of possible solutions that result from the STF's hyper-heuristics decision model (based on STF factors), helps the BTM selectors in the selection of the future BTM profile. The STF starts with the initial set of selected optimal factors that define the BTM's profile. Then the STF's system DMP is launched to find the set of possible solutions in the form of profiles or possible improvements to the current BTM skills, as shown in Fig. 6.

XV. BPM AS A DECISION TREE

The STF's decision tree, results in a set of possible solutions that determine BTM's skills. This tree can be also represented as an implementation of business processes modeling (BPM). Such a solution is optimal, because then the STF knowledge is stored in the business information system [2]. The main advantages for using BPM as a decision tree are:

A. The use of business services.

B. The integration of the STF in the company's business processes and knowledge environment.

C. The use of smart tools, automated workflows, integration and advanced graphical user interfaces, which are making BPM cheap to use.

D. Respecting existing choreography standards.

E. Enabling to deliver quick return on investment & long-term success.

ISBN: 978-1-61804-219-4

F. BPM will enhance the overall business intelligence because the smart use of BPM with STF rules and analytics will help the better decisions for the selection of BTM, with more insights.

XVI. THE STF PROTOTYPE OF THE EMPIRICAL MODEL

The STF's empirical model is built to prove the research proof of concept (POC), which has been developed using the Microsoft Visual Studio 2012 environment [59].

The POC uses the "model view control" (MVC) architectural pattern, that collects the model data. This prototype is a real world decision support system (DSS) that can be used by middle managers [32], as shown in Fig. 7. The POC is a real world system and is considered to be as a concrete managerial benefit.

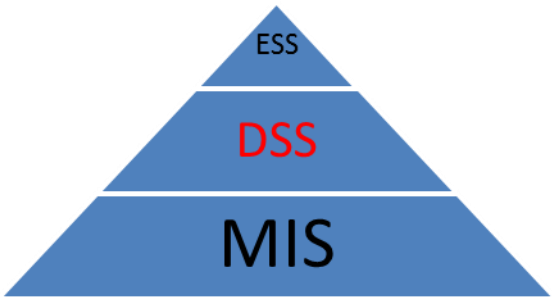

Fig. 7. *Decision systems by management level [32].*

The POC contains the STF's major components, and what will be primarily tested is the reasoning engine, which is based on the AAR heuristics model. This research POC will serve to confirm the research hypothesis and the STF_MHM model; that has a goal function, which calculates the best solution (DSSGoalFunction). Added to that, the authors will use interviews with experts to confirm the POCs outcomes; which means that the STF_MHM is a mixed method based on a real world prototype. The results will be presented in the form of a set of recommendations.

XVII. THE EXPERT'S INTERVIEW

This research phase comes after the hyper-heuristics tree decision model outcomes and is the last phase. This phase will try to confirm the STF's managerial benefits. The interviews will be designed to confirm the outcomes, by a confirmed expert in this domain of business transformation projects.

XVIII. THE STF'S BTM's PATTERN (STFBBTMP)

The authors' aim is to convert their relevant research outcomes into a managerially useful framework [13]; and its hyper-heuristics tree processing model is used as a template that is suitable for a class of problem instances [4].

Therefore, it is planned to create a concrete STF environment that is based on a business process oriented transformation pattern [2]. This STF pattern will be in fact a STF business transformation managers' project pattern (STFBNTMP).

XIX. THE STF'S NEXT RESEARCH PUBLICAITONS AND ITERATIONS

This article presents the STF's empirical model's mixed method, that will transform the experiences made during the proposal and literature review phases, into coherent inputs for the final expert interview phase. For that goal, the researchers have planned the following sets of research activities:

A. STF's empirical phase, planned publications are:

I. Develop a short summary on the STF empirical model, expected delivery date: 01102014. Probably to be submitted to the [62].
II. Develop a research paper [38] on the BTM optimal profile - AofABIS, expected delivery date: 01-04-2014.
III. Develop a full research paper [59] on the STF's empirical model phase - empirical heuristics model implementation, expected delivery date: 01052014.
IV. Develop a full research paper [59] on the STF's empirical model phase - prototype/prove of concept, expected delivery date: 01052014.

B. The final research phase will contain the following steps:

I. Write the draft research report, expected delivery date: 01012014. To verify the coherence.
II. Write the final research report and recommendations for concluding the research, expected delivery date: 01082014.

XX. CONCLUSION

The research empirical phase will try to prove what is the main reason for **BTPs failures**, and will try also to define an optimal profile who is capable of finalizing the implementation phase of a BTP. There has been a lot developed on enabling success in transformation projects, but the authors propose to inspect why BTM fail in the implementation phase of the BTP. That is mainly due to the lack of knowledge in managing business integration and implementation, where there is an important use of business information related technologies.

This is another article in a long series of research articles related to the STF, which is based on a mixed method. The STF factors are the result of the literature review and the surveys outputs. These factors are the base of the **STF's grounded hyper-heuristics research model**. In this article, the focus is on the STF's mixed model's reasoning engine, which is specialized in finding the optimal BTMs' capabilities. These BTM's characteristics needed to holistically manage the design and implement a BTP. More specifically, the authors give an overview on the research grounded hyper-heuristics model, which is a decision support system, integrated in a real world framework, to be used by senior managers [32]).

The most important findings in this phase are:

A) **Knowledge gap:** The STF literature review proved the credibility of a knowledge gap. This gap exists between the traditional management skills building and the complex projects' realities. With the literature

ISBN: 978-1-61804-219-4

review's termination, the authors presented the STF research design and model, based on factors. The researchers proved the existence of a knowledge gap, as well as the necessity of the STF research project [60][52][57].

B) **Mixed Method:** The STF's research uses an unconventional research model in order to create the initial BTM profile. The STF's DMP delivers a set of possible solutions that result from its heuristics decision model. These solutions help the BTM selectors in the selection of the right BTM profile [50]. These mixed models are based on beam search, heuristics; dual-objective decision-making [3].

C) **Managerial benefits:** The qualitative hyper-heuristics decision making process (DMP) model will try to confirm the outcomes of the previous phases (A to D); and deliver managerial recommendations (managerial benefits) that may be used as a template that is suitable for a class of similar problem instances [4]The STF is a just-in-time systems (JIT) managerial framework. The STF can be also used to establish future innovation and transformation related training recommendations; and with that mean, the enterprise avoids the risky traditional business transformation habits, such as "let's change the whole BE", without taking seriously into account the BTM's profile; that can create major problems.

D) **A concrete framework:** The STF research project proposes a concrete framework on how to select, train and evaluate a BTM [59].

E) **Profile:** The empirical phase will try to show that schooling environments produce general profiles that can hardly cope with heterogeneous complexity and fast changes. These high frequency changes are mainly due to the hyper-evolution of technology. Estimating BTM skills require a profound knowledge of the business enterprise architecture, BPs, service oriented technologies and agile business project management issues. That rounds up the profile of an AofABIS [1][2].

F) **STFBTMP :** The STF's research and more precisely, this phase should convert the STF's collected practices and experiences into a management knowledge pattern (STFBTMP), on how to select and train a BTP.

G) The STF proof of concept (POC) and interviews will deliver recommendations on how to improve the BTP's success rates, by selecting and training the right BTM profiles [61].

This research method that is conducted in the context of a cycle of doctorate in business administration was validated by the researcher's supervisor, prof. M. Kalika (BSL).

Acknowledgment

In a work as large as this research project, technical, typographical, grammatical, or other kinds of errors are bound to be missed. Ultimately all mistakes are the authors' responsibility. Nevertheless, the authors encourage feedback from readers identifying errors in addition to comments on the work in general.

It was our great pleasure to prepare this work. Now our greater hopes are for readers to receive some small measure of that pleasure. The authors owe a special debt to Webster University who helped the first author in developing this project.

References

The references are sorted by the importance of the source to the research topic:

[1] SAP, "GBTM: Global Business Transformation Manager Master Certification (SAP Internal). July, 8th – 19th, 2013 in Potsdam, Germany, Business Transformation Academy. SAP, 2013.

[2] SAP, "BTM2: Business Process Management Business Transformation Academy". Germany. 2012.

[3] McMullen, P.R., Tarasewich, P., (2005). "A beam search heuristic method for mixed-model scheduling with setups", Int. J. Production Economics 96 (2005) 273–283. Elsevier.

[4] Vella, A., Corne, D. ; Murphy, C., (2009), "Hyper-heuristic decision tree induction". Sch. of MACS, Heriot-Watt Univ., Edinburgh, UK. Nature & Biologically Inspired Computing, 2009. NaBIC 2009. World Congress. http://ieeexplore.ieee.org/xpl/login.jsp?tp=&arnumber=5393568&url=http%3A%2F%2Fieeexplore.ieee.org%2Fxpls%2Fabs_all.jsp%3Farnumber%3D5393568, December 2nd, 2013

[5] Kalika, "eDBA, research model validation, BSI, Geneva, 2013

[6] A., Farhoomand, "Managing (e)business transformation". UK: Palgrave Macmillan, 2004.

[7] J., Tidd,. "From Knowledge Management to Strategic Competence", 2nd Edition, Imperial College, London, UK, 2006.

[8] J., Tidd, J., Bessant, "Managing Innovation, Integrating Technological, Market and Organizational Change", 4th Edition. USA: Wiley, 2009.

[9] A., Uhl, L., Gollenia, "A Handbook of Business Transformation Management Methodology", Gower. SAP. Germany. 2012.

[10] J, Whitten, L, Bentley '"Systems Analysis and Design Methods". McGraw-Hill & Irvin, 2011. USA.

[11] E., Chanaron, "DBA Workshop", GEM, 2010, Grenoble, France.

[12] Dick, B., (2002). "Action research: action and research" http://www.scu.edu.au/schools/gcm/ar/arp/aandr.html, December 2nd, 2013

[13] Markides, C. "Crossing the Chasm: How to Convert Relevant Research Into Managerially Useful Research", Journal of Applied Behavioral Science, March 2011 vol. 47 no. 1 121-134. London, UK.

[14] Quantitative, "Positivist Research Methods in Information Systems", 2010, http://dstraub.cis.gsu.edu/quant/

[15] M., Hoepft, "Choosing Qualitative Research: A Primer for Technology Education Researchers", Journal of Technology Education, Virginia Tech. 1997. USA.

[16] The Economist, "Inside the machine. A survey of E-management. Special report: E-management". The Economist. 2000, UK.

[17] F., Willaert, "XML-Based frameworks and standards for B2B e-commerce", PhD Research project, Faculteit Economische en Toegepaste Economische Wetenschappen Department. Katholieke Universiteit Leuven, 2001.

[18] IBM, Webinar, " BPM & EA for Better Business Outcomes eKit " http://www-01.ibm.com/software/info/bpm/ekit/bpmea. 2010.

[19] ECS, (2004). www.ecs.org/html/educationIssues/Research/primer/appendixA.asp

[20] Capgemini Consulting, "Business transformation: From crisis response to radical changes that will create tomorrow's business. A Capgemini Consulting survey". France, 2009.

[21] Capgemini, "Trends in Business transformation - Survey of European Executives". Capgemini Consulting and The Economist Intelligence Unit, France, 2007.

[22] Walsh, I., Kefi, H., Baskerville, R., "Managing culture creep: Toward a strategic model of user IT culture". Journal of Strategic Information Systems 19 (2010) 257–280. Journal homepage: www.elsevier.com/ locate/ jsis. Elsevier.

[23] T., Bourner, "'The research process: four steps to success", Arnold, 1996. London. United Kingdom.

[24] A., Jaszkiewicz, R., Sowiński, "The 'Light Beam Search' approach - an overview of methodology and applications", European Journal of Operational Research 113 (1999) 300-314

[25] Birudavolu, S., Nag, B., A Study of Open Innovation in Telecommunication Services: A Review of Literature & Trends. Indian Institute of Foreign Trade, India. 2011).

[26] Bruce, Deakin University, "The literature review", 2010 http://www.deakin.edu.au/library/findout/research/litrev.php#Bruce#Bruce, 2010

[27] Wes, W., "Beyond grounded theory: The use of a heuristic approach to qualitative research". Counselling and Psychotherapy Research: Linking research with practice. Taylor, Francis, 2001.

[28] S., David, D, Linthicum, "Enterprise Application Integration", Addison-Wesley Professional, 2000, USA.

[29] Quinlan,. C., 2011. "Business Research Methods". Dublin City University. Cengage Learning. Ireland. 2011.

[30] Markides, C., 2011. "Crossing the Chasm: How to Convert Relevant Research Into Managerially Useful Research", Journal of Applied Behavioral Science, March 2011 vol. 47 no. 1 121-134. London, UK.

[31] Şeref, Ravindra K. Ahuja, and Wayne L. Winston, "Developing Spreadsheet-Based Decision Support Systems", Michelle M.H. Dynamic Idea Publishing, 2007, Instructor Notes on DSS and data warehouse

[32] Laudon, K., Laudon, J., 2010. Management Information Systems, 11th Edition, Prentice Hall, USA.

[33] TechTerms , 2013, http://www.techterms.com/definition/heuristic, December 2nd, 2013

[34] Oxford Dictionaries, "heuristics", (2013). http://www.oxforddictionaries.com/definition/english/heuristic, December 2nd, 2013.

[35] Trad, A., "COSC DSS, Decision Support Systems – Labs results". Webster university 2013, Geneva, Switzerland.

[36] Trad, A., "The "Selection, and Training framework (STF) for Managers in Business Innovation Transformation Projects" - Overview of the development of the empirical model. IEEE 2013, BAME. Venice, Italy.

[37] Trad, A., Kalpic, D., "The Selection and Training Framework (STF) for Managers in Business Innovation and Transformation Projects - The Design and Implementation of the Research Model", 3rd position awarded paper. IMRA, Croatia, 2013.

[38] Trad, A., Kalpic, D.,. "The Selection and Training Framework (STF) for Managers in Business Innovation and Transformation Projects – The profile of an Architect of adaptive business systems", IMRA, USA. Article to be submitted in 2014.

[39] A., Trad, D. Kalpic, K. Fertalj, "Proactive business monitoring of the IS risk and quality". Proceedings of the 23rd International Conference on Information Technology Interfaces; 2002 June 24-27; Cavtat, Croatia. Zagreb: SRCE University Computing Center, University of Zagreb; 2002. p. 497-502.

[40] A. Trad, D. Kalpic, "Proactive Monitoring of the IS Risk and Quality", ITI 2002, Cavtat, Crotia.

[41] A. Trad, D. Kalpic, "Information Systems Risk and Quality Check (ISRQC)" – Practical Implementation. Proceedings of the International Conference on Information Technology Interfaces; 2002 Pula, Croatia. Zagreb: SRCE University Computing Center, University of Zagreb.

[42] A. Trad, "Audit, Control and Monitoring Design Patterns (ACMDP) for Autonomous Robust Systems (ARS)". International Journal of Advanced Robotic Systems, 2005, Volume y, Number x (200x), ISSN 1729-8806.

[43] A. Trad, "The Mobilere Transformation, by the use of BPEL and SOA", 2008, Geneva, Switzerland.

[44] A. Trad, "GEM DBA Workshop – Research Design" – Poster Presentation, March, 2011, Webster University, Geneva, Switzerland.

[45] A. Trad, D. Kalpic, "The Selection, Training, Follow and Evaluation STF for Managers in Business Innovation Transformation Projects "A Holistic Overview. IEEE 2011, Conference on Information Technology Interfaces; Cavtat, Croatia.

[46] A. Trad, D. Kalpic, "The "Selection, Training, Follow and Evaluation (STF), for Manager's in Business Innovation Transformation Projects - The Human Factor". Conference on Information Technology Interfaces; Cavtat; 2011.

[47] A. Trad, "STF for BTMs. DBA Proposal". Grenoble Ecole de Management, 2011, Grenoble, France.

[48] A, Trad, "The "Selection and Training STF, for Managers in Business Innovation Transformation Projects - The Proposal", GEM, 2011, France.

[49] Trad, A, "STF - The Selection and Training Framework Research Survey System". IBISM, Lausanne, Switzerland. 2013.

[50] Trad, A., Kalpic, D., "The Selection, and Training Framework (STF) for Managers in Business Innovation Transformation Projects" - The Background. , Conference on Information Technology Interfaces; Cavtat, 2013, Croatia.

[51] Trad, A., Kalpic, D., "The Selection, and Training Framework (STF) for Managers in Business Innovation Transformation Projects -The Profile" -. , Conference on Information Technology Interfaces; Cavtat, 2013, Croatia.

[52] Trad, A., Kalpic, D., "The Selection, and Training framework (STF) for Managers in Business Innovation Transformation Projects - The Literature Review". IEEE 2013, Centeris. Portugal

[53] Trad, A., "The Selection, and Training STF for Managers in Business Innovation Transformation Projects - The BPM and services implementation factors". Emerald, 2013, USA

[54] Trad, A., Kalpic, D,, "Transformation Quality and Risk Check (RQRC) – Theoretical Basis". Proceedings of the 23rd International Conference on Information Technology Interfaces; 1999 Jun 15-18; Pula, Croatia. Zagreb: SRCE University Computing Center, University of Zagreb; 1999. p. 497-502.

[55] Trad, A., "STF for BTMs. DBA Proposal." Grenoble Ecole de Management, Grenoble, France. 2011.

[56] Trad A, "The initial Proposal", GEM, France. 2010.

[57] Trad A, "The Selection and Training Framework (STF), for Managers in Business Innovation Transformation Projects - The Final Proposal", GEM, France. 2011.

[58] Trad A, "The Selection and Training Framework (STF) for Managers in Business Innovation Transformation Projects - The literature review", GEM, 2013, France.

[59] Trad, A., Kalpic, D., "The Selection, and Training Framework (STF) for Manager's in Business Innovation Transformation Projects - The proof of concept". 2014, NENED; Zagreb. Croatia. Research paper to be submitted.

[60] Santa Cruz University, Write a literature review . http://library.ucsc.edu/help/howto/write-a-literature-review, 2011.

[61] Kelada, Why do the majority of change initiatives fail and what to do about it - The example of TQM - GEM, Grenoble. 2009.

[62] Trad, A., Kalpic, D., "The Selection, and Training framework (STF) for Managers in Business Innovation Transformation Projects - The Final Interview". IEEE 2014, Centeris. Portugal. Paper to be submitted.

Failure modes of a vehicle component designed for fuel efficiency

M.R. Idris, W.M.Wan Muhamad, S.Z. Ismail

Abstract— Many automotive companies today are striving to build a fuel efficient vehicle due to increasing demand of small compact cars for urban use, high fuel prices and legislative requirements on emission control. This research is part of a concept car project that focuses on a weight reduction program. The component that is subjected to weight loss is known as steering knuckle. This research is to analyze the potential failure modes on a redesigned knuckle that have achieved maximum limit for weight reduction. The original component is then transformed into Finite Element Model (FEM) using HyperWorks software. The weight topologies are tested under different fatigue stresses for identification of crack initiation. A shape optimization method was then employed to verify the potential failures. The results will be presented in comparison to original knuckle design. A recommendation to enhance the component strength will be proposed during the designing stage of the fuel efficient car.

***Keywords*—**Knuckle, Weight reduction, Finite elements, HyperWorks, Fatigue

I. Introduction

In search to find replacement to fossil fuel, automotive manufacturers developed various technologies such as electric vehicle (EV), natural gas vehicle (NGV), biodiesel, hybrid etc. However, during commercialisation, problems pertaining to testing, costs and resources have yet to be resolved. A much radical solution is neede in order to improve fuel efficency.

The weight reduction of vehicle components is also a key to fuel efficiency. Lighter material weights will result in fuel savings. Today, many vehicles are designed with lighter parts/materials in order to reduce its total weight . A simple weight test by author has revealed that by eliminating 20 kg (spare tyre), the extra mileage gain is 8-10 km for every 100km. The test is conducted in the motorway without heavy traffic. The situation is likely to be doubled for city driving.

The weight reduction activities on safety parts often seen as major obstacle to the designers. Any small changes in parameters of parts will affect the material stresses than can cause fatigue or crack initiation.

This work was supported is sponsored by Ministry of Science, Technology and Innovation (MOSTI) Malaysia

M. R Idris is with Universiti Kuala Lumpur, Institute of Product Design and Manufacturing (IPROM), Malaysia (Telephone: 60391795000; fax: 60391795001, email: mrazif@iprom.unikl.edu.my)

W.M.W.Muhamad is with Universiti Kuala Lumpur, Malaysia France Institute(MFI), Malaysia, email: drwmansor@mfi.unikl.edu.my)

S.Z. Ismail is with Universiti Kuala Lumpur, Institute of Product Design and Manufacturing (IPROM), Malaysia (email: s.zubaidah@unikl.edu.my)

Figure 1: Steering Knuckle LH & RH

Figure 2: Steering knuckle assembly

This research is to study the failure modes of components that are subjected to weight reduction, in term of shape and dimension. The selected part is a steering knuckle. This is a safety part which is linked to brake disc and steering linkages. Figure. 1 shows a set steering knuckles that are normally used on cars and each part is weighing 1.5 kg.

The steering knuckle is assembled on the brake disc housing as illustrated in Figure. 2. The research explores the design optimisation using Finite Element Method to evaluate the stress valus under loading constraints. The failure modes of parts will be analysed. Key parameters will be determined to further optimised the dimension (weight lost) and hence to reduce potential failures.

Many think that EVs are bigger and heavier than conventional ones because of their use of large batteries. This might be true for long range vehicles that require big heavy batteries. The battery is usually considered the main component in the EV weight. So, it is important to examine the battery weight in the urban EV model. EV will use a Lithium-ion battery with average specific energy 0.13 kWh/Kg. For a

ISBN: 978-1-61804-219-4

60-mile - 0.2 kWh/mile (97-mile - 0.12 kWh/km) urban vehicle, the total needed battery capacity would be 12 kWh. Therefore, the expected battery weight is about 90 kg which is quite satisfactory for an urban EV. Moreover, the electric motor of an EV is much lighter than the internal combustion engine of a conventional vehicle delivering the same power. In addition to the fact that the EV does not need manual or automatic gearbox, it is also possible to eliminate every mechanical transmission using wheel-drive motors. Furthermore, future advancements in battery technology will make batteries smaller and lighter which will in turn lead to further reductions in weight and size of the EV. [1].

Biodiesel-fuelled diesel engines offer a substantial opportunity to address two major issues facing our global society: energy consumption and global warming. A substantial portion of energy consumption and carbon dioxide emission rates are furnished by the transportation industry, which in the United States, for example, represented nearly 30% of the energy flow and over 31% of the vented CO2.[2]. However, the resources for biodiesel are limited.

The powertrain of a parallel hybrid electric vehicle (PHEV) is a hybrid system of an engine and an electric drive system. Under the control of the advanced vehicle controller unit (VCU), the drive force requested by the driver is optimally distributed between the engine and the motor. The optimal distribution of the drive force is supervised by the vehicle energy management strategy (EMS), which is the kernel part of the real-time control algorithm of the PHEV, and it is one of the key PHEV technologies in which many researchers are engaged. The goal of the EMS is to achieve a high efficiency, energy saving, and low emissions vehicle by controlling the hybrid powertrain system coordinately. This means that the performance of a PHEV is strongly dependent upon the control of the hybrid powertrain system, which includes the engine, electric motor, electrical energy system, automatic clutch and transmission.[3]

Stress-life fatigue analysis was conducted to correlate the crack location between the failed component and the simulation model. A new design proposal was determined with the topology optimization approach, and then design optimization by response surface methodology was effectively used to improve the new clutch fork design. The topology optimization approach used in this study has found an original load balanced optimum material distribution and it is important to know the design space, the boundary conditions and the loads throughout the process. With the results from the topology optimization, design engineer are capable to define a detailed design. Topology optimization has proven very effective in determining the topology of initial design structures for component development in the conceptual design phase. After determining the initial topology, shape optimization can be used for the final design. [4]

High stiffness, high strength, and light weight are important issues when designing vehicle structures. To achieve such goals, the recent applications of CAE based structural optimizations to the design of lightweight vehicle parts with high static and dynamic performances are regarded as efficient approaches. Flatbed trailer is optimized to have a high stiffness-to-mass ratio by applying CAE based optimization tools within consistent problem formulations. Since structural optimizations have not been widely applied to the design of heavy vehicle structures such as a flatbed trailer, substantial improvement in structural performances can be expected by using a systematic optimization procedure. [5]

Optimization methods were developed to have lighter, less cost and may have better strength too. Many optimization types, methods and tools are available nowadays due to the revolution of the high speed computing and software development. There are four disciplines in structural optimization process [6,7,8].

Topology optimization: provides optimum material layout according to certain the design space and loading case.

Shape optimization: supports optimum fillets and the optimum outer dimensions.

Size optimization: to obtain the optimum thickness of a component.

Topography: an advanced form of shape optimization, as it will generate reinforcements such as beads.

Shape optimization refers to the optimal design of the shape boundary of structural components, which is becoming increasingly important in mechanical engineering design. Current interest in structural shape optimization is largely motivated by demands for more cost competitive design throughout the industrial sector. Therefore, considerable effort has been devoted to developing efficient techniques for shape optimization [6]. Shape optimization is expected to further improve a design in achieving certain objectives after topology optimization was performed, such as in this work.

Finite element method used for many type of analysis, such as linear analysis, nonlinear analysis, fatigue analysis and another types. FE analysis was developed to solve the optimization process such as Optistruct linear solver [8], TopShape [9], ANSYS, NASTRAN [10], ABAQUS etc.

II. Research Aim and Objective

This research aims to provide solution to a car designer in optimizing the component structure against the types of failure modes. Designing a light weight component for fuel efficiency is likely to increase the fatigue stress distribution.

This study will identify the potential failure modes of crack initiation using topology and shape optimization approach.

III. Methodology

Topology and Shape optimization was applied to reduce volume or weight of rear knuckle component in a local car model. The approach is shown in Figure 3.

Modeling, simulation and optimization processes used software modules included in Altair's HyperWorks. Utilizing HyperMesh, solid model was imported for finite element modeling where loads and constraints were applied.

Shape optimization process requires shape definition for design variables and HyperMorph was used to conduct such purpose. Then, shape optimization process was conducted

using OptiStruct. Furthermore, Hyperview and Hypergraph were used to display and plot the data for results interpretation.

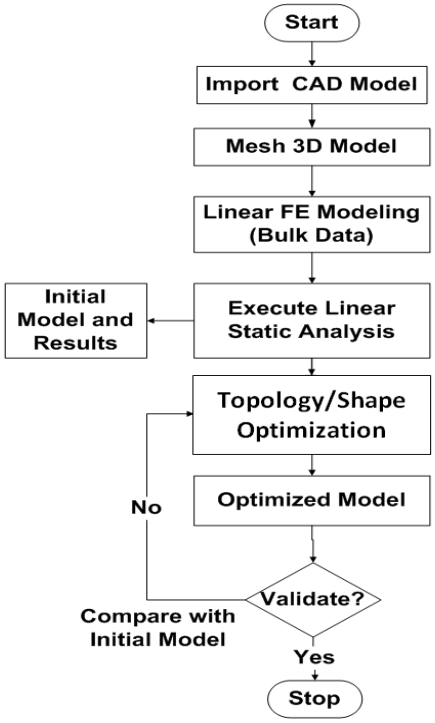

Figure 3: Design optimization flowchart

Shape definition is based on the possible design space that allows some of region in the component to be changed. It depends on the interface and connection condition between the component and other components that are attached to the component.

IV. Model and Numerical Analysis

A. Finite Element Model

Finite element model for knuckle is shown in Figure 4 below.

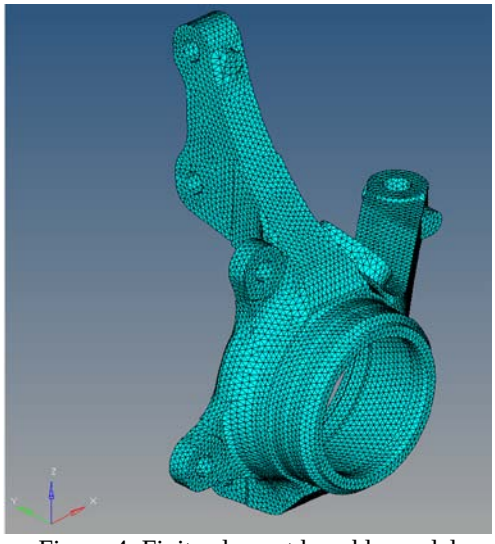

Figure 4: Finite element knuckle model

The applied material properties are presented in Table 1.

Table 1: Material properties of knuckle

Material	Steel
Density	7.85e-9 tonne/mm^3
Poisson's Ratio	0.3
Modulus of elasticity	200000 MPa
Yield Stress	478.32 MPa
Ultimate tensile stress	621 MPA

B. Boundary Conditions and Loading

In actual test performed in a local car manufacturing company, the knuckle is mounted when it subjected to the load. To represent this condition it is constrained from the back with all degree of freedom constraints.

The part must be able to withstand 4000N sinusoidal load and greater than 350000 cycles.

C. Optimization Parameters

The vector of nodal coordinates (**x**) is used to define the shape of knuckles structure in finite element model.

Using the basis vector approach, the structural shape is defined as a linear combination of basis vectors. The basis vectors define nodal locations.

$$\mathbf{x} = \sum DV_i \,.\, BV_i \qquad (1)$$

Where **x** is the vector of nodal coordinates, BV_i is the basis vector associated to the design variable DV_i.

Using the perturbation vector approach, the structural shape change is defined as a linear combination of perturbation vectors. The perturbation vectors define changes of nodal locations with respect to the original finite element mesh.

$$\mathbf{x} = x_o + \sum DV_i \,.\, PV_i \qquad (2)$$

Where **x** is the vector of nodal coordinates, x_o is the vector of nodal coordinates of the initial design, PV_i is the perturbation vector associated to the design variable DV_i. This approach is adopted by the OptiStruct software.

A general optimization or a mathematical programming problem can be stated as follows [11].

$$\text{Find } (X) = \begin{Bmatrix} x_1 \\ x_2 \\ \vdots \\ x_n \end{Bmatrix} \qquad (3)$$

which minimize $f(\mathbf{X})$

subject to the constraints

$g_j(\mathbf{X}) \leq 0,\ j = 1, 2, \ldots, m$

$l_j(\mathbf{X}) = 0,\ j = 1, 2, \ldots, p$

where **X** is an n-dimensional vector called the *design vector*, $f(\mathbf{X})$ is termed the *objective function*, and $g_j(\mathbf{X})$ and $l_j(\mathbf{X})$ are known as *inequality* and *equality* constraints, respectively.

ISBN: 978-1-61804-219-4

The objective of this optimization is to minimize volume while maximum stress of the elements became constraint variable. Design variables were determined using Hypermorph.[12]

Seven shapes were defined (shape 1, shape 2, shape 3, shape 4, shape 5, shape 6 and shape 7) as design variables [9].

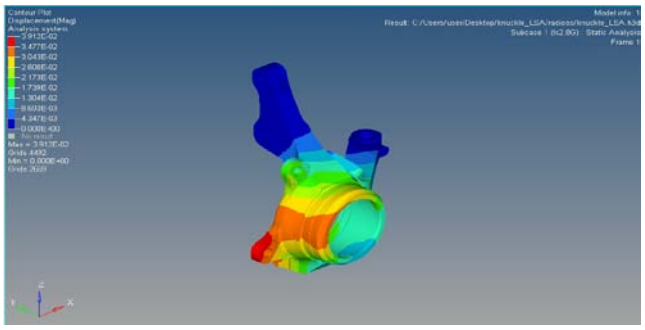

Figure 5: Knuckle analysis (Displacement Contour)

Figure 5 shows the knuckle part that has been drawn in finite element using HyperWork software. The part was analyzed under working loading constraints. The displacement contour indicates one side of part has been subjected to major displacement.

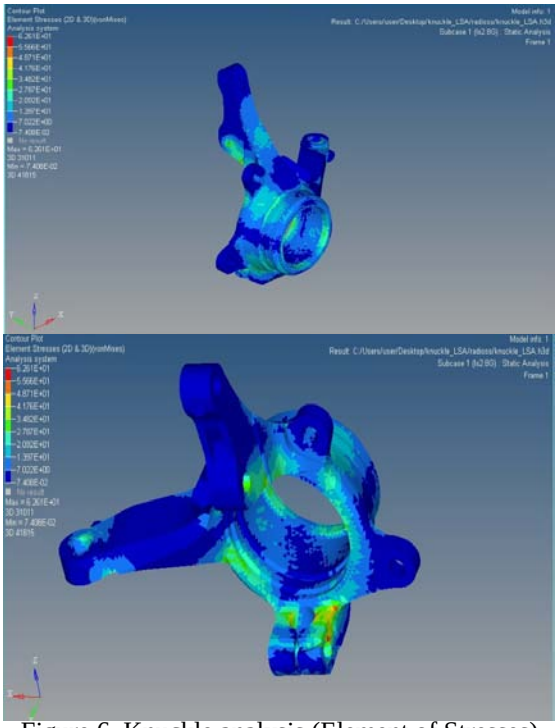

Figure 6. Knuckle analysis (Element of Stresses)

Figure 6 illustrates the state of element stress when part is subjected under loading constraints. The red zones indicate the concentration of stress area where a potential failure (weak point) tends to occur. The failures can be in the form of crack initiation or chip. Meanwhile the green colour zones are subjected to fatigue stress as they have continuous displacement at the same points over time. In this research, the stresses are analysed in 9 regions as shown in Figure 7.

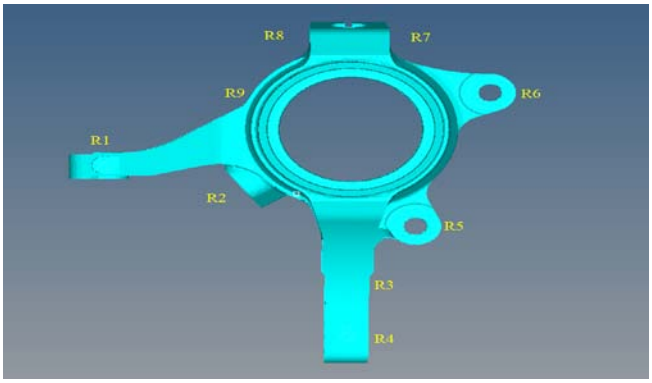

Figure 7: Element of Stress Region (for data collection)

V. Results And Discussion

Topology Optimization

The data for the element of stresses were gathered using the HyperWork Finite element method.

Table 2: Stress values based on region

Region Location	ID Element	Element of Stresses
R1	41416	22.056
	178977	21.659
R2	33550	25.115
R4	169422	23.887
	159392	22.411
	168987	15.639
	100040	33.084
	168819	14.36
R5	167159	22.815
R7	185359	35.696
	31645	38.712
	194183	49.016
R8	133817	38.126
R9	173430	25.31
	168766	28.81
	158717	35.166

The data in Table 2 indicated that R7 (38.712, 49.016) & R8 (38.126) are subjected to higher stress area. However, based on the red zone stress topology (Figure 8 & 9), the stress concentrations were appeared at the mounting holes. This means that under fatigue load condition, both R7 and R8 are likely to fail due to crack initiation.

ISBN: 978-1-61804-219-4

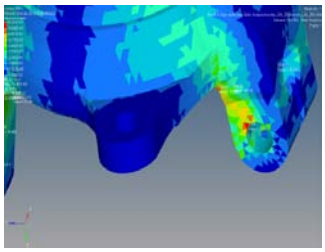

Figure 8: R7

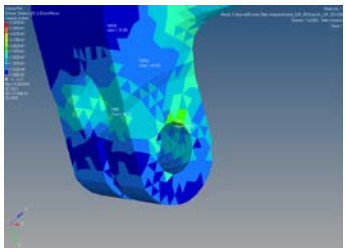

Figure 9: R8

Shape Optimization

Shape definition is based on the possible design space that allows some of region in the component to be changed. It depends on the interface and connection condition between the component and other components that are attached to the component.

Table 3: Stress values based on region

Region Location	ID Element	Element of Stresses
R2	170215	265.287
	163864	197.686
R3	158999	404.124
	169876	298.43
	164975	243.128
	100040	216.217
R5	53344	148.259
R6	133446	191.321
R7	59754	192.57
	185361	247.053
	39479	281.388
	160985	353.481
R8	103931	187.934

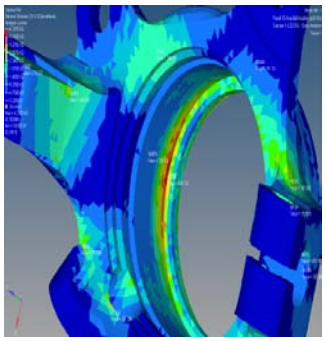

Figure 10: R3

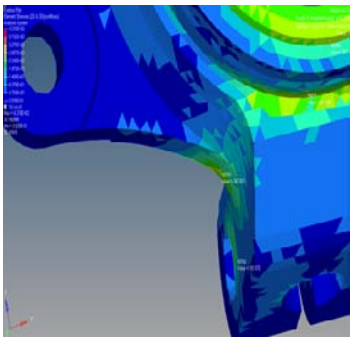

Figure 11: R8

In this research the` weight lost' parameters are defined as to reduce the shape size and its dimensions. For experimentation purposes, the part is subjected to 10 % REDUCTION in thickness, diameters and angles. The part is now redesigned and was tested under the same loading constraints. The results show some stress concentrations have moved to different regions with more severe red zone areas as shown in Fig. 10 and Fig. 11.

VI. Conclusions

Designing a fuel efficient car needs a systematic approach without compromise the safety and quality. Many developments toward new technologies (EV, NGV and hybrid) for fuel efficient and zero emission are taking place. However, the fundamental problems pertaining to batteries life, material costs and other design constraints are yet to be resolved. This research has successfully explored the topology and shape optimization methodologies to reduce component weight and as well as predicting the potential failure modes. This method is found to be useful and reliable during parts development stage.

ACKNOWLEDGEMENTS

This research was sponsored by Ministry of Science, Technology and Innovation (MOSTI) Malaysia TechnoFund Grant. The authors would like to thank PROTON and UniKL for their support.

REFERENCES

[1] Noha Sadek. Urban electric vehicles: a contemporary business case. Eur. Transp. Res. Rev. (2012) 4:27–37. 2012

[2] B.T. Tompkins, H. Song, J.A. Bittle, T.J. Jacobs. Efficiency considerations for the use of blended biofuel in diesel engines. Applied Energy 98 (2012) 209–218. 2012

[3] B. Suh, A. Frank, Y. J. Chung, E. Y. Lee,Y. H. Chang, S. B. Han. Power train System Optimization for a Heavy-duty Hybrid Electric Bus. International Journal of Automotive Technology, Vol. 12, No. 1, pp. 131−139 (2011). 2009

[4] Necmettin Kaya, Idris Karen, Ferruh Ozturk. Materials and Design 31. Re-design of a Failed Clutch Fork Using Topology and Shape Optimization by the Response Surface Method. Materials and Design Volume 31, Issue 6, June 2010, Pages 3008-3014. 2010

[5] Gang-Won Jang, Min-Su Yoon, Jae Ha Park. Lightweight flatbed trailer design by using topology and thickness optimization. Struct Multidisc Optim (2010) 41:295–307. 2009

[6] Altair Hyperworks 10, Altair Engineering Inc., India, 2010.

[7] Kojima,Y., "Mechanical CAE in automotive design", R & D review of Toyota CRLD, Vol 35, No. 4, 2000.

[8] Obayashi S, Tsukahara T. "Comparison of optimization algorithms for aerodynamic shape design". AIAA Journal, Vol. 35, No. 8. 1997.

[9] Richards RA. "Zeroth-order shape optimization utilizing a learning classifier system". PhD Dissertation, Mechanical Engineering Department, Stanford University, 1995.

[10] Yang. R.J., "Design Modeling consideration in Shape Optimization of Solids", Computers & Structures, Vol. 34, Issue 5, 1990

[11] Rao S.S., "Engineering Optimization Theory and Practice", John Wiley & Sons, Inc4th edition, 2009.

[12] HyperMorph Introduction Methods for Morphing Finite Element Models, Altair Engineering Inc., India, 2006.

Dynamical Characteristics of Multifractal Strengths in Multifractal Structures

Jae-Won Jung, Jong-Kil Park, Kyungsk Kim

Abstract—The pattern of stone distribution in the game of Go (Baduk,Weiqi, or Igo) can be treated in the mathematical and physical languages of multifractals. The concepts of fractals and multifractals have relevance to many fields of science and even arts. A significant and fascinating feature of this approach is that it provides a proper interpretation for the pattern of the two-colored (black and white) stones in terms of the numerical values of the generalized dimension and the scaling exponent. For our case, these statistical quantities can be estimated numerically from the black, white, and mixed stones, assuming the excluded edge effect that the cell form of the Go game has the self-similar structure. The result from the multifractal structure allows us to find a definite and reliable fractal dimension, and it precisely verifies that the fractal dimension becomes larger, as the cell of grids increases. We also find the strength of multifractal structures from the difference in the scaling exponents in the black, white, and mixed stones.

Keywords— Multifractals, Generalized dimension, Spectrum, Fractal dimension,Go, Baduk

I. Introduction

For over three decades, there have extensively been an interest for many models having the multifractal structures in the scientific fields such as the physical, biological, engineering, social, and medical sciences. It is certainly worthwhile to study a variety of real systems extended from the fractals [1-3] to the multifractals [4,5] and to reveal a much complicated structure of universal classes, in order to understand essentially its structure and property in nature. However, it is not relatively easy to analyze and understand the elements of particular natural systems, but the mathematical and statistical approaches for the modeling and simulation of natural systems have been led to a field of intensive multifractal research. The investigation of multifractals is up to the present a topic of interdisciplinary research possessing a formidable challenge. It is widely believed that the multifractals has intrinsically and numerically the distributions of the singularities of the scaling exponents on interwoven sets of varying fractal dimensions. Until now, the multifractal formulism using the box-counting method have been represented in terms of its generalized dimension and scaling exponent. Many methods and techniques to analyze and simulate the multifractals have recently been burgeoned: the intermittent nature of turbulence [6,7], the various financial time series [8], the wavelet transform approaches [9], the growing and non-growing networks, and so on. At all events, it is yet delicate to incorporate some universal behavior in the scaling mechanism of multifractals.

Jae-Won Jung is with Applied Meteorology Research Lab, National Institute of Meteorological Research, Seoul 156-720, Korea (e-mail: xewon@naver.com).

Jong-Kil Park is with School of Environmental Sciences Engineering, Atmospheric Environment Information Research Center, Inje University, Gimhae, 621-749, Korea (e-mail: envpjk@inje.ac.kr).

Kyungsik is with Physics Department, Pukyung National University, Busan 608-737, Korea (corresponding author to provide phone: 82-51-629-5562; fax: 82-51-629-5549;e-mail: kskim@pknu.ac.kr).

The Go is a strategic board game which two players use their brain function and decision making to win. the game is also known as the Weiqi, Igo, and Baduk in China, Japan, and Korea, respectively. The Go has been transformed a popular game in a conspicuous way which has a strategic complexity due to the brain's activity in spite of its simple rules. Two players, who alternately place black and white stones, played one Go game on the vacant intersections of a grid of 19×19 lines. One stone, two stones, or a group of stones is captured and removed if it has no empty adjacent intersections surrounded by stones of the opposite color. The game is perfectly ended if one player occupy a larger portion of the board than the opponent. The placing stones close together helps them support each other and avoid the capture. On the other hand, the placing stones that the far apart creates influence across more of the board. The part of the strategic difficulty of the game stems from finding a balance between such conflicting interests. Two players should strive to serve both the defensive and offensive purposes and make a decision between the tactical urgency and the strategic plan.

Historically, the Go originated in ancient China more than 2,500 years ago, although it is not known exactly when the game was invented. After the Go game spread to Korea and Japan in about the 7th century, the board with 19×19 points of a grid have become standard until now. In Korea, there mainly existed the formal competition between Mr. Chang-Ho Lee and Mr. Hun-Hyun Cho, who were the top-rank professional holders of worldwide renown in the world Go community for two decades.

To our knowledge, the structure and property of the Go, the out put of the human brain activity, have not been studied yet in the dynamical mechanism. It is of utility to investigate on the scaling behavior of its structure and property. This present letter is to discuss analytically and numerically the multifractal structure [10] and property of the Go game, in particular Mr. Chang-Ho Lee's game, via the generalized dimension and the scaling exponent. We also find the multifractal strength from the scaling exponents in the Go game.

II. Theoretical Methodology

From the Go game, the interesting aspects concerning multifractals come from the fact that the distribution of stones on the stone board can be nonuniform in a singular way. In particular, there exists an arbitrarily fine-scaled of stones on all grids of the stone board. Such structure of the grids have been called the multifractal structure. This can be characterized by the generalized dimension and scaling exponent that essentially give the dimensions of the dense and sparse grids of the stone. In order to analyze the multifractal feature for the Go game, we

ISBN: 978-1-61804-219-4

review the generalized dimension and the spectrum of our interest in the multifractal formalism. We suppose that all grids existing the self-similar structure are divided into $M(\varepsilon)$ cells of points $\varepsilon x\varepsilon = 1 = M(\varepsilon)$. The generalized dimension in multifractal structures [11] is represented in terms of

$$D_q = \frac{1}{(q-1)} \lim_{\varepsilon \to 0} [\sum_i n_i p_i^q / \ln \varepsilon], \quad (1)$$

where $p_i = n_i/n$ denotes the fractional number of points in the i-th cell, $[(i - 1)\epsilon^2, i\epsilon^2]$, for all cells n. The explicit relations between f_q and D_q, and between α_q and D_q are, respectively, given via the following Legendre transform:

$$f_q = q \frac{d}{dq}(q-1)D_q - (q-1)D_q, \quad (2)$$

and

$$\alpha_q = \frac{d}{dq}(q-1)D_q. \quad (3)$$

Through the generalized dimension D_q and the scaling exponent f_q and α_q, we can simulate and analyze the multifractal measures in the Go game, and these mathematical techniques have been confirmed in empirical investigations of diverse models. From the multifractal singularity spectra f_q associated with Legendre transformation, the multifractal strength of can be quantified by the difference between the maximum and minimum values of α, which is given by

$$\Delta\alpha = \alpha_{\max} - \alpha_{\min}, \quad (4)$$

where $\Delta\alpha$ is an important parameter describing the width of the multifractal spectrum. The larger the $\Delta\alpha$ is, the stronger is the multifractality.

III. Numerical Calculations

In particular, our model analyzes and simulates the 400 Go games of Chang-Ho Lee, played from January 1986 (one final game of 46th Kuksu title in Korea) to January 2003 (one final match with Chang-Hyuk Yu in KBS Baduk title of Korea). Interestingly, we introduce that a grid consists of 18 × 18 points, neglected the edge having 37 points, in order to make a self-similar structure in the Go game. Since one Go board shows 18 × 18 points in arbitrarily one game as neglecting the right and bottom edge, we call it as the excluded edge effect, i.e., the effect that is neglected the edge in a gird concerning 19 × 19 points. It is appropriate to note that in reality the four edges are selected in each Go game, because even excluded edge effect has a slight influence on the victory or defeat in each Go game. Here we simulate each game for the four edges composed as the right and bottom, left and bottom, top and right, and top and left edges. Hence there exist a total of 4 × 400 = 1,600 games in the 400 Go games of Chang-Ho Lee.

$$\alpha + \beta = \chi. \quad (1) \quad (1)$$

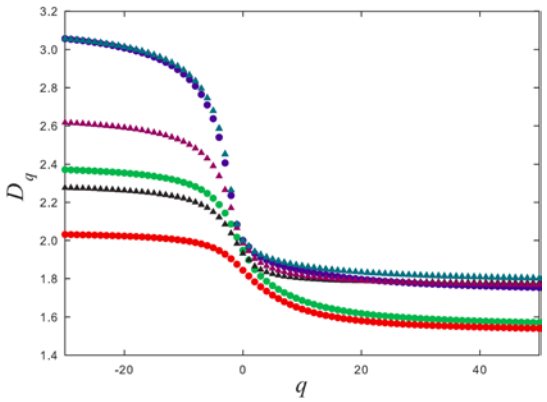

Fig. 1. Spectrum D_q versus q: plots of the 2 × 2 (red circle), 3 × 3 (green circle), and 6 × 6 (blue circle) points for the black stones and of the 2 × 2 (black triangle), 3 × 3 (purple triangle), and 6 × 6 (cyan triangle) points for the mixed (black and white) stones.

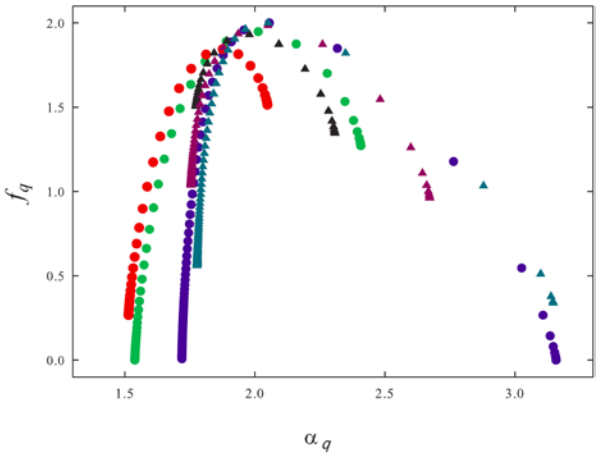

Fig. 2. Spectrum f_q versus α_q: plots of the 2 × 2 (red circle), 3 × 3 (green circle), and 6 × 6 (blue circle) points in the black stones and of the 2 × 2 (black triangle), 3 × 3 (purple triangle), and 6 × 6 (cyan triangle) points for the mixed (black and white) stones.

TABLE I. Summary of values of the fractal dimension D_0 (or DQ=0), the generalized dimension, and the scaling exponent on the distribution of the black, white, and mixed stones consisting of ϵ^2 =2 × 2, 3 × 3, and 6 × 6 points.

stones	points(ϵ^2)	D_0	$D_{-\infty}$	$D_{+\infty}$	$\alpha_{-\infty}$	$\alpha_{+\infty}$	$f_{-\infty}$	$f_{+\infty}$
Black	2 × 2	1.844	2.044	1.521	2.048	1.500	1.514	0.267
	3 × 3	1.948	2.398	1.546	2.407	1.500	1.272	0.000
	6 × 6	2.000	3.129	1.728	3.158	1.720	0.000	0.007
White	2 × 2	1.888	2.165	1.560	2.170	1.555	1.448	0.000
	3 × 3	1.939	2.571	1.647	2.590	1.640	0.000	0.000
	6 × 6	2.000	3.074	1.810	3.097	1.805	0.000	0.647
Mixed	2 × 2	1.932	2.299	1.775	2.308	1.774	1.347	1.507
	3 × 3	1.986	2.657	1.759	2.672	1.750	0.962	1.038
	6 × 6	2.000	3.122	1.784	3.147	1.750	0.339	0.539

In our model of the Go, we choose three kinds of the stone distributions after finishing one Go game: black, white, and mixed stones. The mixed stones mean all stones (black and

ISBN: 978-1-61804-219-4

white) in the case of one game. After we perform the computer simulation, we can analyze the multifractal structure of the black, white, and mixed stones. Figure 1 is the plot of the generalized dimension D_q as a function of q for the three kinds of stones. The spectrum f_q is shown in Fig. 2 for the three kinds of stones. From our computational results it appears that the larger the cell is, the larger is the fractal dimension, i.e. D_0= 1.844 (2×2 points), 1.948 (3×3 points), and 2.000 (6×6 points) for the black stones. In the case of the other two (i.e. white and mixed) stones, the fractal dimension appears as the larger value rather than that of the 2×2 cell, while the fractal dimension in a grid of 6×6 points has the same value D_0= 2.000. The other numerical result for the fractal dimension, generalized dimension, and spectrum for the three stones is summarized in Table 1. For the scaling exponent α_q, our result is from Table 1 that $\Delta\alpha$ is larger as the cell ϵ^2 increases. This means that the larger $\Delta\alpha$ is, the stronger is the multifractal structure. In a similar fashion, we can estimate the strength of multifractality in terms of the range of α in order to identify its multifractal properties.

VI . SUMMARY

In conclusion, the multifractals shed significantly new light on the structural analysis of the Go game, by assuming the excluded edge effect. These results provide insight into some details for a better understanding of the scaling properties based on the multifractal structure. We have shown that the distribution of white stones in 6×6 points can be advanced as a simple rule in contrast to that of the other two (i.e. black and mixed) cases. Emphasis is particularly put on $\Delta\alpha$ to note that the multifractal property is stronger as $\Delta\alpha$ is larger. That is, it means that the situation comes nearer to no mono-fractal property. Its feature that goes near mono-fractal structure means that the game is somewhat non-complex despite its rule. The fractal dimension obtained from the multifractal measures would not be simply compared numerically with other cases, but in our case, it is a coincidence that it becomes a smaller (or larger) fractal dimension as the points of cell goes to a smaller (or larger) value.

In the future, a theoretical understanding of multifractals [12,13] would be an essential development in the advancement of the world Go game. It is expected that the multifractal structure will contribute significantly to a deep and sophisticated understanding of the stunning percentage of victories in the Go game. This sort of research would be likewise of great value in characterizing and categorizing the scaling behavior in detail with the qualitative analysis and numerical calculation performed in other relevant models. In view of statistical quantities of the network, we expect to descibe how the connectivity has influence on the percentage of victories of the winner from local and global efficiencies in the future, and the problem related to the network of complex systems is under investigation for several world Go communities.

This work was supported by Basic Science Research Program through the National Research Foundation of Korea (NRF) funded by the Ministry of Education, Science and Technology (2013R1A1A2008558), by the National Research Foundation of Korea(NRF) Grand funded by the Korea government (MSIP) (2013-065891), and by the Korea Meteorological Administration Research and Development Program under Grant Weather Information Service Engine (WISE) project (153-3100-3133-302-350).

REFERENCES

[1] T. Vicsek, Fractal Growth Phenomena, World Scientifc: Singapore, 1992.

[2] A. Bunde and S. Havlin, Fractals and Disordered Systems: Springer, Berlin, 1996.

[3] H.E. Stanley, L.A.N. Amaral, A.L. Goldberger, S. Havlin, P.Ch. Ivanov, C.-K. Peng, "Statistical physics and physiology: Monofractal and multifractal approaches," Physica A Vol. 270, pp. 309-324, 1999.

[4] B.B. Mandelbrot, The Fractal Geometry of Nature: Freeman, San Francisco, 1983.

[5] M. Barnsley, *Fractals everywhere:* Academic Press, San Francisco, 1988.

[6] A. Aharony, "On Growth and Form," Science Vol. 232, pp. 891-892, 1999.

[7] J.L. McCauley, "Introduction to multifractals in dynamic systems theory and fully developed fluid turbulence," Phys**.** Rep**.** Vol 189, No. 5, pp. 22 5-266, 1990.

[8] G. Lim, S.-Y. Kim, H. Lee, K. Kim and D.-I. Lee, "Multifractal detrended fluctuation analysis of derivative and spot markets," Physica A Vol. 386, pp. 259-266, 2007.

[9] M. Sifuzzaman1, M.R. Isla and M.Z. Ali, "Application of Wavelet Transform and its Advantages Compared to Fourier Transform," J. of Phys. Sci., Vol. 13, pp. 121-134, 2009.

[10] C. Grebogi, E. Ott, and J. A. Yorke, "Chaos, Strange Attractors, and Fra ctal Basin Boundaries in Nonlinear Dynamics," Science Vol. 238, pp.632-638, 1987.

[11] G. Paladin and A. Vulpiani, "ANOMALOUS SCALING LAWS IN MULTIFRACTAL OBJECTS," Phys. Rep. Vol. 156, pp. 147-251, 1987.

[12] J. D. Farmer, "Information Dimension and the Probabilistic Structure of Chaos," Z. Naturforsch Vol. 37A, pp. 1304-1325, 1982.

[13] T. C. Halsey, M. H. Jensen, L. P. Kanadanoff, I. Procaccia, B. I Shraiman, "Fractal measures and their sigularities: The characterization of strange sets," Phys. Rev. B, Vol 33, pp. 1141-1151, 1986.

Mathematical modeling and experimental study of a tubular solid oxide fuel cell

S.A. Hajimolana, M. A. Hussain

***Abstract*—**Experiment and validation of tubular solid oxide fuel cell (SOFC) fuelled with hydrogen is presented in this work. An isothermal mathematical modelling based on first principles is developed. The fuel cell is divided into seven subsystems and the factors such as mass/momentum transfer, diffusion through porous media, electrochemical reactions, and polarization losses inside the subsystems are presented. The model is validated using experimental fuel cell performance data for at 923 and 1023 K. The present model could predict the experimentally observed dependence of current density on cell potential very well at 923–1023 K. It is observed from the experimental data and simulation results that the fuel cell performance at 1023 K is higher than that obtained at 923 K due to reducing the overpotentials in higher operating temperature. The effect of fuel cell temperature pressures, and flow rates on performance is also studied. The results also reveal that the there is an improvement of cell performance when flow rates are enhanced.

***Keywords*—** tubular SOFC, model validation, cell temperature, flow rate, fuel cell performance

I. Introduction

Since the simulation results of modeling is only a prediction and estimation of the real system, an important step in the development of modeling and simulation is validation. Many reported studies in the literatures have not validated their simulation results with experimental data [1-5].

Several research groups have experimentally investigated the use of hydrogen to power SOFCs [6-9]. Calise, et al. [9] studied the thermodynamic and electrochemical performance of a micro-tubular SOFC to characterize the fuel cell polarization at different temperatures. Singhal [10] studied the materials and fabrication methods for different cell components and discussed the performance of cells fabricated using these materials under three different operating temperatures. The effect of various parameters on cell performance and ohmic polarization at a range of temperatures between 872-1072 K with hydrogen as fuel was experimentally studied with Zhao and Virkar [11]. The parameters evaluated were YSZ electrolyte thickness, cathode interlayer thickness, anode support thickness and anode support porosity. Huang and Huang [12] investigated the phenomena of electrochemical promotion of bulk lattice-oxygen extraction in a hydrogen fuelled SOFC. However, in these works the effect of cell temperature, pressure and flow rates on cell performance was not studied in order to investigate which parameters has significant effect on fuel cell performance.

This paper reports on experimental results for validating a tubular solid oxide fuel cell fed with hydrogen. The model is validated using experimental fuel cell performance data between 923 and 1023K. In this range of temperatures, it is expected that material degradation would decrease whilst prolonging the fuel cell lifetime and also result in a reduction in cost due to the utilization of metal materials. The effect of fuel cell temperature on its performance is studied. The effect of fuel cell temperature and flow rates on performance is also studied. The results also reveal that the there is an improvement of cell performance when flow rates are enhanced.

II. Experimental setup

The goal of this test setup was to validate the simulation results with the experimental data. By changing the operating condition in respect to furnace temperature and flow rates, different test points were obtained.

A mixture of zirconium oxide and calcium oxide crystal lattice has been used as the electrolyte. The crystal lattice allows oxide ions to pass through it to reach the anodic surface, where the oxide ions combine with protons to form water. The solid electrolyte is coated on both sides with specialized porous electrode materials. The anode consists of a metallic nickel- and Y2O3-stabilized ZrO2 skeleton, which provides a thermal expansion coefficient comparable to those of the other cell materials, thus limiting the buildup of stresses resulting from a difference in the coefficient of thermal expansion. The cathodic material is strontium-doped lanthanum magnetite (La1-xSrxMnO3, for x 0.10-0.15); its structure, such as that of the anode, is porous to permit rapid mass transport of the reactant and product gases. The cathodic material has low levels of chemical reactivity with the electrolyte, which extends the lifetime of the material. However, it is a poor ionic conductor. The electrochemical reaction occurs when both fuel and air flow into the SOFC separately.

The tubular SOFC is placed inside the furnace, which has a temperature control system and can be adjusted to a desired value. A silver wire is used as a current collector to connect the anode and the cathode respectively, while both current collectors are affixed to the electrodes by means of a silver paste. Air and fuel were preheated in the furnace by increasing the temperature gradually, resulting in an enhancement of the fuel cell temperature as well. Three separate cylinders supply air and fuel (H2 and N2) are fed to the cathodic and anodic sides of the SOFC, respectively. By using a mixing station, it is possible to control the fuel composition accurately. The

M. A. Hussain at the chemical engineering department, university of Malaya, Kuala Lumpur, Malaysia (corresponding author to provide e-mail: mohd_azlan@um.edu.my).

S.A. Hajimolana was the chemical engineering department, university of Malaya, Kuala Lumpur, Malaysia (e-mail: Yashar_molana1@yahoo.com).

furnace is connected to the fuel cell test system which is in turn connected to a PC for controlling and monitoring the system. A schematic diagram and a photo of the experimental set up are shown in Figures 1 and 2, respectively.

A large amount of excess air was used to limit the thermal gradient in the fuel cell. The preparation of the fuel cell for the test involved sensitive procedures. Any change in the fuel cell operating conditions was made very slowly to avoid unnecessary shocks to the very sensitive structures of the SOFC.

N2 was fed to the anode surface without any H2 supply in order to purge and prevent O2 leakage into the anodic feed stream. Then the furnace temperature was increased gradually. The rate of temperature increase was 2 K per hour. When the temperature reached the defined value and became stable, the fuel cell was ready for performing experiments. However, prior to commencement of experiments, N2 was gradually tapered off while H2 flow was increased to a desired value. Within three steps, each step in 10 s intervals, N2 flow rates decreased down to zero while H2 flow rates increased up to 250 cm3/min. Air was injected into the bottom of the cell tube and flowed over the cathodic surface through a gap between the injection tube and the cell tube. The test was started with a furnace temperature of 923 K (intermediate temperature range). The cell performance was characterized by measuring the potential and current. This procedure was repeated again for temperature at 1023 K (high temperature range).

The voltage and current were recorded only after their response reached a steady state condition for 30 min at each temperature setting. In this study the influence of flow pressure and flow rate on the cell performance were also investigated and compared with the simulation results. The air and fuel pressures were changed from 1 to 0.7 atm, air flow rate was increased from 700 to 1030 cm3/min and the fuel flow rate was raised from 175 to 325 cm3/min. The operation temperature of these experiments was 1023 K. The voltage and current were recorded again only after their response reached steady state for 30 min at each pressure and flow rate setting.

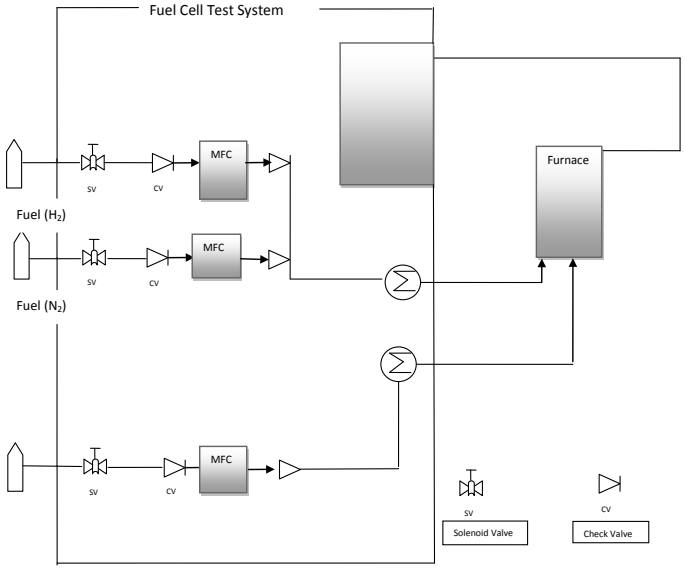

Fig. 1 Schematic diagram of the experimental setup.

Fig. 2 Picture of the fuel cell experimental set up

III. Mathematical Modeling

The tubular SOFC system under study here is single tubular SOFCs. The cell has two tubes, an outer tube and an inner tube [13]. To develop a first-principles isothermal model of the SOFC system, single tubular fuel cell is considered and divided into five subsystems [13]. The fuel cell model is derived by writing mass and/or momentum conservation equations for each of the seven subsystems. The assumption considered in the mathematical formulation is that the gas boundary layers are very small relative to the corresponding radius; therefore, the equations governing the diffusion processes are written in the Cartesian coordinates. Fluid velocities are averaged along the radial direction. Partial pressures and fluid velocities in each subsystem are uniform in every direction. Specific properties such as viscosities, and densities in each subsystem are uniform. Furthermore, outlet partial pressures and velocities are equal to the pressures and velocities inside the subsystem.

The mass/momentum balance inside SS1, SS3 and SS5 are given as follows, respectively:

$$L\frac{d\xi^i_j\rho^i_j}{dt}=u^i_{j_{in}}\xi^i_j\rho^i_{j_{in}}-u^i_j\xi^i_j\rho^i_j+\sum N_jM_j\left(\frac{2r_iL}{r^2_i-r^2_0}\right) \quad (1)$$

$$L\frac{d(u_i\rho_i)}{dt}=(u_{i_{in}})^2\rho_{i_{in}}-(u_i)^2\rho_i+\frac{\rho_{i_{in}}R^*T_{i_{in}}}{M_i}-\frac{\rho_iR^*T_i}{M_i} \quad (2)$$

i is air flow injection tube, air flow inside cathode side, fuel flow inside anode side, j is air, oxygen, nitrogen, hydrogen, w is the wall, Nj is mass transfer by means of diffusion, n is the molar number.

This model assumes that the pressure drop caused by the pipe resistance over the distance L is negligible.

Electrochemical reaction occurs inside the fuel cell (SS4) at

ISBN: 978-1-61804-219-4

the triple phase boundary (TPB), which as a result produces voltage and current.

Fuel cell voltage output is dependent on gas partial pressures and is adversely affected by concentration, activation, and ohmic losses (polarizations or irreversibilities). The electromotive force, reversible open-circuit cell voltage (denoted by Erev) is given by the Nernst equation. However, the actual cell voltage (E) is less than its theoretical open circuit voltage because it is strongly affected by several irreversible losses including activation losses due to irreversibility of electrochemical reactions at the three-phase boundary (TPB), concentration losses due to mass transport resistance in the electrodes (especially for thick anodes as in an anode-supported SOFC) and ohmic losses due to ionic and electronic charge transfer resistances. Actual voltage is thus given by:

$$E = E^o - \eta_{act_{ano}} - \eta_{conc_{ano}} - \eta_{act_{cat}} - \eta_{conc_{cat}} - \eta_{ohm} \quad (3)$$

According to the equivalent circuit approximation, the cell outlet voltage is governed in (Hajimolana et al., 2009). The dynamic model of the SOFC system has 13 first-order ordinary differential equations, which are integrated numerically using MATLAB.

IV. Results and Discussion

A. Experimental and model validation

Validation is achieved through the comparison between simulation results and experimental data from actual system behavior to find the validity and accuracy of the modeling. Blind acceptances of simulation results are not a good basis to make engineering decisions involving financial and time schedule risks. In this work because of limitation of the lab system, the validation was only done to compare the simulation results with experimental data at different cell temperature.

B. Effect of cell temperature

For validation purpose, the effect of cell temperature on fuel cell performance was studied to compare the simulation results with experimental data at 923 (intermediate temperature) and 1023 K (see Figure 2). For this system, at temperatures lower than 873 K, the fuel cell voltage was very low and not sufficient to generate sufficient power. Also at fuel cell temperatures higher than 1073 K, the SOFC faced the risk of durability and degradation of materials. The current–potential plot obtained from this simulation was compared with the experimental data. The present model could predict the experimentally observed dependence of current density on cell potential very well at 923 and 1023 K.

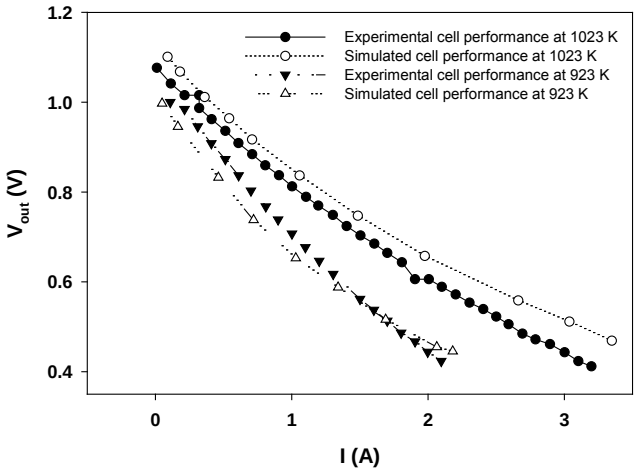

Fig. 2 Experimental and simulated cell performance at two different temperatures.

It is apparent from Figure 2 that the fuel cell performance at 1023 K is greater than that obtained at 923 K. This is because the higher operating temperature reduces the overpotentials. Therefore, high temperature SOFCs provide a highly efficient power generation technology.

C. Effect of flow rate

Figures 3 and 4 depict a comparison between simulation results and experimental data for various fuel and air flow rates for fuel cell operating temperature at 1023 K. The results indicate that cell performance rises when flow rates are enhanced. For example when the fuel flow rate increases from 175 to 325 ml/min the voltage raised from 1.125 to 1.13 V (see Figure 5-10). The trend of these results is also consistent with experimental results reported in the literature [14]. The results also show that the effect of air flow rate on fuel cell performance is more than fuel flow rate.

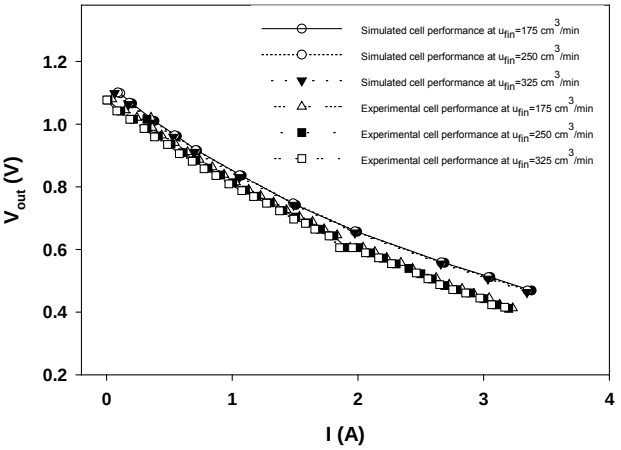

Fig. 3 Experimental and simulated cell performance for various fuel flow rates at 1023 K.

ISBN: 978-1-61804-219-4

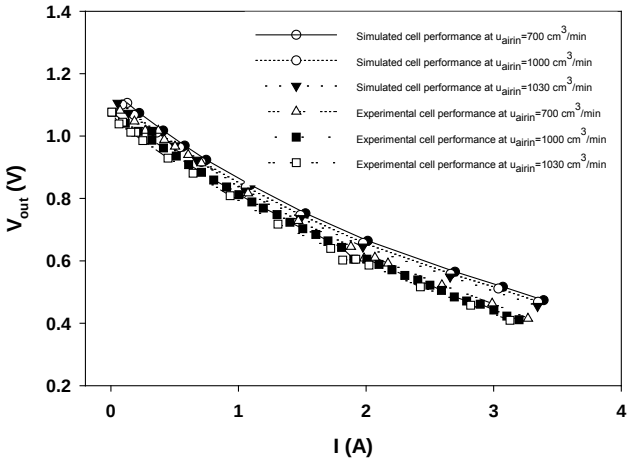

Fig. 4 Experimental and simulated cell performance for various air flow rates at 1023K.

D. Effect of flow pressure

Figures 5 and 6 show a comparison between simulation results and experimental data for various fuel and air pressure for fuel cell operating temperature at 1023 K. It is observed from Figure 8 that when the fuel pressure increases from 0.7 to 1atm, the fuel cell output voltage shows an improvement of 6%. A step increase in the fuel pressure increases the partial pressure of H2 at the TPB, which leads to an improvement of electrochemical reaction rate. As a result, the fuel cell performance increases. Experimental results reported in the literature also confirm this observation [10].

Moreover, Figure 9 shows a 7% improvement of fuel cell voltage when the air pressure increase from 0.7 to 1atm. A step increase in the air pressure increases the partial pressure of O2 at the TPB, which increase the production of electrons with higher voltage. However, the effect of air pressure on fuel cell performance compared to fuel pressure is higher.

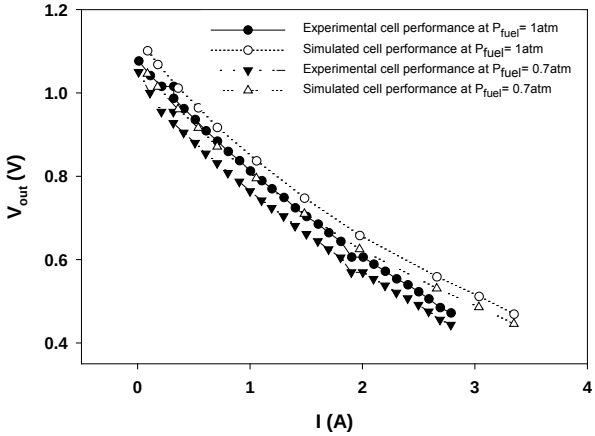

Fig. 5 Experimental and simulated cell performance for various fuel pressures at 1023K.

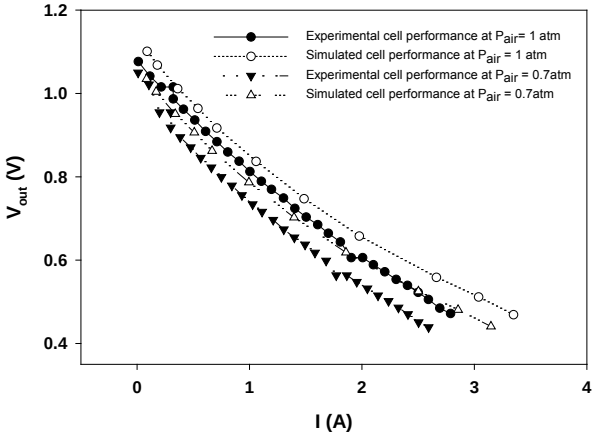

Fig. 6 Experimental and simulated cell performance for various air pressures at 1023K.

V. CONCLUSION

Experiment and validation of tubular SOFC fuelled with hydrogen is presented in this work. The model is validated using experimental fuel cell performance data for at 923 and 1023 K. The present model could predict the experimentally observed dependence of current density on cell potential very well at 923–1023 K. It is observed from the experimental data and simulation results that the fuel cell performance at 1023 K is higher than that obtained at 923 K due to reducing the overpotentials in higher operating temperature.

The effect of flow pressure on fuel cell performance is studied. The results show that the cell performance increase when flow pressure is enhanced. The results also indicate that the effect of air pressure rate on fuel cell performance is more than fuel pressure.

The results also reveal that the there is an improvement of cell performance when flow rates are enhanced. It is observed that the effect of air flow rate on fuel cell performance is more than fuel flow rate. However, it is observed that the effect of flow rates compared to cell temperature and flow pressure on fuel cell performance are not significant, because the temperature and pressure directly can affect the outlet voltage and current.

ACKNOWLEDGMENT

The authors are grateful to the ERGS grant (53-02-03-1100), UMRG (RG114/11AET) and UMRG (RP006G-13ICT) for providing financial assistance to equipment and salary respectively.

REFERENCES

[1] Achenbach E. Three-dimensional and time-dependent simulation of a planar solid oxide fuel cell stack. Journal of Power Sources 1994;49:333-48.

[2]Nagata S, Momma A, Kato T, Kasuga Y. Numerical analysis of output characteristics of tubular SOFC with internal reformer. Journal of Power Sources 2001;101(1):60-71.
[3]Campanari S, Iora P. Definition and sensitivity analysis of a finite volume SOFC model for a tubular cell geometry. Journal of Power Sources 2004;132(1-2):113-26.
[4]Coutelieris FA, Douvartzides SL, Tsiakaras PE. Heat transfer phenomena in a solid oxide fuel cell: An analytical approach. Chemical Engineering Science 2005;60(16):4423-30.
[5]Chakraborty UK. Static and dynamic modeling of solid oxide fuel cell using genetic programming. Energy 2009;34(6):740-51.
[6]Singhal SC. Advances in solid oxide fuel cell technology. Solid State Ion 2000;135(1):305-13.
[7]Suzuki T, Yamaguchi T, Fujishiro Y, Awano M. Fabrication and characterization of micro tubular SOFCs for operation in the intermediate temperature. Journal of Power Sources 2006;160(1):73-7.
[8]Huang CM, Shy SS, Lee CH. On flow uniformity in various interconnects and its influence to cell performance of planar SOFC. Journal of Power Sources 2008;183(1):205-13.
[9]Calise F, Restucccia G, Sammes N. Experimental analysis of performance degradation of micro-tubular solid oxide fuel cells fed by different fuel mixtures. Journal of Power Sources 2010;In Press, Corrected Proof.
[10] Singhal SC. Advances in solid oxide fuel cell technology. Solid State Ionics 2000;135(1-4):305-13.
[11] Virkar AV. A model for solid oxide fuel cell (SOFC) stack degradation. Journal of Power Sources 2007;172(2):713-24.
[12] Huang T-J, Huang M-C. Effect of operating conditions on the electrochemical behavior of hydrogen-fed solid oxide fuel cells. International Journal of Hydrogen Energy 2008;33(19):5073-82.
[13] Hajimolana S, Ahmad., Soroush M. Dynamics and Control of a Tubular Solid-Oxide Fuel Cell. Ind Eng Chem 2009;48:6112-25.
[14] Suwanwarangkul R, Croiset E, Entchev E, Charojrochkul S, Pritzker MD, Fowler MW, et al. Experimental and modeling study of solid oxide fuel cell operating with syngas fuel. Journal of Power Sources 2006;161 308–22.

Experimental testing of a data fusion algorithm for miniaturized inertial sensors in redundant configurations

Teodor Lucian Grigorie, Ruxandra Mihaela Botez, Dragos George Sandu, and Otilia Grigorie

***Abstract*—**The paper presents an adaptive data fusion algorithm which reduces the miniaturized inertial sensors errors by using linear redundant configurations. The algorithm statistical combines the data from sensors, which measure the same quantity, in order to provide better estimates of the accelerations or angular speeds on each of the three axes of an Inertial Measurement Unit (IMU) in a strap-Down inertial navigation system. The sensors (accelerometers or gyros) are disposed in linear arrays along the IMU axes. To experimentally validate the algorithm, some bench tests are performed. In this way are used some accelerometers arrays in two configurations: 1) one accelerometers array with four miniaturized sensors (n=4); and 2) one accelerometers array with nine miniaturized sensors (n=9). Each of the two configurations is tested for three cases of input accelerations, 0 m/s2, 9.80655 m/s2, and -9.80655 m/s2. The system was tested by using an adjustable horizontal table. For the first input acceleration the sensitivity axes of the arrays were directed horizontally, while for the last two values of the input acceleration the axes were directed along the local vertical, oriented upwards and downwards.

***Keywords*—**Redundant inertial navigators, miniaturized sensors, data fusion, experimental testing.

I. Introduction

CURRENTLY, many companies in aerospace industry design and manufacture small vehicles equipped with strap-down miniaturized inertial navigation systems, achieved through the expanded use of nano- and MEMS (micro electro mechanical systems) technologies for the conception of inertial sensors ([1]-[6]). The use of such miniaturized sensors made possible the redundancy for the strap-down inertial navigation systems, by means of different architectures in the sensors dispositions ([6], [7]), and at lower cost, compared to the use of non-miniaturized and very precise inertial sensors. In this way, the design stage of the strap-down inertial navigation systems requires, among other things, the establishing of the inertial sensors disposal architecture in Inertial Measurement Unit (IMU). This architecture is closely correlated with the type of used sensors, but also with their signal processing algorithms. Taking into account that the position monitoring of a vehicle, using inertial methods, necessitates the detection of both acceleration and angular velocity of the vehicle relative to the inertial space, the minimum number of sensors that are required to be used is six (three for acceleration and three for rotation). Usually, the sensors of the two triads are disposed after the axes of a right rectangular trihedral as in Fig. 1.

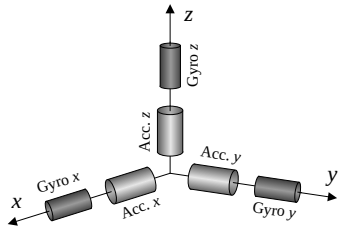

Fig. 1 Classical configuration of IMU sensors

Increased computational power of the navigation processors allows now that the numerical algorithms, becoming more complex, can be run in real time ([8]-[14]). Moreover, strong penetration of inertial sensors market by the miniaturization technologies, allows the realization of strap-down inertial systems with light weight and volume and with extremely low prices compared to non-miniaturized systems. As always, getting a major advantage is based on a compromise, the miniaturization of sensors pays the price in the performances, which are still weak compared with those of non-miniaturized sensors. From this point of view, the miniaturized acceleration and gyro sensors are noisy; for the acceleration sensors, the noise density is between 100 $\mu g/Hz^{1/2}$ and a few hundreds of $\mu g/Hz^{1/2}$, for bandwidths between 100 Hz and 2500 Hz, while for the gyro sensors, the noise density is between 0.0035 $(^o/s)/Hz^{1/2}$, and 0.1 $(^o/s)/Hz^{1/2}$ for bandwidths between 50 Hz and 100 Hz. For the same category of sensors, the noise density may vary from one sensor to another, within 20% of the catalogue value. Noise filtering is not recommended because it can alter the useful signal and, therefore, the sensor output does not reflect exactly the signal applied at the sensor

This work was supported by CNCSIS-UEFISCSU, project PN II-RU, No. 1/28.07.2010, "High-precision strap-down inertial navigators, based on the connection and adaptive integration of the nano and micro inertial sensors in low cost networks, with a high degree of redundance", code TE_102/2010

T. L. Grigorie is with the University of Craiova, 107 Decebal Blvd., 200440, Craiova, Dolj, Romania (phone: +40 251 436447; fax: +40 251 436447; e-mail: lgrigore@elth.ucv.ro).

R. M. Botez is with Ecole de Technologie Superieure, 1100 Notre Dame Ouest, H3C 1K3, Montreal, Qc., Canada (e-mail: ruxandra@gpa.etsmtl.ca).

D. G. Sandu is with In Flight and Research Test Center Craiova, 10 Aviatorilor , Ghercești, Dolj, Romania (e-mail: dragos_sandu@yahoo.com).

O. Grigorie is with the Carol I, High School, 2 Ioan Maiorescu Street, 200418 Craiova, Dolj, Romania (e-mail: ogrigorie@yahoo.com).

input. Besides the noise increase, negative influences on the stability and values of bias, on the scale factor calibration, on the accelerometers' cross-axis sensitivities and on the accelerations sensitivities applied along any gyros given axis appear, all attributed to miniaturization. Analyzing and combining the previously presented, emerges the idea that if in the navigator are used more miniaturized sensors instead of each classical sensor, and data obtained from them are fused with adequate numerical algorithms, one can obtain a high performance level at a price lower than the systems with high performance classical sensors. On the other hand, the large number of sensors has as a consequence the increase of the navigator redundancy degree.

The here presented work is a part of a research project concerning the development of high-precision strap-down inertial navigators, based on the connection and adaptive integration of the nano and micro inertial sensors in low cost networks, with a high degree of redundance, and was realized in collaboration with the École de Technologie Supérieure in Montréal as a consequence of the documentation internships effectuated by the project team members at this university.

The paper presents the experimental validation of such data fusion algorithm which reduces the perturbations of miniaturized inertial sensors by using redundant linear configurations. The results obtained through the numerical simulation of the algorithm were presented by the authors in reference [7]. A redundant linear configuration supposes the mounting of several accelerometers and gyros sensors on each IMU axis (Fig. 2).

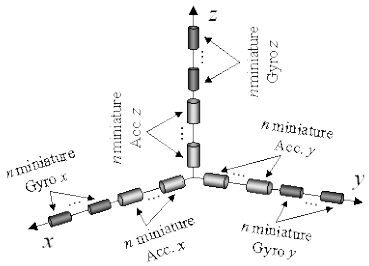

Fig. 2 Redundant linear disposition of IMU sensors

This variant has been adopted since the restrictions imposed to the classical redundant configuration (collinear sensors), in the early years of redundant IMU ('70), by the sensors volume and number (limited, in fact, and by low computing capacity) were removed today. Another argument in favor of this configuration is that of constructive simplicity in front of the architectures generated by the optimal redundant unconventional configurations ([1], [15], [16]). The need to reduce the noise of the sensors in the inertial measurement units by using this kind of algorithms appears as a consequence of the fact that most of the noise spectral components are situated in the band 0-100 Hz, being superimposed on the acceleration and angular speed signals considered useful in navigation applications. So, this noise filtering by using classical methods is not recommended.

II. Data Fusion Algorithm

The inertial navigation principle consists in the detection of the vehicle linear acceleration and angular speeds components in its tri-axial reference frame, followed by their processing using the navigation algorithm with the aim to obtain the vehicle positions, speeds and attitudes. In this way, our idea is to use n miniaturized sensors of acceleration or angular speed for each vehicle frame axis as in Fig. 2. The proposed algorithm integrates all the acceleration or angular speed sensors fixed on the same axis. This algorithm is based on the idea that for the determination of acceleration or angular speed components on the considered axis, each sensor should have a weight inverse proportionally with the standard deviation of the last m samples acquired from it ([7]) (Fig. 3). For redundancy achievement, in the case of malfunctioning or breaking-down of one or more sensors on that axis, they are given null weights and are excluded from calculation.

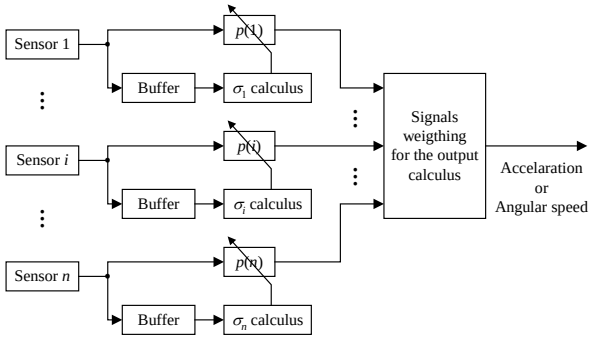

Fig. 3 Sensors data fusion algorithm block scheme

The novelty brought by the proposed algorithm consists in its adaptivity, provided by the permanent change of the weights p_i $(i=\overline{1,n})$ in the measured quantity best-estimate calculus as a function of the statistic properties of the independent measures, given by their σ_i $(i=\overline{1,n})$ dispersions. Many data fusion applications use constant values for the sensors' dispersions, values estimated through prior measurements realized with each of the sensors. In this case we calculate the sensors' dispersions at each time step. To perform this, a buffer should be used to arrange the data in a repeated frames format. As a consequence, if *m* is the number of samples provided by each of the *n* sensors in one second, we use a FIFO (first in first out) buffer to generate data frames of *m* consecutive samples; two consecutive frames superposed with (*m*-1) samples.

Considering c_{ij} as the perturbed j^{th} reading, from the i^{th} sensor on the input axis, the average of *m* consecutive samples acquired from the i^{th} accelerometer is given by the equation

$$\overline{c}_i = \frac{1}{m}\sum_{j=1}^{m} c_{ij}, \tag{1}$$

while the dispersion of the readings is calculated with the next formula

$$\sigma_i^2 = \frac{1}{m}\sum_{j=1}^{m}(c_{ij} - \overline{c}_i)^2. \quad (2)$$

For each sensor, the larger is the weight $p(i)$, the smaller is the standard deviation $\sigma_i = \sqrt{\sigma_i^2}$. Considering $c_{i\,(m+1)}$ as reading no. $m+1$ from the i^{th} sensor, the quantity read by the integrated system of n sensors following $m+1$ steps of signal acquisitions from them is

$$c_{m+1} = \left(\sum_{i=1}^{n} p_i \cdot c_{i\,(m+1)}\right) / \left(\sum_{i=1}^{n} p_i\right). \quad (3)$$

If we considers the sum of the n accelerometers' weights equal with the unit,

$$\sum_{i=1}^{n} p_i = 1 \quad (4)$$

and the inverse proportionality between weight p_i and the standard deviation σ_i given by equalities

$$\sigma_1 \cdot p_1 = \sigma_2 \cdot p_2 = ... = \sigma_n \cdot p_n, \quad (5)$$

then, we obtain the weight associated with the i^{th} sensor with the next expression

$$p_i = (1/\sigma_i) \cdot \left(1/\sum_{k=1}^{n}(1/\sigma_k)\right). \quad (6)$$

Thus, the estimate of the measured quantity (the output of the algorithm) for the $m + 1^{th}$ sample acquired from each sensor in the sensors array is resulted with the formula

$$c_{m+1} = \left(\sum_{i=1}^{n}(c_{i\,(m+1)}/\sigma_i)\right) / \left(\sum_{k=1}^{n}(1/\sigma_k)\right), \quad (7)$$

i.e.

$$c_{m+1} = \frac{1}{\sum_{k=1}^{n}\frac{1}{\sqrt{\sum_{j=1}^{m}(c_{kj} - \overline{c}_k)^2}}} \cdot \sum_{i=1}^{n}\frac{c_{i\,(m+1)}}{\sqrt{\sum_{j=1}^{m}(c_{ij} - \overline{c}_i)^2}}. \quad (8)$$

If one of the sensors breaks down, the standard deviation is null or has very large values. When equation (8) is implemented into the software, the zero value can be conditioned for the malfunctioning sensor weights, if its corresponding standard deviation is null. The same weights will be given to it, if the standard deviation exceeds a maximum limit.

III. Experimental Validation

To experimentally validate the proposed algorithm, bench tests were performed. Two sensors configurations were used: 1) an accelerometers array with four miniaturized sensors (n=4); and 2) an accelerometers array with nine miniaturized sensors (n=9). Each configuration was tested for three cases of input acceleration: 0 m/s2, 9.80655 m/s^2 and -9.80655 m/s^2. The system was tested by using an adjustable horizontal table with a bubble. For the first input acceleration the sensitivity axes of the arrays were directed horizontally, while for the last two values of the input acceleration the axes were directed along the local vertical, oriented upwards and downwards. The data acquisition was performed using a NI-DAQ USB 6210 card with 16 analog inputs (16 bits, and a total sampling rate of 250 kS/s), 4 digital inputs and 4 digital outputs. Matlab/Simulink was used as the application software for the experimental tests; the algorithm's implementation for n=9 is presented in Fig. 4. The sampling rate was 100 samples/s for each of the input channels used. Therefore, the buffers in the algorithm generated data frames of m=100 consecutive samples; two consecutive frames were superposed with m-1=99 samples.

The preliminary step of the experimental tests consisted in the calibration of the nine used accelerometers and their biases compensation ([8]-[10], [14]). For the first configuration of the sensors array (n=4), the independent measures $x_i\,(i=\overline{1,4})$ provided to the algorithm and the resulted $\hat{x}$ estimate are shown in Fig. 5; the figure presents the results for all three of the cases considered for input accelerations (0 m/s^2, 9.80655 m/s^2 and -9.80655 m/s^2). Figs 6 and 7 depict the dispersions of the independent measures and of the $\hat{x}$ estimate, respectively the optimal weights of the independent measures for all three input accelerations. Figs 19 and 20 show an obvious decrease of the amplitude noise was achieved by using the proposed algorithm, thereby confirming its efficacy. The same result is indicated by the values of the mean dispersions of the independent measures $x_i\,(i=\overline{1,4})$ and of the $\hat{x}$ estimate given in Table 1.

Table 1. Values of the mean dispersion of the independent measures and of the $\hat{x}$ estimate for four sensors in array

Input acceleration [m/s^2]	Mean dispersion [(m/s^2)]				
	Sensor 1	Sensor 2	Sensor 3	Sensor 4	Estimate
0	$3.17\cdot10^{-5}$	$3.28\cdot10^{-5}$	$2.05\cdot10^{-5}$	$4.60\cdot10^{-5}$	$6.91\cdot10^{-6}$
9.80655	$3.05\cdot10^{-5}$	$3.13\cdot10^{-5}$	$1.95\cdot10^{-5}$	$4.34\cdot10^{-5}$	$6.66\cdot10^{-6}$
-9.80655	$3.52\cdot10^{-5}$	$3.79\cdot10^{-5}$	$2.29\cdot10^{-5}$	$5.08\cdot10^{-5}$	$8.17\cdot10^{-6}$

Visualizing graphical characteristics in Fig. 7 and analyzing the mean values of the sensors weights, presented in Table 2, one can conclude that the best sensor in array was sensor no. 3 (it took the best weight), while the worst was sensor no. 4 (it took the smallest weight).

From another perspective, according to the values in Table 1, when the sensitivity axis of the sensor array was on the

horizontal plane the dispersion of the estimate was reduced by 1.69 times relative to sensor 3 (the best sensor), by 2.53 times relative to sensor 4 (the worst sensor), and by 2.115 times relative to the average of the mean dispersions for the four sensors in the array.

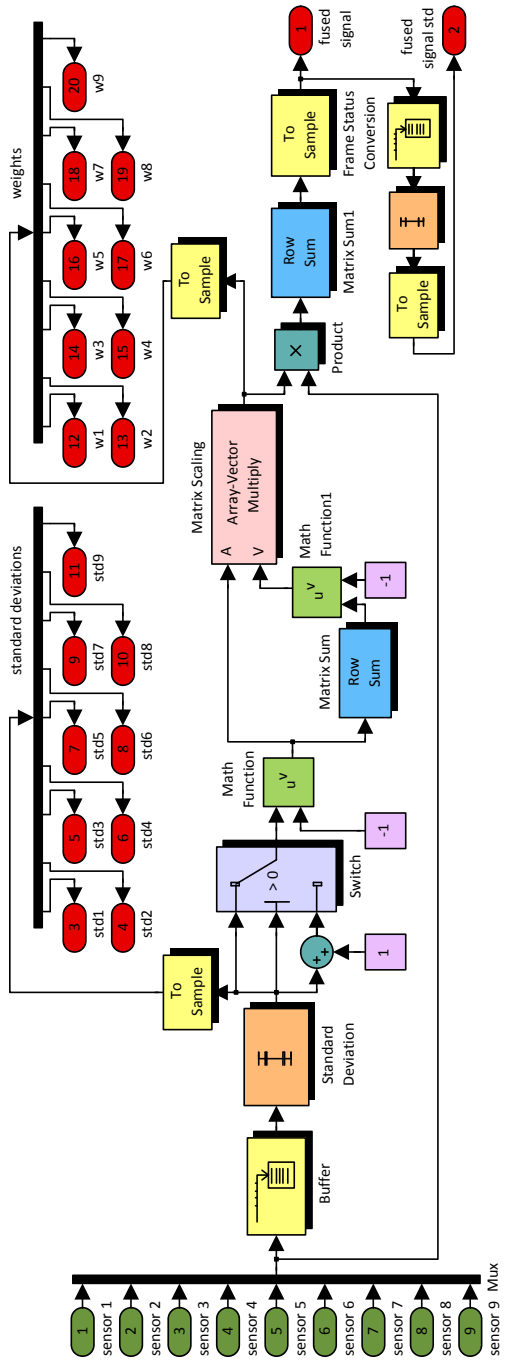

Fig.4 Algorithm Matlab/Simulink model for n=9

When the sensitivity axis of the sensors array was considered on the vertical direction and oriented upwards, the dispersion of the estimate was reduced by 1.68 times relative to sensor 3, by 2.51 times relative to sensor 4, and by 2.112 times relative to the average of the mean dispersions for the four sensors in array. In the final test case for this configuration, when the sensitivity axis of the sensors array was on the vertical direction and oriented downwards, the dispersion of the estimate was reduced by 1.64 times relative to sensor 3, by 2.45 times relative to sensor 4, and by 2.065 times relative to the average of the mean dispersions for the four sensors in array.

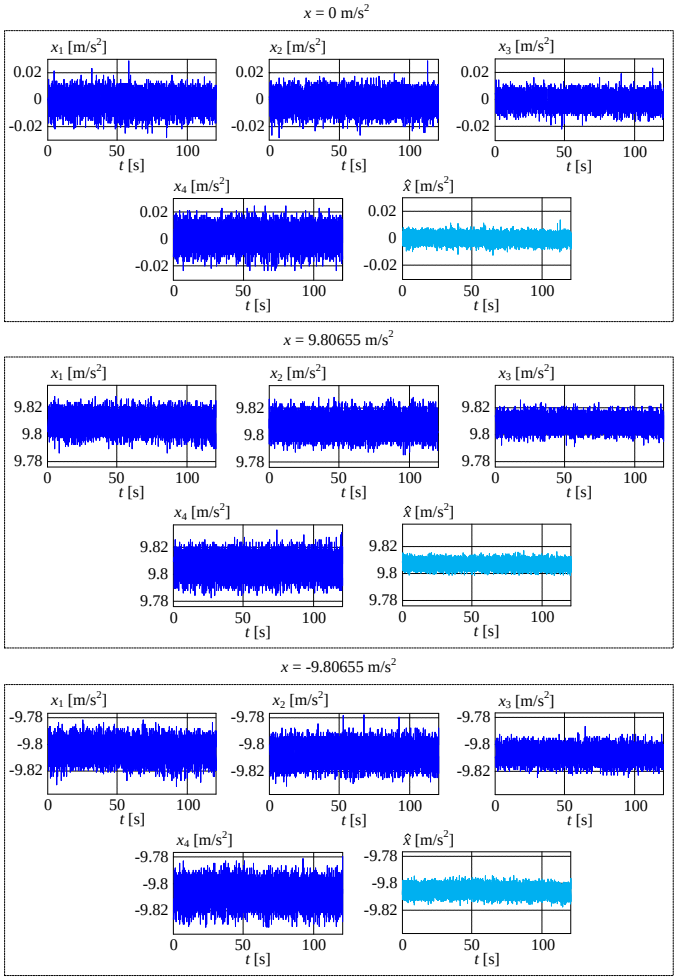

Fig. 5 The independent measures provided to the algorithm and the resulted estimate for n=4

Table 2. Mean values of the sensors weights (n=4)

Input acceleration	Mean weight			
	Sensor 1	Sensor 2	Sensor 3	Sensor 4
0 m/s^2	0.2466	0.2421	0.3067	0.2044
9.80655 m/s^2	0.2453	0.2421	0.3067	0.2057
-9.80655 m/s^2	0.2478	0.2384	0.3072	0.2064

For the second sensors array configuration (n=9), the independent measures provided to the algorithm and the resulted estimate are shown in Fig. 8 (the results for all three considered cases for input accelerations are given in the figure). As in Figs 5 and 6, an obvious decrease in the noise amplitude achieved by using the proposed algorithm can be observed in Fig. 8. The same observation can be drawn from the values of the mean dispersions of the independent measures and of the estimate given in Table 3 for all three testing cases.

ISBN: 978-1-61804-219-4

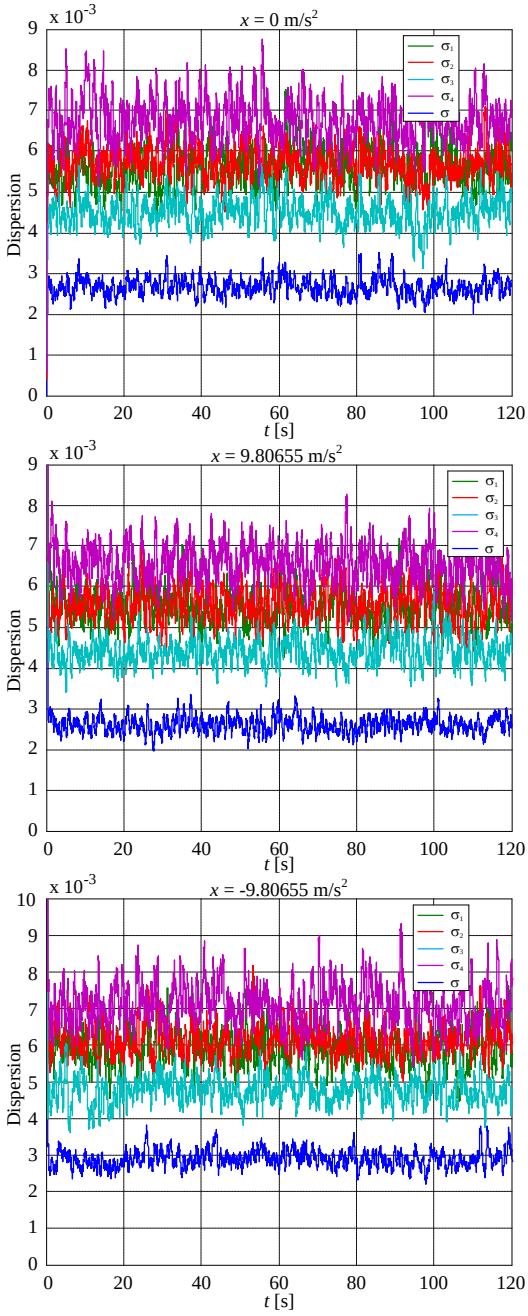

Fig. 6 The dispersions of the independent measures and of the estimate for n=4

Table 3. Values of the mean dispersion of the independent measures and of the estimate for nine sensors in array

	Input acceleration	0 m/s^2	9.80655 m/s^2	-9.80655 m/s^2
Mean dispersion	Sensor 1	$5.509 \cdot 10^{-3}$	$5.411 \cdot 10^{-3}$	$5.809 \cdot 10^{-3}$
	Sensor 2	$5.490 \cdot 10^{-3}$	$5.372 \cdot 10^{-3}$	$5.909 \cdot 10^{-3}$
	Sensor 3	$4.740 \cdot 10^{-3}$	$4.636 \cdot 10^{-3}$	$5.018 \cdot 10^{-3}$
	Sensor 4	$6.440 \cdot 10^{-3}$	$6.054 \cdot 10^{-3}$	$6.553 \cdot 10^{-3}$
	Sensor 5	$7.425 \cdot 10^{-3}$	$5.819 \cdot 10^{-3}$	$6.446 \cdot 10^{-3}$
	Sensor 6	$5.978 \cdot 10^{-3}$	$5.070 \cdot 10^{-3}$	$5.612 \cdot 10^{-3}$
	Sensor 7	$7.338 \cdot 10^{-3}$	$6.069 \cdot 10^{-3}$	$6.561 \cdot 10^{-3}$
	Sensor 8	$8.019 \cdot 10^{-3}$	$6.422 \cdot 10^{-3}$	$7.130 \cdot 10^{-3}$
	Sensor 9	$6.880 \cdot 10^{-3}$	$6.269 \cdot 10^{-3}$	$6.915 \cdot 10^{-3}$
	Estimate	$1.997 \cdot 10^{-3}$	$1.787 \cdot 10^{-3}$	$2.005 \cdot 10^{-3}$

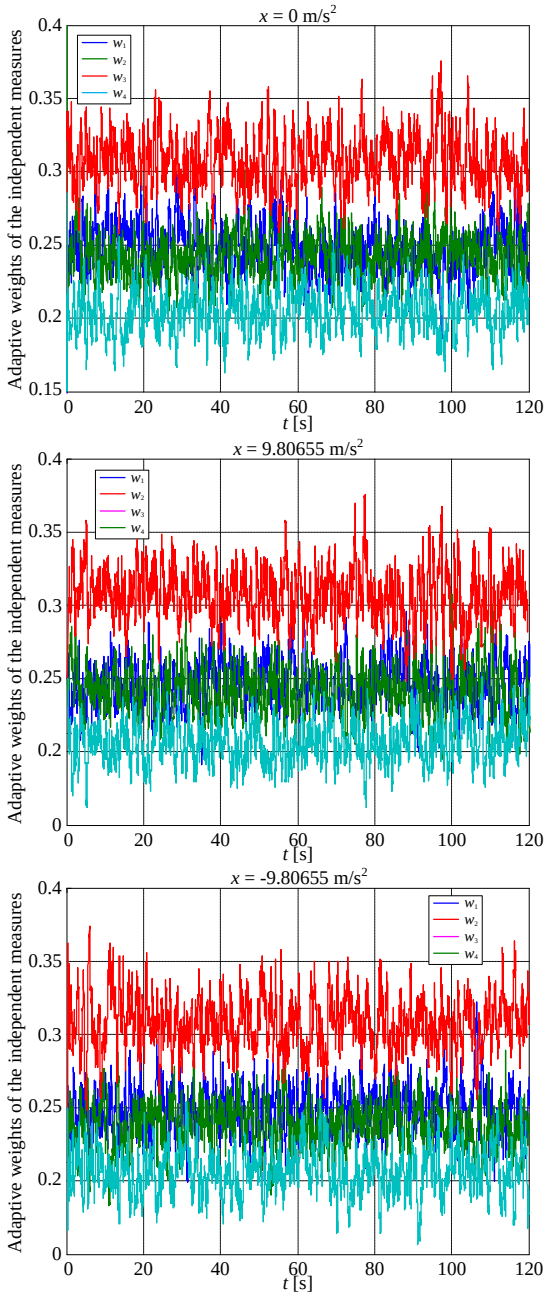

Fig. 7 The weights of the independent measures for n=4

Fig. 8 and data in Table 4 indicate that, for this sensor array configuration, the best sensor was no. 3 (it had the smallest dispersion), while the worst was sensor no. 8 (it had the biggest dispersion). On the other way, according to the values in Table 3, when the sensitivity axis of the sensor array was on the horizontal plane the dispersion of the estimate was reduced by 2.37 times relative to sensor 3 (the best sensor), by 4.01 times relative to sensor 8 (the worst sensor), and by 3.216 times relative to the average of the mean dispersions for the nine sensors in the array. When the sensitivity axis of the sensor array was considered on the vertical direction and oriented upwards, the dispersion of the estimate was reduced by 2.59 times relative to sensor 3, by 3.59 times relative to sensor 8, and by 3.178 times relative to the average of the

ISBN: 978-1-61804-219-4

mean dispersions for the nine sensors in the array. In the final test case for this configuration, when the sensitivity axis of the sensor array was on the vertical direction and oriented downwards, the dispersion of the estimate was reduced by 2.50 times relative to sensor 3, by 3.55 times relative to sensor 8, and by 3.10 times relative to the average of the mean dispersions for the nine sensors in the array.

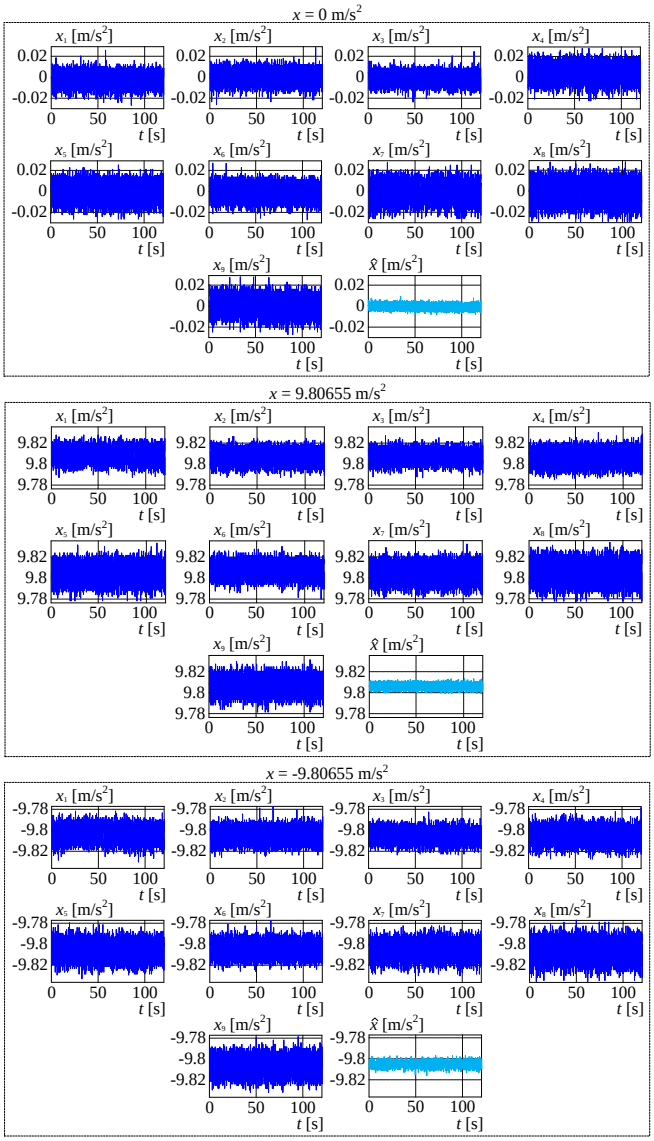

Fig. 8 The independent measures provided to the algorithm and the resulted estimate for n=9

Table 4. Mean values of the sensors weights (n=9)

	Input acceleration	0 m/s²	9.80655 m/s²	-9.80655 m/s²
Mean weight	Sensor 1	0.1262	0.1154	0.1176
	Sensor 2	0.1265	0.1163	0.1154
	Sensor 3	0.1466	0.1346	0.1359
	Sensor 4	0.1079	0.1031	0.1043
	Sensor 5	0.0935	0.1073	0.1059
	Sensor 6	0.1163	0.1231	0.1216
	Sensor 7	0.0947	0.1029	0.1041
	Sensor 8	0.0867	0.0972	0.0958
	Sensor 9	0.1011	0.0996	0.0989

As in the numerical simulations, we can conclude that this algorithm reduces the signal noise power delivered to the navigation processor, proportionally with the integrated sensors number. A high redundancy degree for the strap-down inertial navigation system at a low-cost with respect to more accurate and expensive sensors is also provided.

IV. Conclusion

The paper presented the experimental validation of an adaptive algorithm which reduces the miniaturized inertial sensors errors by using linear redundant configurations in Inertial Measurement Unit. The algorithm determined an estimate of the sensors ideal input (angular speed or acceleration derived from the vehicle dynamics) starting from n sensors unbiased and uncorrelated independent measures. In this way, the estimate was provided under the form of a weighted mean of the n independent measures, and a formula for the optimal weights calculation was deduced.

The experimental validation tests results confirm the algorithm's efficiency for both tested configurations (with four, respectively with nine acceleration sensors in array). The obtained mean dispersion of the estimate acceleration was smaller, by a few times, than the mean dispersions of the signals acquired from each of the acceleration sensor for all three cases considered for input acceleration. As in the numerical simulations, we can conclude that this algorithm reduces the signal noise power delivered to the navigation processor, proportionally with the integrated sensors number.

This algorithm is suitable to be used in strap-down inertial navigators with miniaturized redundant IMUs, which uses more miniaturized sensors instead of each classical sensor.

Acknowledgment

This work was supported by CNCSIS-UEFISCSU, project PN II-RU, No. 1/28.07.2010, *"High-precision strap-down inertial navigators, based on the connection and adaptive integration of the nano and micro inertial sensors in low cost networks, with a high degree of redundance"*, code TE_102/ 2010.

References

[1] J. C. Radix, *Systemes inertiels a composants lies <<Strap-Down>>*, Cepadues-Editions, Ecole Nationale Superieure de l'Aeronautique et de l'Espace SUP'AERO, Toulouse, 1993.

[2] N. Barbour and G. Schmidt, "Inertial sensor technology trends". *IEEE Sensors Journal*, Volume 1, Issue 4, pp: 332-339, Dec. 2001.

[3] J. Bernstein, "An overview of MEMS inertial sensing technology". *Sensors Magazine*, February, 2003.

[4] J. Fraden, *Handbook of Modern Sensors. Physics, Designs, and Applications*. Springer, 3rd ed., 2004.

[5] K. Maenaka, *MEMS Inertial Sensors and Their Applications*. Conference on Networked Sensing Systems, Japan, June 2008.

[6] A Lawrence, *Modern inertial technology: navigation, guidance and control*. Springer Verlag, New York, 1993.

[7] T. L. Grigorie, R.M. Botez, "Modeling and numerical simulation of an algorithm that reduces inertial sensors errors and increases the degree of strap-down navigator redundancy in a low cost architecture", *Transactions of the Canadian Society of the Mechanical Engineering (CSME)*, Vol. 34, No. 1, pp. 1-16, 2010.

[8] R. Rogers, *Applied Mathematics in Integrated Navigation Systems*, Third Edition, Published by AIAA, 2007.
[9] J. Farrell and M. Barth, *The Global Positioning System and Inertial Navigation*. McGraw-Hill, New York, 1999.
[10] D. H. Titterton, *Strapdown inertial navigation technology (2nd Edition).* Institution of Engineering and Technology, 2004.
[11] M. R. Mohamadzadeh, "Practical implementation of new algorithm for restricting data fusion in cloud computing with use of information Kalman filtering". Proceedings of the 2013 International Conference on Systems, Control, Signal Processing and Informatics (SCSI 2013), July 16-19, 2013, Rhodes Island, Greece
[12] M. Ekmanis, "Self-Calibration in Differential Drive Dynamics/ Kinematics Model". Proceedings of the 2013 International Conference on Systems, Control and Informatics (SCI 2013), Venice, Italy, September 28-30, 2013
[13] S Pleshkova and A. Bekiarski, "Integrated Audio Visual Information Processing in Human Robot Interface". 9th WSEAS International Conference on Signal Processing (SIP '10), Catania, Italy, May 29-31, 2010
[14] H. Q. Mahamda, O. Gorgis and L. Reindl, "Design and calibration of an inertial navigation sensor node for precise tracking". 6th WSEAS International Conference on Circuits, Systems, Electronics,Control & Signal Processing, Cairo, Egypt, Dec 29-31, 2007
[15] S. Guerrier, *Integration of Skew-Redundant MEMSIMU with GPS for Improved Navigation Performance*, Master Project, Ecole Polytechnique Federale de Lausanne, June 2008.
[16] A. J. Pejsa, Optimum skewed redundant inertial navigators, *AIAA Journal*, No. 12, pp. 899–902, 1974.

Dynamic Network of Autocatalytic Set Model of Chemical Reactions in a Boiler

A.B. Sumarni and I. Razidah

Abstract—Integration of Autocatalytic Set (ACS) and graph theory has provided a graphical model of combustion process in circulating fluidized bed boiler. Eight important species identified in the process are represented as nodes and the catalytic relationships are represented by edges in the graph. Evolution of the species from the graph has been explored by using adjacency matrix whereby sequence of depleted species over time is highlighted and two species left after the combustion process namely CO and CO_2 is shown conformed to the actual process. In this paper, network of the graphical ACS model is further investigated using left Perron vector of transition matrix. This paper will highlight on the depletion of species over time with regards to the actual process.

***Keywords*—**Autocatalytic Set, Graph Theory, Circulating Fluidized Bed Boiler, Transition Matrix.

I. Introduction

Autocatalytic Set (ACS) concept which was introduced in the early 1860's by Darwin is a revolutionary theory about the origin of life. Ever since then, the concept is introduced in chemistry [1]-[3], in biology [4] and even in mathematics [5] where the latter had initiated the ACS in terms of graph. It is defined as a subgraph, each of whose nodes has at least one incoming link from a node belonging to the same subgraph [5]. Application of this concept is explored in modeling clinical waste incineration process [6].

Recently, the ACS concept is applied in modeling a combustion process in circulating fluidized bed boiler (CFB) [7]. As for the process, eight species which gives significant contribution are identified from chemical reactions that exist during the process namely Coal, Hydrogen (H_2), Oxygen (O_2), water (H_2O), Carbon (C), Carbon Monoxide (CO), Carbon Dioxide (CO_2) and Methane (CH_4). The species is represented as nodes in the graph while directed edge from node *j* to node *i* indicates that species *j* catalyzes the production of species *i* (see Fig. 1). Since the combustion process in CFB is dynamic in nature, the graph undergoes process of evolution. The evolution process of the graph is represented by graph dynamics model whereby evolution of the species is explored using Perron-Frobenious eigenvector (PFE) of adjacency matrix [8].

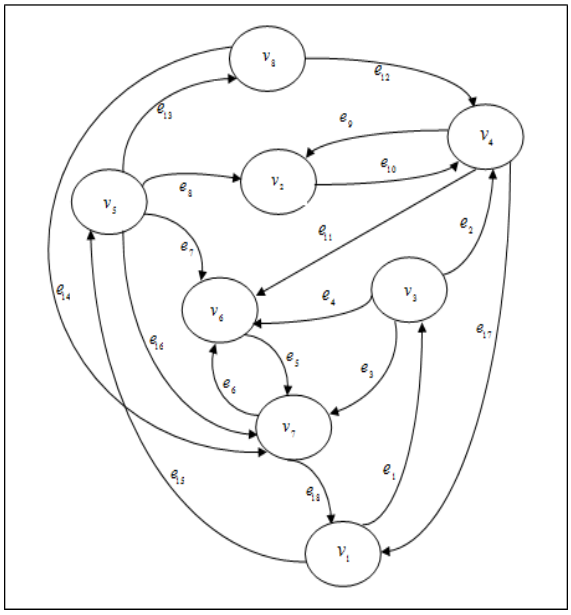

Fig 1. A graph $G(V, E)$ of catalytic relationship among species during combustion process in CFB

In the study, the species was thought as "living" on the node of the graph where it is evolved after certain time *t* and the PFE was used as an indicator to indicate concentration level of each species during the process. The smaller the concentration levels the less significant the species is at particular time *t* and is subsequently deleted. Sequence of depleted species was Methane (CH_4) followed by Oxygen (O_2), Water (H_2O), Hydrogen (H), Carbon (C) and Coal at time t_1, t_2, t_3, t_4, t_5 and t_6 respectively. The result also shows that species left after the combustion process are Carbon Monoxide (CO) and Carbon Dioxide (CO_2) which are in accordance with the actual process. However, O_2 is depleted at the early stage of the process which is at time t_2. This result shows that the model is not really explaining the real process since O_2 is needed to complete the combustion. This situation leads to further investigation on the evolution process of the graph in a long run using another most common matrix representation of a graph namely transition matrix.

This work was supported financially by UiTM Fundamental Research Grant Scheme (FRGS) .

A.B.Sumarni is with the Department of Mathematics, Faculty of Computer & Mathematical Sciences, UiTM Malaysia. (e-mail: sumarni@tmsk.uitm.edu.my).

I. Razidah is a professor from the same department. (e-mail: razidah@tmsk.uitm.edu.my).

In order to explore the dynamical behaviour of the species through the graph, method used in [9] is adopted.

II. Transition Probability Matrix

Transition probability matrix is one of mathematical model that makes it possible to study dynamic complex systems by establishing a finite number of states. If the transition from one state to another is not predetermined, but rather can only be specified in terms of certain probabilities which depend on the previous history of the system, then the process is called a stochastic process [10]. In addition, if the transition depends only on the value of current state, then the process is called a Markov process or Markov chain. It can be explained in the followings:

Let us consider a random process defined by a finite set of states, $N=\{1,...,n\}$ and a sequence $X_0, X_1, X_2, ...$ of random variables taking values in *N*. Any Markov process with finite states is known as *finite Markov chain* if the transition probabilities at step (*k+1*) depend only on the state at step *k*, that is,

$P(X_{k+1}=j \mid X_k=i_k,...,X_0=i_0)= P(X_{k+1}=j \mid X_k=i_k)$ and is described by transition probability matrix $P=\lfloor P_{ij} \rfloor_{i,j\in N}$ where $P_{ij}= P(X_{k+1}=j \mid X_k=i_k)$ for all $i, j \in N$. As for probabilities, the number P_{ij} must lie in the interval $[0,1]$. Furthermore, for any fixed *j*, $p_{1j}+p_{2j}+...+p_{kj}=1$. Every Markov process defines a transition matrix, and conversely [11]. The matrix is also called Markov, probability or stochastic matrices [10]. In particular, a transition matrix is stochastic if each of whose rows (columns) consists of nonnegative real numbers, with each row (column) sums is 1 [12]. This stochastic matrix could predict the state of a system described by a Markov process in future observation times where the prediction is in term of probabilities. In a Markov process, a state vector that approached some limiting fixed vector as the number of observations increased is called a *regular* Markov process.

Definition 1.[10]

A transition matrix is *regular* if some integer power of it has all positive entries.

Thus, for a regular transition matrix *P*, there is some positive integer *m* such that all entries of $P^{(m)}$ are positive. A Markov process which is governed by regular transition matrix is called *regular Markov process*. A study on regular Markov process has significant contribution to the theory of Markov chain which is based on the following Theorem 1.

Theorem 1. [10]

If *P* is a regular transition matrix, then as $n\to\infty$,

$$P^n \to \begin{bmatrix} q_1 & q_1 & \cdots & q_1 \\ q_2 & q_2 & \cdots & q_2 \\ \vdots & \vdots & & \vdots \\ q_n & q_n & \cdots & q_n \end{bmatrix}$$ where q_i are positive numbers such that $q_1+q_2+...+q_n=1$.

Thus, it shows that a system described by a regular Markov process would eventually approach a fixed probability vector $q=(q_1, \ \ldots, \ q_n)^t$. The vector *q* is called *steady state vector* of the regular Markov process. Normally a state transition is represented by directed graph where it can relate to the problem of random walk. The concept of random walk is equivalent to the concept of finite Markov chain. Let us consider a directed graph $G=(V,E)$ with $V=\{1,...,n\}$ and choose some initial nodes. Suppose that at each time step, choose at random a current node and move to this node. The resulting sequence of nodes is called a random walk. The probability of moving from a node *i* to a node *j* is equal to d_i^{-1}, where d_i is the out-degree of node *i*. In other words, transition probability matrix for random walk specifically for unweighted directed graph is given as follows:

$$P(u,v)=\begin{cases} \dfrac{1}{d_u} & \text{if } (u,v)\in E \\ 0 & \text{otherwise} \end{cases} \qquad (1)$$

where d_u denotes the out-degree of vertex *u*.

Transition matrix of a random walk can also be related to Perron-Frobenius Theorem [6]. Although it may not be symmetric, it does have useful property that all of its entries are nonnegative. In order to relate to Perron-Frobenius Theorem, the transition matrix must be irreducible too. If the adjacency matrix A for any strongly connected graph *G* is irreducible, then the transition probability matrix *P* of *G* is also irreducible (regular) [13]. Subsequently, for irreducible transition probability matrix, Perron-Frobenius Theorem provides useful information on eigenvalues of the matrix where eigenvalue of $P, \lambda_1(P)=1$ and if matrix *P* is irreducible(regular) it has exactly one invariant measure x^T, which is positive [14]. Here, invariant measure of the matrix *P* is referring to the left Perron vector (LPF) corresponds to the spectral radius of the matrix. In a dynamic system described by a Markov process through a probability vector, LPF of transition probability matrix *P* is known as a unique steady state vector or stationary distribution vector.

As for combustion process in CFB, by (1), the transition matrix *P* is as follows:

$$P=\begin{bmatrix} 0 & 0 & \frac{1}{2} & 0 & \frac{1}{2} & 0 & 0 & 0 \\ 0 & 0 & 0 & 1 & 0 & 0 & 0 & 0 \\ 0 & 0 & 0 & \frac{1}{3} & 0 & \frac{1}{3} & \frac{1}{3} & 0 \\ \frac{1}{3} & \frac{1}{3} & 0 & 0 & 0 & \frac{1}{3} & 0 & 0 \\ 0 & \frac{1}{4} & 0 & 0 & 0 & \frac{1}{4} & \frac{1}{4} & \frac{1}{4} \\ 0 & 0 & 0 & 0 & 0 & 0 & 1 & 0 \\ \frac{1}{2} & 0 & 0 & 0 & 0 & \frac{1}{2} & 0 & 0 \\ 0 & 0 & 0 & \frac{1}{2} & 0 & 0 & \frac{1}{2} & 0 \end{bmatrix} \qquad (2)$$

ISBN: 978-1-61804-219-4

From the matrix, the following observations are deduced:

i) P is a stochastic matrix since each row sums equal to one and no value is less than 0.
ii) P is a regular transition matrix since for $k=6$, $\left((P^*)^k\right)_{i,j}>0,\ \forall i,j=1,...,n$.
iii) P is irreducible since the corresponding graph is strongly connected.
iv) The largest eigenvalue of P is $\lambda=1$. It is also known as right eigenvalue.

As for $\lambda=1$, the left Perron vector φ of P is

$$\varphi=\begin{bmatrix}0.1696 & 0.0512 & 0.0848 & 0.0901\\ 0.0848 & 0.2191 & 0.2792 & 0.0212\end{bmatrix}^t. \quad (3)$$

It is calculated by solving eigenvector problem or by finding steady state vector q of matrix P by using Theorem 1. It is also known as stationary distribution vector or PageRank vector π [15] where it is used to compute a ranking of nodes in a graph based on the structure of its links. The idea of PageRank is that $\pi(i)$ can be interpreted as the "importance" of i. Thus π defines a linear order on the vertices by treating $i\le j$ if $\pi(i)\le\pi(j)$. Thus, importance of the species represented as nodes in the graph can be measured by its PageRank or its left Perron vector.

III. Methodology

The network of the interaction between species in the combustion process in CFB is represented by 8×8 adjacency matrix. However this species is dynamic in nature in which it is wiped out in the process due to it is not functioning and a new network is evolved after certain time t. Thus, graph dynamics represent dynamical behavior of the species of the combustion process in CFB [6]. The graph $G(V,E)$ is also represented by 8×8 transition matrix in which it described transition of one species to the other species in the process. The process is evolved over time to a stationary state which is described by left Perron vector. The likelihood of species to move to a particular species can be determined from its left Perron vector on each phase of the graph dynamics. The least value of j^{th} element of the row of its left Perron vector indicates the least chance of moving from other species to the species j. Thus species j represented as node j in the graph is considered least important and therefore the existence is insignificant thus can be omitted from that phase. In contrary, the highest value of j^{th} element of the row of its left Perron vector indicates the most important species to the process.

In this section, a procedure to determine the importance of the species based on graph dynamics procedure [6] is adopted. The procedure involved dynamical variables, $V=(v_1,...,v_n)$; n=1,…,8 where v_i stands for the chance of transition from other species to the i^{th} species in the graph $G(V,E)$. It is summarized as follows:

Step 1: Keeping G with n variables fixed and represented by transition matrix P, v_i is evolved for a specified time t, which is large enough for v_i to converge to its steady state. At this particular state, v_i is no longer altered whereby, V can be represented by its left Perron vector. $V_i\equiv v_i(t)$ such that $\sum_{i=1}^{8}V_i=1$.

Step 2: The set L of nodes i with the least value of V_i is determined, i.e. $L=\left\{i\in S\middle|V_i=\min_{j\in S}V_j,\ S=\{1,2,...,n\}\right\}$. This is the set of least important nodes, identifying transition value of a variable in the steady state vector at a specific time t. The least the value of V_i, the least important is the node i. One of the least important node is chosen randomly and is removed from the system along with its links leaving a graph with *s-1* variables.

Step 3: Graph G is now reduced to *s-1* variables. A transition matrix $(s-1)\times(s-1)$ is reconstructed. Other nodes and links of G remain unchanged. All these $v_i(v_i>0)$ is once again evolved to a new steady state at a consequent time t, in which $\sum_{i=1}^{n-1}v_i=1$. The steps are repeated until it produced 2×2 matrix that represent two variables are attained. The whole process occurred at discretely sparse intervals labeled by n = 0,1,…, k. The algorithm for the above procedure is as follows:

Graph Dynamics Algorithm:

Input: Given a transition matrix P.
Output: Compute left Perron vector and reduce the dimension of matrix P.

```
Begin
    read input matrix P_{n×n}
    while n > 2
            find left Perron vector,X
            if x_i < 0
            LPF = −1× X
            else LPF = X
            find min x_i and delete row and column i
            of matrix P
    return P_{n−1×n−1}
end
```

repeat until $P_{2\times2}$

IV. Implementation & Discussion

The procedure explained in the previous section is implemented to the graph $G(V,E)$ in Fig. 1 and its corresponding LPF in (3) using MATLAB-R2009b. At n=0, it is anticipated that v_i evolved until it reached a particular time whereby all variables reached its steady state. This phenomenon is represented by its left Perron vector, φ of P^*. The least important variable corresponds to the least value of the element in the left Perron vector. It is then removed from the system together with their links to give way to the

remaining variables for their interaction which leads to the second update of the process (n=1). A new graph of the remaining variables, now denoted by G_1 is an induced graph of G(V,E). The steps given in the procedure is then repeated until n=6 where only two variables remain in the induced graph. The expected update on each stage of the combustion process given by this dynamic model through the procedure is given in Table I.

TABLE I. UPDATES OF SPECIES IN $G(V,E)$

Updates	Species involved in $G(V,E)$	LPF	x_i deleted
G_0	Coal(v_1), Hydrogen (H_2) (v_2), Oxygen (O_2) (v_3), Water (H_2O) (v_4), Carbon (C) (v_5), CO (v_6), CO_2 (v_7), Methane (CH_4) (v_8)	$X=\begin{pmatrix}0.1696\\0.0512\\0.0848\\0.0901\\0.0848\\0.2191\\0.2792\\0.0212\end{pmatrix}$	Methane (CH_4) (v_8)
G_1	Coal(v_1), Hydrogen (H_2)(v_2) oxygen (O_2)(v_3), water (H_2O) (v_4), carbon (C) (v_5), CO (v_6), CO_2 (v_7)	$X=\begin{pmatrix}0.1714\\0.0571\\0.0857\\0.0857\\0.0857\\0.2286\\0.2857\end{pmatrix}$	Hydrogen (H_2)(v_2)
G_2	Coal(v_1), Oxygen (O_2) (v_3), Water (H_2O) (v_4), Carbon (C) (v_5), CO (v_6), CO_2 (v_7)	$X=\begin{pmatrix}0.1846\\0.0923\\0.0308\\0.0923\\0.2615\\0.3385\end{pmatrix}$	Water (H_2O) (v_4)
G_3	Coal(v_1), Oxygen (O_2)(v_3), Carbon (C)(v_5), CO (v_6), CO_2(v_7)	$X=\begin{pmatrix}0.1818\\0.0909\\0.0909\\0.2727\\0.3636\end{pmatrix}$	Carbon (C) (v_5)
G_4	Coal(v_1), Oxygen (O_2)(v_3), CO (v_6), CO_2(v_7)	$X=\begin{pmatrix}0.1818\\0.1818\\0.2727\\0.3636\end{pmatrix}$	Coal (v_1)
G_5	Oxygen (O_2) (v_3), CO (v_6), CO_2(v_7)	$X=\begin{pmatrix}*\\0.5\\0.5\end{pmatrix}$	Oxygen (O_2) (v_3)
G_6	CO (v_6), CO_2(v_7)	$X=\begin{pmatrix}0.5\\0.5\end{pmatrix}$	-

* 1.0647×10^{-16}

The graph dynamics are shown by the deletion of the species which is regarded as least important during time t. The explanation on the deletion of the species is given in Section III. From the table, Methane (CH_4) is the first species to be deleted followed by Hydrogen (H_2), Water (H_2O), Carbon (C), Coal and then Oxygen (O_2) at time t_1, t_2, t_3, t_4, t_5 and t_6 respectively. The species left at the end of the combustion process indicated by using LPF is shown to be similar to [8]. However, towards the end of the process, at time t_6, Oxygen (O_2) is become least important due to being fully consumed in the combustion process. Thus it is deleted and the deletion at this time is more realistic as compared to [8]. This situation shows that the real process of combustion in CFB is better explained by using LPF of transition matrix of graph $G(V,E)$ in terms of evolution of species.

V. Conclusion

Graph dynamics of combustion process in CFB is presented by using LPF of transition matrix. The result is presented in a form of sequence of depletion species which is due to least important species namely Methane (CH_4) followed by Hydrogen (H_2), Water (H_2O), Carbon (C), Coal and Oxygen (O_2) while species left at the end of the process are Carbon Monoxide (CO) and Carbon Dioxide (CO_2). The dynamics model shows in this work is better explained the actual process as compared to dynamics model using PFE of adjacency matrix in terms of sequence of depleted species over time t.

Acknowledgment

The authors would like to thank the Research Management Institute, Universiti Teknologi MARA Malaysia for the financial support through the Fundamental Research Grant Scheme, Ref: 600-RMI/FRGS 5/3 (8/2013). Their gratitude is also extended to anonymous reviewers for their valuable comments and suggestions.

References

[1] S. A. Kauffman, "Cellular Homeostasis, Epigenesist and Replication in Randomly Aggregated Macromolecular Systems," *Journal of Cybernetics*, vol.1, pp.71-96, 1971.

[2] M. Eigen, "Self-organization of matter and the Evolution of Biological Macromolecules," *Naturwissenchaften*, vol.58, pp.465-523, 1971.

[3] O.E. Rossler, "A System Theoretic Model of Biogenesis," *Z. Naturforschung*. vol.26b, pp.741-746, 1971.

[4] S. A. Kauffman, "Autocatalytic Replication of Polymers," *Journal of Theoretical Biology*, no. 119, 1986.

[5] S. Jain and S. Krishna, "Autocatalytic Sets and the Growth of Complexity in an Evolutionary Model," *Physical Review Letters*. vol. 81, pp. 5684-5687, 1998.

[6] A. Tahir, B. Sabariah, A, Khairil, "Modeling a Clinical Waste Incineration Process Using Fuzzy Autocatalytic Set," *Journal of Mathematical Chemistry*, vol. 47, no.4, pp.1263 – 1273, 2010.

[7] S.A. Bakar, N. A. Harish, F. H. Osman, F. Ismail and S. F. A. Mokhtar, "Autocatalytic set of chemical reactions of fluidized bed boiler" in *Proceedings of International Conference on System Engineering and Technology (ICSET) 2012, Bandung, IEEEXplore*, pp 1-6.

[8] S.A. Bakar, N. A. Harish, R. Ismail, "Graph Dynamics Representation of Chemical Reactions of a Boiler" in *Proceedings of Business Engineering and Industrial Applications Colloquium (BEIAC) 2013, Langkawi*, pp.906-910.

[9] A. B. Sumarni, A. Tahir, B. Sabariah, "Graph Dynamics of Fuzzy Autocatalytic Set of Fuzzy Graph Type-3 of an Incineration Process," *Journal of Fundamental Sciences*, vol. 6, pp. 9-14, 2010.

[10] H. Anton and C. Rorres, *Applications of Linear Algebra. (2th ed.)* New York. John Wiley & Sons, Inc, 1977.

[11] C. Meyer, "Matrix Analysis and Applied Linear Algebra," *SIAM*. Philadelphia, 2000.

[12] A. Berman and R. J. Plemmons, *Nonnegative Matrices in the mathematical Science*, New York. Academic Press Inc, 1979.

[13] K. Costello, (2010, March, 19). Random walks on Directed Graph [online]. Available: www.math.ucsd.edu/~phorn/math261/10_19_notes.pdf

[14] L. Ninove, "Dominant Vectors of Nonnegative Matrices. Application to Information Extraction in Large Graphs".Ph.D Thesis. Universite Chatolique De Louvain, France, 2008.

[15] C. C. Balázs, M. J. Raphaël and D. B. Vincent, "PageRank Optimization in Polynomial Time by Stochastic Shortest Path Reformulation," *LNAI*. Berlin Heidelberg: Springer-Verlag. 6331, 89-103, 2010

Model of advanced calculus for determining the fire resistance of a structural element

Diana ANCAŞ[1] and Bogdan UNGUREANU[1]

***Abstract*—**The article shows an advanced model of calculus with reference to the SAFIR calculus program, wishing for an additional validation of the results obtained this way.
The SAFIR program allows a nonlinear structural analysis in time phases corresponding to temperature increase in transversal section under the action of constant static loads or variables in time.
Thus, in the case of verification by numeric calculus of the structural pillars of Bucharest Tower Center, an additional validation of the advanced model of calculus was taken in consideration by comparing the results offered by the SAFIR program with a relevant test for a pillar experimentally tested for fire at the University of Gent, Belgium, pillar of the same type with those of the Bucharest Tower Center structure (steel I profiles with a cross disposition, with concrete between the visible, unprotected soles of the steel profiles)

***Keywords*—**fire resistance, temperature, thermal response, structural element.

I. Model of calculs

ADVANCED models of calculus (calculus programs) must fulfil the following conditions:

1) To contain separate models of calculus to determine:
- the evolution and distribution of temperature in the structure's elements (thermal response model);
- the mechanical behaviour of the structure or of a random part of the structure (mechanical response model);
- the ability to be utilised in association with any temperature-time evolution curve provided that the properties of the material are known to the targeted temperature domain;
- the reliability on the acknowledged principles and hypotheses of the thermal transfer theory.

2) The thermal response model must consider:
- the proper thermal actions specified in SR EN 1991-1-2;
- the variations of the material properties with temperature;
- to rely on the acknowledged principles and hypotheses of the structural mechanics theory considering the changing of the mechanical properties along with the evolution of the temperature.

3) The mechanical response model must consider:
- the combined effect of the mechanical actions, geometrical imperfections and thermal actions;
- the temperature dependent on mechanical properties;
- the geometric nonlinear effects and nonlinear effects of the materials' properties, including the effect of discharge upon the structural rigidness.

Models of advanced calculus can be utilised for any shape of transversal section. The SAFIR program used to verify by numeric calculus the pillars of Bucharest Tower Center structure fulfils all these conditions. The SAFIR program allows a nonlinear structural analysis in time phases corresponding to temperature increase in transversal section under the action of constant static loads or variables in time.

The calculus of resistance time of a structural element under the action of fire has two stages:
- at the first stage the evolution of temperature in transversal section of the elements is determined, thus considering the degradation of the mechanical characteristics of the materials that make the section;
- at the second stage the response of the structural element under the thermal loads and the highest static loads obtained from the combinations corresponding to special fire grouping is determined.

II. Relevant test to validate the model of calculus

The experimental test relevant for the validation of the advanced model of calculus SAFIR in case of testing the pillars of the structure of Bucharest Tower Cenetr by numeric calculus was taken from the experimental research report REFAO-EUR10828EN [1] of the European Commission from year 1987 where we can find the fire tests conducted by ARBED RECHERCHES on pillars and beams with composite section of steel-concrete, made of steel profiles with concrete between the visible soles.

The fire test for the octagonal pillar with steel profiles with cross disposition, with concrete between the visible soles of the steel profiles was conducted at the fire tests laboratory of the University of Gent, Belgium. The test was used in the current report to additionally validate the SAFIR advanced model of calculus. The transversal section of this pillar that has similar construction to those of the Bucharest Tower Center is shown in Fig. 1 together with the pillar disposition in the experimental setting. Fig. 1 also shows the disposition of the thermo-elements (termocuple) for experimental determining of the temperatures in transversal section.

The test was conducted under the action of the standardized temperature-time curve ISO-834 with a temperature evolution in accordance to article 3.2.1 (1) of SR EN1991-1-2 (also used for the verification by numeric

[1]Diana ANCAŞ, PhD, Faculty of Civil Engineering and Building Services/ Technical University "Gheorghe Asachi" of Iasi, Dimitrie Mangeron 43, Iasi, Romania (e-mail: ancas05@yahoo.com).

[1]Bogdan UNGUREANU, PhD Student, Faculty of Civil Engineering and Building Services/ Technical University "Gheorghe Asachi" of Iasi, Dimitrie Mangeron 43 Iasi, Romania (e-mail: bogdan.ungureanu@tuiasi.ro).

calculus of the fire resistance of structural elements of Bucharest Tower Center).

The material characteristics for concrete were determined on cubes of 200 mm tested at dates close to the fire test date.

On the surfaces exposed to fire, the net heat flow is determined considering the heat transfer by convection and radiation in accordance to paragraph 3.1 of SR EN1991-1-2 "Eurocode 1: Actions upon structures. Part 1-2: General actions-Actions upon fire exposed structures" [2]. This depends on the resulting emittance as a product between the fire emittance and the surface of the element emittance.

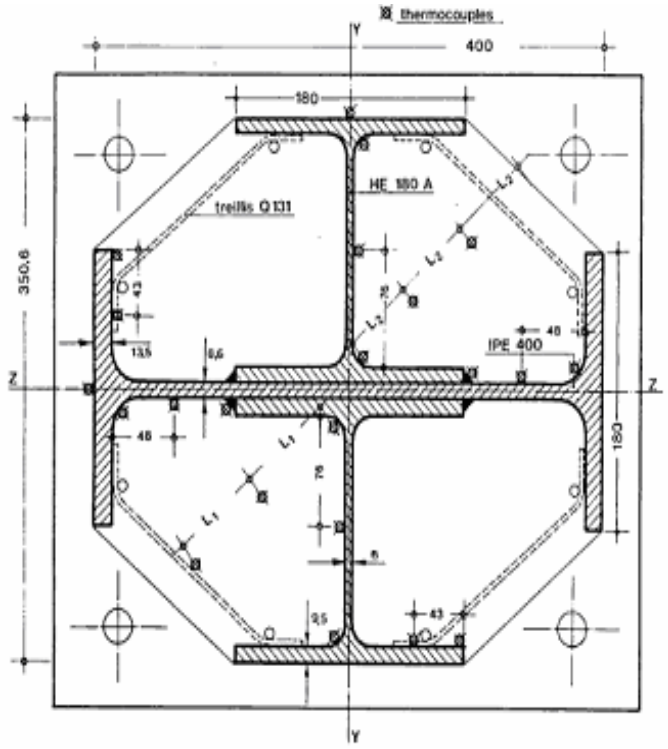

Fig. 1 Experimental specimen [4]

The resulting emittance in case of a fire test depends on the position of the burners in respect with the experimental specimen, furnace size, fuel used and characteristics of furnace walls. Fig. 2 shows the values of the resulting emittances considered for the visible steel surfaces (0.3 and 0.5) and concrete surfaces (0.45) for the octagonal pillar tested in specific conditions of the fire test furnace of the University of Gent as they were given in the ARBED report (fig. 32 of the report). These values were also considered in the SAFIR program numeric calculus.

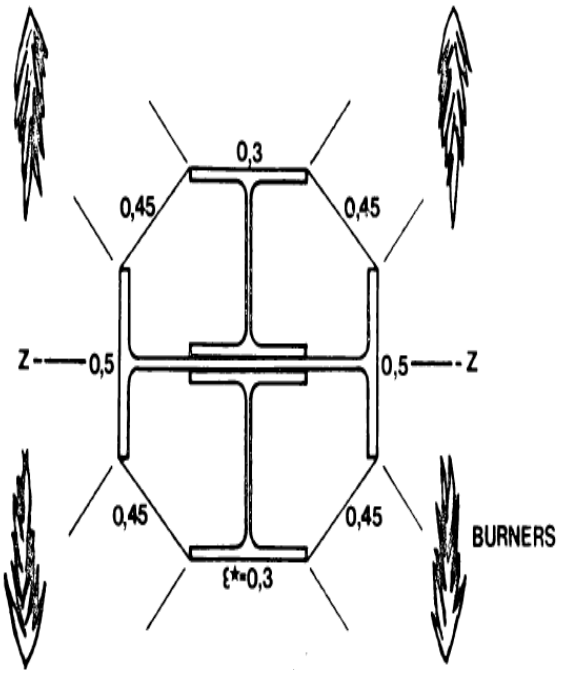

Fig. 2 Resulting emittances for the steel soles and concrete surfaces of the pillar tested in the furnace of the University of Gent [3]

EN 1991-1-2 states that for fire emittance, a value of 1.00 can generally be considered. The emittance of regular steel surface (thus being the case of the profiles used for the octagonal pillar tested for fire) and the emittance of the concrete surface have a value of 0.7. As a consequence, the resulting emittance for steel and concrete in accordance with SR EN1991-1-2 would have a value of 0.7 on the whole perimeter of the tested pillar, a superior value to those of the emittances calculated for the octagonal pillar tested in the furnace of the University of Gent laboratory.

The pillar with octagonal section considered to validate the SAFIR advanced calculus model behaved extremely well at fire test showing a fire resistance of 172 minutes in terms of unprotected exposure of the soles of the steel profiles. The conclusions of the report were that this type of pillar made of steel profiles with a cross disposition, with concrete between the visible soles of the profiles, unprotected, without additional reinforcements, represent an efficient structural solution from fire resistance point of view, capable of enduring the combined action of axis compression with bend along both main directions and attractive not only from architectural point of view. Moreover, the fact that the soles of steel profiles are visible on all four sides of the pillar allows uncomplicated realization of the joints usually used in steel structures. The pillar wasn't additionally reinforced with longitudinal resistance reinforcements as it was in the case of the Bucharest Tower Center structure pillars. Shackles, same as in the case of Bucharest Tower Center structure, were welded on the soles of the metallic profiles together with a constructive longitudinal reinforcement as shown in Fig. 1.

ISBN: 978-1-61804-219-4

III. Validation of Calculus Model

Fig. 3 shows the comparison between experimentally measured temperatures at thermo-elements level [3] and the numeric calculated temperatures at yield time of the experimental specimen of 172 minutes (10,320 seconds) at the same thermo-element level. As one can observe, the SAFIR program gives good results, with close values, covering (higher temperatures), for temperatures calculated at the level of the thermo-element used in fire test. In the numeric calculus, were used for steel and concrete, the values of the emittances determined for the octagonal pillar placed in fire test furnace of the University of Gent, shown above.

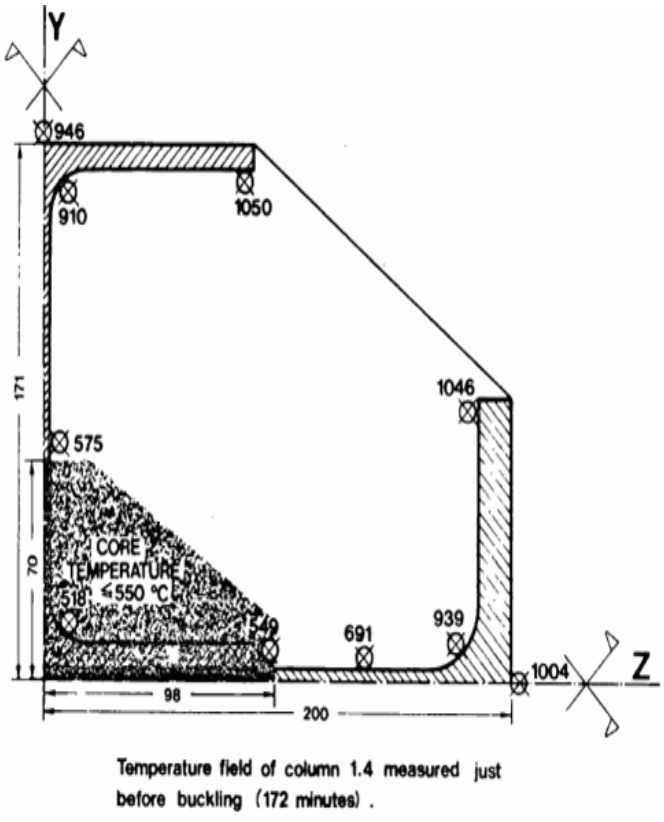

Temperature field of column 1.4 measured just before buckling (172 minutes).

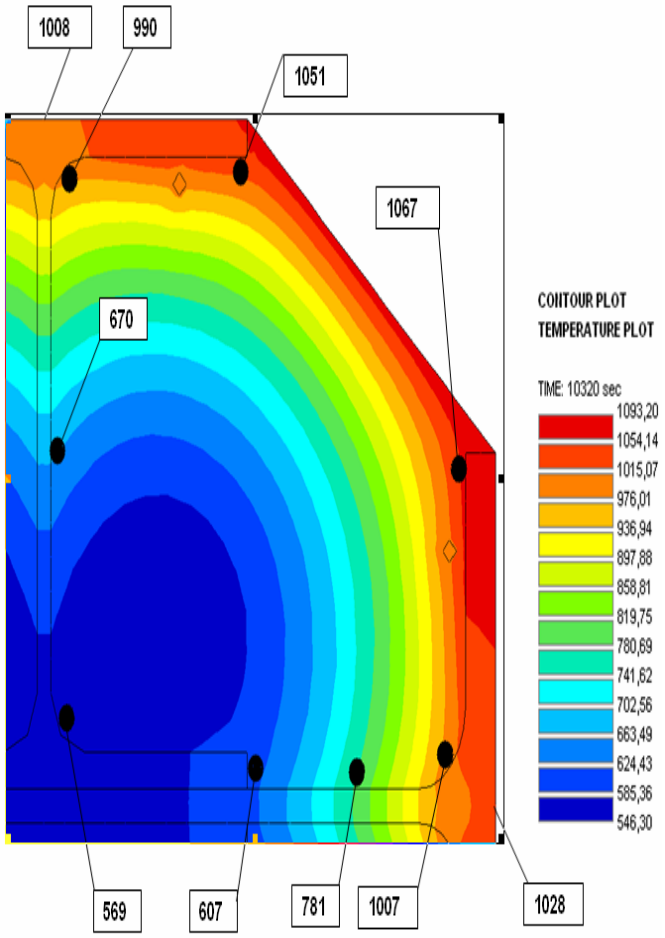

Fig. 3 Distribution of temperature in transversal section and at the thermo-elements level by numeric calculus with the SAFIR program for a period of 172 minutes (10,320 seconds) in comparison with the experimental results [3]

In case of considering a buckling length of 70% of the pillar's length (intermediate situation of articulate-embedded propping of the pillar, between the case of the pillar with perfect articulated propping, perfectly embedded at both ends) the yield time obtained by numeric calculus is of 164 minutes, conservative result but closer to the yield time experimentally determined. This might suggest that in reality, for the experimental specimen, perfect articulations for propping couldn't be realised and that there was a certain degree of embedding at the ends of the experimental specimen. It is worth mentioning the fact that the pillar is leaner (considering its length and characteristics of the transversal section) and thus its behaviour can be affected in cases where propping provides a certain degree of embedding at ends. It is obvious that it is impossible to know for certain the level of embedding at ends realised by the grips of the experimental specimen. Further on, in the sensibility analysis of the calculus model at other critical parameters' level, one would consider as reference the intermediate case of the articulate-embedded bar that is closer to the real situation of experimental trial.

ISBN: 978-1-61804-219-4

In case of considering a buckling length corresponding to the double embedded bar situation (50% of the pillar's length) the yield time obtained by numeric calculus is 188 minutes. It is noticed that the yield time is superior to the time experimentally obtained, which is obvious because in the experimental sett-up a perfect embedding couldn't (and wouldn't) be obtained, no matter how large the real embedding degree at the ends of the specimen had been, considering the gripping details that were made (Fig. 1).

In conclusion, following the sensibility analysis carried out at the level of initial imperfections amplitude (critical parameter for the determination of fire resistance for a structural element) was demonstrated the fact that the SAFIR advanced calculus model gives results in accordance to the principles of engineering: yield time obtained as a result of numeric calculus decreases with the increase of initial imperfections amplitude of the pillar. The yield time decreases from 164 minutes for an imperfection with an amplitude of 1 mm (considering that the experimentally measured imperfections were 0), to 156 minutes for an imperfection with a higher amplitude, of 1/1000 of the pillar length and to 140 minutes for an imperfection with the highest considered amplitude of 1/200 of pillar lengths. It may be highlighted the fact that, as the sensibility analysis shows, the initial imperfections with the amplitude of 1/200 of the pillar length, considered in the fire resistance verification by numeric calculus of the Bucharest Tower Center structure pillars were covering for the results of the calculus.

As shown, the resulting emittances of steel and concrete, in accordance to SR EN1991-1-2 have the value of 0.7 (considering that for fire emittance one can generally consider the value 1.00), a superior (covering) value opposed to the emittances determined for the octagonal pillar tested in the furnace of the University of Gent laboratory. Fig. 4 shows the distribution of temperatures in transversal section for the yield time of the experimental specimen of 172 minutes (10,320 seconds) in case of considering a resulting emittance of value 0.7 for the whole pillar perimeter. It may be noticed that the temperature values are higher, so covering, compared to the temperatures resulted of numeric calculus for emittance values determined in the Gent laboratory, of 0.45 for the concrete surface, of 0.3 and 0.5 for the surfaces of the steel soles (Fig. 3).

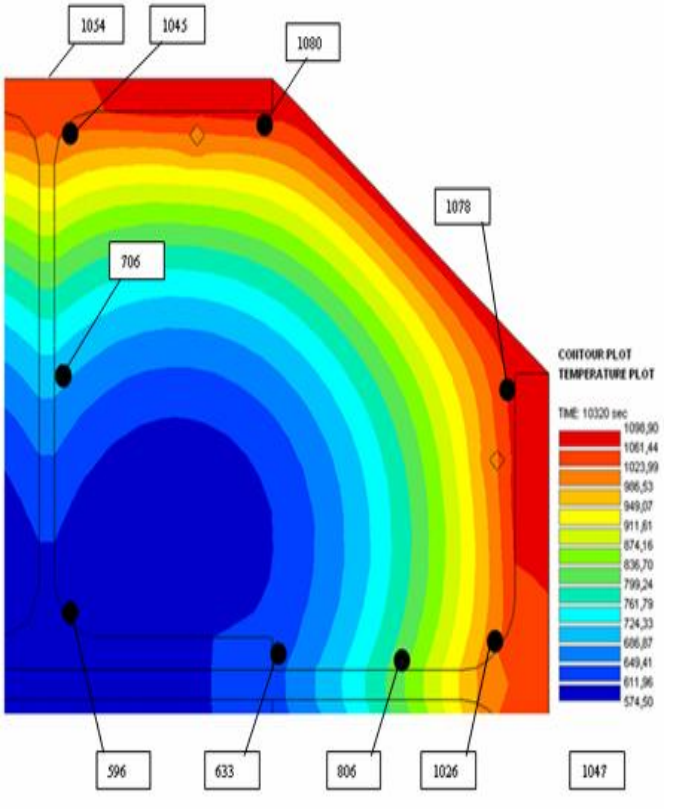

Fig. 4 Distribution of temperature in transversal section corresponding to the yield time of the experimental specimen of 172 minutes (10,320 seconds) considering resulting emittances of 0.70 for exposed surfaces of concrete and steel

The yield time resulted from numeric calculus (buckling length corresponding to the case of articulate-embedded bar, with an amplitude of global imperfection of 1 mm), considering for the resulting emittaces values of 0.70 for exposed surfaces of concrete and steel, is of 152 minutes.

In conclusion, following the sensibility analysis carried out at the level of resulting emittances for steel and concrete surfaces, was proved that the SAFIR advanced calculus model gives results in accordance to the principles of engineering: yield time resulted by numeric calculus decreases with the increase of the values of resulting emittances. The yield time decreases from 164 minutes for resulting emittances of 0.45 for concrete, 0.3 and 0.5 for steel (determined for the fire test furnace of the University of Gent), to 152 minutes for resulting emittances of 0.70 for steel and concrete as foreseen in SR EN 1991-1-2. Higher values for emittances imply a radiation increased component of the net thermal heat flow over unit of surface that, as demonstrated also by numeric calculus, leads to higher temperatures in transversal section and to a lower yield time of the element. It is highlighted the fact that, as the sensibility analysis also shows, the values of the resulting emittances considered in accordance to the SR EN 1991-1-2 for verification by numeric calculus of the fire resistance of Bucharest Tower Center structure pillars, were covering for the results of the calculus.

ISBN: 978-1-61804-219-4

IV. Conclusions

The program for numeric analysis of structures under the action of fire SAFIR is a program renowned and used at international level, follows the principles stated by the Eurocodes, in order to be considered a model of advanced calculus for this type of analysis. In accordance to the conditions stated by Eurocodes for validating models of advanced calculus, the SAFIR program was validated through numerous comparisons both to fire tests and other acknowledged programs.

For the case of verification by numeric calculus of the structure pillars of Bucharest Tower Center, an additional validation of the advanced calculus model was considered, by comparing the results offered by the SAFIR program to a relevant trial, for a pillar experimentally tested for fire at the University of Gent, Belgium, pillar of similar type to those of the Bucharest Tower Center structure (I profile with cross disposition, with concrete between the visible, unprotected soles of the steel profiles).

As expected, the SAFIR program offered, by comparison to the experimental trial, good results with covering values, for temperatures calculated at the level of the thermo-elements used for experimental determining of temperature in transversal section as well as for the fire resistance time. Following the sensibility analysis, necessary for validating a model of advanced calculus, but can also be done for a particular situation, was shown that the SAFIR program gives results in accordance to the principles of engineering. The sensibility analysis was carried out considering various critical parameters to determine the fire resistance of a structural element: buckling lengths, equivalent geometrical imperfections and resulting emittances.

In fire testing the pillars of the Bucharest Tower Center structure, all critical parameters previously enumerated were considered with values to lead to covering results in terms of fire resistance time. Thus, in numeric calculus, the buckling lengths of the pillars were considered equal to the lengths of the elements (the hypothesis of bi-articulate grip of the pillars), the amplitude of equivalent geometrical imperfections was considered of 1/200 of the elements' length and the values of the resulting emittances were considered those indicated by the Eurocodes. All these hypotheses were proved to be covering following the shown numeric calculus and also following the sensibility analysis as well as in comparison to the experimental trial.

In conclusion, the SAFIR advanced numeric calculus model can be considered validated also for the particular situation of the pillars of Bucharest Tower Center structure, where, for their verification, were chosen all the calculus hypotheses that lead to covering results from the fire resistance time point of view.

References

[1] A. D. Ancaş, "*Rezistenţa şi stabilitatea la foc a elementelor din oţel",* Calculul şi alcătuirea structurilor supuse acţiunii incendiului, Partea I, Editura Politehnium, Iaşi, 2008.

[2] SR EN1991-1-2, Eurocod 1: *Acţiuni asupra structurilor. Partea 1-2: Acţiuni generale – Acţiuni asupra structurilor expuse la foc*.

[3] C.E.C. Agreement Number N° 7210-SA/502, *Computer assisted analysis cf the fire resistance of steel and composite concretesteelstructures (REFAO - CAFIR), Commission of the European Communities, Directorate-General, Science, Research and Development*, EUR 10828 EN, ECSC-EEC-EAEC, Brussels, Luxembourg, 1987.

[4] Flucuş I., Şerban M., – *Consideraţii privind comportarea şi protecţia la foc a construcţiilor şi instalaţiilor în contextul legislaţiei actuale în domeniul apărării împotriva incendiilor*, Editura Academica, Bucureşti, 2001.

[5] Skiner, D.M., *Determination of high temperature properties of steel*, BHP Technical bulletin, vol. 16, Melbourne research laboratories, 1992.

[6] Fouquet G., *Exemples d'application du DTU Feu – Acier pour justifier la stabilité au feu d'éléments de structure,* Construction métallique nr. 1, 1994.

[7] M. Konecki, M. Polka, *Extension of the Fire Zone Model with Some Detailed Mass and Heat Transfer*, *Journal of Applied Sciences Research*, 2009, pp. 212-220.

[8] M. J. Hurley, ASET-B: *Comparison of Model Predictions with Fullscale Test Data*, *Journal of Fire Protection Engineering*, Vol. 13, 2003, pp. 37-65.

[9] S. M. Olenik, D.J. Carpenter, *An Updated International Survey of Computer Models for Fire and Smoke, Journal of Fire Protection Engineering*, Vol. 13, 2003, pp. 87-110.

[10] www.nist.gov , *Fire Simulation and Research Software, "Users' Guide to FIRST*, A Comprehensive Single-Room Fire Model," NBSIR 87-3595.

[11] Zaharia R., Dubina D., Duma D., *Validarea unui model de calcul avansat pentru analiza structurilor solicitate la acţiunea focului, Realizări şi preocupari actuale în ingineria construcţiilor metalice, A XII-a Conferinţa Naţională de Construcţii Metalice*, Timişoara, 26-27 Noiembrie 2010, Editura Orizonturi Universitare, ISBN 978-973-638-464-6, 2010.

[12] Flucuş I., Şerban M., – *Consideraţii privind comportarea şi protecţia la foc a construcţiilor şi instalaţiilor în contextul legislaţiei actuale în domeniul apărării împotriva incendiilor*, Editura Academica, Bucureşti, 2001.

[13] M. Konecki, M. Polka, *Extension of the Fire Zone Model with Some Detailed Mass and Heat Transfer*, *Journal of Applied Sciences Research*, 2009, pp. 212-220.

The three different methods for simple definitions of coarse aggregate dimensions

Yasreen G. Suliman, Madzlan B. Napiah, Jr., and Ibrahim Kamaruddin

***Abstract*—** The function of coarse aggregate in the mix is to provide stability to the pavement due to their interlocking behavior between the particles. The shapes of coarse aggregate particles significantly influence their mechanical behavior, as well as the properties and performance of hot mixture asphalt. In order to get the coarse aggregate shape analysis based on length, width, and thickness, many different methods like two-dimension (2D) and manual measurements are normally used. However, this paper utilizes a CT scan machine to measure the shape of aggregate particles via three-dimensional (3D) analysis. In this study, three different methods are used to measure the coarse aggregate dimensions: Manual measurement (caliper), Microscopy measurement, and CT scan measurement. This is done to determine the accuracy and speed of each technique. The results of the three different methods are compared for different sizes of coarse aggregate which are retain on 20mm, 14mm, 10mm, and 5mm sieve size. Pertinent statistical analysis and detailed comparison of the three methods indicates no significant differences between the three methods. They are thus complementary for use. A noticeable drawback of the microscope method is the limitation for the size of coarse aggregate to be measured. The microscope can only capture the full picture for some of 5mm sieves sizes. Bigger than 5mm size, 2 or three captured pictures are required to measure one dimension. The tasking nature of the Manual measurements procedure hinders its utilization for quality control of aggregates on the hot mix asphalt paving construction on a daily basis.

***Keywords*—** Coarse aggregate, manual measurement, microscopy measurement, CT scan measurement.

I. Introduction

HOT mixture asphalt (HMA) pavement has been found as an alternative, to prevent premature failure. Aggregates are granular mineral particles which account for 90–95% of asphaltic mixture by weight and 75-85% of asphaltic mixture by volume [1].

Aggregates are used in a number of different ways in highway construction. In all cases the aggregate used should be strong, tough, durable, and has the ability to be crushed into bulky particles without many flaky particles. The function of coarse aggregate in the mix is to provide stability to the pavement due to the interlocking behavior between the coarse particles. One of major requirements for coarse aggregates used in bituminous mix is the gradation of the material. Good distribution of aggregate could give a strong mixture that reflects on better fatigue resistance [2].

The physical characteristics of aggregate (shape and surface texture) have been found to affect the workability and optimum bitumen content of the mixture. They also affect the asphalt mixture properties and its performance [3], [4], and [5]. A classification of the aggregate shape used in USA is as follows; well-rounded, rounded, sub-rounded, sub-angular and angular [3]. It had been found that grading, shape and surface texture of mineral aggregate affect stiffness of the mixture. The angular particle provides better interlocking property than rounded particles and rough surface of aggregate provides a greater bonding strength with asphalt cement and gives better frictional resistance between particles. This resulted in greater mechanical stability which reflects on the better rutting resistance [6], [7].

Particle shape has an effect on the strength of the aggregate particles; on the bond with cementing materials; and on the resistance to sliding of one particle over another. Atkins [8] found that flat particles, thin particles and needle shaped particles break more easily than cubical particles. Angular particles with rough fractured face allow a better bond with cements than do rounded and smooth gravel particles. Rounded particles provide better workability during compaction but tend to continue to compact under traffic loading due to lack of interlocking property. While angular particles give the asphalt mix a harder consistency making it more difficult to handle and compact. On the other hand it provides a better interlocking than rounded particles [1]. One investigation carried by Janoo et al. [9] found that angularity shape is important not only on the surface layer but they also have significant effect on the base course layer. Another study by Topal and Sengoz [3] found that aggregate shape has effects on the bituminous mixture workability and performance. It was also observed that particle shape has an effect on the air voids content in the mixture.

Some of the researchers noted that shape and surface texture of fine aggregate can affect the workability and optimum

This work was supported by Universiti Teknologi PETRONAS. The authors would like to express their thanks to civil department in Universiti Teknologi PETRONAS for helping in conducting the experiments in their well equipped laboratory

S. G. Yasreen is with the Civil Engineering Department, Universiti Teknologi PETRONAS, Seri Iskandar, 31750, Tronoh, Perak Malaysia (e-mail: yasreen80@yahoo.com or neersay@yahoo.com).

N. B. Madzlan is with the Civil Engineering Department,Universiti Teknologi PETRONAS, Seri Iskandar, 31750 Tronoh, Perak Malaysia (e-mail: madzlan_napiah@petronas.com.my).

K. Ibrahim is with the Civil Engineering Department, Universiti Teknologi PETRONAS, Seri Iskandar, 31750 Tronoh, Perak Malaysia (e-mail: ibrakam@petronas.com.my).

asphalt cement content of the mixture, as well as the asphalt mixture properties. These include stability, air voids in the mixture, and durability [1], [3], and [6].

In wide-ranging shape, angularity and surface texture of aggregates have been shown to directly affect the engineering properties of highway construction materials such as hot mix asphalt concrete, Portland cement concrete, and unbound aggregate layers.

In general, it is preferable to have somewhat equi dimensional rather than flat, thin or elongated particles. The amount of flat and elongated particles in coarse aggregate samples can be determined following ASTM D4791 [10], using a proportional caliper device. To date, no ASTM standard test is available for accurately and rapidly quantifying the shape of aggregates while it is also very important. There are some methods that can be used to measure the aggregate dimensions:

1) Manual measurements (a calliper device). The tasking nature of this procedure hinders its utilization for quality control of aggregates on the hot mix asphalt paving construction on a daily basis.
2) Digital image analysis facilitates rapid measurement of particle characteristics. Numerous researchers have demonstrated the feasibility of using an image analysis system to measure and characterize particles [11]. Image analysis techniques often analyze particles as 2-dimensional objects since only the two-dimensional projection of the particles are captured and measured.
3) Three-dimensional analysis of aggregate particles via 2 cameras is used as in [11].

II. Problem Formulation

Presently, measuring the aggregate dimensions poses unique challenges to engineers. This is due to the tedious nature of many existing techniques. To date there is no standard procedure for accurately and rapidly quantifying the shape of aggregates, which is very essential.

III. Problem Solution

The main objective of this study is to determine the capability of the CT scan machine for measuring the coarse aggregate dimensions. Similarly, this study aims to establish the proper and faster method of measurement among the three methods, to be used in general framework.

IV. METHODOLOGY

The methodology of this study is defined in several steps as follow:

A. Prepare Coarse Aggregate

Coarse aggregate (granite) was washed, dried, and sieved to the single size (retained on 20mm, 14mm, 10mm and 5mm sieve size). This is based on the Malaysian standard specification Jabatan Kerja Raya (JKR) [12]. After preparing the coarse aggregate, the three different methods of measuring the coarse aggregate dimension were applied.

B. Manual Measurement (calliper)

Manual measurements using a digital slide calliper device is a tedious procedure. As mentioned earlier, the tasking nature of this procedure hinders its utilization for quality control of aggregates on the hot mix asphalt paving construction on a daily basis. An alternative method which permits rapid measurements of particle shape is essential for good quality control of aggregates. The calliper used to measure the aggregate dimensions manually is shown in Fig. 1.

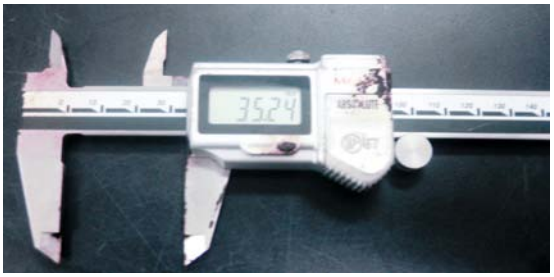

Fig. 1 digital slide calliper

C. Microscopy measurement (2D)

Usually, image analysis techniques treat particles as 2-dimensional objects since only the two-dimensional projection of the particles is captured. Based on the layout of the particle, the two dimensions can be length and width for the first captured image, and then when the second image is captured, the third dimension which is thickness can be measured. The microscope is attached with the computer with the software to show the captured picture and to measure the dimension on the picture as shown in Fig. 2. In this method the full picture capture for the whole particle cannot be obtained because of the limitation of the microscope`s lens. Consequently, the aggregate which has length exceeding 5mm cannot be fully captured. Therefore to get the length of the particle, 2 or 3 pictures need to be captured. This explains why this method is not practical.

Fig. 2 microscopy measurement

D. CT scan measurement (3D)

In this study, three-dimensional analysis of aggregate particles was performed using the CT scan machine as shown in Fig. 3. The particle was placed into a circular plate and the plate was rotated to position the particle properly to enable the device capture one full 3D image. With the aid of the component software, the CT scan machine can measure the

ISBN: 978-1-61804-219-4

long, intermediate, and short particle dimensions (d_L, d_w, and d_t) and based on them, the measurement of the flatness and elongation of the particles can be obtained. Besides flatness and elongation, some other shape factors can also be measured which can be used to better characterize the 3-D shape of particles such as roundness, sphericity and shape factor. Aggregate particles are three-dimensional in nature. Information about the three dimensions of a particle such as long, intermediate, and short particle dimensions (d_L, d_w, and d_t respectively), which can be obtained using one of the three methods illustrated above, is thus essential for proper characterization of the particle.

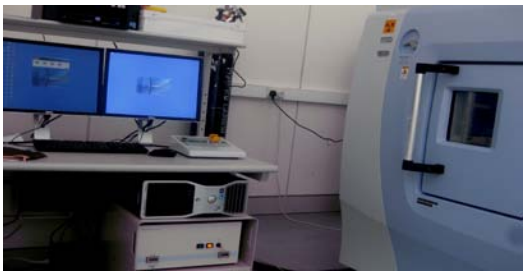

Fig. 3 CT scan measurement

Depending on the general particle characteristics, measurements of the characteristics of few particles i.e. 213 can provide statistically valid information about the size and shape of the particles in a sample. Based on these measurements, the following shape factors can be calculated as cited in [11]:

- Elongation: Elongation is the ratio of longest dimension (d_L) to intermediate dimension (d_w) of a particle.
- Flatness: Flatness is the ratio of intermediate dimension (d_w) to shortest dimension (d_t) of a particle.
- Sphericity applies to coarse aggregate sizes and describes the overall 3-dimensional shape of a particle calculated with equation 1 below. Sphericity has a relative scale of 0 to 1. sphericity value of one (1) indicates a particle has equal dimensions (cubical). The value of sphericity is expressed as Refer to "(1),":

$$Sp = \sqrt[3]{\frac{d_t \times d_w}{{d_L}^2}} \qquad (1)$$

- Shape Factor: Shape Factor, SF, is given as Refer to "(2),":

(1)

$$SF = \frac{d_t}{\sqrt{d_w \times d_L}} \qquad (2)$$

V. RESULTS AND DISCUSSION

A. Manual measurement (calliper)

The results obtained from manual measurement using the digital slide caliper as shown in Fig. 4, are obtained from 100 different particles for aggregate size retain on 5mm, 10mm, 14mm and 20mm sieve size. The results of the three dimensions which are length, width, and thickness for particles are listed in Table 1 for 5mm, 10mm, 14mm and 20mm respectively. The comparison between the other methods was carried out based on statistical analysis (Standard deviation and mean) for the length, width, and thickness for all four different particles sizes.

Fig. 4 example of manual

B. Microscopy measurement

The results obtained from microscopy measurement are obtained from thirteen different particles for each aggregate size (retain on 5mm, 10mm, 14mm and 20mm). The results of the three dimensions which are length, width, and thickness for each particle is measured as shown in Fig. 5 and nominated in Table 2 for 5mm, 10mm, 14mm and 20mm sieve size respectively. The comparison between the other methods was carried out based on statistical analysis (Standard deviation and mean) for the length, width, and thickness for all four different sizes.

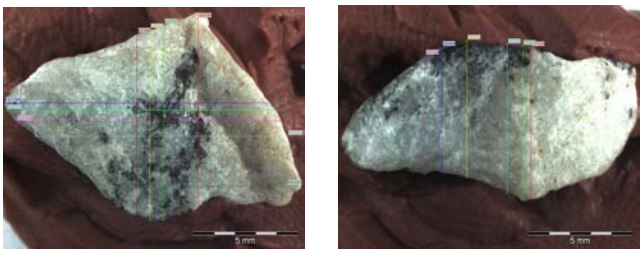

(a) (b)

Fig. 5 example of captured image of length and width (a) and thickness (b)

C. CT scan measurement

The result of the particle`s dimensions is obtained from one captured picture which is full 3D as shown in Fig. 6. A 100 different particles for aggregate size (retain on 5mm, 10mm, 14mm and 20mm sieve size) are used for CT scan measurement. The results of the three dimensions which are length, width, and thickness for particles are shown in Table 3 for 5mm, 10mm, 14mm and 20mm respectively. The comparison between the other methods was carried out based on statistical analysis (Standard deviation and mean) for the length, width, and thickness for all four different particles sizes. Results from microscopy and manual caliper measurements indicate that the CT scan method provides a very efficient and reliable means for measuring all three

particle dimensions simultaneously. Besides flatness and elongation, some other shape factors can also be measured that can be used to better characterize the 3D shape of particles such as sphericity and shape factor.

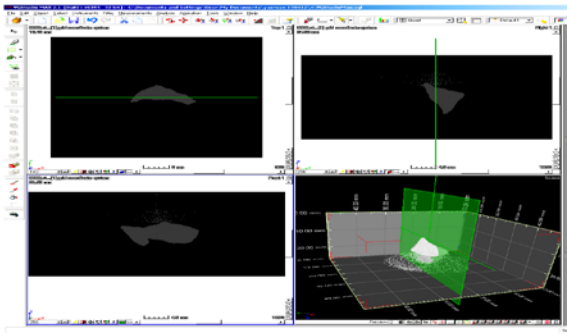

Fig. 6 example of 3D captured image of particles (length, width and thickness) in different section

D. Verification of CT scans Method

To verify the applicability of this proposed method, the measured dimensions of aggregate particles (d_L, d_w, and d_t) from the 3D (CT scan) image analysis method were compared with those from manual and microscopy methods. The three dimensions (d_L, d_w, and d_t) of 100 uniform size aggregate particles retain on 5mm, 10mm, 14mm and 20mm sieve, were measured manually using a calliper. The same particles were then measured using the proposed 3D (CT scan) image analysis method and 52 particles were measured using the microscopy method. The resolution of the image measurement for microscope was about 0.8 mm which was considered to be sufficient for aggregates of the size being examined.

Comparisons of the three dimensions (d_L, d_w, and d_t) determined using manual measurements, microscopy, and CT scan measurement are summarized in table 4, 5, 6, and 7 for coarse aggregate retain in 5mm, 10mm, 14mm, and 20mm sieve size respectively. From Table 4, the average values on the three dimensions (d_L, d_w, and d_t) of these 252 aggregate particles obtained from microscopy measurement, manual measurement and CT scan measurement are 5.154 mm versus 5.958 mm, versus 5.758mm, for the thickness and 14.954mm versus 17.238mm, versus 16.334mm for the length, and 9.554mm versus 10.827mm versus 10.445mm for the width respectively. These values for coarse aggregate retain on 5mm, the same trend it can be found in other coarse aggregate size (retain on 10mm, 14mm, and 20mm) as shown in table 5,6, and 7 respectively. The closeness between the three methods indicates that the proposed method (CT scan) is a good alternative to measure the dimensions of particles. Further, the Total time to perform the CT scan measurements was shorter compared with manual and microscope methods.

The average values of sphericity, elongation, flatness and Shape factor for this group of 252 particles obtained from microscopy, manual and CT scan measurements are 0.614mm versus 0.607mm, versus 0.618mm, for the sphericity and 1.585mm versus 1.610mm, versus 1.575mm for the elongation, and 2.144mm versus 2.112mm versus 2.057mm for the flatness and 0.452mm versus 0.450mm, versus 0.459mm for the shape factor respectively. These values for coarse aggregate retain on 5mm sieve size, the same trend it can be found in others coarse aggregate sizes (retain on 10mm, 14mm, and 20mm) as shown in Tables 5,6, and 7 respectively. Comparisons of sphericity, elongation, flatness and shape factor between manual measurements, microscopy measurement, and CT scan measurements shows that the proposed CT scan measurement method yields comparable results to those made using manual measurements and microscopy measurement.

ISBN: 978-1-61804-219-4

Table 1. dimensions of coarse aggregate retain on 5mm, 10mm, 14mm, and 20mm by using a digital slide calliper

	aggregate retain on 5 mm			aggregate retain on 10 mm			aggregate retain on 14 mm			aggregate retain on 20 mm		
No of sample	Thickness	Length	Width	Thickness	Length	Width	Thickness	Length	Width	Thickness	Length	Width
1	7.55	10.17	10.14	8.36	24.43	14.74	8.51	26.3	24.68	18.40	40.74	28.03
2	4.09	9.66	6.9	8.95	19.18	11.90	16.86	35.5	18.62	15.00	34.96	23.74
3	2.56	20.58	14.46	8.81	27.66	14.83	13.94	25.87	21.02	14.30	46.00	31.14
4	5.85	16.26	10.71	11.55	21.26	16.49	16.8	36.96	20.16	15.58	25.47	24.96
5	4.77	19.02	11.36	11.27	20.17	17.95	15.62	23.22	17.64	22.71	31.81	25.35
6	3.26	18.23	11.48	7.01	21.74	17.15	18.17	31.12	21.38	17.94	31.25	20.71
7	6.61	17.89	12.87	6.54	20.56	20.29	16.57	25.94	19.51	16.70	29.05	23.27
8	3.34	14	11.88	6.34	18.96	17.47	11.12	28.41	19.57	18.22	25.81	22.72
9	5.91	13.23	11.27	13.80	20.25	15.35	9.57	28.51	23.5	16.66	35.36	24.94
10	4.69	17	10.26	10.26	23.47	17.30	11.64	32.25	23.24	19.34	30.33	25.75
11	8.54	18.69	9.28	9.99	26.94	15.02	12.11	35.87	24.66	17.87	27.76	26.65
12	10.1	17.27	11.17	15.69	33.03	18.72	11.67	26.45	20.46	23.95	35.79	28.53
13	6.3	25.69	11.21	7.01	26.71	17.77	18.5	29.09	21.9	16.24	35.16	24.54

Table 2. dimension of coarse aggregate retain on 5mm, 10mm, 14mm, and 20mm by using microscop method

	aggregate retain on 5 mm			aggregate retain on 10 mm			aggregate retain on 14 mm			aggregate retain on 20 mm		
No of sample	Thickness	Length	Width	Thickness	Length	Width	Thickness	Length	Width	Thickness	Length	Width
1	5.6	8.3	6.9	8.12	23.8	14.5	7.7	24	23.6	18.3	40.2	26.5
2	4	9.1	6.4	8.5	18.1	12.1	16.4	32.6	17.6	16	34.3	21.85
3	2.9	18.4	11.9	8.5	26	14	12.3	25.5	20.3	14.4	46.2	31.2
4	6.9	14.9	8.8	12.4	20	15	18	33.3	20.2	15.4	24.7	24.3
5	4.4	16.1	10.2	12.8	19.4	17	14.5	21.8	16.6	20.8	31	20.8
6	2.9	17.5	9.5	6.4	20.7	15.1	16.9	28.6	21.1	18	28.6	20.5
7	6.1	15	12.2	5.2	19.2	17.1	16.4	23.2	17.3	14.2	28	19.9
8	2.7	12.7	11.6	5.8	19.9	16.7	10.7	28.2	19.3	17.3	26	21.5
9	5.4	11.6	9.8	11.5	18.6	14.9	8.6	27.9	22.7	15.6	34.8	20.9
10	4.7	15.1	9.1	8.8	22.7	15.9	12.8	31.2	22.7	18.3	29.1	23.1
11	6.4	16	8.7	10.3	25.2	13.7	10.9	34.7	24.1	18.2	25.8	23.4
12	9.5	15.4	10.6	14.2	32.2	18.9	12.3	24.5	22.1	20.7	34.5	27.2
13	5.5	24.3	8.5	6.4	24.8	15	17.7	25.7	18.7	16.5	32.1	23.1

Table 3. dimension of coarse aggregate retain on 5mm, 10mm, 14mm, and 20mm by using ct scan method

	aggregate retain on 5 mm			aggregate retain on 10 mm			aggregate retain on 14 mm			aggregate retain on 20 mm		
No of sample	Thickness	Length	Width	Thickness	Length	Width	Thickness	Length	Width	Thickness	Length	Width
1	6	9.06	7.32	8.22	23.36	13.76	8.81	26.81	23.86	18.44	40.73	27.53
2	3.79	9.05	7.42	9.14	18.98	11.76	16.82	33.99	17.7	15.03	35.04	23.24
3	2.87	19.69	12.93	8.7	26.8	14.58	13.39	24.68	20.69	14.44	46.17	30.09
4	6.12	15.37	10.48	13.4	21.28	15.64	17.15	34.92	19.58	15.26	24.95	24.08
5	4.51	17.96	11.9	12.24	19.31	17.77	16.96	22.83	18.17	20	31.83	21.78
6	3.03	18.13	10.67	6.9	21.41	16.99	18.14	31.82	20.7	16.06	29.58	20.41
7	6.56	17.66	13.18	5.75	20.6	18.21	15.1	24.43	17.88	16.47	28.3	20.96
8	3.39	14.87	11.35	6.26	20.48	16.99	12.3	27.89	18.9	16.03	25.09	21.95
9	5.74	11.4	9.55	13.85	20	15.3	8.62	28.03	22.15	16.51	35.64	24.03
10	4.79	16.52	10.36	9.33	23.3	15.89	11.5	32.19	23.68	19.82	29.37	22.93
11	8.01	16.46	8.9	9.56	25.29	14.33	10.87	35.5	23.72	16.58	26.18	26.05
12	8.03	15.58	10.32	14.81	32.7	18.58	10.27	24.72	21.85	20.42	35.36	26.82
13	5.06	25.45	11.17	7.27	25.33	16.93	17.77	28.24	24.89	16.23	34.32	22.25

ISBN: 978-1-61804-219-4

Table 4. the average value on the three dimensions (d_L, d_w, and d_t) sphericity elongation, flatness, and shape factor for the three methods for coarse aggregate 5mm sieve size

Methods used in this study	Thickness	Length	Width	Sphericity	Elongation	Flatness	Shape factor
Microscopy measurement	5.154	14.954	9.554	0.614	1.585	2.144	0.452
Manual measurement	5.958	17.238	10.827	0.607	1.610	2.112	0.450
CT scan measurement	5.758	16.334	10.445	0.618	1.575	2.057	0.459

Table 5. the average value on the three dimensions (d_L, d_w, and d_t) sphericity elongation, flatness, and shape factor for the three methods for coarse aggregate 10mm sieve size

Methods used in this study	Thickness	Length	Width	Sphericity	Elongation	Flatness	Shape factor
Microscopy measurement	9.148	22.354	15.377	0.655	1.464	1.848	0.497
Manual measurement	9.766	23.882	15.926	0.655	1.514	1.762	0.514
CT scan measurement	9.421	23.147	15.59	0.657	1.509	1.787	0.509

Table 6. the average value on the three dimensions (d_L, d_w, and d_t) sphericity elongation, flatness, and shape factor for the three methods for coarse aggregate 14mm sieve size

Methods used in this study	Thickness	Length	Width	Sphericity	Elongation	Flatness	Shape factor
Microscopy measurement	13.477	27.785	20.485	0.708	1.367	1.665	0.577
Manual measurement	14.309	30.811	21.606	0.693	1.442	1.661	0.566
CT scan measurement	13.717	29.873	20.786	0.693	1.455	1.652	0.564

Table 7. the average value on the three dimensions (d_L, d_w, and d_t) sphericity elongation, flatness, and shape factor for the three methods for coarse aggregate 20mm sieve size

Methods used in this study	Thickness	Length	Width	Sphericity	Elongation	Flatness	Shape factor
Microscopy measurement	17.208	31.946	23.404	0.742	1.367	1.38	0.643
Manual measurement	18.228	33.704	24.911	0.742	1.359	1.392	0.636
CT scan measurement	17.214	32.658	23.555	0.731	1.391	1.394	0.630

The results are also analyzed based on the standard deviation and the mean for all the coarse aggregate length, width, and thickness for all the aggregate sizes and all the three methods as refer to (3), (4):

$$S_d = \sqrt{\frac{S_1^2}{n_1} + \frac{S_2^2}{n_2}} \quad (3)$$

$$\Delta = \left|\overline{u_1} - \overline{u_2}\right| \quad (4)$$

Where the S_d is the average standard deviation for the parameter of the two methods. i.e. (standard deviation for length by calliper + length by microscopy); S is the standard deviation for one parameter for one method i.e. (standard deviation for length by calliper), n is the number of samples; Δ is the difference between the two means; u is the mean of the one parameter for the one method (mean of the length by calliper). After the S_d and Δ are obtained the correlation of Δ vs. S_d *95% confidence interval is found for all the parameter (length, width, and thickness) for the four different sizes. If the Δ is smaller than the S_d *1.96 (95% confidence interval), that means there is no significant different between the methods. An example is shown below which is done based on values included in Table 8:

$$Sd_{ca,m} = \sqrt{\frac{(4.29233)^2}{13} + \frac{(4.11514)^2}{13}} = 1.649 * 1.96 = 3.232$$

$$\Delta = \left|16.7454 - 14.9538\right| = 1.792$$

As a result 1.792<3.232, which means there is no significant difference between the caliper method and microscope method. Again this correlation is used for comparing the

standard deviation and the difference of the mean between the CT scan method and microscope method and between the caliper method and CT scan method.

Table 8. Descriptive Statistics

Type of Method	Mean	Std. Deviation	N
Length_Calliper	16.7454	4.29233	13
Length_Microscop	14.9538	4.11514	13
Length_CTscan	15.9385	4.41552	13

All the results from the comparison between the three methods showed that there is no significant difference between the three methods. However there are two parameters that did not satisfy the above correlation which are the standard deviation for the calliper and CT scan for width for 20mm sieve size and the standard deviation for the calliper and microscope for width for 5 mm sieve size.

E. Application of Proposed Method:

In this section, the results obtained by applying the proposed CT scan method for three-dimensional analysis of aggregates on standard size retain on 5mm, 10mm, 14mm, and 20mm sieve size. Table 9 below summarizes the results of three dimensions (d_L, d_w, d_t), and other shape parameters of aggregate particles for coarse aggregate retain on 5mm sieve size. For the application of the CT scan method, three or four different sources of the aggregate (granite) will be measured and their dimensions and other shape factors will be compared with these results. Table 9 also summarizes the results of other shape indices such as sphericity, shape factor, and roundness.

Sphericity and shape factor utilize information for all three dimensions (dL, dw, dt) and give a general expression of the "sphericity" of particles.. Roundness utilizes information of area and perimeter from projected images and gives a combined expression for the "shape" and "surface texture" of particles. Particles that have rough surfaces will have larger values of roundness. Clearly, quantified measurements of this type of shape parameters could be correlated against laboratory and field measurement of performance.

I. CONCLUSIONS & FUTURE DIRECTIONS

Based on the results obtained from the three methods, it was found that there is no significant difference between the three methods and they are complementary for use. The manual measurement using the caliper also can be used, but it is a complex method and time consuming. The microscopy method is also a time consuming because it provides only two dimensions. The third dimension requires another picture acquisition. In addition, for one particle you have to take two or three images to get one full dimension of particle.

The results of the study described herein demonstrate that the CT scan method is a promising method for three-dimensional analysis of aggregate particles. This method not only provides an efficient means to measure elongation and flatness, but also provides a more-comprehensive and quantitative means for characterizing morphological characteristics of aggregate particles. These investigations attest to the desirability of adopting the image from CT scan as a useful tool for quantifying morphological characteristics of aggregate particles.

Table 9 .Summary of the 3D (CT scan) of the coarse aggregate retain on 5mm sieve size.

No of sample	Thickness	Length	Width	Roundness	Sphericity	Elongation	Flatness	Shape factor
1	6	9.06	7.32	0.3	0.812	1.238	1.220	0.737
2	3.79	9.05	7.42	0.3	0.700	1.220	1.958	0.463
3	2.87	19.69	12.93	0.1	0.457	1.523	4.505	0.180
4	6.12	15.37	10.48	0.1	0.648	1.467	1.712	0.482
5	4.51	17.96	11.9	0.3	0.550	1.509	2.639	0.308
6	3.03	18.13	10.67	0.3	0.462	1.699	3.521	0.218
7	6.56	17.66	13.18	0.3	0.652	1.340	2.009	0.430
8	3.39	14.87	11.35	0.5	0.558	1.310	3.348	0.261
9	5.74	11.4	9.55	0.3	0.750	1.194	1.664	0.550
10	4.79	16.52	10.36	0.1	0.567	1.595	2.163	0.366
11	8.01	16.46	8.9	0.1	0.641	1.849	1.111	0.662
12	8.03	15.58	10.32	0.1	0.699	1.510	1.285	0.633
13	5.06	25.45	11.17	0.3	0.444	2.278	2.208	0.300
14	8.62	22.4	9.1	0.5	0.539	2.462	1.056	0.604
15	7	11.81	9.83	0.5	0.790	1.201	1.404	0.650
16	8.76	13.46	11.2	0.3	0.815	1.202	1.279	0.713
17	3.74	12.67	10	0.5	0.615	1.267	2.674	0.332
18	5.5	21.75	9.84	0.5	0.485	2.210	1.789	0.376
19	3.7	17.7	12.18	0.1	0.524	1.453	3.292	0.252
20	8.76	17.74	11.25	0.5	0.679	1.577	1.284	0.620
23	5.19	13.24	10.37	0.3	0.675	1.277	1.998	0.443
32	4.52	18.1	14.29	0.5	0.582	1.267	3.162	0.281
33	7.99	22.62	8.93	0.1	0.519	2.533	1.118	0.562
35	5.95	15.8	9.49	0.3	0.609	1.665	1.595	0.486
36	6.31	13.85	9.1	0.3	0.669	1.522	1.442	0.562

ISBN: 978-1-61804-219-4

ACKNOWLEDGMENT

The authors would like to express their thanks to supervisors and civil department in Universiti Teknologi PETRONAS.

REFERENCES

[1] Topal, A. and Sengoz, B., "Evaluations of Compacted Aggregate Resistant Test Compared with the Fine Aggregate Angularity Standards", *Science Direct Journal of Construction and Building Materials*, 2006, pp. 1-6.

[2] Asi, I.M., "Laboratory Comparison Study For the Use of Stone Matrix Asphalt in Hot Weather Climates", *Science Direct Journal of Construction and Building Materials*, Vol. 20, 2006, pp. 982–989.

[3] Topal, A. and Sengoz, B., "Determination of Fine Aggregate Angularity in Relation with the Resistance to Rutting of Hot-Mix Asphalt", *Science Direct Journal of Construction and Building Materials*, Vol. 19, 2005, pp. 155-163

[4] Eyad, M., Dana, O., Thomas, W. and Laith, T., "Correlation of Fine Aggregate Imaging Shape Indices with Asphalt Mixture Performance", *Journal of Transportation Research Record* ISSN 0361-1981, Annual Meeting of the Transportation Research Board No. 80, Washington, 2001, pp. 148-156.

[5] Chapuis, R.P., and Legare, P.P., "A Simple Method for Determining the Surface Area of Fine Aggregate and Filler in Bituminous Mixtures, Effect of Aggregates and Mineral Filler on Asphalt Mixture Performance", ASTM STP 1147, *American Society for Testing and Materials*, Philadelphia, 1992.

[6] Choyce, P.W., "HRA Wearing Course Containing Crushed Rock Fine Aggregate", *Journal of Highways and Transportation*, Institution of Highways and Transportation.

[7] Shen, D.H., Wu, C.M. and Du, J.C., "Performance Evaluation of Porous Asphalt with Granulated Synthetic Light Weight Aggregate", *Science Direct Journal of Construction and Building Materials*, 2007, pp. 1-9.

[8] Atkins, H.N., "Highway Materials Soils and Concretes", Prentice Hall, Fourth edition, 2003.

[9] Janoo, V., Bayer Jr, J.J. and Benda, C.C., "Effect of Aggregate Angularity on Base Material Properties", *Journal of Materials in Civil Engineering*, Nov-Dec. 2004, pp. 614-622.

[10] ASTM, *(1995)*, "Standard Test Method for Flat Particles, Elongated Particles, or Flatand Elongated Particles in Course Aggregate", D 4791-*95*, ASTM, Philadelphia, PA.

[11] J. D. FROST AND J. S. LAI "Digital Analysis of Aggregate Particle Shape**"** School of Civil and Environmental EngineeringGeorgia Institute of Technology Atlanta, Georgia, USA.

[12] Flexible Pavement, "Standard Specification for Road Works", Malaysia: Jabatan Kerja Raya, 1988, pp.

G. Yasreen, Sudan 1980. B.Sc Honours 2-1 in Civil Engineering, and Diploma in Architecture, Faculty of Engineering & Architecture, University of sudan, Sudan university of science & technology, Khartoum State, Sudan, 2001-2006. M.Sc in Civil Engineering, Thesis title: The Performance of Conventional and Polymer Modified Bituminous Mixture Containing Different Types of Sand as Fine Aggregate, Universiti Teknologi PETRONAS Perak, Malaysia 2007-2009. Currently PhD candidate in Civil Engineering, Thesis title: The new design method for best aggregate packing or interlocking mechanism, Universiti Teknologi PETRONAS Perak, Malaysia since 2010.

She published at; Langkawi, Malaysia 2nd European Asian Civil Engineering Forum (EACEF), APSEC 2009. 8th EASTS Surabaya organized by the eastern asia society for transportation studies, 2009. Washington, Transportation Research Board of the National Academies, July 26, 2011. Current research interest in aggregate interlocking or packing mechanism, and previous research interest in fine aggregate properties and polymer modified bitumen.

PhD candidate. Suliman.

A Study on the Influence of using Stress Relieving Feature on Reducing the Root Fillet Stress in Spur Gear

Nidal H. Abu-Hamdeh and Mohammad A. Alharthy

***Abstract*—**The aim of this study was to create stress relieving features to reduce the root fillet stress in spur gear. A pilot model was established to predict von Mises stress at the root fillet of the gear without holes and was used as a reference model. Finite element modeling was adopted using Abaqus® package. The predicted stresses were compared with stresses obtained by AGMA analytical solution. A good agreement was found in the comparison between the calculated and predicted stresses. Then, two other models, namely first model and second model, were built to investigate the effect of various hole parameters (number, diameter, location, angle). The first model was performed by creating hole/holes in the gear body. The second model was performed by creating hole/holes in the face/profile of the gear. The results obtained showed that increasing the diameter size of hole/holes resulted in higher percentage of stress reductions compared to the pilot case. Furthermore, increasing the number of holes resulted in higher percentage of stress reductions compared to the pilot case, but gear rigidity in this case was highly affected.

***Keywords*—** Gear; Stress reduction; Root fillet; Finite element.

I. Introduction

Gears are critical components in the rotating machinery industry. Various research methods; theoretical, numerical, and experimental, have been performed throughout the years regarding gears. One of the reasons why theoretical and numerical methods are preferred is because experimental testing can be particularly expensive. Thus, numerous mathematical models of gears have been developed for different purposes. Some investigators used the method of introducing stress risers to minimize the highest stress in the profile of the gear tooth. The method of hole drilling was tried by Hebbal et al. [1]. They used a two-dimensional finite element modeling of a gear drilled at each tooth centerline. They achieved a 20% reduction in the contact stresses, but they obtained a 139% increase in the bending stress and the maximum deflection increased by about 75%. A reduction of about 9% in the shear stresses was obtained by Wagaj and Kahraman [2] when drilling several holes in the gear profile. Wilcox and coleman [3] conducted a study using finite element modeling for the stress analysis of gear tooth and according to their obtained results they suggested a new formula to determine root stresses. Sayama et al. [4] conducted a study using finite element modeling for the analysis of thin rimmed gear stresses. Their empirically obtained results showed good agreement with their modeling. Elkholy [5] introduced a method to determine tooth load sharing especially for high contact ratio spur gearing. Mohanty [6] suggested an analytical method to calculate the individual tooth load during meshing cycle. He also referred to determination of the locations and sizes of contact zones along the path of contact for high contact ratio gearing. Fredette and Brown [7] used holes drilled across the entire tooth to find the overall effect of hole size and location on the critical stresses in the gear. A slight reduction in the root tensile stress produced a great increase in fatigue life. Litwin et al. [8] and Handschuh [9] applied finite element analysis on a loaded tooth to determine share load, real contact ratio, precision of motion and the stress analysis.

Moriwaki [10] developed a technique named Global Local Finite Element Analysis (GLFEM) and applied it to a gear tooth for its stress analysis. GLFEM is a numerical analysis technique that combines finite element solutions and the classical analytical ones on the basis of the energy principle. He realized that for doing the stress analysis of the gear using the finite element analysis, a load acts at a point on the tooth profile a fine subdivision is required at the applied load point. In GLFEM, no fine subdivision is required for the analysis. This method also guarantees an easy determination of the critical section. The application of finite element method for loaded tooth contact analyses (LTCA) was also performed by Chao and Baxter [11] and Drago and Uppaluri [12]. Chien-Hsing et al. [13] formed a batch module by taking gear systems as testing examples. A simple and practical method was developed, through which this module was enabled which would search for contact nodes and elements and also it would automatically define the contact surfaces for contact analysis. Spitas and Costopoulos [14] studied the idea of making spur gear teeth with circular profile at the root instead of the standard trochoidal root fillet and it was studied numerically using boundary element method. It was demonstrated that the novel circular design surpasses the existing trochoidal design

N. H. Abu-Hamdeh is with the Mechanical Engineering Department, Faculty of Engineering, King Abdulaziz University, P.O. Box 80204, Postal Code 21589, Jeddah, Saudi Arabia, (corresponding author, phone: +966545993930; fax: +966-2-6952181; e-mail: nabuhamdeh@kau.edu.sa / nidal@just.edu.jo).

M. A. Alharthy, was with the Mechanical Engineering Department, Faculty of Engineering, King Abdulaziz University, P.O. Box 80204, Postal Code 21589, Jeddah, Saudi Arabia (e-mail: maharthy@yahoo.com).

of the spur gear tooth fillet in terms of fatigue endurance without affecting the pitting resistance. Kapelevich and Kleiss [15] presented a different approach for the traditional gear design procedure. The approach was direct gear design and allowed analysis of an extensive range of parameters for all possible gear combinations in order to find the most suitable solution for a specific application. This optimum gear solution can exceed the limits of traditional rack generating methods of gear design. Direct gear design for asymmetric tooth profiles opens additional reserves for improvement of gear drives with unidirectional load cycles. Guigand and Icard [16] provided a method for simulating loaded face gear meshing. The method simulated the loaded behavior of face gear meshing and provided some results such as the instantaneous pressure distribution across the whole width of the teeth in contact and loaded transmission error. Beghini and Santus [17] proposed a simple method to minimize the peak to peak transmission error (PPTE) for a spur gear set. Their main goal was to develop a simple method for profile optimization in terms of PPTE, which was the main cause of whining noise in spur gears. Parker and Vijayakar [18] studied the dynamic response of a spur gear pair using a finite element/contact mechanics model. A semi-analytical model close to the tooth surface was matched to a finite element solution away from the tooth surface. Hiremagalur and Ravani [19] studied the effect of backup ratio in spur gear root stresses analysis and design. Backup ratio was considered significant to understand rim failures that start at the tooth root. In their study an analytical approach, based on theory of elasticity, was used to provide a computational formulation in spur gears for root stress calculations. Dally and Riley [20] tried to minimize the stress in a finite plate by drilling a hole in it. They optimized the hole profile for minimizing the photo elastic stress. They performed their study on both circular and square profiles. Yang [21] showed that similar stress reductions are possible in gears. His work was limited to hole placement in the region of relatively low stress of the bending gear tooth.

II. Modeling

Two arrangements of stress risers were adopted in this study. The first arrangement was obtained by creating circular hole/holes in the side of the gear. Different hole locations and hole diameters were examined. The second arrangement was obtained by creating circular hole/holes in a gear profile/face. Different locations and diameters of the holes with different depths were examined. The load was applied as a relative motion of 0.15° between the two gears. It was applied over the pitch diameter and distributed along the tooth face.

A. Pilot Model

A pilot model of two meshing gears was created using computer-aided design software (CAD) SolidWorks, then it was imported into Abaqus FEA software for set up and analysis. Gear was selected with twelve teeth, module of 5 mm, face width of 50 mm, pitch diameter of 60 mm and outside diameter of 70 mm. The material selected was steel (BS970-3 1991 080M40 (EN8)) with modulus of elasticity of 210 GPa and Poisson's ratio of 0.3 and the contact property has a tangential behavior with a coefficient of friction 0.2. The same material and properties were selected for the pinion. Model parameters defined as (d) the hole diameter, (θ) as the angle between the hole center to the Z-axis, and (center-to-center distance) as the distance between the gear center and the hole center as shown in Figure 1.

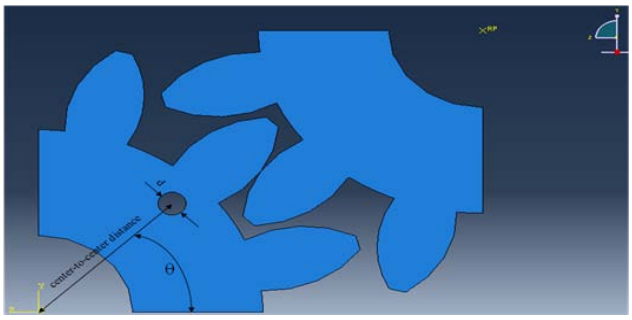

Fig. 1 model parameters used in this study

B. First Model

This model is similar to the pilot model but a circular hole in the side of the gear was created (Figure 2). Different hole diameters with different angles and different center-to-center distance for each diameter were tested. Two, three, and four holes on the side of the gear were also examined. The holes were created with different hole diameters, different angles from vertical and different distance between each hole center and gear center.

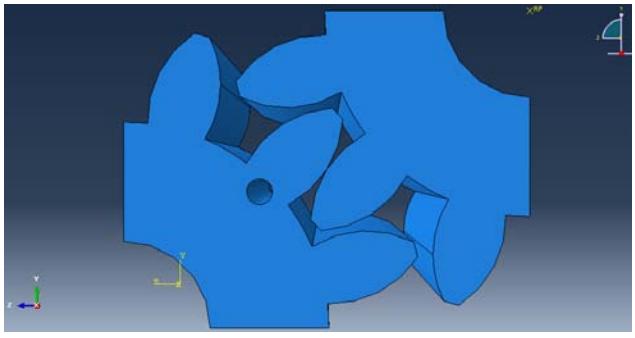

Fig. 2 first model with one hole of 3mm diameter,45° and 22.25 mm center-to-center distance

C. Second Model

This model is similar to the pilot model but circular hole/holes in the gear profile/face with different hole locations, diameters, and depths were examined (Figure 3).

D. Gear Modeling in Abaqus

Finite Element Analysis (FEA) is a numerical method to interpolate an approximate solution to a boundary value

problem. With the basic understanding of how finite element programs work, a finite element model must be created with

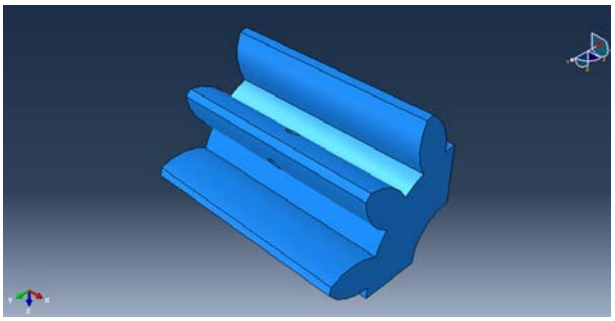

Fig. 3 second model with one hole of 3 mm diameter, the depth is through all, 30 mm center-to-center distance and 25 mm from gear edge

appropriate parameters such as dimensions, loads, constraints, element choice, mesh selection, etc. In a way, creating the finite element model is the most time consuming step of finite element analysis. Users should spend time to create the model as accurately as possible since geometry is one of the critical aspects in FEA. In Abaqus, there are two different methods to construct the model. The first method is to build the model in a computer-aided design (CAD) environment such as SolidWorks, Pro/ENGINEER, or CATIA, and export the model with a file format such as IGES, ACIS, or Parasolid. The file is then imported into Abaqus for set up and analysis. However, the main disadvantage for this method is the CAD geometry data could be lost during the translation of the model, which means the dimensions of the model are no longer exact. The second method is to use Abaqus' internal drawing capabilities to build the model. In this method, no geometry data is lost since the file does not need to be translated. However, the modeling functions in Abaqus are not as good as the other CAD programs; users often encounter difficulties for building complex models due to the interface limitations. It would be ideal if the models are built in a CAD environment and no geometry data are lost during translation. In this study, the first method was adopted by using SolidWorks design library (ANSI Metric).

A three dimensional "3D" quarter model was analyzed using Abaqus® FEA package. Driver gear was assumed infinitely rigid and Driven gear was assumed fixed and deformable. Four boundary conditions were applied. The first boundary condition (BC-1) was applied on a cutting area which is perpendicular and symmetrical on the Z-axis. The second boundary condition (BC-2) was applied on a cutting area which is perpendicular and symmetrical on the Y-axis. BC-3 was applied on an inner face of the gear hole and assumed pinned. BC-4 was applied on a reference point which is a pinion center with a rotating motion of -0.0026 radians.

The pilot and first models were meshed using global mesh size of 2 mm quadratic hexahedral 20-node brick elements with reduced integration type C3D20R, and with nodes spaced at a uniform radial distribution and refined in the holes vicinity. The second model was meshed using global mesh size of 1 mm and 10-noded quadratic tetrahedron elements type C3D10, and with nodes spaced at a uniform radial distribution and refined in the holes vicinity.

III. Results and Discussion

Initially, Von Mises stress at the root fillet was calculated using the gear rating calculation procedure specified in AGMA standards. The following input data for a standard spur gear were used in AGMA calculations; module of 5 mm, 12 teeth on pinion, 20° pressure angle, and 0.3 radius factor was considered for analysis. The gear material having modulus of elasticity equal to 2.1 X 10^5 N/mm^2 and Poisson's ratio equal to 0.3 were assumed in the analysis. The calculated Von Mises stress was obtained and found to be 157 MPa.

A. Pilot Model Results

The aim was mainly to establish a running model to be used as a reference model for this study. To verify the pilot model results, they were compared with results obtained from AGMA standard calculations. The input data for the pilot model were; 12 teeth with module of 5, face width 50 mm, pitch diameter of 60 mm and outside diameter of 70 mm. The material selected was steel with modulus of elasticity (E) of 210 GPa and Poisson's ratio of 0.3, the contact property has a tangential behavior with a coefficient of friction 0.2. The stresses obtained from the pilot model were found to be in close agreement with the calculated stresses based on AGMA standards for the specific geometric configuration of the gear. Therefore the results that follow are given more credibility.

B. First Model Results

In the one-hole case, several single hole arrangements were tested to determine the optimum hole position in the gear. The first set of tests was performed at 45° angle to find best center-to-center distance stress-wise. Figure 4 shows one example of this set where one hole with a diameter of 3 mm was used at 45° from horizontal and 30 mm between hole center and gear center. Stress obtained at the fillet was 189.1 MPa which is higher than pilot case (157 MPa). This means no improvement

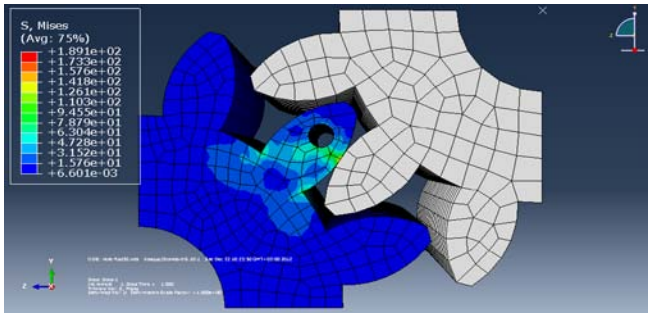

Fig. 4 maximum Von Misses stress obtained from first model of one hole, 30 mm center-to-center and 45°

was made using this arrangement. Figure 5 summarizes the stresses obtained at different center-to-center distance for this arrangement. The optimum case was found at 17 mm center-

to-center distance. The same procedure was repeated but at 30° and 60°, respectively. Figure 6 shows a comparison between stresses obtained for the same hole at 17 mm center-to-center distance at three angles (30°,45°,60°). The results obtained showed that the greater benefit reached when the hole was created at 45° and 60°.

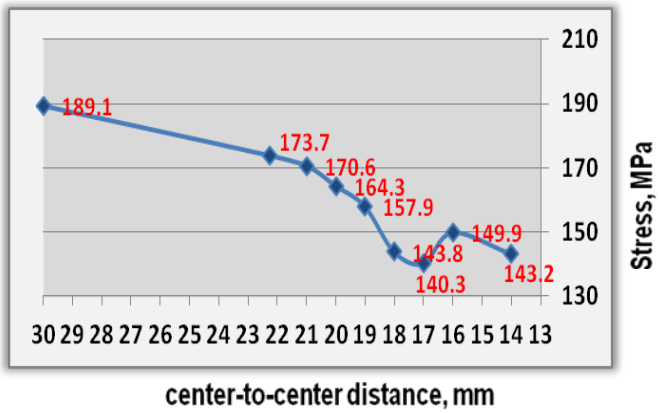

Fig. 5 maximum Von Misses stresses obtained from first model at different center-to-center distance (one hole and 45°)

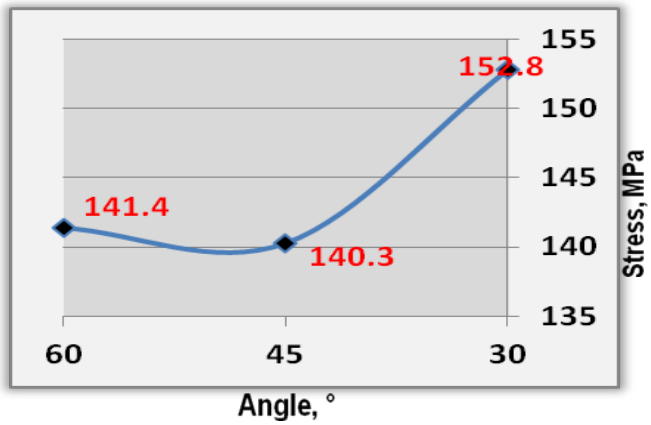

Fig. 6 maximum Von Misses stresses obtained from first model at different angles (one hole and 17 mm center-to-center distance)

The two-hole model consisted of two holes with radius 3 mm each oriented 30° and 60°, respectively, from the Z-axis and the distance between holes' center and gear's center was set at 20 mm as shown in Figure 7. The stress obtained was 127.7 MPa which is about 18.7 % reduction in Von Mises stress. Various arrangements were tested for this model including different diameters, orientation angles, and center-to-center distances for each hole. Some of the results obtained from this model for different combinations of two holes stress reliving features are shown in Figure 8. A maximum of 25% reduction in maximum Von Mises stress was obtained in this analysis.

In the three-hole model, different arrangements of three holes were examined. Figure 9 shows an example of this model. In this case, three holes with the same radius of 3 mm oriented at angles of 30°, 45° and 60°, respectively, from Z-axis. The distance between holes' center and gear center were set as 21, 26 and 21 mm, respectively. The stress obtained for this case was 108.2 MPa which yielded a 31.1 % reduction

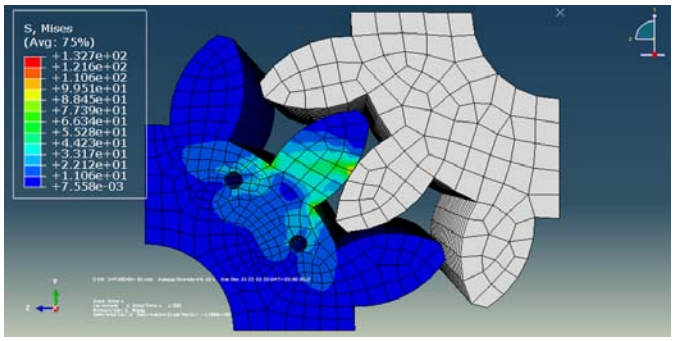

Fig. 7 first model results (two holes 3 mm diameter each / both at 20 mm center distance / oriented at 30° and 60°)

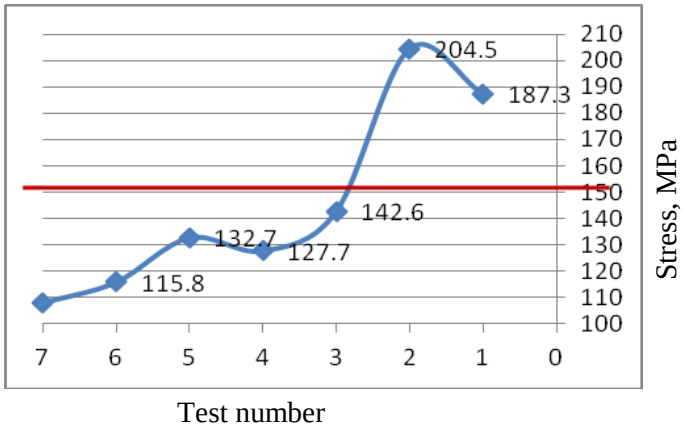

Fig. 8 some maximum Von Misses stresses obtained by applying first model with two holes

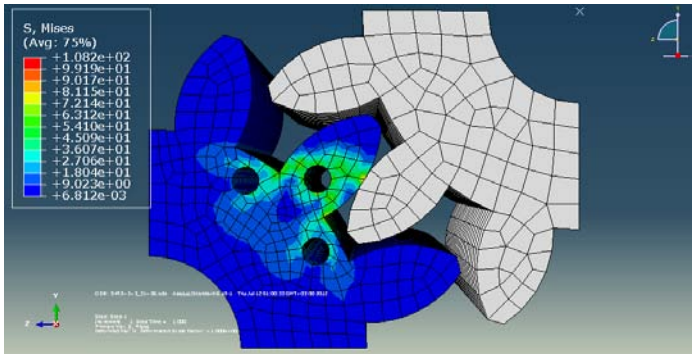

Fig. 9 first model result of maximum Von Misses stresses (three holes 3 mm diameter each / center distance at 21, 26 and 21 mm / oriented at 30°, 45° and 60°)

compared to the pilot case. Again, various arrangements were considered for analysis using this model including different diameters, orientation angles, and center-to-center distances

ISBN: 978-1-61804-219-4

for each hole. Some of the results obtained from this model are shown in Figure 10. It is noted that introduction of more than one stress relieving feature has added advantages.

In the four-hole arrangement, four holes examined with radii of 2, 2, 3 and 2 mm, respectively, oriented at 30°, 45°, 45° and 60° angle from Z-axis, respectively. The center distances were set at 20, 20, 26 and 20 mm, respectively, as shown in Figure 11. Stress reduction was observed and it was about 28% compared to the pilot case but the rim material in this case was much reduced which could affect the strength of the material.

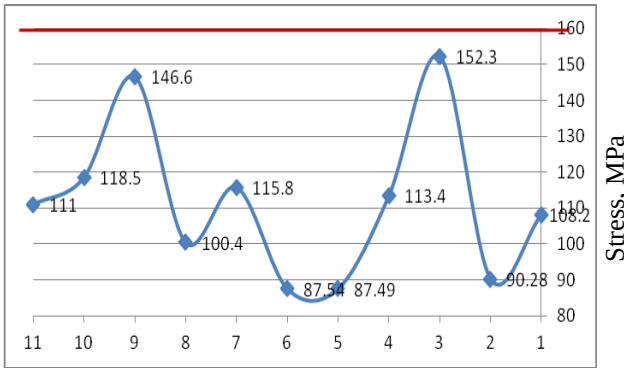

Fig. 10 some maximum Von Misses stresses obtained by applying first model with three holes

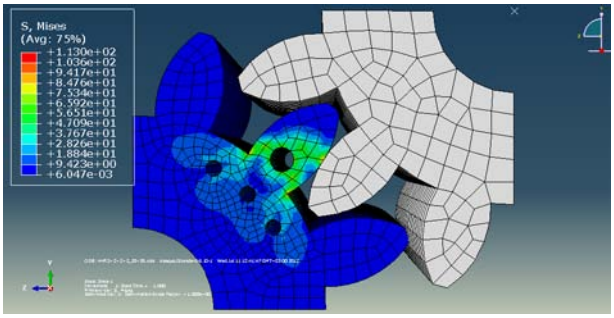

Fig. 11 first model result of maximum Von Misses stresses (four holes with radii 2, 2, 3 and 2 mm / 20, 20, 26 and 20 mm center distances/ oriented at 30°, 45°, 45° and 60° angles)

C. Second Model Results

In this model, circular hole/holes were examined in the gear profile/face using different hole location, diameter, and depth. Many simulation runs were executed to determine the optimum combination of hole location, diameter, and center distance. Mesh size of 1 mm was used in this model as a pilot case. The highest stress obtained was 881.4 MPa. The first simulation run was performed using one hole with a diameter of 3 mm and 30 mm center distance as shown in Figure 12. The stress obtained was 1098 MPa. This means no improvement was accomplished using this arrangement due to reduced contact area which resulted in greater stress. This means no benefits could be obtained from this arrangement.

IV. Conclusion

The aim of this study was to create stress relieving features to reduce the root fillet stress in spur gear. In addition to the

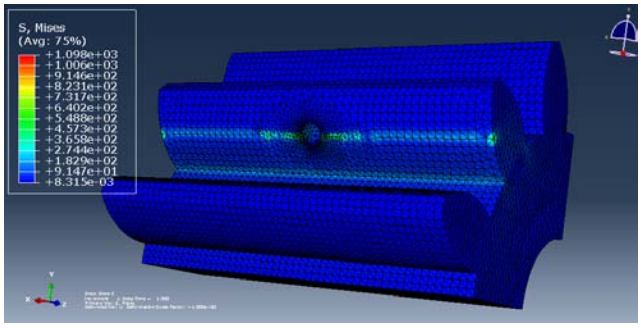

Fig. 12 second model results (one hole of 3 mm diameter/ 30 mm center distance / whole tooth simulated)

pilot model, two extra models implementing finite element simulation were used in this study. The first model was performed by creating hole/holes in the gear body with various diameters, various center distances, and various hole/holes orientation angles from Z-axis. Three cases were used in this model; one hole, two holes, and three holes. The second model was performed by creating hole/holes in the face/profile of the gear with various diameters and center distances. The finite element modeling was performed using Abaqus/CAE 6.10. Firstly, a pilot model with no holes created in the gear body was established to predict stresses at the root fillet of the gear and the results were compared with stresses obtained by AGMA analytical solution. A close agreement in stresses obtained analytically with those obtained from simulation was found. Consequently, the other two models were constructed to examine the effect of creating holes in the gear body as stress relieving features on root fillet stresses. For one hole case, it was found that the best results were obtained when one hole as a stress reliving feature was created at 60° angle from Z-axis. Furthermore, increasing the diameter of hole/holes resulted in higher percentage of stress reductions compared to the pilot case. For the two- and three-hole cases, increasing the number of holes resulted in higher percentage of stress reductions compared to the pilot case, but gear rigidity in this case was questionable. The second model did not produce any reduction of stresses in the root fillet area. On the contrary, stress increased because of the reduction in contact area.

References

[1] M. S. Hebbal, V. B. Math, B. G. Sheeparamatti., "A Study on Reducing the Root Fillet Stress in Spur Gear Using Internal Stress Relieving Feature of Different Shapes," *International Journal of Recent Trends in Engineering*, vol. 1, pp. 163-165, 2009.

[2] P. Wagaj, A. Kahraman., "Influence of Tooth Profile Modification on Helical Gear Durability," *Journal of Mechanical Design*, vol. 124, pp. 501-510, 2002.

[3] L. Wilcox, W. Coleman, "Application of Finite Element to the Analysis of Gear Tooth Stresses," *Journal of Engineering for Industry*, vol. 95, pp. 1139 -1148, 1973.

[4] T. Sayama, S. Oda, K. Umeezawa, "Root Stresses and Bending Fatigue Strength of Welded Structure Gears," presented at the 1981 International Symposium on Gearing & Power Transmissions, Japan, Tokyo.
[5] A. H. Elkholy, "Tooth Load Sharing in High Contact Ratio Spur Gears," *Journal of Mechanisms, Transmissions, and Automation in Design*, vol. 107, pp. 11-16, 1985.
[6] S. C. Mohanty, "Tooth Load Sharing and Contact Stress Analysis of High Contact Ratio Spur Gears in Mesh," presented in the 2002 National Convention of Mechanical Engineers, India, Roukela.
[7] L. Fredette, M. Brown, "Gear Stress Reduction Using Internal Stress Relief Features," *Journal of Mechanical Design*, vol. 119, pp. 518-521, 1997.
[8] J. Lu, F. L. Litwin, J. S. Chen, "Load share and Finite Element Stress Analysis for Double Circular-Arc Helical Gears," Mathematical and Computer Modeling, vol. 21, pp. 13-30, 1995.
[9] R. Handschuh, F. L. Litwin, "A Method of Determining Spiral Bevel Gear tooth Geometry for Finite Element Analysis," NASA TPP-3096m AVSCOM TR -C-020, 1991.
[10] I. Moriwaki, T. Fukuda, Y. Watabe, K. Saito, K., "Global Local Finite Element Method (GLFEM) in Gear Tooth Stress Analysis," Journal of Mechanical Design, vol. 115, pp. 1008-1012, 1993.
[11] H. C. Chao, M. Baxter, H. S. Cheng, "A Computer Solution for the Dynamic Load, Lubricant Film Thickness, and Surface Temperatures in Spiral Bevel Gears," in *Advanced Power Transmission Technology, NASA CP-2210, AVRADCOM TR-82-C-16*, 1981, pp. 345-364.
[12] R. J. Drago, B. R. Uppaluri, "Large Rotorcraft Transmission Technology Development Program," Technical Report (D210-11972- 1-VOL-1), Boeing Vertol Co., NASA Contract NAS3-22143) NASA CR-168116, 1983.
[13] L. Chien-Hsing, C. Hong-Shun, H. Chinghua, C. Yun-Yuan, Y. Cheng-Chung, "Integration of Finite Element Analysis and Optimum Design on Gear Systems," Finite Elements in Analysis and Design, vol. 38, pp. 179-192, 2002.
[14] V. Spitas, T. Costopoulos, C. Spitas, "Increasing the Strength of Standard Involute Gear Teeth with Novel Circular Root Fillet Design," *American Journal of Applied Sciences*, vol. 2, pp. 1058-1064, 2005.
[15] A. L. Kapelevich, R. E. Kleiss, "Direct Gear Design for Spur and Helical Involute Gears," Gear Technology, pp. 29-35, 2002.
[16] M. Guingand, J. P. de Vaujany, Y. Icard, "Analysis and Optimization of the Loaded Meshing of Face Gears," Journal of Mechanical Design, vol. 127, pp. 135-143, 2005.
[17] M. Beghini, F. Presicce, C. Santus, "A Method to Define Profile Modification of Spur Gear and Minimize the Transmission Error," American Gear Manufacturer's Association, Technical Paper, pp. 1-9, 2004.
[18] R. G. Parker, S. M. Vijayakar, T. Imajo, "Non-Linear Dynamic Response of a Spur Gear Pair: Modeling and Experimental Comparison," *Journal of Sound and Vibration*, vol. 237, pp. 433-455, 2000.
[19] J. Hiremagalur, B. Ravani, "Effect of Backup Ratio on Root Stresses in Spur Gear Design," *Mechanics Based Design of Structures and Machines*, vol. 32, pp. 423-440, 2004.
[20] J. W. Dally, W. F. Riley, *Experimental stress Analysis.* New York: McGraw-Hill, 1991.
[21] T. Y. Yang, *Finite Element Structural Analysis*. New York: Prentice-Hall, Englewood Cliffs, 1986.

Computing of Coronary Sinus Pressure performances - Best PICSO Approach

Loay Alzubaidi
College of Computer Engineering and Science
Prince Mohammad Bin Fahd University
Email: Lalzubaidi@pmu.edu.sa

***Abstract*—**Research has found out that PICSO, or else pressure-controlled intermittent coronary sinus occlusion, can considerably relieve myocardium (ischemic cardiac muscle). This is usually done by elevating the venous pressure. There are two mechanisms involved for this to succeed. One of the mechanisms is distention of the venous vessels, a process that induces mechanotransduction. The other mechanism is redistribution of the venous flow to ischemic areas. Mechanotransduction, which occurs in endothelial cells, usually causes changes in the ischemic heart that induce myocardial salvage and myocardial recovery. This is made possible as the results of myocardial deficits are blunted when coronary inflow is limited.

For these extreme side effects to be limited, a mathematical model was relied on to describe the change of the CSP (Coronary Sinus Pressure) during occlusion of the LAD (Left Anterior Descendant) and after reopening of the LAD. In this research paper, the rise and release times of diastolic and systolic plateaus of CSP are computed with use of an automatic computing module. A number of PICSO cycles during the study were computed and analyzed with cycles ranging from 5:3 seconds (inflation: deflation) to 12:8 seconds. The range was varied for the best PICSO cycle to be selected.

***Keywords*—**Coronary Sinus Pressure, Intermittent occlusion, Left Anterior Descendant, Mathematical model, PICSO.

I. Introduction

PISCO has been proposed and studied as a novel method in cardiac surgery and interventional cardiology to salvage myocardium's ischemic areas [1], [2]. The beneficial effects of PICSO as an intervention technique are closely related to an optimal timing of pressure elevation in the coronary venous [3]. As such, a mathematical model has been effectively relied on to put the estimation of release times and occlusion on a rather quantitative basis [4], [5], [6]. The model used comprises of two parts, that each have a three parameter duplicate exponential function[7],[8]. This can be computed as follows:

$$CSP(t) = \begin{cases} A*\exp\{B*[1-\exp(-C*t)]-1\} & when \quad 0 < t < T1 \\ D*\exp\{E*[1-\exp(-\frac{F}{t})]-1\} & when \quad T1 \le t < T2 \end{cases} \qquad (1)$$

Where:

CSP (t) = Coronary sinus pressure (mmHg)

t = Time (s)
T2 = Time – final point of CSP release (s)
T1= Time – final point of CSP occlusion (s)
C, F = Fitting parametric quantity (1/s)
B, E = Fitting parametric quantity (dimensionless)
A, D = Fitting parametric quantity in (mmHg)

The first part of the equation (1a) shows the CSP rise during occlusion (inflation) time.

$$CSP\ (t) = A*\exp\{B*[1-\exp(-C*t)]-1\} \qquad (1a)$$

As described in Fig. 1 below, systolic peaks increased and coincided with the times of the inflammation period. The second part of the equation (1b) shows release of CSP over the deflation period.

$$CSP\ (t) = D*\exp\{E*[1-\exp(-\frac{F}{t})]-1\} \qquad (1b)$$

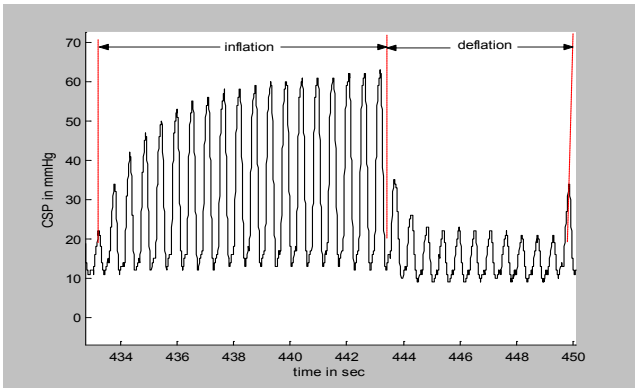

Fig. 1 PICSO cycle with Inflation: deflation time as 10:6 s

As shown in figure 1, the systolic peaks usually decremented and coincided with deflation period times. The diastolic and systolic peaks were matched with non-linear least square based algorithms.

II. METHOD

As the mathematical model equations 1a and 1b and their three parameters A,B,C and D,E,F represent systolic and diastolic (envelope curve) respectively, it can thereby be possible to show the time taken to realize the CSP plateau with

respect to fitted parameters[9],[10].

A. Inflation

The rise time of CSP plateau, was calculated with reliance on equation 1a. The highest level of the CSP (t) in equation 1a is realized when t → ∞ as follows

$$CSP_{(t\to\infty)} = A * \exp(B-1)$$

Since the plateau is not really realized as per mathematical terms, it is of uttermost importance to consider the time taken for it to reach 90 percent of the predicted plateau height. As such, the systolic plateau is 90 percent from the peak value of CSP like demonstrated in figure 2 below:

$$Systolic\ Plateau = 0.9 * A * \exp(B-1) \quad (2)$$

$$Rise\ Time = (1/C) * \ln(-B/\ln(0.9)) \quad (3)$$

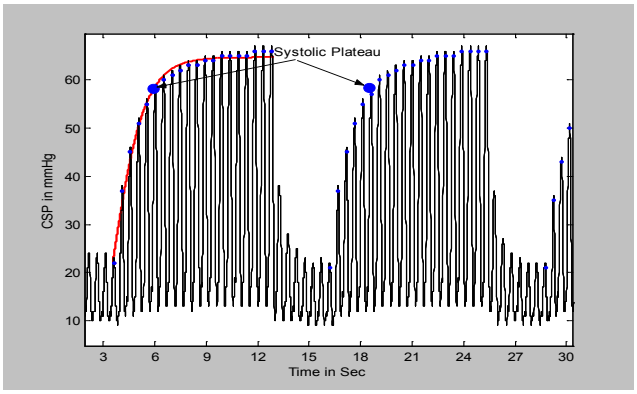

Fig. 2 Systolic Plateau of CSP over inflation

B. Deflation

The release time of the CSP plateau was calculated using equation 1b. The lowest CSP (t) value in equation 1b is realized when t→ ∞.

$$CSP_{(t\to\infty)} = D * \exp(-1)$$

Since a plateau is never actually reached it is meaningful to consider the Plateau is 110% of the predicted height plateau. The plateau is 110% from the lowest value of the CSP as shown in fig 3.

$$Plateau = 1.1 * D * \exp(-1) \quad (5)$$

$$Release\ Time = -F / \ln(1 - \ln(1.1)/E) \quad (6)$$

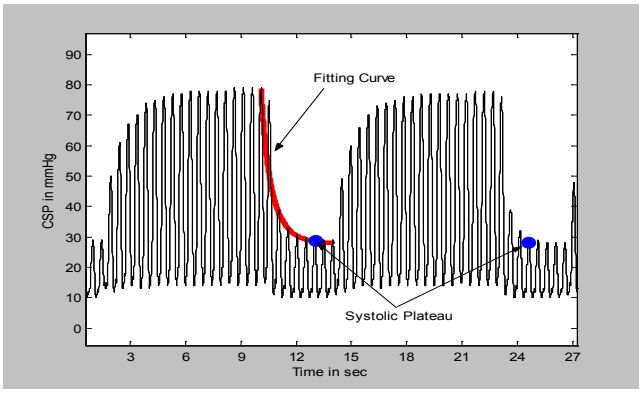

Fig. 3Systolic Plateau of CSP over deflation

III. RESULTS

The automatic computation module calculates the rise and release time of the CSP plateau over the LAD occlusion period and after the reopening of the LAD for 13 animals, basically dogs, pigs and sheep.

A. Automatic calculation of rise and release periods

The rise and release time can be defined as the time taken for the CSP to realize systolic or diastolic (plateau). This can be realized after a prolonged release or occlusion [11], [12]. Fig. 4 below shows the varying rise or inflation times needed to realize the systolic and diastolic plateau with respect to the LAD status of occlusion. During the rise period, the systolic plateau may be realized promptly as soon as the LAD opens.

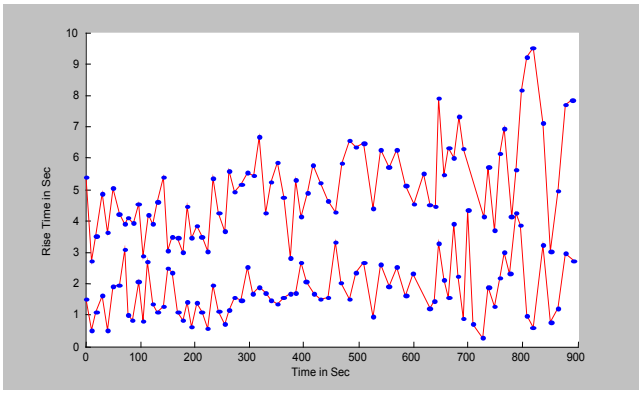

Fig. 4 Rise time for CSP plateaus during the inflation period

The static result of varying rise time over the inflation periods that depends on the opened or occluded LAD for systolic plateau can be demonstrate in fig. 5 below. In figure 5 below, the systolic plateau will be realized in 5.13 +/- 1.00 seconds by reperfusion early and in 5.31 +/- 1.00 seconds by reperfusion late. The systolic plateau will also be realized in 5.89 +/- 1.20 seconds by occluded early and in 5.80 +/- 1.10 seconds by occluded late. A one or two-way ANOVA was carried out to demonstrate the importance of the obvious variance between the LAD positions with respect to rise times. This confirmed that the importance of the difference is evident at $p<0.0083$.

ISBN: 978-1-61804-219-4

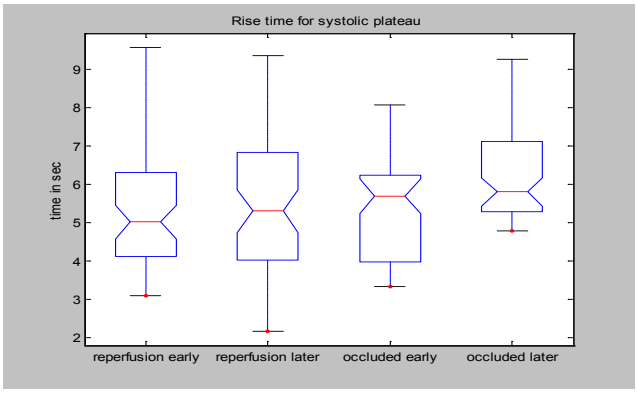

Fig. 5 Rise time to systolic plateau changes in dependence of LAD during the inflation period

The diastolic plateau is realized very promptly when LAD occluded, as demonstrated in figure 6 below. Figure 6 demonstrated the variance in rise time of the diastolic plateau. The diastolic plateau will be realized in 2.02 +/- 0.20 seconds by reperfusion early and in 2.00 +/- 0.50 seconds by reperfusion later. The diastolic plateau is also realized in 1.18 +/- 0.40 seconds by occluded early and in 1.62 +/- 0.20 seconds by occluded late. A significant variance at $p<0.0006$ in rise time over the assorted occlusions could be seen. The systolic plateau can be realized very fast over the deflation period when LAD opens.

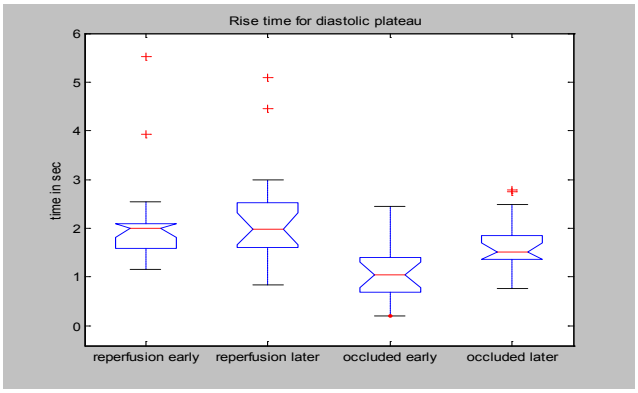

Fig. 6 Rise time to diastolic plateau changes in dependence of LAD during the inflation period

The static result of varying the release time over the deflation period with respect to the opened or occluded LAD for the systolic plateau is shown in figure 7 below. In figure 7 below, the systolic plateau will be realized in 2.46 +/- 0.40 seconds by reperfusion early and in 4.7 +/- 0.80 seconds by reperfusion late. It is also realized in 5.2.0 +/- 0.20 seconds by occluded early and in 5.20 +/- 0.40 seconds by occlude late. There is a significance difference observed at $p<2.1175e-012$ in release time over the assorted occlusion.

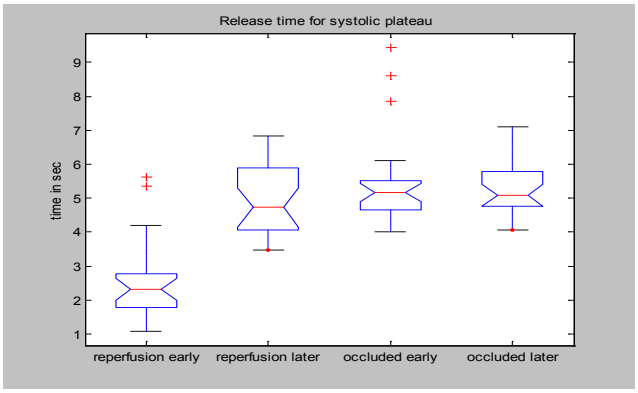

Fig. 7 Release time to systolic plateau changes in dependence of LAD during the deflation period

The diastolic plateau is realized very promptly when LAD opens. The figure 8 below demonstrates the variance of the release time of the diastolic plateau. The diastolic plateau will be realized in 1.21 +/- 0.10 seconds by reperfusion early and in 1.21 +/- 0.25 seconds by reperfusion late. It is also realized in 1.88 +/- 0.40seconds by occluded early and in 1.40 +/- 0.40 seconds by occluded late. A significant difference in release time can be seen at $p<1.0286e-008$.

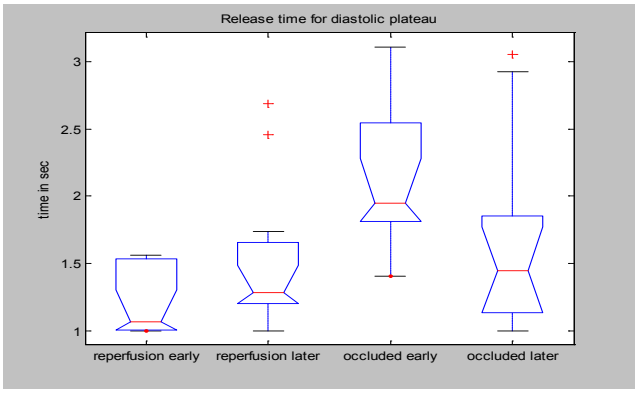

Fig. 8 Release time to diastolic plateau changes in dependence of LAD during the deflation period

B. Best PICSO

The best PICSO cycle can be defined as the cycle during which the ration of rise and release times to realize the CSP plateau is relatively equal to the ratio of inflation time and deflation time. This can be described as follows:

$$\frac{\text{Inflation time}}{\text{deflation time}} \approx \frac{\text{rise time}}{\text{release time}}$$

Over the experiment of various inflation and deflation times ranging from 5:3 seconds to 12:8 seconds, three PICSO type cycles were detected. The three are long PICSO, short PICSO and best PICSO. With respect to the short PICSO cycle, like seen in figure 9 below, the computed systolic plateau will be realized once the inflation period is over. This shows that the inflation time requires extension.

ISBN: 978-1-61804-219-4

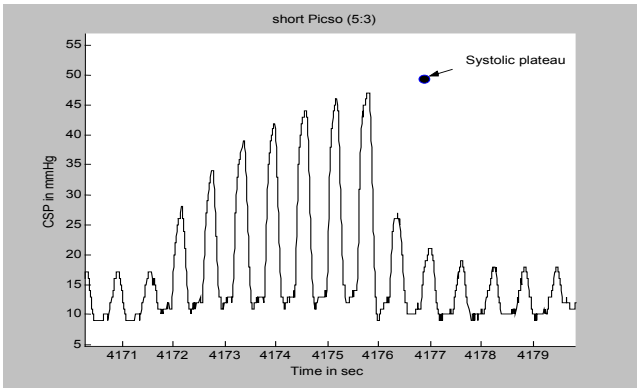

Fig. 9 Systolic plateau of short PICSO cycle

In the long PICSO cycle as demonstrated in figure 10, the computed systolic plateau can be reached before the inflation period ends. This shows that the inflation period should be curtailed.

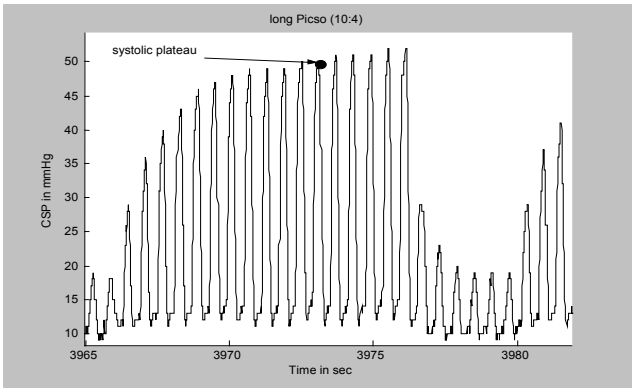

Fig. 10 Systolic plateau of long PICSO cycle

The computed plateaus are approximately realized in the best PICSO cycle when inflation and deflation periods end as demonstrated in figure 11 above.

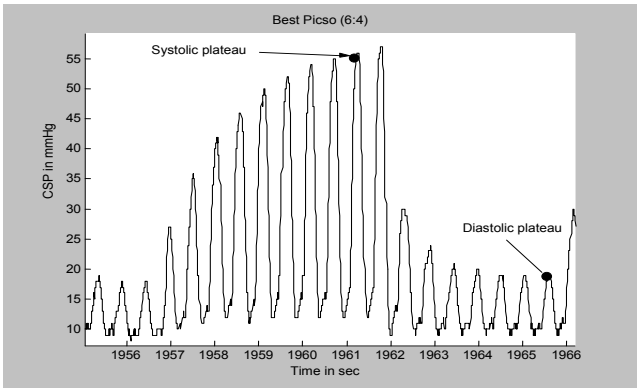

Fig. 11 Systolic plateau of BEST PICSO cycle

The table below demonstrates the different cycles, where the best PICSO delivered is at 6:4 seconds.

Table 1 Best PICSO cycle

Inflation : Deflation (sec)	Rise time (sec)	Release time (sec)	Cycle status
5:3	4.20	2.01	Short
6:3	3.98	2.38	Short
7:3	4.02	2.39	Short
8:3	5.32	2.01	Short
10:3	5.64	2.85	Short
12:3	5.99	2.85	Short
5:4	5.95	3.96	Long
6:4	5.78	3.74	Best
10:4	7.02	3.92	Short

IV. Conclusion

This work has a number of implications for bioinformatics. It provides the implementation of the mathematical model that describes the increment and decrement of the CSP during individual PICSO cycles significantly. The BEST PICSO was calculated in depend on the rise and the release time of the plateaus, with these times calculations we can set the PICSO device to the right inflation/deflation time. For the ONLINE measurement there are two possibilities to set the PICSO device, the first one is by running the device with constant inflation/deflation time (Ex. 5sec/3sec). During the test period (let say 5 PICSO), we calculate the rise and the release times and then adjust the PICSO devices in accordance with our new inflation/deflation times. The second method, which is more intelligent, needs neither a test period nor a constant time setting. With help of ONLINE prediction this method is able to calculate the plateaus and their rise and release time using the first 4-6 systolic peaks. With help of the extracted data we shall be able to determine the setting parameters (inflation/deflation parameters) on the PICSO device.

This research has various implications for bioinformatics. For instance, it offers implementation of a mathematical model that demonstrates increment and decrement of CSP over the individual PICSO cycles. As a matter of importance, the best PICSO cycle was computed with respect to the rise and release times of the specific plateaus. The PICSO device can be set to the right deflation or inflation times with use of these time computations.

Basically, there exist two possibilities of setting the PICSO device for an ONLINE measurement. One of the possibilities is to run the device using an invariable inflation/deflation time, for example 5seconds/3seconds. Over the test period, for example 5 PICSO, the rise and release times can be computed and the PICSO devices adjusted with respect to the novel inflation/deflation times. The second possibility does not require an invariable setting of time. This method, with the aid of an ONLINE prediction, is able to compute the plateaus and their rise/release times. This can be done with the use of the

ISBN: 978-1-61804-219-4

1st 4 to 6 systolic peaks. Once can be able to determine the inflation/deflation parameters on the PICSO device using the extracted data.

REFERENCES

[1] Mohl W, Gueggi M, Haberzeth K, Losert U, Pachinger O, Schabart A, Effects of intermittent coronary sinus occlusion (ICSO) on tissue parameters after ligation of LAD, Bibliotheca Anatomica 1980; PP. 517-521.

[2] Glogar D., Mohl W., Mayr H., Losert U., Sochor H., Wolner E. Pressure-controlled intermitent coronary sinus occlusion reduces myocardial necrosis (Abstract). Am J Cardiol 1982; 49: 1017.

[3] Schreiner W, Neumann F, Schuster J, Froehlich KC, Mohl W. Computation of derived diagnostic quantities during intermittent coronary sinus occlusion in dogs. Cardiovasc Res 1988; 22(4): 265-276.

[4] Schreiner W, Mohl W, Neumann F, Schuster J. Model of the haemodynamic reactions to intermittent coronary sinus occlusion. J Biomed Eng 1987; 9(2): 141-147.

[5] Alzubaidi L, Mohl W, Rattay F. Automatic Computation for Pressure Controlled Intermittent Coronary Sinus. J IJCSI 2010; Vol. 7, Issue 6,pp.285-289.

[6] Alzubaidi L, Mohl W, Method and device for the intermittent occlusion of the coronary sinus US Patent 7780604, 2010.

[7] Alzubaidi L. Accurate methods of calculating the Coronary Sinus Pressure plateau. J IJCSI 2011; Vol. 8, Issue 1,pp.138-140.

[8] Alzubaidi L, Mohl W, Device for the Intermittent Occlusion of the Coronary Sinus. European Patent EP 1753483, 2011.

[9] Kenner T, Moser M, Mohl W, Tied N. Inflow, outflow and pressures in the coronary microcirculation. In: CSI - A New Approach to Interventional Cardiology. Mohl W, Faxon D, Wolner E (editors). Darmstadt: Steinkopff; 1986; 15.

[10] Neumann F, Mohl W, Schreiner W. Coronary sinus pressure and arterial flow during intermittent coronary sinus occlusion. Am J Physiol 1989; 256(3 Pt 2): H906-915.

[11] Moser M, Mohl W, Gallasch E, Kenner T. Optimization of pressure controlled intermittent coronary sinus occlusion intervals by density measurement. In: The Coronary Sinus, Vol. 1. Mohl W, Glogar D, Wolner E (editors). Darmstadt: Steinkopf; 1984; pp.529-536.

[12] Mohl W, Glogar D, Kenner T, Klepetko W, Moritz A, Moser M. Enhancement of washout induced by pressure controlled intermittent coronary sinus occlusion (PICSO) in the canine and human heart. In: The Coronary Sinus, Vol. 1 Mohl W, Glogar D, Wolner E (editors). Darmstadt: Steinkopf; 1984; pp.537-548.

ISBN: 978-1-61804-219-4

Dynamic Graph Model of Evaporation Process in a Boiler System

H. Noor Ainy, A. Tahir& I. Razidah

***Abstract*—**Traditionally, research on graph theory focused on studying the properties of static graphs. However, almost all real networks are dynamic and large in size. Quite recently, study on evolution of variables or processes in the network have led to the integration of the concept of Autocatalytic set (ACS) and Graph theory. Thus, this paper aims to develop the dynamic graph model of an evaporation process in a Boiler system whereby seventeen variables are identified to represent the nodes. Thirty six links which are based on the catalytic relationship among the nodes represent the edges. Based on the concept of ACS, new properties of the graph are revealed. These properties indicate some initial findings that will lead to the further exploration in terms of Fuzzy Graph.

***Keywords*—**Combustion process, Corrosion, Water treatment, Perron-Frobenius eigenvector.

I. Introduction

GRAPH theory provides a mathematical modeling for studying interconnection among elements in natural and man-made systems. Traditionally, research on graph theory focused on studying static graphs. Directed graph is widely used to interpret the interconnection structure underlying the dynamics of the interacting subsystems or variables involve in the process. Recently, study on evolution of variables or processes have become the most active areas of research [1] – [3].

The concept of autocatalysis comes from chemistry. An Autocatalytic Set (ACS) is a set of reactions whose product catalyzes one another. In term of graph theoretic approach, ACS is a subgraph each of the nodes has one incoming link from a node belonging to the same subgraph [4]. Applications of this concept are explored in modeling the clinical waste incineration process and combustion process in a Circulating Fluidized Bed Boiler [2,10]. There are two main processes involve in a typical oxy-fuel combustion boiler system namely, combustion and evaporation process. In power generation plant, steam is used to generate electricity. Steam is produced by evaporation process in the boiler system which involves complex interactions of chemical substances that exist during the process. Since these chemical substances will undergo evolution process, the evaporation process can be represented as the dynamic graph by integrating the concept of Autocatalytic set.

The evaporation process in the boiler system is described in the next section, which is followed by some discussion on the concept of ACS utilized in developing the dynamic graph model. Next, some properties related to the dynamic graph model are revealed.

This work was supported by Universiti Teknologi MARA (UiTM) MALAYSIA .

H. Noor Ainy is with the Department of Mathematics, Faculty of Computer & Mathematical Sciences, UiTM Malaysia. (e-mail: ainy@tmsk.uitm.edu.my).

I. Razidah is a Professor with the same department. (email: razidah@tmsk.uitm.edu.my).

A. Tahir is a Professor in Mathematics from Faculty of Science & Nanotechnology Research Alliance Universiti Teknologi Malaysia (UTM), Skudai, Johor, Malaysia. (e-mail: tahir@ibnusina.utm.my)

II. Evaporation Process in Boiler System

Since corrosion is the main cause of reduced reliability in steam generating systems, proper water treatment to the feedwater system is essential in order to protect tubes and heaters in the boiler system against corrosion. Regardless of feedwater design, the major problems are similar for all types of system [5]. Based on Fig. 1 which is adapted from [3], the feedwater is supplied to the drum where the water is evaporated. The furnace is used to increase the water temperature and eventually to cause evaporation. Thus, circulation of water, steam, and water and steam mixture take place in the drum where steam generated in the drum flows to other systems in the boiler.

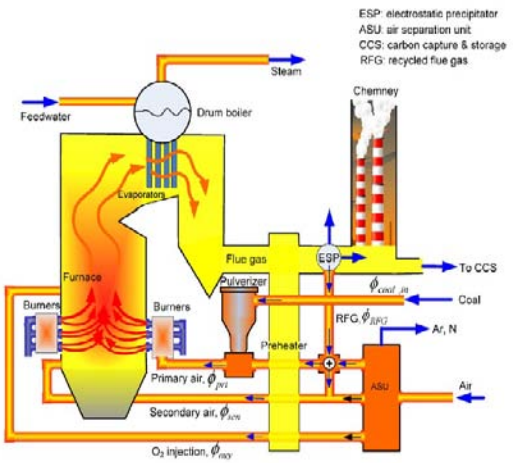

Fig. 1 Evaporation process in oxy- combustion Boiler

The steam drum is the entry point for feedwater and internal chemical treatment. The dynamic graph of evaporation process in drum system depends on chemical reactions in the feedwater-drum system [5].

III. THE AUTOCATALYTIC SET

The concept of Autocatalytic set (ACS) was formally introduced in 1971 by Kauffman, Eigen and Rossler as a set of catalytically interacting molecules. Later, Jain and Krishna [4] had integrated ACS in terms of graph theoretical concept and formalized as follows:

Definition 1: Autocatalytic Set
An autocatalytic set is a subgraph, each of whose nodes has at least one incoming link from a node belonging to the same subgraph.

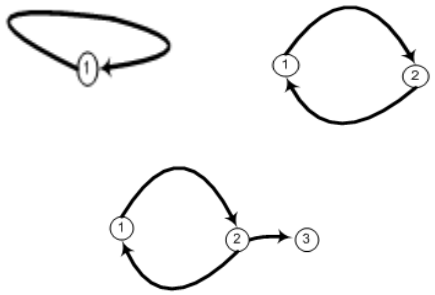

Fig. 2 Examples of ACS

Some examples of ACS are shown in Fig. 2, where a node in a directed graph represents a molecular species and a link from *j* to *i* indicates that *j* is a catalyst for *i*.

A graph with *s* nodes is completely specified by a matrix of order *s*, $A=(a_{ij})$ called the adjacency matrix of the graph. The graph is transformed to a square adjacency matrix, *A* by using definition of adjacency matrix given in [4] where

$$A_{ij}=\begin{cases}1 & if \quad (v_j,v_i)\in E\\ 0 & if \quad (v_j,v_i)\notin E\end{cases} \qquad (1)$$

By using (1), the adjacency matrices of the graphs in Fig. 2 are represented as follows.

a) $[1]$ b) $\begin{bmatrix}0&1\\1&0\end{bmatrix}$ c) $\begin{bmatrix}0&1&0\\1&0&0\\0&1&0\end{bmatrix}$

Here, the adjacency matrix in (1) is the transpose of usual adjacency matrix as defined by [10]. This convection had been adopted by [1, 2] in their works as it is convenient and representative in the context of the dynamical systems.

IV. DYNAMIC GRAPH MODEL OF EVAPORATION PROCESS

A digraph *G* is formally defined by $G=(V,E)$ where *V* is the set of vertices and *E* is the set of arcs or edges; each being a pair of distinct vertices. The set of vertices, *V* which signify chemical substances or variables that play the vital role in the water treatment and evaporation process in feedwater-drum system are identified as Pollution(v_1), Scavengers(v_2), Water(v_3),Metal oxide(v_4), Sodium sulfite(v_5),Oxygen(v_6) ,Nitrogen(v_7),Sodium hydroxide(v_8), Sulfur dioxide (v_9), Hydrogen sulfide(v_{10}), Hydrocloric acid(v_{11}), Sodium chloride (v_{12}), Hydrogen(v_{13}), Copper oxide(v_{14}), Silicon dioxide(v_{15}), Carbon dioxide(v_{16}) and Sulfuric acid(v_{17}). Pollution (v_1) represents the corrosion deposits and gases that is transported to the outside of the feedwater-drum system whereas scavengers (v_2) refers to the chemical treatment which is added to control corrosion. Based on the chemical reactions in [5]–[9], thirty six edges, *E* which represent the links between variables in the water treatment process due to their catalytic relationship are identified. As an example, the link (v_2,v_4) is based on the chemical reaction, $N_2H_4+6FeO_3\rightarrow 4Fe_3O_4+N_2+2H_2O$ [6]. This means that scavengers (v_2) namely hydrazine(N_2H_4) catalyzes the formation of metal oxide,(Fe_3O_4) (v_4)as shown in Fig. 3. Metal oxides prevent contact between metal and oxidizing ions in the boiler tube.

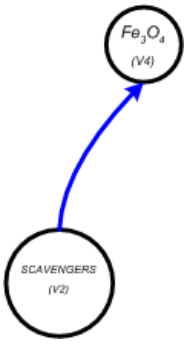

Fig. 3 The link, (v_2,v_4)

Thus, the complete set of *E* is as follows

$$E=\{(v_1,v_2),(v_1,v_3),(v_2,v_3),(v_2,v_4),(v_2,v_5),(v_2,v_7),(v_2,v_8),(v_2,v_{10}),(v_3,v_4),(v_3,v_6),(v_3,v_8),(v_3,v_9),(v_3,v_{10}),(v_3,v_{11}),(v_3,v_{12}),(v_3,v_{13}),(v_3,v_{14}),(v_4,v_1),(v_5,v_{17}),(v_6,v_5),(v_6,v_7),(v_6,v_{14}),(v_6,v_{16}),(v_7,v_1),(v_8,v_3),(v_8,v_{12}),(v_9,v_{17}),(v_{10},v_9),(v_{11},v_3),(v_{11},v_{12}),(v_{12},v_1),(v_{13},v_3),(v_{14},v_1),(v_{15},v_1),(v_{16},v_{15}),(v_{17},v_{11})\}$$

Hence, dynamic graph model of the evaporation process denoted as $G_S(V,E)$ is shown in Fig. 4.

Fig. 4 Dynamic graph model of the evaporation process $G_S(V,E)$

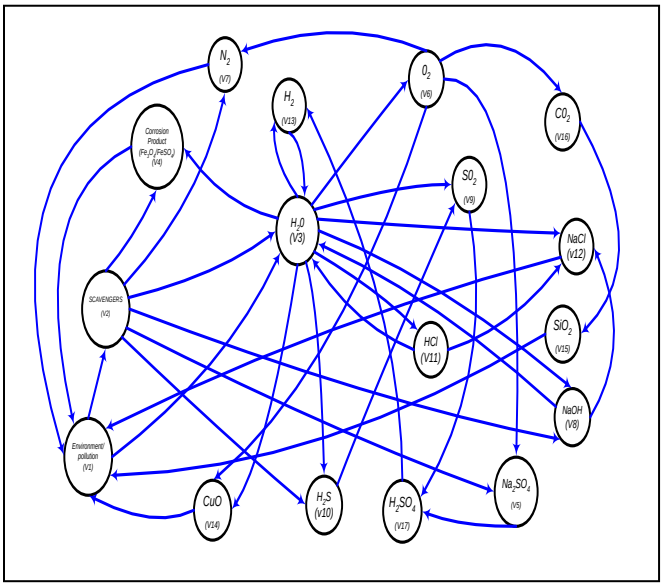

Based on the definition of an Autocatalytic set given in previous section and the description on the catalytic relationship between the chemical substances have provided a proof by construction for the following proposition.

Proposition1: The graph, $G_S(V,E)$ is an Autocatalytic set.

This proposition has inspired to explore further features of the dynamic graph model.

V. Related Properties of the Graph, $G_S(V,E)$

A. Irreducible graph

The first property to explore is to determine whether the graph is reducible or irreducible. A graph is said to be irreducible if each node in the graph has access to every other node. In addition, an irreducible graph is an ACS [4]. Therefore, the graph, $G_S(V,E)$ as shown in Fig. 4 is an ACS, hence, it is an irreducible graph.

B. Adjacency Matrix

The graph, $G_S(V,E)$ represents the network of chemical interaction in the evaporation process where the chemical substances or variables are represented as nodes and directed link from node *j* to node *i* indicates that variable *j* catalyzes the production of variable *i*. Hence, the corresponding adjacency matrix, *A* of the graph, G_S is a nonnegative matrix which is irreducible and primitive [2]. The special feature of the matrix of the graph, G_S is that every row must contain at least one non–zero element. It is also shown that all the elements of principle diagonal of the matrix are zero. This shows that there is no self-replicating of any of variable within the system.

C. Relation of an ACS to Perron-Frobenius eigenvector

The ACS is a useful graph-theoretic concept which can be related to the Perron-Frobenius eigenvector[11]. The Perron-Frobenius eigenvector (PFE) is an indicator of the existence of ACS in a graph. The relation of its corresponding adjacency matrix, *A* to Perron-Frobenious Theorem [11] showed that the largest value known as Perron-Frobenious eigenvalues is $\lambda_1 \geq 1$ for graph $G_S(V,E)$ and its corresponding eigenvector (PFE) is denoted as X_S.

$$A=\begin{bmatrix}
0&1&1&0&0&0&0&0&0&0&0&0&0&0&1&0&0\\
0&0&1&1&1&0&1&1&0&1&0&0&0&0&0&0&0\\
0&0&0&1&0&1&0&1&1&1&1&1&1&1&0&0&0\\
1&0&0&0&0&0&0&0&0&0&0&0&0&0&0&0&0\\
0&0&0&0&0&0&0&0&0&0&0&0&0&0&0&0&1\\
0&0&0&0&1&0&1&0&1&0&0&0&0&1&0&1&0\\
1&0&0&0&0&0&0&0&0&0&0&0&0&0&0&0&0\\
0&0&1&0&0&0&0&0&0&0&0&1&0&0&0&0&0\\
0&0&0&0&0&0&0&0&0&0&0&0&0&0&0&0&1\\
0&0&0&0&0&0&0&0&1&0&0&0&0&0&0&0&0\\
0&0&1&0&0&0&0&0&0&0&0&1&0&0&0&0&0\\
1&0&0&0&0&0&0&0&0&0&0&0&0&0&0&0&0\\
0&0&1&0&0&0&0&0&0&0&0&0&0&0&0&0&0\\
1&0&0&0&0&0&0&0&0&0&0&0&0&0&0&0&0\\
1&0&0&0&0&0&0&0&0&0&0&0&0&0&0&0&0\\
0&0&0&0&0&0&0&0&0&0&0&0&0&0&1&0&0\\
0&0&0&0&0&0&0&0&0&0&1&0&0&0&0&0&0
\end{bmatrix},\quad
X_S=\begin{bmatrix}
0.3846\\0.1496\\0.4647\\0.2388\\0.1284\\0.1807\\0.1284\\0.2388\\0.2735\\0.2388\\0.1807\\0.3438\\0.2414\\0.2509\\0.0273\\0.0703\\0.1563
\end{bmatrix}$$

Since all elements of PFE are non-zero, it can be deduced that the subgraph of the PFE is the entire graph $G_S(V,E)$ which further confirmed that the graph, $G_S(V,E)$ is an ACS. Thus PFE can be considered to be an indicator for the existence of ACS in the graph.

VI. Conclusion

Dynamic graph model of an evaporation process in a Boiler system is developed with Autocatalytic set as its main features. By considering the chemical reactions in the water treatment and evaporation process, seventeen chemical substances are identified to represent the nodes and thirty-six links to represent the edges of the graphical model. In addition, some properties of the graphical model related to adjacency matrix and Perron-Frobenius Theorem are presented. Thus, the relationship of Autocatalytic set and Perron-Frobenius eigenvector has provided a better understanding of the graph representing the evaporation process in the boiler system. It is anticipated that the approach adopted in this work will lead to further research by considering uncertainty or fuzziness in modeling complex dynamical systems.

Acknowledgment

The authors would like to thank Universiti Teknologi MARA Malaysia (UiTM) for the financial support. Their gratitude is also extended to anonymous reviewers for their valuable comments and suggestions.

REFERENCES

1. B. Sabariah, "Modeling of a clinical waste incineration processusing novel fuzzy autocatalytic set: a manifestation of mathematical thinking". Thesis PhD, UTM, Malaysia, 2006.
2. A. B. Sumarni, R. Ismail, and N.A. Harish, "Graph Dynamics Representation of Chemical Reactions of a Boiler", *IEEE Proc of Business Engineering and Industrial Applications Colloquium* (BEIAC) 2013, pp.906-910.
3. A. Haryanto, and K.S. Hong, "Modeling and simulation of an oxy-fuel combustion boiler system with flue gas recirculation",*Computers and Chemical Engineering*, 2011,vol. 35, pp.25-40
4. S. Jain, and S Krishna, "Autocatalytic sets and the growth of complexity in an Evolutionary Model", *Phys. Review.Letters.*1998, vol. 81, pp. 5684-5687.
5. A. Zaki, *Principles of Corrosion Engineering and Corrosion Control*, UK:Heinemainn, 2006.
6. S. Vidojkovic, A. Onjia, B. Motovic, N. Grahovac,, V. Maksimovic, and A. Nastasovic, "Extensive feedwater quality control and monitoring concept for preventing chemistry-related failures of boiler tubes in a subcritical thermal power plant", *Applied Thermal Engineering*, 2013, vol. 59, pp. 683-694.
7. T.M. Treit, "Simulation model a sulfuric acid production process as an integrated part of an energy system", *Simulation Modeling Practice and Th*eory, 2003, vol. 11, pp. 585-596.
8. R.N. Ning, "Discussion of Silica speciation, fouling, control and maximum reduction", *Desalination*, 2002,vol. 151, pp. 67-73.
9. S.C. Srivastava, K.M. Godiwalla, and M.K. Banerjee, "Fuel Corrosion of Boiler and Superheater tubes", *Journal of Material Science,*1997, vol.32, pp. 835-849.
10. A. Tahir, B. Sabariah, and A. K. Anuar, "Modeling clinical incineration process using fuzzy autocatalytic set", *Journal Mathematical Chemistry*, 2010,vol. 47(4), pp.1263-1273.
11. C. R. MacCluer. "The Many Proofs and Applications of Perron's Theorem".*SIAMReview*, 2000,vol 42(3), pp. 487-498.

Using Simulation to Assess the Performance of a Large-scale Supply Chain for a Steel Producer

Raid Al-Aomar, Mahmoud Al-Refaei, Ali Diabat, Mohd. Nishat Faisal, and Ameen Alawneh

***Abstract*—**This paper summarizes the simulation technique and technology used for assessing the Key Performance Indicators (KPIs) for the supply chain of a large-scale steel producer. To this end, a Discrete Event Simulation (DES) model of the underlying supply chain is built, verified and validated, and set to produce a selected set of KPIs that characterize the supply chain performance in terms of responsiveness, efficiency, and productivity. A base model of the steel producer supply chain is first developed based on collected information and the process structure. The model is then verified based on the intended flow and logic of the company supply chain. Special logic is developed into the model to track customer orders and produce the selected set of the supply chain KPIs. The model behavior is validated with company officials and tested using the collected data. Preliminary results were encouraging and were reported in terms of supply chain KPIs. At this stage, the developed simulation model is used to assess and validate the current status of the supply chain performance taking into consideration the key deterministic and stochastic factors across the supply chain (supplies, warehouses, operations, storage, and distribution). In the next implementation stage of the project, further data will be collected and incorporated into the model and the model will be used for scenario analysis and as a platform to optimize (improve) the performance of the supply chain.

***Keywords*—**Performance Measurement, Simulation, Steel Industry, Supply Chain Management.

I. Introduction

SUPPLY Chain Management (SCM) is focused on developing, optimizing, and operating efficient supply chains. Efficient supply chains are commonly characterized by cost effectiveness, lean flow and structure, high degree of integration, speed and accuracy, reliability, and well-chosen Key Performance Indicators (KPIs).

This paper was made possible by the support of an NPRP award number NPRP 4-522-2-188 from the Qatar National Research Fund (a member of the Qatar Foundation). The statements made herein are solely the responsibility of the authors.

Raid Al-Aomar is with the College of Engineering at Abu Dhabi University, UAE (phone: +971-2-501-5763; fax: +971-2-586-0182; e-mail: raid.alaomar@adu.ac.ae).

Mahmoud Al-Refaei is with the department of mathematics & statistics at Jordan University of Science & Technology, Jordan (e-mail: alrefaei@just.edu.jo).

Ali Diabat is with the department of Engineering Systems Management at Masdar Institute of Technology, UAE (e-mail: adiabat@masdar.ac.ae).

Mohd. Faisal is with the department of Management & Marketing at Qatar University, Qatar (e-mail: nishat786@qu.edu.qa).

Adeeb Alawneh is with the department of Mathematics, Statistics & Physics at Qatar University, Qatar (e-mail: aalawneh@qu.edu.qa).

As discussed in [1], a supply chain is an integrated system which synchronizes a series of inter-related business processes that facilitate the flow of goods, money, and information amongst various business entities, e.g. suppliers, manufacturers, distributors, and retailers.

Using KPIs to characterize the performance of the supply chain provides valuable feedback information that can be used to monitor performance, track progress, and rapidly diagnose potential problems. Chae [2] emphasizes the role of KPIs in closing the gap between planning and execution of supply chain operations, and offers guidelines for developing such indicators. Across the searched literature, KPIs are suggested for the four processes in the Supply Chains Operations-Reference (SCOR) framework; Plan, Source, Make, and Deliver [3, 4].

Over the last decade, there has been also an increasing interest in the use of simulation to model the performance of supply chains. Simulation modeling in general and Discrete Event Simulation (DES) in particular has played an increasing role in supply chain design, improvement, and problem-solving. This can be mainly attributed to the tremendous improvement in simulation software and the integration of statistical and optimization methods [5-7].

Simulation is used as an overall representation of the supply chain. It also incorporates variability in terms of demand, lead time, process reliability, etc., into the supply chain model and it is used to assess supply chain performance. Jahangirian *et al.* [8] provide a comprehensive review of the simulation literature. Terzi and Cavalieri [9] survey the literature on the use of simulation in a supply chain context. Other examples of simulation-based supply chain management applications can be found in [10-13]. In the context of steel industry, however, little research is directed at optimizing the supply chain using simulation modeling.

This paper presents the work accomplished so far by a group of researcher towards the fulfillment of one of the tasks in a research project that is aimed at improving the performance of a large-scale supply chain of a steel producer. This task is focused on using simulation to assess the performance of the underlying supply chain. This entails developing a conceptual model of the supply chain, programming the model using WITNESS software tool, validating the model, and setting the model to generate a set of KPIs that depict the performance of the supply chain. The paper also presents preliminary quantitative results of the supply chain KPIs.

ISBN: 978-1-61804-219-4

II. Supply Chain KPIs

A. Supply Chain Description

The targeted supply chain of the steel producer consists of an upstream flow of raw materials from suppliers to the company as well as downstream flow through the distribution channels. An overview of steel production operations is shown in Fig. 1. This process map shows only the set of key activities at the company site including receiving raw materials, main production processes, and shipping finished products to distributors and consumers. In reality, the complete supply company chain includes 17 suppliers, 31 distributers, and 4 types of products (DRI, HBI, Billets, and Rebar).

As shown in Fig. 1, raw materials arrive at the company port from suppliers around the world based on a certain schedule. A material handling process transfers the raw material from the yard to the production facility. Steel manufacturing at QS comprised of four integrated primary units: Direct Reduction (DR), Electric Arc Furnace (EAF) for molten steel production, Continuous Casting (CC), and Rolling Mill (RM). In production, steel is processed through direct reduction to produce Directly Reduced Iron (*DRI*), electrical furnaces to produce *molten steel*, and continuous casting to produce the *billets* and through rolling mills to produce the *rebars* final product and store them in plant's internal storage bays. Orders are then shipped to customers (distributors) locally and around the world on land and in sea. Other auxiliaries that are not included in the model include well-equipped Jetty facilities, a Main Power Substation, Quality Control Center, Maintenance Shops and facilities for sea/fresh water, compressed air, natural gas and a Clinic.

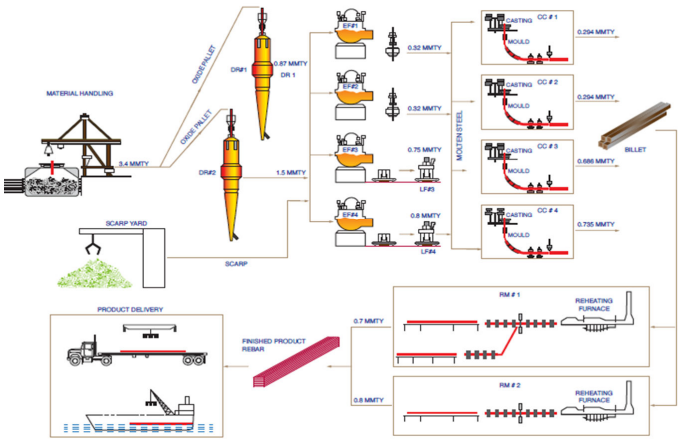

Fig. 1 An overview of the steel production supply chain

B. KPIs Development

Performance measurement is crucial to supply chain management. However, several metrics can be used for evaluating the performance of supply chains. These metrics can be related to critical aspects of the supply chain such as lead time, customer service, cost, and quality. The focus should be placed on the KPIs ability to measure the value-added activities (supply, manufacturing, logistics, and distribution).

In this paper, the supply chain KPIs are designed to provide quantitative measures that are related to the study objectives. Other qualitative measures can be added during the implementation stage. Thus, the simulation model aims at developing a specific set of KPIs to measure the performance of the supply chain and recommending a set of operational KPIs to maintain a high level of supply chain performance.

KPIs are developed based on what is essential for the success of the targeted supply chain in terms of responsiveness, efficiency, and productivity/utilization. To this end, the following KPIs are developed and programmed into the simulation model to quantify the performance of the steel producer's supply chain:

- *KPIs of supply chain responsiveness (customer service level):*
  - Order lead time (OLT): order-to-delivery time. The simulation model tracks the time of each order received by company from each market and a KPI will be produced at the end of the simulation run to average out the lead time of these orders. Simulation results will be validated with the historical data of actual orders lead times at QS.
  - Order fill rate (OFR): Fraction of orders/demand met on time from inventory. The company prefers to fill the received orders from finished items inventory. The objective is to reduce order lead time and to respond flexibly to various customer needs. The fraction of these orders filled is a KPI that depends on inventory size and desired service level.
  - On-time delivery (OTD): A key responsiveness measure is for the supply chain is to be able to deliver orders to different markets on time. The model tracks each order's lead time from initiation to delivery and compare that to a pre-set order due date to estimate the overall percentage of orders delivered on time in each market.

- *KPIs for supply chain efficiency (cost & resources management):*
  - Average inventory level: Amount of inventory across QS measured in units, days of demand, and financial value. This is a key indicator of supply chain efficiency measured in terms of total inventory. Sub measures include:
    - Product Inventory Level (PIL): Average finished product inventory measured in units, days of demand, and financial value.
    - Material Inventory Level (MIL): Average raw material inventory measured in units, days of demand, and financial value.
  - Production Unit Utilization (PUU): This set of KPIs measures the utilization % of the four main production units; Direct Reduction, Electrical Furnace, Continuous Casting, and Rolling Mill.

ISBN: 978-1-61804-219-4

- *KPIs for supply chain productivity:*
  - Orders Delivered Yearly (ODY): This KPI will tally the number of orders that are delivered yearly from each product type. Such measure is directly related to revenue generated from the supply chain and to benchmark with similar world-class industries.
  - Production Unit Yield (PUY): This set of KPIs tracks the yield of the four main production units; Direct Reduction, Electrical Furnace, Continuous Casting, and Rolling Mill.

III. Supply Chain Simulation

This section describes the development of the supply chain simulation model. The model is developed by depicting the key elements in the steel producer supply chain process from suppliers to consumers. The following approach is followed to develop the model:

A. Conceptual model development
B. WITNESS model development
C. Data collection and incorporation
D. KPIs programming
E. Model validation
F. Results reporting

A. Conceptual model

The main functions of steel producer supply chain include procurement, logistics, warehousing, and distribution. Procurement focuses on raw materials, equipment, spares and consumables, and supply contracts. Logistics is focused on customs and transportation. Warehousing is focused on inventory control, warehouse operations (receiving and shipping), and item management. Distribution is a function controlled by the domestic and regional traders (dealers) who order steel products and pick up their orders from the plant. Fig. 2 depicts the generic structure of the conceptual model of the supply chain network.

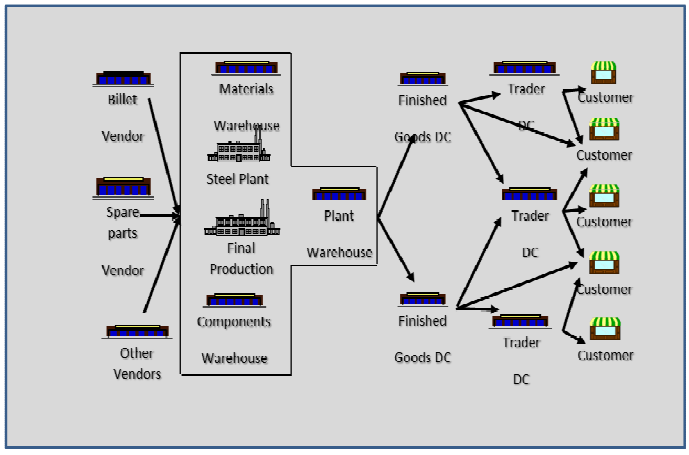

Fig. 2 The supply chain conceptual simulation model

B. WITNESS model

The supply chain simulation model is developed using WITNESS simulation software. WITNESS provides a flexible simulation environment that facilitates the ability to build the model incrementally using modules for each key element of the supply chain (suppliers, warehouses, operations, distributors, and Markets). Each module can be testes as standalone which generates confidence in the validity of the overall model. The model is developed using the following WITNESS modules:

A full WITNESS base model of the supply chain is developed by integrating the operation of the 3 main modules (Suppliers, Production, and Distribution). Logic is developed to integrate the flow and control the material supply, the production operations, and the order fulfillment process. Fig. 3 presents a snapshot of the supply chain WITNESS model in the run mode.

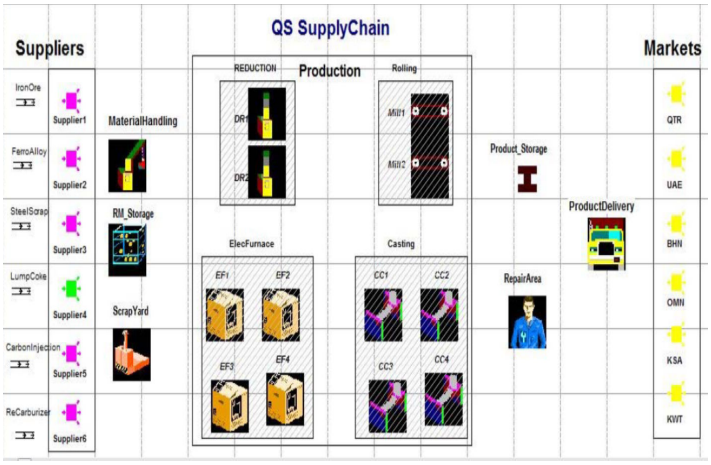

Fig. 3 Snapshot of the supply chain simulation model

C. Data Incorporation

The validity of the supply chain base model in WITNESS is highly driven by the quality of collected data for the different simulation modules. Model data were collected at the three modules through site visits and meetings with subject matter experts. The data includes the detailed supply chain structure, flow directions, rates, and times. Table 1 shows a sample of the data collected from main operations in the supply chain and used in the simulation model.

Process variability and reliability data was also collected to incorporate the realistic behavior of the supply chain into the model and to run the simulation under stochastic conditions. To this end, some collected data were fitted to standard distributions to capture the variability in supplies, processing, and demand.

The data collection will continue in the implementation stage to provide the needed information for scenario analysis and performance improvement.

ISBN: 978-1-61804-219-4

Table 1 Example of collected data from main process operations

Facility	Produced Products	RM Receiving Capacity	Production Capacity	Production Rate (ton/hr)
DR1 Module	DRI	450000	870000	105
DR2 Module	DRI/HBI	450000	1500000	187.5
EF/CC1/2	Molten Steel/Billets	450000	640000	78.5
EF3/CC3	Molten Steel/Billets	450000	750000	95
EF4/CC4	Molten Steel/Billets	450000	800000	99
Rolling Mill - 1	Rebar	20000	700000	87.5
Rolling Mill - 2	Rebar	30000	800000	110

D. KPIs Programming

As discussed earlier, the simulation model is set to produce a specific set of KPIs to characterize the supply chain performance in terms of responsiveness, efficiency, and productivity. The defined KPIs were programmed into the simulation model using WITNESS commands and built-in functions based on the data collected and information available. The model is set to generate KPIs only for the re-bar product using the Iron Ore raw material. Later in this implementation stage, all other products and raw materials will be added to the model.

The model is set to generate these KPIs in the simulation report at the end of run time. The selected set of KPIs will be further enhanced in the implementation stage of the study with more involvement of the supply chain experts of subject matters.

E. Model Validation

Model validation is crucial for the successful implementation of the supply chain model. The objective is to make sure that the results generated by the model actually reflect the reality of steel producer supply chain. This is step is also essential before running scenario analysis and optimization algorithms that aim at improving the performance of the supply chain. To validate the results of the simulation model, one major product, Re-Bar (Reinforcement Bar), is first simulated using the common raw material from suppliers (Iron Ore Billet). Only local market is simulated at this point as it represents the majority of products distribution (about 26 of the 33 distributors are actually in the local market). Other markets information will be incorporated in the model at a later stage of the implementation.

The first validation run was set under deterministic conditions (without incorporating variability in demand, supply, production cycle times, and equipment reliability). The model was able to generate results that are for the most part close to the expected behavior of the process. Cases in which the results deviated from the actual (expected) behavior of the process were justified based on the selected run conditions and the assumptions of the model. To further validate the model, another run is set using the full capacity of steel production (all units of DR, EF, CC, and RM). Since all other run conditions are kept the same, we would expect to see the model able to accommodate larger number of orders in a shorter lead time. This was exactly the case in model results.

To incorporate a more realistic behavior into the model, the simulation is run under variability conditions in supplies, processing, and demand. In addition, the company-provided reliability data for production units are incorporated into the model. The main sources of variability include; supplies variability, cycle/processing times variability at the 4 steel production units, process reliability, and ordering variability.

F. Results Reporting

Based on the data collected and information available so far, the WITNESS model is developed, tested (verified), and used to generate an assessment of the defined KPIs. The model is set to generate a full Model Output Report in Excel format at the end of run time. Simulation Run Controls are set to a warm-up period of 7 days, a Run time of 365 days, and 5 Replications. Table 2 presents a summary of the preliminary simulation results of the supply chain KPIs. The unit flow in the model is set to one-thousand ton of steel and all cycle times and schedules are in days. A full Model Output Report in Excel format is also generated from the model.

Table 2 Summary of preliminary results of KPIs simulation

Category	KPI		Run1	Run 2	Run 3	Run 4	Run 5
Responsiveness	OTD		97.92%	92.62%	88.70%	98.02%	95.32%
	OLT		0.23 days	0.35 days	0.71 days	0.25 days	0.19 days
	OFR		87.96%	85.71%	81.02%	88.91%	85.32%
Efficiency	PIL		11,352	11,311	10,568	24,722	11,242
	MIL		22,665	26,019	12,355	46,472	76,530
	PUU	DR	66.6%	76.7%	57.5%	66.7%	67.2%
		EF	43.17%	48.23%	49.22%	58.31%	48.81%
		CC	43.15%	48.13%	48.91%	59.12%	48.54%
		RM	77.44%	78.11%	69.55%	77.11%	78.03%
Productivity	ODY		140	151	152	142	153
	PUY	DR	1317	1315	1315	1312	1319
		EF	1320	1321	1323	1318	1320
		CC	1320	1321	1323	1318	1320
		RM	1312	1314	1311	1316	1315

IV. Discussion

Preliminary simulation results showed that the model is ready as a flexible template to assess the defined set of supply chain KPIs under similar to real-world conditions. The model has generated KPIs values (shown in Table 2) that reflect the provided information. For example the model reports an average of 148 order delivery per year with an average order lead time of about half day (this is for local market only and running only one product full capacity). In the implementation stage, these results will be compared to last year records to assess current situation and suggest improvement. The closer the values of the KPIs to actual supply chain performance the higher the credibility of the model and the data used in the model. Only a sample results and a sample of collected data were presented since multiple enhancements are expected in the upcoming implementation stage.

In the implementation phase of the project, the preliminary results will be discussed with the company officials to validate

the KPIs and a full-blown simulation model of the supply chain will then be used to drive improvement of the supply chain performance. At a later stage, the model will be used as a template for optimization with Simulated Annealing. The flexibility of DES model will facilitate the validation of current performance and the prediction of the future performance. The simulated KPIs will be also used as performance criteria in the supply chain optimization study.

Further work that will take place in the implementation phase of the project includes the following:

- Further validation of the structure, logic, data, and results of the WITNESS simulation model of the supply chain.
- More involvement of company officials and further data collection on the performance of the supply chain.
- Simulating and analyzing several operational and what-if scenarios of the supply chain (experimental design of simulation).
- Linking and analyzing the results of a Linear Programming (LP) deterministic model to the results of the stochastic simulation model.
- Integrating the simulated annealing optimization algorithm into the WITNESS simulation model of the supply chain.
- Optimizing the total cost of the supply chain and running multi-criteria optimization of supply chain KPIs.

V. Conclusion

This paper has presented a summary of the effort and the results achieved by the project researchers in completing a task of a research project on optimizing the performance of the supply chain for a steel producer. This task is focused on developing a WITNESS simulation model to simulate the supply chain KPIs. Most of the relevant simulation data is collected and incorporated into the model to implement the conceptual model and develop current state quantitative results of the supply chain KPIs. The selected set of KPIs characterizes the supply chain performance in terms of responsiveness, efficiency, and productivity. The model is verified based on the flow and logic information of the company supply chain. Special logic is developed into the model to track customer orders and produce the selected supply chain KPIs. The paper has presented samples of the structured main modules of the WITNESS model and samples of model logic for supply, production, storage, and distribution. Preliminary results in terms of supply chain KPIs were obtained from the model. In the implementation stage, the model will be validated with the supply chain subject matter experts and further data will be collected to simulate several real-world scenarios and optimize (improve) the performance of the supply chain.

References

[1] H. Min and G. Zhou, "Supply chain modeling: Past, present and future," in *Computers & Industrial Engineering*, vol. 43, pp. 231–249, 2002.

[2] B. K. Chae, "Developing key performance indicators for the supply chain: and industry perspective," in *Supply Chain Management: An International Journal*, vol. 14(6), pp. 422-428, 2009.

[3] S. Chopra and P. Meindl, *Supply Chain management; Strategy, Planning, and Operations.* Prentice Hall, 2007.

[4] C. Bozarth and R. B. Handfield, *Introduction to Operations and Supply Chain Management*, 2nd ed., Prentice Hall, 2008.

[5] J. Banks (editor), *Handbook of Simulation, Principles, Methodology, Advances, Applications, and Practice.* John Wiley, 1998.

[6] A. Law, *Simulation Modeling and Analysis, 4th ed.*, McGraw-Hill College, 2006.

[7] B. L. Nelson, J. Banks, J. S. Carson, and D. M. Nicol, *Discrete-Event System Simulation, 3rd ed.,* Prentice Hal, 2006.

[8] M. Jahangirian, T. Eldabi, A. Naseer, L. K. Stergiouslas, and T. Young, "Simulation in manufacturing and business: A review," in *European Journal of Operational Research*, vol. 203, pp. 1-13, 2010.

[9] S. Terzi, and S. Cavalieri, "Simulation in the supply chain context: a survey," in *Computers in Industry*, vol. 53, pp. 3-16, 2004.

[10] F. Longo and G. Mirabelli, "An advanced supply chain management tool based on modeling and simulation," in *Computers & Industrial Engineering*, vol. 54, pp. 570–588, 2008.

[11] J. Y. Jung, G. Blau, J. F. Pekny, G. V. Reklaitis, and D. Eversdyk, A simulation based optimization approach to supply chain management under demand uncertainty. In Computers & Chemical Engineering, vol. 28, pp. 2087-2106, 2004.

[12] T. Yoo, H., Cho, and E., Yücesan, Hybrid algorithm for discrete event simulation based supply chain optimization, in *Expert Systems with Applications*, vol. 37, pp. 2354–2361, 2010.

[13] F. Campuzanu and J. Mua, Supply Chain Simulation: A System Dynamics Approach for Improving Performance, Springer, 2011.

[14] J. Heidrich, "Implementation of supply chain management systems in steel industry," in *Industry Management*, vol. 18(5), pp. 46-49, 2002.

[15] K. Walker, "Ingredients for a Successful Supply Chain Management System Implementation," in *Supply Chain Forum*, vol. 10(1), pp. 44–50, 2009.

Optimization of White Hide Deliming Process

D. Janáčová, H. Charvátová, P. Mokrejš, V. Vašek, O. Líška

Abstract—In this paper we focused on the optimization of the pelt deliming which is one of the operation that prepares the skin material for the main manufacturing operation, tanning. Nowadays is the deliming in light of the ecology and economy inconvenient. The most used deliming preparations are ammonium salts of strong acids that cause pollution of technological sewerage water and which clearing is very expensive. In addition by the deliming process is used up large amount of wash liquid and electric energy for working of the equipment. It is needful in addition to the substitution of the ammoniac deliming preparation by nonammoniac to minimize operating costs for the achievement of the required level of deliming.

For the optimization process of deliming it is possible to set up an access of the indirect modelling that is based on make-up of mathematical models coming out of study of the physical operation mechanism. Displaced limy-ions are on the skin material fixed partially, part can be removed by pure water and the rest deliming agent (chemical deliming). The process is diffusion nature, it is characterized by the value of diffusion effective coefficient and so called structure power of the removing item to the solid phase. The mentioned parameters belong to input data that are appropriate for the automatic control of deliming process.

Keywords—Hide deliming, optimization, unreacted core model.

I. Introduction

DELIMING of the pelt is part of tannery operations of natural skin process. By the deliming purpose is cut down pH of pelt at the value appropriate for the following manufacturing operations. In practice is deliming realized in two on itself consequential levels. Firstly the lime is removed from pelt that is exposed propeller shaft in the skin material in washing process of pelt by water (simple deliming) and the slaked lime is subsequently removed by the help of the appropriate chemical preparation that is bound to skin material (chemical deliming). At present is deliming inconvenient from the economical and ecological point of view. The most used deliming preparations are ammonium salts of strong acids which cause ammoniacal pollution of technological sewage water that must be subsequently purify. In addition large amount of wash liquid and electrical energy for the working equipment are used up by the deliming process. Therefore is needful besides substitution of ammoniac deliming preparations by nonammoniac to minimize operating costs for achievement of the level deliming.

In order to the deliming process optimization can be applied an access of the indirect modelling that is based on assemblage of mathematic models that usually result from their own physical mechanism study of the appropriate operation. By the concrete research is concerned the constant setting that characterize actual processes and determination parameters of deliming process kinetics whereas it is possible to result from it that the reaction proceeding in heterogeneous are followed by sharing of material and warm so that their parameters are independent on the system construction..

II. Mathematical Description of Chemical Deliming

To achieve higher levels of the processed leathers quality, consumption of water greatly increases. Therefore it is necessary used to reduce the content of calcium hydroxide in the pelts by chemical deliming. Chemical deliming consists in the chemical reaction between calcium hydroxide and deliming agent. It breaks chemical bonds between calcium hydroxide and pelt (pelt) producing unbound salt, that is removed by non-chemical washing.

To simplify the process, we have assumed a low concentration of diffusing component. This assumption is based on the real tanning experience. Speed of deliming process is monitored by dependence of the increasing concentration of neutral calcium salt in the bath. It is justified when the concentration of deliming agent is much higher than concentration of calcium in the pelt and deliming agent is not bound to the pelt.

Model "unreacted core" implies that the process will occur on the outer surface of the pelt and the active components penetrate into unreacted layer which surrounds the core of unmodified pelt.

This work was supported by the European Regional Development Fund under the project CEBIA-Tech No. CZ.1.05/2.1.00/03.0089 and by the Ministry of Education, Youth and Sports of the Czech Republic.

D. Janáčová, Tomas Bata University in Zlín, Faculty of Applied Informatics, Department of Automation and Control Engineering, nám. T. G. Masaryka 5555, 760 01 Zlín, Czech Republic; phone: +420 576 035 274; fax: +420 576 032 716; (e-mail: janacova@fai.utb.cz)

H. Charvátová, Tomas Bata University in Zlín, Faculty of Applied Informatics, Department of Automation and Control Engineering, nám. T. G. Masaryka 5555, 760 01 Zlín, Czech Republic (e-mail: charvatova@fai.utb.cz)

P. Mokrejš, Tomas Bata University in Zlín, Faculty of Technology, Department of Polymer Engineering, nám. T. G. Masaryka 5555, 760 01 Zlín,

V. Vašek, Tomas Bata University in Zlín, Faculty of Applied Informatics, Department of Automation and Control Engineering, nám. T. G. Masaryka 5555, 760 01 Zlín, Czech Republic (e-mail: vasek@fai.utb.cz).

O. Líška, Technical University of Košice, Mechanical Engineering Faculty, Department of Automation, Control and Human Machine Interactions, Letná 9, 042 00 Košice, Slovak Republic, (e-mail:ondrej.liska@tuke.sk)

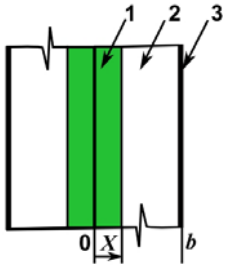

Fig. 1: Unreacted core model

1 – part of the pelt, which has not yet been processed -„unreacted core“ , 2 – processed part of the pelt, 3 – boundary layer

$$D\frac{\partial^2 c_1}{\partial x^2}=\frac{\partial c_1}{\partial t},\quad (x_m < x < b\ ,\ t>0) \tag{1}$$

$$c_p\frac{\partial x_m}{\partial t}=D\frac{\partial c_1}{\partial x}(x_m,t) \tag{2}$$

$$V_0\frac{\partial c_{10}}{\partial t}(t)=-D\cdot S\frac{\partial c_1}{\partial x}(b,\ t) \tag{3}$$

$$c_1(x_m,\ t)=c_s \tag{4}$$

$$c_1(b,t)=c_0(t) \tag{5}$$

$$c_1(x,0)=c_p \tag{6}$$

$$c_{10}(0)=c_{p1} \tag{7}$$

Equation (1) describes diffusion through the reacted part of the pelt. Equation (2) describes movement speed of the boundary. Equations (3) **Chyba! Nenalezen zdroj odkazů.**– (7) are boundary and initial conditions.

The used symbols mean:

A - sorption equilibrium constant (determined from Langmuir isotherm), [1];
b - half thickness of the pelt, [m];
c_0 - concentration of $Ca(OH)_2$ in the bath, [kg · m^{-3}];
c_{10} - concentration of $CaSO_4$ (unbound salt) in the bath, [kg · m^{-3}];
c_A - concentration of $Ca(OH)_2$ bound to the pelt, [kg · m^{-3}];
c_p - initial concentration of $Ca(OH)_2$ in the pelt, [kg · m^{-3}];
c_{p1} - initial concentration of $CaSO_4$ [kg · m^{-3}];
c_s - total initial concentration of $Ca(OH)_2$ in the system, [kg · m^{-3}];
C - dimensionless concentration of $Ca(OH)_2$, [1];
C_0 - dimensionless conc. of $Ca(OH)_2$ in the bath, [1];
C_S - total dimensionless initial concentration of $Ca(OH)_2$ in the pelt, [1];
D - diffusion effective coefficient of washed component from the pelt, [m^2.s^{-1}];
Fo - Fourier number (dimensionless time), [1];
Na - soaked number (ratio of V_0 / V) , [1];
S - area of the pelt, [m^2];
t - time, [s];
V - volume of the pelt, [m^3];
V_0 - volume of the deliming bath, [m^3];
x - space coordinate, [m];
x_m - space coordinate of the moving boundary, [m];
X - dimensionless space coordinate, [1].

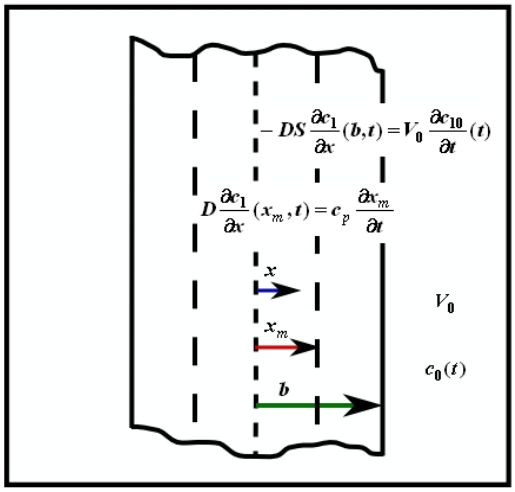

Fig. 2 Model of the chemical deliming

Fig. 3 shows concentration field of deliming agent penetration to the pelt. Fig 10 depicts concentration field of washing out calcium sulphate (unbound salt) from the pelt.

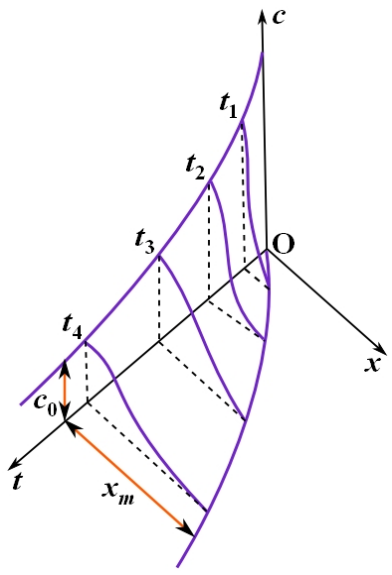

Fig. 3 Concentration field of deliming agent penetration to the pelt

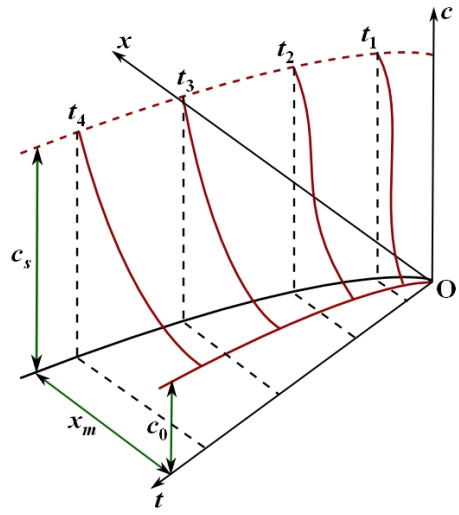

Fig. 4 Concentration field of washing out calcium sulphate (unbound salt) from the pelt

On condition that time progress (reacted) interface in the pelt is slow and that the dependence of the salt concentration will linear from this interface to pelt surface for description of the chemical deliming can be used so called quasistationary model thereby the relation (1) – (7) will simplify to the form:

$$c_p \frac{\mathrm{d}x_m}{\mathrm{d}t} = D \frac{c_s - c_0}{x_m} \tag{8}$$

$$c_0 V_0 = S\, x_m \left(c_p - \frac{c_s - c_0}{2} \right) \tag{9}$$

After dimensionless quantity implementation:

$$C_0 = \frac{c_0}{c_p}, \quad F_o = \frac{D \cdot t}{b^2 (1 + A)}, \quad X = \frac{x}{b}, \quad C_s = \frac{c_s}{c_p} \tag{10}$$

by condition

$$C_{10}(0) = 0 \tag{11}$$

we´ve got the solution:

$$F_{\square} = 4Na^2 (2 - C_s) \left\{ \frac{C_s}{(2 - 2C_s)^3} \ln\left[\frac{C_s (2 - C_s - C_{10})}{(C_s - C_{10})(2 - C_s)} \right] + \right.$$
$$+ \frac{2(2 - C_s)^2 C_s - (2 - C_s) C_s^2 - (2 - C_s)^3}{2(2 - 2C_s)^3} \left[\frac{1}{(2 - C_s - C_{10})^2} - \frac{1}{(2 - C_s)^2} \right] +$$
$$\left. + \frac{C_s (2C_s - 2)}{(2 - 2C_s)^3} \left[\frac{1}{(2 - C_s - C_{10})} - \frac{1}{2 - C_s} \right] \right\}. \tag{12}$$

Dimensionless concentration field of unfixed salt in the bath is designed in the following Fig. 5.

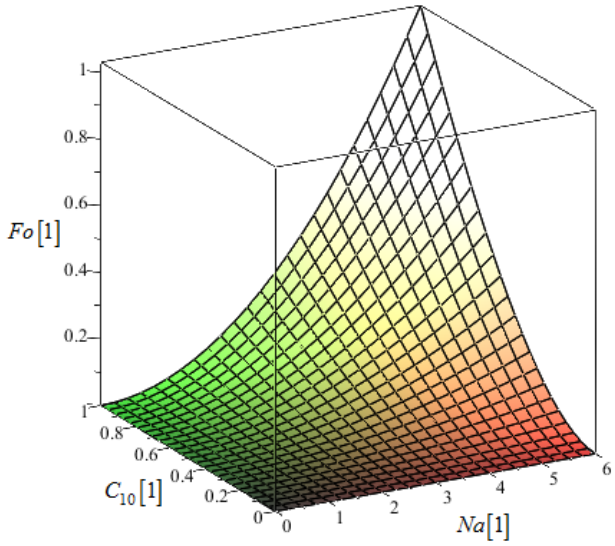

Fig. 5 Process of dimensionless concentration of non-fixed salt in the deliming bath depending up the dimensionless time and the dimensionless volume bath.

III. The Deliming Process Optimization

The set up mathematical models and their solutions provided us to make a proposal for the deliming process optimization, whereas first of all we insisted on economical aspects. For this purpose is needful to find a point in which shall be implement a transformation from simple deliming to chemical deliming so that occur to the saving of total costs at the given operation.

By determination of the breaking point was firstly needful to set up the cost function for simple and chemical bath washing of the pelt. From the appropriate cost function can be determined the optimal amount of washing water if you like the chemical preparation necessary for successful implementation of the appropriate operation. By setting up of the cost function for the pelt washing by water we supposed that by clear water is possible to remove from the skin material firstly free calcium ions and that the general operating costs N_c at the given operation are given by sum of costs for used electrical energy for equipment work NE and costs for used up washing water N_v

$$N_C = N_V + N_E \tag{13}$$

whereas the costs for used up energy are given by product of specific price for the energy K_E, time t and electromotor input for the working equipment P

$$N_E = K_E \cdot P \cdot t \tag{14}$$

Costs for used up wash water are given by product of the specific price for wash water K_V and wash water capacity V_0.

$$N_V = K_V \cdot V_0 \tag{15}$$

For the total costs fixing depending up non-dimensional consumption of wash water was firstly needful to set up for the appropriate soaked number Na the dependence of the

wash level y determining the effectivity of deliming process at non-dimensional time Fo

$$y = \frac{Na}{\varepsilon(1+A)+Na} - 2\frac{Na^2}{\varepsilon(1+A)}\sum_{n=1}^{\infty}\frac{\exp\left(-F_o q_n^{\,2}\right)}{\varepsilon(1+A)+\frac{q_n^{\,2}Na^2}{\varepsilon(1+A)}+Na} \qquad (16)$$

and from it to determine non–dimensional time needful for getting the appropriate wash level. The determination of this time subsequently made possible to set together the appropriate cost function

$$N_C = K_V \cdot Na \cdot V + \frac{K_E \cdot P \cdot F_o \cdot b^2 \cdot (1+A)}{D} \qquad (17)$$

By the cost function setting for the chemical washing we proceeded accordingly. However we supposed that by the chemical agent action will take place the fermentation of structure between calcium ions and collagen fibres whereby the relation for dependence determination of wash level on non – dimensional time is simplificated to form

$$y_{CH} = \frac{Na}{\varepsilon+Na} - 2\frac{Na^2}{\varepsilon}\sum_{n=1}^{\infty}\frac{\exp\left(-F_o q_n^{\,2}\right)}{\varepsilon+\frac{q_n^{\,2}Na^2}{\varepsilon}+Na} \qquad (18)$$

and cost function has a form

$$N_{CH} = K_{CH} \cdot Na \cdot V + \frac{K_E \cdot P \cdot F_o \cdot b^2}{D}. \qquad (19)$$

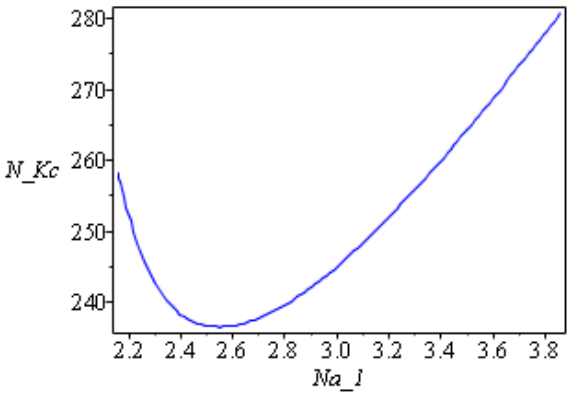

Fig. 6 Cost function for non-chemical washing

For parameters:
A = 10; P = 10 kW; b = 2 mm; ε= 0; 5; Na = 2;D = 6:10^{-9} m^2.s^{-1};
K_v = 60 Kč.m^{-3}; K_E = 3 Kč.kW^{-1}h^{-1}

The used symbols mean:

K_E – price for electrical energy unit, [Kč.kWh^{-1}];
K_{CH} – price for chemical agent unit, [Kč.m^{-3}];
K_V – price for wash water unit, [Kč.m^{-3}];
N_C – final operating costs for simple washing of pelt, [Kč];
N_E – costs for electrical energy consumption for simple, chemical washing of pelt , [Kč];
N_{CH} – final operating costs for chemical washing of pelt, [Kč];
N_V – costs for wash water consumption, [Kč];
P – electromotor input for equipment working, [KW];
y – level of simple bath washing, [l];

IV. Conclusion

In this work was proven that by so complicated materials such as pelt can be applied indirect modelling, it means the quantitative description of the set technologic operation running for the processes optimization of the natural polymer manipulation. In our work we targeted the optimization process possibilities of the pelt deliming.

Designed mathematic models provided us for setting of the cost function, it means dependence of the main operating costs on the technologic water consumption.

References

[1] Crank, J. The Mathematics of Diffusion, Clarendon Press, Oxford, 2 nd Ed., 1975
[2] Charvátová, H. Modeling of pelt chemical deliming.(Dissertation work), Zlín: Tomas Bata University in Zlín, Zlín, 2007. (in Czech)
[3] K. Kolomazník, et al., "Modeling of Raw Hide Soaking", in WSEAS Transactions on Information Science and Applications, Hellenic Naval Academy, Ostrava Poruba, 2005.
[4] Kaul, S. N., Nandy, T., Szpyzrkowitz, L., Gautam, A., Khanna, D. R. (2005). Waste Water Management With Special Reference to Tanneries. Discovery Publishing

Dagmar Janáčová is a Professor in the Department of Automation and Control Engineering, Faculty of Applied Informatics, Tomas Bata University in Zlín. Her research activities include: modeling of treatment processes of natural polymers, transport processes, recycling of tannery waste, and optimization and ecological approach of tannery processes. She has received the following honors: Diploma of England, XXIII IULTCS Congress, London, 11–14 September, 1997; Gold Medal - EUREKA EU Brussels 1997; Special Prize, Ministry of Agriculture, Belgium, 1997.

Hana Charvátová is a research worker at the Department of Automation and Control Engineering, Faculty of Applied Informatics, Tomas Bata University in Zlín. Her research activities include recycling technology and modeling of natural and synthetic polymers treatment.

Pavel Mokrejš is an Associate Professor in the Department of Polymer Engineering, Faculty of Technology of Tomas Bata University in Zlín. His research activities include: treatment of liquid and solid waste form tannery industry, treatment of leather waste from shoe industry, utilization protein hydrolysates, biodegradable casings and films, and isolation of proteins from untraditional sources.

Vladimír Vašek is a Professor in the Department of Automation and Control Engineering, Faculty of Applied Informatics, of Tomas Bata University in Zlín. His research activities include: microcomputer applications in technology processes, computer monitoring and control systems, and discrete deterministic controllers approach of tannery processes. He has received the following honors: Diploma of England, XXIII IULTCS Congress, London, 11–14 September, 1997; Gold Medal - EUREKA EU Brussels 1997; Special Prize, Ministry of Agriculture, Belgium, 1997.

Ondrej Líška is an Associate Professor in the Department of Automation, Control and Human Machine Interactions of Technical University of Košice. His research activities include automatic control of machines and processes, monitoring and visualization of processes, sensor systems for automation and control, control with the use of advanced management methods.

Some aspects of using shift registers based on 8 degree irreducible polynomials

Mirella A. Mioc and Mircea Stratulat

Abstract—The Linear Feedback Shift Register is a well-known subject in many major analyses. Usually LFSR functions in a Galois Field GF(2^n), meaning that all the operations are done with arithmetic's modulo n degree Irreducible Polynomials, as these polynomials influence the performance of the Linear Feedback Shift Register functioning. The whole analysis of functioning for irreducible polynomials of 8 degree proves that almost all obtained results are in the same time distribution.

Keywords: Cryptosystem, Irreducible polynomials, Pseudo-Random Sequence, Shift registers.

I. INTRODUCTION

A code-breaking machine appeared as one of the first forms of a shift register early in the 40's, in Colossus. It was a five-stage device built of vacuum tubes and thyratrons. Many different implementation forms were developed along the years.

The LFSR (Linear Feedback Shift Register) is the basis of the stream ciphers and most often used in hardware designs.

A string of memory cells stored a string of bits and a clock pulse can advance the bits with one position in that string.

For each clock pulse it is produced the new bit in the string using the XOR of certain positions.

The basis of every LFSR is developed with a polynomial, which can be irreducible or primitive.[4]

A primitive polynomial satisfies some additional mathematical conditions and determines for the LFSR to have its maximum possible period, meaning (2^n-1), where n is the number of cells of the shift register or the length.

LFSR can be built based on XOR (exclusive OR) circuits or XNOR (exclusive denied OR).

The difference of status is, of course, the equivalent status will be 1, where it was 0. For an n bits LFSR, all the registers will be configured as shift registers, but only the last significant register will determine the feedback.

An n bits register will always have n + 1 signals.

Every LFSR works by taking the XOR of the selected bits in its internal state and any LFSR containing all zero bits will never move to any other state, so one possible state must be excluded from any cycle.

An LFSR is composed of memory cells connected together as a shift register with linear feedback. In digital circuits a shift register is formed by flip-flops and EXOR gates chained together with a synchronous clock.

Shift registers are a form of sequential logic like counters.

Always the shift registers produce a discrete delay of a digital signal or waveform. Considering that a shift register has n stages, the waveform is delayed by n discrete clock times.

Usually the naming of the shift register follows a type of convention shown normally in digital logic, with the least significant bit on the left.

According to the communication protocol, the signals will be addressed, not the registers. There are n+1 signals for each n-bit register. Always the next state of an LFSR is uniquely determined from the previous one by the feedback network.

Any LFSR will generate a sequence of different states starting with the initial one, called seed.

A feedback shift register is composed of:

- a shift register
- a feedback function.

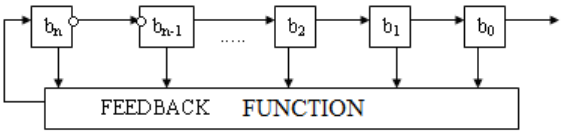

Fig.1. Feedback Shift Register Scheme

An LFSR can be represented as a polynomial of variable x referred to as the characteristic polynomial or the generator polynomial.

A LFSR is a shift register, whose input bit is given from a linear function of the initial status.

The initial value of the register is called seed and the sequence produced is completely determined by the initial status.

Because the register has a finite number of possible statuses, after a period the sequence will be repeated.

If the feedback function is very good chosen the produced sequence will be random and the cycle will be very long.

There are two kinds of implementation for LFSR [6]:

- Fibonacci implementation
- Galois implementation.

ISBN: 978-1-61804-219-4

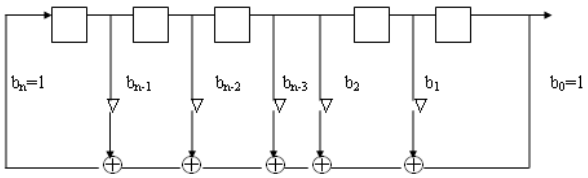

Fig. 2. Fibonacci implementation

In Fibonacci form the weight for any status is 0, when there isn't any connection and 1 for sending back.

Exceptions of this are the first and the last one, both connected, so always on 1.

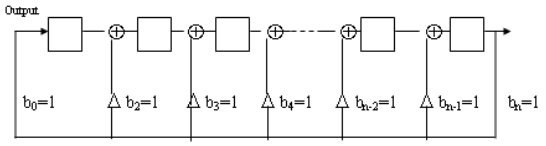

Fig.3. Galois implementation

In Galois implementation there is a Shift Register, whose content is modified each step at a binary value sent to the output.

In Galois configuration the single bit shifted out is XORed with several bits in the shift register and in conventional configuration each new bit input to the shift register is the XOR of several bits in the register.

Comparing the two scheme of representation it is shown that the weight order in Galois is opposite the one in Fibonacci.

From the hardware point of view, Galois implementation is fastest than Fibonacci because of the reduced number of XOR gates in feedback and so it is much more used.

There are some industries in which Fibonacci form is referenced as SSRG (Simple Shift Register Generator) and Galois as MRSRG (Multiple-Return Shift Register Generator).

There are two types of LFSR from the utilization point of view: the well-known LFSR, that is an "in-tapping" LFSR and the "out-tapping" LFSR.

The "in-tapping" LFSR is usually called a MISR (Multiple Input Shift Register).

Cycle codes belong to algebraically codes for errors detecting.

This experiment develops an analysis of a Linear Feedback Shift Register and a Multiple Input – output Shift Register.

By using a primitive polynomial in the polynomials modulo 2 as modular polynomial in the polynomial multiplication it can be created a Galois Field of order 2^n with a polynomial beginning with x^n.

Such kind of field can be denoted as $GF(2^n)$ or GF(n) and one of the famous applications for that is in the Rijndael Algorithm (AES), where n=8.

Beginning with 2000 Rijndael [5] cryptosystem is officially the Advanced Encryption System (AES).

The old DES (Data Encryption Standard) [7] was broken from Electronic Frontier Foundation in three days. The two authors Joan Daemen and Vincent Rijman from Holland chose to use a Galois Field GF (2^8) with the following generator polynomial.

$$P(x)=x^8+x^4+x^3+x+1 \quad (1)$$

or '11B' in hexadecimal representation.

All arithmetical operations are developed in a Galois group.

The Shift Register Cryptosystems variant has been developed from the evolution of the encrypting techniques [11]. Such a cryptosystem is based upon generating a sequence in a finite field and for obtaining it a Feedback Shift Register is used.

There are some methods for using LFSR to build secure ciphers.

For increasing the strength of the output from an LFSR, often it is used another LFSR for controlling how often it is stepped.

Another technique uses three LFSRs with different periods and it is known as the Geffe generator.

Usually it is necessary to combine the methods for obtaining more elaborate constructions.

Almost all applications of using shift registers representing generator polynomials need to be developed in a finite field.

Evariste Galois demonstrated that a field is an algebra with both addition and multiplication forming a group. Some ground information from Algebra demonstrated the importance of working with irreducible polynomials and primitive polynomials. Also the importance of using shift registers in cryptosystems based on irreducible polynomials is demonstrated in increasing the security obtained.

The Linear Feedback Shift Registers are used in a variety of domains:

- Pattern Generators;
- Testing [1], [14];
- Optimized counters [2]
- Data Encryption/ Decryption;
- Built-in Self-Test (BIST) [6], [7];
- Digital Signal Processing
- Pseudo-random Number Generation(PN)
- Scrambler/Descrambler
- Data Integrity
- Checksums;
- Signature Analyzer [3];
- Error Correction;
- Wireless communications.

II. MATHEMATICAL BACKGROUND

A finite field (FF) or Galois Field (GF), so named in honour of Evariste Galois, in abstract algebra is a field that contains only finitely many elements.

Finite fields are important in algebraic theory, number theory, Galois theory, cryptography and coding theory [12].

It's possible to classify the finite fields by size.

So, for each prime p and positive integer k there is exactly one finite field up to isomorphism of size p^k.

Each finite field of size q is the splitting field of the polynomial $x^q - x$.

Similarly the multiplicative group of the field is a cyclic group.

Finite fields have applications in many areas of mathematics and computer science, including coding theory [16] and others.

The finite fields are classified as follows:

- The number of elements or order, of a finite field is of the form p^n, where p is a prime number called the characteristics of the field, and n is a positive integer.
- There exists a finite field with p^n elements for every prime number p and positive integer n.
- Any two finite fields with the same number of elements are isomorphic. It means that under same remaining of the elements of one of these, both its addition and multiplication tables become identical to the corresponding table of the other one.

The use of a naming scheme for finite fields that specifies only the order of the field is justified by this classification.

Notations for a finite field can be: F_p^n and $GF(p^n)$.

Arithmetic in a finite field is different from the standard integer arithmetic.

In the finite field there are a limited number of elements and the result of any operation performed is an element within that field.

Each finite field is not infinite, but despite this there are infinitely many different finite fields and their cardinal (number of elements) is necessarily of the form p^n where p is a prime number and n is a positive integer.

Two finite fields of the same size are isomorphic.

The prime p is called the characteristic of the field and the positive integer n is called the dimension of this field over its prime field.

Finite fields are used in a variety of applications as in classical coding theory in linear block codes such as BCH (Bose Chaudhuri Hocquenghem) and RS (Reed Solomon) and in cryptography algorithms such as DES (Data Encryption Standard) and Rinjdael encryption algorithm (AES).

A binary polynomial f(x) of degree n has the form:

$$f(x) = x^n + a_{n-1}x^{n-1} + \ldots + a_1 x + a_0$$

where a_i are binary coefficients.

Binary polynomials are added and multiplied in the normal manner of adding and multiplying polynomials except that the resulting coefficients are reduced modulo two.

A binary polynomial f(x) divides polynomial h(x) provided one can find a binary polynomial g(x) such that f(x)g(X)=h(x). For example let $f(x) = x^3 + x + 1$ and $h(x) = x^7 + 1$, then from Example 3 f(x) divides h(x) since f(x)g(x) = h(x) where $g(x) = x^4 + x^2 + x + 1$.

A binary polynomial f(x) is said to be *irreducible* if its only divisors are 1 and f(x). For example one can show that $x^3 + x + 1$ is an irreducible polynomial. It can be shown that if f(x) is an irreducible binomial polynomial of degree n then f(x) is a divisor of $x^{2n-1} + 1$.

An irreducible binomial polynomial on degree n is primitive if f(x) is not a divisor of x^r+1 for any *r* less than 2^n-1. For example x^3+x+1 is a primitive polynomial since

$x^3 + x + 1$ does not divide $x^r + 1$ for r less than 7.

The binary vector and power representations are two other methods of denoting $GF(2^n)$. As before let f(x) be a primitive binomial polynomial of degree n. Let z be a number such that f(z) = 0.

- Binary Vector Representation

For each element $h(z) = a_0 + a_1 z + \ldots + a_{n-1}z^{n-1}$ in $GF(2^n$ one can define a binary n-tuple by identifying:

$h(z)=\{a_0, a_1, \ldots, a_{n-1}\}$

- Power Representation

It can be shown that since f(x) is a divisor of $x^{2n-1} + 1$ and not a divisor of $x^r + 1$ for t less than 2^n-1 then $z^{2n-1} = 1$ and that $z^i \neq z^j$ for $i \leq j \leq 2^n-1$. Using the exponential notation $z^0 = 1$, $GF(2^n)$ can be defined in terms of z^i as:

$GF(2^n) = \{ z^0, z^1, z^3, .., z^{2n-2}\} \cup \{0\}$

This is defined to be the power representation of $GF(2^n)$. Since every non-zero element in $GF(2^n)$ can be expressed as a power of z this element is a *generator* of $GF(2^n)$.

For most applications of $GF(2^n)$ to cryptography, the value of n is large and it is impossible to construct a complete look-up table for the field. In transmission of data the binary n-tuple representation (a_0, a_1, ..., a_{n-1}) is used. The discrete log problem is that, given the binary n-tuple representation of an element in $GF(2^n)$, find its power representation. For large n this is an intractable problem. The reverse problem of given the power representations find the binary n-tuple representation can be easily solved by using the division algorithm as follows:

- Let $a = z^i$ be an element of $GF(2^n)$ defined by primitive polynomial f(x);
- By division algorithm $x^i = q(x)f(x) + r(x)$ where degree of r(x) < n or 0;
- By substitution $z^i = q(z)f(z) + r(z)$ which implies that $z^i = f(z)$.

For security reasons it was demonstrated that the maximum number of pseudo-random sequences is obtained by using irreducible polynomials [15].

III. Experimental Results and Mathematical Calculus

The main subject of analysis the functioning of linear feedback shift register (LFSR) and multiple input output shift register has the irreducible polynomials for degree 4, 8 and 16 [10].

All the analysis is based on the three possible implementations for LFSR [17].

First of all were developed programs for simulating the functioning for the three different types of implementations for comparing the obtained results for 4 degree irreducible polynomials [8].

For all analysis functioning of LFSR for 8 degree irreducible polynomials a complete presentation was made in [9].

In the following table there are presented all the 30 irreducible polynomials of 8 degree.

Table I. The 8 degree irreducible polynomials

1.	1	1	0	1	1	0	0	0	1
2.	1	0	1	1	1	0	0	0	1
3.	1	1	0	1	0	1	0	0	1
4.	1	0	1	1	0	1	0	0	1
5.	1	0	0	1	1	1	0	0	1
6.	1	1	1	1	1	1	0	0	1
7.	1	0	1	1	0	0	1	0	1
8.	1	1	1	1	1	0	1	0	1
9.	1	1	0	0	0	1	1	0	1
10.	1	0	1	0	0	1	1	0	1
11.	1	0	0	1	0	1	1	0	1
12.	1	0	0	0	1	1	1	0	1
13.	1	1	1	0	1	1	1	0	1
14.	1	1	0	1	1	1	1	0	1
15.	1	1	1	0	0	0	0	1	1
16.	1	1	0	1	0	0	0	1	1
17.	1	0	1	1	0	0	0	1	1
18.	1	1	1	1	1	0	0	1	1
19.	1	1	0	0	0	1	0	1	1
20.	1	0	0	1	0	1	0	1	1
21.	1	0	0	0	1	1	0	1	1
22.	1	0	1	1	1	1	0	1	1
23.	1	1	0	0	0	0	1	1	1
24.	1	1	1	1	0	0	1	1	1
25.	1	1	1	0	1	0	1	1	1
26.	1	0	1	1	1	0	1	1	1
27.	1	1	1	0	0	1	1	1	1
28.	1	1	0	0	1	1	1	1	1
29.	1	0	1	0	1	1	1	1	1
30.	1	0	0	1	1	1	1	1	1

It was developed a simulation program for the functioning on LFSR of 8 degree for the Galois implementation [9].

In the following it will be presented an analysis for the irreducible polynomial:

$$P(x) = x^8 + x^6 + x^5 + x^3 + 1 \quad (2)$$

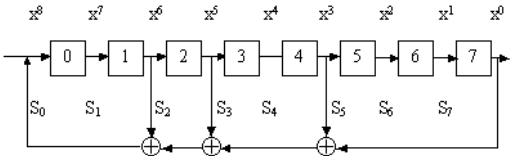

The weights for each position are shown in the next rows:

$$S_0 = 1\ P(x) \quad (3)$$
$$S_1 = x\ P(x) \quad (4)$$
$$S_2 = x^2\ P(x) \quad (5)$$
$$S_3 = (x^3 + x)\ P(x) \quad (6)$$
$$S_4 = (x^4 + x^2 + x)\ P(x) \quad (7)$$
$$S_5 = (x^5 + x^3 + x^2)\ P(x) \quad (8)$$
$$S_6 = (x^6 + x^4 + x^3 + x)\ P(x) \quad (9)$$
$$S_7 = (x^7 + x^5 + x^4 + x^2)\ P(x) \quad (10)$$

First of all in this analysis it was verified with the simulation program for each weight the result, which is the same with the result of the polynomial division and also with the result obtained from the simulation table.

It is presented only the situation of the 7-th weight and after that the next table contains all the other results for all the weights.

All the analysis is referring the results obtained for the Galois implementation.

The result is obtained by the quotient division between the result of multiplying the remainder (the results from Fibonacci implementation) and x^8, and the used irreducible polynomial.

S_7

$(x^{15}+x^{14}+x^{13}+x^{12}+x^{11}+x^{10}+x^9+x^8)(x^7+x^5+x^4+x^2)=$

$=x^{22}+x^{21}+x^{20}+x^{19}+x^{18}+x^{17}+x^{16}+x^{15}+x^{20}+x^{19}+x^{18}+x^{17}+x^{16}+x^{15}+x^{14}+x^{13}+x^{19}+$

$x^{17}+x^{16}+x^{15}+x^{14}+x^{13}+x^{12}+x^{17}+x^{16}+x^{15}+x^{14}+x^{13}+x^{12}+x^{11}+x^{10}=$

$=x^{22}+x^{21}+x^{19}+x^{18}+x^{14}+x^{13}+x^{11}+x^{10}$

$x^{22}+x^{21}+x^{19}+x^{18}+x^{14}+x^{13}+x^{11}+x^{10}$ | $x^8+x^6+x^5+x^3+1$

$x^{22}+x^{20}+x^{19}+x^{17}+x^{14}$ | $x^{14}+x^{13}+x^{12}+x^{11}+$

$x^{21}+x^{20}+x^{18}+x^{17}+x^{13}+x^{11}+x^{10}$ | $x^{10}+x^9+x^8+x^7+x^6+$

$x^{21}+x^{19}+x^{18}+x^{16}+x^{13}$ | x^5+x^3+x+1

$x^{20}+x^{19}+x^{17}+x^{16}+x^{11}+x^{10}$

$x^{20}+x^{18}+x^{17}+x^{15}+x^{12}$

$x^{19}+x^{18}+x^{16}+x^{15}+x^{12}+x^{11}+x^{10}$

$x^{18}+x^{17}+x^{16}+x^{14}+x^{11}$

$x^{18}+x^{17}+x^{15}+x^{14}+x^{12}+x^{10}$

$x^{18}+x^{16}+x^{15}+x^{13}+x^{10}$

$x^{17}+x^{16}+x^{14}+x^{13}+x^{12}$

$x^{17}+x^{15}+x^{14}+x^{12}+x^9$

$x^{16}+x^{15}+x^{13}+x^9$

$x^{16}+x^{14}+x^{12}+x^{11}+x^8$

$x^{15}+x^{14}+x^{11}+x^9+x^8$

$x^{15}+x^{13}+x^{12}+x^{10}+x^7$

$x^{14}+x^{13}+x^{12}+x^{11}+x^{10}+x^9+x^8+x^7$

$x^{14}+x^{12}+x^{11}+x^9+x^6$

$x^{13}+x^{12}+x^8+x^7+x^6$

$x^{13}+x^{11}+x^{10}+x^8+x^5$

$x^{11}+x^7+x^5+x^5$

$x^{11}+x^9+x^8+x^6+x^3$

$x^9+x^8+x^7+x^5+x^3$

$x^9+x^7+x^6+x^4+x$

$x^8+x^6+x^5+x^3+1$

x^4+x+1

$(x^4+x+1)x^8=x^{12}+x^9+x^8$

$x^{12}+x^9+x^8$ | $x^8+x^6+x^5+x^3+1$

$x^{12}+x^{10}+x^9+x^7+x^4$ | x^4+x^2

$x^{10}+x^8+x^7+x^4$

$x^{10}+x^8+x^7+x^5+x^2$

$x^5+x^4+x^2$

Table II. Calculus for S7

	SR_0	SR_1	SR_2	SR_3	SR_4	SR_5	SR_6	SR_7
	0	0	0	0	0	0	0	0
1	0	0	0	0	0	0	0	1
1	1	0	0	0	0	0	0	1
1	1	1	0	0	0	0	0	1
1	0	1	1	0	0	0	0	1
1	1	0	1	1	0	0	0	1
1	0	1	0	1	1	0	0	1
1	1	0	1	0	1	1	0	1
1	1	1	0	1	0	1	1	1
0	0	1	1	0	1	0	1	1
0	0	0	1	1	0	1	0	1
0	0	0	0	1	1	0	1	0
0	1	0	0	0	1	1	0	1
0	0	1	0	0	0	1	1	0
0	1	0	1	0	0	0	1	1
0	0	1	0	1	0	0	0	1
0	0	0	1	0	1	0	0	0
			x^2		x^4			

Table III. The weights for Galois implementation for $P(x) = x^8+ x^6+ x^5+ x^3+1$

The weight	The result
7	$x^4+ x^2$
6	$x^6+ x^5+ x^4+ x^2+ 1$
5	$x^7+ x^6+ x^5+ x^4+ 1$
4	$x^7+ x^3+ x^2$
3	$x^7+ x^6+ x$
2	$x^7+ x^6+ x + 1$
1	$x^5+ x^4$
0	$x^6+ x^4+ x^2+ 1$

The next program was developed for analysis of all 8th degree irreducible polynomials. There are 30 different processings for each polynomial and in the main program it was counted the time for each situation. The program was executed in linux and it was necessary to use – lrt option for accessing time specific functions.

```
#include <stdio.h>
#include <stdlib.h>
#include <time.h>

#include    "prelucrareA0.c"
#include    "prelucrareAl.c"
#include    "prelucrareA2.c"
#include    "prelucrareA3.c"
#include    "prelucrareA4.c"
#include    "prelucrareA5.c"
#include    "prelucrareA6.c"
#include    "prelucrareA7.c"
#include    "prelucrareA8.c"
#include    "prelucrareA9.c"
#include    "prelucrareAlO.c"
#include    "prelucrareAll.c"
#include    "prelucrareAl2.c"
#include    "prelucrareA13.c"
#include    "prelucrareAl4.c"
#include    "prelucrareA15.c"
#include    "prelucrareA16.c"
#include    "prelucrareAl7.c"
#include    "prelucrareAl8.c"
#include    "prelucrareA19.c"
#include    "prelucrareA20.c"
#include    "prelucrareA21.c"
#include    "prelucrareA22.c"
#include    "prelucrareA23.c"
#include    "prelucrareA24.c"
#include    "prelucrareA25.c"
#include    "prelucrareA2 6.c"
#include    "prelucrareA27.c"
#include    "prelucrareA28.c"
#include    "prelucrareA29.c"
struct timespec tstart={0,0}, tend={0,0};

FILE *pf,*fin;
int k,x[23],Lung;

void afis(int tab[],int n)
{
   int i;

   if(k==1)
   {
   printf("     ");
   fprintf(pf,"     ");
   }
   else
   {
      fprintf(pf,"x^%d.",Lung-k+1);
      printf("x^%d.",Lung-k+1);
   }

   for (i=0;i<n;i++)
   {
      printf(" %d ",tab[i]);
      fprintf(pf," %d ",tab[i]);
   }
   fprintf(pf,"\n");
   printf("\n");
}

typedef void (*prel_t)(int n, int knt, int a[],int s[]);

prel_t preltab[30] =
{prelucrareA0,prelucrareA1,prelucrareA2,prelucrareA3,prelucrareA4,prelucrareA5,prelucrareA6,prelucrareA7,prelucrareA8,prelucrareA9,prelucrareA10,prelucrareA11,prelucrareA12,prelucrareA13,prelucrareA14,prelucrareA15,prelucrareA16,prelucrareA17,prelucrareA18,prelucrareA19,prelucrareA20,
```

```
prelucrareA21,prelucrareA22,prelucrareA23,prelucrareA24,pr
elucrareA25,prelucrareA26,prelucrareA27,prelucrareA28,prel
ucrareA29};

int main(int argc, char *argv[])
{

   if(argc==1)
   {
   printf("Lipsa nume la functia prelucrare. (1 ,2 ,3 ...)\n");
   exit(EXIT_FAILURE);
   }
   else
   {

      int s[50],a[50],i,j,numprel;

      pf=fopen("LFSR8_Schema_A.txt","a");
      if(!pf)
      {
      printf("Eroare la deschiderea fisierului
LFSR8_Schema_A.txt !!!\n");
      exit(EXIT_FAILURE);
      }

      fin=fopen("lfsr8.txt","r");
      if(!fin)
      {
      printf("Eroare la deschiderea fisierului lfsr8.txt !!!\n");
      exit(EXIT_FAILURE);
      }

      for(i=0;i<8;i++)
      s[i]=0;

      if(fscanf(fin,"%d",&Lung)!=1)
      {
      printf("Eroare la citirea lungimii polinomului!\n");
      exit(EXIT_FAILURE);
      }

      for(i=0;i<Lung;i++)
         if(fscanf(fin,"%d",&x[i])!=1)
      {
         printf("Eroare la citirea indicelui %d\n",i);
         exit(EXIT_FAILURE);
      }

   numprel = atoi(argv[1]);

      clock_gettime(CLOCK_MONOTONIC, &tstart);
      k=1;

      printf("Se foloseste functia: %d!\n",numprel);
   fprintf(pf,"Se foloseste functia: %d!\n",numprel);

   for(i=0;i<Lung+1;i++)
      {
      afis(s,8);
      preltab[numprel-1](8, i, a, s);
         for(j=0;j<8;j++)
         s[j]=a[j];
      }

      clock_gettime(CLOCK_MONOTONIC, &tend);

      printf("Executarea buclei a durat: %.5f secunde.\n\n",
        ((double)tend.tv_sec + 1.0e-9*tend.tv_nsec) -
        ((double)tstart.tv_sec + 1.0e-9*tstart.tv_nsec));
      fprintf(pf,"Executarea buclei a durat: %.5f secunde.\n\n",
        ((double)tend.tv_sec + 1.0e-9*tend.tv_nsec) -
        ((double)tstart.tv_sec + 1.0e-9*tstart.tv_nsec));

      fclose(pf);
      fclose(fin);
      return 0;
   }
}
```

In this program it was used an input file (lfsr8.txt) containing the input data polynomial and another output file (LFSR8_Schema_A.txt) containing the output sequences while the time is measured for each execution of functioning simulation for all the 30 irreducible polynomials of 8th degree.

The following table contains the time measured in seconds.

Table IV. Results of the main program

	Time 10bits	Time 16 bits	Time 255 bits
prelucrareA0	0.00083	0.0002	0.02697
prelucareA1	0.00016	0.00022	0.00361
prelucareA2	0.00007	0.00016	0.00389
prelucareA3	0.00012	0.00021	0.00373
prelucareA4	0.00016	0.00015	0.00384
prelucareA5	0.00012	0.00022	0.02516
prelucareA6	0.00017	0.00013	0.00364
prelucareA7	0.00012	0.00024	0.00414
prelucareA8	0.0002	0.00022	0.0039
prelucareA9	0.0008	0.00019	0.00392
prelucareA10	0.00018	0.00021	0.00397
prelucareA11	0.00011	0.00016	0.00346
prelucareA12	0.00018	0.00016	0.00425
prelucareA13	0.00007	0.00019	0.00397
prelucareA14	0.00016	0.00022	0.00424
prelucareA15	0.00022	0.00021	0.00696
prelucareA16	0.00015	0.00023	0.00387
prelucareA17	0.00007	0.00022	0.00405

prelucareA18	0.00013	0.00016	0.00377
prelucareA19	0.00015	0.00015	0.00396
prelucareA20	0.00017	0.0002	0.00446
prelucareA21	0.00017	0.00021	0.01093
prelucareA22	0.00012	0.00016	0.00382
prelucareA23	0.00016	0.00015	0.00396
prelucareA24	0.00016	0.0002	0.00399
prelucareA25	0.00007	0.00017	0.00825
prelucareA26	0.00015	0.00025	0.00351
prelucareA27	0.00013	0.00022	0.00377
prelucareA28	0.00012	0.00021	0.00374
prelucareA29	0.0002	0.00019	0.00382

The next two graphics show the obtained results from the execution of the main program for each of all 30 degree 8 irreducible polynomials for three different situations depending on the entrance data polynomial.

The lengths of the entrance polynomials were 10, 16, 255bits. The maximum length of sequences is 2^8-1 [13].

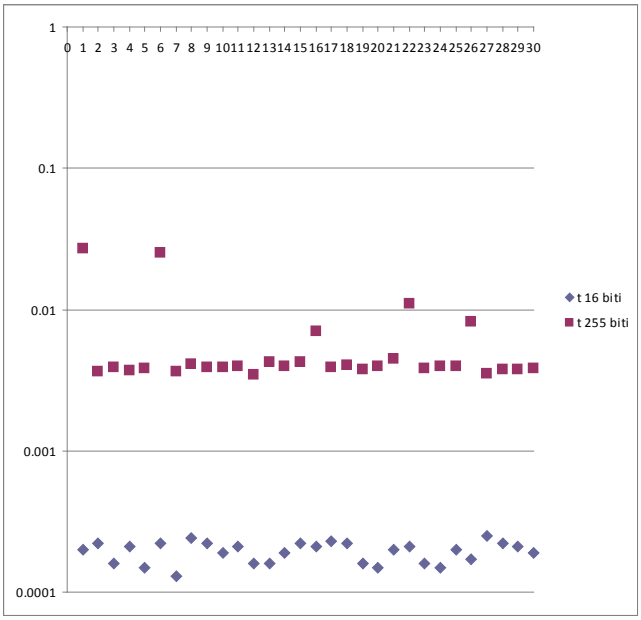

Fig.5. Graphic containing the results for 16, 255 bits

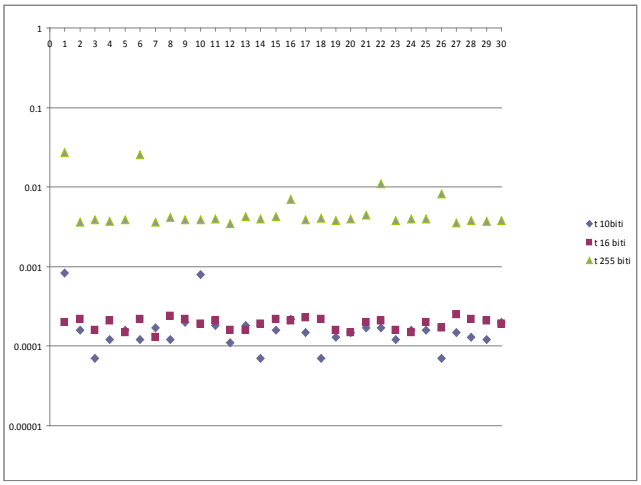

Fig.6. Graphic containing the results for 10, 16, 255 bits

The distribution obtaining in function of the lengths of data entrance polynomial shows that time depends of input length, but for lengths that are quit close the processing times obtain are also close (this can be seen in Fig.6 results for 10 and 16 bits inputs).

Time does not change so much depending on which one of the 30 different 8^{th} degree irreducible polynomials has been used.

IV. CONCLUSION

The whole analysis of functioning for irreducible polynomials of 8 degree proves that almost all obtained results are in the same distribution of time.

The aspect of security was taken into consideration, so that the used polynomials are all irreducible or primitive polynomials.

Another important aspect presented in this analysis is the discovery of the new formula for the calculation of the weights used for obtaining the final result.

This formula was tested for all the situations referring to degree 8 irreducible polynomials and the final conclusion is that the mathematical relations discovered are correct.

A shift register is a device whose function is to shift its contents into adjacent positions within the register or, for the end position, out of the register.

The main practical uses for a shift register are:

- the delay of a serial bit stream;
- the convert between parallel and serial data.

This study focuses on a comparative study of different types of implementations for a Linear Feed-back Shift Register for 8 degree irreducible polynomials. The results of all these experiments were used for obtaining some graphics showing the time distribution.

ISBN: 978-1-61804-219-4

REFERENCES

[1] Abramovici M., Breuer M. A., Friedman A. D., Digital Systems Testing and Testable Design, Computer Science Press,1990;

[2] Alfke P., Efficient Shift Registers, LFSR,Counters, and Long Pseudo-Random Sequence Generators,XAPP 052, July 7,1996.

[3] Alvarez R., Martinez F.-M., Vicent J.-F., Zamora A., A Matricial Public Key Cryptosystem with Digital Signature, *WSEAS TRANSACTIONS on MATHEMATICS* Manuscript , vol.7,No.4,2008, pp. 195-204.

[4] Angheloiu I., Gyorfi E., Patriciu V.V., Securitatea şi protecţia informaţiei în sistemele electronice de calcul, Ed. Militară, Bucureşti, 1986.

[5] Daemen J., Rijmen V., "*The Design of Rijndael: AES - The Advanced Encryption Standard"*, Springer-Verlag, 2002.

[6] Goresky M., Klapper A., Fibonacci And Galois Representations of Feedback with Carry Shift Registers, December 4, 2004;

[7] Matsui M., The First Experimental Cryptanalysis of the Data Encryption Standard.In Advances in Cryptology, *Proceedings of Crypto'94*, LNCS 839, Y. Desmedt, Ed., Springer-Verlag, 1994.

[8] Mioc M. A., Simulation study of the functioning of LFSR for grade 4 Irreducible Polynomials, WSEAS Conference ISPRA, 21-23 February, 2009.

[9] Mioc M. A., Study of Using Shift Registers in Cryptosystems for Grade 8 Irreducible Polynomials, *WSEAS Conference SMO*, 23-25 September 2008.

[10] Mioc M. A., An analyze of functioning for a linear feed-back shift register and a multiple input-output shift register, Buletinul Stiintific al Universitatii „Politehnica" din Timisoara, Seria ELECTRONICA si TELECOMUNICATII, Transactions on electronics and communications, Tom 50(64), Fascicola 2, 2005.

[11] Schneier B., *Applied Cryptology: Protocols, Algorithms, and Source Code in C*, John Wiley and Sons, New York, 1996;

[12] Shannon C.E., Mathematical Theory of Communication, 1948.

[13] Solomon G., Shift register sequences, Aegean Park Press, Laguna Hills, Canada, 1967.

[14] Tsui F., *LSI/VLSI Testability Design*, McGraw-Hill Book Company, 1987.

[15] Udar S., Kagaris D., LFSR Reseeding with Irreducible Polynomials, *IOLTS 2007*, pp. 293-298

[16] Van Lint J.H., Introduction to Coding Theory, 2nd ed., Springer-Verlag, USA, 1992.

[17] Vlăduţiu M., Crişan M., Tehnica testării echipamentelor automate de prelucrare a datelor, Editura Facla, Timişoara, 1989.

Long Term Forecast of Water Desalination Investments in an Arid City: Case of Riyadh, Saudi Arabia

Yasir Khalid and Abdel Hamid Ajbar*

***Abstract*—**Situated in an arid region, the Kingdom of Saudi Arabia is confronting a momentous challenge to cope with rising water scarcity and shrinking water supply. Home of about five million people, the capital, Riyadh, is one of the densely populated cities of the country, and its population is growing by 3% per year. Water demand of the city is fulfilled through local ground water resources with a 48% share while the rest of the supply comes from desalination plants. With rising water demand and retirement of old plants, a considerable gap will exist between water supply and water demand. This research develops a methodology for the prediction of desalination needs for the city residential water until year 2030, and suggests the suitable type and size of desalination plants to bridge theanticipated water supply-demand gap. Following the assessment of water deficit, the total investments needed to build future desalination facilities are also estimated. Because of the uncertainties surrounding the parameters affecting the growth of long term water demand, three scenarios are presented: A low growth scenario, high growth scenario and the most likely scenario. These scenarios are used to provide three estimations of long term investments in needed desalination plants to satisfy the projected water deficit.

***Keywords*—**Water scarcity, desalination plants, economics, supply demand gap analysis, Saudi Arabia.

I. Introduction

Access to fresh water is one of the most important development and infrastructure challenges faced by the Kingdom of Saudi Arabia (KSA).The country has no perennial rivers or lakes, and its renewable water resources are less than 100 cubic meters per capita, well below the 1000 cubic meters per capita benchmark commonly used to denote water scarcity [1]. The annual population growth of 3% [2] puts a considerable strain on the available water resources. Domestic water demand increased at an annual growth rate of 6% i.e. from 200 million m^3/y in 1970 to 2063 million m^3/year in 2010 [2]**.**In order to satisfy the needs for a growing population, the kingdom is currently relying on desalination plants to satisfy around half of the water demand. Building desalination plants is, however, a costly and time consuming process. It is therefore of importance that policy makers have a reliable estimate of the long term water desalination needs in order to implement the appropriate capital expenditures in the development plans and to avoid any shortage in the domestic water supply..

Riyadh city, with a population of around five millions, compromises more than one fourth of the total population of Saudi Arabia. Being the capital and an important industrial center, it is a focal point for local and international immigration with 30% of the population being non-Saudi [3]. Rapidly rising population, large investments in social and physical infrastructure and enviable outdoor activities have exerted enormous pressure on the existing water facilities of Riyadh.

At present, Riyadh water supplies come from local ground water (48%) while the rest comes from two thermal multi-stage flash (MSF) distillation plants and one membrane-based reverse osmosis (RO) plant installed on the gulf sea [3-4]**.** MSF plants have completed their life cycle and are working under extension period. A new plant at Ras Al-Khair (RAK) is gearing up to be installed in the near future. With the stoppage of old plants, a severe water shortage will occur in near future even with the inclusion of RAK desalination plant.

This research involves an analysis of Riyadh's water supply and demand and goes on to calculate the water deficit until year 2030. Moreover it will also suggest the suitable type of new desalination plants to be installed based upon acceptable practice and standards, followed by the estimation of the required investments.

II. Riyadh's Water Resources

A. Supply Side

On the supply side, the city receives around 48% of its resources from local ground water, after being treated by reverse osmosis plants [3-4]. The other part of water supply comes from three desalination plants MSF I (starting year 1982, capacity of 118,447m^3/day), MSF II (starting year 1983, capacity of 815,185m^3/day) and reverse osmosis (starting year 2002, capacity of 78,182m^3/day)[5]. The water supply system in the city is also characterized by large unaccounted for water (UFW), estimated to be 30% of the water supply [6].

B. Water Demand

Desalination water is used primarily in the residential sector. Agricultural and industrial sectors make use of treated ground

Yasir Khalid is a researcher in the Department of Chemical Engineering, King Saud university, P.O. Box 800, Riyadh 11421, Saudi Arabia (email:ykhalid@ksu.edu.sa).

Abdel Hamid Ajbar (corresponding author) is a professor in Chemical Engineering Department, King Saud university (phone:++966-11-4676850; fax:++966-1-4678770;email:aajbar@ksu.edu.sa)

ISBN: 978-1-61804-219-4

water. For the residential sector, the typical household in the city uses about 47% of its total water use in the bathroom. The toilet makes up 27%, while the shower and sink use 20%. Laundry makes up 21%, faucets 16% while the leaks are estimated to be around 17% [6]. The residential per capita water consumption in the city is estimated in 2011 to be 308 liters per day [6]

III. CURRENT DESALINATION PLANTS FOR RIYADH CITY

Two desalination technologies are used to supply water to Riyadh city. The thermal multi-stage flash (MSF) is the dominant desalination technology and has a share of about 90%of the total desalinated water supplied to the city while the rest of the desalinated water comes from the membrane-based reverse osmosis (RO) plants [7]. In MSF process, seawater is pressurized and heated to the maximum desalination plant temperature and is then discharged into chambers maintained slightly below the saturation vapor pressure of water. This causes a fraction of its water content to flash into steam. The flashed steam is stripped of suspended brine droplets as it passes through a mist eliminator, and then condenses on the exterior surface of heat transfer tubing. The condensed liquid drips into trays as a water suitable for human consumption. The other desalination plant installed is reverse osmosis (RO) which uses hydraulic pressure as its energy source for desalting seawater. In this process, seawater is driven under pressure through a semipermeable membrane, generally of organic material, to separate water from salts.

MSF plants are known to be energy extensive but they have the advantage of producing both fresh water and electricity (co-generation). RO plants, on the other hand, require far less energy but are known to be negatively affected by the short life of their membranes. However, recent innovations in membrane and pre-treatment technologies have made the RO process more competitive.

III-METHODOLOGY FOR ESTIMATION OF DESALINATION NEEDS

A. Scenario Development for Water Demand

The starting point for the determination of desalination needs is the estimation of long term water demand. The authors [3] have recently conducted a study to determine the long term water demand of the city (Fig.1).Uncertainties about population growth, economic growth and water management were taken into consideration in developing the three scenarios shown in Fig.1.

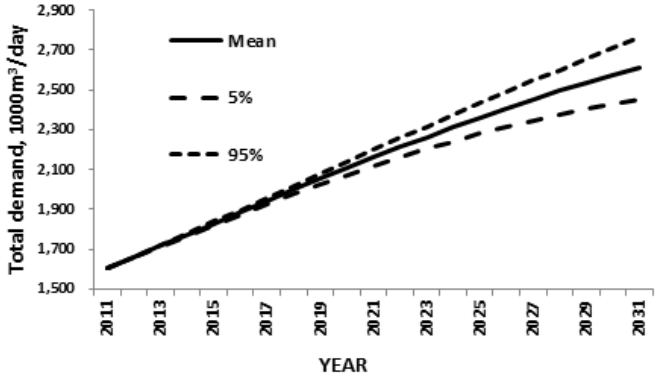

Fig. 1 Water Demand for Riyadh City [3]

The predicted water demand is represented by an interval within which 90% of potential demand would normally fall. A 90 percent confidence interval is formed by the values of the 5^{th} and 95^{th} percentiles i.e. one may feel confident that 90 percent of all forecast possibilities will fall within this interval for any forecast year. The 5% scenario would represent roughly the scenario associated with small growth of water demand. The 95% scenario would roughly be associated with very high growth of water demand. The mean value would represent the most likely scenario.For example, the year's 2030 projected water demand of 2610 $x10^3$ m^3/day would lie between the limits of 2451$x10^3$ m^3/day (5% demand scenario) and 2766$x10^3$ m^3/day (95% demand scenario). Using the above mentioned forecasted water demand, the water deficit between the projected demand and available water supplies in the coming years can be calculated.

B. Assessing the Water Supply from 2011-2030

A common life cycle of desalination plants is 20-25 years depending upon the type of technology. Refurbishment of the existing old plants provides an extension of plant lifetime by more than 15 years. On this basis and assuming a 40-year life design, [8-9], the MSF I and MSF II desalinations plants will complete their life span in year 2023 and year 2024 respectively. The amount of water supplied by local ground water resources (906,644 m^3/day) is assumed to remain the same from year 2011 to year 2030. The desalinated water to be supplied from Ras Al-Khair plant (900,000 m^3/day) in 2014 [5] is also considered

C. Analyzing Water Supply-Demand Gap

Fig.2 represents the total water supply from year 2011 to 2030. The starting water supply for all scenarios is 1,918,458 m^3/day in 2011 which raises to 2,818,458 m^3/day in 2014 with the addition of RAK plant, then reduces to 1,884,826m^3/day with the retiring of old MSF plants and remains constant until 2030.

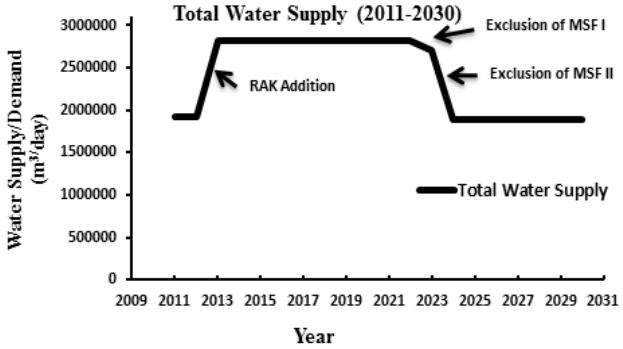

Fig. 2 Total Water Supply for the City (2011-2030)

The total water supply/demand gap for all three different scenarios is shown in Fig. 3 with two different zones. The first zone corresponds to the time in which supply exceeds the demand while the second zone indicates the time period where demand is outstripping the supply. Its starting point is year 2024 where supply and demand curves intersect each other and is shown by an angular upward arrow. For the 95% scenario, the water deficit for year 2024 is 23% which grows to 32% (881,174m^3/day) until year 2030. For the 5% demand scenario there will be water deficit of 17% in year 2024 which rises to 23% (566,174 m^3/day) in year 2030 while for the mean (most likely scenario) the deficit figure for year 2024 is 20% and reaches up to 28% (725, 125m^3/day) in year 2030.

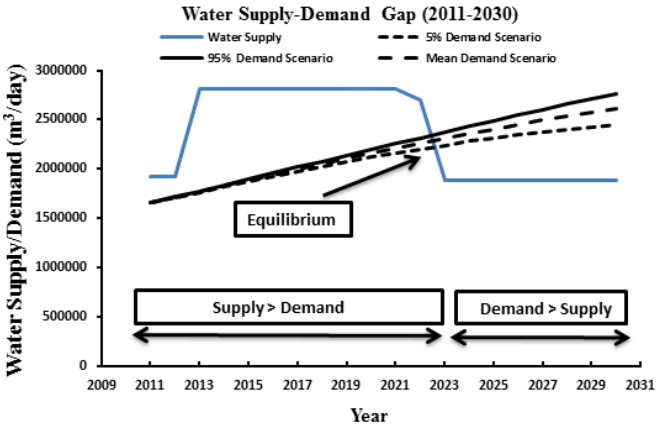

Fig. 3 Supply-Demand Curve for the three Scenarios

D. *Selection of Suitable Location*

Desalination plants should be installed in a place where interconnections to the power distribution and water supply networks are economically and technically feasible [10]. These include the possibility of effective usage of current road infrastructure for the plants already in operation and the utilization of existing fuel network in order to use existing network facility. Proper utilization of residential multifaceted of existing plants is another key factor that has to be considered while selecting an appropriate location. In the light of above discussion, the necessity of water for Riyadh city will be served by Al-Jubail city, located in the Eastern province of the country. The old plants that are located in the same city (Al-Jubail) have already completed their life span and are working under life extension program and can be de-commissioned with minimum environmental effect.

E. *Selecting Suitable Desalination Technology*

The next significant task is the selection of suitable desalination technology. A comparison among the two dominant technologies is presented in the following Table 1. The table shows results of comparison using two different criteria: Non-computable (i.e. qualitative) criteria and computable (i.e. quantitative) criteria.

Table 1 Comparison between leading desalination technologies[11-12]

Description	**MSF**	**RO**
Maintenance and Reliability	High	Average
Power generation dependency	High	Low
Robustness	High	Less than MSF
Future technology options	Low	High
Flexibility	Low	High
Environmental Impact	High	Low
Feed Water Sensitivity	Low	High
Computable Criteria (Based upon 15 MIGD (68,184 m^3/day) Plant)		
Description	MSF	RO
Unit Operating Cost ($/m^3)	1.07	0.76
Annual Operating Cost (M$/year)	26.63	18.92
Operating Cost (OPEX) (20) (M$)	532	378.28
Capital Cost (CAPEX) (M$)	(9*15)=135	(7.5*15)=112.5
Total Cost (M$)	667	490.78

The above comparisons show that RO is dominant over MSF in most of the addressed cases. There is today a better understanding of pre-treatment requirements for the RO process.However for Riyadh city where population is increasing at a rapid rate and industrialization is expanding, putting more stress on power needs, the desalination plant coupled with power plant provides a benefit of better utilization of fuel. MSF desalination plants are economically feasible since by allowing cogeneration of water and electricity, the cost of the plant is distributed over two products (water and electricity).The choice of MSF plants looks promising as the old MSF plants infrastructure can be easily used with the new similar plants.

F. *Selection of Plant Size*

The size and number of units for the selected technology depends upon the respective maximum number of units in running at the moment of installation and technology advancement. MSF units are moving towards bigger size. The biggest MSF plant having unit capacity of 16.7 million gallons per day (MIGD)(i.e. 75,898 m^3/day) is in operation in Shouhat (United Arab Emirates) while other units having capacity 20 MIGD are in construction phase in Ras Al-Khair . In this context we will use (16.7 MIGD=75,898m^3/day) MSF unit

ISBN: 978-1-61804-219-4

size as it carries acceptable practice and standards of working for longer period of time.

IV. Economic Analysis of Total Investment

This section deals with the total investment needed for MSF plants with a unit capacity of 16.7 MIGD which is a bench mark capacity for MSF evaporators as described in the previous section. Economic analysis includes the estimation of capital costs (CAPEX) and operating costs (OPEX). MSF desalination costs depend on a number of site specific factors such as feed water characteristics, product water quality, plant capacity and energy. Cost calculations are done using the following relations while the results are shown in Table 2

- Annual Operating Cost=Unit Operating Cost*Plant Capacity
- OPEX=Annual Operating Cost*20 years (Plant life cycle is considered to be 20 years [13])
- CAPEX= Unit Capital Cost* Plant Capacity

Table 2 Cost Summary for 16.7 MIGD Plant

Description	**Units**	**Cost**
Parts	(US $/m^3)	0.01
Chemicals	(US $/m^3)	0.05
Labor	(US $/m^3)	0.08
Amortized Capital Cost	(US $/m^3)	0.42
Thermal Energy	(US $/m^3)	0.31
Electrical Energy	(US $/m^3)	0.20
Unit Operating Cost	(US $/m^3)	1.07
Annual Operating Cost for 16.7 MIGD	M$/year	29.64
Operating Cost(OPEX) (20 years)	M$ (US)	593
Capital costs(CAPEX)	M$ (US)	150.3
Total Cost(CAPEX+OPEX)	M$ (US)	743.3

Table 3 shows the total investment needed for building the desalination plants for all three scenarios.

V. Conclusion

This paper has presented a case study on how to estimate the long term desalination plants for an arid and desalination-dependent city. The problem is a challenging one, given that it requires in the first stage the determination of water demand. Given the uncertainties surrounding the population growth and economic growth (linked to fluctuating oil prices), the determination of water demand has to be made using a probabilistic approach using three scenarios.

Table 3Number of units and total investment

Scenario	Plant Capacity(MIGD)	Number of Units Needed	Theoretical possible units	Total Investment (billion US$)
5 %	128.81	7.7	8	5.94
95 %	194.25	11.6	12	8.92
Mean	159.86	9.6	10	7.43

Following this step, this research work estimated the gap between the total water demand and available water resources for two decades (2011-2030). The research predicts water gaps of 124.81 MIGD, 159.86 MIGD and 194.25 MIGD for three probable scenarios until year 2030. Moreover it was shown that with the retiring of old MSF plants, the installation of the same type of plants looks promising based upon past experience and long lifetime. The evaporator capacity was chosen based upon the available acceptable practice. The number of units required against the predicted gap for all three scenarios were also calculated. For 124.81 MIGD gap, 8 units wills serve the purpose while for 159.86 MIGD and 194.25 MIGD the required number of units is 10 and 12 respectively. The total investment needed for building the desalination plants for all three scenarios was calculated. The maximum investment is for the 95% demand scenario which is 8.92 billion dollars and the minimum investment is 5.94 billion dollars for the optimistic (5%) scenario. The most likely (mean) scenario requires 7.13 billion dollars. These findings will definitely ease water authorities to build the new desalination plants on fast-track basis to cope with the chronic water shortage problem.

References

[1] A. Giansiracusa. (2010) "Coping with Scarcity: Saudi Arabia and Water,"Available:http://www.stimson.org/spotlight/coping-with-scarcity-saudi-arabia-and-water/.

[2] O. K. M. Ouda. "Water demand versus supply in Saudi Arabia: current and future challenges," *Int. J. Wat. Resour.D.* 2013. DOI:10.1080/07900627.2013.837363.

[3] I. Almutaz, E. Ali, Y. Khalid, A.H. Ajbar."A long-term forecast of water demand for a desalinated dependent city: case of Riyadh City in Saudi Arabia,"*Desalin.Water Treat*. vol.51, pp. 5934–5941, 2013.

[4] I. Almutaz, A.H. Ajbar and E. Ali. "Determinants of residential water demand in an arid and oil rich country: A case study of Riyadh city in Saudi Arabia," *IJPS*, vol.7, pp. 5787-5796, 2012.

[5] SWCC. "Saline Water Conservation Corporation, Annual Report", no. 38." pp. 16-23, 2011.

[6] MOWE. (2011). Ministry of Water and Electricity, Riyadh, Saudi Arabia

[7] IAEA (2002) "Status of design concepts of nuclear desalination plants." International Atomic Energy Agency,Available:http://wwwpub.iaea.org/mtcd/publications/pdf/te_1326_web.pdf

[8] C. Sommariva, H. Hogg and K. Callister. "Forty-year design life: the next target Material selection and operating conditions in thermal desalination plants,"*Desalination*, vol. 136, pp. 169-176, 2001.

[9] R.G. Raluy, L. Serra and J. U. A. Valero. "Life-cycle assessment of desalination technologies integrated with energy production systems." *Desalination*, vol. 167, pp. 445–458, 2004.
[10] N. X. Tsiourtis. "Criteria and procedure for selecting a site for a desalination plant." *Desalination*, vol.221, pp. 114–125, 2008.
[11] GWI/WDR. (2012), "Technology choice still open at Yanbu 3." Water Desalination Report,Availablehttp://www.globalwaterintel.com/archive/13/10/general/technology-choice-still-open-yanbu-3.html
[12] G. Ejjeh, L. Awerbuch. (2009)"Challenges of Integration of Desalination, Power, Energy, Environment and Security." World Energy Council, Dubai, Available: http://64.190.51.133/Programs/CFFS/CFFSDubai/Innovations_in_Water__Energy_Technologies1.pdf
[13] A. A. Mabrouk, "Techno-economic analysis of tube bundle orientation for high capacity brine recycles MSF desalination plants," *Desalination*, vol. 320, pp. 24–32, 2013.

Modified ABC Variant (JA-ABC4) for Performance Enhancement

Noorazliza Sulaiman, and Junita Mohamad-Saleh

***Abstract*—**Optimization algorithms developed based on bio-inspired algorithms (BIAs) have solved various optimization problems. Among them, Artificial Bee Colony (ABC) algorithm, a swarm-intelligence-based (SI) algorithm has attracted the attention of optimization researchers. It is because it has demonstrated tremendous results in comparison with other optimization algorithms such as Genetic Algorithm (GA), Differential Evolution (DE) algorithm and Particle Swarm Optimization (PSO) algorithm. Besides that, it is also known to be simple and flexible. However, ABC may be trapped in local optima and has slow convergence speed. Although ABC variants have been proposed by various researchers, none of them can solve both problems simultaneously. Thus, this work presents a new modified ABC algorithm referred to as JA-ABC4 with the objectives to diligently avoid premature convergence and enhance convergence speed. The proposed algorithm has been compared with the standard ABC and other existing ABC variants on ten commonly used benchmarks functions. The performance results have shown that the proposed algorithm has yielded the best performance compared to the standard ABC and two other good ABC variants (BABC1 and IABC) in terms of convergence speed and global minimum achievement.

***Keywords*—**Artificial bee colony, Bio-inspired algorithm, convergence speed, swarm-intelligence-based algorithm.

I. Introduction

Inspired by the behaviors of nature, bio-inspired algorithms (BIAs) have been applied to solve various optimization problems as shown by works of [1]-[4]. BIAs are metaheuristic method that has promising results in solving those problems [5]. They have been implemented to overcome the problems of high computational cost and premature convergence tendency that numerical methods have faced [3]. BIAs basically consist of several classes and among the most prominent classes are swarm-intelligence-based (SI) algorithms. Many optimization algorithms have been developed based on SI and examples of them are Ant Colony Optimization (ACO) algorithm [6], Particle Swarm Optimization (PSO) algorithm [7] and many more. These algorithms have shown tremendous performance in solving various problems such as the travelling salesman problem [8], power loss minimization [9], environmental economic dispatch [10] and many more. One SI method that has recently attracted the attention of optimization researchers is Artificial Bee Colony (ABC) algorithm.

ABC has been proposed by Karaboga in 2005 [11] and it is inspired from the foraging behavior of honeybees [12]. Many optimization researchers show their interest in it since it has shown efficiency in solving various optimization problems as well as demonstrated excellent performance in comparison with other prominent optimization algorithms such as Genetic Algorithm (GA), Differential Evolution (DE), Particle Swarm Optimization (PSO) algorithms and few others [12]-[14]. Apart from that, its control parameters are easy to tune and its implementation is simple and flexible [12].

In spite of its excellence performance, it actually suffers from few limitations which are premature convergence tendency on multimodal function due to local minima trappings and slow convergence speed on unimodal functions [15], [16]. ABC is known to be good in exploration but poor in exploitation. Moreover, it does portray extreme self-reinforcement. Many researchers have come out with the proposal of various ABC variants [15]-[21] with the aims to solve the problems. However, none of them are able to solve to problems simultaneously [15], [16], [19]. This is due to the exploration and exploitation processes which have to be balanced in order for the algorithm to perform well and maintain its robustness [17], [20], [21]. Thus, this work proposes a modified ABC variant named JA-ABC4. Few modifications have been done to the standard ABC algorithm to balance out the exploration and exploitation capabilities of the algorithm. The effects are for the algorithm to persistently avoid local optima trapping and show faster convergence speed, simultaneously.

II. Artificial Bee Colony (ABC) Algorithm & Variants

A. Standard ABC algorithm

In order to complete each generation, the standard ABC algorithm has three performance-deciding phases. They are employed-bees, onlooker-bees and scout-bee phases. The algorithm starts when the employed-bees have been randomly assigned with food sources available around the hive or search-space. Food sources represent the possible solution for

This work is supported by Ministry of Higher Education (MOHE) FRGS Grant No: 203/PELECT/6071247.

J. Mohamad-Saleh is with School of Electrical & Electronic Engineering, Universiti Sains Malaysia, 14300 Nibong-Tebal, Penang, Malaysia (corresponding author ‘s phone: 604-599-6027; fax: 604-594-1023; e-mail: jms@ usm.my).

N. Sulaiman is with School of Electrical & Electronic Engineering, Universiti Sains Malaysia, 14300 Nibong-Tebal, Penang, Malaysia (e-mail: noorazlizasulaiman@gmail.com).

the problems. Then, the nectar-amount of food sources which is the fitness of the possible solution is being calculated. After that, employed-bees explore the neighborhood of food sources associated to it and update its food source using mutation equation or solution search equation given as:

$$z_{ij} = y_i + \phi(y_{ij} - y_{kj}) \quad (1)$$

where z_{ij} represents the candidate solution of i_{th} food source with j_{th} dimension. y_{ij} is j_{th} dimension of i_{th} food source and y_{kj} represents j_{th} dimension of k_{th} food source. Subscripts *i* and *k* are the mutually exclusive food sources, j Є [1,2,…D] and *D* is the dimension of search space. Subscripts *j* and *k* are randomly chosen numbers and φ is a random number within [-1,1].

The equation has directed the interaction among the possible solutions which results in a new possible solution called candidate solution. This candidate solution will be evaluated with the old possible solution using greedy-selection mechanism. This mechanism is used to select the fitter possible solution between the candidate solution and the old possible solution. Once the fitter possible solution has been chosen, the employed-bees associated with this potentially fitter possible solution share it with the onlooker-bees, in the onlooker-bees phase. Onlooker-bees use fitness-proportion selection scheme in choosing the possible solutions to be updated. The action of onlooker-bees is also dependent upon the probability value, *P*i:

$$P_i = fit_i / \sum_{i=1}^{SN} fit_i \quad (2)$$

where P_i is the probability of *i*-th food source, fit_i is the fitness value of *i*-th food sources and *SN* represents the number of food sources. Then, the onlooker-bees explore the neighborhood of the selected-possible solution and update it using (1). Later, greedy-selection mechanism is applied in choosing the fitter possible solution. Finally, in scout-bee phase, the possible solution which has become exhausted and can no longer be improved over a user-defined control parameter *limit* [20] will be abandoned [17]. The employed-bees associated with this possible solution will become scout-bees and will take subsequent flight to discover a new possible solution to replace the abandoned possible solution. This is done by randomly searching the search space [12] using the equation:

$$y_i^j = y_{\min}^j + rand(0,1)(y_{\max}^j - y_{\min}^j) \quad (3)$$

where y^j_{min} and y^j_{max} is the lower and upper limit of the search space, respectively. *rand (0, 1)* is a function which randomly generates numbers within [0,1]. More details of ABC can be found in [12].

B. ABC Variants

G-best guided ABC (GABC) algorithm has been proposed by Zhu and Kwong in 2010 [17]. It uses the information of global best possible solution (g-best) in the solution search equation. Thus, it has the capability to improve exploitation. The proposed solution search equation has enhanced the exploitation of the algorithm by driving the candidate solution towards a global best solution. Hence, the candidate solution becomes fitter with each generation. However, the algorithm has been found to be slow in convergence rates [16].

Best-so-far ABC (BsfABC) algorithm has been proposed by Banharnsakun *et al.* in 2011 [18]. It has incorporated new solution search equation for the onlooker-bees to improve convergence rate and increase the performance of the algorithm. Nevertheless it seems to be computationally intensive and the solution search utilized during onlooker bee phase is found to be local in nature. Thus, the possibility to be trapped into local optima is high. This has made BsfABC insufficient in solving complex optimization problems [15], [16].

Improved ABC (IABC) algorithm has been introduced by Gao and Liu in 2011 [19]. Two improved solution search equations have been proposed in this work together with the chaotic systems and the opposition-based learning method during initialization. Besides that, parameter *p* has been introduced to control the emergence of both solution search equation. Nonetheless, this variant is actually poor in exploitation. This is proven when the algorithm is not capable in dealing with Rosenbrock function [19].

Gao *et al.* [20] have recommended global best ABC (BABC) in 2012. They have incorporated new modified solution search equation into the standard ABC to replace the old one, creating two BABC algorithms named BABC1 and BABC2. The solution search equation for BABC1 has driven the new solution around the best solution while the solution search equation of BABC2 explores the search space randomly around the best solution. However, the algorithm has suffered from insufficient in exploration. This limitation leads the variant to premature convergence when solving complex multimodal optimization problems [16].

An analysis has been carried out and the results have shown that IABC and BABC1 exhibit the best performances among all. Thus, these two have been chosen as the compared algorithms in this work.

The standard ABC algorithm is known to be good in exploration but poor in exploitation [17], [20], [21] resulting the inefficiency of ABC to solve premature convergence tendency and slow convergence speed problems. Although the above-mentioned variants aim to overcome these, they are actually not capable to solve those limitations simultaneously. Thus, this paper proposes a new ABC variant referred to as JA-ABC4 as the problem solver. This new ABC variant basically is the extension of the variant that has been proposed in the work of [22].

III. Modified ABC (JA-ABC4) Algorithm

The inefficiency of the standard ABC is due to (1) which

directs the interaction between y_{ij} and y_{kj}. y_{ij} is the possible solution to be updated while y_{kj} is a random possible solution. It means that the random possible solution is being chosen regardless of its fitness value. Hence, in any case, if fitter random possible solution (y_{kj}) is selected, the candidate solution would be fitter as well. The problem comes when the equation chooses any poor possible solution for the interaction. The resulting candidate solution would be dragged close to the poor possible solution. Hence, the candidate solution would be poor and drifted away from the global minimum.

Therefore, in this work, new stages have been inserted before the employed-bee phase in order to overcome the problem. These new stages have directed the algorithm to identify few poor possible solutions and then update the solution around global best (gbest) solution using the mutation equation inspired from [20]:

$$z_{ij} = y_{best,j} + \phi(y_{ij} - y_{kj}) \quad (4)$$

where z_{ij} represents the candidate solution of i_{th} food source with j_{th} dimension. $y_{best,j}$ is best food source, y_{pj} represents j_{th} dimension of p_{th} food source and is randomly chosen. Subscripts *i*, *k* and *p* are the mutually exclusive food sources and the rest of the parameter are the same as (1).

Equation 4 has generated candidate possible solution which definitely should be fitter than the previous and then substituted the poor possible solution. This will create a fitter population since employed-bees and onlooker-bees would then update these fitter possible solutions in the next phases. Thus, the population now is fitter yet diverse population. By doing so, the convergence speed of the algorithm has been increased.

Since the population now is a fitter population, there is a possibility for the algorithm to be trapped in the local optima. Thus, in order to avoid this, the mutation equation of the employed-bees in employed-bees phase has been modified. This modification has inspired by the mutation equation found in [19] and [15]. The mutation equation of JA-ABC4 is:

$$z_{ij} = y_{r1,j} + \phi(y_{r2,j} - y_{r3,j}) + \psi(y_{r4,j} - y_{best,j}) \quad (5)$$

where $y_{r1,j}$, $y_{r2,j}$, $y_{r3,j}$ and $y_{r4,j}$ are *r1*, *r2*, *r3* and *r4-th* food sources with j_{th} dimension. Subscripts *r1*, *r2*, *r3* and *r4* refer to the mutually exclusive food sources, Ψ is a random number within [0,T], where T is a user defined number and the rest of the parameter are the same as (1) and (4).

The first two terms of (5) are inspired from the equation proposed in [19]. This equation aims to enhance the exploration capabilities of the algorithm as the equation is known for its randomness [19]. Thus, this will cater the possibility for premature convergence tendency of the algorithm. The last term of the equation targets to balance out the exploration and exploitation capabilities of the algorithm [23]. The overall equation should exhibit faster convergence speed and efficiently avoid local minima, simultaneously.

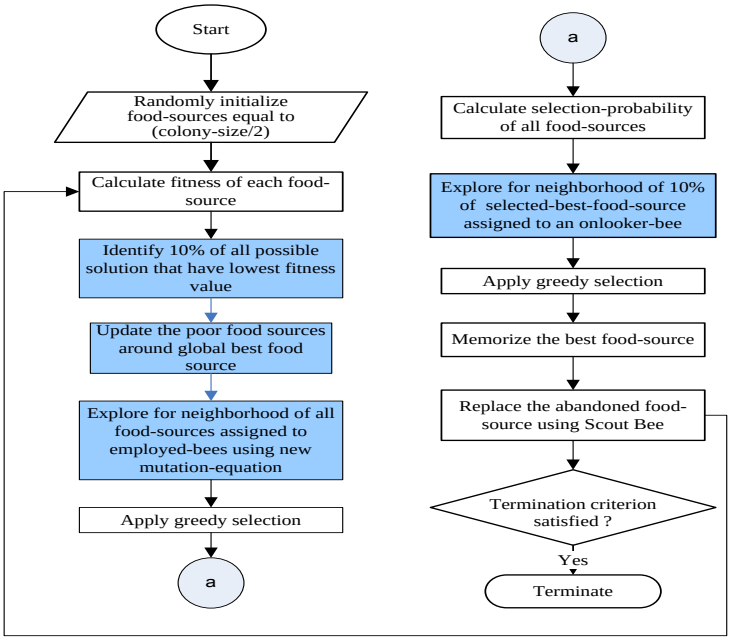

Fig. 1 The flowchart of JA-ABC4

The next modification is to make sure that the overall algorithm demonstrates balanced exploration and exploitation capabilities. This is done by directing the onlooker-bees to update only few most-fit selected-possible solutions. Thus, with only few possible solutions to be updated, the exploitation capability of onlooker-bees has been enhanced and the algorithm is expected to converge faster.

This proposed modified ABC variant has been simulated on ten commonly used benchmark functions which are Griewank (f_1), Rastrigin (f_2), Rosenbrock (f_3) Ackley (f_4), Schwefel (f_5), Himmelblau (f_6), Sphere (f_7), Step (f_8), Bohachevsky 2 (f_9) and RS Schwefel's 2.22 (f_{10}) as listed in Table I.

IV. EXPERIMENTAL SETTINGS

Besides being tested on ten commonly used benchmarks functions as listed in Table I, the performance of proposed algorithm, JA-ABC4 has also been compared with the standard ABC (ABC) [12] and two best-performed ABC variants, i.e. global best ABC (BABC1) [20] and improved ABC (IABC) [19].

For all algorithms, the dimension of the benchmark function has been set to 30, the population size has been set to 50, number of generation has been limited to 1000 and parameter *limit* has been set as D×SN, where D represents the dimension of the search space and SN is the number of food sources. The *T-value* for JA-ABC4 has been set to 0.5 [15] and the *p-value* of IABC has been set to 0.25 [19]. As for global solution validation, each of the compared algorithms including JA-ABC4 has been set to simulate for 30 times on each benchmark function [15]. All these values follow those used and recommended in the literature [12], [13], [15], [17], [19], [20], [21].

ISBN: 978-1-61804-219-4

Table I. Benchmark functions

Function	Function Name	InitializationRange
f1	RS Griewank	±600
f2	RS Rastrigin	±15
f3	RS Rosenbrock	±15
f4	RS Ackley	±32
f5	RS Schwefel	±500
f6	RS Himmelblau	±600
f7	RS Sphere	±600
f8	RS Step	±600
f9	RS Bohachevsky 2	±100
f10	RS Schwefel's 2.22	±100

V. Results and Discussion

Figs. 2 to 7 show the performance results of the proposed algorithm, JA-ABC4 in comparison with the standard ABC and two best-performed ABC variants i.e. BABC1 and IABC.

The performance results have shown the superiority of JA-ABC4 compared to other algorithms in terms of convergence speed and global minimum. From Fig. 2, it has depicted that the standard ABC and BABC1 have failed to reach the optimum solution. Although IABC did reach the global optimum but the convergence speed of JA-ABC4 is faster than IABC. Also, JA-ABC4 has efficiently reached global minimum. Figs. 1 and 4 show that JA-ABC4 exhibits faster convergence speed than other compared algorithms while the rest of the graphs have also illustrated the superb performance of JA-ABC4 compared to other algorithms in terms of convergence speed and avoiding local minima trapping.

Table II summarizes the statistical results obtained for each of the benchmark functions. It shows the average and standard deviation of 30 runs for each of the compared algorithms. It is clear from the statistics in Table II that JA-ABC4 is the most outstanding ABC variant.

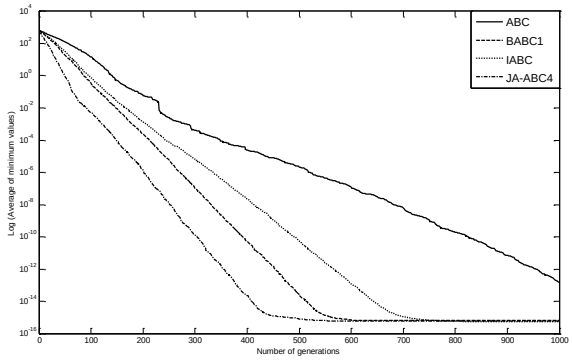

Fig.2 Performance result of compared algorithms on *f1*

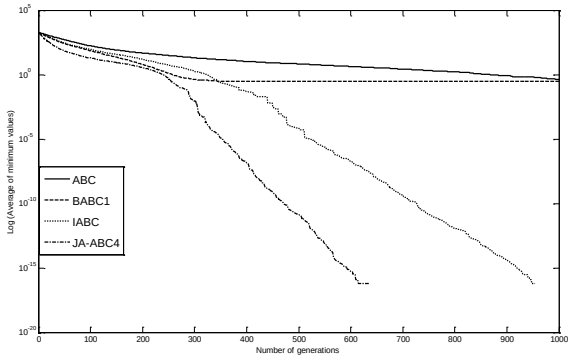

Fig.3 Performance result of compared algorithms on *f2*

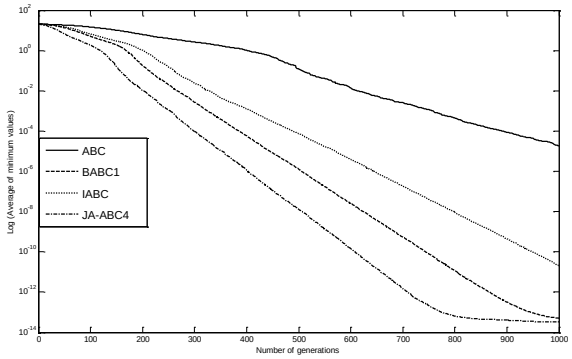

Fig.4 Performance result of compared algorithms on *f4*

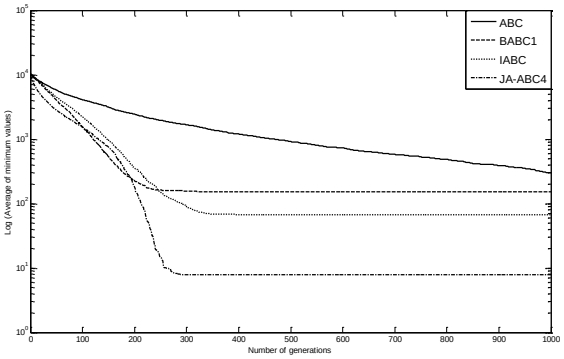

Fig.5 Performance result of compared algorithms on *f5*

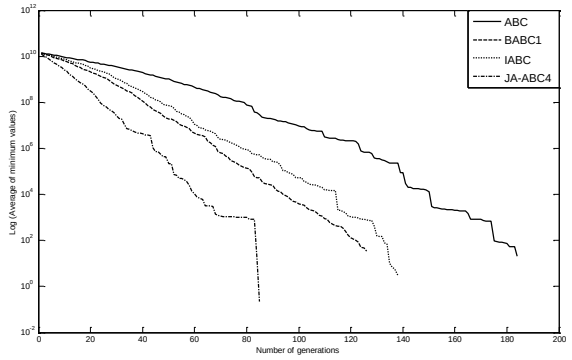

Fig.6 Performance result of compared algorithms on *f6*

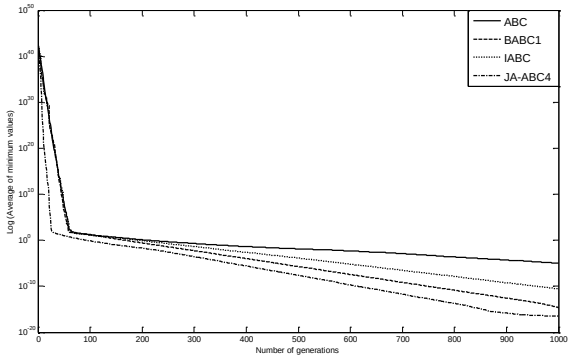

Fig.7 Performance result of compared algorithms on *f10*

Table II. Performance results of the compared optimization algorithms

Functions	Algorithms	Average	Std Deviation
f1	ABC	1.47E-13	1.65E-13
	BABC1	6.22E-16	1.50E-17
	IABC	5.40E-16	4.82E-17
	JA-ABC4	**5.34E-16**	**1.09E-17**
f2	ABC	3.77E-01	5.87E-01
	BABC1	2.98E-01	4.64E-01
	IABC	0.00E+00	0.00E+00
	JA-ABC4	**0.00E+00**	**0.00E+00**
f3	ABC	9.03E-01	1.11E+00
	BABC1	3.04E+01	3.30E+01
	IABC	5.63E+00	5.85E+00
	JA-ABC4	**4.54E+00**	**1.39E+00**
f4	ABC	1.82E-05	1.12E-05
	BABC1	4.86E-14	7.52E-15
	IABC	1.97E-11	6.75E-12
	JA-ABC4	**3.26E-14**	**4.24E-15**
f5	ABC	2.96E+02	1.20E+02
	BABC1	1.54E+02	1.33E+02
	IABC	6.71E+01	8.62E+01
	JA-ABC4	**7.90E+00**	**3.00E+01**
f6	ABC	-7.83E+01	1.55E-07
	BABC1	**-7.82E+01**	**4.09E-01**
	IABC	-7.83E+01	1.21E-14
	JA-ABC4	-7.83E+01	1.40E-14
f7	ABC	4.53E-10	3.99E-10
	BABC1	6.66E-16	1.10E-16
	IABC	5.49E-16	9.03E-17
	JA-ABC4	**5.03E-16**	**1.17E-17**
f8	ABC	4.82E-10	5.12E-10
	BABC1	6.37E-16	1.02E-16
	IABC	5.38E-16	9.62E-17
	JA-ABC4	**5.14E-16**	**1.09E-17**
f9	ABC	3.85E-08	4.32E-08
	BABC1	4.57E-16	1.36E-16
	IABC	4.09E-16	1.42E-16
	JA-ABC4	**3.87E-16**	**1.42E-16**
f10	ABC	1.07E-05	5.44E-06
	BABC1	2.44E-15	1.79E-15
	IABC	2.64E-11	39.63E-12
	JA-ABC4	**3.42E-17**	**2.38E-17**

VI. CONCLUSION

The paper proposes JA-ABC4, a new ABC variant with the objectives to enhance the performance of ABC algorithm in terms of avoiding premature convergence and improving the convergence speed. The performance results obtained clearly exhibited the excellent performance of the JA-ABC4 as compared to others on various commonly used benchmark functions. This has suggested that the proposed algorithm has the potential to solve complex optimization problems. For future work, the proposed algorithm shall be tested to solve real-world applications.

ACKNOWLEDGMENT

The authors acknowledge the Ministry of Higher Education (MOHE) FRGS Grant No: 203/PELECT/6071247 for the financial support.

REFERENCES

[1] Y. Hendrawan, and H. Murase, "Bio-inspired feature selection to select informative image features for determining water content of cultured Sunagoke moss," *Expert Systems with Applications*, vol. 38, no. 11, pp. 14321-14335, 2011.

[2] H. A Kurid, T. S. Alnusairi, and H. S. Almujahed, "OBAME: optimized bio-inspired algorithm to maximize search efficiency in P2P databases," *Procedia Computer Science*, vol. 21, no. 0, pp. 60-67, 2013.

[3] M. Rocha, R. Mendes, O. Rocha, I. Rocha, and C. E. Ferreira, "Optimization of fed-batch fermentation processes with bio-inspired algorithms," *Expert Systems with Applications*, vol. 41, no. 5, pp. 2186-2195, 2014.

[4] B. B. Youssef, "Parallelization of a bio-inspired computational model for the Simulation of 3-D multicellular tissue growth," *Procedia Computer Science*, vol. 20, no. 0, pp. 391-398, 2013.

[5] S. Binitha, and S. S. Sathya, "A survey of bio inspired optimization algorithms," *International Journal of Soft Computing and Engineering (IJSCE)*, ISSN, pp. 2231-2307, 2012.

[6] M. Dorigo, V. Maniezzo, and A. Colorni, "Ant system: optimization by a colony of cooperating agents," *IEEE Transactions on Systems, Man, and Cybernetics, Part B: Cybernetics*, vol. 26, no.1, pp. 29-41, 1996.

[7] J. Kennedy, and R. Eberhart, "Particle swarm optimization," in Proceedings IEEE International Conference on Neural Networks, Perth, 1995, pp. 1942-1948.

[8] C. Ding, Y. Cheng, and M. He, "Two-level genetic algorithm for clustered traveling salesman problem with application in large-scale TSPs," *Tsinghua Science and Technology*, vol. 12, no. 4, pp. 459-465, 2007.

[9] H. Tehzeeb-Ul-Hassan, R. Zafar, S. A. Mohsin, and O. Lateef, "Reduction in power transmission loss using fully informed particle swarm optimization," *International Journal of Electrical Power & Energy Systems*, vol. 43, no. 1, pp. 364-368, 2012.

[10] M. Basu, "Economic environmental dispatch using multi-objective differential evolution," *Applied Soft Computing*, vol. 11, no. 2, pp. 2845-2853, 2011.

[11] D. Karaboga, "An idea based on honey bee swarm for numerical optimization," Technical Report-TR06, 2005.

[12] D. Karaboga, and B. Akay, "A comparative study of artificial bee colony algorithm," *Applied Mathematics and Computation*, vol. 214, no. 1, pp. 108-132, 2009.

[13] D. Karaboga, and B. Basturk, "A powerful and efficient algorithm for numerical function optimization: artificial bee colony (ABC) algorithm," *Journal of Global Optimization*, vol. 39, no. 3, pp. 459-471, 2007.

[14] D. Karaboga, and B. Basturk, "On the performance of artificial bee colony (ABC) algorithm," *Applied Soft Computing*, vol. 8, no. 1, pp. 687-697, 2008.

[15] A. G. Abro, and J. Mohamad-Saleh. " Enhanced global-best artificial bee colony optimization algorithm," in *Sixth UKSim/AMSS European*

Symposium on Computer Modeling and Simulation (EMS), Valetta, 2012, pp. 95-100.
[16] A. G. Abro, and J. Mohamad-Saleh, "An enhanced artificial bee colony optimization algorithm," *Recent Advances in Systems Science and Mathematical Modelling*, D.S. Nikos Mastorakis, Valeriu Prepelita, Ed. WSEAS Press, 2012, pp. 222-227.
[17] G. Zhu, and S. Kwong, "Gbest-guided artificial bee colony algorithm for numerical function optimization," *Applied Mathematics and Computation*, vol. 217, no. 7, pp. 3166-3173, 2010.
[18] A. Banharnsakun, T. Achalakul, and B. Sirinaovakul, "The best-so-far selection in artificial bee colony algorithm," *Applied Soft Computing*, vol. 11, no. 2, pp. 2888-2901, 2011.
[19] W. Gao, and S. Liu, " Improved artificial bee colony algorithm for global optimization," *Information Processing Letters*, vol. 111, no. 17, pp. 871-882, 2011.
[20] W. Gao, S. Liu, and L. Huang, "A global best artificial bee colony algorithm for global optimization," *Journal of Computational and Applied Mathematics*, vol. 236, no. 11, pp. 2741-2753, 2012.
[21] W. F. Gao, and S. Y. Liu, "A modified artificial bee colony algorithm. Computers & Operations Research, 2012. 39(3): p. 687-697.
[22] N. Sulaiman, J. Mohamad-Saleh, and A. G. Abro, "A modified artificial bee colony (JA-ABC) optimization algorithm," in *Proceedings of the International Conference on Applied Mathematics and Computational Methods in Engineering*, Rhodes Island, 2013, pp 74-79.
[23] A. G Abro, "Performance enhancement of artificial bee colony optimization algorithm," Ph.D. thesis, School of Electrical & Electronic Engineering Universiti Sains Malaysia, 2013.

J. Mohamad-Saleh received her B.Sc (in Computer Engineering) degree from the Case Western Reserve University, USA in 1994, the M.Sc. degree from the University of Sheffield, UK in 1996 and the Ph.D. degree from the University of Leeds, UK in 2002. She is currently an Associate Professor in the School of Electrical & Electronic Engineering, Universiti Sains Malaysia. Her research interests include computational intelligence, tomographic imaging and soft computing.

N. Sulaiman received her B.Eng (in Electrical & Electronics Engineering) degree from the Universiti Teknologi PETRONAS, Malaysia in 2010. She is currently a Ph.D. candidature in the School of Electrical & Electronic Engineering, Universiti Sains Malaysia. Her research interest includes computational intelligence and power system.

Brain Emotional Learning Based Intelligent Controller via Temporal Difference Learning

Javad Abdi
Department of Electrical and Computer Engineering, NazarAbad Center, Islamic Azad University, Karaj, Alborz, Iran
e-mail: javad.abdi@kiau.ac.ir

Azam FamilKhalili
Department of IT & Computer Engineering, Amirkabir University of Technology Tehran, Iran
e-mail: a.familkhalili@aut.ac.ir

Modeling emotions has attracted much attention in recent years, both in cognitive psychology and design of artificial systems. Far from being a negative factor in decision-making, emotions have shown to be a strong faculty for making fast satisfying decisions. In this paper, we have adapted a computational model based on the limbic system in the mammalian brain for control engineering applications. Learning in this model based on Temporal Difference (TD) Learning. We applied the proposed controller (termed BELBIC) for a simple model of a submarine. The model was supposed to reach the desired depth underwater. Our results demonstrate excellent control action, disturbance handling and system parameter robustness for TDBELBIC. The proposal method, regarding the present conditions, the system action in the part and the controlling aims, can control the system in a way that these objectives are attained in the least amount of time and the best way.

Key Words: Artificial neural networks; Temporal difference; Brain Emotional Learning Based Intelligent Controller; heating, ventilating and air conditioning

I. INTRODUCTION

In these year, design of computational intelligent systems have received significant attentions. Control technique and application based on Artificial Neural Networks (ANNs) [1], Genetic Algorithms (GA) [2] and Fuzzy Inference System (FIS) [3] are among them. Emotional Learning is a psychologically motivated algorithm which is a family of intelligent algorithms [4].

Recently, biologically motivated intelligent computing has been successfully employed for solving different types of problems [5] [6]. Capability of learning is the greatest benefits of an intelligent system from a classical one. A common attribute of the learning process is the adaptation of the system parameters to better tackle the changing environment. One type of evaluation is based on emotional cues, which evaluate the impact of the external stimuli on the ability of the system both to function effectively in the short term and to maintain its long term prospects for survival [7]. Emotional learning is one of the learning strategies based on emotional evaluations. This learning process occurs in the brain Limbic system in mammalian brains [8].

Moren and Balkenius [9] presented a neurologically inspired computational model of the Amygdala and the Orbitofrontal Cortex in the Limbic System which is based on brains. A new model of control algorithm called Brain Emotional Learning Based Intelligent Controller (BELBIC) has been suggested [10]. By direct and indirect approaches, two different approaches are developed.

Applying this controller for eliminating stator oscillations through fin placement was done in [11]. Application of BELBIC in Speed control of an interior permanent magnet synchronous motor was shown in [12] and in [13] a modified version of BELBIC was utilized in heating, ventilating and air conditioning (HVAC) control problem that is multivariable, nonlinear and non-minimum phase. In [14] other HVAC called micro-heat exchanger was the scope of BELBIC application. In [15], this controller used for controlling an identified model of a washing machine and in [16] this controller with multi objectives constraints was tuned for washing machine with evolutionary algorithms where it is possible to have a trade-off between energy consummation and other control objectives.

The BELBIC controller used for many application such as power system [17], active queue management [18], aerospace launch vehicle [19], interior permanent magnet synchronous motor system [20], flight simulation servo system [21], delayed systems [22] and other uncertain nonlinear systems [23].

Lucas has some reviews on successful control engineering and decision making applications, in which BEL has been used for satisfying action selection based on artificial emotions. He also demonstrated the capability of BELBIC including high levels of adaptability, disturbance rejection, and fault tolerance by implementing it with neural network [24].

As mentioned, in real time control and decision systems, Emotional Learning is a powerful methodology due to its simplicity, low computational complexity and fast training where the gradient based methods and evolutionary algorithms are hard to be applied because of their high computational complexity [25] [26].

Although this controller was applied in many simulation and real control tasks but the previous actions are not considered in these studies and the simulation and implementation were done in limited simulation or real time. In this article the TD learning algorithm used in BELBIC controller to improved version of this controller, and it is introduced and applied to control submarine plant.

The structure of the paper is as the following. In Section 2 the limbic model of mammalian brain and original model of BELBIC as an applied model is

presented. Section 3 present the control schema based on TD learning is demonstrated. In Section 4, the linear single input single output (SISO) system: submarine model and TD learning are presented, respectively. the implementation of the original BELBIC on control of Submarine Model is demonstrated in this section. The internal instability of controller in simulation plant model and real plant are shown, too. Finally in Section 6 the conclusion part is discussed.

II. An Applied model: Structure of the Limbic System

Motivated by the success in functional modeling of emotions in control engineering applications [27] [28] [29], the main purpose of this research is to use a structural model based on the limbic system of mammalian brain, for decision making and control engineering applications.

The emotional processes is done by the Limbic System, as part of the mammalian creatures' brain. The Limbic System located in the cerebral cortex consists mainly of following components: Amygdala, Orbitofrontal Cortex, Thalamus, Sensory Cortex, Hypothalamus, Hippocampus and some other less important areas. Fig. 1 shows a simple graphical of limbic system in human brain [30].

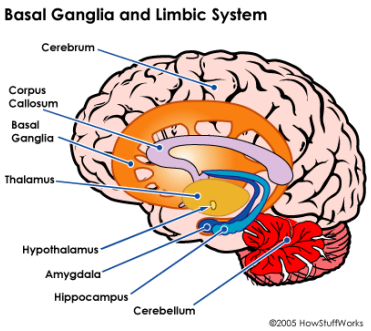

Fig. 1: The structure of the main components of Limbic System [30]

Amygdala which is a small almond-shaped in sub-cortical area is play role in the emotional system. This component is placed in a way to communicate with all other Sensory Cortices and areas within the Limbic System. For In this section the all parts of Limbic system are describe.

The studies show that a stimulus and its emotional consequences are associated in the Amygdala area [31]. A powerful area but small of the brain, the amygdala is located below the hypothalamus and helps the mammalian process the world at large. The amygdala is in charge of for regulating emotions, affecting our relationships and well-being. It also plays a part in causing arousal. Automatic reactions like fear are in large part caused by the amygdala. Amygdala are believed to mediate inherently emotionally charged stimuli as well as coarsely resolved stimuli in general [32].

The Thalamus signal going to the Amygdala evades the processes involved in the Sensory Cortex and other components of the system. Therefore, Amygdala receives a non-optimal but fast stimulus from the Thalamus which among the input stimuli is often known as a characteristic signal [33].

Hippocampus is the next to the Amygdala and part of the forebrain, which is shaped somewhat like a seahorse. The hippocampus is key in creating new memories and helps mammalian with spatial orientation and sleep patterns.

The cerebral cortex is the largest, most apparent part of the brain. It is the outer layer of the brain that is the main source of human intelligence. The surface of the cortex is grey matter and has six different layers with many neural networks. Beneath these layers is white matter and when all of these are put together we are given a huge number of connections that facilitate our ability to think, feel, and reason.

The cerebral cortex has two hemispheres and each hemisphere helps to manage different things and perform various tasks. Both the hemispheres can communicate with one another, and can be divided into four different lobes.

The corpus callosum connects the brain's two hemispheres together. It is a huge bundle of nerve fibers that allows information to pass between the two parts of the brain. The corpus callosum allows for optimal performance from the brain.

As mentioned, there are two approaches to intelligent and cognitive control. In the indirect approach, the intelligent system is utilized for tuning the parameters of the controller. We have adopted the second, so called direct approach, where the intelligent system, in our case the computational model termed TDBELBIC, is used as the controller block. Fig. 2 present a structural engineering model of this System. TDBELBIC is essentially an action generation mechanism based on sensory inputs and emotional cues. In general, these can be vector valued, although in the benchmarks discussed in this paper for the sake of illustration, one sensory input and one emotional signal (stress) have been considered.

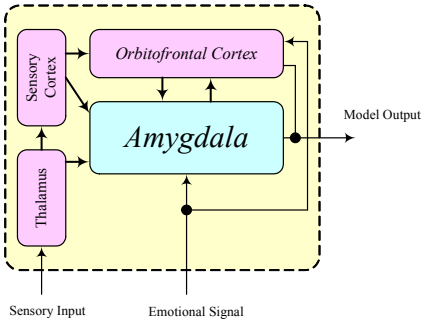

Fig. 2. The abstract structure of TDBELBIC

The emotional learning occurs mainly in amygdala. The learning rule of amygdala is given in formula (1).

$$\Delta G_a = k_1.\max(0, EC - A) \quad (1)$$

where G_a is the gain cin amygdala connection, k_1 is the learning step in amygdala and EC and A are the values of emotional cue function and amygdala output at each time. The term max in the formula (1) is for making the learning changes monotonic, implying that the amygdala gain can never be decreased. This rule is for modeling the incapability of unlearning the emotion signal (and consequently, emotional action), previously learned in the amygdala [34] [35]. Similarly, the learning rule in orbitofrontal cortex is shown in formula (2).

$$\Delta G_o = k_2.(MO - EC) \quad (2)$$

where G_o is the gain in orbitofrontal connection, k_2 is the learning step in orbitofrontal cortex and MO is the output of the whole model, where it can be calculated as formula (3):

$$MO = A - O \quad (3)$$

In fact, by receiving the sensory input S, the model calculates the internal signals of amygdala and orbitofrontal cortex by the relations in (4) and (5) and eventually yields the output.

$$A = G_a.S \quad (4)$$

$$O = G_o.S \quad (5)$$

Since amygdala does not have the capability to unlearn any emotional response that it ever learned, inhibition of any inappropriate response is the duty of orbitofrontal cortex.

III. Implementation

Controllers based on emotional learning have shown very good robustness and uncertainty handling properties [27] [29], while being simple and easily implementable. To utilize our version of the Moren-Balkenius model as a controller, we note that it essentially converts two sets of inputs into the decision signal as its output. We have implemented a closed loop configuration using this block (termed TDBELBIC) in the feed forward loop of the total system in an appropriate manner so that the input signals have the proper interpretations. The block implicitly implemented the critic, the learning algorithm and the action selection mechanism used in functional implementations of emotionally based (or generally reinforcement learning based) controllers, all at the same time [27] [28] [29]. The structure of the control circuit we implemented in our study is illustrated in Fig. 3. The functions we used in emotional cue and sensory input blocks are given in (6) and (7),

$$EC = W_1.e + W_2.CO \quad (6)$$

$$SI = W_3.PO + W_4.\dot{PO} \quad (7)$$

where EC, CO, SI and PO are emotional cue, controller output, sensory input and plant output and the W_1 through W_4 are the gains must tuned for designing a satisfactory controller.

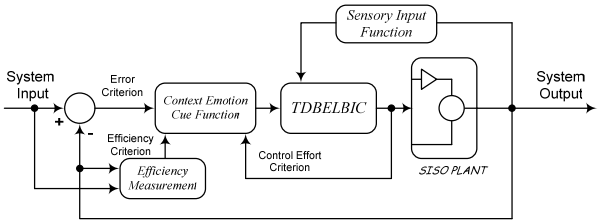

Fig. 3. Control system configuration using TDBELBIC

IV. Simulations

We confirmed the capability of TDBELBIC by performing some simulations. It must be mentioned that in the all simulations outlined below, we implemented the set-point control strategy with the desired value of 1. The descriptions of simulations are given below:

A Linear SISO System: Submarine Model

In this simulation, we considered a simple model of a submarine. The model was supposed to reach the desired depth underwater. The quantitative model is represented via (8).

$$G(s) = \frac{0.1(s+1)^2}{s(s^2+0.09)} = \frac{0.1s^2+0.2s+0.1}{s^3+0.09s} \quad (8)$$

We implemented the control circuits in MATLAB SIMULINK package. The output of the system with a simple feedback and the output of the system with a TDBELBIC controller are given in Fig. 4.

B TD(Lambda) Learning

Most of new learning algorithms like reinforcement learning, Q-learning and the method of temporal differences are characterized by their fast computation and in some cases lower error in comparison with the classical learning methods. Fast training is a notable consideration in some control applications. However, in prediction applications, two more desired characteristics of a good predictor are accuracy and low computational complexity.

In reinforcement learning, there is no teacher available to give the correct output for each training example, which is called unsupervised Learning. The output produced by the learning agent is fed to the environment and a scalar reinforcement value (reward) is returned. The learning agent tries to adjust itself to maximize the reward. [36] [37]

Often that the actions taken by the learning agent to produce an output will affect not only the immediate reward but also the subsequent ones. In this case, the immediate reward only reflects partial information about the action. It is called delayed-reward. [37] [38]

TD learning is a type of reinforcement learning for solving delayed-reward prediction problems. Unlike

ISBN: 978-1-61804-219-4

supervised learning, which measures error between each prediction and target, TD uses the difference of two successive predictions to learn that is Multi Step Prediction. The advantage of TD learning is that it can update weights incrementally and converge to a solution faster [39].

In a delay-reward prediction problem, the observation-outcome sequence has the form $x_1, x_2, ..., x_m, z$ where each x_t is an observation vector available at time t, $1 \le t \le m$ and z is the outcome of the sequence. For each observation, the learning agent makes a prediction of z, forming a sequence: $P_1, P_2, ..., P_m$.

Assuming the learning agent is an artificial neural network, update for a weight w of the network with the classical gradient descent update rule for supervised learning is:

$$\Delta w = -\alpha \nabla_w E = -\alpha \sum_{t=1}^{m} (P_t - z) \nabla_w P_t \qquad (9)$$

Where α is the learning rate and $\nabla_w E$ is the gradient vector, $\partial E / \partial w$ of the mean square error function:

$$E = \frac{1}{2} \sum_{t=1}^{m} (P_t - z)^2 \qquad (10)$$

In [38], Sutton derived the incremental updating rule for equation (9):

$$\Delta w_t = \alpha (P_{t+1} - P_t) \sum_{k=1}^{t} \nabla_w P_k \qquad (11)$$

For t=1,2,....,m where $P_{m+1} \xrightarrow{def} z$

To emphasize more recent predictions, an exponential factor λ is multiplied to the gradient term:

$$\Delta w_t = \alpha (P_{t+1} - P_t) \sum_{k=1}^{t} \lambda^{t-k} \nabla_w P_k \qquad (12)$$

where $0 \le \lambda \le 1$

This results in a family of learning rules, TD(Lambda) , with constant values of λ.

But there are 2 special cases:

First, when λ=1, Eq. (12) falls back to Eq. (11), which produces the same training result as the supervised learning in Eq. (9). Second, when λ=0, since $0^0 = 1$, Eq. (12) becomes

$$\Delta w_t = \alpha (P_{t+1} - P_t) \nabla_w P_k \qquad (13)$$

I can extended the Eq. (13) for BELBIC and made Eq. (14) for TDBELBIC.

$$\Delta G_{Ot} = \alpha (z - P_t) \nabla G_O P_t \qquad (14)$$

Which has a similar form as Eq. (9). So the same training algorithm for supervised learning can be used for TD(0).

V. Conclusion

In Fig. 4, you can observe the results of simulating the diagram block Fig. 3. The results, based on TD learning, are compared to Orbitofrontal Cortex learning in a shared TDBELBIC structure. The outcomes suggest that TD based learning in faster than Orbitofrontal Cortex learning. But faster learning is increased for maximum overshoot. Both of the learning is incremental, however, their memory output signals are presented in figures 5, 6. The increase rates represent their learning speed.

Paying attention to the achievements in the emotional controls founded a computational model, based on the Limbic system, for mammals' brain via time series learning. The paper tried to develop this method for answering more complicated issues and achieving difficult goals.

To do this, the ability of the learning module the emotional controller, was increased achieving based a brain computational model means of TD learning for credit assignment. TD learning, has easier computations because of using it's own experience. The methods resemble human behavioral learning.

Appendix: Body of BELBIC Algorithm

```
function E=belbic(x)
global OLD
A = OLD(1) ;
O = OLD(2) ;
V = OLD(3) ;
W = OLD(4) ;

S=x(1);

Rew=x(2);

%----------------intial learning( alpha & beta )
alpha=0.1;

beta=0.4;
%-------------------------------
   DV=alpha*max(0,Rew-A)*S;
   y=A-O-Rew;
   DW=beta*y*S;
   V=V+DV;
   W=max(0,W+DW);
   A=S*V;
   O=S*W;
   OLD = [ A ; O ; V ; W ] ;
   E=A-O;
```

References

K.S. Narendra, and K. Parthasarathy, "Identification and control of dynamical systems using neural networks," *IEEE Trans. on Neural Networks,* vol. 1, no. 1, pp. 4-27, 1990.

R.J. Wai, J.D. Lee, and K. H.Su, "Supervisory enhanced genetic algorithm control for indirect field-oriented induction motor drive," *Proceedings IEEE International Joint Conference on Neural Networks,* vol. 2, pp. 1239-1244, 2004.

T.M. Takagi, and M. Sugeno, "Fuzzy identification of systems and its applications to modeling and control," *IEEE Trans. on Systems, Man, and Cybernetics,* vol. 15, no. 1, pp. 122-132, 1985.

H. Zhang, S. Liu, and S.Y. Yang, "An emotion-based behavior coordination approach to autonomous mobile robots," *Proceedings of the International Conference on Sensing, Computing and Automation*, vol. 1, pp. 249-254, 2006.

C. Lucas, D. Shahmirzadi, and M. Biglarbegian, "Co-evolutionary Approach to Graph-Coloring Problem," *Technical Journal of Amirkabir University of Technology*, vol. 14, nO.54, pp. 363-369, 2003.

M. Sipper, and M. Tomassini, "Convergence to Uniformity in A Cellular Automaton via Local Co-evolution," *International Journal of Modern Physics*, vol. 8, no. 5, pp. 1013-1024, 1997.

D. Shahmirzadi, *Computational Modeling Of The Brain Limbic System And Its Application In Control Engineering*, Master dissertation, Texas A&M University, U.S.A., 2005.

S. Maren, "Long-Term Potentiation in the Amygdala: A Mechanism for Emotional Learning and Memory," *Trends in Neurosciences*, vol. 22, no. 12, pp. 561-567, 1999.

J. Moren, and C. Balkenius, "A Computational Model of Emotional Learning in the Amygdala," *Cybernetics and Systems,* vol. 32, no. 6, pp. 611-636, 2000.

C. Lucas, D. Shahmirzadi, and N. Sheikholeslami, "Introducing BELBIC: Brain Emotional Learning Based Intelligent Controller," *International Journal of Intelligent Automation and Soft Computing*, vol. 10, no.1, pp. 11-22, 2004.

C. Lucas, D. Shahmirzadi, and H. Ghafoorifard, "Eliminating Stator Oscillations through Fin Placement," Journal of Engineering Simulation ,vol. 3, no. 1, pp 3-7, March 2002.

R.M. Milasi, C. Lucas, and B.N. Araabi, "Speed Control of an Interior Permanent Magnet Synchronous Motor Using BELBIC," *5th International Symposium on Intelligent Automation and Control, World Automation Congress, WAC 2004*, Seville, Spain, June 28-July1, ISIAC 116, 2004.

N. Sheikholeslami, D. Shahmirzadi, E. Semsar, C. Lucas, and M. J. Yazdanpanah, "Applying Brain Emotional Learning Algorithm for Multivariable Control of HVAC Systems," *International Journal of Intelligent and Fuzzy Systems*, vol. 17, no. 1, pp. 35-46, 2006.

H. Rouhani, M. Jalili, B.N. Araabi, W. Eppler, and C. Lucas, "Brain emotional learning based intelligent controller applied to neuro-fuzzy model of micro-heat exchanger," *Expert Systems with Applications*, vol. 32, pp. 911-924, 2007.

R.M. Milasi, C. Lucas, and B.N. Araabi, "Intelligent Modeling and Control of Washing Machine Using Locally Linear Neuro- Fuzzy (LLNF) Modeling and Modified Brain Emotional Learning Based Intelligent Controller (BELBIC)," *Asian Journal of Control*, vol. 8, no. 4, 2005.

R.M. Milasi, M.R. Jamali, and C. Lucas, "Intelligent Washing Machine: A Bioinspired and Multi-Objective Approach," *International Journal of Control, Automation, and Systems*, vol. 5, no. 4, pp. 436-443, August 2007.

R. Mohammadi, C. Lucas, and B.N. Araabi, "A novel controller for a power system based BELBIC," *Proceedings of World Automation Congress*, vol. 18, 2004, pp. 409-420, 2001.

M.J. Kharaajoo, "Application of brain emotional learning based intelligent controller (BELBIC) to active queue management," *International Conference on Computational Science, Lecture Notes in Computer Science*, vol. 3037, pp. 662-665, 2004.

A.R. Mehrabian, C. Lucas, and J. Roshanian, "Aerospace launch vehicle control: An intelligent adaptive approach," *Aerospace Science and Technology*, vol. 10, no. 2, pp. 149-155, 2006.

R. Mohammdi, C. Lucas, B.N. Arraabi, T.S. Radwan, and M.A. Rahman, "Implementation of emotional controller for interior permanent magnet synchronous motor drive," *Industry Applications Conference*, vol. 4, pp. 1767-1774, 2006.

Z. Ziyang, W. Daobo, and W. Zhisheng, "Flight simulation servo system based on learning based intelligent controller," *Proceedings of the Fourth International Conference on Impulse and Hybrid Dynamic Systems*, pp. 1372-1375, 2007.

A. Torabi, M. Boroushaki, and G. Vosoughi, "Design a brain emotional learning based intelligent controller (BELBIC) in delayed systems," *14th- International conference of Iranian Society of Mechanical Engineering (ISME2006)*, Isfehan, Iran, 2006.

A.R. Mehrabian, and C. Lucas, "Emotional Learning Based Intelligent Robust Adaptive Controller for Stable Uncertain Nonlinear Systems," *International Journal of Intelligent Technology (IJIT)*, vol. 1, no. 1, pp. 34-40, 2005.

C. Lucas, "BELBIC and Its Industrial Applications: Towards Embedded Neuro-emotional Control Codesign," *Chapter Book, Integrated Systems Design and Technology 2010*, M. Fathi, A. Holland (Ed.), F. Ansari and C. Weber (Co-Eds.), vol. 3, pp. 203-214, 2011.

R.W. Picard, E. Vyzas, and J. Healey, "Toward machine emotional intelligence: Analysis of affective physiological state," *IEEE Transactions on Pattern Analysis and Machine Intelligence,* vol. 23, no. 10, pp. 1175-1191, 2001.

M. Fatourechi, C. Lucas, and A.K. Sedigh, "Reducing Control Effort by means of Emotional Learning," *Proc. of 9th Iranian Conf. on Electrical Engineering, ICEE'01*, Tehran, Iran, vol. 41, pp. 1-8, 2001.

C. Balkenius, and J. Moren, "A Computational Model Of Emotional Conditioning In The Brain," *Proceeding of the workshop on Grounding Emotions in Adaptive Systems,* Zurich, 1998.

J.R. Jang, "ANFIS: Adaptive-Network-Based Fuzzy Inference System," *IEEE Transaction on Systems, Man and Cybernetics,* vol. 23, no. 3, 1993.

A.A. Savinov, "An Algorithm for Induction of Possibilities Set-Valued Rules by Finding Prime Disjunctions," *4th On-line World Conference on Soft Computing in Industrial Applications (WSC4),* September 21-30, 1999.

D. Purves, G.J. Augustine, D. Fitzpatrick, L.C. Katz, A. LaMantia, J.O. McNamara, and S.M. Williams, *Neuroscience* , Sinauer Associates, 2001.

J.E. LeDoux, *In Search of an Emotional System in the Brain: Leaping from Fear to Emotion and Consciousness*. Cambridge, MA: MIT Press, 1995.

A. Ohman, and S. Mineka, "Fears, Phobias, and Preparedness: Toward and Evolved Module of Fear and Fear Learning," *Journal of Psychological Review*, vol. 108, no. 3, pp. 483-522, 2001.

J.P. Kelly, *The Neural Basis of Perception and Movement*, Principles of Neural Science, London. UK: Prentice Hall, 1991.

M.H. Voigt, "Fuzzy evolutionary algorithms" *Technical Report 92-038, International Computer Science Institute (ICSI), 1947 Center Street, Suite 600, Berkeley, CA, 94704,* June 1992.

J. Chen, E. Antipov, B. Lemieux, W. Cedeno, and D.H. Wood, "DNA Computing Implementing Genetic Algorithms," *Preliminary Proceedings DIMACS Workshop On Evolution As Computation,* pp: 39-49 , DIMACS, Piscataway NJ, January 1999.

J. Abdi, C. Lucas, A.F. Khalili, C. Lucas, and A.K. Sedigh, "The Role of Truncated Temporal Difference Learning (TTDL) with Functional Approximators in Reduction of Time and Computational Costs of Reinforcement Learning," *Journal of Iranian Association of Electrical and Electronics Engineers*, vol. 1, no. 1, P.P. 4-19, Spring 2004.

D. Eby, R.C. Averill, William F. Punch III, and E.D. Goodman, "Evaluation of Injection Island GA Performance on Flywheel Design Optimization," *Proceedings, Third Conference on Adaptive Computing in Design and Manufacturing, Plymouth, England,* Springer Verlag, April 1998.

R.S. Sutton, "Learning to Predict by the Methods of Temporal Differences," *Machine Learning,* vol. 3, pp. 9-44, 1988.

R.S. Sutton, "Generalization in Reinforcement Learning: Successful Examples Using Sparse Coarse Coding," *To Appear in Advances in Neural Information Processing Systems 8,* 1995.

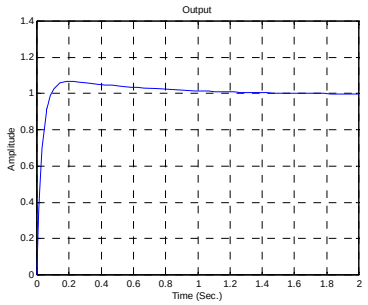

BEBIC Output

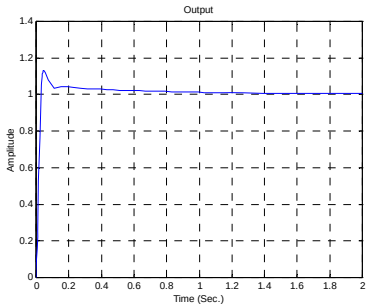

TDBEBIC Output

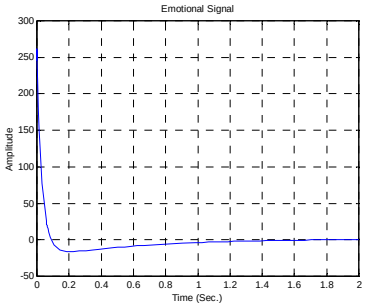

BELBIC Emotional Signal

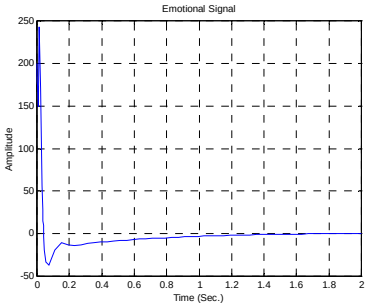

TDBELBIC Emotional Signal

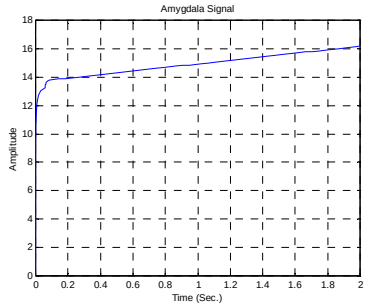

Amygdala BELBIC Output

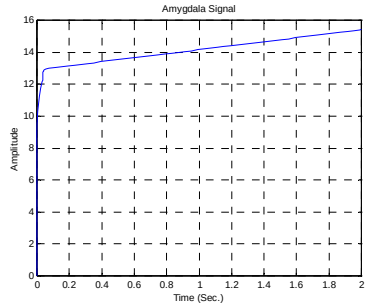

Amygdala TDBELBIC Output

Fig. 5. Comparison of BELBIC and OFC Learning with BELBIC and TD Learning

(i)

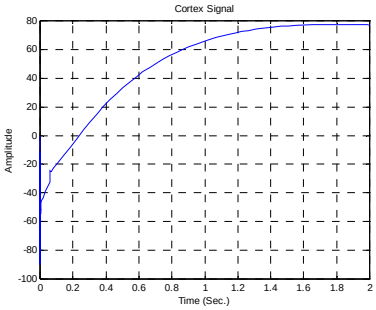

Cortex Output

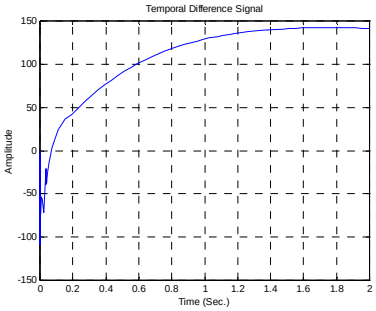

TD Learning Output

Fig. 6. Comparison of BELBIC and with TDBELBIC Memory

ISBN: 978-1-61804-219-4

Multiscale Convergence Optimization in Constrained Molecular Dynamics Simulations

N. Nafati

APSM Team. ICN. UMR7272.
Scientific University of Nice. France.
Courriel : Nicolas.Nafati@unice.fr

***Abstract*—These instructions give you guidelines for preparing papers for IEEE Transactions and Journals. Use this document as a template if you are using Microsoft *Word* 6.0 or later. Otherwise, use this document as an instruction set. The electronic file of your paper will be formatted further at IEEE. Paper titles should be written in uppercase and lowercase letters, not all**

Abstract-The energy analysis is essential for studying chemical or biochemical reactions but also for characterizing interactions between two protagonists. Molecular Dynamics Simulations are well suited to sampling interaction structures but under minimum energy. To sample unstable or high energy structures, it is necessary to apply a bias-constraint in the simulation, in order to maintain the system in a stable energy state. In MD constrained simulations of "Umbrella Sampling" type, the phenomenon of ligand-receptor dissociation is divided into a series of windows (space sampling) in which the simulation time is fixed in advance. A step of de-biasing and statistical processing then allows accessing to the Potential Force Medium (PMF) of the studied process.

In this context, we have developed an algorithm that optimizes the DM computation time regarding each reaction coordinate (distance between the ligand and the receptor); and thus can dynamically adjust the sampling time in each US-Window. The data processing consists in studying the convergence of the distributions of the coordinate constraint and its performance is tested on different ligand-receptor systems. Its originality lies in the used processing technique which combines wavelet thresholding with statistical-tests decision in relation to distribution convergence.

In this paper, we briefly describe a Molecular Dynamic Simulation, then by assumption we consider that distribution data are series of random-variables vectors obeying to a normal probality law. These vectors are first analyzed by a wavelet technique, thresholded and in a second step, their law probability is computed for comparison in terms of convergence.

In this context, we give the result of PMF and computation time according to statistic-tests convergence criteria, such as Kolmogorov Smirnov, Student tTest, and ANOVA Tests. We also compare these results with those obtained after a preprocessing with Gaussian low-pass filtering in order to follow the influence of thresholding. Finally, the results are discussed and analyzed regarding the contribution of the muli-scale processing and the more suited criteria for time optimization.

***Index* Keywords: Molecular Dynamic Simulations. Umbrella Sampling. Potential Force Medium (PMF). Convergence. Ligand – Receptor. Wavelet Thresholding. Statistical-Tests Decision. Normal Probality Law. Kolmogorov Smirnov. Student tTest. ANOVA. Gaussian low-pass filtering.**

I. INTRODUCTION

Molecular Dynamics (MD) is a sampling space based on iterative numerical integration of the equations of Newton motion. Since the time scales accessible to MD simulations are several orders of magnitude less than the time of chemical reactions, we may introduce a bias to increase the likelihood of sampling rare or unlikely events. In fact, when the energy barrier between two states to be sampled is less than KT (K: Boltzmann constant. T: system temperature in °K), the probability can be obtained in simulations at equilibrium. In the case of larger barriers, the state of higher energy will not be reached and a harmonic potential sampled must be inserted in order to obtain the Hamiltonian suitable sampling. The addition of this harmonic potential is called Umbrella-Sampling (U.S.), where the force constant of this potential is another parameter at equilibrium (or reaction coordinate at equilibrium) . This way provides a sampling that does not follow the Boltzmann statistics, but improves sampling in the vicinity of a chosen value of reaction coordinate [9][10][14].

The sampling technique is therefore constrained so as to cut the energy path connecting an initial state to a final state of the reaction in several windows, as shown in the fig1. .

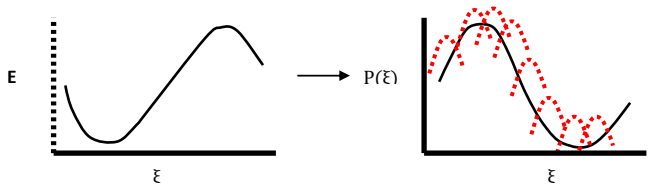

Fig1.: Schematic overall sampling by Umbrella Sampling technique under a harmonic constraint. The left curve shows the energy according to the reaction coordinate. The right one shows the probability as a function of the same parameter. The red curves having the umbrella-shaped sample windows are Umbrella-Sampling.

According to Boltzmann statistics [10][13][17][20][23], Potential Strength Medium (PMF) noted F is given by the following formula:

$$\mathbf{F}(\boldsymbol{\xi}) = -\mathbf{K_B T}\,\mathbf{ln}(\mathbf{P}(\boldsymbol{\xi})) \quad \textbf{(1)}$$

Where P(ξ) is the probability distribution that represents the number of times that the system samples the reaction coordinate. The expression of P(ξ) and hence of the PMF are modified in the case of sampling constraint. The WHAM (Weigthed Average Histogram Analysis) [9][14] software aims to determine the PMF through the calculation of some constants induced by the harmonic constraint.

As indicated in Fig1, two successive harmonic potential sampling windows, with a recovery given rate, lead to PMF identification up to a constant. The expression of this constant is:

$$\mathbf{ln}\left(\langle e^{\beta V_1(\xi)}\rangle\right) - \mathbf{ln}\left(\langle e^{\beta V_2(\xi)}\rangle\right) \quad \textbf{(2)}$$

The WHAM program corrects the value of PMF in each window by calculating the constants from (2) through the recovery of successive US windows, and thus provides the values of PMF (kcal/mol) depending on the reaction coordinate.

II. Problem Context:

A molecular dynamics simulation [10] consists in several steps of calculation:

-Energy minimization processing.

-Thermalization processing in which the protein complex is heated up to 300 °K. During this phase the thermal noise increa-ses.

-Equilibration phase processing: the energy of the system becomes minimum.

-Production Data phase: data are collected in order to compute the PMF.

The Amber software is used to achieve all these steps, and to reach among other things, different distributions of coordinate reaction (Distance between molecules), expressed in Angstroms. Each distribution is a distance-vector including a deterministic and random component. These distribution-vectors are measured at a given time in a sampling window-time whose size is set in advance. The present random component in each distribution is due to thermal agitation. The random thermal noise explains that noise components due to thermal agitation may have all sorts of values from low frequencies to very high frequencies. It greatly influences the number of iterations of the temporal sampling under a constraint reaction coordinate.

During the production phase, data distributions are collected by moving the US window along the spatial axis sampling. Therefore this sampling is directed or forced because the system is maintained in an energy potential well. Then the distribution distance estimator depends only on the distance, so the directed sampling allows to overcome the other freedom degrees.

To obtain efficient estimators of the distance-distribution, the US windows must be relatively long (approximately about several tens nanoseconds) and this for a large protein complex of approximately 5000 atoms. Consequently, our work has focused on developing algorithms that use short time windows centered around each spatial sampling. Our algorithm combines the wavelet and gaussian filtering processing with statistical convergence criteria. Our simulations have shown that this combination can reduce the cost of computing time.

III. Data Formulation:

In our study, we consider that during a Dynamic Molecular Simulation, each distribution $\boldsymbol{X_i}_{\,0\le i\le N-1}$ is obtained as a stochastic measure which represents a temporal sample at a given distance. In other words, the constrained spatial sampling proceeds as follows: for each distance $\boldsymbol{D_j}_{\,0\le j\le M-1}$ from $\boldsymbol{D_0}$ to $\boldsymbol{D_{M-1}}$, we collect each distribution $\boldsymbol{X_i}_{\,0\le i\le N-1}$ at time $\boldsymbol{t_{i-1}} + \boldsymbol{\Delta t}$ until the convergence of their probability distribution, then we increment the distance and repeat the process until $\boldsymbol{D_{M-1}}$.

The objective of our molecular modeling is to obtain measurements of the vibrational micro-state of the protein complex at a given distance. To do this, we have to accumulate a large number of statistical data which represent the probability distribution of the micro-states system. This statistic depends on the thermodynamics complex.

So, we denote that each distribution is a random measure such that :

$$\boldsymbol{X} = \boldsymbol{X_d} + \boldsymbol{\varepsilon}$$

Where $\boldsymbol{X_d}$ is the determinist component, and $\boldsymbol{\varepsilon}$ is the noise component.

ISBN: 978-1-61804-219-4

So, at every spatial sampling step, we collected a series of distributions: $\{X_0, X_1, X_2, X_3, X_4, \dots, X_{N-1}\}$ whose limit mainly depends on the speed of the probability convergence. This series is considered as a set of independent random variables, supposed to follow a normal distribution.

IV. Removing Noise with Wavelet Transformation

A. A brief overview of wavelets

The Continuous Wavelet Transform (CWT) [3][19][25] gives a time-frequency representation of signals. A wavelet transform is a convolution of a signal X(t) with a set of functions which are generated by translations and expansions of a main function. The main function is known as the mother wavelet and the translated or expanded functions are called wavelets. Mathematically, the CWT is given by:

the translated or expanded functions are called wavelets. Mathematically, the CWT is given by:

$$\boldsymbol{W(a,b) = \frac{1}{\sqrt{a}} \int X(t)\psi(\frac{t-b}{a})\, dt} \quad \textbf{(3)}$$

Here $\boldsymbol{b}$ is the time translation parameter and $\boldsymbol{a}$ is the expansion parameter of the wavelet. Ψ is the mother wavelet which is non-zero only on a certain interval.

The Discrete Wavelet Transform (DWT) is similar to the Fourier transform in that a signal is decomposed in terms of a basis set of functions. In Fourier transforms the basis set involves sines and cosines and the expansion has a single parameter. In wavelet transform the expansion has two parameters and the functions (wavelets) are generated from a single "mother" wavelet [8].

Any signal can be decomposed as:

$$\boldsymbol{X(t) = \sum_a \sum_b c_{ab}\, \psi_{ab}(t)} \quad \textbf{(4)}$$

Where the two-parameter coefficients are given by

$$\boldsymbol{c_{ab}(a,b) = \int X(t)\, \psi_{ab}(t)\, dt} \quad \textbf{(5)}$$

And the wavelets $\boldsymbol{\psi_{ab}}$ obey the condition

$$\boldsymbol{\psi_{ab}(t) = 2^{\frac{a}{2}}\, \psi(2^a t - b)} \quad \textbf{(6)}$$

B. Removing Noise with the DWT

"De-noising" a signal with the DWT involves three steps [1][5][8][15]:

1. Transform the input signal **X** with the DWT (X is a vector whose dimension is equal to N).

2. Force to zero all transform coefficients whose magnitude falls below some percentage of the maximum magnitude. This is a thresholding operation in which the threshold is adaptively computed or not. In our simulation, we used an adaptative soft thresholding with a universal threshold [1][5][15]. given by:

$$\boldsymbol{T = \sigma \sqrt{\frac{2\log(N)}{N}}} \quad \textbf{(7)}$$

Where σ is the standard deviation of X.

3. Inverse DWT.

IV. Principle of Statistical Tests

A hypothesis test (or statistical test) is an approach that aims to provide a decision rule which, on the basis of sample results, leads to make a choice between two statistical hypothesis. These two hypothesis are disjoint, in other word mutually exclusive.

Significance level of the test :

There is a risk, agreed in advance, of wrongly rejecting the null hypothesis H_0 when it is true, it is called the significance level of the test and the corresponding probability is noted α:

$$\boldsymbol{\alpha = P\,(\,\textbf{To Reject } H_0 \mid \textbf{when } H_0 \textbf{ is true}\,)} \quad \textbf{(8)}$$

At this level of significance, we affect to the statistic sampling distribution a rejection region of the null hypothesis (also called the critical region or **C**ritical **P**robability ($\mathbf{P_c}$)). The area of this region is the probability α. For example, choosing α = 0.05 means that sampling variable can take in 5% of cases, a value belonging to the rejection area of $\mathbf{H_0}$. The sampling distribution matches to a complementary region, called region of acceptance of $\mathbf{H_0}$ (or region of non-rejection) whose probability is equal to 1 - α.

From this point, we use different stochastic tests as convergence criteria. These criteria are focused on α as a threshold of acceptation or rejection of any convergence hypothesis. We set α error to 0.05 in our simulations.

As we said before, our data are samples (distance distributions) coming from the same population, which follows a probability law supposed to be normal $\mathcal{N}(\mu, \sigma)$. In our simulations we use non-parametric [2][4][6,7][12][16][21] and parametric statistic-tests [11][18][22][24] in order to find the best statistic-tests convergence criteria.

The statistical tests are:

- The parametric test of student (tTest), to test the sample average convergence, assuming that the variance is known.

- The non-parametric Kolmogorov Smirnov test, another non-parametric alternative to the tTest for independent samples.

ISBN: 978-1-61804-219-4

- The Anova non-parametric test, to check if the difference between the sample averages can be attributed to random sampling or to the fact that the samples are really significantly different [18].

A. *Student Convergence criteria*

Convergence of sequences of random variables is an important concept in probability theory and statistics, in particular the study of stochastic processes. For example, several random variables from the same population converge to the same probability.

In this article, we assume that (X_i) is a sequence of real random variables, and that all these variables are defined on the same probability space.

Let $(\boldsymbol{F_0, F_1, F_2, \ldots\ldots, F_{N-1}})$ be the repartition functions, associated with random variables $(\boldsymbol{X_0, X_1, X_2 \ldots\ldots, X_{N-1}})$. **F** is the repartition function of the random variable $\boldsymbol{X}$. In other words, $\boldsymbol{F_i(x)}$ is defined by $\boldsymbol{F_i(x) = P(X_i \leq x)}$ and $\boldsymbol{F}$ by $\boldsymbol{F(x) = P(X \leq x)}$. It is said that $\boldsymbol{X_{N-1}}$ converges to $\boldsymbol{X}$ in probability if :

$$\mathbf{lim}_{N\to\infty}\, \boldsymbol{P}(|\boldsymbol{X_N - X}| \geq \boldsymbol{\epsilon}) = \mathbf{0} \qquad \mathbf{(9)}$$

The distributions $(\boldsymbol{X_0, X_1, X_2 \ldots\ldots, X_{N-1}})$ are considered as a set of independent random variables and are measured at each constraint spatial sampling step. In principle they should converge at a given time. [Our goal is to reduce the iteration numbers and then the cost in time of molecular dynamic simulation.

Student's **tTest** [21][22] can be used to statistically test the hypothesis of equality of random variables average following a normal distribution and with unknown variance.

So the bilateral symmetrical confidence interval for the mean $\boldsymbol{\mu}$ can be written as:

$$\boldsymbol{IC(n)} = \left[\bar{\boldsymbol{x}} - \boldsymbol{t}^{\boldsymbol{n-1}}_{\boldsymbol{1-\alpha/2}}\cdot\sqrt{\frac{\boldsymbol{S}}{\boldsymbol{n}}}\,, \bar{\boldsymbol{x}} + \boldsymbol{t}^{\boldsymbol{n-1}}_{\boldsymbol{1-\alpha/2}}\cdot\sqrt{\frac{\boldsymbol{S}}{\boldsymbol{n}}}\right] \qquad \mathbf{(10)}$$

where

tTest is the fractile of order $\mathbf{1 - \frac{\alpha}{2}}$ of St(n-1) Student Law. Most **tTest** statistics have the form: $\mathbf{tTest} = \frac{\mathbf{Z}}{\mathbf{s}}$, where **Z** and **s** are functions of the data. Typically, $\boldsymbol{Z}$ is designed to be sensitive to the alternative hypothesis (its magnitude tends to be larger when the alternative hypothesis is true), whereas *s* is a scaling parameter that allows the distribution of **tTest** to be determined.

And

$\bar{x} = \frac{1}{n}\ \sum_{i=1}^{n} x_n$ is the average estimator

$\boldsymbol{s} = \frac{\boldsymbol{1}}{\boldsymbol{n-1}}\ \sum_{\boldsymbol{i=1}}^{\boldsymbol{n}}(\boldsymbol{x_i} - \bar{\boldsymbol{x}})^{\boldsymbol{2}}$ is the unbiased estimator of the variance.

B. *Kolmogorov-Smirnov (ksTest) criteria*

The **two-sample ksTest** is one of the most useful and general nonparametric methods for comparing two samples, as it is sensitive to differences in both location and shape of the empirical cumulative distribution functions [12][16].

The Kolmogorov–Smirnov test may also be used to test if two underlying one-dimensional probability distributions differ. In this case, the Kolmogorov–Smirnov statistic is:

$$\mathbf{D_n} = \ \mathbf{sup_x}|\mathbf{F_n(x) - F(x)}| \qquad \mathbf{(11)}$$

where $\mathbf{sup_x}$ is the supremum of the distances set. If the sample comes from a distribution F(x), then $\mathbf{D_n}$ converges to 0 almost surely**.** Kolmogorov strengthened this result, by effectively providing the rate of this convergence.

$$\mathbf{F_n(x)} = \frac{\mathbf{1}}{\mathbf{n}}\sum_{\mathbf{i=1}}^{\mathbf{K}}\mathbf{I_{X_{i\leq x}}} \qquad \mathbf{(12)}$$

Where $\mathbf{I_{X_{i\leq x}}}$ is the indicator function, equal to 1 if $\mathbf{X_i} \leq \mathbf{x}$ and equal to 0 otherwise.

Under null hypothesis, the sample comes from the distribution **F(x)** and $\sqrt{\mathbf{n}}\mathbf{D_n}$ converges to the Kolmogorov distribution, which does not depend on **F**. This result may also be known as the **Kolmogorov theorem** [12].

C. *One-way ANOVA test criteria*

In statistics, one-way ANalysis Of VAriance (abbreviated one-way ANOVA) is a technique used to compare mean-values of two or more samples.

ANOVA is a collection of statistical models used to analyze the differences between group mean-values and their associated procedures (such as "variation" among and between groups). In ANOVA setting, the observed variance in a particular variable is partitioned into components attributable to different sources of variation. In its simplest form, ANOVA provides a statistical test of whether or not the mean-values of several groups are equal, and therefore generalizes tTest to more than two groups.

The normal-model based ANOVA analysis assumes the independence, normality and homogeneity of the variances of the residuals. **Significance testing** ANOVA is a good example for explaining why very many statistical tests represent ratios of explained to unexplained variability. Here, we base this test on a comparison of the variance due to the between-groups variability (called *Mean Square Effect*, or

MS_{effect}) with the within-group variability (called *Mean Square Error*, or Ms_{error}). Under the null hypothesis (that there are no mean differences between groups in the population), we would still expect some minor random fluctuation in the mean-values for the two groups when taking small samples. Therefore, under the null hypothesis, the variance estimated based on within-group variability should be about the same as the variance due to between-groups variability. We can compare those two estimates of variance via the *F* test (see also Fisher Distribution), which tests whether the ratio of the two variance estimates is significantly greater than 1. When a statistical test provides a highly significant ratio, we can conclude that the mean-values for the two groups are significantly different from each other.

VI. Algorithm Architecture:

The Proposed algorithm is :

Step_1: Production by the Program XLeap from Amber of the Coordinate Topology Files of the complex system under study.

Step_2: Initializing input parameters (initial and final distance coordinates of the complex system.

Step_3: Calculation calibration process step.

Step_4: Production step in which molecular dynamic simulation provides data-distribution. Each iteration have to take into account the output file "restart " of the previous step as a coordinate file (Input CRD File).

Step_5: Data outputs Collection, namely the distribution of distance from the file dump.

Step_6: Subband decomposition of collected data and thresholding high frequency components. Or preprocessing by a gaussian filter of the collected data distribution.

Step_7: Data Reconstruction after the suppression of the micro-states noise. Or collecting the smooth data distribution.

Step_8: Evaluation of the convergence statistic-criteria. If the probability distribution doesn't converge then begin the process since step_4. If not the program goes on.

Step_9: Recording of production results and incrementing of the US step.

Step_10: If the final distance is not reached, then loop from step_3, if not, stop the process.

V. Simulations and Results:

Our simulations have been made on two systems:

-**System_1**: a mixture of one molecule of NaCl (saline) and water in a box of 12 Angstroms long.

-**System_2**: Deca-Alanine, a peptide consisting of ten residues of alanine with an alpha helix form, in vacuum.

Distance distributions are considered by assuming independent random variables following a normal law probability. Their number at a given constrained distance depends strongly on the used convergence criteria.

Distance distributions are considered by assuming independent random variables following a normal law probability. Their number at a given constrained distance depends strongly on the used convergence criteria.

A. Simulation number one:

Below we give the results of the PMF in the case of System_1 and for windows of 16000 steps in time. The spatial sampling is 0.2 Angstrom. The sampling time step is 0.002 ps. The initial distance is equal to 0.5 Angstroms and the final distance is equal to 10 Angstroms. For System_2 we have the same parameters except for the distance varying from 12 to 35 Angstroms.

In this first simulation, we used a simple and effective criteria which is a parametric statistical test of normality, leading to the Confidence Interval of normality with a given confidence level [4,5]. This confidence interval contains 99% of the population when the distribution is following a normal (or Gaussian) law of probability. The character of normality is given by the probability:

$$\mathbf{P(IC_{Max} \leq X \leq IC_{Min})} \qquad \mathbf{(13)}$$

$$\mathbf{and\ IC_{Max} = \mu + 3\sigma\ \ when\ \ IC_{Min} = \mu - 3\sigma}$$

From this, we deduced the following parametric criteria:

$$\mathbf{Criteria\_1 = |IC_{1_{Min}} - IC_{2_{Min}}|} \qquad \mathbf{(14)}$$

$$\mathbf{Criteria\_2 = |IC_{1_{Max}} - IC_{2_{Max}}|} \qquad \mathbf{(15)}$$

Below we give the PMF simulation in the case of System_1 whose window size is 16000 temporal steps. The convergence normality criteria are: Criteria_1 and Criteria_2. Their values are each fixed to 0.2, 0.1, and 0.05.

Below we give the PMF simulation in the case of System_1 whose window size is 16000 temporal steps. The convergence normality criteria are: Criteria_1 and Criteria_2. Their values are each fixed to 0.2, 0.1, and 0.05.

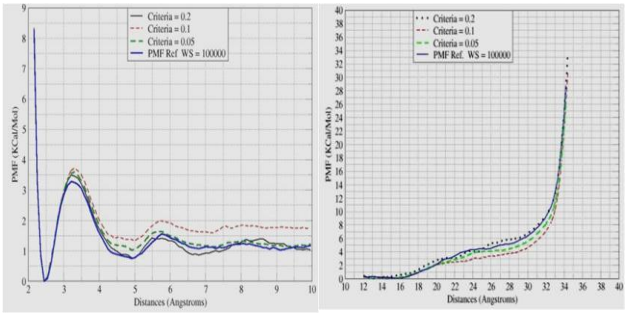

Fig2.: On the left we give the PMFs of system_1, on the right those of system_2; these for different thresholds of the normality criteria. The Umbrella Sampling Window Size (USWS) is fixed to 16000. The blue curve represents the Reference PMF (Ref. PMF) whose USWS is fixed respectively to 40000 for system_1 and 100000 for system_2. All these curves except the Ref. PMF are obtained after the convergence of their probability.

The following figure shows the time cost of these results in function of the threshold criteria values and the Umbrella Sampling Window size.

	System_1		System_2	
Criteria Threshod Values	USWS = 16000	Ref. USWS = 40000	USWS = 16000	Ref. USWS = 100000
0.2	3.232 ns	7.680 ns	40.704 ns	46.400 ns
0.1	4.576 ns		40.736 ns	
0.05	7.296 ns		42.240 ns	

Fig3.: Time costs of simulations for different test-threshold values and sizes of the Umbrella Sampling Window Size.

Observation and Discussion:

we can note that the computation time is low for the criteria threshold value of 0.2 and with PMF close to the PMF reference for both system_1 and sytsem_2 complexes. The used normality convergence criteria indicate that improvement in terms of computation time is possible for adequate test criteria threshold values. Thermal agitation induces duplication of information related to the remaining degrees of freedom. A non-optimal threshold does not filter some parasite micro-states which make information redundant, so the knowing of all the micro-states is not required to measure the PMF. In this context we assume that pre-processing the distributions could improve the convergence speed.

B. Simulation number two:

The purpose of this simulation is to see the impact of the pre-processing by a low-pass Gaussian filter and statistical convergence criteria such as Anova, tTest and skTest. The simulation conditions are identical to that of the previous case.

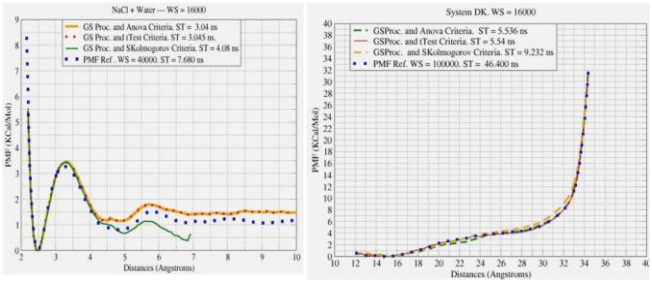

Fig4.: On the Left and right, we give respectively the PMF of system_1 and system_2 for different statistical conver-gence criteria. The distributions of micro-vibration states are pre-processed by Gaussian low-pass filter. One can see the duration of each simulation (Simulation Time=ST) according to statistical criteria. The window size (USWS) is set to 16000 steps for each simulation. Also one gives the reference curve PMF (Ref. PMF) whose size is set to 40000 for system_1, and 100000 for system_2.

Note that the pre-processed distributions by a gaussian low pass filter brings a significant gain in terms of time of the probability convergence. The simulation time is reduced by a factor of two for system_1 and 10 for system_2 when the convergence criteria such as ANOVA and tTest are used. Results of skTest are less satisfactory.

C. Simulation number three:

Here distributions obtained during a sampling time at a given distance are pre-processed by a denoising technique. It involves a wavelet methodology where high frequencies are thresholded (see Fig5.). The used wavelet belongs to the family of bio-orthogonal wavelet (Cubic Spline) and the chosen thresholding method is a universal soft thresholding technique. In order to see the influence of this denoising process, distributions are decomposed and thresholded until level 8. Then the signal is reconstructed and its probability is compared to the previous one by using different convergence criteria such as : skTest, tTest and finally Anova Test.

Observation and Discussion:

The PMF values in case of multi-scale distributions analysis are shown above (Fig5.). We can see that the cost in computation time is generally less than those of PMFs references. In system_1, a gain of 2ns to 3ns was observed in the case of tTest and ANOVA test criteria. However in the case of skTest, divergence was observed at the beginning of the simulation.

For the Alanine complex, the computation time of each simulation is measured about 7 times lower than the reference simulation one (46.400 ns). This is in the case of tTest and ANOVA test. Regarding skTest, the computation time increased significantly (about twice the reference time).

It is also noted for the system_2 that convergence is almost perfect with respect to the PMF reference for all statistical

tests.

CONCLUSION

The performance of the algorithm thus developed, is based on the efficiency of the stochastic convergence criteria, combined with an adaptative pre-processing. This allows to use a succession of short size windows iterated until a convergence. One reminds that a long Umbrella Sampling Window for a big protein complex leads to several days of calculation.

Here distributions of reaction coordinates are pre-processed by a methodology involving a low pass-filter, or a wavelet soft thresholding. It significantly improves and reduces the computation time of the simulations.

The results show that fact of pre-processing all micro-vibrations of high frequencies reduces the computation time. The Umbrella Sampling Method with short windows is used to perform a constrained temporal sampling.

We can assume that the use of narrow bandwidth filters eliminates some useful information (some vibrational frequencies) from the entropy, and then causes the PMF to take inifinite values.

The given algorithm unquestionably allows a reduction of the iteration number and so the time of simulation.

[5] M. Farge, "Wavelet transforms and their applications to turbulence," Ann. Rev. Fluid Mech. , 24:395–457, 1992.

VIIII. REFERENCES

[1] A., Azzalini, M. Farge, and K. Schneider. "Nonlinear wavel et thresholding: a recursive method to determine the optimal denoising threshold," Appl. Comput. Harmon. Anal. 18(2), pp.177–185, Oct. 2004.

[2] V. Bagdonavicius, J. Kruopis, M.S. Nikulin, "Non-parametric tests for complete data," ISTE&WILEY: London&Hoboken, 2011.

[3] H. O. Bartelt, K. H. Brenner, and A.W. Ohman, "The wigner distribution function and its optical production," *Optics Communications*, 32, pp. 32-38,1980.

[4] G. W. Corder & D. I. Foreman, "*Nonparametric Statistics for Non-Statisticians: A Step-by-Step Approach*," Wiley, 2009.

[5] M. Farge, "Wavelet transforms and their applications to turbulence," Ann. Rev. Fluid Mech. , 24:395–457, 1992.

[6] Gibbons, Jean Dickinson and Chakraborti, Subhabrata "*Nonparametric Statistical Inference*," 4th Ed. CRC, 2003.

[7] T. P. Hettmansperger, J. W. McKean, "*Robust nonparametric statistical methods,"* Kendall's Library of Statistics. 5 (First ed.). London: Edward Arnold.

[8] I. Johnstone and B. Silverman, "Wavelet treshold estimators for data with correlated noise," J. R. Stat. Soc., Ser. B. Stat. Methodol. 59,pp.319–351,1997.

[9] S. Kumar, J. M. Rosenberg, D. Bouzida, R. H. Swendsen, P.A. Kollman P. A., "Multidimensional Free-Energy Calculations Using the Weighted Histogram Analysis Method," Journal of Computational Chemistry, 16, 11, pp.1339-1350. 1995.

[10] L. Charlier, "Etude des Interactions moléculaires entre molécules odorantes et protéines impliquées dans les premières étapes de la perception olfactive," Thèse de Doctorat. Université de Nice-Sophia Antipolis, Octobre, 2009.

[1] A., Azzalini, M. Farge, and K. Schneider. "Nonlinear wavel et thresholding: a recursive method to determine the optimal denoising threshold," Appl. Comput. Harmon. Anal. 18(2), pp.177–185, Oct. 2004.

[2] V. Bagdonavicius, J. Kruopis, M.S. Nikulin, "Non-parametric tests for complete data," ISTE&WILEY: London&Hoboken, 2011.

[3] H. O. Bartelt, K. H. Brenner, and A.W. Ohman, "The wigner distribution function and its optical production," *Optics Communications*, 32, pp. 32-38,1980.

[4] G. W. Corder & D. I. Foreman, "*Nonparametric Statistics for Non-Statisticians: A Step-by-Step Approach*," Wiley, 2009.

[5] M. Farge, "Wavelet transforms and their applications to turbulence," Ann. Rev. Fluid Mech. , 24:395–457, 1992.

[6] Gibbons, Jean Dickinson and Chakraborti, Subhabrata "*Nonparametric Statistical Inference*," 4th Ed. CRC, 2003.

[7] T. P. Hettmansperger, J. W. McKean, "*Robust nonparametric statistical methods,"* Kendall's Library of Statistics. 5 (First ed.). London: Edward Arnold.

[8] I. Johnstone and B. Silverman, "Wavelet treshold estimators for data with correlated noise," J. R. Stat. Soc., Ser. B. Stat. Methodol. 59,pp.319–351,1997.

[9] S. Kumar, J. M. Rosenberg, D. Bouzida, R. H. Swendsen, P.A. Kollman P. A., "Multidimensional Free-Energy Calculations Using the Weighted Histogram Analysis Method," Journal of Computational Chemistry, 16, 11, pp.1339-1350. 1995.

[10] L. Charlier, "Etude des Interactions moléculaires entre molécules odorantes et protéines impliquées dans les premières étapes de la perception olfactive," Thèse de Doctorat. Université de Nice-Sophia Antipolis, Octobre, 2009.

Artificial Neural Networks Algorithms for Earthquake Forecasts

Mostafa Allameh Zadeh, A. Mohseni

Abstract-Recent advances in machine learning make it possible to design efficient prediction algorithms for earthquake forecasts. Self Organizing Feature Maps (SOFM) technique can be used to detect precursory seismic activation or quiescence and make earthquake forecast.Here we apply the SOFM method for optimal forecasting of large earthquakes in Iran, using the data catalogue maintained by IIEES. The purpose of this paper is to describe the use of the neural network model to generate synthetics data catalogue in the local regions and propose a fast algorithm for synthetic earthquake catalog generation based on an original catalog. More specifically, we also propose a Monte Carlo simulation model which can generate data from a small number of earthquake aftershocks and discusses the relationship between the complexity of an earthquake and its aftershocks. This is a very stimulating article about the very important issue of making reliable decisions under uncertainty. This article shows how machine-learning techniques can be complemented with provably valid measures of accuracy and reliability. The experiments show this model can open new possibilities for earthquake forecasts.

Keywords—Pattern informatics, earthquake, forecasting, seismicity, Neural

I. Introduction

The Earth's crust is clearly extremely complex and it is generally accepted that earthquakes are a chaotic phenomenon. Thus, as in the case earthquake forecasting must be considered on a statistical basis (Allamehzadeh and Mokhtari, 2003; Madahizadeh and Allamehzadeh, 2009). A

Fundamental question is whether the statistical properties of seismicity patterns can be used to forecast future earthquakes. Premonitory seismicity patterns were found for some strong earthquakes in Iran.

Premonitory seismicity pattern informatics (PI) approach has been proposed by RUNDLE et al. (2002), TIAMPO et al. (2002a, b, c).

This approach is based on the strong space-time correlations that are responsible for the cooperative behavior of driven threshold systems and arises both from threshold dynamics as well as from the mean field (long range) nature of the interactions. The PI technique can be used to detect precursory seismic activation or quiescence and make earthquake forecasts.

The purpose of this paper is to study the applicability of the pattern Recognition (PR) algorithm for forecasting large earthquakes in Iran. As an example, we will present a forecast of large (M>5) earthquakes during the time period 1990-2013 in the Alborz region:

the region that includes the epicenter of the 1990 Rudbar earthquake. First, we will briefly introduce the PR method. Next, we will describe the earthquake catalogues used in this paper.

II. Pattern Recognition

We suggest that the SOM is capable of identifying cohesive patterns of nonlinear measurements that would be difficult to identify using traditional linear data reduction procedures and that neural networks will be increasingly valuable in the analysis of a wide range of complex behaviors.

In this study we have employed the self-organizing map (SOM) in gene expression data

Analysis (figure 1). The SOM is an unsupervised neural network algorithm, which has been used

with great level of success in various clustering and visualization earthquakes aftershocks (see Allamehzadeh and Mokhtari, 2003; Allamehzadeh and Abbassi, 2005). Moreover, several studies report that for a noisy data set the SOM outperforms hierarchical clustering and many other clustering methods in various critical areas such as noise tolerance, speed and robustness (Mangiameli, Chen,&West, 1996; Chen et al., 2002; Gibbons & Roth, 2002).

Researchers in China have suggested that neural networks ensembles and support vector machines could be used to predict the magnitudes of strong earthquakes [5, 16], but more research needs to be done to corroborate their findings.

The purpose of this study is analysis and visualization of earthquake catalog data obtained from IIEES networks on simulation data using the SOM. The SOM has been used earlier in clustering

aftershocks patterns by Allamehzadeh et al., 2003.

Rather than attempt to issue earthquake predictions, we hope to analyze past data for periodic patterns that may advance our understanding of earthquake dynamics.

With the exception of a brief period in the 1970s, earthquake prediction was generally considered to be infeasible by seismologists. Then, in 1975, Chinese scientists ordered the evacuation of Haicheng one day before a magnitude 7.3 earthquake struck. This led to a flurry of optimism toward earthquake prediction [9, 11], which was subsequently checked by the failed prediction of the magnitude 7.8 Tangshan earthquake of 1976.

Another failure occurred in Parkfield, California in the early 1980s. Up to then, magnitude 6.0 earthquakes had occurred at fairly regular 22-year intervals. This led researchers to predict that an earthquake would strike by 1993; no such earthquake arrived until 2004. To this day, the Haicheng earthquake remains the only successful earthquake prediction in history.

This paper describes a method for estimating earthquake recurrence interval and coefficient of variation from historic earthquake records by using SOM algorithms.

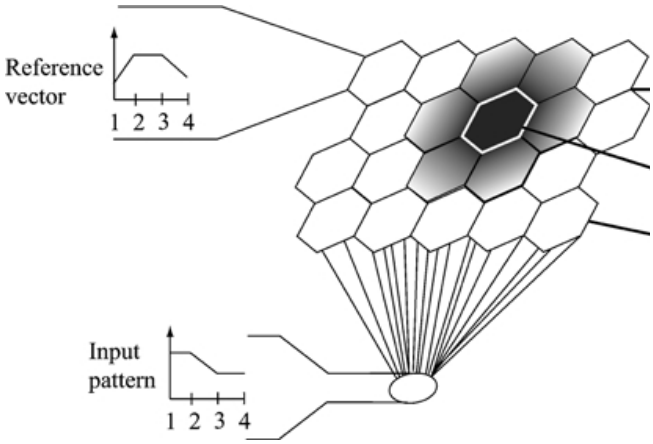

Fig. 1 Idea of the SOM. All neurons contain a reference vector, whose dimension is the same as the dimension of the input data. Earthquake location expression pattern is compared to all reference vectors and the neuron containing the closest reference (black with white boundaries) is permitted to update with neurons belonging to the neighborhood region (shaded).

Statistical practice between recurrence estimation and earthquake probability calculations can be a concern [e.g., Savage, 1991, 1992]. Optimally, we would have enough observations of earthquake intervals to fill out recurrence PDFs; these would eliminate the epistemic uncertainties surrounding recurrence parameters, and define the uncertainty inherent in earthquake recurrence.

As will be shown, Machine learning algorithms fitting tends to be most useful on short sequences and seems primarily sensitive to the histogram of the data. Results reflect epistemic uncertainties by showing the range and uncertainty in distribution parameters that are consistent with observations and their uncertainties.

In many pattern recognition systems, the methodology frequently used is the statistical approach, whereby decision theory derived from statistics of input patterns is used to design a classifier

[13]. Although this paradigm has been successfully applied to solve various problems in pattern classification, it has difficulty in expressing structural information unless an appropriate

choice of features is made possible. Furthermore, this approach requires much heuristic information to design a classifier [14]. Neural-networks-based paradigms, as new means of

implementing various classifiers based on statistical and structural approach, have been proven to possess many advantages for classification because of their learning ability and good generalization.

▪ III. METHODS

The methods described in this paper differ from other recurrence parameter estimation techniques. Most commonly, variants of maximum-likelihood techniques are applied to observed series to estimate recurrence parameters [e.g., Geller, Robert J. and Jackson, David D. and Ka-

gan, Yan Y. and Mulargia, Francesco (1997)]. The methods used to extract knowledge from earthquakes time series are described in this section. The goal is to find patterns in data that precede the appearance of earthquakes with a given magnitude by using Quadratic Neural Networks (QNN) and Radial Base Function (RBF) Neural Networks.

In many pattern recognition systems, the methodology frequently used is the statistical approach, whereby decision theory derived from statistics of input patterns is used to design a classifier

[13]. Although this paradigm has been successfully

applied to solve various problems in pattern classification, it has difficulty in expressing structural information unless an appropriate choice of features is made possible. Furthermore, this approach requires much heuristic information to design a classifier [14]. Neural-networks-based paradigms, as new means of implementing various classifiers based on statistical and structural approach, have been proven to possess many advantages for classification because of their learning ability and good generalization

[9]–[12], [14]–[16]. Generally speaking, multilayered networks (MLNs), usually coupled with the back propagation (BP) algorithm, are most widely used in face recognition [9]. Yet, two major criticisms are commonly raised against the BP algorithm: 1) It is computationally intensive because of its slow convergence speed and 2) there is no guarantee at all that the absolute minima can be achieved. On the other hand, RBF neural networks have recently attracted extensive interests in the community of neural networks for a wide range of applications [17]–[29]. The salient features of RBF neural networks are as

follows.

As the goal is to find patterns that precede quake occurrences, the magnitude of the current earthquake, Mb, has been forced to be the only attribute in the consequent.

The Mb attribute has been divided in three non-overlapped intervals: [3.0, 3.5) or small earthquakes, [3.5, 4.4) or medium earthquakes, and [4.4, 6.2] or large earthquakes (note that the largest retrieved earthquake magnitude is 6.2). Tables 1 show the data catalog is used for extracted to large, medium and small earthquakes, respectively. Note that ΔMw and Δt represent the increment of the b–value and the time elapsed between the previous and current earthquake, respectively. Also, the magnitude of the earthquake occurred prior the current one, Mw, has been covered only by one rule. Finally, all rules have been assessed by means of three well-known and widely used indices: Confidence, support, and lift [6].

Table1. Earthquakes used in this study

N	Date							Location			Magnitude
	Year	Month	Day	Hour	Min	Sec		Latitude (N)	Longitude (E)		Mw
1	1677	1	1	0	0	0		54.2	27.9		6.4
2	1703	1	1	0	0	0		54.9	26.6		6.8
3	1824	8	28	0	0	0		52.4	29.8		7.1
4	1890	3	25	0	0	0		53.7	28.8		7.1
5	1902	7	9	0	3	38		56.3	27.1		6.3
6	1927	5	9	0	10	31		56.7	27.7		6.4
7	1949	4	24	0	4	22		56.5	27.3		6.3
8	1956	10	31	0	14	3		54.7	27.3		6.6
9	1961	6	11	0	5	10		54.5	27.8		6.6
10	1972	4	10	6	2	6		52.8	28.4		6.7
11	1977	3	21	52	21	18		56.4	27.6		6.7
12	1990	11	6	53	18	45		55.5	28.2		6.6
13	1999	3	4	28	5	38		57.2	28.3		6.6
1	1919	10	24	0	20	32		62.05	26.11		5.8
2	1926	5	19	33	21	13		58.9	26.3		5.7
3	1929	9	3	0	12	7		62.07	26.59		6.3
4	1945	11	27	15	21	56		63.5	25		8.0

ISBN: 978-1-61804-219-4

N	Date							Location			Magnitude
	Year	Month	Day	Hour	Min	Sec		Latitude (N)	Longitude (E)		Mw
5	1972	8	6	20	1	12		61.14	24.99		5.5
6	1979	1	10	45	15	5		60.99	26.491		6.1
7	1989	12	7	34	12	59		58.965	25.918		6.0
8	1992	1	30	0	5	22		62.88	24.25		5.9
9	2005	3	13	58	3	31		62	26.73		6.0
1	1824	6	2	0	0	0		51.5	29.7		6.1
2	1864	12	7	0	20	0		45.98	33.38		6.3
3	1868	8	1	0	20	0		52.5	34.9		6.4
4	1875	3	21	0	15	0		50.5	30.5		5.9
5	1890	2	7	0	0	0		51.22	34.18		6.3
6	1903	9	25	0	1	20		58.23	35.18		6.0
7	1907	3	31	0	14	12		50	30		6.1
8	1917	7	15	0	17	58		45.82	33.48		6.3
9	1923	9	22	0	20	47		56.63	29.51		6.7
10	1927	11	12	0	14	46		47.38	32.53		6.1
11	1929	7	15	0	7	44		49.48	32.08		6.1
12	1937	4	7	0	18	30		52.1	34.8		5.6
13	1939	11	4	0	10	15		48.52	32.4		6.1
14	1948	7	30	43	3	30		49.12	31.41		5.8
15	1957	3	16	46	0	43		52.87	34.91		5.6
16	1958	5	5	64	5	21		44.79	35.69		5.6
17	1962	6	29	15	22	35		48.76	32.21		5.7
18	1972	2	28	85	18	44		51.1	29.74		5.5
19	1980	12	18	0	12	34		44.25	35.89		6.2
20	1989	5	27	36	20	8		50.892	30.148		6.0
21	1998	8	5	15	14	27		46.266	33.183		5.6
22	2002	9	25	23.9	22	28		49.327	32.076		5.6
23	2008	8	27	12.5	21	52		47.36	32.23		5.8
24	2010	7	30	28.2	13	50		59.36	35.17		5.5
1	1868	8	1	0	20	0		52.5	34.9		6.4
2	1890	2	7	0	0	0		51.22	34.18		6.3
3	1903	9	25	0	1	20		58.23	35.18		6.0
4	1923	9	22	0	20	47		56.63	29.51		6.7
5	1937	4	7	0	18	30		52.1	34.8		5.6
6	1957	3	16	46	0	43		52.87	34.91		5.6
7	1962	9	4	20	13	30		49.72	35.56		5.7
8	2010	7	30	28.2	13	50		59.36	35.17		5.5
1	1641	2	5	0	18	0		46.1	37.9		6.7
2	1648	3	31	0	24	0		43.5	38.3		6.5
3	1696	4	14	0	0	0		43.9	39.1		7.0
4	1715	3	8	0	6	0		43.9	38.4		6.6
5	1840	7	2	0	19	0		43.9	39.5		7.3
6	1930	5	6	0	22	34		44.6	38.24		7.1
7	1957	12	13	0	1	45		47.8	34.55		6.8
8	1976	11	24	15	12	22		44	39.1		7.0
1	1909	1	23	0	2	48		49.13	33.41		7.4
2	1920	5	25	0	11	39		46.5	33.5		5.6
3	1932	5	7	0	14	54		45	36.2		5.7

ISBN: 978-1-61804-219-4

N	Date							Location			Magnitude
	Year	Month	Day	Hour	Min	Sec		Latitude (N)	Longitude (E)		Mw
4	1939	1	25	0	11	2		50.81	30.93		5.7
5	1941	6	10	0	20	38		46.84	33.5		5.8
6	1944	6	28	33	2	57		45	36		5.8
7	1951	6	9	53	11	22		49.8	32.26		6.2
8	1960	3	24	0	23	21		51	31.25		6.1
9	1967	1	11	14	11	20		45.66	34.07		5.6
10	1978	12	14	21	7	5		49.634	32.128		6.2
11	1988	3	30	43	2	12		50.179	30.845		5.9
12	2006	3	31	17	1	17		48.73	33.74		6.1
1	1911	4	18	0	18	14		57.05	31.25		6.4
2	1933	10	5	0	13	29		57.07	34.52		6.2
3	1948	7	5	0	13	53		57.73	29.88		6.1
4	1978	9	16	54	15	35		57.382	33.243		7.4
5	1998	3	14	5	19	40		57.589	30.13		6.6
6	2005	2	22	12	2	25		56.81	30.76		6.4
1	1903	3	22	0	14	35		59.71	33.16		6.2
2	1923	11	29	0	3	36		59.4	33.62		5.8
3	1941	2	16	0	16	39		58.9	33.4		6.2
4	1947	9	23	0	12	28		58.7	33.7		6.9
5	1962	4	1	0	0	45		58.87	33.21		5.8
6	1968	8	31	12	10	47		58.96	34.04		7.1
7	1979	11	27	34	17	10		59.754	34.057		7.1
8	1997	6	25	8	19	38		59.435	33.916		5.9
1	1854	11	0	0	0	0		59.38	30.58		5.7
2	1923	9	14	0	8	10		59.33	28.97		5.8
3	1932	9	8	0	7	25		58.66	30.99		5.8
4	1960	8	23	15	8	58		59.85	29.09		5.7
5	1969	11	7	80	18	34		59.98	27.82		6.1
6	1980	1	1	56	2	45		60.346	27.341		5.5
7	2003	12	26	6	1	56		58.268	28.95		6.6
8	2010	12	20	58.1	18	41		59.24	28.35		6.5
1	1780	1	1	0	0	0		59	36		6.5
2	1804	1	1	0	0	0		57.18	36.33		5.8
3	1808	6	26	0	0	0		54.32	35.25		6.5
4	1931	8	8	0	8	54		57.63	35.56		5.7
5	1940	5	4	0	21	1		58.5	35.75		6.5
6	1953	2	12	10	8	15		54.88	35.39		6.5
7	1971	5	26	17	2	41		58.14	35.53		5.6
8	1979	12	9	3	9	12		56.82	35.105		5.6
9	2010	8	27	13.1	19	23		54.48	35.58		5.7
1	1838	1	1	0	0	0		59.96	29.5		6.9
2	1905	6	19	0	1	27		59.98	29.89		6.8
3	1927	7	7	0	20	6		62.26	27		6.3
4	1934	6	13	0	22	10		62.64	27.63		7.0
5	1950	9	24	0	22	56		60.7	34.5		6.0
6	1979	12	7	59	9	23		59.849	34.078		6.1
7	1994	2	24	13	0	11		60.51	30.79		6.3

ISBN: 978-1-61804-219-4

N	Date							Location			Magnitude
	Year	Month	Day	Hour	Min	Sec		Latitude (N)	Longitude (E)		Mw
8	1997	5	10	13	7	57		59.81	33.847		7.2
1	1786	10	1	0	0	0		45.77	38.36		6.2
2	1844	5	13	0	0	0		47.97	37.5		6.8
3	1862	12	19	0	5	0		47.8	39.3		6.2
4	1879	3	22	0	3	42		47.85	37.8		6.6
5	1896	1	4	0	18	28		48.32	37.7		6.6
6	1905	1	9	0	6	17		47.8	37.9		6.1
7	1924	2	19	0	7	1		48.32	39		6.8
8	1940	7	11	18	1	23		47.6	39.5		5.5
9	1976	2	3	57.5	16	40		48.326	39.898		5.6
10	1997	2	28	9	12	57		48.07	38.109		6.1
11	2002	6	22	11	2	58		49.02	35.597		6.5
1	856	12	22	0	0	0		54.14	36.23		7.3
2	958	2	23	0	0	0		51.35	35.82		7.3
3	1177	5	0	0	0	0		50.83	35.92		7.1
4	1209	0	0	0	0	0		59.22	36.05		7.3
5	1389	2	0	0	0	0		58.75	36.25		7.3
6	1405	11	23	0	0	0		58.75	36.25		7.3
7	1485	8	15	0	0	0		50.45	36.43		7.1
8	1608	4	20	0	0	0		50.5	36.37		7.3
9	1695	5	11	0	5	0		57.46	37.1		6.9
10	1825	0	0	0	0	0		52.45	36.05		6.6
11	1830	3	27	0	0	0		52.28	35.73		7.0
12	1851	6	0	0	0	0		58.5	36.78		6.8
13	1890	7	11	0	6	0		54.6	36.6		7.2
14	1957	7	2	0	0	42		52.45	36.05		7.1
1	1810	1	1	0	0	0		57.12	37.85		6.4
2	1833	1	1	0	0	0		58.1	37.3		6.2
3	1871	12	23	0	0	0		58.3	37.25		7.1
4	1893	11	17	0	19	36		58.4	37.12		7.0
5	1904	11	9	0	3	28		59.77	36.94		6.4
6	1929	5	1	0	15	37		57.8	37.7		7.1
7	1985	10	29	5	14	23		54.899	36.901		6.2
8	1997	2	4	8	10	37		57.312	37.729		6.5
1	1665	6	1	0	0	0		52.08	37.75		6.4
2	1678	1	1	0	0	0		52.6	36.3		6.5
3	1780	1	8	0	19	6		49.29	38.12		7.3
4	1854	10	1	0	15	0		50	38		6.0
5	1895	7	8	0	22	0		53.7	39.1		7.5
6	1935	4	11	0	23	14		53.3	36.35		6.6
7	1980	5	4	19	18	35		49.019	38.048		6.6
8	1990	6	20	10	21	0		49.222	36.997		7.4
9	2000	11	25	33	18	9		49.938	40.23		6.8

Statistical learning theory is for small-sample statistics. And support vector machine is a new machine learning method based on the statistical learning theory. The support vector machine not only has solved certain problems in many learning methods, such as small sample, over fitting, high dimension and local minimum, but also has a higher generalization (forecasting) ability than that of

ISBN: 978-1-61804-219-4

artificial neural networks. The strong earthquakes in Iran are related to a certain extent to the intensive seismicity along the main plate boundaries in the world; however, the relation is nonlinear. In the paper, we have studied this unclear relation by the support vector machine method for the purpose of forecasting strong earthquakes in Iran.

The used methodology is quite different from the usual seismotectonic methods that allow delineating seismogenic zones and calculating the seismic hazard inside these zones.

In the Alborz region, Gorshkov (2006) define seismogenic nodes prone to earthquakes M>6 and characteristic geomorphological-gelogical features that discriminate seismogenic nodes from non-seismogenic ones. Morphostructural nodes are formed around intersections or junctions of two or several lineaments. The nodes have been obtained by the morphostructural zoning (MZ) method. The compiled MZ map shows the hierarchical block-structure of the Alborz region, the network of boundary zones separating blocks formed at the intersections of boundary zones. The pattern recognition algorithm RBF was defined other nodes capable of such size earthquakes using topographic, morphometric, and morphostructural parameters that describe the nodes. Nodes prone to M>6 exhibit the high topographic contrast and the increased fragmentation of the crust. Results of the work were pointed out the high seismic potential of the Alborz region: this study was identified a number of seismogenic nodes, where the target earthquakes have not yet been recorded.

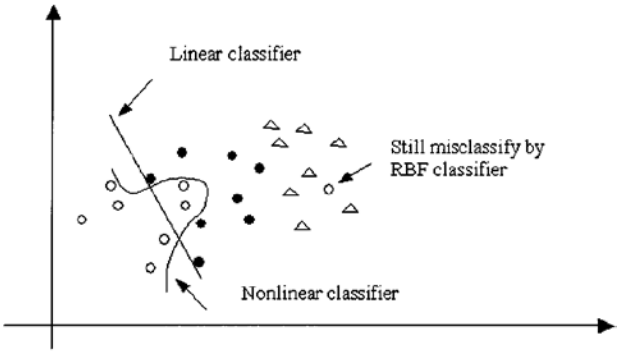

Fig. 2 An RBF neural classifier versus a linear classifier.

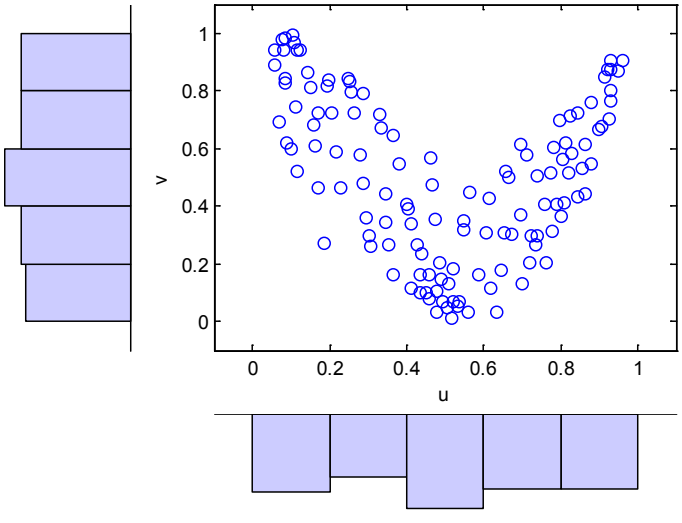

Fig. 3 shows the predicted of pattern recognition of Alborz region by this methods.

Machine learning will give us greater insight into the patterns underlying earthquake activity, even if we cannot predict the time, location, and strength of the earthquakes accurately, Machine learning algorithms available for us to understand and predict patterns of earthquakes activity.

ISBN: 978-1-61804-219-4

Regression techniques have been widely used for forecasting time series [5]. Thus, an empirical study on sea water quality prediction can be found in [7]. The authors transformed quantitative data into statistical moments, and constructed a tree to estimate the forecasting interval of the target variable. Last, the problem of predicting the machinery degradation and trending of fault propagation before reaching the alarm was studied in [12]. In particular, the authors proposed an approach based on regression trees to forecast such time series.

IV. Conclusions

Earthquake data from two particular areas of the Iranian plate have been successfully mined by means of two different techniques: QNN and the RBF algorithm. In particular, QNN with a confidence of 83.0% and a lift of 5.6 on average have been discovered and a regression-tree with an error of 0.35 has been built. Both techniques have discovered the great influence that the b–value has in earthquakes occurrences as its variation along with the time elapsed have shown to be useful to model different earthquakes. Thus, the patterns discovered before an earthquake takes place may be useful in subsequent predictions.

It is well known that if the dimension of the network input is comparable to the size of the training set, which is the usual case in pattern recognition of earthquake, the system will easily bring about overfitting and result in poor generalization. In this paper, a general design approach using an RBF neural classifier for face recognition to cope with small training sets of high-dimensional problem is presented.

References

- 2007 Working Group on California Earthquake Probabilities (2008), Working Group on California Earthquake Probabilities (2008), The Uniform California Earthquake Rupture Forecast, Version 2. Available: http://pubs.usgs.gov/of/2007/1437/ of 2007-1437 text.pdf
- [2] Allamehzadeh, M., M. Abbassi. “Recognition of seismic precursory activities using Self-Organizing Feature maps Neural Network” International Journal Diaster Advances, Vol I, (2008).
- [3] Allamezadeh, M., M. Mokhtari, “Prediction of Aftershokcs Distribution using Self-Organizing Feature maps (SOFM) and its Application on the Birjand-Ghaen and Izmit Earthquakes”Journal of Seismology and Earthquake Engineering (JSEE): Fall 2003. Vol. 5. No. 3. Page: 1-15.
- [4] 2007 Working Group on California Earthquake Probabilities (2008), The Uniform California Earthquake Rupture Forecast, Version 2. Available: http://pubs.usgs.gov/of/2007/1437/ of2007-1437 text.pdf
- [4] Press, Frank (1975), Earthquake Prediction. Scienti_c American, 232.5:14.
- [5] Liu, Yue and Wang, Yuan and Li, Yuan and Zhang, Bofeng and Wu, Gengfeng (2004), Earthquake Prediction by RBF Neural Network Ensemble. Advances in
- Neural Networks - ISNN 2004, 3174:13-17.
- [6] Stark, P. B. (1997), Earthquake prediction: the null hypothesis. Geophysical Journal International, 131: 495499. doi: 10.1111/j.1365-246X.1997.tb06593.x
- [7] USGS, Google Earth/KML Files. Available: http://earthquake.usgs.gov/learn/kml.php
- [8] USGS, Quaternary Faults in Google Earth. Available: http://earthquake.usgs.gov/hazards/qfaults/google.php
- [9] Wang, Kelin and Chen, Qi-Fu and Sun, Shihong and Wang, Andong (2006), Predicting the 1975 Haicheng earthquake. Bulletin of the Seismological Society of
- America, 96.3:757-795. doi:10.1785/0120050191
- [10] Wang, Wei and Liu, Yue and Li, Guo-zheng and Wu, Geng-feng and Ma, Qin-zhong and Zhao, Li-fei and Lin, Ming-zhou (2006), Support vector machine method for orecasting future strong earthquakes in Chinese mainland. Acta Seismologica Sinica, 19: 30-38.
- [11] S. Lawrence, C. L. Giles, A. C. Tsoi, and A. D. Back, “Face recognition:
- A convolutional neural-network approach,” IEEE Trans. Neural Networks, vol. 8, pp. 98–113, Jan. 1997.
- [12] S.-H. Lin, S.-Y. Kung, and L.-J. Lin, “Face recognition/detection by probabilistic decision-based neural network,” IEEE Trans. Neural Networks, vol. 8, pp. 114–132, Jan. 1997.
- [13] K. Fukunaga, Introduction to Statistical Pattern Recognition, 2nd ed. San Diego, CA: Academic Press, 1990.
- [14] H. H. Song and S. W. Lee, “A self-organizing neural tree for large-set pattern classification,” IEEE Trans. Neural Networks, vol. 9, pp. 369–380, Mar. 1998.
- [15] C. M. Bishop, Neural Networks for Pattern Recognition, New York: Oxford
- Univ. Press.
- [16] Wang, Wei and Liu, Yue and Li, Guo-zheng and Wu, Geng-feng and Ma, Qin-zhong and Zhao, Li-fei and Lin, Ming-zhou (2006), Support vector machine method for
- forecasting future strong earthquakes in Chinese mainland. Acta Seismologica Sinica, 19: 30-38.
- [16] J. L. Yuan and T. L. Fine, “Neural-Network design for small training sets of high dimension,” IEEE Trans. Neural Networks, vol. 9, pp. 266–280, Jan. 1998.
- [17] J. Park and J. Wsandberg, “Universal approximation using radial basis

- functions network," Neural Comput., vol. 3, pp. 246–257, 1991.
-
- [18] F. Girosi and T. Poggio, "Networks and the best approximation property," Biol. Cybern., vol. 63, pp. 169–176, 1990.
-

Modeling of Nonlinear Systems using Parallel OBF-WAVELET Networks Model

H. Zabiri, M. S. Fadzil, L. D. Tufa and M. Ramasamy

***Abstract*—**In present work, a nonlinear system identification using parallel linear-plus-nonlinear model is developed. A linear Orthonormal Basis Filters (OBF) model is integrated with nonlinear Wavelet Network (WN) model in parallel structure. The overall nonlinear model is taken as the sum of these two models and analyzed using Van de Vusse reactor to observe the effectiveness and its performance within the model development region as well as under extrapolating conditions. The result showed that the proposed parallel OBF-WN is performing better than other conventional model in both regions of operations

***Keywords*—**Modeling, Nonlinear systems, OBF, Wavelet networks.

I. Introduction

INcontrol area, mathematical modeling is a backbone in determining the capacity and capability of the system. Mathematical models are classified into two categories: black box (purely empirical model) and white box (traditional physical modeling)[1]. White box models are derived from fundamental principles such as mass and energy balances. However, they tend to be highly complex and generally are difficult and very time consuming to be developed. Nonlinear black box models, on the other hand, mainly aim to determine a mathematical model of process dynamics that matches observed input/output data according to some objective matching criteria. Hence, they have certain advantages over the white box models in terms of development time and efforts [2].

In nonlinear system identification using black box models such as neural networks (NN), one possible approach is to use a parallel combination of linear-plus-NN models[3]. This parallel combination through the usage of residuals is very attractive in two ways: viz. (1) a nonlinear model that is not properly developed performs worse than a linear one, hence by having a linear model developed in the first step ensures that reasonable models are obtained, and (2) applying the NN on the residuals (inputs and residuals as network input and output) ensures that the overall nonlinear model performs at least as good as or better than the linear model. One recent approach is the parallel OBF-NN model developed by [2](see Figure 1). The developed OBF-NN model has been shown to have better extrapolation capability in comparison to the conventional NN model.

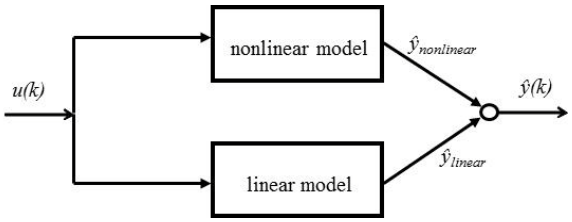

Fig. 1 The nonlinear model is used supplementary in parallel to a linear model

Though NN has been recognized as a successful class of nonlinear models, there is no structured construction procedure for determining the number of hidden layers and neurons in the network model [4]. Wavelet networks, on the other hand, do not suffer from such drawback, and are also efficient in approximating any static nonlinearity [4]. Efficient construction algorithms for defining the Wavelet networks structure are available [5].

In the developing world with a variety of sophisticated technology, wavelet networks have been proven successful in the areas of classification and identification problem[6]. Development of wavelet networks comes from combination of neural networks and wavelet theory. This type of nonlinear model has their own capabilities of catching essential features in "frequency-rich" signals that contribute to their strength. Wavelet networks have advantages over neural networks where both the position and the dilation of the wavelets are optimized besides the weights.

In this paper, the performance of the previously developed parallel OBF-NN model is evaluated by replacing the nonlinear NN model with Wavelet networks (WN), resulting in parallel OBF-WN model. The proposed model is shown in Figure 2. The objective of the paper is to analyze whether the proposed OBF-WN model can simultaneously identify nonlinear systems as well as improving the extrapolation

This work was supported by Universiti Teknologi PETRONAS.

H. Zabiri is with Universiti Teknologi PETRONAS, Bandar Seri Iskandar, 31750 Tronoh Perak Malaysia (corresponding author phone: 605-368-7625; fax: 605-365-6176; e-mail: haslindazabiri@petronas.com.my).

M. S. Fadzil is with Universiti Teknologi PETRONAS, Bandar Seri Iskandar, 31750 Tronoh Perak Malaysia (e-mail: sepusmat91@gmail.com).

T. D. Lemma is with Universiti Teknologi PETRONAS, Bandar Seri Iskandar, 31750 Tronoh Perak Malaysia (e-mail: lemma_dendena@petronas.com.my).

M. Ramasamy is with Universiti Teknologi PETRONAS, Bandar Seri Iskandar, 31750 Tronoh Perak Malaysia (e-mail: Marappagounder@petronas.com.my).

capability of the previous model.

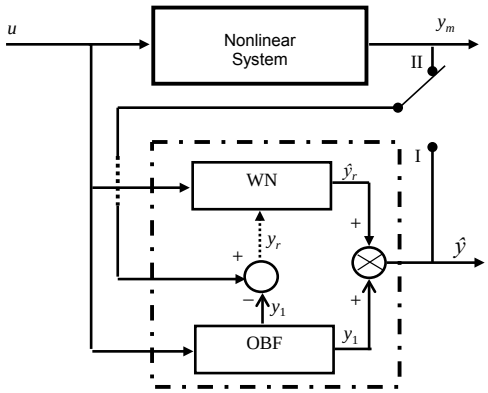

Fig. 2 The Proposed sequential identification of residuals-based parallel OBF-plus-WN models (I: simulation, II: prediction configuration)

II. Methodology

Parallel combination of OBF-WN is developed using the following procedures that are divided into two major parts: (A) Training and (B) Validation.

A. Training: Parallel OBF-WN model

As stated before, in order to develop a parallel proposed model, a parsimonious linear Laguerre model is identified first. The single-input single-output (SISO) for Orthonormal Basis Filter(OBF) model can be expressed as follows:

$$\hat{y}(k+1) = \left(\sum_{i=1}^{N} c_i L_i(q) \right) u(k) + e(k) \quad (1)$$

where$N$ is the number of orthonormal basis filter, c_i are the optimal OBF model parameters, $L_i(q)$ are the orthonormal basis filters, q is forward shift operator, $u(k)$ is input to the system, and $e(k)$ is the system white noise.

For SISO nonlinear model, the wavelet network (WN) function is based on the following function expansion:

$$f(x) = \sum_i w_{a,b}^{\ i} a_i^{-n/2} \psi((x-b_i)/a_i) \quad (2)$$

where$a$ and b are the dilation and translation parameters, respectively. Function Ψ is termed as "mother wavelet" and is selected as radial function [5] and w represents the weights.

Theoverall model output then is the summation of both thelinear dynamic model and the nonlinear model.

$$\hat{y}_f(k) = y(k) + f(k) \quad (3)$$

Simple algorithm to identify the OBF-WN model can be described as follow:

1. Develop OBF model to get y_{OBF}
2. Calculate the predicted residual using
   $y_{RES} = y_{ACTUAL} - y_{OBF}$
3. Develop the WN model using y_{RES} as outputs of the WN model.

For the input data, (75%) of the generated data is set into the training while (25%) for validation test sets. The aim is to evaluate how effective the model generalizes (predicts) when subjected to out-of-sample data that is not used during the identification stage.In this step, the most important is to observe the graphical plots between model output and measured process output as well as by using numerical test defined by Root Mean Square Error (RMSE).

$$RMSE = \sqrt{\frac{\sum_{i=1}^{n} (y - \hat{y})^2}{n}}$$

where

y is measured output

$\hat{y}$ is predicted value of y

B. Validation: Extrapolation Analysis

Extrapolation is a term used when a model is forced to perform prediction in regions beyond the space of the original training data. Continuous stirred tank reactors (CSTR) are often encountered in industrial applications and one of the operating units widely considered in the control literature. To evaluate the proposed model performance, the CSTR case study used as the demo problem in MATLAB Neural Network Predictive Control Toolbox is used. New out-of-sample data are generated in the validation part by using 9%, 20% and 28% decrease in w_1 (flow of the inlet into CSTR) below the original training range of the model. The new data is used to validate the proposed model and compared against the previously established parallel OBF-NN model

III. Results and Discussions

A. Parallel OBF-WN model development

The corresponding input-output data used to develop the proposed model is as shown in Figure 3.

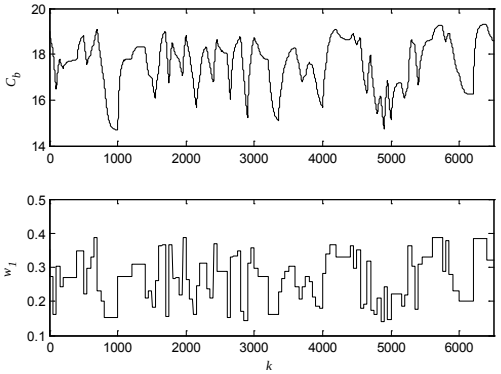

Fig. 3 Input-output data set

Developing the linear OBF model using this data, it is observed that the linear OBF model seem to be able to identify only 69% of the process variations as shown in Figure 4. Moreover, Figure 5 indicates the significant presence of nonlinearity in the system due to a strong pattern in the

residual behavior.

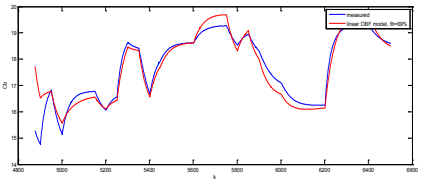

Fig. 4 Measured and estimated output for linear Laguerre model

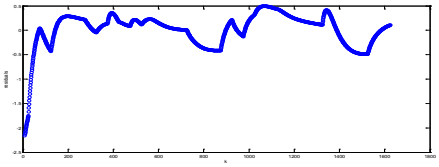

Fig. 5 Residuals of the linear OBF model

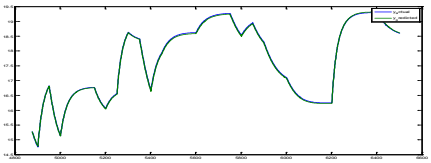

Fig. 6 Measured and estimated output for the OBF-WN model for model development

The analysis in Table 1 shows the performance comparisons between the previously developed parallel OBF-NN and the proposed parallel OBF-WN model done on the validation data set.

Table 1 Identification RMSE: Comparison on the validation sets

Case Studies	Parallel OBF-NN	Parallel OBF-WN
Plant	0.0008	0.000574

From Table 1, it is shown that the proposed OBF-WN model is able to identify the nonlinear CSTR system since the error on the validation data set is comparably similar to OBF-NN.

In order to apply this model under extrapolating conditions, this identification result is important to ensure that both models are comparably similar in the model development stage. Using the same optimal parameters obtained in this stage, both models are then subjected to the extrapolating conditions in the next section.

B. Extrapolation using Parallel OBF-WN model

Figures 7, 8 and 9 show the measured and predicted values of the product outlet concentration, $\underline{C_b}$ for decrease of 9%, 20% and 28% in the w_1 below the original training range. The resulting RMSE comparison between the two models for the three test sets are shown in Figure 10. Parallel OBF-WN seems to show an excellent prediction performance with the RMSE is 0.186, 0.1814 and 0.1803 which are generally smaller or comparable to the parallel OBF-NN.

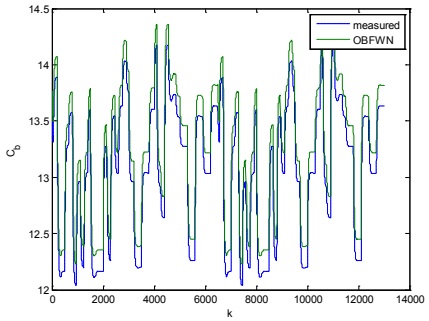

Fig. 7 9% decrease in w_1

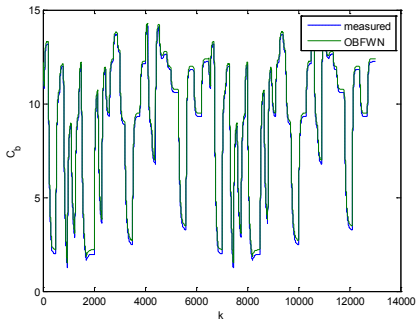

Fig. 8 20% decrease in w_1

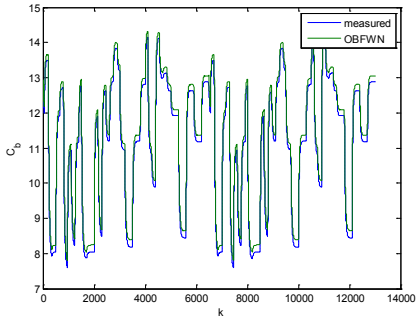

Fig. 9 28% decrease in w_1

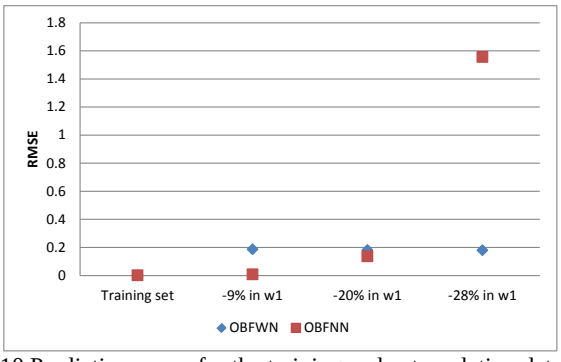

Fig. 10 Prediction errors for the training and extrapolation data sets

IV. CONCLUSIONS

In this study, it has been shown that the Orthonormal Basis Filter (OBF) plus Wavelet Networks (WN) model is able to identify nonlinear systems efficiently and to extrapolate beyond the regions of original range encountered during the model development phase. Future works may involve the

integration of the proposed model in a closed-loop nonlinear predictive controller environment to test its capability under control loop.

ACKNOWLEDGMENT

The authors would like to thank University Teknologi PETRONAS for the funding provided for this study.

REFERENCES

[1] L. Ljung, Perspectives on system identification, *Annual Reviews in Control*, 34 (2010), pp. 1-12.
[2] H. Zabiri, M. Ramasamy, L.D. Tufa, A. Maulud, Integrated OBF-NN models with enhanced extrapolation capability for nonlinear systems, *Journal of Process Control*, 23 (2013), pp. 1562-1566.
[3] J. Sjöberg, Q. Zhang, L. Ljung, A. Benveniste, B. Delyon, P.-Y. Glorennec, H. Hjalmarsson, A. Juditsky, Nonlinear black-box modeling in system identification: a unified overview, *Automatica*, 31 (1995), pp. 1691-1724.
[4] P. Aadaleesan, N. Miglan, R. Sharma, P. Saha, Nonlinear system identification using Wiener type Laguerre–Wavelet network model, *Chemical Engineering Science*, 63 (2008), pp. 3932-3941.
[5] R.K.H. Galvao, V.M. Becerra, J.M.F. Calado, P.M. Silva, LINEAR–WAVELET NETWORKS, *Int. J. Appl. Math. Comput. Sci.*, 14 (2004), pp. 221-232.
[6] S.A. Billings, Wei, H., New Class of Wavelet Networks for Nonlinear System Identification, *IEEE TRANSACTIONS ON NEURAL NETWORKS*, 16 (2005), pp. 862-874.

Authors Index

ISBN: 978-1-61804-219-4